



University
of Glasgow

Colquhoun, Ross (2015) *Production and characterisation of CorGlaes pure 107 degradable polymer composites*. PhD thesis.

<http://theses.gla.ac.uk/6352/>

Copyright and moral rights for this thesis are retained by the author

A copy can be downloaded for personal non-commercial research or study, without prior permission or charge

This thesis cannot be reproduced or quoted extensively from without first obtaining permission in writing from the Author

The content must not be changed in any way or sold commercially in any format or medium without the formal permission of the Author

When referring to this work, full bibliographic details including the author, title, awarding institution and date of the thesis must be given



University
of Glasgow

**Production and Characterisation of CorGlaes[®] Pure 107
Degradable Polymer Composites**

Ross Colquhoun

Submitted in fulfilment of the requirements for the degree of Doctor of Philosophy

Supervised by Professor K.E. Tanner

University of Glasgow

School of Engineering

Biomedical Engineering Division

March 2015

Abstract

Phosphate glass fibre polymer composites have the potential to be utilised as degradable orthopaedic implant devices with modifications to the glass fibre composition allowing for materials with tailorable mechanical properties and degradation rates. Accordingly such materials could be advantageous for the development of alternative cranioplasty implant devices. In collaboration with an industrial sponsor, a promising composition of phosphate glass was characterised to assess its potential as a composite reinforcing agent along with the applicability of different composite configurations as possible cranioplasty implants.

The CorGlaes[®] Pure 107 phosphate glass was found to demonstrate suitable dissolution rates for cell culture whilst vibrational spectroscopy and analytical chemistry techniques confirmed its structural features and suitability for fibre manufacturing. The mechanical properties of its bulk and fibre formats were determined to be in line with alternate PG compositions but initial biocompatibility screenings of glass samples using human osteosarcoma cells found this composition to be cytotoxic. This was believed to be due to localised pH changes or from the release of Zn²⁺ ions towards cytotoxic levels. The absence of a carbonated hydroxyapatite layer formation when immersed in simulated body fluid also indicated that this glass composition possessed no *in vitro* bioactivity.

Composite materials based on CorGlaes[®] Pure 107 fibres in a polylactic acid (PLA) matrix at a 0.2 fibre volume fraction (V_f) were found to exhibit mechanical properties within the same region as those reported for cranial bones. However rapid dissolution of the reinforcing fibres (due to autocatalysis) led to premature reductions in the composite mechanical properties and resulted in a cytotoxic response during *in vitro* cell culture. The introduction of a secondary hydroxyapatite filler phase into the CorGlaes[®] Pure 107 composite to counteract the acidic pH led to changes in the samples mechanical properties and degradation media pH. However this failed to retard the fibre dissolution rate in 0.15 V_f composites. At a 0.01 V_f , the inclusion of HA produced biocompatible composites compared to the HA free equivalent and was attributed to the reduction of preferential Zn²⁺ ion release from the glass fibres due to the pH buffering at the fibre-matrix interface. However the low V_f required to achieve biocompatible composites made the CorGlaes[®] Pure 107 fibres unsuitable as a primary composite reinforcing agent.

Consequently phosphate glass fibre composites may be suitable for cranioplasty applications with future hybrid composites allowing for the design of implant materials that are capable of eliciting an immediate *in vivo* response whilst retaining its long term mechanical properties.

Acknowledgements

I would to thank my supervisors, Prof Liz Tanner and Prof Nikolaj Gadegaard for giving me this opportunity and their unwavering support, encouragement and guidance throughout the course of my work. I also wish to thank Prof Matt Dalby for his thoughtful advice and useful discussions as well as acknowledge the financial support provided by the EPSRC.

Thanks to Dr Tom Gilchrist and Giltech Ltd for agreeing to collaborate on this project, the supply of materials and to my industrial supervisors, Mr David Healy and Mr Ian West for their expertise, enthusiasm and assistance that they have provided. I would also like to thank the entire Giltech Ltd staff for always making me feel welcome during my visits.

I wish to express my gratitude to all the research, technicians and support staff across the various departments I have worked at in the University of Glasgow who have helped make this work possible. I am especially grateful to Mr John Davidson and Mrs Carol-Anne Smith for their respective help with mechanical testing and cell culture studies.

I would like to thank Alex Vasiev for his insightful discussions, advice and his shared interest in coffee as well as all the other friends I have made during my project.

Finally I would to thank Stacey for reminding me of my life outside of research as well as my parents for their continued love, support and patience throughout the course of my work.

Authors Declaration

I declare that, except where explicit reference is made to the contribution of others, that this thesis is the result of my own work and has not been submitted for any other degree at the University of Glasgow or any other institution.

Ross Colquhoun

Table of Contents

| | |
|---|-----------|
| Abstract | 1 |
| Acknowledgements | 2 |
| Authors Declaration | 3 |
| Table of Contents | 4 |
| List of Figures | 11 |
| List of Tables | 32 |
| Nomenclature | 36 |
| 1 Giltech Ltd | 40 |
| 1.1 CorGlaes [®] Technology | 40 |
| 1.1.1 CorGlaes [®] Pure 107 | 40 |
| 2 Introduction | 41 |
| 2.1 Aims of Thesis | 43 |
| 3 Literature Review | 44 |
| 3.1 Bone | 44 |
| 3.1.1 Definition and Function | 44 |
| 3.1.2 Composition and Physiology | 45 |
| 3.1.2.1 Composition | 45 |
| 3.1.2.2 Bone Cells | 46 |
| 3.1.2.3 Bone Remodelling | 46 |
| 3.1.3 Structure of Bone | 48 |
| 3.1.3.1 Macrostructure | 49 |
| 3.1.3.2 Microstructure | 51 |
| 3.1.3.3 Sub-microstructure | 53 |
| 3.1.3.4 Nanostructural and Sub-nanostructures | 54 |
| 3.1.3.5 Lamellar and Woven Bone | 55 |
| 3.1.4 The Human Skull | 56 |
| 3.1.4.1 Anatomy | 56 |
| 3.1.4.2 Structure | 57 |
| 3.1.5 Mechanical Properties of Bone | 58 |
| 3.1.5.1 Overview | 58 |

| | | |
|---------|---|-----|
| | 5 | |
| 3.1.5.2 | Cortical Bone | 59 |
| 3.1.5.3 | Cancellous Bone | 60 |
| 3.1.5.4 | Cranial Bones | 61 |
| 3.1.6 | Fracture of Bone | 62 |
| 3.1.6.1 | Skull Fracture | 62 |
| 3.1.6.2 | Fracture Repair | 64 |
| 3.2 | Biomaterials for Bone Augmentation | 67 |
| 3.2.1 | Natural Biomaterials for Bone Augmentation | 67 |
| 3.2.1.1 | Autografts | 67 |
| 3.2.1.2 | Allografts | 68 |
| 3.2.2 | Artificial Biomaterials for Bone Augmentation | 69 |
| 3.2.2.1 | Tissue Response to Artificial Biomaterials | 69 |
| 3.2.2.2 | Metals | 71 |
| 3.2.2.3 | Degradable Polymers | 72 |
| 3.2.2.4 | Calcium Phosphate Ceramics | 76 |
| 3.2.2.5 | Bone Cements | 78 |
| 3.2.2.6 | Glasses | 80 |
| 3.2.2.7 | Glass-Ceramics | 83 |
| 3.2.3 | Composites | 84 |
| 3.2.3.1 | Overview | 84 |
| 3.2.3.2 | Composite Biomaterials | 90 |
| 3.3 | Cranioplasty | 93 |
| 3.3.1 | Overview | 93 |
| 3.3.2 | Cranioplasty Plate Materials | 93 |
| 3.3.2.1 | Auto- and Allogenic Bone | 93 |
| 3.3.2.2 | Metals | 93 |
| 3.3.2.3 | PMMA | 94 |
| 3.3.2.4 | Polymers | 95 |
| 3.3.2.5 | Ceramics | 96 |
| 3.3.2.6 | Composites | 97 |
| 3.3.3 | Cranioplasty Complications | 98 |
| 3.4 | Phosphate Glasses | 99 |
| 3.4.1 | Definition and Theory of Glass Formation | 99 |
| 3.4.2 | Manufacturing of Phosphate Glasses | 100 |
| 3.4.3 | Structure and Classification | 101 |

| | | |
|----------|--|------------|
| 3.4.4 | Dissolution Mechanisms | 105 |
| 3.4.5 | Bioactivity Mechanisms | 106 |
| 3.4.6 | Compositions for Bone Tissue Augmentation | 107 |
| 3.4.6.1 | Ternary Compositions | 108 |
| 3.4.6.2 | Complex Compositions | 109 |
| 3.4.7 | Phosphate Glass Fibres | 114 |
| 3.4.7.1 | Bulk vs. Fibre Properties | 114 |
| 3.4.7.2 | Fibre Manufacturing | 114 |
| 3.4.7.3 | Biomedical Applications | 115 |
| 3.4.8 | Phosphate Glass Fibre Composites | 118 |
| 3.4.9 | Composite Modifications | 122 |
| 4 | Principles of the Technique Used | 124 |
| 4.1 | Structural and Thermal Properties | 124 |
| 4.1.1 | X-ray Diffraction (XRD) | 124 |
| 4.1.2 | Fourier Transform Infrared Spectroscopy (FTIR) | 125 |
| 4.1.3 | Raman Spectroscopy | 128 |
| 4.1.4 | Differential Scanning Calorimetry (DSC) | 129 |
| 4.2 | Microhardness Testing | 131 |
| 5 | Characterisation of CorGlaes[®] Pure 107 Composition | 132 |
| 5.1 | Outline | 132 |
| 5.2 | Materials and Methods | 134 |
| 5.2.1 | CorGlaes [®] Pure 107 Phosphate Glass Manufacturing | 134 |
| 5.2.1.1 | Bulk Monoliths | 134 |
| 5.2.1.2 | Annealed Disks | 134 |
| 5.2.1.3 | Powder Samples | 134 |
| 5.2.2 | XRD | 135 |
| 5.2.3 | FTIR | 135 |
| 5.2.4 | DSC | 135 |
| 5.2.5 | Density | 136 |
| 5.2.6 | Flexural Strength and Elastic Modulus | 136 |
| 5.2.7 | Microhardness Testing | 137 |
| 5.2.7.1 | Sample Preparation | 137 |
| 5.2.7.2 | Hardness and Fracture Toughness | 137 |
| 5.2.8 | Dissolution | 138 |

| | | |
|----------|---|------------|
| 5.2.8.1 | Dissolution Rate | 138 |
| 5.2.8.2 | Ion Release | 140 |
| 5.2.9 | Bioactivity | 140 |
| 5.2.9.1 | Preparation of Simulated Body Fluid (SBF) | 140 |
| 5.2.9.2 | c-SBF Immersion | 142 |
| 5.2.10 | Biocompatibility | 143 |
| 5.2.10.1 | Cell Culture Precursor Solutions | 144 |
| 5.2.10.2 | <i>In Vitro</i> Cell Culture and Cell Seeding | 147 |
| 5.2.10.3 | MTT Assay | 148 |
| 5.2.10.4 | Live/Dead [®] Staining | 150 |
| 5.3 | Results | 152 |
| 5.3.1 | XRD | 152 |
| 5.3.2 | FTIR | 152 |
| 5.3.3 | DSC | 154 |
| 5.3.4 | Density | 156 |
| 5.3.5 | Flexural Strength and Elastic Modulus | 156 |
| 5.3.6 | Hardness and Fracture Toughness | 156 |
| 5.3.7 | Dissolution | 158 |
| 5.3.7.1 | Dissolution Rate | 158 |
| 5.3.7.2 | Ion Release | 159 |
| 5.3.8 | Bioactivity | 160 |
| 5.3.9 | Biocompatibility | 162 |
| 5.3.9.1 | MTT Assay | 162 |
| 5.3.9.2 | Live/Dead [®] Staining | 163 |
| 5.4 | Discussion | 165 |
| 5.5 | Conclusions | 184 |
| 6 | Characterisation of CorGlaes[®] Pure 107 Fibres | 185 |
| 6.1 | Outline | 185 |
| 6.2 | Materials and Methods | 186 |
| 6.2.1 | Fibre Manufacturing | 186 |
| 6.2.2 | XRD and DSC | 187 |
| 6.2.3 | Raman Spectroscopy | 187 |
| 6.2.4 | Fibre Diameter | 187 |
| 6.2.5 | Tensile Testing | 188 |
| 6.2.5.1 | Weibull Analysis | 189 |

| | | |
|----------|--|------------|
| 6.2.5.2 | Fibre Fracture Analysis | 190 |
| 6.2.6 | Silane Treated CorGlaes [®] Pure 107 Fibres | 191 |
| 6.2.7 | Fibre Dissolution Rate | 192 |
| 6.2.8 | Fibre Bioactivity | 193 |
| 6.3 | Results | 194 |
| 6.3.1 | XRD | 194 |
| 6.3.2 | DSC | 194 |
| 6.3.3 | Raman Spectroscopy | 197 |
| 6.3.4 | Fibre Diameter | 198 |
| 6.3.5 | Tensile Testing | 199 |
| 6.3.6 | Dissolution Rate | 202 |
| 6.3.7 | Fibre Bioactivity | 203 |
| 6.4 | Discussion | 208 |
| 6.5 | Conclusions | 222 |
| 7 | CorGlaes[®] Pure 107 Fibre Composites as Potential Cranioplasty Plates | 223 |
| 7.1 | Outline | 223 |
| 7.2 | Materials and Methods | 224 |
| 7.2.1 | CorGlaes [®] Pure 107 Glass Fibre Mats | 224 |
| 7.2.2 | Composite Precursors | 224 |
| 7.2.2.1 | Fibre Pre-Pregs | 224 |
| 7.2.2.2 | Matrix Sheets | 226 |
| 7.2.3 | Composite Manufacturing | 226 |
| 7.2.4 | Mechanical Properties | 229 |
| 7.2.5 | Degradation | 231 |
| 7.2.5.1 | Weight Loss and Mechanical Properties | 231 |
| 7.2.5.2 | Ion Release | 233 |
| 7.2.6 | DMEM Degradation | 233 |
| 7.2.7 | Bioactivity | 233 |
| 7.2.8 | Biocompatibility | 234 |
| 7.3 | Results | 235 |
| 7.3.1 | Pre-Preg Orientation | 235 |
| 7.3.2 | Mechanical Properties | 235 |
| 7.3.3 | Degradation | 238 |
| 7.3.3.1 | Weight Loss and Mechanical Properties | 238 |
| 7.3.3.2 | Ion Release | 242 |

| | | |
|----------|--|------------|
| 7.3.4 | DMEM Degradation | 243 |
| 7.3.4.1 | Weight Loss and Mechanical Properties | 243 |
| 7.3.4.2 | Ion Release | 246 |
| 7.3.5 | Bioactivity | 250 |
| 7.3.6 | Biocompatibility | 253 |
| 7.4 | Discussion | 255 |
| 7.5 | Conclusions | 274 |
| 8 | Modified CorGlaes[®] Pure 107 Fibre Composite | 275 |
| 8.1 | Outline | 275 |
| 8.2 | Materials and Methods | 276 |
| 8.2.1 | Silane Treated CorGlaes [®] Pure 107 Composites | 276 |
| 8.2.2 | CorGlaes [®] Pure 107 Fibre-Particle Hybrid Composites | 276 |
| 8.2.3 | Hybrid Composite Precursors | 277 |
| 8.2.3.1 | Fibre Pre-Pregs | 277 |
| 8.2.3.2 | Matrix Sheets | 278 |
| 8.2.4 | Hybrid Composite Manufacturing | 278 |
| 8.2.5 | Development of CorGlaes [®] Pure 107 Hybrid Composites | 279 |
| 8.2.5.1 | Optimisation of Hybrid Composite Degradation | 280 |
| 8.2.5.2 | Optimisation of Biocompatible Hybrid Composites | 283 |
| 8.2.6 | Mechanical Testing and Degradation | 285 |
| 8.2.7 | Biocompatibility of CorGlaes [®] Pure 107 Hybrid Composites | 285 |
| 8.2.7.1 | Cell Culture Precursor Solutions | 285 |
| 8.2.7.2 | MTT Assay | 286 |
| 8.2.7.3 | Coomassie Brilliant Blue | 286 |
| 8.2.7.4 | SEM Imaging | 288 |
| 8.2.8 | Ion Release | 289 |
| 8.2.9 | Hybrid Composite Bioactivity | 289 |
| 8.3 | Results | 290 |
| 8.3.1 | Silane Treated CorGlaes [®] Pure 107 Composites | 290 |
| 8.3.1.1 | Mechanical Properties | 290 |
| 8.3.1.2 | Degradation | 291 |
| 8.3.2 | Optimisation of Hybrid Composite Degradation | 294 |
| 8.3.2.1 | Mechanical Properties | 294 |
| 8.3.2.2 | Degradation | 296 |
| 8.3.3 | Optimisation of Biocompatible Hybrid Composites | 299 |

| | |
|----------------------------------|------------|
| | 10 |
| 8.3.3.1 MTT Assay | 299 |
| 8.3.3.2 Coomassie Brilliant Blue | 300 |
| 8.3.3.3 SEM Characterisation | 304 |
| 8.3.3.4 Mechanical Properties | 309 |
| 8.3.3.5 Degradation | 310 |
| 8.3.3.6 Ion Release | 313 |
| 8.3.3.7 Bioactivity | 315 |
| 8.4 Discussion | 320 |
| 8.5 Conclusions | 339 |
| 9 Discussion | 341 |
| 10 Conclusions | 346 |
| 11 Future Work | 348 |
| Appendix A | 350 |
| References | 351 |
| Publications | 370 |

List of Figures

Chapter 2

- Figure 2.1.1. a) Illustration of potential CorGlaes[®] Pure 107 multi-component composite being applied as a cranioplasty implant material [Modified from Aitasalo et al. (2014)] and b) Magnified section showing the position of the implant in relation to the surrounding physiological tissue [Modified from Nganga et al. (2012)]......42

Chapter 3

- Figure 3.1.1. Illustration of human skeleton with examples of different bone types (long, short, flat, irregular and sesamoid) [Modified from Hamill (2006) Biomechanical Basis of Human Movement].44
- Figure 3.1.2. Illustration of a) Osteonal remodelling of cortical bone showing osteoclast resorption at the cone front along with the bone forming osteoblast cells. The blood supply (Bs) at the centre of the new Haversian canal and distance travelled are also shown over a 56 day period and b) Remodelling of cancellous bone showing the trench formed across the trabeculae [Reproduced from Brickley (2010) The Bioarchaeology of Metabolic Bone Disease].48
- Figure 3.1.3. Seven level hierarchy structure found in the diaphysis of the long bone across the macro- to nanometre scale showing the diversity in structural arrangement [Reproduced from Rho et al. (1998)]......49
- Figure 3.1.4. Illustration of a) Partial frontal section of tibia (long bone) with the different regions and structural components labelled and b) Sagittal section of the tibia (lateral view) showing distribution of cortical and cancellous bone throughout the tissue [Reproduced from Patton (2014) Survival Guide for Anatomy & Physiology].50
- Figure 3.1.5. Sagittal section through a long bone showing the outer shell of cortical bone with concentrations of cancellous bone at the epiphyses [Reproduced from Khurana (2009) Bone Pathology].50
- Figure 3.1.6. Internal microscopic structure of the diaphysis from a long bone showing the cortical and cancellous regions as well as the osteons found in the cortical bone tissue [Reproduced from Patton (2013) Survival Guide for Anatomy & Physiology].51

- Figure 3.1.7. Illustration of a) Transverse section of an osteon in cortical bone and b) Individual trabeculae of cancellous bone at the microstructural level [Reproduced from Belinha (2014)]......52
- Figure 3.1.8. a) Depiction of three different osteonal types 1) Transversely 2) Longitudinally 3) Intermediately orientated as viewed by polarised light microscopy and the associated osteonal lamella arrays as described by the orthogonal plywood model [Reproduced from Giraud-Guille (1988)] b) Illustration of twisted plywood model showing alternation of fibre orientations between adjacently concentric lamellae. [Reproduced from Adler (2000) Bone Diseases: Macroscopic, Histological, and Radiological Diagnoses of Structural Changes in the Skeleton].....53
- Figure 3.1.9. Nanostructural hierarchy of bone showing the collagen fibre bundles in the osteons of cortical bone to be composed of a single collagen fibre that consists of tropocollagen molecules and hydroxyapatite crystals [Reproduced from Roesler (2007)]......55
- Figure 3.1.10. Sub-nanostructural level of cortical bone showing the staggered arrangement of the tropocollagen molecules and hydroxyapatite crystals in a collagen fibre [Reproduced from Olszta et al. (2007)]......55
- Figure 3.1.11. Illustration of skull (lateral view) showing the bones that make up the cranium, facial and mandible bones [Reproduced from Martini (2007) Anatomy and Physiology].....56
- Figure 3.1.12. a) Left lateral view of posterior half of skull showing radiographic features and tri-layered structure of the cranium [Modified from Gallucci (2007) Radiographic Atlas of Skull and Brain Anatomy] and b) Illustration of the basic architecture and sandwich structure of the flat bones (such as those in the cranium) [Reproduced from Orchard & Nation (2014) Cell Structure & Function].57
- Figure 3.1.13. Contributions from the matrix (collagen) and reinforcing (hydroxyapatite) phases of bone showing the influence from each component on the mechanical properties of normal bone [Reproduced from Burr (2013) Basic and Applied Bone Biology].58

- Figure 3.1.14. a) Comparison of stress-strain curves between cortical and trabecular (cancellous) bone with the bending and compression of individual trabeculae represented by the linear elastic region and b) Power-law relation between the elastic modulus and apparent density for an isotropic section of cancellous bone [Reproduced from Narayan (2009) Biomedical Materials].
.....60
- Figure 3.1.15. Examination of skull fractures showing a) Lateral radiograph of skull with comminuted fracture and b) CT scan of skull showing depressed fracture of the left parietal bone (large arrow) and epidural hematoma (small arrow) [Reproduced from Demetriades & Lewton, (2011)]......64
- Figure 3.1.16. Illustration of a) Restoration of fractured bone union through hematoma and subsequent hard callus formation via the deposition of woven bone and b) Conversion of woven bone to lamellar bone and restoration of the medullary cavity [Modified from Porth (2011) Essentials of Pathophysiology: Concepts of Altered Health States]......65
- Figure 3.2.1. Reconstruction of radial fracture containing a critical size defect (CSD) a) Resection of fibrous tissue b) Implantation of bone graft with locking compression plate as well as a haemostatic agent and c) Post-operative CT images of defect site after 9 months showing metallic plates and allograft bone [Reproduced from Calori et al. (2011)]......68
- Figure 3.2.2. Images of a-b) Canine radius with implanted glass tube after sixty one days of implantation performed by Sir William Macewan - stored at the Hunterian Museum in the University of Glasgow and c) Drawing of histological section after retrieval of glass tube from canine radius [Reproduced from Tanner & Dalby (2010) Guest Editorial]......81
- Figure 3.2.3. Number of papers published between 1990-2010 under the field of "bioactive glass" compiled from a search of Web of Science [Reproduced from Rahaman et al. (2011)]......81
- Figure 3.2.4. Comparison of the elastic modulus vs density (i.e. specific modulus) for different monolithic and fibre composite materials [Reproduced from Hull & Clyne (1996) An Introduction to Composite Materials]......85
- Figure 3.2.5. Comparison of different filler types used in composite design [Reproduced from Mallick (1997)]......85
- Figure 3.2.6. Comparison of different types of composite configurations using different fillers [Reproduced from Gurdal et al. (1999)]......86

- Figure 3.2.7. Illustration of FRPC showing a) Elastic modulus (E), shear modulus (G) and Poisson's ratio (ν) of the fibre (E_f , G_f , ν_f) and matrix (E_m , G_m , ν_m) constituents in a unidirectional fibre reinforced composite and b) Elastic properties of composite with regards to global axis running parallel (x_1) and transverse (x_2) to the primary fibre axis with the elastic modulus (E_1 , E_2) as well as the shear modulus (G_{12}) and Poisson's ratio (ν_{12}) labelled relative to the applied axis coordinates. [Reproduced from Gurdal et al. (1999)]......87
- Figure 3.2.8. Comparison of different fibre architectures used in various composite laminate designs [Reproduced from Gurdal et al. (1999)]......88
- Figure 3.2.9. Illustration of interfacial debonding, fibre fracture and fibre pull-out during composite fracture [Reproduced from Mallick (1997)]......88
- Figure 3.2.10. Illustration of a hybrid polymer composite that incorporates short fibres and particles into the matrix phase [Reproduced from Fu et al. (2009)]......89
- Figure 3.2.11. Overview of the different composite materials being developed for tissue reconstruction at different anatomical sites [Reproduced from Ramakrishna et al. (2001)]......91
- Figure 3.3.1. Manufacture and implantation of a titanium cranioplasty plate for frontal skull reconstruction showing a) Simulation of reconstruction using CAD/CAM software based on CT scan data b) Manufactured titanium plate and c) Surgical implantation and fixation of titanium plate for frontal basis reconstruction [Reproduced from Spetzger et al. (2010)]......94
- Figure 3.3.2. Navigation assisted reconstruction of a large skull defect using a PMMA cranioplasty plate fixed with titanium screws [Reproduced from Spetzger et al. (2010)]......95
- Figure 3.3.3. Polymer cranioplasty plates a) MEDPOR[®] Surgical implant [Reproduced from Liu et al. (2004)] b) MEDPOR[®] Titan cranial plate for temporal reconstruction with reinforcing titanium mesh visible [Reproduced from <http://www.stryker.com> (Accessed 14/09/2014) and c) Patient specific customised pre-fabricated PEEK implant plate from 3D CT data [Reproduced Harris et al. (2014)].96
- Figure 3.3.4. Illustration of a fibre reinforced cranioplasty plate design that combines high performance non-resorbable glass fibres with a porous layer containing bioactive glass (BG) particles [Reproduced from Vallittu et al. (2015)]......97

- Figure 3.4.1. Enthalpy-Temperature diagram showing formation of crystalline and glassy materials as well as the effect of cooling rate on glass formation [Reproduced from Shelby (2005) Introduction to Glass Science and Technology].99
- Figure 3.4.2. Random network structure of a vitreous phosphate glass generated by P-tetrahedra linked by P-O-P covalent bonds [Modified from Jones & Clare (2012)]......101
- Figure 3.4.3. Classification of PG networks based on Q^i terminology showing decreasing BO's as Q^n decreases [Modified from Brow (2000)]......102
- Figure 3.4.4. Change in P-O-P glass structure from the addition of MOs (CaO/Na₂O) into the phosphate network and the formation of ionic bonds between the phosphate groups - Note that due to the single positive charge of the Na⁺ ion, the PG network is depolymerised but no ionic bonding between chains occurs [Modified from Jones & Clare (2012)]......102
- Figure 3.4.5. Hydration reaction that produces the formation of a hydrated surface layer across the glass surface due to the exchange of the sodium with hydrogen ions in water (Na-H) [Reproduced from Gao et al. (2004)]......105
- Figure 3.4.6. Breakage of P-O-P bonds in a PG network from the attack of H₂O water molecules after the initial surface hydration reaction [Reproduced from Gao et al. (2004)]......106
- Figure 3.4.7. Sequence of reactions occurring across surface of silica based bioactive glasses with surface reactions (1-5) and cellular events (6-11) labelled [Reproduced from Hench (1998) Bioactive materials: The potential for tissue regeneration].107
- Figure 3.4.8. 2D map of a) Glass forming region and b) Corresponding dissolution rates of phosphate glasses in the P₂O₅-CaO-Na₂O system [Reproduced from Uo et al. (1998)]......109
- Figure 3.4.9. Representation of a) Melt spinning b) Solid pre-form downdrawing and c) Fibre updrawing techniques employed in PGF production [Reproduced from Wallenberger, (2010)].114
- Figure 3.4.10. Images of PGF tows a) (P₂O₅)₅₀-(CaO)₁₆-(MgO)₂₄-(Na₂O)₆-(Fe₂O₃)₄ [Reproduced from Hasan et al. (2012)] and b) (P₂O₅)₅₀-(CaO)₄₀-(Na₂O)₅-(Fe₂O₃)₅ fibres - the change in colour was attributed to the composition of the glass [Reproduced from Ahmed et al. (2010)]......117

| | |
|---|-----|
| Figure 3.4.11. Weight loss of “as used” and annealed PGF-PLA composites (0.14V _f) over 6.5 weeks of degradation in deionised water [Reproduced from Ahmed et al. (2009)]. | 120 |
|---|-----|

Chapter 4

| | |
|--|-----|
| Figure 4.1.1. Illustration of coherent X-ray beams striking a series of hkl lattice planes a distance d_{hkl} apart in a crystalline material at an incident angle θ and the resultant optical path difference ($2s$) [Reproduced from Mittemeijer (2010) Fundamentals of Materials Science: The Microstructure-Property Relationship Using Metals as Model Systems]. | 124 |
| Figure 4.1.2. Representation of a covalent bond between two atoms of mass m_1/m_2 as a spring model system with spring stiffness k . | 125 |
| Figure 4.1.3. Molecular vibrations from the available degrees of freedom found in a CO ₂ molecule when exposed across a range of mid-infrared radiation frequencies during FTIR. | 126 |
| Figure 4.1.4. Scattering of an incident laser source (ν_0) by a sample and the resultant Rayleigh (ν_0) and Raman scattering ($\nu_0 \pm \nu_m$) during Raman spectroscopy [Reproduced from Ferraro (2003) Introductory Raman Spectroscopy]. | 128 |
| Figure 4.1.5. Configuration of thermal analysis equipment a) Dual heating of sample (S) and reference (R) pans in DTA and b) Independently temperature controlled DSC set up of sample (S) and reference (R) pans [Reproduced from Brown (2001) Introduction to Thermal Analysis: Techniques and Applications]. | 130 |
| Figure 4.1.6. Idealised DSC thermogram curve for a glassy material with key thermal properties/events indicated [Reproduced from Jones & Clare (2012)]. | 131 |

Chapter 5

| | |
|---|-----|
| Figure 5.2.1. Illustration of radial crack lengths (c) emanating from the Vickers indent on a material sample surface [Reproduced from Bhushan (1998) Handbook of Micro/Nano Tribology]. | 138 |
| Figure 5.2.2. Process flowchart of CorGlaes [®] Pure 107 disk bioactivity after immersion in c-SBF for 336 hours of immersion. | 143 |
| Figure 5.2.3. Process flow chart for assessing the biocompatibility of CorGlaes [®] Pure 107 disks using an MTT assay and a Live/Dead [®] cell staining kit. | 144 |
| Figure 5.3.1 XRD trace of CorGlaes [®] Pure 107 composition of phosphate glass over 5-85° 2θ with no crystallisation peaks and a broad halo centred at $2\theta = 23^\circ$. | 152 |

- Figure 5.3.2. FTIR vibrational spectra of the CorGlaes[®] Pure 107 phosphate glass over a) The complete mid-IR range (4000-400cm⁻¹) and b) The 1400-400cm⁻¹ wavenumber range showing absorption peaks and shoulders corresponding to the glass's structure with the wavenumber of identified spectral features labelled.153
- Figure 5.3.3. DSC trace of the CorGlaes[®] Pure 107 phosphate glass over the pre-programmed heating cycle with deviations in the baseline indicative of endo- and exothermic events.....155
- Figure 5.3.4. Magnified section of CorGlaes[®] Pure 107 DSC thermogram (Figure 5.3.3) showing the glass transition temperature at 436°C from the intersection of tangents.155
- Figure 5.3.5 Magnified DSC thermogram of CorGlaes[®] Pure 107 (Figure 5.3.3) showing the crystallisation onset temperature from the intersection of tangents.....156
- Figure 5.3.6. Optical image of CorGlaes[®] Pure 107 disk surface after Vickers micro indentation with a 300g load showing an indent diagonal (d₁) and crack length (c₁) emanating from indent site. [scale bar = 50µm].....157
- Figure 5.3.7. a) Weight loss during dissolution of CorGlaes[®] Pure 107 disks immersed in distilled water at 37°C with the overlaid trendline plotted through the origin indicative of the glass's dissolution rate and b) Extract pH of CorGlaes[®] Pure 107 disk dissolution media showing the formation of an acidic pH after 72 hours (standard deviation $\leq \pm 0.34$).158
- Figure 5.3.8. a) Daily ionic concentrations and b) Accumulative ionic concentrations in the immersion media over the first 168 hours of CorGlaes[®] Pure 107 disk dissolution in distilled water at 37°C.159
- Figure 5.3.9. FTIR of CorGlaes[®] Pure 107 disk surfaces after immersion in c-SBF at 37°C for 24, 72, 120, 168 and 336 hours.160
- Figure 5.3.10. a) Weight loss during the immersion of CorGlaes[®] Pure 107 disks in c-SBF at 0.1 cm² ml⁻¹ and b) Extract pH of c-SBF media during bioactivity analysis of CorGlaes[®] Pure 107 disks (standard deviation $\leq \pm 0.01$).161
- Figure 5.3.11. Viability of MG63 cells cultured in CorGlaes[®] Pure 107 disk extract media over 24 and 96 hours of dissolution and evaluated by MTT assay after 24 hours of incubation at 0.1, 10, 50, 100 vol% extract concentrations.162

Figure 5.3.12. Live/Dead[®] cell viability staining of Thermanox[®] coverslip controls (a-c) and CorGlaes[®] Pure 107 disks (d-l) showing reduced MG63 cell viability when cultured on CorGlaes[®] Pure 107 disks with increasing incubation period compared to the cell spreading observed on the positive controls (Thermanox[®]) [All scale bars = 10µm].163

Figure 5.3.13. Comparison of CDMEM pH over the corresponding incubation period for Live/Dead[®] cell cytotoxicity testing of CorGlaes[®] Pure 107 disks compared to a blank CDMEM control (standard deviations $\leq \pm 0.01$) - the media change at 96 hours corresponding to the cell culture protocol is also included.164

Figure 5.4.1. Illustration comparing the XRD results between a crystalline and amorphous material of the same composition highlighting the correspondence of sharp and broad peaks between both results [Modified from Suryanarayana & Norton (1998)].165

Figure 5.4.2. FTIR spectra showing a) The deconvolution of a phosphate glass FTIR spectrum over the 1200-800cm⁻¹ range and b) An equivalent FTIR spectrum of the CorGlaes[®] Pure 107 composition illustrating the potential for similar band overlapping [Reproduced from Lucacel et al. (2009)].166

Figure 5.4.3. Variation in thermal properties (T_g, T_{oc}, PW) with the increasing substitution of a) Mg for Ca [Reproduced from Morikawa et al. (2013)] or b) Sr for Ca [Reproduced Jones & Clare (2012)] into phosphate glass compositions showing a clear difference between non-linear (i.e. mixed cation effects) and linear PW relationships respectively.168

Figure 5.4.4. Comparison of CorGlaes[®] Pure 107 phosphate glass density with Bioglass[®] 45S5 and alternate ultra-, meta- and polyphosphate glass compositions intended for biomedical applications [Data from Abou Neel et al., 2008; Devi et al., 2010; Khor et al., 2011; Jones & Clare, 2012; Lee et al., 2013; Sharmin et al., 2014].170

Figure 5.4.5. Comparison between the flexural strength and elastic modulus of the CorGlaes[®] Pure 107 glass with BioGlass[®] 45S5, cortical bone, hydroxyapatite along with alternate PG compositions intended for biomedical applications [Data from Thompson & Hench, 1998; Kokubo et al., 2003; Abou Neel et al., 2009; Ratner et al., 2012].171

Figure 5.4.6. Comparison of CorGlaes[®] Pure 107 glass hardness with different PG compositions and Bioglass[®] 45S5 [Data from Jones & Clare (2012) and Weiss et al. (2014)].173

Figure 5.4.7. Increase in hardness, fracture toughness and elastic modulus with substitution of MgO or TiO₂. Note: the elastic moduli reported here were determined from the hardness data and was excluded from the previous analysis that used three and four point bend techniques (Figure 5.4.5) [Reproduced from Weiss et al. (2014)]......174

Figure 5.4.8. Comparison of CorGlaes[®] Pure 107 fracture toughness with Bioglass[®] 45S5 and alternate phosphate glass compositions [Data from Jones & Clare (2012) and Weiss et al. 2014].175

Figure 5.4.9. Dissolution of glass compositions showing a) Delayed release of Ti⁴⁺ ions from the glass with increasing concentration of TiO₂ (mol%) [Reproduced from Novajra et al. (2011)] and b) Changes in media pH during the dissolution of glass samples with increasing concentrations of MgO (mol%) [Reproduced Lee et al. (2013)].177

Figure 5.4.10. Variation in Zn²⁺ and Mg²⁺ ion release from a (P₂O₅)₅₅-(ZnO)₃₀-(MgO)₁₅ glass in different media pH buffer solutions (0.24-0.43 cm² ml⁻¹) at ambient temperature [Data from Khor et al. (2011)].178

Figure 5.4.11. Comparison of CorGlaes[®] Pure 107 phosphate glass dissolution rate with a selection of different ultra-, meta- and polyphosphate glass compositions measured under near identical testing conditions in distilled water or PBS at 37°C [Data from Franks et al., 2002; Navarro et al., 2003; Ahmed et al., 2004; Skelton et al., 2007; Abou Neel et al., 2009; Hasan et al., 2012]. ...179

Chapter 6

Figure 6.2.1. Images of a) Gravity fed melt spinning fibre manufacturing plant with ceramic bushing and stainless steel drum labelled and b) Image of CorGlaes[®] Pure 107 fibres [scale bar = 100mm].....186

Figure 6.2.2. Illustration of sample housing frames employed in tensile testing of CorGlaes[®] Pure 107 fibres showing a) Housing frame dimensions b) Fixation of sample specimens [Reproduced from BS ISO 11566:1996] and c) Image of testing configuration showing a card housing prior to cutting of the support frame.....188

| | | |
|----------------|---|-----|
| Figure 6.3.1. | XRD profile of CorGlaes [®] Pure 107 fibres showing the amorphous structure of the fibres produced under the operating conditions specified in section 6.2.1..... | 194 |
| Figure 6.3.2. | DSC thermogram of CorGlaes [®] Pure 107 fibres over a thermal cycle from 25°C to 1200°C..... | 195 |
| Figure 6.3.3. | DSC thermogram of CorGlaes [®] Pure 107 fibres with the glass transition temperature identified as 432°C from the tangent intersection (Magnified section from Figure 6.3.2)..... | 195 |
| Figure 6.3.4. | Crystallisation onset temperature of CorGlaes [®] Pure 107 fibres identified from the intersection of lines on the DSC thermogram (magnified section of Figure 6.3.2)..... | 196 |
| Figure 6.3.5. | DSC thermogram of CorGlaes [®] Pure 107 fibres showing multiple crystallisation peaks and its liquidus temperature (magnified section of Figure 6.3.2)..... | 196 |
| Figure 6.3.6 | Raman spectrum of CorGlaes [®] Pure 107 fibres over the 1400-100cm ⁻¹ wavenumber range with peaks corresponding to the structural features of the CorGlaes [®] Pure 107 composition..... | 197 |
| Figure 6.3.7. | SEM images of CorGlaes [®] Pure 107 fibres with measurements of the diameters used to determine the average cross sectional area [scale bars = 10µm , 2µm]..... | 198 |
| Figure 6.3.8. | a) Force-displacement plot and b) Stress-strain plot of a tensile tested ≈Ø20µm CorGlaes [®] Pure 107 fibre at a cross-head speed of 1mm s ⁻¹ | 199 |
| Figure 6.3.9. | Determination of Weibull modulus (<i>m</i>) from CorGlaes [®] Pure 107 fibre tensile test data based on the gradient of the plotted trendline. | 200 |
| Figure 6.3.10. | Corrected probability of failure based on the Weibull statistical analysis of the CorGlaes [®] Pure 107 fibre tensile test data. | 200 |
| Figure 6.3.11. | Variation in experimental CorGlaes [®] Pure 107 tensile strength with theoretically determined surface flaw type and size. | 201 |
| Figure 6.3.12. | Comparison of CorGlaes [®] Pure 107 fibre dissolution up to 168 hours in various immersion media showing a) Dry weight loss over time and b) Media pH throughout the immersion period with the replacement of DMEM at 96 hours of immersion (standard deviation ≤ ± 0.07)..... | 202 |
| Figure 6.3.13. | Comparison of CorGlaes [®] Pure 107 fibre dissolution rate against the initial ionic conductivity of the immersion media after 24 hours of immersion.. | 203 |

- Figure 6.3.14. Media pH of c-SBF during bioactivity testing of CorGlaes[®] Pure 107 fibres over 336 hours of immersion showing the decrease in pH with prolonged immersion (standard deviation $< \pm 0.02$).203
- Figure 6.3.15. FTIR spectra of CorGlaes[®] Pure 107 fibres after immersion in c-SBF for up to 336 hours (2 weeks) with the formation and suppression of broad peaks over the immersion period labelled accordingly.....204
- Figure 6.3.16. Comparison of Raman spectra obtained from CorGlaes[®] Pure 107 fibres prior to bioactivity testing [T_0] and after 336 hours of immersion [$T_{336\text{Hour}}$] in c-SBF at 37°C with the peaks labelled.205
- Figure 6.3.17. SEM Images of CorGlaes[®] Pure 107 fibres prior to bioactivity testing [T_0] and after immersion in c-SBF at various points over a 336 hour period showing the changes across the fibre surface at a) T_0 b) 0.5 c) 1 d) 3 e) 6 f) 12 g) 24 h) 48 i) 168 j) 336 hours of immersion [scale bar = 2 μm] and k) Image of CorGlaes[®] Pure 107 fibres on 25mm SEM mounting stubs after each immersion period in c-SBF prior to SEM imaging (moving counter-clockwise from T_0 as indicated) showing the decreasing amount of retrievable fibre with increasing immersion time from $T_0 \rightarrow T_{336\text{Hour}}$206
- Figure 6.3.18. SEM images of CorGlaes[®] Pure 107 fibres after immersion in c-SBF a-b) Fibre cross-section showing an outer surface layer of 400.4 nm and 550.6nm thickness respectively after 12 hours of immersion [scale bar = 1 μm] c-e) Surface precipitation and cracking on fibres after 168 hours of immersion [scale bar = 20 μm] and f) Surface deposition onto fibres after 336 hours of immersion [scale bar = 10 μm].....207
- Figure 6.4.1. DSC thermogram of $\text{P}_2\text{O}_5\text{-CaO-MgO-Na}_2\text{O-TiO}_2$ glass system between 1mm glass frit and fine powder samples showing the formation of two crystalline phases/peaks in the glass powder corresponding to the formation of $\text{Ca}_2\text{P}_2\text{O}_7$ and CaMgP_2O_7 [Reproduced from Jones & Clare (2012)].209
- Figure 6.4.2. Force-displacement plot of a rejected tensile tested CorGlaes[®] Pure 107 fibre sample showing evidence of several fractures due to the presence of multiple fibres being accidentally secured to the housing card during sample preparation.....211

| | | |
|------------------|--|-----|
| Figure 6.4.3 | Comparison of CorGlaes [®] Pure 107 fibre tensile properties with alternate phosphate glass fibre compositions of similar $\approx 20\mu\text{m}$ diameter, tested according to ISO 11566:1996 [Data from Ahmed et al., 2008; Cozien-Cazuc et al., 2008; Hasan et al., 2012; Haque et al., 2013; Sharmin et al., 2014]. | 212 |
| Figure 6.4.4. | Comparison of CorGlaes [®] Pure 107 fibre Weibull modulus (m) and normalising stress (σ_0) with alternate PGF's tested according to ISO 11566:1996 [Data from Ahmed et al., 2008,2009; Cozien-Cazuc et al., 2008; Sharmin et al., 2014]. | 214 |
| Figure 6.4.5. | Comparison of CorGlaes [®] Pure 107 fibre dissolution rates in distilled water and PBS compared with alternate PGF compositions [Data from Rinehart et al., 1999; Cozien-Cazuc et al., 2009; Haque et al., 2013; Sharmin et al., 2014]. | 218 |
| Figure 6.4.6. | a) FTIR absorption spectra of various semi-amorphous metal pyrophosphate salts over $2000\text{-}400\text{cm}^{-1}$ wavenumber range [Reproduced from Leeuwen et al. (2012)] and b) FTIR of CorGlaes [®] Pure 107 fibres after 336 hours of immersion in c-SBF ($1400\text{-}400\text{cm}^{-1}$). | 219 |
| Figure 6.4.7. | SEM image of phosphate glass fibres after 24 hours of immersion in PBS at 37°C showing significant cracking and peeling of the outer surface layer [Reproduced from Rinehart et al. (1999)]. | 221 |
| Chapter 7 | | |
| Figure 7.2.1. | Illustration of manufacturing method for producing random continuous fibre mats (RCM) from a CorGlaes [®] Pure 107 fibre tow a) Expansion of fibres parallel to fibre tow b) Collection around a hand driven mandril and c) Cutting and removal from mandril into RCM mats [Modified from Mallick (1997) Composites Engineering Handbook]. | 224 |
| Figure 7.2.2. | Back-lit illuminated images of a) $100\times 50\text{mm}$ section of UD solvent cast CorGlaes [®] Pure 107 fibre pre-preg [scale bar = 10mm] b) $100\times 50\text{mm}$ section RCM solvent cast CorGlaes [®] Pure 107 fibre pre-preg [scale bar = 10mm] c) Orientation axis used in OrientationJ results d) Unidirectional (UD) control image and e) Randomly orientated control image (generated by MATLAB). | 225 |
| Figure 7.2.3. | Compression moulding press used to produce PLA matrix sheets and CorGlaes [®] Pure 107 composites. | 226 |

- Figure 7.2.4. Illustration of a) Alternating film stacking technique with PLA matrix sheets and CorGlaes[®] Pure 107 fibre pre-pregs [Reproduced from Gibson & Månson (1992)] b) Sequential lay up of matrix films and fibre pre-pregs under heat and pressure inside the cavity mould [Reproduced from Gibson & Månson (1992)] c) 130x80mm stainless steel cavity mould used for composite manufacturing [scale bar = 10mm] and d) 130x80mm 0.2V_f RCM composite plate marked for further cutting stages of sample manufacturing [scale bar = 10mm].227
- Figure 7.2.5. Illustration of a) Cutting specifications for samples cut along the length direction of the composite (A) and samples cut along the width direction of the composite (B) and b) 3-point bend testing arrangement used to test the CorGlaes[®] Pure 107-PLA composites and control samples [Reproduced from BS EN ISO 14125:1998].229
- Figure 7.2.6. Image of 60x15x2mm 0.2V_f RCM composite sample used in degradation testing with the three exposed cross-sectional faces indicated [scale bar = 10mm].232
- Figure 7.3.1. Stress-strain plots of CorGlaes[®] Pure 107 fibre (filler), NatureWorks[®] 3001D PLA polymer (matrix) and 0.2V_f RCM composite with the ultimate stress (σ_f/σ_m) and strain at failure (ϵ_f/ϵ_m) of each precursor phase indicated.236
- Figure 7.3.2. Variation in flexural strength and elastic modulus of CorGlaes[®] Pure 107 fibre-PLA composites with increasing fibre volume fraction (0→0.2V_f) and different fibre architectures (RCM and [0/90]_{3S}) alongside a PLA control.236
- Figure 7.3.3. Comparison of experimental composite primary elastic modulus (E₁) with that predicted by the rule of mixtures model over different composite fibre volume fractions (0→0.2V_f) and architectures (RCM, [0/90]_{3S}).237
- Figure 7.3.4. Comparison between stress-strain plots of 0.2V_f RCM and 0.2V_f [0/90]_{3S} composites obtained from three point bend testing according to BS EN ISO 14125:1998.237
- Figure 7.3.5. Degradation of 0.2V_f RCM and 0.2V_f [0/90]_{3S} composites in distilled water at 37°C along with a PLA control over 1008 hours (six weeks) showing a) Wet weight and b) Dry weight losses.238

- Figure 7.3.6. Media pH during 1008 hour (six week) degradation of 0.2V_f RCM and 0.2V_f [0/90]_{3S} composites along with a PLA control in distilled water at 37°C.239
- Figure 7.3.7. Comparison of a) Flexural strength and b) Elastic modulus during degradation of 0.2V_f RCM and 0.2V_f [0/90]_{3S} composites as well as a PLA control over 1008 hours (six weeks) in distilled water at 37°C.240
- Figure 7.3.8. a) Fracture surfaces of degraded 0.2V_f RCM CorGlaes[®] Pure 107 composite samples after gold coating, SEM images of b) 0.2V_f RCM composite after 168 hours of degradation [scale bar = 100µm] c) 0.2V_f RCM composite showing breakdown of fibre-matrix interface due to fibre dissolution after 168 hours [scale bar = 10µm] d) 0.2V_f RCM composite after 336 hours of immersion [scale bar = 100µm] e) 0.2V_f RCM composite after 504 hours of immersion [scale bar = 10µm] f) PLA control fracture surfaces after 1008 hours of degradation [scale bar = 100µm].241
- Figure 7.3.9. a) Daily ionic concentrations and b) Total accumulative ionic concentrations from 0.2V_f RCM composites over initial 168 hours of degradation in distilled water at 37°C.242
- Figure 7.3.10. Comparison of a) Wet weight and b) Dry weight during degradation of 0.2V_f RCM composites in distilled water and DMEM over 1008 hours (six weeks) at 37°C.243
- Figure 7.3.11. Comparison of media pH during 0.2V_f RCM composite degradation in distilled water and DMEM at 37°C over 1008 hours (standard deviation in DMEM ≤ ± 0.06).244
- Figure 7.3.12. Comparison of a) 0.2V_f RCM composite flexural strength (standard deviation in DMEM ≤ ± 4 MPa) and b) 0.2V_f RCM composite elastic modulus during sample degradation in distilled water and DMEM over 1008 hours of degradation (standard deviation in DMEM ≤ ± 0.8 GPa)...245
- Figure 7.3.13. a) Daily ion release from 0.2V_f RCM composite during degradation in DMEM and b) Accumulative ion release from 0.2V_f RCM composite during degradation in DMEM over initial 168 hours.246
- Figure 7.3.14. Daily sodium ionic concentration in DMEM during degradation of 0.2V_f RCM composite degradation over 168 hours.247

- Figure 7.3.15. a) Surface image of the 0.2V_f RCM composite after 366 hours of degradation in DMEM [scale bar = 5mm] and b-d) SEM images of 0.2V_f RCM composite fracture sites after 336 hours of degradation in DMEM showing the formation of precipitants within the voids created by fibre dissolution [scale bars = 30µm, 10µm and 5µm].....248
- Figure 7.3.16. Comparison of FTIR spectra obtained from the precipitate formed during degradation of the 0.2V_f RCM composite in DMEM with the CorGlaes[®] Pure 107 composition and that obtained during bioactivity testing of CorGlaes[®] Pure 107 fibres after 336 hours of immersion in c-SBF.249
- Figure 7.3.17. XRD trace of surface precipitate formed after 336 hours of 0.2V_f RCM composite degradation in DMEM showing an amorphous structure and halo at $2\theta \approx 30^\circ$249
- Figure 7.3.18. Images of 15x15x2mm 0.2V_f RCM composite samples over various immersion periods in c-SBF showing the formation of a surface precipitate with prolonged duration in c-SBF [scale bar = 10mm].250
- Figure 7.3.19. Comparison of 0.2V_f RCM composite wet weight during degradation in distilled water (SA:V = 0.21 cm² ml⁻¹), DMEM (SA:V = 0.21 cm² ml⁻¹) and c-SBF (SA:V = 0.1 cm² ml⁻¹).....250
- Figure 7.3.20. Comparison of media pH during degradation of 0.2V_f RCM composite in distilled water (SA:V = 0.21 cm² ml⁻¹), DMEM (SA:V = 0.21 cm² ml⁻¹) and c-SBF (SA:V = 0.1 cm² ml⁻¹).....251
- Figure 7.3.21. FTIR spectra of composite planar faces after immersion in c-SBF for up to 336 hours over a) 4000-400cm⁻¹ and b) 1400-400cm⁻¹ wavenumber ranges.252
- Figure 7.3.22. Comparison of degradation media cytotoxicity from NatureWorks[®] 3001D PLA and CorGlaes[®] Pure 107 fibre-PLA composites with increasing fibre volume fraction (0→0.2V_f) on MG63 cell viability using MTT assay.....253
- Figure 7.3.23. Media extract pH from composite samples and positive controls after 24 and 96 hours of degradation used in MTT assay.254
- Figure 7.3.24. Degradation extract concentration from 0.2V_f RCM CorGlaes[®] Pure 107 composite on MG63 cell viability using MTT assay after 24 and 96 hours of degradation.....254

- Figure 7.4.1. SEM of a degraded $0.2V_f$ RCM composite with the riverlines created from fibre degradation illustrating the shift in fibre dispersion due to the extrusion of the polymer matrix from the mould during manufacturing [scale bar = $100\mu\text{m}$].257
- Figure 7.4.2. Comparison of $0.2V_f$ and $0.2V_f [0/90]_{3S}$ composite mechanical properties with the composite precursor materials, cortical/parietal bone and HAPEX[®] [Data from Motherway et al., 2009; Ratner, 2012; Tjong, 2012].258
- Figure 7.4.3. Comparison of PGF composites mechanical properties with $0.2V_f$ RCM and $0.2V_f [0/90]_{3S}$ CorGlaes[®] Pure 107 composites – arranged by increasing V_f [Data from Ahmed et al., 2008; Khan et al., 2010; Ahmed et al., 2011; Felfel et al., 2012; Han et al., 2013].259
- Figure 7.4.4. Comparison of $0.2V_f$ RCM composite and PLA control wet weight over initial 24 hours of degradation showing equal rates of media uptake in both samples after 4 hours of degradation.260
- Figure 7.4.5. Comparison of $0.2V_f$ RCM composite wet and dry weight over 1008 hours of immersion in distilled water at 37°C261
- Figure 7.4.6. Correlation between the daily ionic concentrations of the degradation media and the $0.2V_f$ RCM composite wet weight over the initial 168 hours of immersion showing reductions in the ions released from the composite as the majority of the CorGlaes[®] Pure 107 fibres degraded.262
- Figure 7.4.7. Optical microscope images of a $\sim\text{Ø}220\mu\text{m}$ CorGlaes[®] Pure 107 filament bonded to a glass coverslip with 3001D PLA and immersed in distilled water at 37°C showing a) Fibre-matrix interface at T_0 and b) Breakdown of the fibre-matrix interface after 336 hours of immersion due to the wicking of moisture along the fibre-matrix interface [scale bar = $100\mu\text{m}$].263
- Figure 7.4.8. Comparison of stress-strain plots from initial (T_0) composite/control samples and after 1008 hours (six weeks) of degradation in distilled water at 37°C265
- Figure 7.4.9. Comparison of $0.2V_f$ composite degradation with the targeted degradation rate of the composite elastic modulus.266
- Figure 7.4.10. Degradation of a $15\times 15\times 2$ mm $0.2V_f$ RCM composite samples in 0.1 vol% sodium azide-DMEM ($\text{SA}:\text{V} = 0.21 \text{ cm}^2 \text{ ml}^{-1}$) with the localised yellow discolouration of the media after 48 hours of degradation signalling an acidic environment surrounding the sample.267

| | |
|--|-----|
| Figure 7.4.11. Comparison of stress-strain plots for 0.2V _f RCM composites after 1008 hours of degradation in distilled water and DMEM..... | 268 |
| Figure 7.4.12. Comparison of Ca ²⁺ , Mg ²⁺ and Zn ²⁺ accumulative ionic concentrations during the degradation of the 0.2V _f RCM composites in DMEM and distilled water (DMEM normalised with respect to its initial ionic concentrations before composite degradation i.e. T ₀)..... | 269 |
| Figure 7.4.13. Comparison of FTIR spectra obtained from precipitates during immersion of composites in c-SBF and DMEM as well as CorGlaes [®] Pure 107 fibres in c-SBF. | 271 |
| Figure 7.4.14. Variation in 0.2V _f RCM CorGlaes Pure 107 composite CDMEM degradation media extract after 96 hours at different concentrations (vol%) with the yellow discolouration indicating a highly acidic media..... | 273 |
| Figure 7.4.15. Effect of 0.2V _f RCM composite extract on the MTT results collected in acellular media showing false positive readings generated by possible influences from the dissolution of the reinforcing fibres. | 273 |

Chapter 8

| | |
|--|-----|
| Figure 8.2.1. Cyclic relationship between the CorGlaes [®] Pure 107 fibre dissolution and the HA buffering effect on the surrounding media pH. | 276 |
| Figure 8.2.2. Image of a solvent cast Ø150mm 0.2V _{HA} -PLA matrix sheet obtained from a 10 w/v % solution of a HA-PLA slurry after 24 hours of solvent evaporating in a fume cabinet [scale bar = 10mm]..... | 278 |
| Figure 8.2.3. Process flow chart for development of CorGlaes [®] Pure 107 fibre HA filler hybrid composites. | 279 |
| Figure 8.2.4. Variation in different calcium phosphate compound solubility with pH (solubility expressed as Ca concentration) [Reproduced from Dorozhkin (2013) Self-Setting Calcium Orthophosphate Cements]..... | 283 |
| Figure 8.2.5. Image of a 60x15x2mm 0.2V _f RCM composite (left) and 0.15V _f -0.2V _{HA} hybrid composite (right) showing the change in colour of the hybrid sample due to the inclusion of hydroxyapatite (HA) particles into the pre-preg and matrix phases..... | 285 |
| Figure 8.3.1. Typical stress-strain plots obtained from the mechanical testing of 0.2V _f RCM and 0.2V _f RCM-APS silane treated composites | 290 |
| Figure 8.3.2. Comparison of 0.2V _f RCM-APS composite mechanical properties with the previous 0.2V _f RCM samples and parietal bone [Data from Motherway et al. (2009)]..... | 290 |

- Figure 8.3.3. Comparison of silane treated $0.2V_f$ RCM-APS composites a) Wet weight and b) Dry weight with previous $0.2V_f$ RCM data over 1008 hours (six weeks) of degradation in distilled water at 37°C291
- Figure 8.3.4. Media pH during degradation of silane treated $0.2V_f$ RCM-APS composite and $0.2V_f$ RCM samples for up to 1008 hours of immersion in distilled water at 37°C292
- Figure 8.3.5. Comparison of silane treated $0.2V_f$ RCM-APS and $0.2V_f$ RCM composite a) Flexural strength and b) Elastic modulus during degradation in distilled water at 37°C for up to 1008 hours (six weeks).293
- Figure 8.3.6. Comparison of stress-strain plots obtained from $0.2V_f$ RCM samples and $0.15V_f$ - V_{HA} hybrid composites as well as a $0.2V_{\text{HA}}$ control.294
- Figure 8.3.7. Comparison of flexural strength and elastic modulus of the different hybrid composite configurations shown in Figure 8.3.6 and control materials as well as parietal bone [Data from Motherway et al. (2009)].294
- Figure 8.3.8. SEM images of mechanically tested $0.15V_f$ - $0.1V_{\text{HA(NHD)}}$ composite fracture faces prior to degradation [i.e. T_0] with HA particles and the pull out of HA particles during mechanical testing shown by arrow 1 and 2 respectively [scale bar = $100\mu\text{m}$, $50\mu\text{m}$, $20\mu\text{m}$, $10\mu\text{m}$].295
- Figure 8.3.9. Comparison of a) Wet weight and b) Dry weight during the degradation of different hybrid composite configurations and control samples over 1008 hours of immersion in distilled water at 37°C296
- Figure 8.3.10. Comparison of media pH during degradation of hybrid composites and control samples over 1008 hours of immersion in distilled water at 37°C297
- Figure 8.3.11. Comparison of hybrid and control composite samples a) Flexural strength and b) Elastic modulus during degradation in distilled water at 37°C over 1008 hours.298
- Figure 8.3.12. MTT assay of MG63 cell viability from the degradation extracts of composite materials containing $0.01V_f$ and $0.05V_f$ with $0V_{\text{HA}} \rightarrow 0.1V_{\text{HA}} \rightarrow 0.2V_{\text{HA}}$ filler volume fractions as well as a $0.05V_f$ - $0.2V_{\text{TCP}}$ sample after 24 and 96 hours of degradation.299
- Figure 8.3.13. Comparison of media pH after 24 and 96 hours of different hybrid composite sample degradation in DMEM (standard deviations $< \pm 0.04$).300

- Figure 8.3.14. Coomassie staining of MG63 cells cultured after 24 hours for a-c) Thermanox[®] coverslips, d-f) PLA, g-i) 0.2V_{HA}, j-l) 0.01V_f and m-o) 0.01-0.2V_{HA} samples at x5, x10 and x20 magnifications [scale bars = 500µm, 250µm and 100µm].....301
- Figure 8.3.15. Coomassie staining of MG63 cells cultured after 96 hours on a-c) Thermanox[®] coverslips, d-f) PLA, g-i) 0.2V_{HA}, j-l) 0.01V_f and m-o) 0.01-0.2V_{HA} samples at x5, x10 and x20 magnifications [scale bars = 500µm, 250µm and 100µm].....302
- Figure 8.3.16. Coomassie staining of MG63 cells cultured after 168 hours on a-c) Thermanox[®] coverslips, d-f) PLA, g-i) 0.2V_{HA}, j-l) 0.01V_f and m-o) 0.01-0.2V_{HA} samples at x5, x10 and x20 magnifications [scale bars = 500µm, 250µm and 100µm].....303
- Figure 8.3.17. SEM images obtained after 24 hours of MG63 cells cultured on (a, d, g) PLA, (b, e, h) 0.01V_f and (c, f, i) 0.01V_f-0.2V_{HA} samples at x800 and x1500 magnification [scale bars = 10µm].....305
- Figure 8.3.18. SEM images obtained after 96 hours of MG63 cells cultured on (a, d, g) PLA, (b, e, h) 0.01V_f and (c, f, i) 0.01V_f-0.2V_{HA} samples at x800 and x1500 magnification [scale bars = 10µm].....306
- Figure 8.3.19. SEM images obtained after 168 hours of MG63 cells cultured on (a, d, g) PLA, (b, e, h) 0.01V_f and (c, f, i) 0.01V_f-0.2V_{HA} samples at x800 and x1500 magnification [scale bars = 10µm].....307
- Figure 8.3.20. Comparison of MG63 cells cultured on (a,d) PLA, (b,e) 0.01V_f and (c,f) 0.01V_f-0.2V_{HA} after 168 hours of immersion at x300 magnification [scale bars = 100µm].308
- Figure 8.3.21. Stress-strain plots obtained from the three point bend testing of 0.01V_f-0.2V_{HA} hybrid samples as well as 0.01V_f and 0.2V_{HA} control samples.....309
- Figure 8.3.22. Comparison of flexural strength and elastic modulus of 0.01V_f-0.2V_{HA} hybrid composite with 0.01V_f and 0.2V_{HA} control samples as well as those recorded for the parietal bone [Data from Motherway et al. (2009)]......309
- Figure 8.3.23. Comparison of a) Wet weight and b) Dry weight of 0.01V_f-0.2V_{HA}, 0.01V_f and 0.2V_{HA} samples during 1008 hours of degradation in distilled water at 37°C.310
- Figure 8.3.24. Comparison of media pH during the degradation of 0.01V_f-0.2V_{HA}, 0.01V_f and 0.2V_{HA} samples after 1008 hours of immersion in distilled water at 37°C.311

- Figure 8.3.25. Comparison of a) Flexural strength and b) Elastic modulus of $0.01V_f$ - $0.2V_{HA}$, $0.01V_f$ and $0.2V_{HA}$ samples during 1008 hours of degradation in distilled water at 37°C312
- Figure 8.3.26. Comparison of daily ionic concentrations from a) $0.01V_f$ and b) $0.01V_f$ - $0.2V_{HA}$ samples during the first 168 hours of degradation in distilled water.313
- Figure 8.3.27. Comparison of the accumulative ionic media concentrations from a) $0.01V_f$ and b) $0.01V_f$ - $0.2V_{HA}$ composites over the initial 168 hours of degradation in distilled water.314
- Figure 8.3.28. FTIR spectra obtained from the planar surfaces of a $0.01V_f$ composite, $4\mu\text{m}$ hydroxyapatite particles and a $0.01V_f$ - $0.2V_{HA}$ hybrid composite over the $1400\text{-}400\text{cm}^{-1}$ wavenumber range showing the overlapping of HA and PLA bands in the hybrid composite spectrum.315
- Figure 8.3.29. Comparison of FTIR spectra obtained after the immersion of $0.2V_{HA}$ composites in c-SBF for 24, 72, 120, 168 and 336 hours over the a) $4000\text{-}400\text{cm}^{-1}$ and b) $1400\text{-}400\text{cm}^{-1}$ wavenumber ranges.317
- Figure 8.3.30. Comparison of FTIR spectra obtained after the immersion of $0.01V_f$ composites in c-SBF for 24, 72, 120, 168 and 336 hours over the a) $4000\text{-}400\text{cm}^{-1}$ and b) $1400\text{-}400\text{cm}^{-1}$ wavenumber ranges.318
- Figure 8.3.31. Comparison of FTIR spectra obtained after the immersion of $0.01V_f$ - $0.2V_{HA}$ composites in c-SBF for 24, 72, 120, 168 and 336 hours over the a) $4000\text{-}400\text{cm}^{-1}$ and b) $1400\text{-}400\text{cm}^{-1}$ wavenumber ranges.319
- Figure 8.4.1. Comparison between a) Unsized and b) Sized glass fibre surfaces showing the reduction in flaw size severity through the use of a silane surface treatment [Reproduced from Zinck et al. (2001)].320
- Figure 8.4.2. Illustration of the compromised fibre-matrix interface in the $0.15V_f$ - $0.2V_{HA(NHD)}$ samples due to the high HA pre-preg volume fraction ($0.33V_{HA-pp}$) [Modified from Cech et al. (2013)].322
- Figure 8.4.3. Wet weight of PLA and $0.2V_{HA}$ composite over initial 168 hours of immersion in distilled water at 37°C showing increased water absorption due to the presence of HA (standard deviation of PLA $\leq \pm 0.03\%$).325
- Figure 8.4.4. Comparison of media pH during the degradation of different composite configurations over the initial 24 hours of immersion in distilled water at 37°C326

- Figure 8.4.5. Comparison of media pH between 0.2V_{HA} and 3001D PLA samples over 168 hours of degradation in distilled water at 37°C.....326
- Figure 8.4.6. SEM images after 168 hours MG63 cell culture on 0.01V_f-0.2V_{HA} hybrid composites with a) The appearance of surface damage and spherical particles labelled [scale bar = 10µm] and b) Magnified section of isolated area showing hollow/damaged nature of selected particle [scale bar = 2µm].331
- Figure 8.4.7. Comparison between sample wet weight over first 168 hours of degradation between 0.01V_f, 0.01V_f-0.2V_{HA} and 0.2V_{HA} samples with the inclusion of HA in the hybrid composite samples obscuring the decrease in wet weight through fibre dissolution.332
- Figure 8.4.8. Comparison between the accumulative ion release from 0.01V_f and 0.01V_f-0.2V_{HA} composites over the initial 168 hours of degradation showing a marked decrease in the total concentration of Zn²⁺ and increase in (PO₄)³⁻ and Ca²⁺ ions release from the 0.01V_f-0.2V_{HA} hybrid composite.....335
- Figure 8.4.9. Comparison of Zn²⁺ accumulative ionic release and media pH against the immersion period for 0.01V_f and 0.01V_f-0.2V_{HA} samples336
- Figure 8.4.10. Comparison of precipitates from 0.01V_f-0.2V_{HA} and 0.2V_f RCM composites after immersion in c-SBF over the 4000-400cm⁻¹ wavenumber range.338

List of Tables

Chapter 3

| | | |
|--------------|---|----|
| Table 3.1.1. | Typical composition (wt.%) and Ca/P ratio of the hydroxyapatite mineral phase found in bone [Reproduced from Neira (2011) An efficient approach to the synthesis of a calcium phosphate bone cement and its reinforcement by hydroxyapatite crystals of various particle morphologies].45 | 45 |
| Table 3.1.2. | Summary of the three stages encountered during bone remodelling for cortical and cancellous bone [Modified from Boccacini (2007)].47 | 47 |
| Table 3.1.3. | Anisotropic and asymmetric properties of human femoral cortical bone mechanically tested at different axis [Reproduced from Winkelstein (2012) Orthopaedic Biomaterials].59 | 59 |
| Table 3.1.4. | Comparison of mechanical properties collected from the compression testing of human cancellous bone obtained from different anatomical sites [Reproduced from Nahum (2002) Accidental Injury: Biomechanics and Prevention].61 | 61 |
| Table 3.1.5. | Strain rate dependence on the flexural strength and elastic modulus of the frontal and parietal bones of an adult skull [Data from Motherway et al. (2009)].62 | 62 |
| Table 3.1.6. | Summary of different types of complex skull fracture encountered.63 | 63 |
| Table 3.2.1. | Generalised mechanical properties of typical metal and metal alloys used in orthopaedic applications [Reproduced from Yaszemski (2003) and Mow (2005)].72 | 72 |
| Table 3.2.2. | Comparison of material properties between different degradable polymers commonly used in orthopaedic applications [Reproduced from Sultana (2012) Biodegradable Polymer Based Scaffolds for Bone Tissue Engineering, Eglin (2008) Biodegradable Polymeric Materials For Osteosynthesis: Tutorial, and Dumitriu (2001) Polymer Biomaterials, Revised and Expanded].75 | 75 |
| Table 3.2.3. | Comparison of mechanical properties between calcium phosphate ceramic biomaterials and bone [Data from Kokubo et al. (2003), Domb (2011) Biodegradable polymers in clinical use and clinical development and Hench (2013) Introduction to bioceramics].78 | 78 |

| | | |
|------------------|---|-----|
| Table 3.2.4. | Typical physical and mechanical properties of bone cements [Reproduced from Yaszemski (2003)]. | 79 |
| Table 3.2.5. | Compositional comparison between commercially available Bioglass [®] 45S5, BonAlive [™] and StronBone [®] products as well as the 13-93 glass composition [Data from Jones & Clare (2012) and Hench (2012)]. | 82 |
| Table 3.2.6. | Material properties of Bioglass [®] 45S5 [Data from Jones & Clare (2012)]. | 83 |
| Table 3.2.7. | Comparison of mechanical properties between commercially available glass-ceramic materials [Data from Holand & Beall (2012)]. | 84 |
| Table 3.2.8. | Description of different composite designs [Data from Gurdal et al. (1999)]. | 86 |
| Table 3.2.9. | Examples of different composites from the literature and those commercially available for use as orthopaedic fracture fixation plates, pins and screws. | 92 |
| Table 3.4.1. | Common modifier oxides (MOs) used in phosphate glass compositions showing their atomic weight, ionic radius and charge-to-size ratio (arranged by increasing ionic radius). | 103 |
| Table 3.4.2. | Description of various phosphate glass structures and network characteristics showing the P ₂ O ₅ content, Q ⁱ terminology and structure. | 104 |
| Table 3.4.3. | Potential modifier cations for PG compositions aimed at bone tissue regeneration. | 110 |
| Table 3.4.4. | Ternary and quaternary glass compositions with alternative MOs suited for bone regenerative applications showing the molar tested by various authors. | 110 |
| Chapter 4 | | |
| Table 4.1.1. | Vibrational modes and corresponding frequencies of a CO ₂ molecule found from FTIR analysis [Data from Smith (2011) Fundamentals of Fourier Transform Infrared Spectroscopy, Second Edition]. | 127 |
| Chapter 5 | | |
| Table 5.1.1. | Summary of techniques typically employed in the characterisation of glasses intended for bone tissue regenerative applications. | 133 |
| Table 5.2.1. | Data collection and media replacement during 1008 hour dissolution of CorGlaes [®] Pure 107 disks in distilled water at 37°C. | 139 |
| Table 5.2.2. | Comparison of ionic concentrations between SBF-K9, c-SBF and human blood plasma [Reproduced from Kokubo et al. (2003)]. | 141 |

| | | |
|--------------|--|-----|
| Table 5.2.3. | Reagent chemicals for preparing 1 litre of corrected simulated body fluid (c-SBF) [Reproduced from Chavan et al. (2010)]..... | 142 |
| Table 5.2.4. | Reagents for preparing 1 litre of HEPES saline solution..... | 145 |
| Table 5.2.5. | Reagents for the preparing 1 litre of Versene solution. | 145 |
| Table 5.2.6. | Reagents used in preparation of 262.5 ml of an antibiotic mix solution.... | 146 |
| Table 5.2.7. | Supplements used to produce 565ml of completed Dulbecco's Modified Eagles Medium (CDMEM)..... | 147 |
| Table 5.2.8. | MTT assay of CorGlaes [®] Pure 107 disks dissolution extracts..... | 149 |
| Table 5.2.9. | Steps describing the Live/Dead [®] stain of MG63 cells cultured on the surface of CorGlaes [®] Pure 107 disks..... | 151 |
| Table 5.3.1. | Assignments of spectral features identified from the CorGlaes [®] Pure 107 FTIR spectrum over the 1400-400cm ⁻¹ wavenumber range to the corresponding phosphate structural features..... | 154 |
| Table 5.4.1. | Comparison of the thermal properties and thermal processing windows (PWs) of different metaphosphate, polyphosphate and pyrophosphate glasses intended for biomedical applications..... | 167 |

Chapter 6

| | | |
|--------------|--|-----|
| Table 6.2.1. | Procedure for the silane treatment of fibres as described by Khan et al. (2011)..... | 191 |
| Table 6.2.2. | Ionic concentrations of acellular DMEM cell culture media, c-SBF and PBS [Data from Kokubo et al. (2003) and Lutišanová et al. (2011)]. | 192 |
| Table 6.3.1. | Thermal properties of CorGlaes [®] Pure 107 fibres. | 197 |
| Table 6.3.2. | Assignments of spectral features identified in the Raman spectrum of the CorGlaes [®] Pure 107 fibres to the phosphate structural features. | 198 |
| Table 6.4.1. | Comparison of phosphate glass fibre diameters used as reinforcing agents in polymer composite devices intended for orthopaedic applications. | 210 |
| Table 6.4.2. | Variation in tensile modulus (Eqn 6.2.2) with lower, average and upper range of fibre diameters (section 6.3.4) with the maximum tensile force (0.288N) recorded during the tensile testing of CorGlaes [®] Pure 107 fibres. | 213 |

Chapter 7

| | | |
|--------------|---|-----|
| Table 7.2.1. | Manufacturing specifications of CorGlaes [®] Pure 107-PLA composites. ... | 228 |
| Table 7.2.2. | Immersion period and sample data during degradation of composite and control samples over 1008 hours in distilled water at 37°C. | 231 |

| | | |
|--------------|--|-----|
| Table 7.3.1. | Comparison of fibre anisotropy in UD and RCM fibre pre-pregs as defined by the primary orientation and coherency of their alignment using MATLAB control images and ImageJ [®] software. | 235 |
| Table 7.4.1. | Comparison of average sample toughness based on the area under the stress-strain plots recorded for each type of composite and control sample shown in Figure 7.3.4. | 256 |

Chapter 8

| | | |
|--------------|--|-----|
| Table 8.2.1. | Specifications for precursor materials used in the manufacture of CorGlaes [®] Pure 107 hybrid composites with HA filler. | 281 |
| Table 8.2.2. | Specifications for pre-preg and matrix phases of CorGlaes [®] Pure 107 composites with HA filler. | 282 |
| Table 8.2.3. | Specifications for fibre pre-pregs and matrix precursor materials used for the manufacturing of CorGlaes [®] Pure 107 hybrid composites. | 284 |
| Table 8.2.4. | Weight and number of precursor sheets used in the manufacture of CorGlaes [®] Pure 107 composites. | 284 |
| Table 8.2.5. | Reagent chemicals involved in preparation of CCE cell fixative solution. | 286 |
| Table 8.2.6. | Reagent chemicals used in the preparation of the Coomassie stain. | 287 |
| Table 8.2.7. | Procedure for Coomassie staining of cells cultured on CorGlaes [®] Pure 107 composite samples. | 287 |

Appendix A

| | | |
|------------|--|-----|
| Table A.1. | Mechanical properties of the different composite configurations manufactured in chapter 7. | 351 |
| Table A.2. | Mechanical properties of the different modified composite configurations manufactured in chapter 8. | 351 |

Nomenclature

| | |
|-------------------|--|
| A | Sample surface area |
| A_f | Fibre cross-sectional area |
| b | Specimen width |
| c | Average indent crack length |
| c_{flaw} | Flaw depth |
| C_g | Atomic packing density |
| d | Average indent diagonal length |
| D_r | Dissolution rate |
| E | Elastic modulus |
| E_1 | Longitudinal (primary) elastic modulus |
| E_{comp} | Composite elastic modulus |
| E_f | Fibre tensile modulus |
| E_m | Matrix modulus |
| F | Maximum load |
| F_f | Fibre maximum tensile force |
| h | Specimen thickness |
| H | Sample hardness |
| H_v | Vickers hardness |
| i | i^{th} tensile strength value |
| IFFS | Interfacial shear stress |
| k | System compliance factor |
| K_{IC} | Fracture toughness |

| | |
|-------------|--|
| k_{sp} | Solubility product constant |
| L | Specimen span |
| L_f | Fibre gauge length |
| m | Weibull modulus |
| MFI | Melt flow index |
| MO | Modifier oxide |
| N | Total number of specimens tested |
| n | An integer |
| n_0 | Correction factor depending upon composite fibre orientation |
| n_1 | Correction factor dependent upon fibre length |
| OD_{570e} | Mean optical density measured for each dissolution extract |
| OD_{570b} | Mean optical density value of the positive control media |
| P | Indentation load |
| P_F | Probability of failure |
| PG | Phosphate glass |
| PGF | Phosphate glass fibre |
| pm | Picometre |
| PW | Processing window |
| q | Weight loss |
| Q^i | Terminology used to describe phosphate structural groups |
| R | Fibre radius |
| RCM | Random continuous mat |
| SA | Surface area |
| s' | Beam mid-point deflection ¹ |

| | |
|-------------|---|
| s'' | Beam mid-point deflection ² |
| t | Time |
| T_g | Glass transition temperature |
| T_{lq} | Liquidus temperature |
| T_m | Melt temperature |
| T_{oc} | Crystallisation onset temperature |
| T_p | Crystallisation peak temperature |
| UD | Unidirectional |
| U_m | Total bonding energy |
| V | Volume |
| V_f | Composite fibre volume fraction |
| V_{HA} | Composite HA volume fraction |
| V_{HA-m} | Composite matrix sheet HA volume fraction |
| V_{HA-pp} | Composite fibre pre-preg HA volume fraction |
| W | Wavenumber |
| w_a | Sample weight in air |
| w_c | Composite weight |
| w_f | Composite fibre weight |
| W_f | Composite fibre weight fraction |
| W_{HA} | Composite HA weight fraction |
| w_{HA} | Composite HA weight |
| W_m | Composite matrix weight fraction |
| w_m | Composite matrix weight |
| w_o | Initial sample weight |

| | |
|-----------------|--|
| w_s | Sample weight suspended in media |
| w_t | Sample weight at time t_x |
| $Y(c, R)$ | Crack geometry constant |
| δ | Non-dimensional indenter geometry constant |
| ΔF | Differential between F' and F'' corresponding to s' and s'' |
| ΔF_B | Difference in force corresponding to the selected strain limits |
| ΔL_B | Difference in cross-head displacement corresponding to the strain limits |
| Δs | Differential between deflections s' and s'' |
| ϵ_f | Fibre strain at failure |
| ϵ_f' | Flexural strain ¹ |
| ϵ_f'' | Flexural strain ² |
| ϵ_m | Matrix strain at failure |
| ρ | Sample density |
| ρ_f | Fibre density |
| ρ_{HA} | HA density |
| ρ_L | Immersion media density |
| ρ_m | Matrix density |
| σ | Tensile strength |
| σ_0 | Normalising stress |
| σ_f | Fibre tensile strength |
| σ_{comp} | Composite flexural strength |
| τ_b | Interfacial shear bond strength |

1 Giltech Ltd

Giltech Ltd are a Scottish company (based in Ayr) focused on the development of medical devices using their range of haemocompatible, biodegradable controlled release technologies for applications such as wound management, urology as well as vascular grafting. These include a range of soluble phosphate glasses, alginates and patented delivery methods that have been previously developed into products such as its alginate based Sorbsan[®] wound care management system and infection resistant Silverline[®] urinary catheters ^[1].

1.1 CorGlaes[®] Technology

CorGlaes[®] is Giltech's range of soluble phosphate based glasses that incorporate active metal ions into their composition to tailor the dissolution rates and ion release profiles. These glasses are typically manufactured according to application specific compositions and can be supplied in a range of material formats (e.g. powder, fibres). Furthermore, previous *in vitro* results using human and animal cell lines on different CorGlaes[®] compositions have also demonstrated the potential applicability of this technology platform as an orthopaedic biomaterial ^[1].

1.1.1 CorGlaes[®] Pure 107

CorGlaes[®] Pure 107 is a quinary composition of ultraphosphate glass development by Giltech Ltd that substitutes specific concentrations (mol%) of magnesium (Mg) and zinc (Zn) into the initial phosphate (P), calcium (Ca) and sodium (Na) CorGlaes[®] system. This glass was selected for this project by Giltech Ltd with a view to its application as either a standalone biomedical implant or in its fibre form as a composite reinforcing agent.

Due to the commercial confidentiality of the project, the precise composition of the CorGlaes[®] Pure 107 glass was not disclosed and consequently all conclusions based on the obtained results have been developed with this restriction in mind. However it was confirmed that the CorGlaes[®] Pure 107 composition contained 55 mol% P₂O₅ as well as low concentrations (mol%) of zinc and sodium. Additionally, the precursor compounds used in the manufacturing of the CorGlaes[®] Pure 107 glass are assumed to have been composed of those typically used in phosphate glass manufacturing (i.e. P₂O₅, CaO, Na₂O, MgO and ZnO).

2 Introduction

The reconstruction of cranial defects typically involves the use of auto- or allograft bone, titanium or PMMA based materials to improve neurological function, protect cerebral tissue and provide cosmetic restoration. However each material possesses specific disadvantages and the occurrence of post-operative infection at the treatment site is a major threat to the success of the implant ^[2, 3].

Combined with their high radiolucency, specific moduli and impact strengths, pre-formed fibre reinforced composites are viewed as an attractive alternative to current cranioplasty plate materials. Accordingly, multi-structured dense-porous composite implant designs such as those using non-resorbable E-glass fibres, bioactive glass particles and a bisphol-a-glycidyl methacrylate/triethyleneglycoldi-methacrylate (pBisGMA-pTEGDMA) matrix have been previously investigated by Aitasalo et al. (2014) for cranioplasty plate applications. This clinical study found that all patients treated with these composites displayed no inflammatory reactions or acute systematic toxicities with good functionality and aesthetic results ^[4, 5].

Given the issues with existing materials and emphasis on infectious prevention, bioactive phosphate glass fibre (PGF) reinforced composites could be advantageous for cranioplasty plate materials. The use of a degradable matrix material along with the antibacterial properties of specific phosphate glass compositions could subsequently allow for the manufacturing of degradable cranioplasty implant materials that facilitate the complete restoration of the skull defect with the host's native bone tissue. Consequently the development of a dense PGF reinforced polymer composite with mechanical properties similar to those of the cranial bones was intended to provide an initial investigation into the suitability of these materials for cranioplasty plate applications. Such composites may be pre-formed to the defect contours and could be bonded to a porous composite foam system, mimicking the structure of cranial bone. This design would be similar to that tested by Aitasalo et al. (2014) with the porous foam scaffold allowing for bone tissue ingrowth whilst the dense PGF polymer composite exterior provided both fixation and mechanical protection (Figure 2.1.1) ^[4, 6].

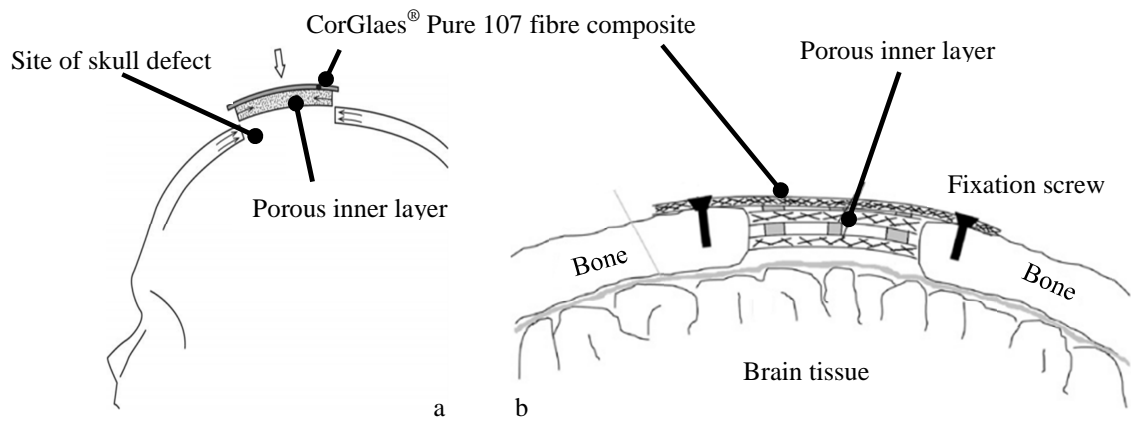


Figure 2.1.1. a) Illustration of potential CorGlaes® Pure 107 multi-component composite being applied as a cranioplasty implant material [Modified from Aitasalo et al. (2014)] and b) Magnified section showing the position of the implant in relation to the surrounding physiological tissue [Modified from Nganga et al. (2012)].

Accordingly the development of a PGF composite as a potential cranioplasty plate component was conducted through a series of iterative steps intended to sequentially characterise the selected glass composition and then the properties of the resulting composite materials.

Chapter 3 of this thesis presents a review of the literature concerning the general physiology, structure and mechanical properties of bone with additional information on the specific properties of the skull's cranial bones. This continues with a breakdown of the biomaterials typically used in orthopaedic applications as well as an overview of the general principles behind composite materials. These concepts are carried forward as the current cranioplasty plate materials are reviewed before the fundamentals and compositional evolution of phosphate glasses (PGs) and PGF composites for hard tissue regeneration are examined. The basic mode of operation behind key analytical chemistry techniques related to this work is then reviewed in chapter 4. The subsequent development of the CorGlaes® Pure 107 composite is then broken down throughout chapters 5 to 8 that each contains their own materials and methods, results, discussion and conclusions.

To expand on this, the structural characterisation along with the mechanical and *in vitro* properties of the CorGlaes® Pure 107 glass and applicability of its fibres as a composite reinforcing agent are investigated in chapters 5 and 6 respectively. This is carried into chapter 7 where the manufacture and testing of CorGlaes® Pure 107 composites through different interdisciplinary techniques is conducted to assess its initial and degenerative

properties. Modification and optimisation of the initial composite configuration based on the previous data obtained from chapter 7 is reported in chapter 8 whilst an overall discussion and conclusion on the project work is found in chapters 9 and 10 respectively. Lastly the future direction of this work is outlined in chapter 11.

2.1 Aims of Thesis

The main aims of this thesis was to develop and investigate a degradable PGF reinforced composite as a potential cranioplasty plate implant component using the CorGlaes[®] Pure 107 composition of phosphate based glass.

Accordingly the aims of this project were:

1. To investigate the suitability of the CorGlaes[®] Pure 107 phosphate glass composition as a biomaterial.
2. To mechanically, chemically and biologically characterise the CorGlaes[®] Pure 107 fibres and evaluate their potential as a composite reinforcing agent.
3. To develop and examine different CorGlaes[®] Pure 107 fibre reinforced polymer composite configurations to assess their potential as a part of a degradable cranioplasty plate.

It should also be noted that the characterisation and analysis performed here was composed of the general multidisciplinary techniques typically employed at the laboratory scale for the testing of glass and biomedical composites as discussed by Mustafa & Tanner (2011) and was not intended to reach *in vivo* testing during this project ^[7].

Furthermore as an initial design criterion, it was decided that the PGF composite plate must aim to retain at least 80% of its initial mechanical properties over a six week degradation period in order to satisfy the mechanical requirements of its intended application. However this may be later refined and extended given the reduced rate of skeletal regeneration in the skull compared to other anatomical sites ^[8-10].

3 Literature Review

3.1 Bone

3.1.1 Definition and Function

Composites are a group of materials composed of two or more components which have characteristics and properties derived from its constituent materials. Bone tissue is an example of a bioceramic composite and is constructed of an organic matrix reinforced by an inorganic ceramic phase. This tissue is found in the vertebrate endoskeleton (Figure 3.1.1) and enables various mechanical as well as physiological processes in the body. This includes crucial metabolic activities (such as the supply of red blood cells - haematopoiesis) and mineral homeostasis by acting as a reservoir for the body's salts. Meanwhile the high mechanical properties of bone provide structural support, attachment sites for muscles (that permit skeletal locomotion) and grant protection to the body's internal organs. Furthermore the dynamically responsive nature of bone allows its structure to be adapted according to the mechanical demands of its loading environment and continually repair itself through a naturally occurring remodelling process ^[11-13].

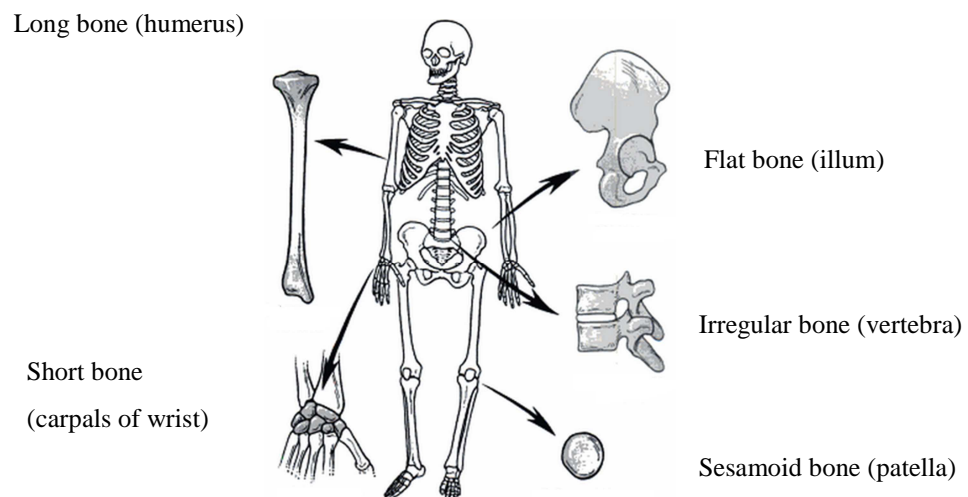


Figure 3.1.1. Illustration of human skeleton with examples of different bone types (long, short, flat, irregular and sesamoid) [Modified from Hamill (2006) Biomechanical Basis of Human Movement].

A complete human skeletal system is composed of over two hundred unique bones with a diverse range of geometrical and structural architectures. These are dependent upon

various factors including its anatomical site (due to the associated mechanical loading), age, sex or required physiological function and are generally classified according to their type or location (Figure 3.1.1) ^[11-13].

3.1.2 Composition and Physiology

3.1.2.1 Composition

As mentioned in section 3.1.1, bone is often considered as a composite consisting of an organic matrix (composed mainly of collagen) reinforced by an inorganic ceramic phase of bone mineral. However despite the various structural organisations of this tissue throughout the body, its fundamental composition remains relatively constant.

Orientated type I collagen fibrils account for $\approx 90\%$ of bone's organic matrix and provide flexibility to the tissue with the remaining matrix contents assigned to non-collagenous proteins such as fibronectin, osteopontin, osteocalcin and bone sialoproteins. Analysis of the mineral phase shows that it constitutes 60-70% of bone's wet weight and is a reservoir for the human body's calcium, phosphorous, sodium and magnesium content. These are stored as imperfect crystalline structures, mainly in the form of 20-80nm long, 2-5nm thick plate-like crystals of non-stoichiometric hydroxyapatite ($\text{Ca}_{10}(\text{PO}_4)_6(\text{OH})_2$) (Table 3.1.1) and are responsible for providing the majority of bone's stiffness, hardness and strength. Additionally, the inclusion of 5-8 % water in bone is considered to play a crucial role in its viscoelastic properties and facilitates nutrient transport throughout the tissue ^[12, 14, 15].

Table 3.1.1. Typical composition (wt.%) and Ca/P ratio of the hydroxyapatite mineral phase found in bone [Reproduced from Neira (2011) An efficient approach to the synthesis of a calcium phosphate bone cement and its reinforcement by hydroxyapatite crystals of various particle morphologies].

| wt.% | | | | | | | | | | | Ca/P |
|------------------|--------------------|--------------------|---------------|--------------|------------------|------------------|---------------|--------------|-----------------------------|----------------------|------|
| Ca^{2+} | PO_4^{3-} | CO_3^{2-} | Na^+ | K^+ | Mg^{2+} | Sr^{2+} | Cl^- | F^- | $\text{P}_2\text{O}_7^{4-}$ | H_2O | |
| 36.6 | 17.1 | 4.8 | 1.0 | 0.07 | 0.6 | 0.05 | 0.1 | 0.1 | 0.07 | 10 | 1.65 |

3.1.2.2 Bone Cells

Despite only accounting for approximately 2% of its organic matrix the cells in bone are vital to its growth and repair. These consist of the four different cell types described below:

Osteoprogenitor cells - Also known as osteogenic cells, these are mesenchymal stem cells (MSC's) with the ability to differentiate into osteoblasts, chondroblasts, bone marrow stromal cells or fibroblasts (depending on the local stimuli). These cells are located within the periosteum as well as the endosteum membranes of the bone tissue and are capable of being reactivated during bone fracture repair ^[16, 17].

Osteoblasts - Derived from osteoprogenitor cells, these large polygonal cells are critical to the growth and repair of bone. Osteoblast cells secrete type I collagen and the glycosaminoglycan's necessary to form the organic matrix of bone as well as producing the previously mentioned non-collagenous proteins. These cells also facilitate the mineralisation process and are capable of producing receptors involved in the differentiation of osteoclasts ^[16, 17].

Osteocytes - These cells make up 90% of all cells in bone and are involved in the cell signalling processes that facilitate maintenance of the bone matrix and metabolic activities (through the bone remodelling process). Osteocytes are derived from mature osteoblasts that have become entrapped during bone deposition and enclosed in a calcified cavity of bone matrix during remodelling (known as a lacuna). These entrapped cells are unable to produce bone matrix and as a result differentiate into osteocytes ^[16-19].

Osteoclasts - Large multinucleated cells responsible for the resorption of mineralised matrix through the release of bone-resorbing acids as well as enzymes for collagen resorption. Osteoclasts are derived from the fusion of multiple monocyte/macrophage cells into a single cell and are regulated by hormones such as calcitonin and growth factors including interleukin 6 (IL-6). These cells reside in resorption pits and facilitate the release of mineral salts from the calcified bone matrix to support mineral homeostasis ^[16-18].

3.1.2.3 Bone Remodelling

The concept of modern bone remodelling is largely attributed to the work of Frost (1961) and is routinely described as a continually occurring physiological process where old bone is replaced with new tissue through a series of coordinated interactions between different

cells. This process maintains the mechanical strength of bone (through the repair of cracks) whilst allowing it to adapt its architecture, mass and density to meet the local mechanical loading regime (as described by Wolff's Law). Bone remodelling also serves to control mineral homeostasis and is regulated from both systematic and local factors as well as mechanical stimuli. However the precise control mechanisms behind the remodelling of bone remain ambiguous ^[17, 20-22].

The remodelling of bone occurs across the skeleton at structures referred to as bone multicellular units (BMUs). These are primarily composed of osteoclasts and osteoblasts which facilitate the resorption and formation of bone respectively. In cortical bone these BMUs form a 150-200 μm diameter cylindrical cutting cone (also known as a Howship's lacunae) that burrow through the mineralised tissue at a rate of 20-40 $\mu\text{m day}^{-1}$. In cancellous bone the remodelling occurs through the formation of 40-60 μm deep trenches as osteoclasts travel across individual trabeculae at rates of up to 25 $\mu\text{m day}^{-1}$. The remodelling process at these BMUs for cortical and cancellous bone can be summarised by the 3 phases described in Table 3.1.2 and is illustrated in Figure 3.1.2 ^[20, 22-25].

Table 3.1.2. Summary of the three stages encountered during bone remodelling for cortical and cancellous bone [Modified from Boccacini (2007)].

| Phase | Description |
|---------------------------|--|
| Activation/ Resorption | Initiates when partially differentiated pre-osteoclasts migrate to the bone surface and form multinucleated osteoclast cells that remove the mineralised component (i.e. hydroxyapatite). This phase can last for approximately two weeks. |
| Reversal | Mononuclear cells prepare the surface for new bone deposition by removing the resorption remnants and provide signals for the differentiation/migration of osteoblast cells. This phase can last four to five weeks. |
| Formation | Osteoblasts deposit new bone matrix in the region between old and new bone forming a cement line. This matrix material is then calcified at the mineralisation front until the resorbed area is completely replaced by new bone tissue. This phase can take up to four months to be completed. |

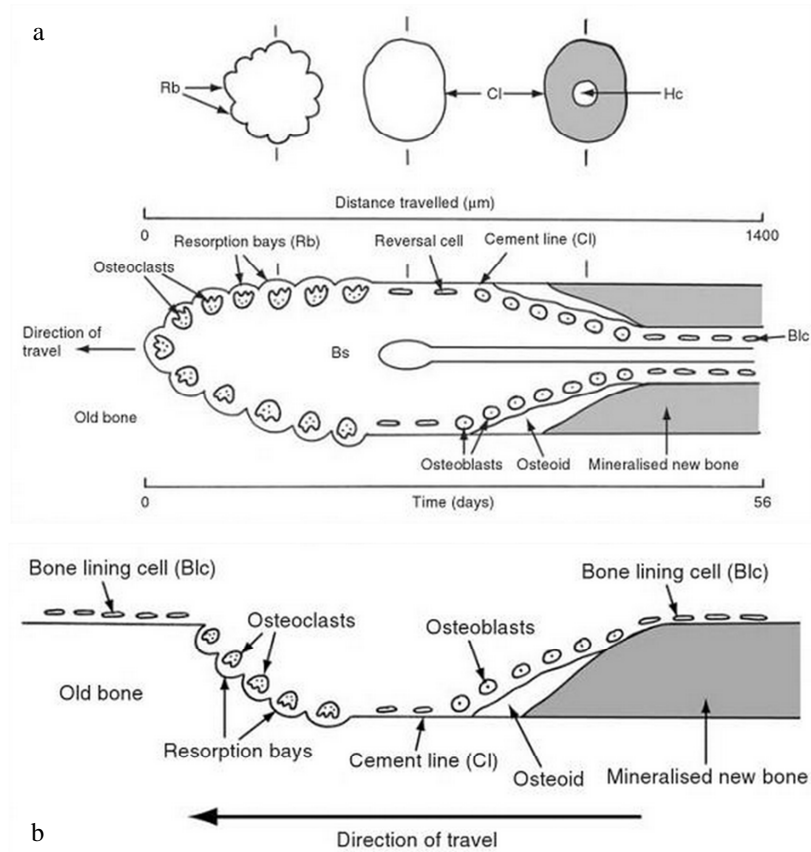


Figure 3.1.2. Illustration of a) Osteonal remodelling of cortical bone showing osteoclast resorption at the cone front along with the bone forming osteoblast cells. The blood supply (Bs) at the centre of the new Haversian canal and distance travelled are also shown over a 56 day period and b) Remodelling of cancellous bone showing the trench formed across the trabeculae [Reproduced from Brickley (2010) *The Bioarchaeology of Metabolic Bone Disease*].

In an adult skeleton the rate of bone resorption and formation are balanced in order to maintain a constant bone mass with studies estimating that the entire mass of an adult skeleton is replaced approximately every ten years. However irreversible reductions in a body's total bone mass can occur from pathological conditions such as osteopenia or osteoporosis ^[20-22].

3.1.3 Structure of Bone

Bone is a hierarchically structured composite that displays various degrees of organisational architecture across the macro- to nanoscale. This is based on the mechanical and metabolic optimisation of the tissue that has been classically characterised over

different levels of hierarchy. However the number of levels defining this hierarchy has typically been user-defined with examples of four (Currey et al. 2012) and seven levels (Weiner & Wagner, 1998) commonly reported (Figure 3.1.3) ^[19, 26-28].

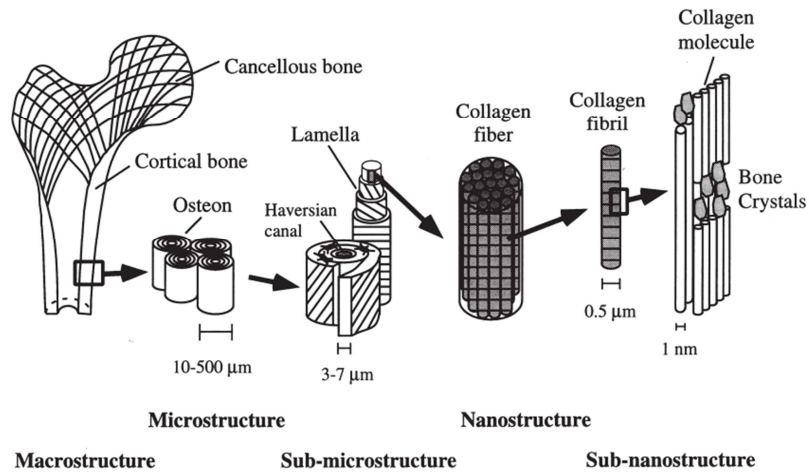


Figure 3.1.3. Seven level hierarchy structure found in the diaphysis of the long bone across the macro- to nanometre scale showing the diversity in structural arrangement [Reproduced from Rho et al. (1998)].

3.1.3.1 Macrostructure

At the macroscopic scale the structure of mature bone tissue is considered to be composed of either a high density, high modulus tissue (cortical) or high porosity mechanically weak structure (cancellous) with the proportions of each distinct phase dependent upon the bones function.

Cortical bone (also known as compact bone) is mainly found in the long bones (e.g. femur, tibia, radius, ulna) as well as the flat bones (e.g. ribs and skull) and is the primary source of mechanical support in the skeleton (Figure 3.1.4). Cortical bone makes up approximately 80 wt.% of a human's total skeletal mass and forms the bone's outer shell with greater concentrations found at anatomical sites subjected to significant mechanical loading. This shell surrounds the bone marrow contained in the medullary canal of the diaphysis with variations in cortical bone concentrations across the epiphysis reflecting the distribution of mechanical loading throughout the long bone (Figure 3.1.5) ^[12, 29-32].

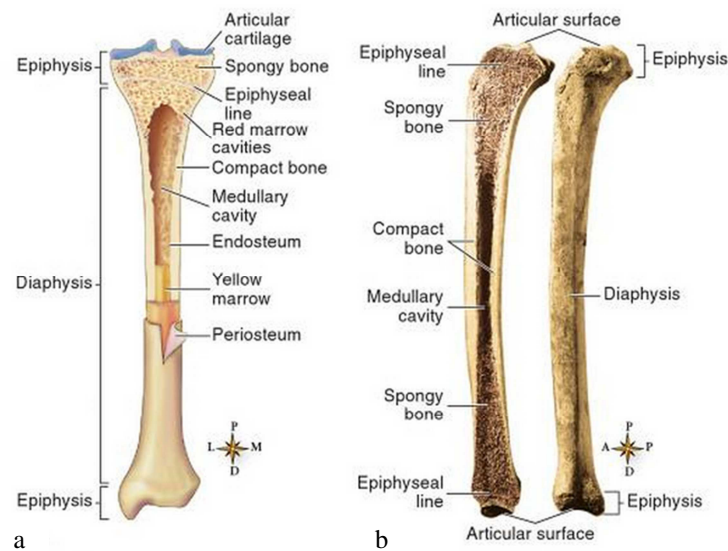


Figure 3.1.4. Illustration of a) Partial frontal section of tibia (long bone) with the different regions and structural components labelled and b) Sagittal section of the tibia (lateral view) showing distribution of cortical and cancellous bone throughout the tissue [Reproduced from Patton (2014) Survival Guide for Anatomy & Physiology].

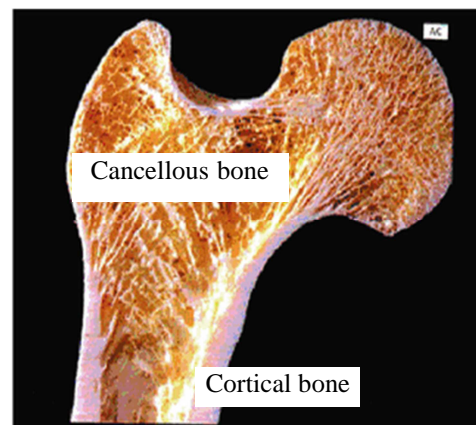


Figure 3.1.5. Sagittal section through a long bone showing the outer shell of cortical bone with concentrations of cancellous bone at the epiphyses [Reproduced from Khurana (2009) Bone Pathology].

Cancellous bone (also known as trabecular or spongy bone) can be idealised as an organised open-cell lattice of short $200\mu\text{m}$ thick, $1000\mu\text{m}$ long tubular struts or plates of bone matrix called trabeculae that are adjacently spaced by $300\text{-}1500\mu\text{m}$ (apparent density $\approx 0.3 \text{ g cm}^{-3}$). This bone structure is primarily concentrated in the epiphyses and metaphyses of long bones as well as in flat and irregular shaped bones such as the vertebrae (Figure 3.1.1). The high porosity of trabecular bone (50-90 vol.%) subsequently provides a high surface contact area for bone marrow, blood vessels and connective tissues

that facilitate its role in haematopoiesis and mineral homeostasis. However due to this porosity, cancellous bone possess a severely reduced compressive strength compared to cortical bone and is consequently found at anatomical sites generally free from any significant mechanical loading. Yet this internal structure does allow for the absorbance of compressive energies and subsequent distribution of stresses throughout the bone to occur such as at areas below the surface of joints ^[12, 29, 30].

3.1.3.2 Microstructure

At the microstructural level (i.e. 10-500 μ m) the exterior and interior surfaces of bone are covered by thin membranes involved in the vascularisation, growth and remodelling of bone (Figure 3.1.6) ^[32].

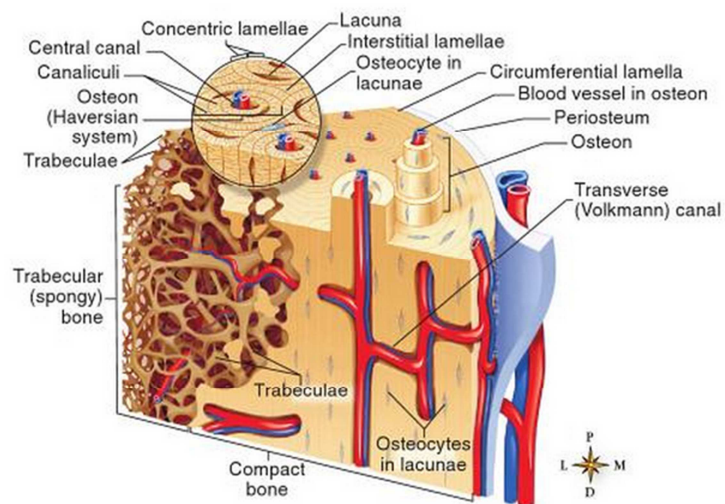


Figure 3.1.6. Internal microscopic structure of the diaphysis from a long bone showing the cortical and cancellous regions as well as the osteons found in the cortical bone tissue [Reproduced from Patton (2013) Survival Guide for Anatomy & Physiology].

The periosteum is a highly vascularised dense fibrous membrane of connective tissue that covers the exterior surfaces of bone (except at sites near joints) and acts as a transitional layer between the bone and overlying soft tissue/musculature (Figure 3.1.6). This layer contains blood vessels and nerves as well as the MSCs that are involved in bone growth whilst the interior surfaces are lined by a thin membrane called the endosteum that contains osteoprogenitor cells (section 3.1.2.2) ^[12].

Microstructurally the basic repeating unit of cortical bone is a cylindrical element called an osteon or Haversian system (Figure 3.1.6) which is typically orientated along their long axis according to the principal stress direction. These structural units are composed of a 20-100 μm diameter central canal (known as a Haversian canal) that houses a blood vessel as well as nerve fibres. Each Haversian canal is successively surrounded by concentric 3-7 μm thick layers of mineralised bone matrix (called lamella) that are separated by 0.1 μm thick sheets of interlamellar cement (Figure 3.1.7). These Haversian systems are consequently linked by a series of smaller blood vessels (called Volkmanns canals) that occur perpendicularly to the osteons and originate from either the periosteum or endosteum to create a network of blood vessels throughout the bone (Figure 3.1.6) ^[12, 14, 25].

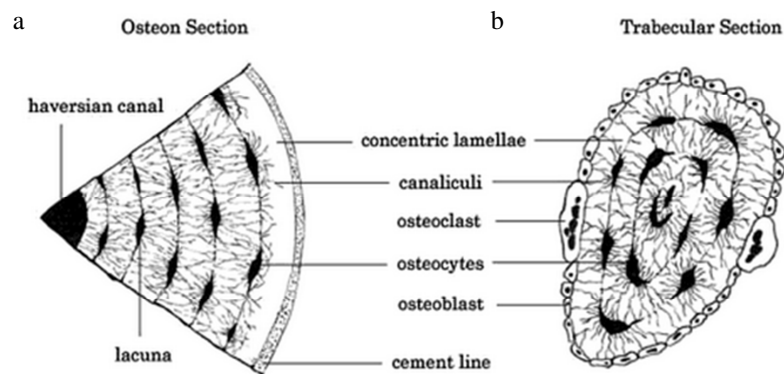


Figure 3.1.7. Illustration of a) Transverse section of an osteon in cortical bone and b) Individual trabeculae of cancellous bone at the microstructural level [Reproduced from Belinha (2014)].

Alternatively the trabeculae of cancellous bone are composed of concentric lamellae that develop into disk shaped sections and form its branched open structural network. Similar to the osteons of cortical bone, these trabeculae can be preferentially oriented along the principal stress direction (in areas such as the vertebrae) or isotropically distributed depending on the mechanical loading regime. However these trabeculae structures do not display the same osteonal units or interstitial mechanisms (i.e. Haversian canals) as found in cortical bone (Figure 3.1.7). As a result, cancellous bone is typically vascularised directly from the surrounding haemopoietic tissue ^[12, 14, 25].

3.1.3.3 Sub-microstructure

Each layer of osteonic lamellae surrounding the Haversian canal of cortical bone is considered to be composed of orientated arrays of mineralised collagen fibres. Yet concepts behind the precise arrangements and mechanisms that stimulate fibre orientation between lamella remain controversial with various models adopted based on the interpretation of experimental data (e.g. microscopically, X-ray diffraction) ^[11, 33].

Based on early work using polarised light microscopy (Gebhardt, 1905; Ascenzi & Bonnucci, 1967) the variation in dark, bright and dark/bright fields was believed to represent the presence of three different types of osteons in cortical bone (Figure 3.1.8a). These were classified by the alignment of parallel arrays of collagen fibres in each lamella either longitudinally (dark), transversely (bright) or intermediately (dark/bright) to the long axis of the Haversian canal. This led to the concept of an orthogonal plywood model in the lamella with fibres limited to two orientations that alternated by 90° between each concentric lamella (i.e. longitudinal/transverse) or intermediately composed of both ^[11, 34, 35].

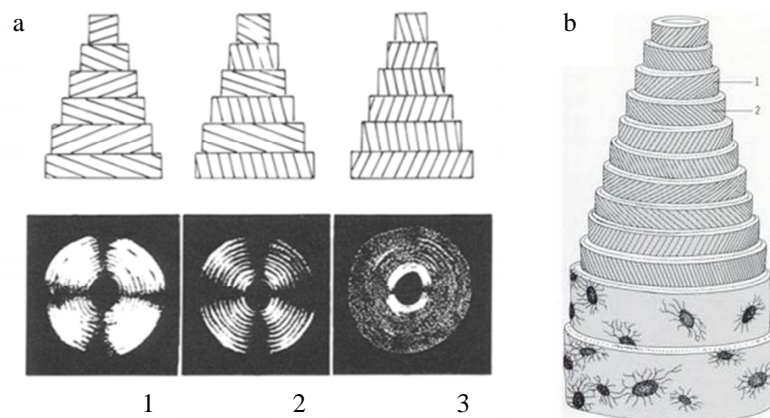


Figure 3.1.8. a) Depiction of three different osteonal types 1) Transversely 2) Longitudinally 3) Intermediately orientated as viewed by polarised light microscopy and the associated osteonal lamella arrays as described by the orthogonal plywood model [Reproduced from Giraud-Guille (1988)] b) Illustration of twisted plywood model showing alternation of fibre orientations between adjacently concentric lamellae. [Reproduced from Adler (2000) Bone Diseases: Macroscopic, Histological, and Radiological Diagnoses of Structural Changes in the Skeleton].

However the use of alternative techniques (e.g. scanning electron microscope) has led to other osteonal models being developed such as the twisted plywood model of collagen fibres as proposed by Giraud-Guille (1988) (Figure 3.1.8). This model depicts the fibres in each lamella as running in a continually spiralling manner around the Haversian canal that are rotated from plane to plane with fibre orientations alternated inversely between each concentric layer. Based on this concept, the three distinct birefringence patterns are attributed to the gradual change in orientation from two distinct structural arrangements as oppose to the three in the orthogonal plywood model. A random orientation of collagen fibres in each lamella has also been proposed with the variation in polarised light attributed to changes in the collagen fibre density instead of alternate orientations (Marotti & Muglia, 1995). Under this model high density and low density fibre lamella were associated with dark and bright bands respectively ^[11, 34, 36].

Although the specific mechanisms behind fibre orientation remain a subject of debate, the mechanical testing of cortical bones has found that sites typically loaded *in vivo* under tension or compression displayed responsive preferential collagen fibre orientations. As a result, discrete areas of longitudinal (tensile) and transverse (compressive) collagen fibre orientations were found in response to the respective loading regimes. This subsequently supports the theory that the mechanical stimulus plays a highly influential role in dictating the collagen fibre alignment throughout cortical bone (Ascenzi & Bonucci, 1967) ^[17, 26, 37].

3.1.3.4 Nanostructural and Sub-nanostructures

The collagen fibres in the lamella of bone are composed of intimately arranged collagen fibril sub-units that are each constructed from the association of multiple 1.5nm diameter, 300nm length tropocollagen molecules (Figure 3.1.9) ^[38, 39]. Tropocollagen is the basic structural unit of collagen and its molecules subsequently consist of three coiled polypeptide chains which, through hydrogen bonding, are structurally arranged as a right handed triple helix. Each tropocollagen molecule is self-assembled with neighbouring molecules into a staggered fibril arrangement with 40nm gaps between the head and tail of each tropocollagen molecule and a 67nm periodicity (due to the 40nm gap and 27nm overlap). These gaps then act as nucleation sites for the formation of $\approx 100 \times 25 \times 2$ nm platelets of hydroxyapatite (HA) that are orientated along the fibrils long axis (Figure 3.1.10) ^[38-40].

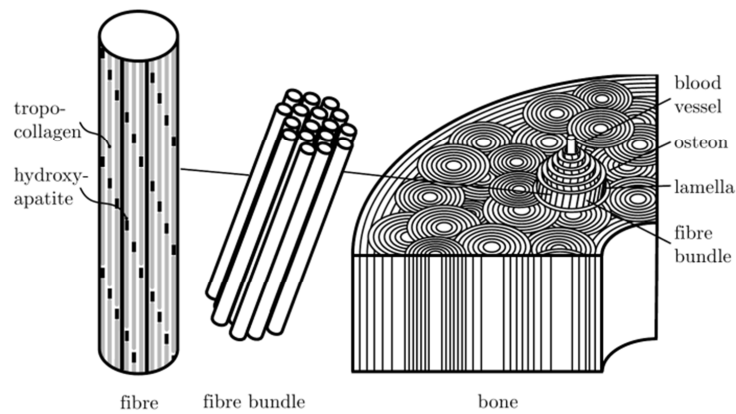


Figure 3.1.9. Nanostructural hierarchy of bone showing the collagen fibre bundles in the osteons of cortical bone to be composed of a single collagen fibre that consists of tropocollagen molecules and hydroxyapatite crystals [Reproduced from Roesler (2007)].

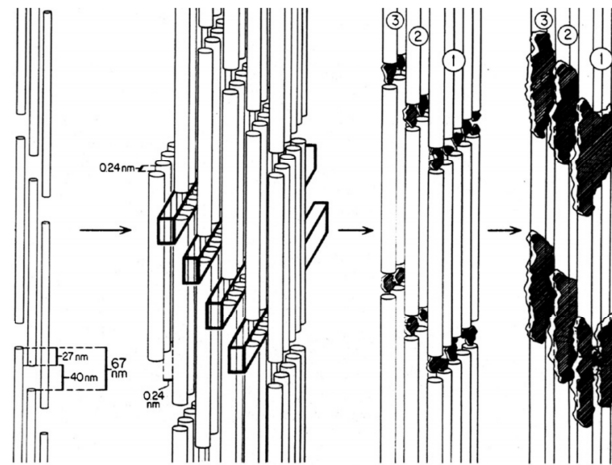


Figure 3.1.10. Sub-nanostructural level of cortical bone showing the staggered arrangement of the tropocollagen molecules and hydroxyapatite crystals in a collagen fibre [Reproduced from Olszta et al. (2007)].

3.1.3.5 Lamellar and Woven Bone

As previously discussed in section 3.1.3.3, the submicroscopic level of mature bone is composed of mineralised lamellar tissue with organised collagen fibres orientated relative to the stress state environment to provide the bone with optimised mechanical properties (i.e. anisotropic). This structure is contrasted by the disorganised irregular collagen fibre arrangement found in woven bone (also known as primary, fibre or reticular bone) that is encountered during embryonic development or during bone fracture repair. The rapid formation of this tissue ($>4\mu\text{m day}^{-1}$) is believed to provide the body with a means of quickly reacting to alterations in the mechanical environment (such as those encountered

during growth). However its disorganised structure and corresponding isotropic properties are unsuitable for efficiently providing long term stability. As a result woven bone is gradually replaced by lamellar bone ($<1\mu\text{m day}^{-1}$) during childhood and is generally not found in the adult skeleton except during the early stages of fracture repair or from certain pathological conditions such as Paget's disease [12, 17, 41].

3.1.4 The Human Skull

3.1.4.1 Anatomy

The skull refers to the osseous framework of the head in the overall skeleton and is composed of 22 irregularly shaped flat bones that make up the facial (splanchnocranium), mandible and cranium sub-divisions of the skull (Figure 3.1.11) [42].

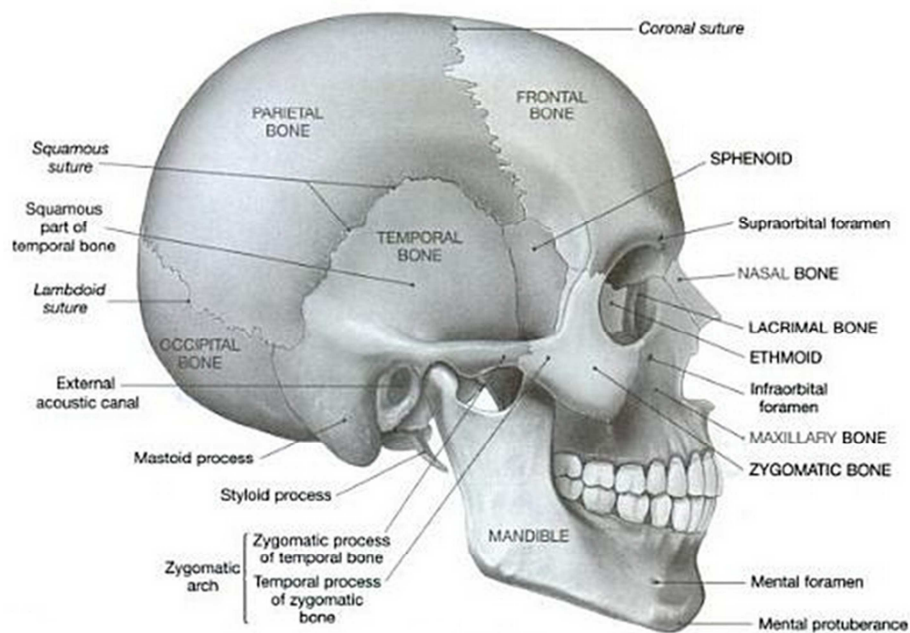


Figure 3.1.11. Illustration of skull (lateral view) showing the bones that make up the cranium, facial and mandible bones [Reproduced from Martini (2007) *Anatomy and Physiology*].

The cranial base and vault designate further sub-groups of the cranium bones which when combined form the cranial vault that surrounds and protects the delicate brain tissue. Also known as the calvarium, it is composed of the frontal, occipital, sphenoid, ethmoid as well as two parietal and two temporal bones, which are fused together by morphologically jagged joints (referred to as sutures). In an adult skeleton these sutures are composed of

dense fibrous tissue with the sagittal, coronal, lambdoidal and squamosal sutures regarded as the major joints of the cranial vault ^[43-45].

3.1.4.2 Structure

At the macroscopic scale, flat bones like the scapula, ribs and those composing the cranial vault are formed as a three layered composite sandwich structure. In the cranial bones this consists of a homogenously structured cancellous bone (known as a diploë) that is situated between upper (ectocranial) and lower (endocranial) tables of dense cortical bone (Figure 3.1.12). This structural organisation provides the high mechanical properties required to protect the brain tissue (from the tables of cortical bone) whilst the porous energy absorbing layer reduces the bone weight without compromising its strength ^[46-48].

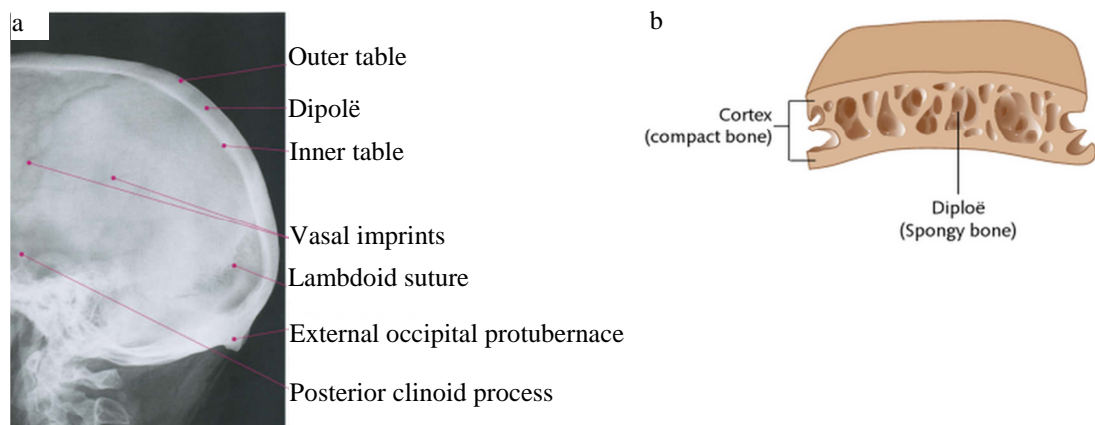


Figure 3.1.12. a) Left lateral view of posterior half of skull showing radiographic features and tri-layered structure of the cranium [Modified from Gallucci (2007) Radiographic Atlas of Skull and Brain Anatomy] and b) Illustration of the basic architecture and sandwich structure of the flat bones (such as those in the cranium) [Reproduced from Orchard & Nation (2014) Cell Structure & Function].

Characterisation of the cranial bones has determined a general thickness $>5\text{mm}$ with the endocranial layer of cortical bone typically possessing a lower thickness and bone density than the ectocranial bone. These properties are believed to stem from the localised stress microenvironments found in the ectocranial layer due to the presence of anchorage sites for masticatory and nuchal musculature. This subsequently imparts areas of highly localised orientations and distinct anisotropy due to the associated mechano-stimulated effects

especially in areas such as the parietal bone where significant muscle attachment sites exist. Such anchorage effects are not encountered at the endocranial layer and consequently imply that the influence of mechanical stimuli plays a significantly diminished role in the remodelling of cranial bones. Yet when considered as a whole element (i.e. as a three layered structure), cranial bone tissue is generally idealised as a linear elastic and isotropic material with acknowledgement of its minor degree of in-plane anisotropy on its outer table ^[46, 49-51].

3.1.5 Mechanical Properties of Bone

3.1.5.1 Overview

The mechanical properties of bone are attributed to its composition (section 3.1.2.1) which, similar to conventional engineering composites, generates its mechanical properties through the reinforcement of a ductile organic matrix with a high modulus ceramic reinforcing phase (Figure 3.1.13). However its mechanical properties are also a conglomerate of the bones microarchitecture, material properties (e.g. mineral density, apparent density) and testing method. Consequently it is general convention to consider the mechanical properties of cortical and cancellous bone as separate entities in order to effectively evaluate their mechanical properties with regards to the dominating factors described. Yet due to these influences it is also often acknowledged that no true value can be considered “correct” for the precise mechanical properties of an entire bone microstructure type and thus mechanical data is typically expressed as a set range of values [33, 49, 52]

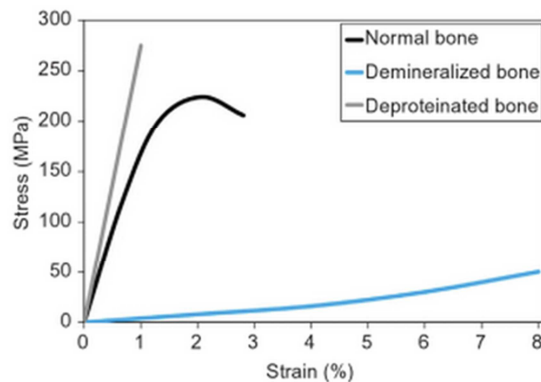


Figure 3.1.13. Contributions from the matrix (collagen) and reinforcing (hydroxyapatite) phases of bone showing the influence from each component on the mechanical properties of normal bone [Reproduced from Burr (2013) Basic and Applied Bone Biology].

3.1.5.2 Cortical Bone

When considering the diaphysis of a long bone (Figure 3.1.4), cortical bone can be considered as a transversely isotropic material that exhibits an increased elastic modulus when tested parallel to its longitudinal axis compared to the radial or circumferential directions. These heterogeneous properties are due to the structural orientations of the osteons and collagen fibres that generate anisotropic properties throughout cortical bone (section 3.1.3.2 and 3.1.3.3). As such, the elastic modulus of cortical bone can increase by up to ≈ 1.5 times in the longitudinal direction (Table 3.1.3). This variation is further demonstrated by the change in mechanical properties obtained under different testing techniques, anatomical locations or tissue age. Yet a consistent range of values for the mechanical properties of cortical bone have been reported despite these variations and influencing factors that approximate its tensile strength, elastic modulus and Poisson's ratio as 100-130 MPa, 17-30 GPa and 0.3-0.4 respectively ^[11, 49, 52-54].

Table 3.1.3. Anisotropic and asymmetric properties of human femoral cortical bone mechanically tested at different axis [Reproduced from Winkelstein (2012) Orthopaedic Biomaterials].

| Mechanical Properties | Longitudinal | Transverse | Shear |
|-----------------------------------|----------------|----------------|---------------|
| Elastic modulus (GPa) | 17.9 \pm 3.9 | 10.1 \pm 2.4 | |
| Ultimate tensile stress (MPa) | 135 \pm 15.6 | 53 \pm 10.7 | |
| Ultimate compressive stress (MPa) | 205 \pm 17.3 | 131 \pm 20.7 | |
| Modulus (GPa) | | | 3.3 \pm 0.4 |
| Ultimate stress (MPa) | | | 65 \pm 4 |

Due to its viscoelastic behaviour, cortical bone also shows increased strength and elastic modulus values with an increasing strain rate that is coupled with a ductile to brittle transition in its failure behaviour (Schaffler et al. 1989). Furthermore, daily activities have been estimated to place *in vivo* strain rates of 0.001-0.01 s⁻¹ on cortical bone with the changes in its mechanical properties shown to follow a power law correlation according to the applied strain rate (Carter & Hayes, 1976) ^[12].

3.1.5.3 Cancellous Bone

As an interconnected lattice structure the mechanical testing of cancellous bone has showed that under compression its mechanical behaviour is likened to an open celled foam with the compressive stress-strain behaviour of this tissue demonstrating its considerable levels of energy absorption compared to cortical bone. This is evident by the large compressive strains observed post-yield given the relatively low mass of cancellous bones (Figure 3.1.14a). However cancellous bone also possesses varying degrees of isotropy depending on the anatomical site and associated mechanical loads. For isotopic cancellous bone (such as that in the proximal humerus) the elastic modulus can be related to the bones apparent density following the power-law relationship shown in Figure 3.1.14b^[30, 55].

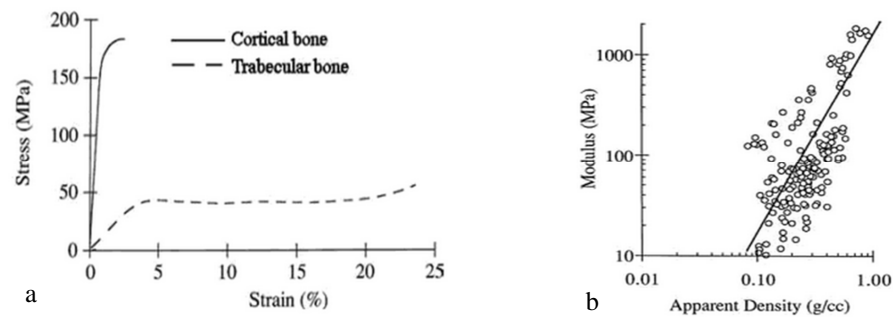


Figure 3.1.14. a) Comparison of stress-strain curves between cortical and trabecular (cancellous) bone with the bending and compression of individual trabeculae represented by the linear elastic region and b) Power-law relation between the elastic modulus and apparent density for an isotropic section of cancellous bone [Reproduced from Narayan (2009) Biomedical Materials].

Yet in regions of anisotropic cancellous bone (e.g. vertebrae) where the trabeculae are generally aligned along the primary loading axis the same considerations must be accounted for as detailed in cortical bone (such as the testing method and direction of loading). Accordingly cancellous bone displays higher mechanical properties in compression compared to tension or shear when tested along its primary axis and is considered to possess extremely limited viscoelasticity that is only observed at relatively high strain rates (10 s^{-1}). As a result cancellous bone is generally regarded as a non-linear viscoelastic material with generalised strength, modulus and Poisson ratio values frequently stated as ranging between 0.1-37 MPa, 0.01-3 GPa and 0.3-0.4 respectively (Table 3.1.4)^[11, 54-57].

Table 3.1.4. Comparison of mechanical properties collected from the compression testing of human cancellous bone obtained from different anatomical sites [Reproduced from Nahum (2002) *Accidental Injury: Biomechanics and Prevention*].

| Author | Anatomical site | Ultimate Strength (MPa) | Elastic Modulus (GPa) |
|-----------------------------|-----------------|-------------------------|-----------------------|
| Schoenfeld et al. (1974) | Proximal femur | - | 0.02-0.97 |
| Brown and Ferguson (1980) | Proximal femur | 2.1-16.2 | 0.05-2.25 |
| Ciarello et al. (1986,1991) | Distal femur | 18.6 | 0.007-0.8 |
| Pugh et al. (1973) | Distal femur | - | 0.41-1.52 |
| Williams and Lewis (1982) | Proximal tibia | 1.5-6.7 | 0.01-0.5 |
| Hvid and Hansen (1985) | Proximal tibia | 13.8-116.4 | 0.004-0.430 |
| Lindahl (1976) | Vertebrae | 4.6 | 0.055 |
| McElhaney et al. (1970) | Vertebrae | 4.13 | 0.151 |
| Struhl et al. (1987) | Vertebrae | 0.06-15 | 0.01-0.43 |

3.1.5.4 Cranial Bones

Investigations into the behaviour of the skull bones have shown that its response to traumatic loading is intrinsically linked to its mechanical properties and anatomical features. As already discussed in section 3.1.4.2, the tri-layered structure of the calvarial bones provide a mechanically strong and light weight system due to the combination of a porous cancellous layer between sheets of high density cortical bone. This architecture is analogous to an engineering sandwich structure with the dipolë layer acting as an energy absorbing core that facilities increased bone thickness without significantly increasing its weight ^[46, 47].

For cranial bones a large variation in the mechanical properties of these tissues has been reported which has been primarily attributed to morphological influences such as the sample size and shape (Motherway et al. 2009). However further discrepancies have arisen from factors such as the tissue preservation methods as well as the testing technique and its specifications (e.g. test speed, quasi-static/dynamic loading). This consequently limits inter-study comparisons due to discrepancies and conflicting data (Evans & Lissner, 1956; Roberts & Melvin, 1968; McElhaney et al., 1970; Wood et al., 1971; Peterson et al., 2002; Motherway et al., 2009). Yet such studies have shown some degree of continuity by

primarily testing the frontal and parietal bones of the calvaria using compression, tensile or bending tests ^[46, 49, 50].

From this, the generally accepted mechanical properties of the adult cranial bones have averaged values for the flexural strength and elastic modulus as 80-140 MPa and 5-15 GPa respectively (McElhaney et al., 1970; Hubbard, 1971; Wood, 1971; Motherway et al., 2009). Furthermore, experimental data (Table 3.1.5) has shown these properties to be rate-dependant ^[46, 50, 58].

Table 3.1.5. Strain rate dependence on the flexural strength and elastic modulus of the frontal and parietal bones of an adult skull [Data from Motherway et al. (2009)].

| Bone | Strain rate (s ⁻¹) | Flexural Strength (MPa) | Elastic Modulus (GPa) |
|----------|--------------------------------|-------------------------|-----------------------|
| Parietal | 21.09 | 84.50 | 10.33 |
| | 30.83 | 82.98 | 9.44 |
| | 109.43 | 123.12 | 12.80 |
| Frontal | 21.77 | 90.80 | 4.35 |
| | 26.28 | 102.60 | 4.87 |
| | 103.98 | 126.91 | 16.34 |

Additionally, impact investigations on cranial bones relating to those experienced during blunt trauma injuries have examined the tolerances of the calvaria bones using a 28mm indenter (Allsop et al. 1993). The data collected on the impact energies required to initiate fracture were observed to vary across the frontal (8700 kPa), parietal (7100 kPa) as well as the temporal bones (5700 kPa) and correlated with the reported alterations in thickness and density of the different calvaria bones ^[49].

3.1.6 Fracture of Bone

3.1.6.1 Skull Fracture

The fracture of bone tissue is highly site specific and is dependent on various factors including the magnitude, direction, loading rate and duration of applied force that can

ultimately lead to fracture when the maximum strain limits or applied forces to the bone are exceeded.

A skull fracture typically refers to a localised injury sustained to one or multiple calvaria bones due to a direct impact with sufficient force as to cause the bone to fracture. Classification of these fractures has traditionally been based on the presence of a scalp laceration (i.e. open fracture) or its location (e.g. vault and basilar fractures). However due to their potentially complex and diverse nature the classification of skull fracture types is typically limited to the generalised definitions described below ^[8, 49, 59, 60].

Linear fracture - Accounts for 80% of all skull fractures and are most likely to occur in the frontal, parietal or occipital calvaria bones. These injuries involve a single fracture occurring across one or multiple bones that passes through its entire thickness and can be sub-categorised into fractures of relatively small size (hairline fractures) or linear separation fractures that are characterised by a separation distance of 3mm between the fractured segments.

Complex fracture - Fracture of the skull bone containing multiple fracture lines that are interconnected and can be sub-divided into the various types including multiple-linear, stellate, comminuted and depressed fractures (Table 3.1.6).

Table 3.1.6. Summary of different types of complex skull fracture encountered.

| Complex Fracture | Description |
|------------------|--|
| Multiple-linear | Intersection of multiple linear fracture lines. |
| Stellate | Star shaped multiple fractures. |
| Comminuted | Fracture of skull into multiple fragments (Figure 3.1.15). |
| Depressed | Skull caves inwards towards the brain (Figure 3.1.15). |

Lastly a diastatic fracture is one that has occurred along a cranial suture and is considered rare compared to the other fracture types.

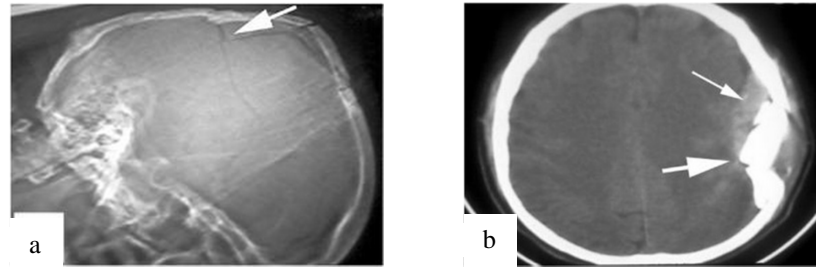


Figure 3.1.15. Examination of skull fractures showing a) Lateral radiograph of skull with comminuted fracture and b) CT scan of skull showing depressed fracture of the left parietal bone (large arrow) and epidural hematoma (small arrow) [Reproduced from Demetriades & Lewton, (2011)].

Furthermore it has been shown that the type of fracture encountered can be directly linked to the area over which the force has been applied during impact. In force trauma this corresponds to a greater probability of a linear fracture occurring at larger impact areas (e.g. $>13 \text{ cm}^2$) compared to the depressed fracture types commonly encountered at smaller, more focalised areas of impact (e.g. 5 cm^2)^[49].

3.1.6.2 Fracture Repair

Fracture repair is a complex auto-activated mechanism which attempts to restore damaged bone tissue to its original anatomical architecture and function. This can occur through either direct (primary) or secondary (indirect) healing processes with the method of fracture repair controlled by the biomechanical conditions at the fracture site. These factors include the degree of mechanical loading, fracture gap size and vascularisation with the presence of adverse conditions (e.g. excessive motion or poor vascularity) potentially leading to delayed or complete non-unions of the fractured bone ends^[57, 61, 62].

Primary fracture healing can only occur in cases of extreme fracture stability that are free from any relative motion with a minimal fracture gap size. Under these conditions osteoclasts are able to tunnel across the fracture line to form a cutting cone at the site of damaged bone tissue. The subsequent deposition of bone matrix by osteoblasts during remodelling then restores the continuity of the Haversian systems and union of the bone fragments^[61, 62].

Alternatively at a fracture site where some degree of biomechanical motion is present a secondary healing process of fracture repair occurs and involves the formation of a callus followed by endochondral ossification as illustrated for a long bone in Figure 3.1.16^{[57, 61,}

^{62]}. In secondary healing, immediately after fracture the local environment consists of various damaged soft tissues (e.g. muscle, tendon and ligaments) and dead bone from the ruptured blood vessels that leads to the formation of a hematoma (i.e. blood clot) at the fracture site. This hematoma is typically formed within 48 hours of fracture and is shown by inflammation at the fracture site. After several days this hematoma is replaced with granulation tissue composed of fibroblasts, collagen, osteoblasts and osteoclasts (recruited from pluripotent MSCs). As the necrotic tissue is removed, capillaries are introduced with collagen fibres and cartilaginous tissue deposited by fibroblasts that form a reparative soft callus. This callus provides a degree of mechanical stability to the fracture site whilst preventing disruption of the newly forming blood vessels. The formation of a hard callus by endochondral ossification then converts the soft callus into woven bone with membranous bone formation restoring union to the bone fracture ends. Finally, tissue remodelling and restoration of the bones functionality occurs through the conversion of woven bone into lamellar bone (known as consolidation). This subsequently restores the medullary cavity as well as the bone architecture and can continue for months or even years after the fracture has been clinically classified as healed ^[57, 61, 63, 64].

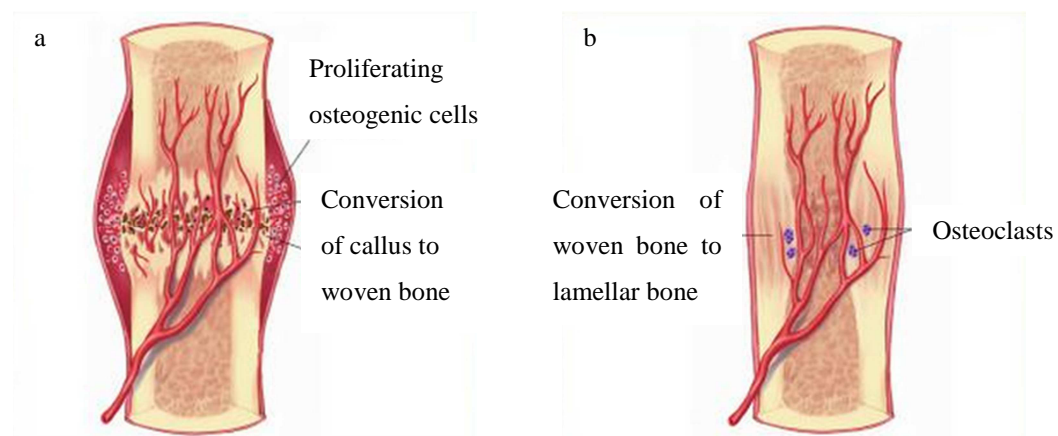


Figure 3.1.16. Illustration of a) Restoration of fractured bone union through hematoma and subsequent hard callus formation via the deposition of woven bone and b) Conversion of woven bone to lamellar bone and restoration of the medullary cavity [Modified from Porth (2011) *Essentials of Pathophysiology: Concepts of Altered Health States*].

Given that the majority of bone fractures are typically treated through methods that exhibit some degree of motion (e.g. sling or cast immobilisation as well as internal or external fixation) secondary bone healing is the most commonly encountered process. Yet consideration should also be taken regarding the allowable amplitude of motion (limited to

0.2–1mm at a fracture gap <2mm) due to the inhibition of osteoblastic behaviour observed at high strain values. In the case of a linear skull fracture, no treatment is required and bone repair follows the same principles as those previously described. However the restoration of skull bone tissue is considered to occur at a slower rate compared to that observed for long bones ^[8, 10, 62].

3.2 Biomaterials for Bone Augmentation

The damage and fracture of bone can occur from a variety of incidents that include events of high energy trauma or bone resection procedures (due to a tumour or infection). However studies have estimated that of the 7.9 million annual fractures occurring in the United States, $\approx 10\%$ will be affected by delayed or non-unions of the fractured bone due to an impairment of the physiological bone repair process. This can stem from the misalignment and non-continuity of the fractured bones (e.g. comminuted fracture) or presence of a critical sized defect (CSD). These are believed to be dependent on the bone type with 30mm, 50mm, and 60mm gaps considered critical for the radius/ulna, femur/tibia and humerus in humans respectively. As a result, surgical intervention is often required through the use of fracture fixation devices and bone graft materials in order to stabilise the defect site and restore continuity to the fractured bones ^[65-67].

Furthermore when considering a bone graft material it is necessary to consider the different material properties that can be advantageous to the *in vivo* bone forming response. This includes its potential to retain viable osteoprogenitor cells during transplantation (osteogenic), ability to stimulate MSCs from the surrounding host tissue into bone forming cell lineages (osteinduction) and facilitate bone growth across its surface (osteoconduction) ^[68].

3.2.1 Natural Biomaterials for Bone Augmentation

Natural biomaterials for bone augmentation typically involve the use of autogenous and/or allogeneic bone grafts that are intended to be used as bone defect fillers in order to bridge the CSD and restore bone union.

3.2.1.1 Autografts

Autogenous bone (collected from the patient's own tissue) has established itself as the gold standard of bone grafting material for the treatment of bone tissue defects due to its osteoconductive, osteoinductive and osteogenic properties. These materials are typically extracted from the iliac crest, proximal tibia or distal femur and given that they are harvested from the patient's own tissue any potential immunogenic response is eliminated. Depending on the application, autogenous bone can provide a supply of vascularised cortical or cancellous bone but is hampered by its limited supply especially in elderly and paediatric patients. The bone harvesting process can also significantly lengthen the surgical

procedure with post-operative complications associated with 8.5-20% of autologous bone grafts that are generally related to the patients donor site. Such complications can include nerve damage, sepsis, pelvic instability, hernia, chronic pain, iatrogenic fracturing as well as ureteral and arterial injuries ^[69-71].

3.2.1.2 Allografts

As of 2005, allogeneic bone is estimated to account for 35% of all bone grafts performed in the United States and involves the harvesting and transplant of bone tissue from a separate individual to the intended patient (Figure 3.2.1) ^[71, 72].

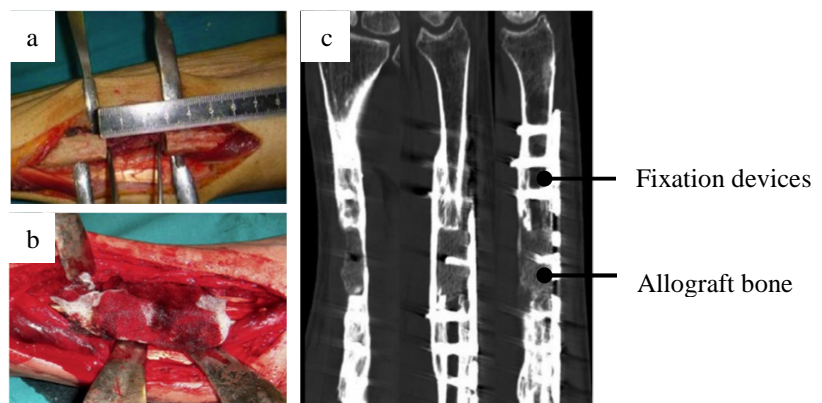


Figure 3.2.1. Reconstruction of radial fracture containing a critical size defect (CSD) a) Resection of fibrous tissue b) Implantation of bone graft with locking compression plate as well as a haemostatic agent and c) Post-operative CT images of defect site after 9 months showing metallic plates and allograft bone [Reproduced from Calori et al. (2011)].

Allografts are intended to alleviate the issues identified with autologous bone (such as donor supply or increased surgical duration) and have also been used to develop commercially available allograft-based bone substitute materials. These products utilise demineralised bone matrix (DBM) which are made available from bone banking facilities in a variety of formats such as dowels, strips and chips to meet the surgical requirements. This subsequently allows the surgeon greater options and has led to allograft bone being the primary bone substitute in total hip arthroplasty (THA) procedures ^[70, 73, 74]. Once implanted, allogeneic bone follows the kinetics of physiological bone-tissue remodelling and is gradually replaced by newly formed bone as the fracture is repaired ^[71, 72].

In order to avoid disease transmission between the donor and recipient, a strict screening process for diseases such as the human immunodeficiency virus (HIV) and Hepatitis C is required. This is coupled with regulated radiation, freezing or freeze drying pre-treatments to allografts in order to further alleviate the potential risk of disease transmission or immunogenic reactions. However these techniques have also been shown to induce changes to the graft material and its biological properties (e.g. mechanical properties, vascularisation) whilst also adversely affecting its osteoinductivity and osteoconductivity. These methods also destroy any viable cells within the allograft bone and thus eliminate any osteogenic potential. As a result the application of structural allografts is associated with a 15-20% failure rate due to the occurrence of fractures and non-unions ^[70, 71, 73, 74].

This lack of osteoinductivity in allograft bone has been addressed by the development of allograft based composites via the inclusion of collagen, non-collagenous proteins and growth factors. These materials are typically combined with cancellous chips or ceramics to further improve their osteoconductivity with commercial DBM-based allograft products available as DBX[®] (Synthes, USA) and Orthoblast[®] (Citagenix, CAN) ^[70, 72-74].

3.2.2 Artificial Biomaterials for Bone Augmentation

3.2.2.1 Tissue Response to Artificial Biomaterials

A biocompatible material has been commonly defined as “one which possesses the ability to perform with an appropriate host response in a specific application” (Boutrand, 2012) ^[75]. Furthermore, according to Hench (2013), no biomaterial can be considered as truly inert and upon implantation will inevitably elicit a response from the host tissue at the material interface. This type of reaction is dependent upon the implant’s material properties that include its composition, morphology, porosity, dimensions (relative to the defect size) and the mechanical loading conditions. However these host reactions are further complicated by tissue specific influences such as the anatomical site, patient health, age, vascularisation and damage incurred from the surgical procedure itself. Consequently the resulting tissue-implant interactions of a biomaterial can be summarised by four generalised reactions according to Hench (2013) ^[76]. These are cytotoxic, encapsulation, bonding to the surrounding tissue and resorption.

To consider in greater detail, a cytotoxic response from an implanted material is clearly undesirable with the occurrence of localised cell death or migration of chemicals released by the foreign material potentially causing systematic damage to the patient.

The most commonly encountered response to an implanted material is its gradual encapsulation with fibrous tissue that isolates the foreign body from the host tissue as part of a protective mechanism. This type of response is typically elicited from the implantation of an inert metal or polymer based device as well as biologically inactive ceramics (the so called 1st generation biomaterials). Sufficient loading of these encapsulated implant devices and interfacial movement can then lead to an increased thickness of the fibrous capsule which eventually results in the loosening of the implant and its subsequent failure. To combat this, porous ceramic coatings are commonly applied to these inert materials in order provide a route for tissue ingrowth and biological fixation ^[76].

Alternatively implanted materials can form an interfacial bond with the surrounding host tissue. In the case of bone this is through the precipitation of a hydroxyl-carbonate apatite (HCA) layer across the materials surface after implantation (2nd generation biomaterials) which is analogous to the composition found in the mineral phase of bone (section 3.1.2.1). This can then act as a substrate for the proliferation and differentiation of osteoblasts that inhibit the materials fibrous encapsulation. Fusion between the implant surface and surrounding tissue is then achieved through the incorporation of collagen fibrils into the HCA layer. Materials displaying this type of tissue response are termed to be *bioactive* and are defined by Hench (2013) as “a material that elicits a specific biological response at the interface of the material which results in the formation of a bond between the tissue and material”. Investigations into this type of response have identified a variety of materials capable of displaying this bioactive behaviour that include synthetic calcium phosphates (e.g. HA, tri-calcium phosphate) as well as certain glass and glass-ceramic compositions. These bioactive materials have since been utilised as either standalone implants or used to improve the tissue response of inert materials through the development of bioactive composites and surface deposited bioactive coatings. Additional investigations have also shown how the bioactive fixation of these materials can display a diverse range of bonding mechanisms, bonding rates, interfacial layer thickness and bond strengths ^[76].

The degree of a material's bioactivity can be rated according to its bioactivity index (I_B) which is defined as “the time required for more than 50% of the materials interface to bond with the native bone tissue” Hench (1991). This rate of bioactivity is influenced by the materials composition as well as its microstructure and has allowed for different classes of bioactivity to be categorised. This includes the class A bioactivity ($I_B > 8$) that is capable of bonding to both hard and soft tissues (e.g. Bioglass[®] 45S5) or class B ($I_B < 8$) which is limited to only hard tissues (e.g. synthetic HA) ^[77].

Finally materials exhibiting a resorbable response are intended to gradually degrade over time and eventually be replaced by the host tissue. This concept is considered to be the optimal method of addressing interfacial stability with the intention that the damaged tissue will be regenerated instead of being replaced by the implant. Such degradable biomaterials can elicit inert or bioactive responses and include degradable devices manufactured from different polymers, ceramics and glasses. However the application of degradable biomaterials is coupled with the difficulty in synchronising their resorption rates with the rate of new tissue formation as well as maintaining suitable mechanical properties as they degrade ^[76].

3.2.2.2 Metals

Metallic biomaterials have the potential to be manufactured into a range of high strength implant devices of various architectures that exhibit reproducible and predictable long term material properties under *in vivo* load bearing conditions. For orthopaedic applications, implants based on 316L stainless steel, cobalt-chrome (Co-Cr) alloys as well as commercially pure titanium (CPTi) and its alloys are considered to be the most frequently used metals for osteosynthesis devices (i.e. bone fracture fixation). This is due to their high mechanical properties (Table 3.2.1) and good corrosion resistance ^[78-81].

However 316L stainless steel can be susceptible to localised corrosion at sites depleted of oxygen (such areas underneath the screws of fracture fixation plates) and as a result implants based on 316L stainless steel have generally been used for relatively short term implant devices where removal during secondary revision surgery is expected ^[78, 79]. More generally, metallic implants can induce stress shielding in the surrounding bone - a phenomena that arises due to the mismatch between the elastic modulus of the native bone and metal implant. The resulting absence of mechanical stimulus to the bone can then lead to osteopenia in the surrounding bone tissue (i.e. reduced bone density) which can ultimately cause bone weakening, localised bone atrophy and possible bone fracture after implant removal. The permanent nature of metallic orthopaedic biomaterials also makes them susceptible to long term complications such as wear, migration and late foreign body reactions as well obscuring radiographic and topographic techniques ^[79-82].

Table 3.2.1. Generalised mechanical properties of typical metal and metal alloys used in orthopaedic applications [Reproduced from Yaszemski (2003) and Mow (2005)].

| | 316L (ASTM F138) | Co-Cr alloys (ASTM F75) | CPTi (ASTM F67) | Ti alloy (Ti-6Al-4V) |
|---|---------------------|----------------------------|--------------------|-------------------------|
| Elastic Modulus (GPa) | 190 | 210-253 | 110 | 116 |
| Yield Strength (MPa) | 792 | 448-841 | 485 | 897-1034 |
| UTS (MPa) | 930 | 655-1277 | 760 | 965-1103 |
| Fatigue Strength (MPa) | 241-820 | 207-950 | 300 | 620-689 |
| Hardness (HV) | 130-180 | 300-400 | 120-200 | 310 |
| Elongation at Fracture (%) | 43-45 | 4-14 | 14-18 | 8 |
| Fatigue Limit (at 10^7 Cycles, R= -1) (MPa) | 241-276 | 207-310 *725-950 | 300 | 620-689 |

*Power metallurgy produced, hot-isostatically pressed.

3.2.2.3 Degradable Polymers

The use of degradable polymers for fracture fixation devices has been driven by the temporary nature of the fracture repair process and the long term complications observed with permanent implant devices. Degradable polymers are consequently considered advantageous for orthopaedic applications given their temporary nature (section 3.2.2.1), lower elastic modulus (reducing stress shielding) and compatibility with radiography. This is coupled with their ability to be easily manufactured into relatively complex shapes using conventional processing techniques. As a result, degradable polymers have been used to develop commercially available internal fracture fixation devices (e.g. plates, rods, pins and screws) which after implantation are intended to slowly transfer mechanical loading back to the regenerating bone as the device gradually degrades [78, 79, 83].

Yet despite the wide range of degradable polymers from natural and synthetic origin, only the synthetic polyesters are considered practical for orthopaedic applications. This is due to their material properties and susceptibility to hydrolytic degradation processes that can provide suitable degradation rates with relatively non-toxic by-products. Of these the polylactides (PLA) and polyglycolides (PGA) along with their subsequent copolymers

are regarded as the most widely used members of this polymer family. However alternative biopolymers such as polyhydroxybutyrate (PHB) and polyhydroxybutyrate-co-valerate (PHBV) as well as polycaprolactone (PCL) have also received interest for bone engineering devices ^[78,79].

PLA and PGA are synthesised by ring opening polymerisation with the extra methyl group of the PLA structure making it more hydrophobic and less crystalline compared to PGA. The ester bond of PLA is also more resistant to hydrolytic degradation and due to the presence of an asymmetric α -carbon atom, three different PLA isomers can exist as L-lactic acid, D-lactic or DL-lactic. Each can be used to form polymers of poly(L-lactic) acid (PLLA) or poly(D,L-lactic) acid (PDLA) along with the manufacturing of poly-L-lactide-co-DL-lactide (PDLLA) or polyglycolide-co-poly lactide (PGLA) copolymers (if combined with PGA) ^[84]. Consequently through the formation of different co-polymer variations, materials with different molecular compositions, molecular weights (M_w) and degree of crystallinity can be developed with tailorable material properties. With regards to this, it is generally accepted that high molecular weight polymers with high degrees of crystallinity will degrade more slowly than a completely amorphous, low molecular weight alternative ^[83, 85].

Upon immersion, the degradation of the PLA or PGA occurs through a homogenous hydrolytic degradation process whereby water absorption results in cleavage and reductions to the polymer chain length. Through this process, the polymers molecular weight (M_w) is gradually reduced in what is described as the 'quasi-stable' stage of polymer degradation with the sample weight, shape and mechanical properties remaining unchanged. This stage continues until the 'loss-of-strength' phase where decreases in the polymers elastic modulus are observed despite no loss in sample weight. The final stage is characterised by significant reductions in the sample weight until it is completely disintegrated and is known as the 'structure-disruption' stage. For poly(α -hydroxyacid) materials (i.e. PLA or PGA), the hydrolysis of these ester bonds produces lactic acid or glycolic acid by-products (from PLA and PGA respectively) which are expelled from the body through catabolic pathways. However being acidic, these by-products can accelerate the polymer degradation rate through autocatalytic effects and can also accumulate at the centre of a polymer device. This can lead to a dramatic loss in the mechanical properties of the device as well as a delayed inflammatory response due to its internal degradation and sudden burst release of acidic by-products. Efforts to minimise these reactions have been

achieved through the inclusion of alkaline salts (e.g. calcium acetate) as filler materials or antibodies of anti-inflammatory mediators into the implant ^[85, 86].

Yet the implementation of polymer fracture fixation devices is limited at load bearing sites as a result of their relatively low mechanical properties (Table 3.2.2) as well as the accelerated polymer degradation rates that can occur from *in vivo* cyclic loading ^[85, 87, 88]. Accordingly, degradable polymer devices must be considerably thicker than their metallic equivalent in order to achieve properties suitable for fracture fixation (e.g. 2mm for PLLA compared to 1.5mm for metal). This added thickness may then make degradable polymer devices unsuitable for certain fractures such as those encountered in hand surgery ^[78, 79, 85].

Table 3.2.2. Comparison of material properties between different degradable polymers commonly used in orthopaedic applications [Reproduced from Sultana (2012) Biodegradable Polymer Based Scaffolds for Bone Tissue Engineering, Eglin (2008) Biodegradable Polymeric Materials For Osteosynthesis: Tutorial, and Dumitriu (2001) Polymer Biomaterials, Revised and Expanded].

| Material Property | PLLA | PDLLA | PGA | PHB | PHBV-10% | PHBV-11% | PHBV-20% | PCL |
|---|-----------|---------|-----------|-----|----------|----------|----------|-----------|
| Density (g cm ⁻³) | 1.25–1.29 | 1.27 | 1.50–1.69 | | | | | 1.06–1.13 |
| *Structure | SC | Am | C | | | | | SC |
| Crystallinity (%) | ≈40 | | >50 | ≈80 | ≈60 | | 35 | |
| Melt Temp. [T _m] (°C) | 175 | 180 | 230 | 171 | 140 | 145 | 130 | 57 |
| Glass Transition Temp. [T _g] (°C) | 53-64 | 50 - 57 | 36-45 | 1 | | 2 | | -62 |
| Tensile strength (MPa) | 50 | 29 | - | 36 | 25 | 20 | 20 | 16 |
| Elastic Modulus [E] (GPa) | 2.7 | 1.9 | 7.0 | 3.5 | 1.2 | 1.1 | 0.8 | 0.4 |
| Elongation [ε _B] (%) | 3.3 | 5.0 | 15-20 | 8 | 20 | 17 | 50 | 300-500 |
| Impact strength (J m ⁻¹) | | | | 60 | 110 | | 350 | |
| Degradation (months) | >24 | | 6-12 | | | | | >24 |

*C = Crystalline, SC = Semi-crystalline, Am = Amorphous

PHB is considered to be an advantageous alternative to current polymer biomaterials such as PLA, PGA or their copolymers as a result of its material properties. This includes its high biocompatibility as well as its 3-hydroxybutyrate acid degradation by-product that is found as a naturally occurring metabolite in human blood and consequently fails to illicit any form of inflammatory response. The piezoelectric nature of PHB is also an attractive option for developing so-called orthopaedic ‘smart materials’ that are capable of producing strain generated potentials at the tissue-implant interface. However the implementation of PHB is limited by its mechanically brittle nature and thermal instability^[89-91].

Such issues have been alleviated by the inclusion of randomly distributed hydroxyvalerate (HV) monomer units (0-24 mol%) throughout the PHB polymer chain structure to produce copolymers with reduced crystallinity and increased ductility/thermal stability. The variation in HV concentration and associated changes to the polymers mechanical properties and degradation rates (due to the changes in its M_w and crystallinity) subsequently allow for the development of polyhydroxybutyrate-co-valerate (PHBV) polymer compositions with tailored properties specific to the implant application (Table 3.2.2). Yet studies have shown that the *in vivo* hydrolysis reactions of PHB and PHBV can be catalysed by non-specific esterase and lysozyme enzymes secreted by the body’s immune system. This has led to accelerated rates of polymer degradation being observed *in vivo* compared to those measured *in vitro*. These materials are also significantly more expensive than conventional biopolymers and can exhibit variations in their material properties^[92-94].

Lastly PCL is a semi-crystalline hydrophobic polymer generally used in pharmaceutical products or wound dressings and due to its low tensile strength, low elastic modulus as well as its high elongation (Table 3.2.2) is considered unsuitable for load bearing orthopaedic applications without a suitable reinforcing agent^[83].

3.2.2.4 Calcium Phosphate Ceramics

Due to the limited supply, expense and potential dangers of natural bone graft materials (section 3.2.1) attention has focused on developing alternative “off the shelf” bone graft products. These would ideally be capable of providing surgeons with a readily available, easy-to-use graft material with reproducible results in an almost unlimited supply^[69, 73, 74].

Synthetic calcium phosphate ceramics such as alpha- or beta-tricalcium phosphate (α -, β -TCP, $\text{Ca}_3(\text{PO}_4)_2$, Ca/P = 1.5) and HA ($\text{Ca}_{10}(\text{PO}_4)_6(\text{OH})_2$, Ca/P = 1.67) have been clinically

used since the 1980s in orthopaedic and dentistry fields for applications including maxillofacial reconstruction and as a generalised bone defect filler. This appeal has been due to their compositional similarity to the apatite mineral phase of bone alongside their high biocompatibility, bioactivity and osteoconductivity. Due to their high density and crystallinity these materials possess high compressive strengths with slow degradation rates and over the last three decades have seen significant product differentiation. This diversification has been driven by the differences in physical properties that can be achieved from relatively small alterations to their chemical composition and crystalline structure. Consequently a range of commercially available synthetically manufactured HA, α -TCP, β -TCP and biphasic calcium phosphate (BCP) mixtures of HA/TCP (Ca/P = 1.5-1.67) products have been introduced. These include ApaPore[®] (ApaTech, UK), Vitoss[®] (Orthovita, USA) as well as Ceraform[®] (Teknimed, France) and can be supplied as solid or porous preformed shapes, generalised wedges/blocks or in granule/paste formats. Further product optimisation has also been achieved through adequate control and tailoring of the porosity which has been shown to play a key role in influencing the rate of osteointegration as well as the materials inherent biocompatibility [69, 73, 74, 95-97].

The diverse performance of these calcium phosphate ceramics is apparent by the greater physiochemical resorption rates possessed by TCP (solubility, $K_{sp} = 10^{-25.5}$ for α -TCP and $10^{-28.9}$ for β -TCP at 25°C) which undergoes osteoclastic resorption *in vivo*. This is in contrast to HA ($K_{sp} = 10^{-116.8}$ at 25°C) which is considered to have marginal degradation rates in its sintered form (e.g. multiple years) and consequently serves a more permanent nature. For BCP the rates are dependent upon the composition ratios and are intermediate between those displayed by TCP and HA [69, 72, 73, 98-100].

As with their other material properties, the mechanical properties of calcium phosphates can vary significantly based upon their composition, architecture and crystallinity. However as bone graft materials, calcium phosphate ceramics suffer from low fracture toughness which confines their use to non-load bearing sites (Table 3.2.3). It also makes them difficult to shape or trim intraoperatively and can limit the quality of the implant interface which can inhibit bone formation [53, 76, 95, 101].

Table 3.2.3. Comparison of mechanical properties between calcium phosphate ceramic biomaterials and bone [Data from Kokubo et al. (2003), Domb (2011) Biodegradable polymers in clinical use and clinical development and Hench (2013) Introduction to bioceramics].

| Material Property | Ca-P ceramics (Generalised) | Dense HA | Porous HA | Cortical bone | Cancellous bone |
|---|--------------------------------|-------------|--------------|------------------|--------------------|
| Compressive strength (MPa) | 30-900 | 500-1000 | 0.21-0.41 | 100-230 | 2-12 |
| Flexural/Tensile Strength (MPa) | 30-200 | 115-200 | - | 50-150 | 10-20 |
| Strain to failure (%) | - | - | - | 1-3 | 5-7 |
| Elastic Modulus (GPa) | 30-103 | 80-110 | 0.001-0.83 | 7-30 | 0.05-0.5 |
| Fracture Toughness [K_{IC}] (MPa m ^{1/2}) | <1 | ~1 | - | 2-12 | - |

Natural derived HA (from bovine or coralline sources) presents another group of bioactive materials with an interconnected macroporous structure similar to that of cancellous bone (section 3.1.3.1). Such structures have traditionally been difficult to achieve in synthetically produced calcium phosphate ceramics and their natural source results in an impure form of HA containing trace elements of Mg, Sr, CO₃, F, as well as Na. These impurities are considered to be advantageous for biological processes and may install a therapeutic effect into the graft material compared to synthetically pure HA. However in general, the performance of synthetic and naturally derived HA are considered to be similar with natural HA also possessing equally poor mechanical properties ^[69, 102, 103].

3.2.2.5 Bone Cements

Initially developed for dental applications in the 1930s, these non-resorbable acrylic-based polymeric materials quickly became an attractive option as an implant material for orthopaedic surgery. Such materials have continued to be extensively applied in modern

orthopaedic procedures for filling osseous defects or as a grouting agent for the fixation of surgical prosthesis that includes hip or knee arthroplasties, vertebroplasty, kyphoplasty as well as in craniofacial or maxillofacial reconstruction. These two component solid-liquid phase systems are typically referred to as ‘bone cements’ and involve the bulk polymerisation of a liquid methyl methacrylate (MMA) monomer after it has been mixed with a poly(methyl methacrylate) (PMMA) powder ^[79, 104, 105].

The use of bone cements are advantageous in orthopaedic surgery due to their low cost and suitable mechanical properties that, once hardened, allow immediate structural support (Table 3.2.4) ^[91]. Despite principally operating on the same composition for over fifty years, seventy different commercial bone cement products are now available. This diversification has been based on changes to the molecular weight of the PMMA as well as the inclusion of other components such as radiopacifiers, antibiotics and therapeutic elements ^[79, 106, 107].

Table 3.2.4. Typical physical and mechanical properties of bone cements [Reproduced from Yaszemski (2003)].

| Material Property | Value |
|---|------------|
| Density (g cm ⁻³) | 1.10-1.23 |
| Water sorption (%) | 0.5 |
| Shrinkage after setting (%) | 2.75-5.0 |
| Ultimate compressive strength (MPa) | 72.6-114.3 |
| Compressive modulus (GPa) | 1.94-3.18 |
| Compressive strain before fracture (%) | 5.0-7.5 |
| Ultimate tensile strength (MPa) | 23.6-49.2 |
| Tensile elastic modulus (GPa) | 1.58-4.12 |
| Tensile strain before fracture (%) | 0.86-2.49 |
| Shear strength (MPa) | 42.7-50.2 |
| Fracture toughness [K _{IC}] (MPa m ^{1/2}) | 1.03-2.32 |

However bone cements are typically not bioactive, relying on a mechanical interlock at the bone-cement interface in order to be fixated and lack any osteoinductive or

osteoconductive potential ^[106]. Another disadvantage of bone cement is its potential fragmentation and the corresponding foreign body reactions that can be elicited by the host tissue from the wear debris. This can ultimately lead to aseptic loosening of a prosthetic and the development of chronic complications. The polymerisation of MMA during its application also produces a significantly high exothermic response with peak temperatures reaching between 80-124°C which, without sufficient irrigation, can cause necrosis in the surrounding tissue ^[79, 104, 106].

Alternatively calcium phosphate cements (CPC) are two or three component systems that function in a similar manner to PMMA and are used for filling small sized osseous defects. However in contrast to the polymerisation reactions of acrylic based cements, CPC function through a complex precipitation process of calcium phosphate crystals. The powder phases of these cements can consist of compounds such as dicalcium phosphate-anhydrite (DCPA), tetra-calcium phosphate (TTCP), mono-calcium phosphate monohydrate (MCPM), calcium carbonate (CaCO₃), amorphous calcium phosphate (ACP) or α -TCP. These are mixed with water and sodium phosphate (Na₃PO₄) to act as an accelerator ^[10, 69, 95].

Given the composition of these calcium phosphates, the clinical advantages to using CPC cements lie in their excellent biocompatibility, bioactivity and osteoconductive properties as well as their ability to degrade by osteoclastic resorption and be gradually remodelled into new bone. This is further complimented by the low temperature precipitation reactions that occur during the hardening of these cements (<40°C). However CPCs are not suitable for load bearing applications (requiring osteosynthesis) and consequently have limited clinical applications ^[10, 69, 95].

3.2.2.6 Glasses

The idea of glass as a tissue regenerative material was first investigated over 100 years ago in Glasgow when Sir William Macewen implanted a glass tube into the medulla of a canine model after a 28.6mm resection of its radius bone. Retrieval of the tube after approximately nine weeks showed that a firm union in the radius had been re-established and that new osseous tissue had proceeded to grow into two-thirds of the glass tube (Figure 3.2.2) ^[108].

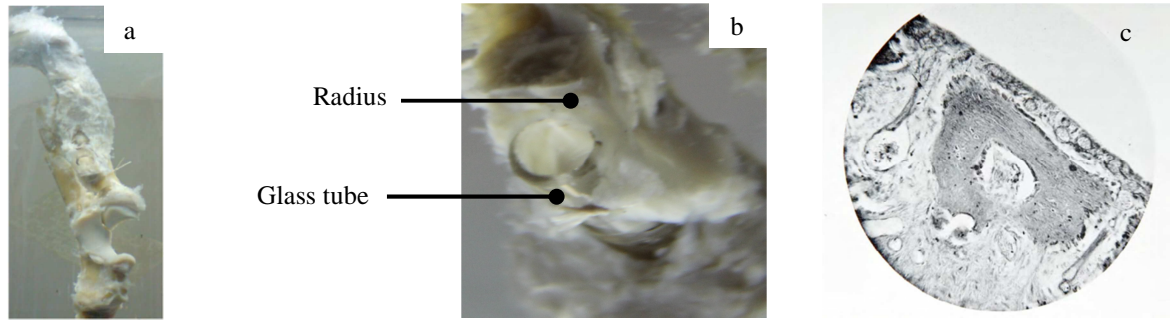


Figure 3.2.2. Images of a-b) Canine radius with implanted glass tube after sixty one days of implantation performed by Sir William Macewan - stored at the Hunterian Museum in the University of Glasgow and c) Drawing of histological section after retrieval of glass tube from canine radius [Reproduced from Tanner & Dalby (2010) Guest Editorial].

Degradable bioactive glasses are an attractive option for bone tissue regenerative applications due to their ability to bond to hard tissue (as well as potentially soft tissues) and completely degrade *in vivo* at rates controlled by the glass's composition. This is coupled with their ability to stimulate advantageous extracellular and intracellular responses from the release of its constituent ions that can potentially lead to an increased rate of bone formation (i.e. osteoinduction). Bioactive glasses can be based on a number of glass forming networks (e.g. silicate-, borate- or phosphate based) with the inclusion of additional components (such as zinc, copper, fluoride, strontium and boron) allowing for a wide range of potential glass compositions to be manufactured. Due to this compositional flexibility, a continued increase in the development and application of bioactive glasses has been observed worldwide (Figure 3.2.3) ^[109-111].

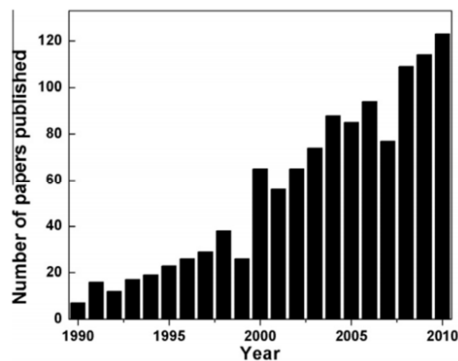


Figure 3.2.3. Number of papers published between 1990-2010 under the field of "bioactive glass" compiled from a search of Web of Science [Reproduced from Rahaman et al. (2011)].

However despite the wide range of available glass formulations, the silicate based Bioglass[®] 45S5 composition (Table 3.2.5) is considered to be the gold standard of bioactive glasses and has been the most widely researched glass for biomedical applications. This composition was discovered by Larry Hench over 40 years ago and was the first material found capable of bonding to bone through the formation of an HCA layer (which was later termed “bioactivity” – section 3.2.2.1) ^[109-111]. Consequently Bioglass[®] 45S5 has been successfully exploited in its particulate form for clinically treating periodontal disease and as a bone filler material through the development of Perioglas[™] and Novabone[™] products respectively (Novabone Products LLC, USA). Similar particulate/granule systems have also been developed from alternate silicate based compositions and include the commercially available BonAlive[®] (Biomaterials Ltd, Finland) and StronBone[™] (RepRegen Ltd, UK) ^[109, 111, 112].

Table 3.2.5. Compositional comparison between commercially available Bioglass[®] 45S5, BonAlive[™] and StronBone[®] products as well as the 13-93 glass composition [Data from Jones & Clare (2012) and Hench (2012)].

| Material | Composition (mol%) | | | | | | |
|--|--------------------|-------------------|-------|-------------------------------|------|------------------|-----|
| | SiO ₂ | Na ₂ O | CaO | P ₂ O ₅ | SrO | K ₂ O | MgO |
| Bioglass [®] 45S5 ^[109] | 46.13 | 24.35 | 26.91 | 2.60 | - | | |
| BonAlive [™] (S53P4) ^[109] | 53.80 | 22.70 | 21.80 | 1.70 | - | | |
| StronBone [®] ^[113] | 44.47 | 27.26 | 21.47 | 4.42 | 2.39 | | |
| 13-93 ^[109] | 54.6 | 6 | 22.1 | 1.7 | - | 7.9 | 7.7 |

As bulk monoliths, Bioglass[®] 45S5 has been successfully implanted in patients as a middle ear prosthesis in order to replace damaged ossicles and treat cases of conductive hearing loss. However the commercial success of this product has been restricted by the poor intraoperative workability of the material. The mechanical properties of Bioglass[®] 45S5 and other bioactive glass systems have also generally limited their clinical applications to anatomical sites free of any significant mechanical loading without additional metallic fixation devices (Table 3.2.6) ^[109, 110, 112].

Table 3.2.6. Material properties of Bioglass[®] 45S5 [Data from Jones & Clare (2012)].

| Material Property | Value |
|--|--|
| Density | 2.7 g cm ⁻³ |
| Glass transition temperature [T _g] | 538°C |
| Glass crystallisation onset temperature [T _{oc}] | 677°C |
| Glass Melt Temperature [T _m] | 1224°C |
| Thermal Expansion Coefficient | 1.51x10 ⁻⁶ °C ⁻¹ |
| Tensile Strength | 42 MPa |
| Youngs Modulus | 35 GPa |
| Fracture Toughness | 0.6 MPa m ^{1/2} |
| Vickers Hardness | 5.75 GPa |

Furthermore the poor thermal workability of silicate based bioactive glasses can make them prone to crystallisation (which has a detrimental effect on a glass's bioactivity). As a result, research has also examined the use of borosilicate, borate and phosphate based glasses. However investigations into other glass compositions have also been driven by the uncertainty over the long term effects of SiO₂ *in vivo* ^[109, 114].

3.2.2.7 Glass-Ceramics

Alternatively heat-treatments can be used to partially convert glass compositions from their completely amorphous structure into one that is primarily crystalline (commonly referred to as glass-ceramics). These can be manufactured to possess superior properties compared to the initial parent glass and can be machined into a variety of shapes (such as artificial vertebrae implants) whilst displaying a bioactive response similar to that observed from bioactive glasses ^[115, 116].

Based on this ceramming process (i.e. conversion to crystalline phases) a variety of glass-ceramics can be manufactured with different material properties through adequate control over the size and concentration of the developing crystalline phases (Table 3.2.7). The commercial development of glass-ceramic materials has resulted in several biomedical products being released such as Cerabone[®] A-W (Botiss Biomaterials, Germany) and Bioverit[®] (Vitron Spezialwerkstoffe GmbH, Germany). However despite their improved

mechanical properties (compared to bioactive glasses) they are still considered too brittle to be used at sites that experience sufficient mechanical loading ^[115-117].

Table 3.2.7. Comparison of mechanical properties between commercially available glass-ceramic materials [Data from Holand & Beall (2012)].

| Material Property | Glass-Ceramic | | |
|--|---------------------------|-------------------------|--------------------------|
| | Cerabone [®] A-W | Bioverit [®] I | Bioverit [®] II |
| Density (g cm ⁻³) | 3.07 | 2.8 | 2.5 |
| Flexural Strength (MPa) | 215 | 140-180 | 90-140 |
| Compressive Strength (MPa) | 1080 | 500 | 450 |
| Youngs Modulus (GPa) | 118 | 70-88 | 70 |
| Vickers Hardness (GPa) | 0.680 | 5 | 8 |
| Fracture Toughness (MPa m ^{1/2}) | 2.0 | 1.2-2.1 | 1.2-1.8 |

3.2.3 Composites

3.2.3.1 Overview

From a mechanical and biological perspective, a single material can often fail to meet the *in vivo* demands encountered within the human body.

Composites are typically defined as a group of materials composed of at least two physically or chemically different constituent phases separated by a distinct interface (Thomas et al., 2012; Balasubramanian, 2013) ^[118, 119]. This commonly involves the homogenous distribution of a brittle, high modulus (E_f) reinforcing filler within a continuous ductile low modulus (E_m) matrix phase. The incorporation of this filler phase typically leads to a general increase in the elastic modulus (E_{comp}), strength (σ_{comp}) and other mechanical properties but a reduction in the strain at failure compared to the matrix phase as the volume or weight content of filler is increased (i.e. volume or weight fraction - V_f , W_f respectively). This increase in mechanical properties is due to the transfer and distribution of externally applied stresses through the matrix to the high modulus reinforcing filler via the filler-matrix interface. Consequently due to their potentially high specific elastic modulus/strength (Figure 3.2.4), increased fatigue resistance, lower thermal

coefficient and high impact energies, composites are considered to be an advantageous alternative to traditional metal devices. However due to the breadth of available literature on composite materials, only a brief summary is presented here [96, 118, 120, 121].

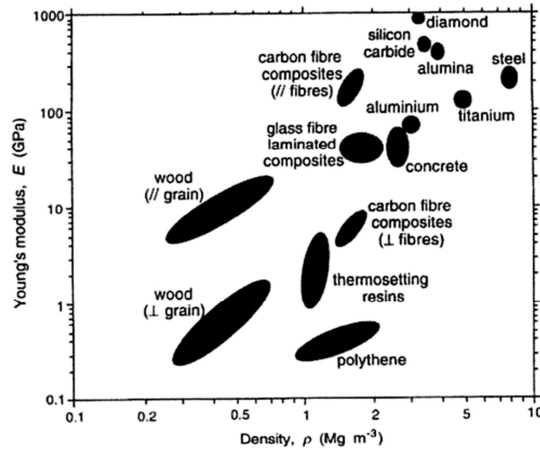


Figure 3.2.4. Comparison of the elastic modulus vs density (i.e. specific modulus) for different monolithic and fibre composite materials [Reproduced from Hull & Clyne (1996) *An Introduction to Composite Materials*].

Furthermore composites also offer the ability to tailor their mechanical properties to meet the demands of a specific application via alterations to different material parameters. These include the choice and associated mechanical properties of each constituent phase, filler form (Figure 3.2.5), the reinforcing phase distribution (i.e. geometrical orientations), filler concentration as well as the condition of the filler-matrix interface (e.g. coupling agents). As a result, a variety of composite configurations can be produced (Figure 3.2.6) with the classifications of these materials typically derived from the nature of their constituents (Table 3.2.8) [96, 118, 122, 123].

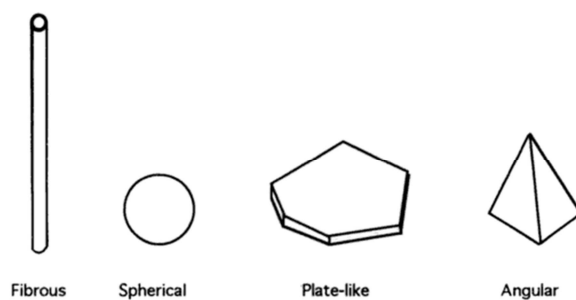


Figure 3.2.5. Comparison of different filler types used in composite design [Reproduced from Mallick (1997)].

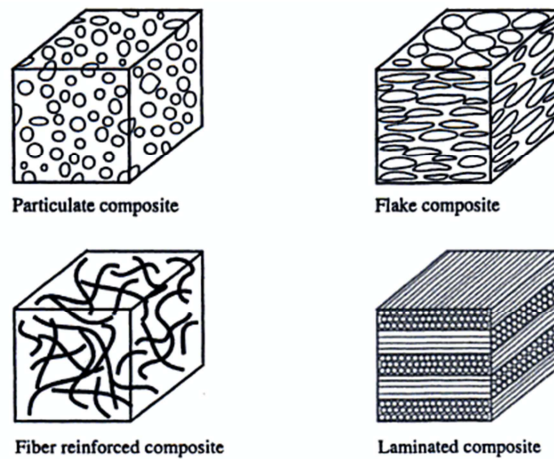


Figure 3.2.6. Comparison of different types of composite configurations using different fillers [Reproduced from Gurdal et al. (1999)].

Table 3.2.8. Description of different composite designs [Data from Gurdal et al. (1999)].

| *Composite Type | Description |
|------------------|--|
| Nano- | Nano- fibres or particles embedded within the matrix. |
| Particulate | Employs the random distribution of isometric particles ($\geq 1\mu\text{m}$). |
| Flake | Uses the random distribution of thin, high aspect ratio flakes/platelets that can provide some degree anisotropy if properly aligned. |
| Fibre-reinforced | Sub-categorized into continuous or discontinuous fibre reinforced composites that utilize long or short fibres respectively. |
| Laminated | Combined stacks of aligned or randomly orientated composite fibre laminates. Laminate layers (also known as pre-pregs) are manufactured by impregnating fibres with a polymer resin. |

*Composites can be dense or of a porous foam like architecture depending on the manufacturing technique.

Yet despite the different types of composite configurations, fibre reinforced composites are considered by Gurdal et al. (1999) to be the most predominantly used form due to the increase in mechanical properties that can be achieved (Figure 3.2.7). This is due to the higher aspect ratios encountered with fibres (i.e. larger surface areas per unit volume) and consequent increase in stress transfer compared to particles - where reinforcement of the sample occurs parallel to the fibres axis (x_1/E_1). Accordingly, fibres suitable for composite

reinforcement should possess a uniform diameter along with a high elastic modulus, high ultimate tensile strength and suitable stability during handling^[96, 123-125].

Fibre reinforced polymer composites (FRPC) can be manufactured from a variety of fibre types including continuous or discontinuous glass or carbon fibres through methods such as extrusion or injection moulding techniques. However the ability to also manufacture composites with anisotropic properties by aligning the reinforcing fibres is considered to be a major advantage compared to isotropic particulate composites or monolithic materials (Ratner et al. 2012)^[96]. This is due to the ability to tailor the composite material properties (via the fibre orientation) in relation to the primary direction of the applied stresses. Yet when considering the illustration shown in Figure 3.2.7, the alignment of parallel reinforcing fibres in the x_1 direction consequently offers lower reinforcement in the transverse direction (x_2/E_2). As such, laminated composite designs incorporating linear fibre pre-pregs of consecutively alternating orientations (e.g. 0° , 45° , 90°) have been used alongside various two dimensional and three-dimensional weave/woven designs to further modify and tailor the fibre composite material properties (Figure 3.2.8)^[96, 121-123, 126].

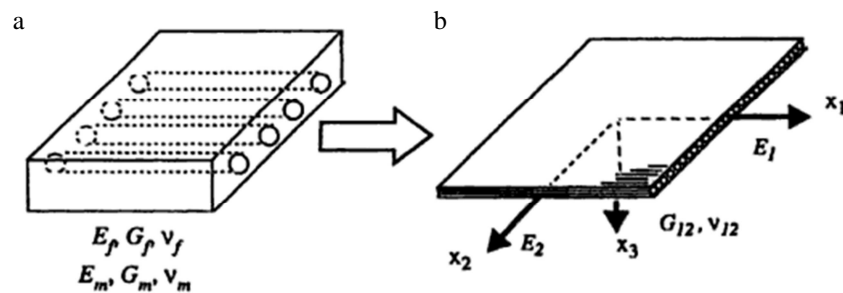


Figure 3.2.7. Illustration of FRPC showing a) Elastic modulus (E), shear modulus (G) and Poisson's ratio (ν) of the fibre (E_f , G_f , ν_f) and matrix (E_m , G_m , ν_m) constituents in a unidirectional fibre reinforced composite and b) Elastic properties of composite with regards to global axis running parallel (x_1) and transverse (x_2) to the primary fibre axis with the elastic modulus (E_1 , E_2) as well as the shear modulus (G_{12}) and Poisson's ratio (ν_{12}) labelled relative to the applied axis coordinates. [Reproduced from Gurdal et al. (1999)].

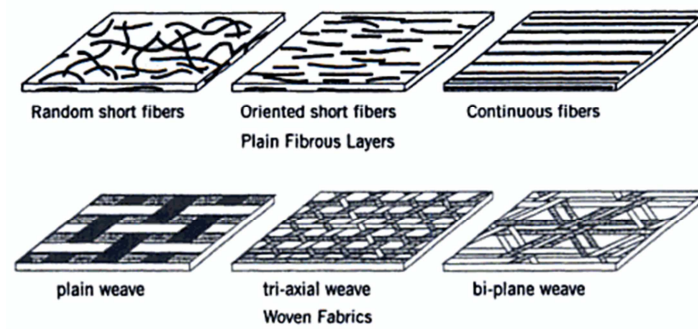


Figure 3.2.8. Comparison of different fibre architectures used in various composite laminate designs [Reproduced from Gurdal et al. (1999)].

In fibre-reinforced composites, the major stress field at the fibre-matrix interface is experienced as shear and as a result, the degree of reinforcement for a specific composite configuration is dependent upon the interfacial shear bond strength (τ_b) of the fibre-matrix interface. Consequently when mechanically loaded, the failure of fibre composite materials traditionally occurs through fibre fracture (for weaker fibres) or when the interfacial shear stresses (IFSS) exceed the interfacial bond strength ($IFSS > \tau_b$). However the fibre-matrix interface is also influential to the fracture toughness of a composite specimen with interfacial debonding and fibre pull out regarded by Mallick (1997) as the primary energy absorbing mechanisms during composite failure. To expand on this, the interfacial debonding can disrupt the crack pathway and cause it to shift from its initial direction (through the fibre) to propagation along the fibre surface (Figure 3.2.9). Additionally if the reinforcing fibres fracture at locations away from the crack plane then the composite fracture toughness can increase due to the friction encountered during fibre pull-out [122, 127].

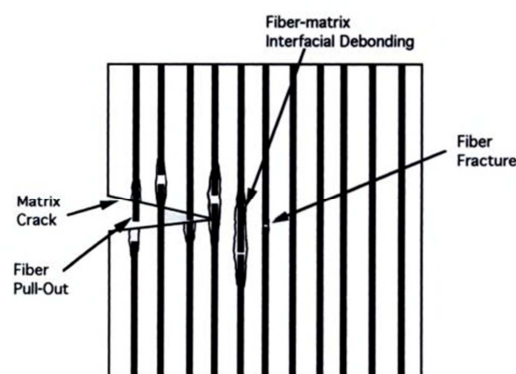


Figure 3.2.9. Illustration of interfacial debonding, fibre fracture and fibre pull-out during composite fracture [Reproduced from Mallick (1997)].

As previously discussed, the enhanced mechanical properties of fibre reinforced composites are related to the quality of the fibre-matrix interface which is dependent upon the ability to successfully infiltrate the fibres with polymer resin. In polymer reinforced laminate composites this can be expressed by a modified version of Darcy's Law that describes the anisotropic viscous flow of the polymer phase during composite processing (Eqn 3.2.1). Based on Darcy's law, improved polymer infiltration can be achieved when a lower viscosity resin (i.e. higher processing temperature) and increased pressure differential/gradient is applied for a set fibre construct of permeability $[K]$ ^[122].

$$[U] = -\frac{[K]}{\mu} \nabla P$$

Eqn 3.2.1

where $[U]$ = superficial velocity, ∇P = pressure gradient, μ = viscosity of the flowing resin and $[K]$ is the permeability tensor of the fibre reinforcement.

In addition to the previously discussed mechanisms of tailoring composite material properties, further modifications can also be achieved through the development of hybrid composite designs. These look to simultaneously incorporate different types of reinforcing phases due to the potential synergistic effects between the two different filler types. Examples of this include the production of composite materials with good fracture toughness (via fibre-pull out and crack deflection mechanisms), impact resistance, thermal shock and wear resistance from the combination of fibres and particles (Figure 3.2.10) ^[128].

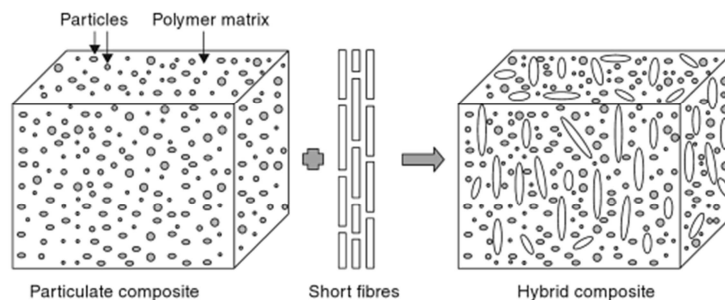


Figure 3.2.10. Illustration of a hybrid polymer composite that incorporates short fibres and particles into the matrix phase [Reproduced from Fu et al. (2009)].

3.2.3.2 Composite Biomaterials

Given the advantages and flexibility in composite mechanical properties, implant design has also looked to utilise such concepts for the application of polymer composite devices with mechanical properties targeted at a desired tissue or specific anatomical site. Such materials have been investigated for a range of tissue reconstructive applications using a variety of different matrix and filler materials including carbon, polymer (i.e. self-reinforcing) or glass (Figure 3.2.11). This also includes architectural variations such as the use of dense or porous composite materials. However due to the breadth of the available literature surrounding the development and characterization of such composite biomaterials only dense glass/ceramic-polymer composites have been considered here ^[129].

In orthopaedic applications, the development of polymer composites using a brittle, high modulus bioactive ceramic or glass reinforcing filler phase alongside a synthetic or natural (e.g. collagen, chitosan etc.) polymer matrix has been investigated since the 1980s. This has been due to the natural ceramic-polymer composite composition of bone (section 3.1.2.1) as well as the flexibility in material design and mechanical properties that can be achieved with composite materials. Consequently these materials have been investigated with the aim that the bioactive filler phase mechanically reinforces the low modulus ductile matrix as well as confer *in vivo* bioactivity to the inert polymer that would typically undergo fibrous encapsulation (Tanner, 2010). Similar to its mechanical properties, this degree of bioactivity can also be tailored via alterations to the bioactive filler concentration, morphology and its distribution (e.g. surface area-to-volume ratios and volume fraction) ^[86, 130, 131].

One of the most successful biomedical composites based on this bioactive ceramic-polymer composite concept has been through the reinforcement of a high-density polyethylene (HDPE) matrix with 40 vol% HA microparticles. Such composites possess an elastic modulus (4.4 ± 0.7 GPa) in the lower region of cortical bone whilst retaining a ductile failure mode. The development of this composite material has since led to its commercial success for orbital floor prosthesis, middle ear implants and maxiofacial surgery reconstructive applications under the tradename HAPEXTM. However, HAPEXTM is non-resorbable and according to Tjong (2012) is unsuitable for major load bearing orthopaedic applications due to its low mechanical strength ^[132, 133].

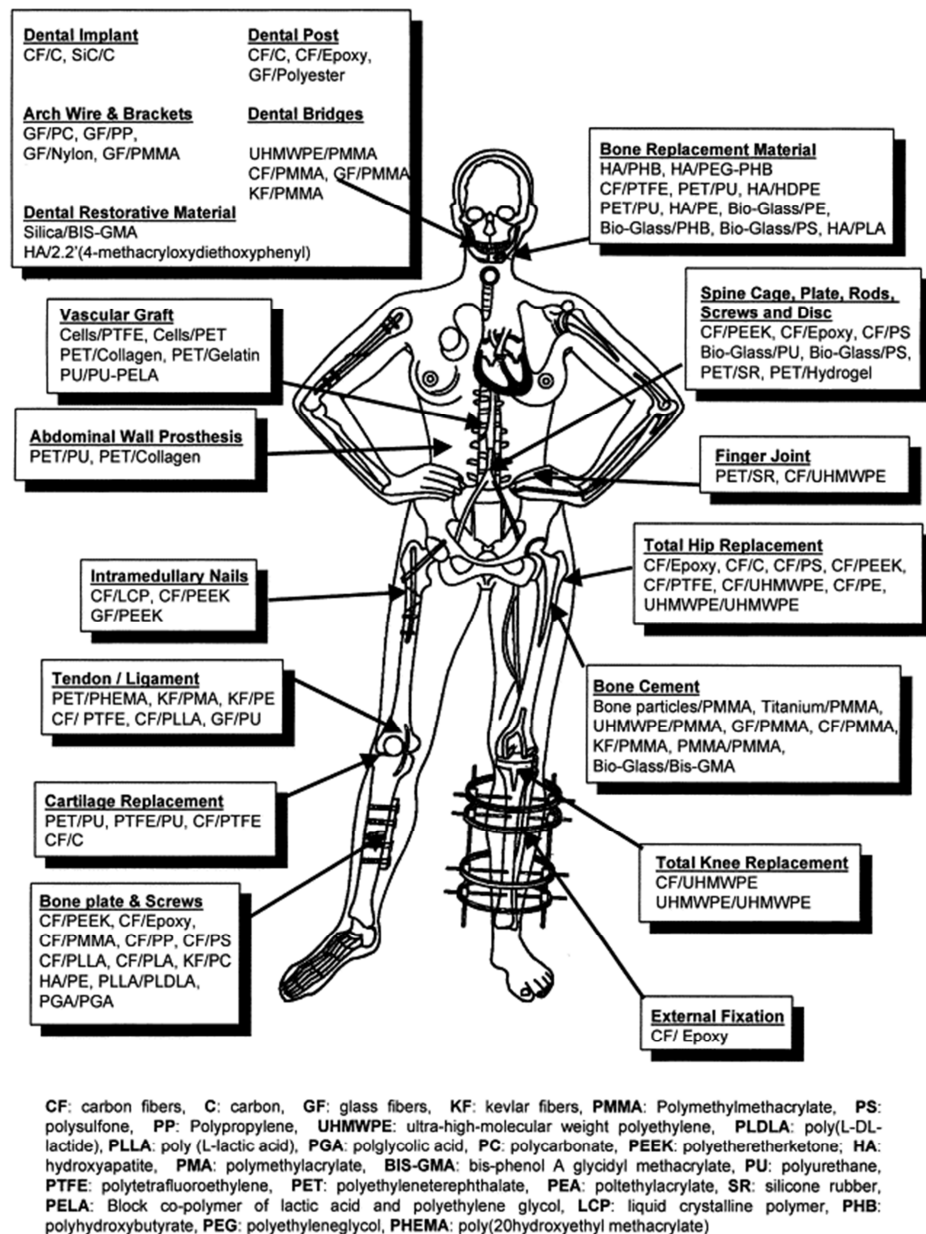


Figure 3.2.11. Overview of the different composite materials being developed for tissue reconstruction at different anatomical sites [Reproduced from Ramakrishna et al. (2001)].

The development and application of degradable composite materials has been viewed as an attractive alternative to traditional metallic orthopaedic implant devices (section 3.2.2.1). This is due to the time-dependent reduction in mechanical properties of such materials and their subsequent ability to gradually transfer mechanical loading to the regenerating tissue as the implant degrades. As discussed in section 3.2.2.3, this would help alleviate any stress-shielding problems (such as those encountered with metallic implant devices – section 3.2.2.2) whilst also eliminating any long term cytocompatibility issues or need for secondary removal surgery. Furthermore by altering the material configuration and precursor materials, composite biomaterials have the ability to be developed with tailored

degradation rates aimed at matching specific tissue formation rates across different anatomical sites. Accordingly a variety of composite configurations using degradable materials have been investigated that have been primarily focused on applications such as fracture fixation plates, pins or screws (Table 3.2.9). In degradable materials the inclusion of basic calcium phosphate compounds has also been used in applications to mediate the acidic degradation of the polymer matrix and buffer any pH effects (such as the lactic acid and autocatalysis effects observed during PLA degradation – section 3.2.2.3) [7, 86, 131, 134].

However the major challenge in the development of such materials is, according to Chen et al. (2012), achieving materials that are not only biodegradable but are also mechanically stable after implantation. This is due to the counterintuitive relationship between mechanical strength and material degradation. Consequently authors such as Pietrzak & Eppley (2000) have indicated that degradable orthopaedic devices should typically aim to retain at least 80% of their mechanical properties after six to eight weeks of degradation [9, 86].

Table 3.2.9. Examples of different composites from the literature and those commercially available for use as orthopaedic fracture fixation plates, pins and screws.

| Author/Product | Matrix | Filler | Filler Conc. |
|-----------------------------------|------------------------------------|----------------------------|--------------|
| Doyle et al. (1991) [7] | PHB | HA Particles | 40 vol.% |
| Shikinami & Okuno (1999) [7] | PLA | HA Particles | 50 wt.% |
| Russias et al. (2006) [135] | PLA | HA Whiskers | 70-85 wt.% |
| Misra et al. (2007) [7] | PHB | Bioglass [®] 45S5 | 20 wt.% |
| Zhou et al. (2009) [136] | PLLA | Phosphate Glass Particles | 10 wt.% |
| Felfel et al. (2013) [137] | PLA | Phosphate Glass Fibres | 30 vol.% |
| Charles et al. (2013) [138] | *Self-Reinforced PLLA-HA (15 wt.%) | | |
| SmartPins (Bionx, USA) [139] | *Self-Reinforced PLLA | | |
| FIXSORB 30 (Takiron, Japan) [139] | PLLA | HA Particles | 30 wt.% |
| BioComposite (Arthrex, USA) [139] | PLLA | BCP Particles | 30 wt.% |

*Self-reinforced (SR) composites incorporate matrix and reinforcing fibres of the same basic thermoplastic polymer family where the matrix has a significantly lower melt temperature compared to the polymer fibres.

3.3 Cranioplasty

3.3.1 Overview

Cranioplasty is a surgical procedure aimed at repairing a cranial vault defect such as those produced by incidents of neurosurgical trauma where sections of calvarial bone have been surgically removed (also known as a craniectomy). The subsequent closure of the defect site is then performed in order to physically protect the underlying brain, provide suitable cosmetic results and improve neurological symptoms. These defects typically range from 12-178 cm² and can be corrected through a range of different native or synthetic cranioplasty plate materials ^[140-142].

3.3.2 Cranioplasty Plate Materials

3.3.2.1 Auto- and Allogenic Bone

The use of autologous bone tissue in cranioplasty was introduced in the 1950s and corrects the defect using the section of bone (i.e. bone flap) previously removed during the earlier craniectomy surgery. This route is considered to be the simplest option given the advantages of autologous material (section 3.2.1.1) and likely correlation with the defect contours. However they can suffer from relatively high infection rates ($\approx 33\%$) ^[2, 140, 142].

Alternatively cranioplasty procedures utilising allogeneic bone can be performed using a split-graft technique where the inner and outer tables of a donor's calvarium are separated. The outer table is then used to correct the cranial defect whilst the inner table remains with the donor. This technique is considered to provide aesthetically pleasing results however it is unsuitable for large defects and suffers from the same allograft bone issues discussed in section 3.2.1.2 ^[2, 140].

3.3.2.2 Metals

Since their initial use during the 1940s, titanium and its alloys have become the only metallic biomaterial currently used in cranioplasty and is considered to be the material of choice for the treatment of moderate to large sized craniectomy defects. This has been due to its good biocompatibility, high strength-to-weight ratio, malleability and comparatively low radiopacity at a reduced cost to alternate metals. Furthermore modern titanium implants can be pre-fabricated using 3D CAD/CAM technology to achieve customised 2-4mm thick cranioplasty plates (Figure 3.3.1) that match the defect contours ^[2, 143].

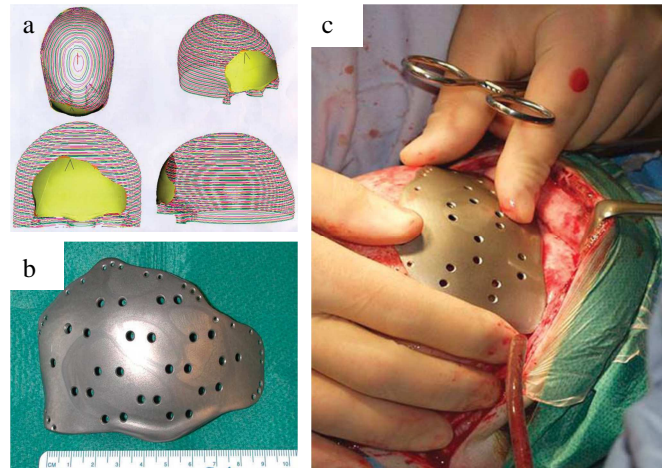


Figure 3.3.1. Manufacture and implantation of a titanium cranioplasty plate for frontal skull reconstruction showing a) Simulation of reconstruction using CAD/CAM software based on CT scan data b) Manufactured titanium plate and c) Surgical implantation and fixation of titanium plate for frontal basis reconstruction [Reproduced from Spetzger et al. (2010)].

Yet despite its higher radiolucency, titanium can continue to generate significant artefacts in both CT and MR imaging that can hinder the postoperative review of patients especially where large reconstructions have been performed. Its application is also associated with patient discomfort in extreme weather conditions due to its high thermal conductivity ^[2].

3.3.2.3 PMMA

Polymethyl-methacrylate (PMMA) has become increasingly popular for cranioplasty due to its ease of handling and intraoperative flexibility that permits its application in technically challenging reconstructive craniectomy defects with cosmetically pleasing results. This is further complimented by the lightweight, non-magnetic and low thermal conduction of the resulting implant that can possess mechanical properties similar to bone for a comparatively lower cost than the titanium equivalent ^[2, 140, 143].

The application of PMMA during a cranioplasty procedure typically involves the manual moulding of the paste as it sets to fit the defect contours to produce 3-6mm thick plates. This plate is then secured using low profile titanium fixation devices (Figure 3.3.2) with large scale cranioplasty procedures commonly incorporating a titanium reinforcing mesh to combat the inherent brittleness of PMMA (Table 3.2.4) ^[2, 140, 143].

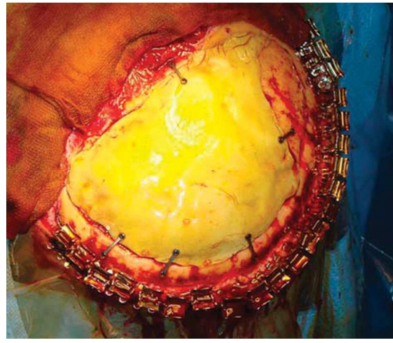


Figure 3.3.2. Navigation assisted reconstruction of a large skull defect using a PMMA cranioplasty plate fixed with titanium screws [Reproduced from Spetzger et al. (2010)].

Besides its brittle nature, the exothermic temperatures during the polymerisation of PMMA has been a major concern due to the risk of potentially damaging the surrounding tissue (i.e. dura mater, cerebral cortex etc.). Consequently the PMMA must be constantly irrigated with saline during polymerisation and contour shaped before being removed from the defect site whilst still in a deformable state ^[144-146]. Additionally PMMA implants are considered to have a high rate of extrusion and infection (reported to be $\approx 24\%$) with further concerns relating to its suitability in paediatric operations due to its inability to accommodate cranial growth ^[2, 143].

3.3.2.4 Polymers

The development of porous polyethylene (PE) with $\text{\O}100\text{-}250\mu\text{m}$ pores offers an implant material that can be easily cut, shaped and sutured intraoperatively and is capable of tissue ingrowth from the surrounding skull bone tissue. Compared to PMMA, porous PE can reduce the overall duration of the surgical procedure at an equivalent cost and has been sold in different sizes as MEDPOR[®] or MEDPOR[®] Titan (Stryker[®], USA) implant materials (Figure 3.3.3a,b). However due to its low mechanical properties (even with mechanical reinforcement) the use of porous PE has been limited to small cranial defects ^[143, 147].

Polyetheretherketone (PEEK) is a semi-crystalline, non-degradable thermoplastic polymer that has been widely used in spinal surgery since 1998 due to its inert nature, light weight, radiolucency and mechanical properties that approach those of cortical bone. Due to these features and previous clinical results, PEEK has now been suggested as a future cranioplasty plate material using 3D CT scanning data to create patient specific plates

(Figure 3.3.3c). Initial publications on the performance of PEEK cranioplasty implants have reported promising results however no long term data is yet available [2, 143].

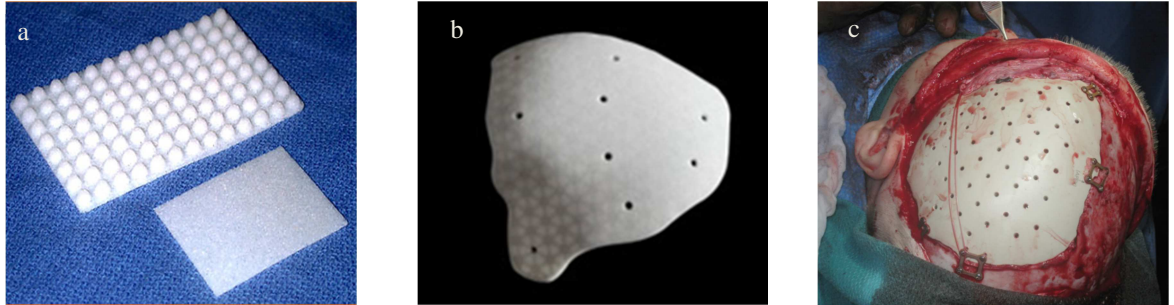


Figure 3.3.3. Polymer cranioplasty plates a) MEDPOR® Surgical implant [Reproduced from Liu et al. (2004)] b) MEDPOR® Titan cranial plate for temporal reconstruction with reinforcing titanium mesh visible [Reproduced from <http://www.stryker.com> (Accessed 14/09/2014) and c) Patient specific customised pre-fabricated PEEK implant plate from 3D CT data [Reproduced Harris et al. (2014)].

3.3.2.5 Ceramics

Calcium phosphate ceramics have held a particular interest as cranioplasty plate materials and are predicted to be important in developing future alloplastic cranioplasty implants [143, 148]. This has subsequently seen the development of preformed porous Ca-P implants with interconnected porosities such as the range of HA cranioplasty devices offered by Fin-Ceramica® (Italy). However as discussed in section 3.3.2.4, the brittleness of calcium phosphates renders them highly susceptible to fracture especially during device fixation and is further compounded by their inability to be moulded intraoperatively [143, 149].

The development of HA based cements has allowed cranioplasties to be performed with ceramic materials that could be easily manipulated during surgery in a similar manner to PMMA. These products are supplied as BoneSource® (Stryker, USA) or Norian SRS® (DePuy Synthes, CH/USA) with titanium meshes commonly integrated into the cement during the reconstruction of large scale defects to improve their mechanical properties. Yet the application of these cements is limited by their relative expense and reported high rates of infection [2, 150, 151].

3.3.2.6 Composites

The application of particulate or fibre reinforced composites as cranioplasty devices has been investigated with a range of material configurations. These have include use of HA reinforced HDPE as well as hydrolytically stable carbon, S-glass or E-glass fibres in different polymer resins (e.g. PEEK, bisphol-a-glycidyl methacrylate/triethyleneglycoldimethacrylate) [4-6, 152-155]. Due to the inert nature of these reinforcing fibres, these implant materials have also incorporated bioactive glass particles such as Bioglass[®] 45S5 or BonAlive[™] into their composite structure (section 3.2.2.6). However unlike the dense composites intended for fracture fixation plates, cranioplasty composites have been developed with dense-porous sandwich like architectures in order for the material to possess suitable mechanical properties whilst allowing for cellular ingrowth (Figure 3.3.4) [5].

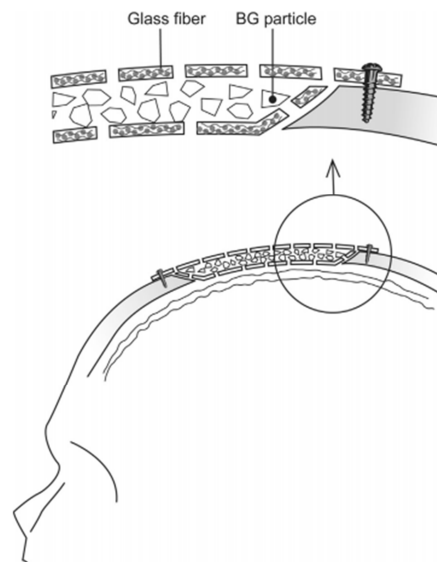


Figure 3.3.4. Illustration of a fibre reinforced cranioplasty plate design that combines high performance non-resorbable glass fibres with a porous layer containing bioactive glass (BG) particles [Reproduced from Vallittu et al. (2015)]

Additional considerations in cranioplasty fibre composite design also related to the lack of a defined mechanical loading regime at anatomical sites across the calvarium. As a result, the use of continuous bi-directional or fibre weaves/fabrics are considered by Vallittu et al. (2015) to be the preferred option compared to the selective orientation and advantageous anisotropic properties found in fibre composite fracture fixation plates (section 3.2.3.1) [5].

3.3.3 Cranioplasty Complications

Despite being considered a physiologically and technically straightforward operation, high complication rates in cranioplasty procedures are common ($\approx 30\%$) and can include patient symptoms such as infection, haematoma, headache and seizures. However these complication rates will vary and are dependent upon the patient's radiography/surgical history, age, procedure duration and primary pathology as well as the cranioplasty site, size and implant material used [140, 141, 156].

Post-operative infection is the most common and significant complication in cranioplasty procedures due to its serious consequences and is regarded by Thavarajah et al. (2012) as one of the key drivers in the diversification and evolution of cranioplasty plate material technology. Retrospective studies on cranioplasty procedures have found these infection rates to range from 5-9% with *Staphylococcus epidermidis*, *Staphylococcus aureus* and *Propionibacterium* identified as the predominant infectious bacteria. These infections are believed to be caused by skin microbiota and their occurrence is influenced by disrupted wound healing, the duration between craniectomy and cranioplasty, prior procedures as well as inflammatory responses [3, 142, 156].

If an infected case is confirmed, the complete removal of the cranioplasty plate is required before a series of broad-spectrum and systemic antibiotic agents is conducted over six to eight weeks. A replacement cranioplasty procedure is then performed after 6-13 months. However the continued rise of antimicrobial resistant infections has placed greater emphasis on preventative measures rather than the current post-operative treatments with the financial implications of treating cranioplasty plate infections estimated to be £9,283 per case to the National Health Service (NHS) according to O'Keeffe et al. (2012) [3, 141, 142, 156].

3.4 Phosphate Glasses

3.4.1 Definition and Theory of Glass Formation

Given the range of manufacturing methods and materials capable of forming glasses, the definition of a glassy material has been typically based on its material characteristics. Accordingly glasses are defined by Shelby (2005) as “an amorphous solid completely lacking in long range, periodic atomic structure, and exhibiting a region of glass transformation behaviour”^[157].

The principles of glass formation can be explained when considering a heated melt of fixed volume that is subsequently cooled at a controlled rate to room temperature. As the temperature drops below the samples melt temperature (T_m) a crystalline state is typically formed that displays a short or long range periodic atomic arrangement. This transition is driven by the tendency of the thermodynamic system to fall to its lowest energy state and is signified by the sharp drop in enthalpy shown in Figure 3.4.1^[157].

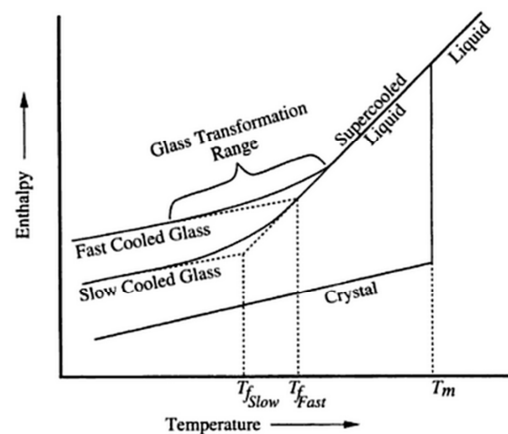


Figure 3.4.1. Enthalpy-Temperature diagram showing formation of crystalline and glassy materials as well as the effect of cooling rate on glass formation [Reproduced from Shelby (2005) Introduction to Glass Science and Technology].

However, if a sample is cooled below its T_m without crystallisation then the materials structure continues to rearrange with decreasing temperature as kinetic factors (i.e. viscosity) overrule the thermodynamic system. Progressive cooling of the liquid and the corresponding increases in viscosity then lead to its structure becoming fixed without any atomic arrangement. This behaviour is represented by the gradual slope in Figure 3.4.1 as the enthalpy deviates from the equilibrium state (observed by the formation of a crystalline material) and is defined as the range of glass transition. The so-called ‘frozen liquid’ can

now be considered as a glassy material. Additionally since deviation from the equilibrium state is dictated by kinetic factors, the rate at which the melt is cooled will ultimately control the temperature at which the sample enters this glass transition region. Thus if a material was to be cooled at a reduced rate then the glass transition temperature (T_g) would shift to lower values with the atomic arrangement of the resulting glass reflective of its arrangement prior to its deviation from the equilibrium state (Figure 3.4.1) ^[109, 157].

Furthermore given the range of materials capable of forming a glass, the American Society for Testing and Materials (ASTM) has defined a glass as any material that has been “cooled from the melt without crystallising”. Accordingly the formation of glassy materials is dependent upon achieving cooling rates high enough for kinetic factors to dominate the thermodynamic system and prevent crystallisation. For a typical inorganic silicate melt (used in the manufacture of windows and drinking vessels) this corresponds to a relatively slow $\approx 20^\circ \text{ min}^{-1}$ whilst the generation of metallic glasses requires rapid cooling rates of $\approx 2^\circ \text{ sec}^{-1}$ ^[109, 157].

3.4.2 Manufacturing of Phosphate Glasses

Phosphate glasses (PGs) have conventionally been manufactured from a melt quenching technique that involves the mixing and heating of raw materials inside a platinum or ceramic crucible to form a homogenous melt. These temperatures typically range between 800-1300°C with the selection and quantity of each precursor based on the calculated proportions of each glass component in order to achieve a specific glass composition (mol%). This melt is then rapidly cooled between two metal plates or poured into water with the production of bulk monoliths achieved using a preheated graphite or metal mould. Monolith samples are then typically subjected to an annealing cycle where they are slowly cooled from a predetermined value to room temperature at a controlled rate in order to alleviate any residual internal stresses in the glass that were generated as it was initially cast ^[109, 157].

Other methods of PG production include relatively modern sol-gel techniques that allow glasses to be produced at comparatively lower temperatures from a polymer-type reaction of a compositionally specific solution. Due to the lower temperatures, sol-gel glasses can incorporate drugs and growth factors as well as allow for development of polymer-glass hybrid materials. However sol-gel PGs are reported to be especially fragile and possess dissolution rates unsuitable for most biomedical applications ^[109].

3.4.3 Structure and Classification

The theory of a glass's structure includes the influential studies by Zachariasen (1932) who proposed the formation of a three dimensional structural network from silicates or phosphorus pentoxide (P_2O_5) glass forming compounds. Further studies by Hägg and Van Wazer challenged these concepts and proved that phosphate glasses could also be composed of large one dimensional molecular groups. This evidently led to glass structure models being described in terms of the short range bonding information and long range length scales throughout the materials overall structure^[157, 158].

PGs are based on the P_2O_5 glass former with the orthophosphate P-tetrahedron (PO_4^{3-}) the basic structural unit that is able to form covalent bonds with any surrounding P-tetrahedrons via the molecule's three free oxygen atoms. Due to their ability to bridge between P-tetrahedrons, these oxygen atoms are generally referred to as bridging oxygen's (BOs) and allow for the formation of chains, rings or branching network structures of orthophosphate units to be generated (via the P-O-P bonds). This three dimensional random network of covalently bonded P-tetrahedrons (as described by Zachariasen, 1932) for a simple vitreous P_2O_5 glass ($v\text{-}P_2O_5$) is represented in Figure 3.4.2^[109, 158].

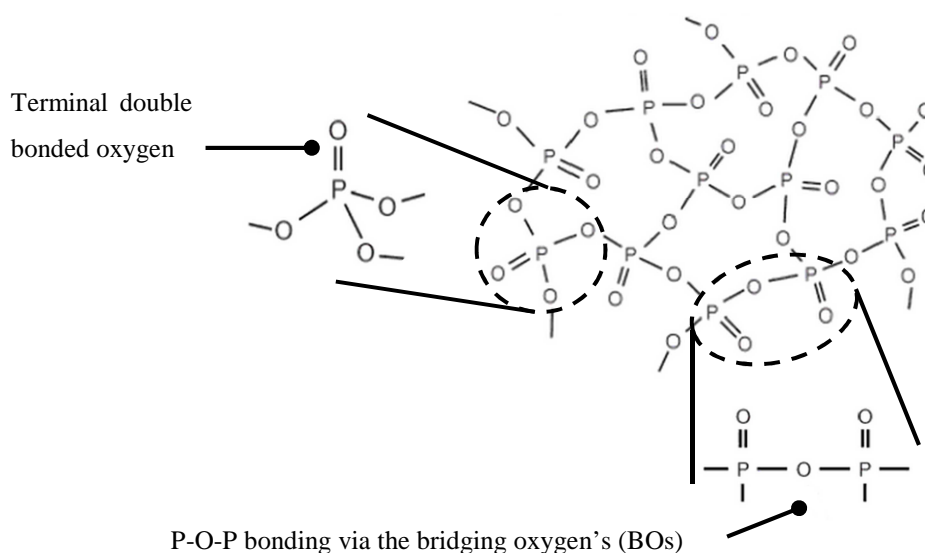


Figure 3.4.2. Random network structure of a vitreous phosphate glass generated by P-tetrahedra linked by P-O-P covalent bonds [Modified from Jones & Clare (2012)].

The corresponding structure of a PG network is typically classified under the Q^i terminology where i represents the number of available BOs per P-tetrahedron (Figure 3.4.3). This classification is dictated by the PG composition and is influenced by the

addition of alkali or alkaline earth metal ions into the PG structure. These ions are intended to modify the glass's structure and have been typically used to improve the poor durability and hygroscopic nature of ν - P_2O_5 glasses. These additional compounds are commonly referred to as network modifier oxides (MOs) and allow for the production of PGs with tailored material properties based on their specific composition [158].

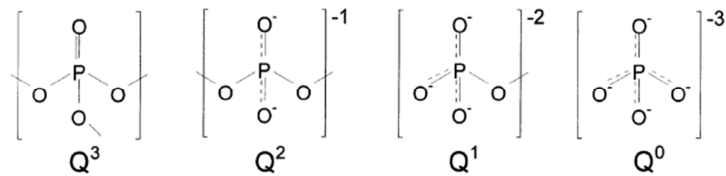


Figure 3.4.3. Classification of PG networks based on Q^i terminology showing decreasing BO's as Q^n decreases [Modified from Brow (2000)].

These modifier oxides can include compounds such as magnesium oxide (MgO), calcium oxide (CaO) or titanium dioxide (TiO_2) and their introduction cleaves the P-O-P bonds in the PG network. This subsequently generates ionic bonds between the non-bridging oxygens (NBOs) of different phosphate groups/chains which are often described as forming a chelate-like structure (Figure 3.4.4). This consequently disrupts the PG network and is known as network depolymerisation [109].

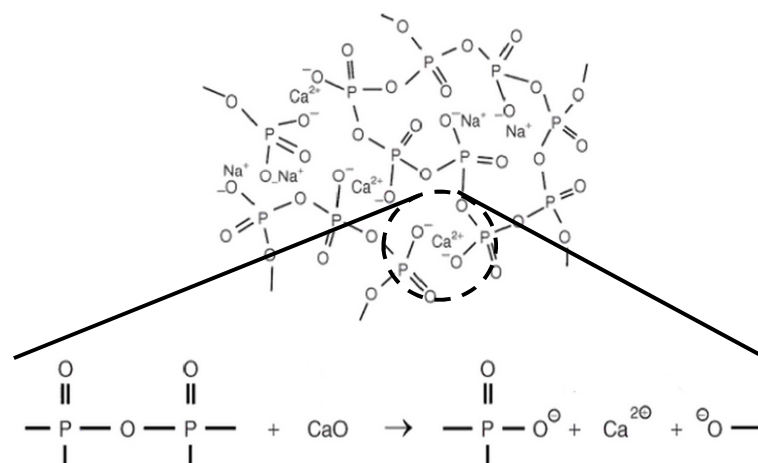


Figure 3.4.4. Change in P-O-P glass structure from the addition of MOs (CaO/ Na_2O) into the phosphate network and the formation of ionic bonds between the phosphate groups - Note that due to the single positive charge of the Na^+ ion, the PG network is depolymerised but no ionic bonding between chains occurs [Modified from Jones & Clare (2012)].

As a result, the random three dimensional crosslinked P-tetrahedra network (Q^3) in a ν - P_2O_5 glass can shift to one consisting of linear polymer-like phosphate chains of decreasing length (Q^2/Q^1) to a glass composed of isolated orthophosphate groups (Q^0) as the concentration of MOs is increased (i.e. $Q^3 \rightarrow Q^2 \rightarrow Q^1 \rightarrow Q^0$). For a binary PG this shift in Q^i classification can be described by the pseudo-reaction $2Q^n + R_2O \rightarrow 2Q^{n-1}$ (where R is a metal atom and n refers to the Q^i network classification) ^[158, 159].

The resulting PG networks from MO addition typically consist of both covalent and ionic bonding and allows for a vast range of potential PG compositions with tailored properties to be achieved from the use of specific MOs and their relative concentrations (mol%). These include the glass's thermal stability (i.e. its tendency towards crystallisation), mechanical properties and its dissolution rate (D_r) which can be altered by several orders of magnitude depending on the atomic radius and valence of the selected MO cations ^[109]. Some commonly utilised MOs along with their related properties are shown in Table 3.4.1. Additionally the increased PG network disruption caused by the number of different MOs can also influence the glass properties ^[109, 160, 161].

Table 3.4.1. Common modifier oxides (MOs) used in phosphate glass compositions showing their atomic weight, ionic radius and charge-to-size ratio (arranged by increasing ionic radius).

| MO/Cation | Atomic weight of cation (amu) ^[146] | Ionic radius of cation (pm) ^[146] | Charge-to-size ratio |
|-------------------|--|--|----------------------|
| B_2O_3/B^{3+} | 10.810 | 41.0 | 0.0731 |
| Fe_2O_3/Fe^{3+} | 55.845 | 75.0 | 0.0400 |
| MgO/Mg^{2+} | 24.305 | 86.0 | 0.0232 |
| ZnO/Zn^{2+} | 65.380 | 88.0 | 0.0227 |
| TiO_2/Ti^{4+} | 47.867 | 100.0 | 0.0400 |
| CaO/Ca^{2+} | 40.078 | 114.0 | 0.0175 |
| Na_2O/Na^+ | 22.989 | 116.0 | 0.0086 |
| La_2O_3/La^{3+} | 138.905 | 117.2 | 0.0255 |
| Sr_2O_3/Sr^{2+} | 87.620 | 132.0 | 0.0151 |

A summary of PG classification based on the glass former content (P_2O_5 mol%), Q^i terminology and corresponding network structure is shown in Table 3.4.2. It should also be noted that due to the difficulty in achieving compositions with an exact stoichiometry of 50 mol% P_2O_5 , metaphosphate glasses are often considered as a long chained polyphosphate glass^[109, 158]. Furthermore pyrophosphate glasses (also known as invert glasses) are formed by the interactions of cations and phosphate groups and not from a random network or entangled phosphate chains^[109].

Table 3.4.2. Description of various phosphate glass structures and network characteristics showing the P_2O_5 content, Q^i terminology and structure.

| Classification ^[109, 158] | P_2O_5 (mol%) | Q^i ^[158] | Structure ^[158] |
|--------------------------------------|--------------------|------------------------|---|
| Vitreous P_2O_5 | 100 | Q^3 | Cross-linked random network of Q^3 tetrahedra |
| Ultraposphate | >50 | Q^3/Q^2 | 50-75 mol%: randomly linked Q^3/Q^2 >75-80 mol%: resembles ν - P_2O_5 |
| Metaphosphate | 50 | Q^2 | Q^2 phosphate polymeric chains of infinite length and ring type structures |
| Polyphosphate | <50 | Q^2/Q^1 | Q^2 chains of various lengths terminated by Q^1 P-tetrahedra |
| Pyrophosphate | <33.3 | Q^1 | Phosphate dimers ($P_2O_7^{4-}$) with isolated phosphate tetrahedra (PO_4^{3-}) |
| Orthophosphate | N/A | Q^0 | (PO_4^{3-}) phosphate tetrahedra |

Finally, intermediate oxides represent an additional glass component with the capability of functioning as either a MO or a network former. The introduction of these intermediate oxides can thus allow for the generation of hydration resistant covalent bonds to be introduced into the glass's backbone (e.g. P-O-M-O-P, where M represents an intermediate metal atom). Examples of these intermediate oxides include those based on magnesium (Mg), iron (Fe), aluminium (Al) and zinc (Zn)^[109].

3.4.4 Dissolution Mechanisms

The dissolution rate (D_r) of a PG can vary over more than four orders of magnitude and is dictated by the glass composition/thermal history and immersion conditions (e.g. temperature, pH, static/dynamic media flow, media ionic concentration and surface area-to-volume ratio). It is however generally accepted that PG dissolution is a two stage process and that it is consistent with a typical polymer hydration model where the initial diffusion of water into the glass surface leads to the release of phosphate chains through hydrolysis of the PG network (section 3.2.2.3). Furthermore PGs are considered to typically degrade congruently with the resulting dissolution products and changes to the ionic concentrations in the aqueous media reflective of the glass's composition^[111, 162, 163].

Upon immersion in aqueous media, it is believed that water molecules penetrate into the surface of the phosphate glass leading to the formation of a smooth hydrated layer across the sample at the glass-water interface. The formation of this hydrated layer occurs in tandem with an immediate ion exchange reaction between the Na^+ ions in the glass and the waters H^+ ions at the phosphate chain ends (Figure 3.4.5)^[163].

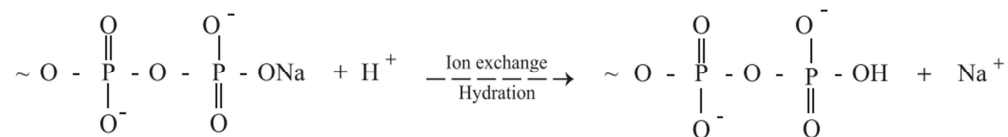


Figure 3.4.5. Hydration reaction that produces the formation of a hydrated surface layer across the glass surface due to the exchange of the sodium with hydrogen ions in water (Na-H) [Reproduced from Gao et al. (2004)].

Given that this ion exchange process occurs immediately, the formation of this hydrated layer is governed by the diffusion rate of water molecules into the bulk glass which is strongly affected by the composition of the PG. This is due to the resulting crosslinks/chelated network structures formed from the introduction of suitable MOs and their ability to retard the diffusion of water molecules into the glass network which consequently improves the durability of the glass^[163].

Once formed, this hydrated layer propagates inward into the glass and is followed by the hydration of entire P-O-P chains that are then disentangled and released into the aqueous environment (Figure 3.4.6). The liberation of these phosphate chains is coupled with the

release of the glass's modifier cations with the linear dissolution rate of a PG reflective of the release kinetics of its phosphate chains ^[109, 163].

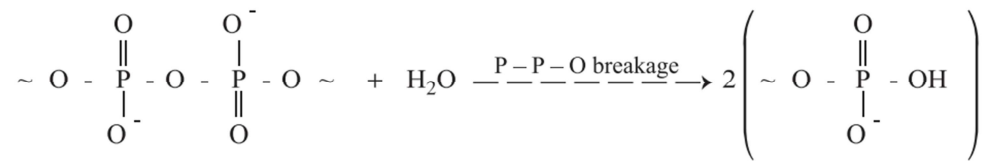


Figure 3.4.6. Breakage of P-O-P bonds in a PG network from the attack of H₂O water molecules after the initial surface hydration reaction [Reproduced from Gao et al. (2004)].

The dissolution process of PGs is consequently considered by Bunker et al. (1984) to follow two separate kinetic periods which are described by an initial decelerating dissolution period obeying $q \propto t^{1/2}$ law (where q represents weight loss). This is then believed to be accompanied by a linear rate of time dependant dissolution ($q \propto t$). However these mechanisms are challenged by Delahaye et al. (1998) who attributes the initial decrease in PG D_r to the gradual increase in media ionic concentration as the glass begins to degrade. Accordingly Delahaye et al. (1998) believes that the dissolution kinetics of a PG should be considered as following a single linear time-dependant relationship ($q \propto t$) throughout the entire dissolution process ^[162, 164]. Furthermore it should be added that the dissolution rate of a PG must be considered with respect to its immersion conditions as accelerated dissolution rates will typically occur when samples are immersed low pH, elevated temperature environments and/or at high surface area-to-volume ratios.

3.4.5 Bioactivity Mechanisms

The mechanisms of bioactivity have been widely investigated for silica based glass compositions such as Bioglass[®] 45S5 and have been shown to be dependent upon a glass's chemical reactivity in physiological media. Accordingly the stages of HCA surface layer formation *in vivo* have been well characterised by Hench to follow a sequence of initial surface reactions prior to a series of cellular events as described in Figure 3.4.7. However in contrast, very little has been reported on the bioactivity mechanisms of silica free phosphate glass compositions that fail to display any sort of silica rich surface layer formation which is considered vital for providing nucleation sites for the Ca²⁺ and (PO₄)³⁻ ions to accumulate and eventually crystallise/precipitate into HCA ^[76, 165-167].

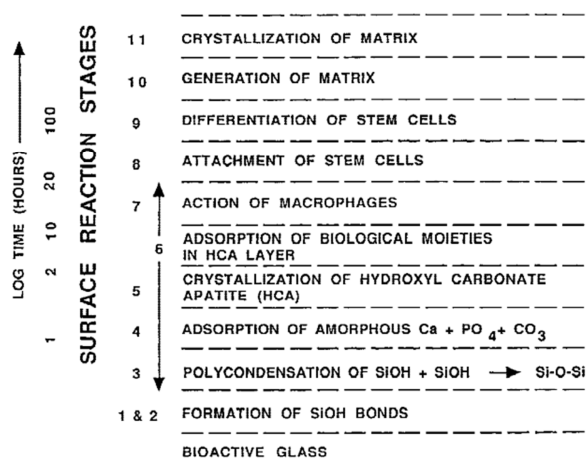


Figure 3.4.7. Sequence of reactions occurring across surface of silica based bioactive glasses with surface reactions (1-5) and cellular events (6-11) labelled [Reproduced from Hench (1998) Bioactive materials: The potential for tissue regeneration].

However authors such as Kasuga et al. (2005) have discussed how in silica free glass compositions the nucleation of bone like apatite can be formed from alternate groups such as Ti-OH, Ta-OH, Zr-OH, Nb-OH, -COOH and PO₄H₂. Furthermore in comparison to the SiO₂ rich gel layer found in silica based glasses, the formation of a calcium phosphate gel layer in PGs is also believed to play an important role in apatite layer formation^[168]. Yet glasses possessing low dissolution rates (i.e. increased durability) are considered to exhibit a poor bioactive response due to their inhibition of the dissolution-precipitation reactions required for apatite formation. In contrast Gayathri Devi et al. (2010) and Mohammadi et al. (2012) have also discussed how the acidic pH formed from a rapidly degrading phosphate glass can also inhibit apatite formation^[169, 170].

3.4.6 Compositions for Bone Tissue Augmentation

The continued interest in the development of new versatile materials for bone tissue regeneration has driven the demand for novel materials with adjustable levels of bioactivity and biodegradation rates. PGs are an advantageous group of materials with the potential for use in hard tissue regeneration due to their ability to be formed from compositions chemically similar to the mineral phase of bone and completely degrade at highly controllable rates. This is further complimented by the ability of PGs to be metabolised by natural processes occurring in the body and stimulatory effects elicited *in vivo* from the ions released during PG dissolution^[160, 171, 172].

The range of PG compositions produced by the addition of MO's has led to a broad spectrum of glasses being developed for the regeneration of bone tissue defects from different glass systems (i.e. binary → complex multicomponent systems). Consequently given the breadth of available literature, only compositions utilising a P₂O₅ glass former concentration of 40-55 mol% and intended for the purposes of bone tissue defect regeneration will be briefly summarised here.

3.4.6.1 Ternary Compositions

Glasses based on the ternary P₂O₅-CaO-Na₂O system as developed by Uo et al. (1998) offer potential as degradable scaffold materials for bone regeneration due their biocompatible dissolution products and compositionally dependant dissolution rates (D_rs). Development of this system continued with a range of studies characterising the compositional effects of different MO concentrations on the various properties of the resulting glasses. This work by Uo et al. (1998) and follow up studies (Franks et al., 2000; Ahmed et al., 2004; Skelton et al., 2007) consequently established that the D_r of a PG decreased with a reduction in P₂O₅ or increase in CaO concentration. This behaviour was due to changes in the glass structure and improvements to the network strength from enhanced ionic cross-linking between the NBOs of different phosphate chains. This was attributed to the disruptive monovalent Na⁺ being replaced with divalent Ca²⁺ cations. Dissolution testing revealed that the PG D_r appeared to follow a linear decrease as the CaO concentration was raised but also that non-linear trends existed when examining systematic alternations to the glass's P₂O₅ content that also affected its biocompatibility. Such non-linear trends were also seen in its thermal properties and were proposed by Ahmed et al. (2004) to be associated with changes to the network packing density due to the presence of small Q¹ pyrophosphate units in glasses with a 45 mol% P₂O₅ composition. However a general trend was reported over a set P₂O₅ content with elevated glass transition (T_g) and crystallisation (T_c) temperatures observed as the concentration of CaO was increased and the network was strengthened^[173]. A comparison of PG D_r in different media by Franks et al. (2000) also showed that reductions in the D_r could be achieved using high ionic strength media such as Hank's Balanced Salt Solution (HBBS) due to an ionic buffering effect^[173-176].

The *in vitro* testing of PG compositions in this system using MG63 and HOS cell lines (Salih et al., 2000; Bitar et al., 2004; Skelton et al., 2007) examined the relationship between a glass's D_r and its biocompatibility. The results obtained from the culture of cells

incubated in dissolution extracts or using direct contact cultures established that the D_r of a PG (and thus its composition) were critical to achieving biocompatible glasses. Correlating with previous data, the *in vitro* results showed that increases in the CaO content (mol%) produced samples with beneficial cell culture responses due to their reduced D_r . This effect was related to the associated ion release rates, pH changes and cell anchorage mechanisms (from the surface integrity) that influenced cell proliferation and expression of antigens like bone sialoprotein, osteonectin and fibronectin [160, 173-180].

Consequently from the range of glass compositions investigated, the glass forming regions and compositional dependence of this system was mapped using 2D ternary diagrams (Figure 3.4.8). Such illustrations also highlighted the limitations in the glass forming region of the P_2O_5 -CaO- Na_2O system and potential D_r that are critical to achieving biocompatible glasses [176].

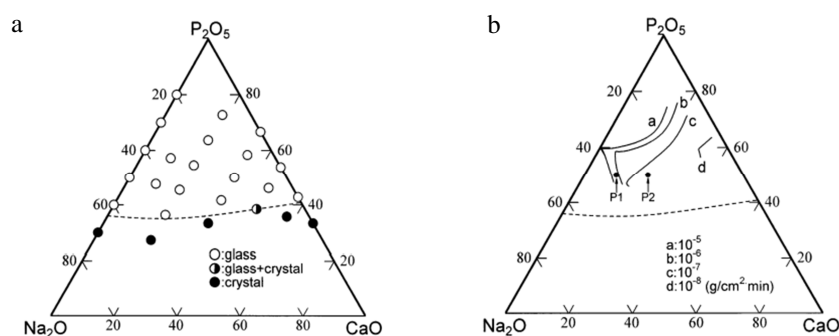


Figure 3.4.8. 2D map of a) Glass forming region and b) Corresponding dissolution rates of phosphate glasses in the P_2O_5 -CaO- Na_2O system [Reproduced from Uo et al. (1998)].

3.4.6.2 Complex Compositions

The addition and substitution of alternate MOs in more complex glass compositions has typically been based upon the introduction of cations with greater charge-to-size ratios than the previous P_2O_5 -CaO- Na_2O system. This has been in order to achieve glasses with an enhanced network strength (and consequently reduced dissolution rates) through the improved ionic cross-linking between phosphate groups/chains. Additionally the controlled release of specific MO cations from tailored PG compositions was anticipated to induce beneficial *in vivo* responses at the treatment site of the bone tissue defect (Table 3.4.3) [181-183]. Some example ternary and quaternary compositions incorporating alternative MOs based on the initial P_2O_5 -CaO- Na_2O system are shown in Table 3.4.4.

Table 3.4.3. Potential modifier cations for PG compositions aimed at bone tissue regeneration.

| Cation | Biological Function/Role |
|-----------|---|
| B^{3+} | Role in bone growth - suspected to replicate effects of oestrogen ^[184] |
| Mg^{2+} | Stimulates bone formation, increase bone cell adhesion and stability ^[185, 186] . |
| Zn^{2+} | Stimulates bone formation, regulates transcription of osteoblast genes ^[185, 186] . |
| Sr^{2+} | Beneficial to <i>in vivo</i> bone formation, possible treatment of osteoporosis ^[185, 186] . |

Table 3.4.4. Ternary and quaternary glass compositions with alternative MOs suited for bone regenerative applications showing the molar tested by various authors.

| | Author | Composition |
|------------|--|--|
| Ternary | Khor et al. (2011) ^[187] | $(P_2O_5)_{70-x}(ZnO)_{30}(MgO)_x$ x: 0, 5, 8, 10, 13, 15, 18, 20 mol% |
| | Lucacel et al. (2012) ^[182] | $(P_2O_5 \cdot CaO)_{100-x}(ZnO)_x$ x: 0, 0.1, 0.5, 1, 10, 50 mol% |
| Quaternary | Knowles et al. (2001) ^[181] | $(P_2O_5)_{45}-(CaO)_x-(Na_2O)_{55-x-y}-(K_2O)_y$ x: 0→25, y: 20, 24, 28, 32 mol% |
| | Franks et al. (2002) ^[188] | $(P_2O_5)_{45}-(CaO)_{32-x}-(Na_2O)_{23}-(MgO)_x$ x: 0→22 mol% |
| | Salih et al. (2007) ^[189] | $(P_2O_5)_{50}-(CaO)_{40-x}-(Na_2O)_{10}-(ZnO)_x$ x: 0→20 mol% |
| | Abou Neel et al. (2009) ^[190] | $(P_2O_5)_{50}-(CaO)_{30}-(Na_2O)_{20-x}-(TiO_2)_x$ x: 0, 1, 3, 5 mol% |
| | Abou Neel et al. (2009) ^[191] | $(P_2O_5)_{50}-(CaO)_{30}-(Na_2O)_{20-x}-(Sr)_x$ x: 0, 1, 3, 5 mol% |
| | Morikawa et al. (2013) ^[192] | $(P_2O_5)_{50}-(CaO)_{45-x}-(MgO)_x-(TiO_2)_5$ x: 0→45 mol% |

Alternative ternary glass compositions such as those assessed by Khor et al. (2011) were intended to generate PGs with improved durability due to the smaller atomic radii and larger charge-to-size ratios of Mg^{2+} and Zn^{2+} that could also provide an advantageous response *in vivo* (Table 3.4.3). The characterisation of PGs incorporating increasing amounts of MgO into ultra- and metaphosphate compositions showed decreases to the glass D_r . The increased durability was associated with the formation of more hydration resistant P-O-Mg-O-P bonds within the glass's network structure compared to the existing P-O-P backbone. Additionally, Khor et al. (2011) highlighted how the lower basicity of the oxygen atoms in these P-O-Mg-O-P bonds (due to the higher charge-to-size ratio of the Mg^{2+} cation) would limit their attraction to the positive H^+ ions of the H_2O molecules. Hence as the MgO concentration (mol%) increased, glass compositions were developed that displayed D_r s considered suitable for osteoblast cell adhesion and proliferation ($0.3\text{--}1.7 \times 10^{-2} \text{ mg cm}^{-2} \text{ hr}^{-1}$) as suggested by Bitar et al. (2004) and Parsons et al. (2004). Dissolution testing in buffered media of different pH also suggested that the preferential leaching of Zn^{2+} ions from PG samples would occur when samples were degraded in acidic media - contrasting the typical congruent PG dissolution behaviour (section 3.4.4) ^[178, 187, 193]. Meanwhile Lucacel et al. (2012) found that the inclusion of ZnO caused an inhibitory effect to PG bioactivity due to the glass's decreased dissolution rate ^[182].

Investigations into more complex quaternary PG systems (Franks et al., 2002; Abou Neel et al., 2009; Lee et al., 2013) showed that greater concentrations of MgO and TiO_2 resulted in increasing glass biocompatibility due to the formation of samples with reduced D_r s. As previously reported, this decrease in glass dissolution rate was attributed to the inclusion of modifier cations with comparatively higher charge-to-size ratios. Studies by Lee et al. (2013) also demonstrated that the atomic weights and structural bond lengths of different MOs could also further manipulate a glass's properties when developing new compositions. Meanwhile an analysis of glass bioactivity discussed the ability of Mg^{2+} ions to be beneficially substituted into apatite layers with Abou Neel et al. (2009) highlighting the potential of Ti^{4+} ions to improve the bioactivity of a PG. The reduced D_r and improved strength of the glasses structural networks was also reflected by shifts in the thermal properties. This was evident by the marked increase in the T_g and T_c in glasses with increasing concentrations (mol%) of either MgO or TiO_2 due to the increased energy required to break the structural bonds in the glass network. Changes to the density of these PG compositions was also reported and related to the comparative atomic weights of the metal atoms in the substituted MOs (Table 3.4.1) ^[183, 188, 190, 194].

Conversely the addition of increasing quantities of ZnO as a direct substitute for CaO in quaternary PG compositions (Salih et al., 2007; Abou Neel et al., 2008) produced glasses with gradually decreasing biocompatibility. These findings were linked to increases in the glass's dissolution rate that subsequently led to the formation of an acidic pH environment over the dissolution period and the rapid release of Zn^{2+} ions to cytotoxic levels. Meanwhile localised surface pH effects were also considered to have led to the poor biocompatibility observed in glasses containing relatively low amounts of ZnO. Based on the thermal data obtained using DSC, the inclusion of increasing concentrations of ZnO resulted in a gradual decrease in the glasses T_g and T_c . This behaviour was attributed to a weaker glass network structure being generated as the concentration of ZnO increased due to the difference in bond strengths between the stronger Ca^{2+} and weaker Zn^{2+} . This hypothesis would correlate with the observed thermal results but contradicts the previous literature and commonly accepted theories on PG structural modification via the inclusion of MOs with increasing charge-to-size ratios (Table 3.4.1) as discussed in section 3.4.3 and 3.4.6.1. Regardless it was concluded that when using ZnO as a MO, the appropriate ion release rates of Zn^{2+} ions should be carefully considered ^[109, 189, 195].

Increases to a glass's dissolution rate were also observed in compositions incorporating K_2O or SrO (Knowles et al., 2001; Marikani et al., 2008; Neel et al., 2009). These results could be clearly explained by the weaker glass structure stemming from the larger ionic radius of K^+ or Sr^{2+} cations and its increased disruption to the glass network. The replacement of the Na^+ with K^+ also corresponded to an increase in the density and hardness of the glass. Additional factors on the behaviour of K_2O containing PGs has been proposed by Knowles et al. (2001) relating to the occurrence of a mixed cation effect on the examined glass compositions. However no correlation between the influences of the mixed cation effect on a glass's dissolution rate has yet been reported ^[181, 191, 196].

The development of metaphosphate glasses with improved thermal stability via the substitution of CaO with MgO was examined by Morikawa et al. (2013) due to the difference in ionic radius and bond energy between Mg^{2+} and Ca^{2+} . This improvement was also attributed to an increase in the number of glass components whilst it was suspected that mixed cation effects could be responsible for the non-linear trends observed in the glass's thermal stability over different compositions. The effect of Mg^{2+} addition on the glass properties was also found to differ between meta- and invert glass compositions ^[192].

As shown by Morikawa et al. (2013), further flexibility in a glass's D_r and thermal stability could be achieved from an increased number of MOs (see also section 3.4.3). This has

since led to the characterisation of more complex multicomponent glasses such as those formed from quinary and septenary glass systems ^[145, 197].

Glasses of a $(\text{P}_2\text{O}_5)_{45}-(\text{CaO})_{(30-x)}-(\text{Na}_2\text{O})_{20}-(\text{CoO})_x-(\text{TiO}_2)_5$ (x : 0, 5, 10, 15 mol%) composition were investigated by Lee et al. (2013) who examined the potential structural and biological advantages from the incorporation and controlled release of cobalt (Co). Yet early investigations showed that despite a reduction in the glass's D_r with increasing Co concentration (mol%), the growth of MG63 cells on samples containing 15 mol% Co appeared to be inhibited. These results subsequently highlighted the need for further optimisation in this glass system and tailoring of ion release rates in order to achieve the desired cellular response. Evidence of a possible enhancement to the glass's thermal stability was also apparent by the relative increase in the crystallisation onset temperature (T_{oc}) ^[145]. The analysis of glasses by Novajra et al. (2011) that substituted K_2O with increasing quantities of TiO_2 in a $(\text{P}_2\text{O}_5)_{50}-(\text{CaO})_{30}-(\text{Na}_2\text{O})_9-(\text{SiO}_2)_3-(\text{MgO})_3-(\text{K}_2\text{O})_{(5-x)}-(\text{TiO}_2)_x$ (x : 0, 2.5, 5 mol%) system have also been investigated. These results were found to correlate with previous data that introduced cations of increasing charge-to-size ratios (Franks et al., 2002; Abou Neel et al., 2009) ^[188, 190, 197].

Meanwhile Weiss et al. (2014) investigated the substitution of Na_2O with TiO_2 or MgO into a P_2O_5 - CaO - Na_2O - SrO glass to develop quinary compositions with improved durability. Characterisation of these samples found that improved durability, thermal stability and mechanical properties were obtained from the incorporation of either 5 mol% TiO_2 or MgO . The expected change in glass properties was associated with an increase to the network's strength due to the advantageous properties of either Mg^{2+} or Ti^{4+} ions and their higher bonding energy ($394.3 \text{ kJ mol}^{-1}$ and $662.2 \text{ kJ mol}^{-1}$ respectively) compared to Na^+ ($257.2 \text{ kJ mol}^{-1}$). A direct comparison between the effects of MgO and TiO_2 on the PG properties also showed that the incorporation of 5 mol% TiO_2 generated samples with an increased density, hardness, fracture toughness and reduced D_r compared to MgO glass's. This was due to the greater bond energy and charge-to-size ratios of the Ti^{4+} ions that were able to act more readily as an intermediate oxide compared to Mg^{2+} ions ^[172].

However besides the stimulatory ions listed in Table 3.4.3, the inclusion of silver (Ag) in PG compositions has also been investigated for potential orthopaedic applications due to its broad antimicrobial properties against multi drug resistant bacterial strains. Consequently such studies have demonstrated how the inclusion of 5 mol% Ag into a glass system can severely limit the attachment and growth of bacteria ^[198, 199].

3.4.7 Phosphate Glass Fibres

3.4.7.1 Bulk vs. Fibre Properties

Owing to the difference in thermal and mechanical pre-history incurred during manufacturing, the structure and properties of phosphate glass fibres (PGFs) can deviate significantly from bulk monoliths of an identical PG composition. This relates to the frozen-in anisotropy of the phosphate chain network parallel to the fibres primary axis as a result of the mechanical drawing stress and rapid quenching (10^{-2} - 10^{-3} seconds) commonly experienced during manufacturing. The resulting change in internal structure is typically reflected by the fibres increased tensile modulus whilst the tensile strength is representative of the fibre surface quality ^[109, 160, 200, 201].

3.4.7.2 Fibre Manufacturing

Continuous PGFs have conventionally been manufactured from a melt spinning technique where droplets are drawn down directly through a nozzle from a temperature adjusted glass melt under the influence of gravity and hydrostatic pressure. These drops are then attenuated by mechanical tension and collected around a rotating drum (Figure 3.4.9a). Furthermore by altering the manufacturing conditions such as the glass melt viscosity, hydrostatic pressure, bushing nozzle diameter and drum speed (rpm), the glass fibre diameter and fibre-to-fibre spacing can be controlled. Alternative methods such as downdrawing from solid preforms and updrawing configurations have been also been developed for fibre production (Figure 3.4.9b,c) but suffer from poor efficiencies compared to melt spinning techniques ^[109, 160, 202, 203].

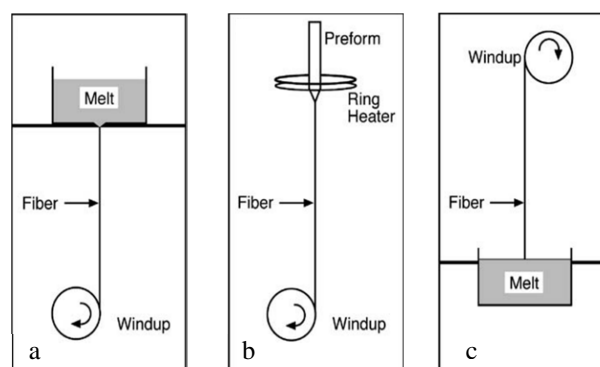


Figure 3.4.9. Representation of a) Melt spinning b) Solid pre-form downdrawing and c) Fibre updrawing techniques employed in PGF production [Reproduced from Wallenberger, (2010)].

However not all glass compositions are suitable for fibrillation and the ability to form PGFs are dependent upon achieving a glass melt of suitable viscosity (typically between $10^3 - 10^6$ Pa·s) without crystallisation of the glass occurring. This crystallisation is undesired due to its ability to prevent fibre drawing, reduce fibre mechanical properties and limit fibre bioactivity. Consequently the ease of forming fibres has typically been dictated by a glass composition's processing window (PW) that is reflective of its thermal stability and is defined as the temperature range between the T_g and T_{oc} with PW values of $>100^\circ\text{C}$ preferred for fibre drawing ^[109].

3.4.7.3 Biomedical Applications

PGFs have gained attention for a range of potential biomedical applications with particular interest in the regeneration of soft tissues (e.g. muscle and ligament), nerve repair and biosensors due to their suitable chemistry and morphology. Such studies include those by Ahmed et al. (2004) who examined the potential of iron doped PGFs in a (P_2O_5) - (CaO) - (Na_2O) - (Fe_2O_3) system as cell delivery vehicles for treating muscular diseases. Similar cell seeding and transplantation constructs were also investigated by Bitar et al. (2004) on a $(\text{P}_2\text{O}_5)_{50}$ - $(\text{Na}_2\text{O})_{(4-y)}$ - $(\text{CaO})_{46}$ - $(\text{Fe}_2\text{O}_3)_y$ (y : 0, 1, 2, 3, 4 mol%) composition for repairing the bone-ligament interface through the co-culture of osteoblast and fibroblasts cell types. However PGF have also gained considerable interest as degradable composite reinforcing agents in novel bone fracture fixation plates, pins or screws ^[178, 194, 204].

The development and systematic characterisation of $\text{Ø}8\text{-}40\mu\text{m}$ fibres based on the previously proven biocompatible ternary P_2O_5 - CaO - Na_2O glass system was examined by Ahmed et al. (2004) for any compositional dependence on the processability of PGFs. The analysis of compositions with varying P_2O_5 and CaO concentrations showed that fibres could not be manufactured from ternary polyphosphate glasses of ≤ 45 mol% P_2O_5 . This was attributed to the low P_2O_5 content of the glass and its resulting short-chained network structure that upon heating, produced melts of unsuitably low viscosity with a tendency towards crystallisation. Compositional influences from the substitution of Na_2O with increasing amounts of CaO displayed the expected increase in glass T_g and decrease in dissolution rate, confirming the same compositionally dependant properties in the fibres as previously reported for bulk samples (Uo et al., 1998; Franks et al., 2000). Further examination on the dependence of PGF manufacturing conditions showed the expected decrease in fibre diameter with increasing pulling speed (i.e. drum rpm) whilst glass composition was found to have no influence on the resulting fibre diameter. A comparison

between bulk and fibre forms of identical glass compositions also showed that fibres displayed a higher D_r and T_g compared to their bulk equivalent which was attributed to surface area effects and difference in thermal history^[174, 176, 205].

In contrast, dissolution studies by Patel & Knowles (2006) examined the effects of SiO_2 addition into a quinary PGF $(\text{P}_2\text{O}_5)_{50}-(\text{CaO})_{30}-(\text{Na}_2\text{O})_{(15-x)}-(\text{Fe}_2\text{O}_3)_5-(\text{SiO}_2)_x$ (x : 0, 1, 3, 5 mol%) composition in order to accelerate the D_r without substantially altering the dissolution media pH. Dissolution testing subsequently confirmed the increased D_r in glasses containing 5 mol% SiO_2 whilst it appeared that the pH changes produced by PGF dissolution were suitably buffered by the cell culture media. This was coupled with a general trend of increasing the glass's thermal properties (T_g , T_c) as the SiO_2 concentration increased^[206].

Further dissolution studies on the effects of aqueous aging to the mechanical properties and real-time dissolution mechanisms of PGFs were examined by Cozien-Cazuc et al. (2008, 2009) on a $(\text{P}_2\text{O}_5)_{40}-(\text{Na}_2\text{O})_{20}-(\text{CaO})_{16}-(\text{MgO})_{24}$ (mol%) composition. Initial tensile testing of $\text{Ø}10\text{-}40\mu\text{m}$ fibres prior to degradation showed that the annealing of fibres decreased the tensile strength from 484 MPa to 288 MPa. It was proposed that this was related to the development of a tensile surface layer containing shallow surface defects across the fibres that acted as initiators for fibre failure following Griffiths theory of brittle fracture. However the annealing process also showed an apparent increase in the tensile modulus from 44 GPa to 52 GPa. Mechanical testing of degraded fibres found that the modulus of as-prepared and annealed samples remained unchanged during immersion whilst the tensile strength of annealed fibres appeared to improve over time^[201, 207].

Data collected from each sample set consequently demonstrated that the annealing of PGFs could provide significant improvements to maintaining the mechanical properties of fibres compared to the application of a 1 wt.% 3-aminopropyltriethoxyethyl (APS) sizing agent^[207]. This was evident by the results which showed that the use of a sizing agent failed to significantly retard the PGF D_r due to the leaching of the sizing agent into the surrounding media. However it was predicted that different preparation techniques or an alternative choice of surface treatment could successfully enhance PGF durability. In contrast the reduced D_r of annealed fibre samples was coupled with smooth fibre topographies compared to the pitting corrosion observed during the dissolution of as-prepared fibres^[201, 208].

Further characterisation and environmental aging on a range of quinary compositions has been conducted to assess the suitability of several fibre systems for biomedical applications (Hasan et al., 2012; Haque et al., 2013; Sharmin et al., 2014). The testing of a $(\text{P}_2\text{O}_5)_{40}\text{-(MgO)}_{24}\text{-(CaO)}_{16}\text{-(Na}_2\text{O)}_{16}\text{-(Fe}_2\text{O}_3)_4$ (mol%) composition was examined by Haque et al. (2013) due to the previously reported advantages of Fe_2O_3 in improving glass durability by Ahmed et al. (2004). Tensile testing of these fibres showed that the filaments displayed tensile strengths of 250-300 MPa and a tensile modulus between 50-70 GPa [194, 209-211].

The analysis of $(\text{P}_2\text{O}_5)_{40}\text{-(MgO)}_{24}\text{-(CaO)}_{16}\text{-(Na}_2\text{O)}_{(20-x)}\text{-(Fe}_2\text{O}_3)_x$ (x : 0, 2, 4 mol%) and $(\text{P}_2\text{O}_5)_{(50-y)}\text{-(MgO)}_{24}\text{-(CaO)}_{16}\text{-(Na}_2\text{O)}_y\text{-(Fe}_2\text{O}_3)_4$ (y : 0, 5, 7.5 mol%) PGF compositions were assessed by Hasan et al. (2012) (Figure 3.4.10). Similarly a $(\text{P}_2\text{O}_5)\text{-(Na}_2\text{O)}\text{-(MgO)}\text{-(CaO)}\text{-(B}_2\text{O}_3)$ system incorporating B_2O_3 was examined by Sharmin et al. (2014) for meta- and polyphosphate glass fibre compositions. These modifier oxides were selected based on previous data (Ahmed et al., 2004; Sharmin et al., 2013) regarding their influence on improving sample durability, thermal stability and *in vivo* response [184, 194, 210, 211].

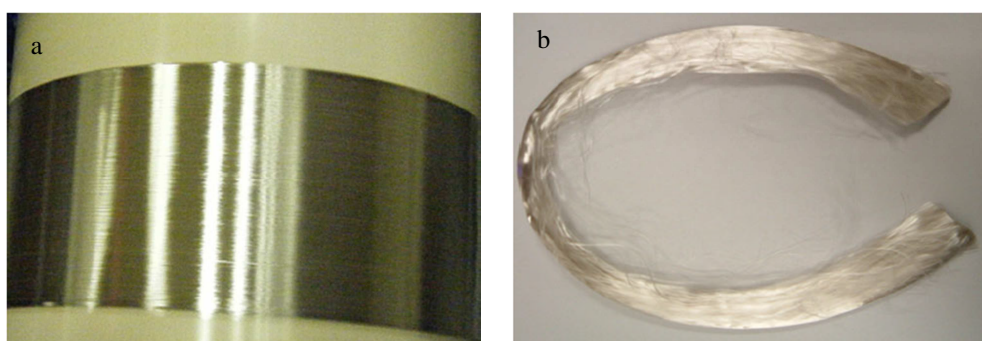


Figure 3.4.10. Images of PGF tows a) $(\text{P}_2\text{O}_5)_{50}\text{-(CaO)}_{16}\text{-(MgO)}_{24}\text{-(Na}_2\text{O)}_6\text{-(Fe}_2\text{O}_3)_4$ [Reproduced from Hasan et al. (2012)] and b) $(\text{P}_2\text{O}_5)_{50}\text{-(CaO)}_{40}\text{-(Na}_2\text{O)}_5\text{-(Fe}_2\text{O}_3)_5$ fibres - the change in colour was attributed to the composition of the glass [Reproduced from Ahmed et al. (2010)].

Both studies showed that the production of fibres could be achieved with compositions of 40-45 mol% P_2O_5 in contrast to the limits previously observed in the ternary system examined by Ahmed et al. (2004). This was due to the higher chain lengths as a result of the increased number of glass components and ability of Fe_2O_3 or B_2O_3 to act as both a network former and modifier oxide (i.e. as an intermediate oxide). The formation of hydration resistant P-O-Fe-O-P or P-O-B-O-P bonds in the networks backbone and

enhanced ionic cross-link densities produced the expected trends by reducing the glass's D_r and improving its PW. Enhanced tensile properties were also observed as the MO increased with tensile strengths as high as 1200 ± 146 MPa recorded by Sharmin et al. (2014). However it was also highlighted that compositions exhibiting very low D_r ($1.8 \times 10^{-6} \text{ g cm}^{-2} \text{ hr}^{-1}$) appeared to reduce the cellular activity compared to similar compositions with higher dissolution rates. It was therefore suggested that target specific glass D_r s would be required for eliciting an advantageous cellular response according to the desired application (Hasan et al. 2012) ^[184, 205, 210, 211].

3.4.8 Phosphate Glass Fibre Composites

Despite the range of material properties and biological responses elicited by PGs they remain unsuitable for load bearing applications due to their poor mechanical properties. Consequently numerous studies have examined the potential of incorporating PGFs into degradable polymers to produce resorbable bioactive fibre reinforced composite materials intended for replacing traditional metallic fracture fixation devices such as pins, plates, nails and screws (Felfel et al. 2013). This has been due to the advantages that a completely degradable fixation device presents in eliminating problems such as stress shielding and secondary revision surgery as discussed in section 3.2.2.2. The use of PGFs also allows for the degradation behaviour of these composites to be tailored for the treatment site and dictate the rate of load transfer to the remodelled tissue whilst simultaneously releasing stimulatory ions. Additionally PGFs possess advantages over alternative reinforcing materials such as those derived from natural origin (e.g. flax, hemp, jute, kenaf, abaca) that are considered to possess inconsistent dimensions and mechanical properties ^[212-214].

Accordingly the majority of studies have been aimed at developing PGF laminate composites via the compression moulding of fibre pre-pregs and polymer matrix sheets to generate materials with mechanical properties similar to those of cortical bone. However equally important is the rate at which these mechanical properties decline which, for a fracture fixation plate should aim to match the rate of bone formation whilst allowing the gradual transfer of loading to the native tissue as it strengthens over a 8-12 week period. As a result, investigations into various PGF compositions, fibre architectures, volume fractions and other composite modifications have been conducted with different polymer matrix materials ^[178, 215-221].

Composites of $0.06V_f$ and $0.18V_f$ utilising a PCL matrix with binary $(P_2O_5)_{50}-(CaO)_{50}$ (mol%) fibres were investigated by Ahmed et al. (2008) with as-prepared and annealed fibres. Mechanical testing of composites showed that no improvement to the flexural strength was observed from the reinforcement of PCL with PGFs. However an increase in the elastic modulus was observed in composites that increased from 0.5 GPa to a maximum of 2.4 GPa with $0.18V_f$ that was within the range of trabecular bone. Higher V_f composites also saw greater ionic concentrations in the degradation media which were consistent with the relative amount of fibres in each composite configuration. Comparisons also indicated that the fibre volume fraction and surface area effects may dominate composite degradation behaviour ^[215].

Further studies of polyphosphate $(P_2O_5)_{35}-(CaO)_{27.5}-(MgO)_{9.5}-(Na_2O)_{22.5}-(TiO_2)_{5.5}$ (mol%) fibres were conducted by Brauer et al. (2008) to assess the fracture behaviour and *in vitro* response of a reinforced organic methacrylate modified oligolactide composite. As expected, the incorporation of TiO_2 was shown to improve the PW of the glass and allowed for the production of $\varnothing=125\mu m$ glass fibres from the glass melt without crystallisation. The resulting composites were found to have similar mechanical properties to cortical bone whilst mechanical testing showed a fibrous fracture mode when tested in 3- or 4-point bending. This was regarded as the desirable failure mode for biomedical implants due to the possibly serious consequences that could result from the sudden failure of an implant. However SEM imaging at the composite fracture sites also showed evidence of sample delamination that indicated poor interlaminar bonding. The culture of composites with murine MC3T3-E1 cells showed that these materials also possessed suitable biocompatibility ^[211, 217, 221].

The retention of mechanical properties and biocompatibility of PGF-PLA composites was examined by Ahmed et al. (2009) who characterised samples using a $(P_2O_5)_{50}-(CaO)_{40}-(Na_2O)_5-(Fe_2O_3)_5$ (mol%) composition of as-prepared or annealed fibres. Composites were generated by the incorporation of 10mm length non-woven fibres ($\varnothing=20-25\mu m$) into a PLA matrix at a 0.14 fibre volume fraction (V_f). As expected, the inclusion of PGFs increased the modulus and flexural strength of the PLA from 2.5 to 5GPa and 50 to 90MPa respectively. However the degradation of samples in deionised water at $37^\circ C$ showed that the mechanical properties were reduced by $\approx 50\%$ after 6.5 weeks. This degradation was coupled with an increased weight loss (Figure 3.4.11) as well as a decrease in media pH (≈ 4) from the dissolution of the reinforcing fibres and formation of phosphoric acid (H_3PO_4) that was believed to have accelerated the PGF D_r through autocatalysis effects.

Comparisons with annealed PGF composites found these samples to exhibit similar initial mechanical properties whilst the degradation results showed these samples to possess an improved degree of mechanical property retention due to the reduced PGF D_r [218].

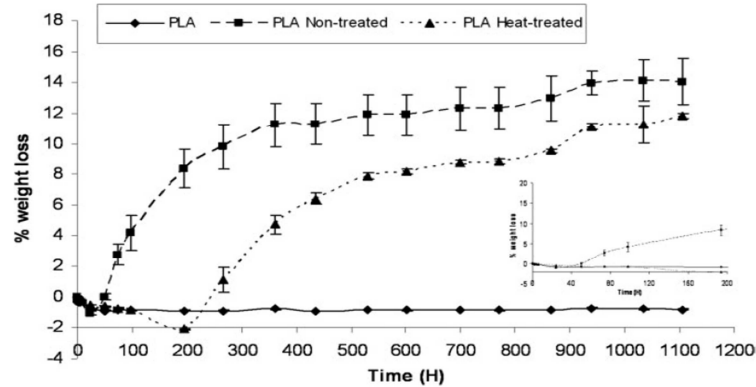


Figure 3.4.11. Weight loss of “as used” and annealed PGF-PLA composites ($0.14V_f$) over 6.5 weeks of degradation in deionised water [Reproduced from Ahmed et al. (2009)].

The culture of MG63 cells on both composite configurations also showed that the reduced D_r of the annealed fibres produced samples with improved biocompatibility compared to as-prepared fibre composites. However despite the improved cellular response, the mechanical properties of all samples remained below those of cortical bone which was attributed to the relatively low composite V_f [201, 207, 218]. Interestingly a polyphosphate $(P_2O_5)_{40}-(MgO)_{24}-(CaO)_{16}-(Na_2O)_{16}-(Fe_2O_3)_4$ (mol%) fibre composite investigated by Felfel et al. (2012) displayed improved durability which was attributed to the tighter packing structure of the phosphate chains in the polyphosphate glass structure. However the applicability of this composition as a composite reinforcing agent was hampered by its reported difficulty to manufacture continuous fibres without fracture compared to metaphosphate glasses [222].

Work on a $(P_2O_5)_{50}-(CaO)_{40}-(Na_2O)_5-(Fe_2O_3)_5$ (mol%) PGF composition was performed by Ahmed et al. (2011) who investigated the influence of fibre architectures on the mechanical properties and degradation of PGF composite samples. The study also investigated higher composite fibre volume fractions to achieve samples with improved mechanical properties closer to those exhibited by cortical bone. Composites of $0.2V_f$, $0.3V_f$ and $0.4V_f$ were produced from chopped 10mm fibre length non-woven mats as well as $0.2V_f$ unidirectional (UD) and $[0/90]$ cross-ply architectures. Mechanical testing of these samples showed the expected increase in flexural strength and elastic moduli with

increasing fibre volume fraction that were found to be accurately predicted by the rule of mixtures. A comparison across different fibre architectures at $0.2V_f$ also showed that [0/90] composites possessed the lowest mechanical properties compared to the highest exhibited by the UD materials. This was due to the stress loads being more axially distributed along the fibre lengths in the UD continuous fibres with regards to the loading axis used during mechanical testing (section 3.2.3). However all composite materials showed a rapid decrease in both flexural strength and elastic modulus after 10-20 days of immersion in deionised water at 37°C with an acidic media formed ($\text{pH}\approx 3.0$) after 5 days of immersion [219].

Long term, these degradation profiles subsequently showed that the acidic pH would gradually return towards initial values and reflected the near complete dissolution of the reinforcing PGFs. Further comparisons also revealed that the rate of water absorption and loss of mechanical properties occurred more rapidly in UD and [0/90] composites compared to chopped fibre samples. This was attributed to the relative ease at which water could wick along the continuous fibre architectures compared to the 10mm discontinuous fibres and demonstrated the influence of fibre architecture on the initial mechanical properties as well as those during sample degradation [219].

The characterisation of bulk monoliths and PGF-PCL composites using PG's doped with SiO_2 and Fe_2O_3 was evaluated by Mohammadi et al. (2012) over a range of $(\text{P}_2\text{O}_5)_{50}-(\text{CaO})_{40}-(\text{SiO}_2)_{10-x}-(\text{Fe}_2\text{O}_3)_x$ (x : 0, 5, 10 mol%) compositions. Comparisons using 10mm length, $\approx 10\text{-}20\mu\text{m}$ diameter PGF's in a PCL matrix ($0.18V_f$) revealed that the ion release rates were greater in $x=5$ mol% composites compared to the equivalent bulk monoliths. This was believed to have resulted from the different surface area-to-volume ratios between the bulk glass and those found at the fibre-matrix interface of the composite. However further comparisons between glasses with increased hydrolytic stability (10 mol% Fe_2O_3) showed that similar ion release profiles could be generated between bulk and composite samples. The incorporation of Fe_2O_3 was also shown to produce glasses with reduced surface polarity and surface energy which was attributed to the decreased concentration of hydroxyl groups (Si-OH) on the glass surface. The results consequently indicated that the ion release rates of PGF composites were dictated by the glass composition and were heavily influenced by the fibre-matrix interface [169].

Meanwhile Han et al. (2013) showed that an increase in mechanical properties could be achieved from the use of multiple fibre mats compared to a single pre-preg lamina during compression moulding. This was due to the improved polymer infiltration when using

multiple fibre mats and quality of the fibre-matrix interface (section 3.2.3.1). The introduction of screw holes in different fibre architectures also showed that significantly greater surface damage was incurred in UD fibre composites compared to random and mixed (i.e. UD + random) composite fibre constructs ^[223].

3.4.9 Composite Modifications

A review of various PGF-polymer composite studies has highlighted how various sample configurations can generate materials with a range of mechanical properties (e.g. 80–200 MPa flexural strength and 5–25 GPa elastic moduli). However a common factor throughout these studies has been the inability of these materials to retain adequate mechanical properties over a prolonged immersion period due to the rapid dissolution of the reinforcing PGFs. These results have been attributed to the breakdown of the fibre-matrix interface and has consequently led to a minimum PGF dissolution rate of 2×10^{-4} mg cm⁻² hr⁻¹ being identified by Hasan et al. (2012) in order to manufacture orthopaedic PGF composites with adequate mechanical properties during sample degradation ^[221, 224].

As shown previously by Mohammadi et al. (2012), alterations to the PGF surface properties via compositional modifications can have significant effects on the quality of the fibre-matrix interfacial adhesion which is crucial for the efficient distribution of mechanical loading across the reinforcing phase. Alternatively chemical coupling agents have been applied to modify the PGF surfaces in order to improve the composite interfacial properties and introduce a degree of hydrophobicity at the interface ^[169, 220, 225].

Due to the multitude of available coupling agents, a cross-examination of their effectiveness was investigated on Ø=9x2mm glass rods and fibres of a quinary (P₂O₅)₄₅-(CaO)₁₆-(MgO)₂₄-(Na₂O)₁₁-(Fe₂O₃)₄ (mol%) composition (Haque et al., 2010; Hasan et al., 2013). These agents included 3-aminopropyl-triethoxysilane (APS), Glycerol 2-phosphate disodium salt (GP), 3-phosphonopropionic acid (PPA), etidronic acid (EA), hexamethylene diisocyanate (HDI), amino phosphoric acid (APA) and sorbitol/sodium ended PLA oligomers (S/Na-PLA). Analysis of the treated samples showed that only APS, EA and HDI appeared to covalently bond to the glass surfaces whilst also being the only treatments that created hydrophobic surfaces. Furthermore it was found that increased concentrations of coupling agents did not directly reflect improvements to τ_b values of the fibre-matrix interface. Degradation testing of the treated rods showed reductions to the glasses D_r could be produced by HDI, APS, EA, Na-PLA and PPA coupling agents ^[220, 226].

Meanwhile follow up biocompatibility studies by Hasan et al. (2013) showed that despite all treatments demonstrating adequate biocompatibility, poor cell responses were observed with the use of HDI or Na-PLA compared to APS, GP and EA treatments ^[227]. Further studies using APS, HDI and S-PLA coupling agents in a $\approx 0.2V_f$ UD PGF-PLA composite of a $(P_2O_5)_{45}-(CaO)_{16}-(MgO)_{24}-(Na_2O)_{11}-(Fe_2O_3)_4$ (mol%) composition using $\varnothing=20\mu m$ fibres were evaluated by Hasan et al. (2013). Assessment and comparison of the treated fibre composite's mechanical properties, degradation and biocompatibility showed that improved initial mechanical properties were achieved with APS and S-PLA treated fibres. A difference in water uptake and final mechanical properties compared to untreated control samples also confirmed that these coupling agents provided improvements to the composites mechanical properties during degradation ^[224]. Similar results were also found by Khan et al. (2011) using $(P_2O_5)_{40}-(CaO)_{16}-(MgO)_{24}-(Na_2O)_{20}$ (mol%) APS silane treated fibres in a $0.1V_f$ PGF-PCL composite. The results indicated that glass surface reactions and the possible formation of a polysiloxane coating on the fibre surfaces were responsible for the decreased fibre dissolution rate found in treated fibre composites ^[228]. However other surface treatments have also been investigated such as those by Liu et al. (2013) on $(P_2O_5)_{45}-(CaO)_{16}-(MgO)_{24}-(Na_2O)_{11}-(Fe_2O_3)_4$ (mol%) fibres which were sputter coated with thin films of magnesium. This aimed at increasing the composite interfacial bonding by improving the mechanical interlock at the fibre-matrix interface ^[208]. However when incorporated into a PCL matrix ($0.2V_f$), the magnesium coated fibres (10mm random non-woven) showed no statistically significant improvement to the initial composite mechanical properties ^[225].

Alternatively attempts at controlling the dissolution of $(P_2O_5)_{51.04}-(CaO)_{21.42}-(Na_2O)_{25.51}-(SiO_2)_{2.03}$ (mol%) fibres in a methacrylate-modified oligolactide matrix were studied by Kobayashi et al. (2010) who incorporated 20 wt.% $CaCO_3$ into a hybrid composite design. Mechanical characterisation of the composites showed that the inclusion of $CaCO_3$ had a significant effect of the dissolution media pH whilst altering the failure behaviour of the composites from a ductile to brittle fracture mode. However, no mechanical testing or *in vitro* data was provided over the ten days of degradation to fully assess the composite performance after $CaCO_3$ addition ^[229].

4 Principles of the Technique Used

4.1 Structural and Thermal Properties

4.1.1 X-ray Diffraction (XRD)

X-ray diffraction (XRD) is an analytical tool used to investigate a crystalline material's atomic or molecular structure and is based on the scattering, interference and diffraction of a monochromatic incident X-ray radiation source by the samples internal atomic arrangement. From this concept, the structural characterisation of a material is achieved by the detection of diffraction peaks (i.e. constructive interference) at specific incident angles following Bragg's Law (Eqn 4.1.1) as illustrated in Figure 4.1.1 ^[230-232].

$$n\lambda = 2d\sin\theta$$

Eqn 4.1.1

where n = an integer, λ = wavelength of incident X-ray, θ = angle of incident X-ray, d = spacing between planes in the atomic lattice

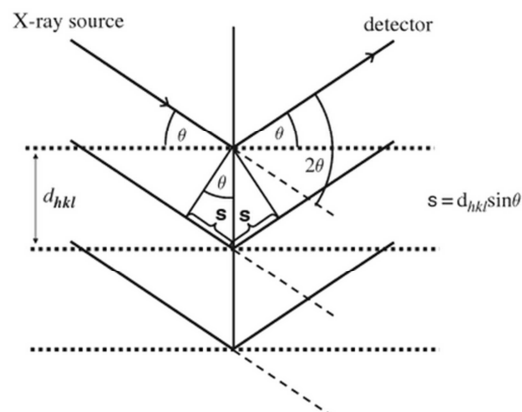


Figure 4.1.1. Illustration of coherent X-ray beams striking a series of hkl lattice planes a distance d_{hkl} apart in a crystalline material at an incident angle θ and the resultant optical path difference ($2s$) [Reproduced from Mittemeijer (2010) Fundamentals of Materials Science: The Microstructure-Property Relationship Using Metals as Model Systems].

From Eqn 4.1.1 it is apparent that for diffraction peaks to occur, the optical path difference between two scattered X-ray beams must be equal to a positive integer of the source wavelength (Figure 4.1.1). Hence by scanning across a range of 2θ angles, the

identification of all possible diffraction directions in a material lattice can be obtained with the results typically expressed as plots of 2θ against intensity. From this the fundamental properties of the crystalline state can be obtained through the use of a materials reference database (e.g. ICDD, International Centre for Diffraction Data) in conjunction with the detected diffraction peaks, measured intensities and calculated basal spacings ^[230, 231, 233].

4.1.2 Fourier Transform Infrared Spectroscopy (FTIR)

Fourier transform infrared spectroscopy (FTIR) is a method of vibrational spectroscopy used to analyse a material's molecular structure by the vibrational modes that occur from the absorption of an incident infrared (IR) radiation source.

For a molecule to absorb IR light, a periodic change in the dipole moment (P) of the molecule must occur (in IR active molecules) with greater levels of polarity producing a more intense IR absorption ^[234]. However this absorption can only occur at specific resonant frequencies that are determined by the molecular structure, atomic masses and structural bonding within the material sample. For a simple covalently bonded diatomic molecule this natural vibrational mode can be represented by a spring model system (Figure 4.1.2) with its natural vibrational frequency (ν_m) described by Hooke's law (Eqn 4.1.2) ^[235].

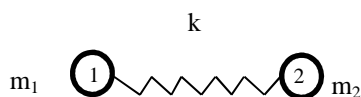


Figure 4.1.2. Representation of a covalent bond between two atoms of mass m_1/m_2 as a spring model system with spring stiffness k .

$$v_m = \frac{1}{2\pi} \sqrt{\frac{k}{\mu}}$$

$$\mu = \frac{m_1 * m_2}{(m_1 + m_2)}$$

Eqn 4.1.2

where v_m = frequency of vibration, k = force constant of bond strength and μ = reduced mass of a diatomic molecule, m_1 and m_2 are atomic masses of atoms 1 and 2 respectively.

However when analysing polyatomic molecules of different atomic masses, bond strengths and structures, a multitude of natural frequencies can exist in a material sample. These frequencies become even more complex when the molecules available degrees of freedom are considered which, for a molecule of n atoms, follows the $3n-6$ and $3n-5$ rule of thumb for non-linear and linear molecules respectively. For example, a simple linear diatomic carbon dioxide (CO_2) molecule ($n = 3$) containing 4 rotational degrees of freedom (Figure 4.1.3) is characterised by the vibrational frequencies outlined in Table 4.1.1 ^[234, 236, 237].

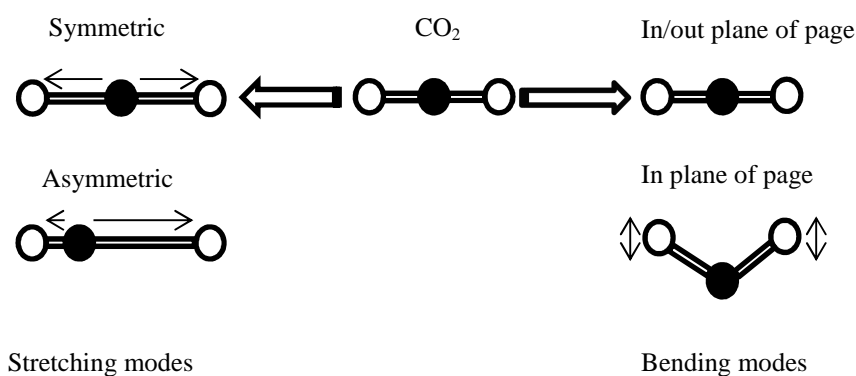


Figure 4.1.3. Molecular vibrations from the available degrees of freedom found in a CO_2 molecule when exposed across a range of mid-infrared radiation frequencies during FTIR.

Table 4.1.1. Vibrational modes and corresponding frequencies of a CO₂ molecule found from FTIR analysis [Data from Smith (2011) Fundamentals of Fourier Transform Infrared Spectroscopy, Second Edition].

| Vibration Mode | Frequency (Hz) | Comment |
|------------------------------|-----------------------|---|
| Symmetric stretching | N/A | IR inactive vibration |
| Asymmetric stretching | 7.05×10^{13} | |
| Bending in/out plane of page | 1.99×10^{13} | Equivalent vibrations – same frequency |
| Bending in plane of page | 1.99×10^{13} | |

It is upon this basis that FTIR is capable of identifying a material sample through the absorption of mid-IR radiation corresponding to the sample's natural molecular vibrations due to its specific molecular structure. These results are typically expressed as plots of IR absorbance against wavenumber where the incident radiations wavenumber is defined as the inverse of the signal wavelength. This relationship is described by Eqn 4.1.3 with a complete FTIR scan commonly expressed over the 4000-400cm⁻¹ wavenumber range [234, 238].

$$W = \frac{1}{\lambda} = \frac{\nu}{c}$$

Eqn 4.1.3

where W = wavenumber, λ = wavelength, c = velocity of light and ν = frequency

From these plots, the characterisation of a material is typically conducted through the analysis of the identified functional group (4000-1000cm⁻¹) and fingerprint regions (\approx 1000-400cm⁻¹) of the spectrum in conjunction with the use of a reference spectrum database [234].

4.1.3 Raman Spectroscopy

Raman spectroscopy is an alternate form of vibrational spectroscopy that compliments FTIR by probing the molecular structure of a sample using the polarised scattering of monochromatic UV, visible or near infrared laser light. However compared to FTIR, the theory of Raman scattering is more complex and has been briefly summarised here with further insight available from the literature ^[239].

In Section 4.1.2 it was shown that a diatomic molecule will vibrate with a natural frequency ν_m and that in order for the molecule to absorb IR radiation a change in the dipole moment (P) of the molecule must occur. However Raman active molecules require a change in the polarity of the molecule to occur during its normal mode of vibration. Consequently the exposure of a Raman active sample to intense laser light of frequency (ν_0) alters the polarizability (α) of the molecule to induce an oscillating dipole moment (P) that scatters the incident light ^[240].

This scattered light will consist of strong Rayleigh scattering (frequency ν_0) and weak Raman scattering (frequency $\nu_0 \pm \nu_m$) which is used in Raman spectroscopy to measure the shift in incident frequency (Figure 4.1.4). Raman scattering can be represented by either the Stokes ($\nu_0 - \nu_m$) or anti-Stokes ($\nu_0 + \nu_m$) lines with an analysis of the Stokes shift considered the common convention due to its higher intensities ^[241]. These shifts are typically represented as a change in the incident wavenumber (Eqn 4.1.3) with the results plotted as a function of the signal intensity against Raman shift (wavenumber). From these plots the identification and concentration of a molecular species can be determined from its measured intensity with each peak corresponding to a specific Raman shift of the incident light source ^[242].

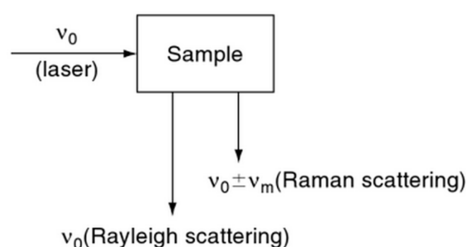


Figure 4.1.4. Scattering of an incident laser source (ν_0) by a sample and the resultant Rayleigh (ν_0) and Raman scattering ($\nu_0 \pm \nu_m$) during Raman spectroscopy [Reproduced from Ferraro (2003) Introductory Raman Spectroscopy].

4.1.4 Differential Scanning Calorimetry (DSC)

During heating a solid state material will undergo phase transformations as the atoms and molecules gain energy and break down their structural bonds (e.g. solid to liquid phase transformation). Thermal analysis (TA) techniques consequently provide a method of accurately measuring and understanding the multiple phase transformations a material can undergo as it gains and loses energy [243].

Typically the TA of a material sample has been performed using differential thermal analysis (DTA) or differential scanning calorimetry (DSC) equipment in order to measure endothermic and exothermic events as a sample is heated and/or cooled. In both techniques a controlled thermal cycle is typically performed with an empty sample pan acting as an inert reference within the equipment's heating cell. However DSC differentiates itself from DTA by its ability to provide quantitative data on a material's thermal properties as a result of the data obtained [244, 245].

DTA operates via the process of simultaneously heating a material sample and reference pan following a pre-programmed thermal cycle under a constant heat input (Q) in order to raise the temperature of the pans (ΔT) following Eqn 4.1.4. This technique is suited to applications requiring extreme temperatures ($\sim 2400^\circ\text{C}$) or where greater flexibility in volume size or crucible form is needed with a classical DTA set up shown in Figure 4.1.5 [244-246].

$$\Delta T = \frac{Q}{C_p}$$

Eqn 4.1.4

where ΔT = differential between initial and final material temperature, Q = thermal energy required to satisfy ΔT , C_p = specific heat capacity of sample

Consequently as both pans are heated, the resulting temperature differential (ΔT_{DTA}) between the material sample (T_s) and reference pan (T_r) are recorded with deviations representative of thermal events in which energy has either been absorbed (endothermic) or released by the sample (exothermic). These results are subsequently displayed as plots of

ΔT_{DTA} against T_r with the general convention that endothermic processes are shown in the negative direction ^[157, 246-248].

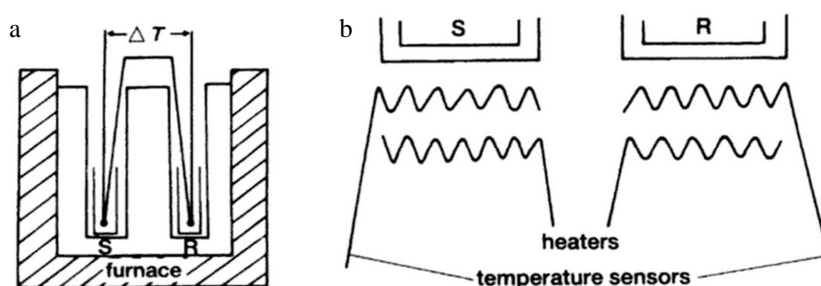


Figure 4.1.5. Configuration of thermal analysis equipment a) Dual heating of sample (S) and reference (R) pans in DTA and b) Independently temperature controlled DSC set up of sample (S) and reference (R) pans [Reproduced from Brown (2001) Introduction to Thermal Analysis: Techniques and Applications].

Similar to DTA, a typical DSC unit comprises of a sample and reference pan that are simultaneously exposed to a controlled heating cycle. However unlike DTA, the design of a DSC system allows the temperature of each pan to be independently measured and controlled (Figure 4.1.5). This allows the instrument to account for the differences in thermal capacity (C_p) between the sample and reference pan to ensure both are heated at identical rates (dT/dt) by modulating the rate of energy supplied to each pan. DSC thus measures the difference in required heat flow rates (dQ/dt) needed to maintain both pans at an identical heating rate throughout the thermal cycle (Eqn 4.1.5) ^[243-246].

$$\frac{dQ}{dt} = \frac{C_p dT}{dt}$$

Eqn 4.1.5

where t = time

Like DTA, the deviations in dQ/dt between the two pans represent the occurrence of thermal events as more or less thermal energy is supplied to the pans in order to accommodate for the absorption or release of energy during phase transformations and are

plotted against T_r . A schematic of an idealised DSC thermogram for a glassy material is shown in Figure 4.1.6 and shows the glass transition (T_g), crystallisation onset (T_{oc}), crystallisation peak (T_p) and liquidus temperatures (T_{lq})^[109, 243]. The liquidus temperature is defined as the temperature at which thermodynamic equilibrium is achieved between the solid and liquid phases in the glass and crystal formation is unstable^[249].

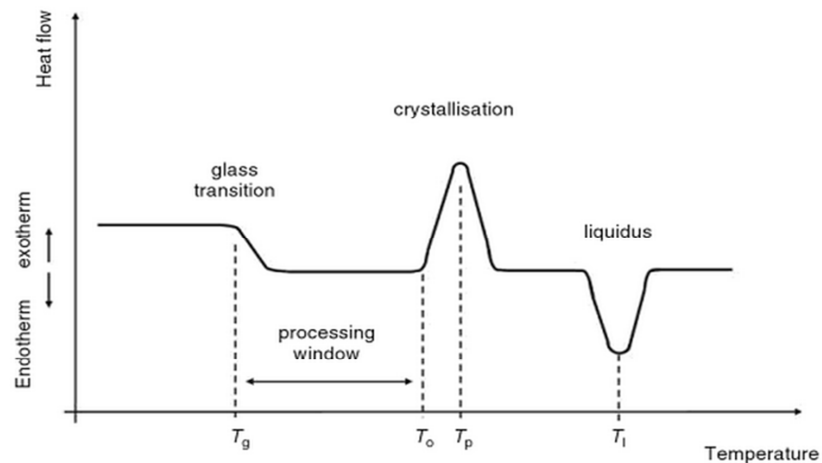


Figure 4.1.6. Idealised DSC thermogram curve for a glassy material with key thermal properties/events indicated [Reproduced from Jones & Clare (2012)].

4.2 Microhardness Testing

Microhardness testing is a widely used method of determining the hardness of a material by analysing an indent profile formed when a diamond indenter of specified dimensions is depressed onto a sample surface under a known load for a controlled duration. These indents can be performed using a Vickers or Knoop indenter and are assessed optically to measure the indent diagonals (d_1/d_2) in order to determine the indent area (Vickers) or projected area (Knoop). From this a microhardness value is calculated using the ratio of applied load to the indent area^[11, 250, 251].

5 Characterisation of CorGlaes[®] Pure 107 Composition

5.1 Outline

Material testing was conducted in order to characterise the different properties of the CorGlaes[®] Pure 107 glass.

The review of the literature has shown that the characterisation of glass formulations requires the analysis of various material properties using a diverse range of techniques relating to the interdisciplinary aspects of biomaterials science. Previous studies have often focused on a range of properties that have typically included its dissolution characteristics, *in vitro* biocompatibility and bioactivity as well as its structural/thermal properties [173, 174, 179, 205, 210, 252]. Table 5.1.1 presents an overview of the experimental techniques commonly employed in the characterisation of glass compositions intended for biomedical applications.

Table 5.1.1. Summary of techniques typically employed in the characterisation of glasses intended for bone tissue regenerative applications.

| Material Property | Analysis Technique/Method |
|---|--|
| Dissolution | Dissolution rate ^[173, 174, 179, 181, 187, 189, 190, 206, 210, 253, 254] Ion release ^[173, 179, 187, 189, 190, 206, 253] Dissolution media pH ^[173, 179, 181, 187, 189, 190, 206, 210, 253, 254] |
| Thermal parameters | Differential thermal analysis (DTA) ^[173, 189, 190, 206, 210, 253-256] Differential scanning calorimetry (DSC) ^[190, 253] |
| Structural characterisation | Nuclear magnetic resonance (NMR) ^[173, 190, 257] X-ray diffraction (XRD) ^[159, 173, 187, 190, 253-258] Energy dispersive X-ray (EDX) ^[210, 254] X-ray photoelectron spectroscopy (XPS) ^[190, 210] Raman spectroscopy ^[159, 258] Fourier transform infrared spectroscopy (FTIR) ^[159, 190, 210, 256] |
| Bioactivity | Immersion in simulated body fluid (SBF) ^[159, 252, 255, 256] |
| <i>In vitro</i> cell culture and biocompatibility | Neutral red uptake (NRU) ^[210] MTT assay ^[177, 210, 259-261] Alkaline phosphate (AP) activity ^[210, 254, 259-261] Live/Dead [®] staining ^[195, 253] AlamarBlue [®] assay ^[176, 210, 254] |
| Density | Archimedes principle ^[190, 210, 253] |

5.2 Materials and Methods

5.2.1 CorGlaes[®] Pure 107 Phosphate Glass Manufacturing

5.2.1.1 Bulk Monoliths

CorGlaes[®] Pure 107 monoliths were prepared using a melt quench technique by placing the designated precursor materials at specific weights inside a silica crucible. This was then heated to 1050°C and held for 120 minutes to form a homogenous melt. The molten CorGlaes[®] Pure 107 glass was then cast across a steel plate and allowed to cool before the resulting glass monolith was broken into fragments and stored inside polyethylene (PE) bags. This material preparation was performed by Giltech Ltd.

5.2.1.2 Annealed Disks

For characterisation of the CorGlaes[®] Pure 107 composition, Ø15x2mm melt quenched disks were produced by manually pressing a small pool of the remelted CorGlaes[®] Pure 107 cullet inside a custom profiled graphite mould. The disks were then subjected to an annealing cycle by being placed inside a 420°C preheated oven which was then raised to 465°C at 5°C min⁻¹ and held at this temperature for 60 minutes. Samples were then subsequently cooled to room temperature at 1°C min⁻¹ to complete the annealing process. This material preparation was performed by Giltech Ltd.

5.2.1.3 Powder Samples

CorGlaes[®] Pure 107 powder samples were generated by feeding glass fragments into a Hosokawa ACM10 hammer mill grinder (Hosokawa Micron, UK) which were comminuted under pre-set speed and airflow conditions to produce ≈15µm particles. Powder samples were stored without any further annealing stages inside PE bags. This material preparation was performed by Giltech Ltd.

5.2.2 XRD

The CorGlaes[®] Pure 107 phosphate glass structure was characterised by XRD on powder samples using a D5000 X-ray diffractometer (Siemens AG, Germany) and monochromatic Cu K α radiation (1.5418Å). The analysis was performed at a scanning step rate of 0.02° over 2 θ values from 5 to 85°. XRD was performed at the School of Chemistry, University of Glasgow by Mr Andrew Monaghan.

5.2.3 FTIR

FTIR spectra were recorded using a Spectrum One FT-IR Spectrometer (PerkinElmer, USA) on CorGlaes[®] Pure 107 powder samples. The production of KBr disks typically used in the preparation of FTIR samples was omitted due to the Attenuated Total Reflectance (ATR) accessory attached to the FTIR equipment. Scans were obtained in absorbance mode across the 4000–400cm⁻¹ wavenumber range at a resolution of 8cm⁻¹ with 16 scans performed per spectra and analysed using the equipment's Spectrum[®] software (PerkinElmer, USA). FTIR was performed at the Centre for Textile Conservation, University of Glasgow.

5.2.4 DSC

Thermal analysis of the CorGlaes[®] Pure 107 glass was evaluated by differential scanning calorimetry (DSC) using a STA 449 F1 Jupiter[®] - Simultaneous TGA-DSC equipment (Netzsch, Germany) on crushed glass monolith fragments (<3mm). The DSC was performed by heating samples to 1200°C at 10 °C min⁻¹ inside an inert nitrogen atmosphere before cooling at 30°C min⁻¹ with air as the purge gas. Phase transformation temperatures were then analysed by the instrument's Proteus[®] software (Netzsch, Germany) and Eqn 5.2.1 used to determine the glass's processing window (PW). As discussed in section 3.4.7.2, the PW (Figure 4.1.6) is believed to reflect a glass's thermal stability (i.e. its tendency towards crystallisation) and due to its consistency in the literature was selected over alternative models such as the Hruby criterion ^[109, 120, 262]. DSC was performed by Dr Fiona Sillars at the Advanced Materials Research Laboratory (AMRL), University of Strathclyde.

$$PW = T_{oc} - T_g$$

Eqn 5.2.1

where PW = processing window ($^{\circ}\text{C}$), T_{oc} = glass crystallisation onset temperature ($^{\circ}\text{C}$) and T_g = glass transition temperature ($^{\circ}\text{C}$).

5.2.5 Density

The density of the CorGlaes[®] Pure 107 phosphate glass was determined using Archimedes principle by recording the weight of a disk sample in air (w_a) and whilst suspended within a suitable media (w_s) of known density (ρ_L). Measurements were carried out in triplicate on three glass disks ($n = 3$) using distilled water as the immersion media and the sample density calculated by Eqn 5.2.2 ^[157]. Data was collected using a $\pm 0.1\text{mg}$, Pioneer[™] analytical balance (Ohaus, USA) with an attached density measurement kit.

$$\rho = \frac{(w_a * \rho_L)}{(w_a - w_s)}$$

Eqn 5.2.2

where ρ = sample density (g cm^{-3}), ρ_L = immersion media density (g cm^{-3}), w = sample weight in air (g) and w_s = sample weight suspended in media (g).

5.2.6 Flexural Strength and Elastic Modulus

Mechanical testing of the CorGlaes[®] Pure 107 phosphate glass had been previously assessed by The Welding Institute (Cambridge, UK) following a 4-point bend method according to ASTM C158-02 using an Instron 5567 B723 (Instron, USA). Samples ($n = 24$) were tested at a cross-head speed of 0.5 mm min^{-1} using a 30kN load cell with the data used to calculate the glass's flexural strength and elastic modulus ^[263, 264]. This data was provided by Giltech Ltd.

5.2.7 Microhardness Testing

5.2.7.1 Sample Preparation

CorGlaes[®] Pure 107 disks were prepared by being ground down with WS Flex 18C silica carbide paper (Hermes Abrasives, Germany) over a range of grades (P240-1200 grit) using a Metaserv[®] universal polisher (Buehler, USA) with distilled water applied as a cooling agent. Disks were then polished using MetaDi[®] Supreme diamond polishing compounds (Buehler, USA) of decreasing particle size (15→6→1 μm) and finally cleaned in an Ultra 8000 ultrasonic bath (James Products Limited, UK) for three minutes. To ensure adequate surface quality prior to testing, the polished sample surfaces were visually inspected by an Eclipse ME600 optical microscope (Nikon, Japan).

5.2.7.2 Hardness and Fracture Toughness

Microhardness testing of CorGlaes[®] Pure 107 disks was performed using a Vickers microhardness indenter due to the reduced sensitivity of the Vickers technique to the initial sample surface conditions ^[11, 250]. Microhardness testing on polished disks was conducted with a 300g indentation load using a Wilson Wolpert Micro-Vickers 401MVA (Buehler, USA) at an indentation dwell time of five seconds. This indentation load was selected based on previous Vickers hardness testing by Clément et al. (1999) and was performed under atmospheric conditions at ambient temperature with five microhardness tests each performed on three disk samples ($n = 3$) ^[265]. The resulting indent diagonals (d_1/d_2) were then measured using the optical microscopy equipment attached to the testing unit and a Vickers hardness value calculated from Eqn 5.2.3 ^[266].

$$H_V = \frac{1.854 * P}{d^2}$$

Eqn 5.2.3

Where H_V = Vickers hardness (HV), P = indentation load (kg), d = average indent diagonal length (mm).

Vickers hardness (HV) was converted to GPa using a 0.009807 conversion factor ^[267].

From the microhardness testing, the fracture toughness of the CorGlaes[®] Pure 107 composition was also determined using the radial crack lengths (c) emanating from the indent depressions of each Vickers microhardness test (Figure 5.2.1) using Eqn 5.2.4 [266, 268].

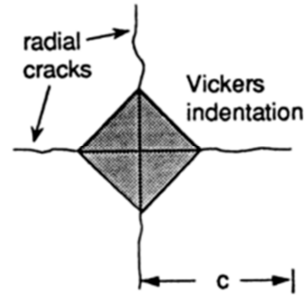


Figure 5.2.1. Illustration of radial crack lengths (c) emanating from the Vickers indent on a material sample surface [Reproduced from Bhushan (1998) Handbook of Micro/Nano Tribology].

$$K_{IC} = \delta \left(\frac{E}{H} \right)^{1/2} \left(\frac{P}{c^{3/2}} \right)$$

Eqn 5.2.4

where K_{IC} = fracture toughness ($\text{MPa m}^{1/2}$), E = elastic modulus (GPa), H = sample hardness (GPa), P = indentation load (mN), c = average indent crack length (μm), δ = non-dimensional indenter geometry constant, 0.016 ± 0.004 for radial median cracks resulting from Vickers indentation [266, 269].

5.2.8 Dissolution

5.2.8.1 Dissolution Rate

Dissolution studies on the CorGlaes[®] Pure 107 glass were performed on three glass disks ($n = 3$) using distilled water at a $0.18 \text{ cm}^2 \text{ ml}^{-1}$ surface area-to-volume ratio (SA:V) and stored individually inside polystyrene universal tubes within a 37°C incubator for 1008

hours (six weeks). Due to its frequent use in the literature, this experimental configuration was selected over a dynamic flow system such as that used by Rinehart et al. (1999) or Giltech Ltd^[270].

During immersion, samples were periodically removed, dried and weighed (± 0.1 mg Pioneer[™] analytical balance - Ohaus, USA) along with measurements of the dissolution media pH (HI 221 pH Meter - Hanna Instruments, USA) as outlined in Table 5.2.1. The samples were then returned to fresh media until the next measurement point.

Table 5.2.1. Data collection and media replacement during 1008 hour dissolution of CorGlaes[®] Pure 107 disks in distilled water at 37°C.

| Immersion Period (hours) | Data | Measurement Points/Media Change |
|---|---------------------------|---|
| 0, 24, 48, 72, 96, 120, 144, 168 [1 week] | Sample weight Media pH | At each immersion period, media replaced after each measurement. |
| 168, 336, 504, 672, 840, 1008 [6 weeks] | Sample weight Media pH | At each immersion period, media replaced at each measurement and every 72 to 96 hours between measurements. |

Collected weight data was then analysed using Eqn 5.2.5 and plotted against the dissolution period (hours) with the addition of a linear trendline describing the CorGlaes[®] Pure 107 dissolution rate in $\text{mg cm}^{-2} \text{ hr}^{-1}$ [145, 173, 183].

$$\text{Weight loss per unit area} = \frac{w_o - w_t}{A}$$

Eqn 5.2.5

Where w_o = initial sample weight (mg), w_t = sample weight at time t_x (mg) and A = sample surface area (cm^2).

5.2.8.2 Ion Release

Coordinating with the dissolution data in section 5.2.8.1, the ionic concentrations of the dissolution media were also measured from extracts obtained every 24 hours over the first 168 hours of glass disk immersion (Table 5.2.1). These were measured for the Ca^{2+} , Mg^{2+} , Zn^{2+} and Na^{+} cations as well as the $(\text{PO}_4)^{3-}$ anion corresponding to the CorGlaes[®] Pure 107 composition (section 1.1.1).

The Ca^{2+} , Mg^{2+} and Zn^{2+} cation concentrations were assessed using an AAnalyst[™] 400 Atomic Absorption Spectrometer (Perkin Elmer, USA) at 422.7nm (Ca^{2+}), 285.2nm (Mg^{2+}) and 213.9nm (Zn^{2+}) wavelengths with a nitrous oxide-acetylene flame used to compensate for phosphate interference. Sodium (Na^{+}) concentration was determined by flame emission using a 410 Flame Photometer (Sherwood Scientific, UK).

Orthophosphate anion concentration was measured using a Technicon AutoAnalyser (Seal Analytical, UK) that is comprised of a segmented flow system with an air bubble used to isolate samples. The $(\text{PO}_4)^{3-}$ anion was used as an indicator for the different phosphate anions that could be released during glass dissolution (e.g. $(\text{P}_2\text{O}_7)^{4-}$, $(\text{P}_3\text{O}_9)^{3-}$, $(\text{P}_3\text{O}_{10})^{5-}$) similar to that performed by Skelton et al. (2007) and Khor et al. (2011). All daily/accumulative ionic concentrations were expressed in mg l^{-1} and plotted over the first 168 hours of immersion for each ionic species^[175, 187, 190]. Ion release was measured at the School of Chemistry, University of Glasgow by Mr Michael Beglan.

5.2.9 Bioactivity

The bioactivity of the CorGlaes[®] Pure 107 phosphate glass was assessed using a protein-free acellular, simulated body fluid (SBF) in order to replicate the *in vivo* conditions at the laboratory scale^[271].

5.2.9.1 Preparation of Simulated Body Fluid (SBF)

For bioactivity testing of the CorGlaes[®] Pure 107 composition, corrected SBF (c-SBF) was initially prepared. Corrected SBF differentiates itself by accounting for the SO_4^{2-} ion deficiency found in the original SBF-K9 formulation first developed by Kokubo et al. and used by Hench et al. as well as multiple other authors. The ionic constituents of these solutions are compared with human blood plasma in Table 5.2.2^[53, 271, 272].

Table 5.2.2. Comparison of ionic concentrations between SBF-K9, c-SBF and human blood plasma [Reproduced from Kokubo et al. (2003)].

| Ion | SBF-K9 (mM) | c-SBF (mM) | Human Blood Plasma (mM) |
|--------------------------------|-------------|------------|-------------------------|
| Na ⁺ | 142.0 | 142.0 | 142.0 |
| K ⁺ | 5.0 | 5.0 | 5.0 |
| Mg ²⁺ | 1.5 | 1.5 | 1.5 |
| Ca ²⁺ | 2.5 | 2.5 | 2.5 |
| Cl ⁻ | 148.8 | 147.8 | 103.0 |
| HCO ₃ ⁻ | 4.2 | 4.2 | 27.0 |
| HPO ₄ ²⁻ | 1.0 | 1.0 | 1.0 |
| SO ₄ ²⁻ | 0 | 0.5 | 0.5 |

The c-SBF was prepared by sequentially adding each reagent (Table 5.2.3) to a polypropylene (PP) bottle containing 750ml of distilled water which was maintained at 37°C and vigorously agitated by magnetic stirring. Each reagent was only added after the previous had completely dissolved. All apparatus used (beakers, bottles, spatulas etc.) were cleaned prior to c-SBF preparation by rinsing with a dilute hydrochloric acid (HCL) solution and then washed consecutively with distilled water. After the addition of the final chemical reagent, the solution pH was buffered to 7.25 at 37°C using 1M HCl with further distilled water added to create a final solution volume of 1000ml^[272].

Table 5.2.3. Reagent chemicals for preparing 1 litre of corrected simulated body fluid (c-SBF) [Reproduced from Chavan et al. (2010)].

| Stage | Reagent | Quantity (g) |
|-------|--|--------------|
| 1 | NaCl | 7.996 |
| 2 | NaHCO ₃ | 0.350 |
| 3 | KCl | 0.224 |
| 4 | K ₂ HPO ₃ ·3H ₂ O | 0.228 |
| 5 | MgCl ₂ ·6H ₂ O | 0.305 |
| 6 | 1M HCl | 40ml |
| 7 | CaCl ₂ | 0.278 |
| 8 | Na ₂ SO ₄ | 0.071 |
| 9 | (CH ₂ OH) ₃ CNH ₂ | 6.057 |

To check solution stability, 50ml of prepared c-SBF solution was placed in a cleaned PP bottle and stored inside an incubator at 37°C for 48 hours to ensure no spontaneous precipitation had occurred.

5.2.9.2 c-SBF Immersion

The bioactivity of CorGlaes[®] Pure 107 disks was assessed in triplicate ($n = 3$) by recording the initial sample weight (± 0.1 mg Pioneer[™] analytical balance, Ohaus, USA) before individually immersing disks within c-SBF at a $0.1 \text{ cm}^2 \text{ ml}^{-1}$ surface area-to-volume ratio inside cleaned PP bottles. Containers were placed inside an incubator at 37°C with the c-SBF replaced every 72 hours. Samples were extracted after 24, 72, 120, 168 as well as 336 hours (two weeks) of immersion and washed in acetone (VWR, USA) to halt any further surface reactions occurring before the samples were weighed again. Samples were then stored inside a desiccator unit for further analysis with any precipitate characterised following the flow chart described in Figure 5.2.2 with the weight loss of the glass disks in c-SBF calculated by Eqn 5.2.5. The media pH of the c-SBF was also recorded at each immersion period using a HI 221 pH Meter (Hanna Instruments, USA) with the weight loss and media pH plotted over the 336 hours of immersion [182, 273].

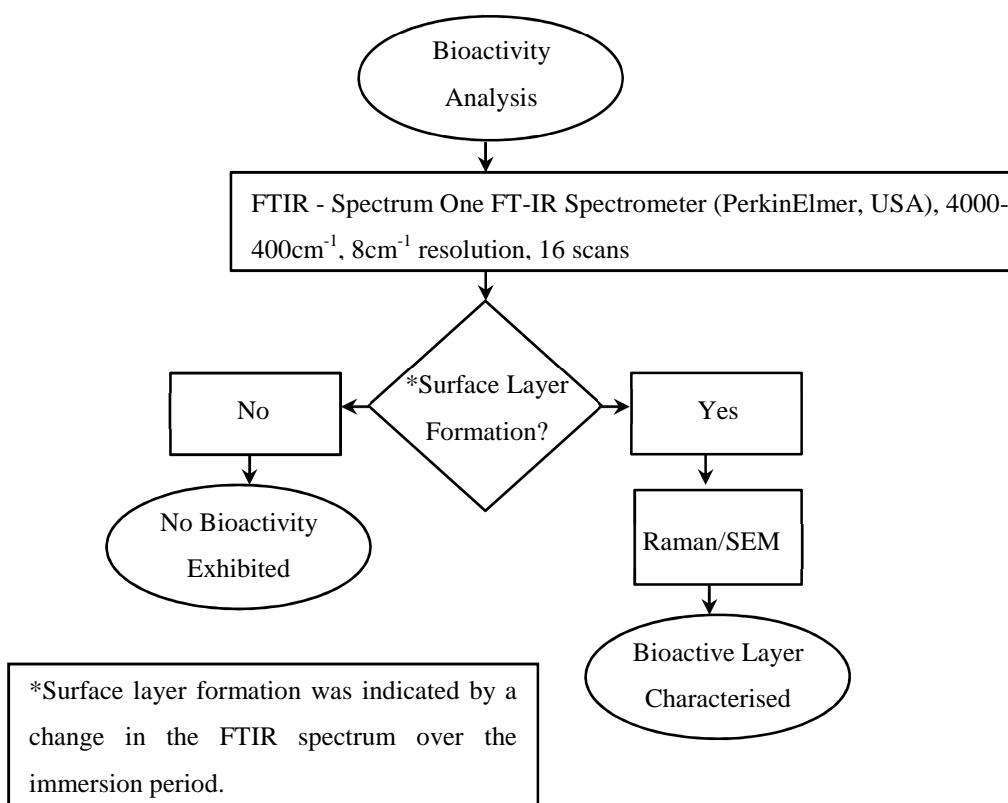


Figure 5.2.2. Process flowchart of CorGlaes[®] Pure 107 disk bioactivity after immersion in c-SBF for 336 hours.

If a surface layer precipitate was found by FTIR, then Raman spectroscopy was to be performed using a LabRAM HR (Horiba Jobin Yvon, France) with a Ventus 532 laser (Ventus, USA) over a 1500-100cm⁻¹ wavenumber range. Spectra were to be collected in triplicate ($n = 3$) from a 532.17nm laser line with a 10% OD objective and 600 grating over a 10 second accumulation period. Images of the CorGlaes[®] Pure 107 disk surfaces were also to be captured using a Sigma VP SEM (Carl Zeiss, Germany) in SE and BSE modes using a 20kV accelerating voltage. Raman spectroscopy and SEM was to be performed at the School of Chemistry and the School of Geographical and Earth Sciences, University of Glasgow respectively.

5.2.10 Biocompatibility

The procedures for biocompatibility testing and preparing precursor solutions for *in vitro* cell culture were conducted following the instructions and recipes at the Centre for Cell Engineering (CCE), University of Glasgow.

Biocompatibility of the CorGlaes[®] Pure 107 composition was assessed from a combination of MTT assay and a Live/Dead[®] Cell Viability/Cytotoxicity Kit (Life Technologies, USA) on disk samples following the process flow chart shown in Figure 5.2.3.

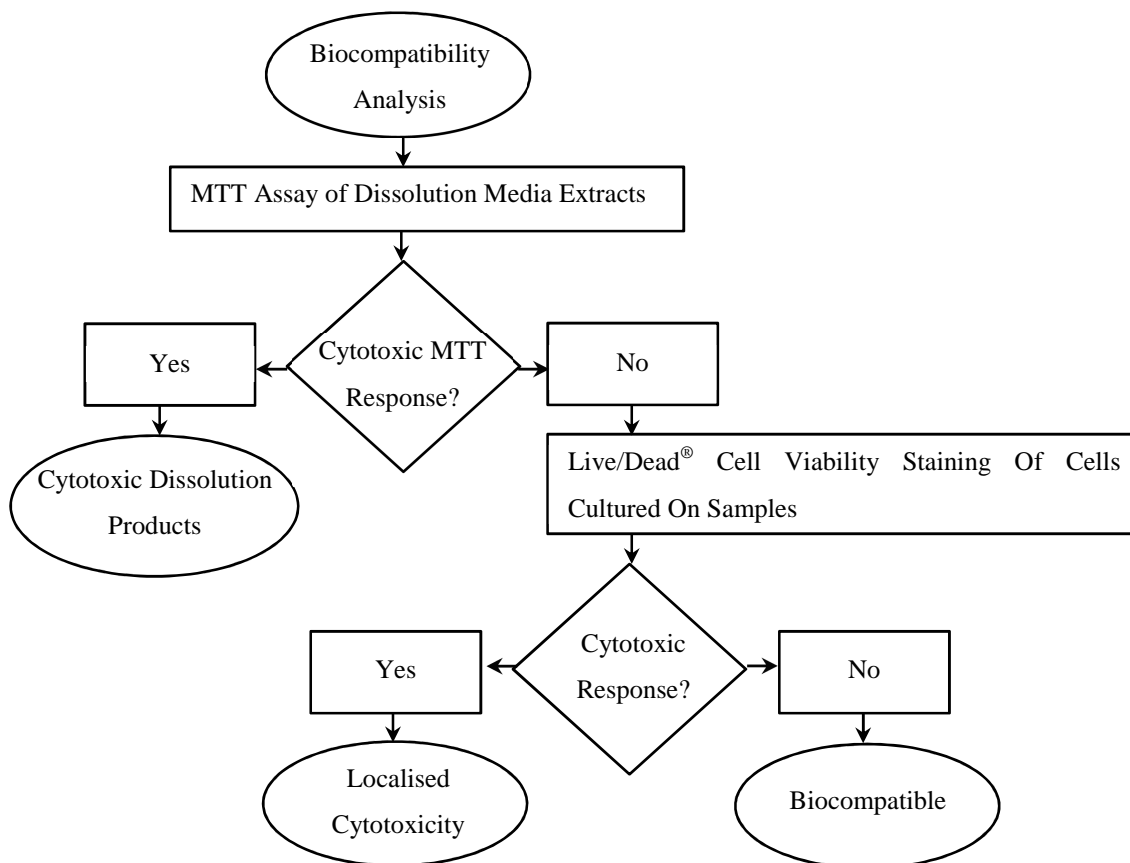


Figure 5.2.3. Process flow chart for assessing the biocompatibility of CorGlaes[®] Pure 107 disks using an MTT assay and a Live/Dead[®] cell staining kit.

5.2.10.1 Cell Culture Precursor Solutions

HEPES buffered saline solution

HEPES saline solution is a zwitterionic chemical buffering agent and was prepared by adding the reagents outlined in Table 5.2.4 to 1000ml of distilled water. The pH of the resulting solution was then adjusted to 7.5 using 5M NaOH and dispensed in 100ml vials before being autoclaved and stored in a fridge at 4°C.

Table 5.2.4. Reagents for preparing 1 litre of HEPES saline solution.

| Reagent | Quantity |
|----------------------------|----------|
| Sodium chloride | 8g |
| Potassium chloride | 0.4g |
| d-glucose | 1g |
| HEPES (Sigma-Aldrich, USA) | 2.38g |
| 0.5% phenol red | 2ml |

Versene solution

Versene is a chelating agent based on an ethylenediaminetetraacetic acid (EDTA) solution and is used in conjunction with Trypsin to allow cells to be dissociated from the surface of a culture flask into a suspension. The Versene solution was prepared by adding the reagents outlined in Table 5.2.5 to 1000ml of distilled water and the pH adjusted to 7.5 using 5M NaOH. The Versene solution was dispensed into 20ml vials, autoclaved and stored in a fridge at 4°C [274, 275].

Table 5.2.5. Reagents for preparing 1 litre of Versene solution.

| Reagent | Quantity |
|--|----------|
| Sodium chloride | 8g |
| Potassium chloride | 0.4g |
| d-glucose | 1g |
| HEPES (Sigma-Aldrich, USA) | 2.38g |
| Ethylenediaminetetraacetic acid (EDTA) | 0.2g |
| 0.5% phenol red | 2ml |

Trypsin-Versene solution

Trypsin is an enzyme used to remove cells from the surfaces of culture vessels by hydrolysing specific peptide bonds in the adhered cells and is combined with Versene in order to improve its activity. Trypsin-Versene solutions were prepared by adding 2ml of Trypsin (Sigma-Aldrich, USA) to 20ml of Versene under a laminar flow hood and were stored in a fridge at 4°C prior to use ^[274, 275].

Antibiotic mix

In order to prevent the growth of contaminating bacteria during cell culture an antibiotic solution (AB) was prepared by mixing the reagents outlined in Table 5.2.6. The AB solution was then aliquoted into sterile 20ml glass vials and stored in a freezer at -20°C.

Table 5.2.6. Reagents used in preparation of 262.5 ml of an antibiotic mix solution.

| Reagent | Volume (ml) |
|---|-------------|
| L-glutamine | 150 |
| Penicillin-Streptomycin | 100 |
| Fungizone [®] Antimycotic (Life Technologies, USA) | 12.5 |

Phosphate buffered saline

Phosphate buffered saline (PBS) was prepared from PBS tablets (P4417, Sigma-Aldrich, USA) by dissolving one tablet in 200ml of deionised water to yield 0.01M phosphate buffer, 0.0027M potassium chloride and 0.137M sodium chloride (pH = 7.4). The resulting media was then sterilised by autoclaving and stored at ambient temperature.

Cell culture medium

As supplied Dulbecco's Modified Eagles Medium (DMEM) (Sigma-Aldrich, USA) was received as a basal media containing various quantities of amino acids, salts, vitamins and

glucose, but lacked the essential proteins or growth promoting agents necessary for cell culture. For this media to be considered complete, further supplements were added to 400ml of DMEM as outlined in Table 5.2.7. Supplements were added sequentially after passing through a Minisart 0.2µm syringe filter (Sartorius Stedim Biotech, Germany) with completed DMEM (CDMEM) divided into 25cm³ flasks and stored in a freezer at -20°C.

Table 5.2.7. Supplements used to produce 565ml of completed Dulbecco's Modified Eagles Medium (CDMEM).

| Reagent | Volume (ml) |
|--|-------------|
| DMEM | 400 |
| Medium 199 | 100 |
| Foetal Bovine Serum (FBS) | 50 |
| Antibiotic Mix (AB) [From Table 5.2.6] | 10 |
| Sodium Pyruvate | 5 |

5.2.10.2 *In Vitro* Cell Culture and Cell Seeding

For *in vitro* testing of the CorGlaes[®] Pure 107 composition, a human osteosarcoma derived cell line, MG63, was selected to perform preliminary biocompatibility testing due to its widely accepted role as an accurate model of osteoblastic behaviour and availability [177, 178]. The MG63 cell lines were cultured within 75cm³ flasks inside a 37°C humidified atmosphere incubator with 5% CO₂ to maintain the required culture media pH.

For sample cell seeding, the required media (Trypsin-Versene, HEPES, CDMEM) was heated to 37°C using a hot water bath and confluent cells dissociated from the culture flask by removing the CDMEM culture media, washing twice with HEPES saline solution then adding 5ml of the Trypsin-Versene solution for 90 seconds. The flask medium and dissociated cells were then transferred to a universal centrifuge tube containing 5ml of fresh CDMEM and centrifuged at 1400 rpm for four minutes to generate a cell pellet. The pellet was then re-suspended in 1ml of CDMEM with the specific cell concentration (cells ml⁻¹) determined using a hemocytometer.

5.2.10.3 MTT Assay

The MTT assay is a quantitative method of *in vitro* cytotoxicity testing based on the cleavage of a water soluble tetrazolium salt, (3-[4,5-dimethylthiazol-2-yl]-2,5-diphenyl-tetrazolium bromide) by NADH- or NADPH-dependant dehydrogenases to generate insoluble blue formazan crystals. These crystals are subsequently solubilised by the introduction of a suitable organic solvent with the optical density (OD) of the resulting solution measured by spectrophotometry at a detection wavelength between 570nm and 590nm. Since the cleavage of the tetrazolium salt (MTT) can only occur in respiring mitochondria, the optical density (i.e. absorbance) of the formazan solution can consequently be used as a means of accurately evaluating viable cells. Advantages of this technique include its ease, reproducibility and reported correlation between *in vitro* and *in vivo* results ^[276-279].

MTT assay protocol

The *in vitro* cytotoxicity of the CorGlaes[®] Pure 107 disk degradation by-products was evaluated following the MTT assay protocol outlined by BS EN 10993-5:2009. Glass disks were initially sterilised by immersing in a 70 vol% ethanol-water solution for one hour and sequentially rinsed three times in the ethanol solution before being washed twice with HEPES saline solution. Samples were then placed within a 12 well cell culture plate and allowed to degrade in CDMEM at a 1.25 cm² ml⁻¹ surface area-to-volume ratio inside a 5% CO₂, 37°C incubator for 24 and 96 hours. Disks were degraded in triplicate ($n = 3$) for each immersion period with the extracted dissolution media diluted with CDMEM to 100, 50, 1, and 0.1 vol%. Positive and negative control media were prepared from CDMEM and a 1 vol% Triton-X100 (Sigma-Aldrich, USA)/CDMEM solution respectively ^[280].

For the MTT assay, MG63 cells were cultured in 100µl per well of CDMEM at a cell concentration of 1x10⁵ cells ml⁻¹ within a 96 well plate for 24 hours following a plate layout in accordance with BS EN 10993-5:2009 to evaluate each extract concentration in triplicate ($n = 3$). After 24 hours, the culture media was aspirated and replaced with the diluted extracts from the CorGlaes[®] Pure 107 disks alongside the control media and incubated for 24 hours before performing the MTT assay following the steps described in Table 5.2.8 ^[280].

Table 5.2.8. MTT assay of CorGlaes® Pure 107 disks dissolution extracts.

| Step | Activity |
|------|--|
| 1 | Under a laminar flow hood, a 5mg ml ⁻¹ thiazolyl blue tetrazolium bromide (Sigma-Aldrich, USA) solution was prepared using sterile PBS to a total volume that ensured 100µl could be distributed in each sample well. |
| 2 | The cell culture media was removed and each sample well was rinsed with 100µl of sterile PBS. |
| 3 | 100µl of the thiazolyl blue tetrazolium bromide solution was added to each sample well before the plate was wrapped in foil and incubated for 60 minutes. |
| 4 | After incubation, the solution was removed and 100µl of dimethylsulfoxide (DMSO) (Sigma-Aldrich, USA) was added to each well. The culture plate was then transferred to a FLUOstar OPTIMA spectrophotometric plate reader (BMG LabTech, Germany) operating at a detection wavelength of 570nm. |

From the spectrophotometric results, the cell viability of each well corresponding to a specific CorGlaes® Pure 107 media extract concentration or control was assessed by Eqn 5.2.6. The MTT data was then statistically analysed by two-way analysis of variance (ANOVA) using MS Excel (Microsoft, USA).

$$\text{Percentage Cell Viability} = 100 * \frac{OD_{570e}}{OD_{570b}}$$

Eqn 5.2.6

where OD_{570e} = mean optical density measured for each dissolution extract (or control) and OD_{570b} = mean optical density value of the positive control media.

5.2.10.4 Live/Dead[®] Staining

The Live/Dead[®] Cell Viability/Cytotoxicity Kit (Life Technologies, USA) is a dye-based membrane integrity system of determining cell viability from the interactions of membrane permeable and membrane impermeable dyes with cells cultured on a sample surface.

From the membrane impermeable ethidium homodimer-1 (EthD-1), dead cells can be determined from the dyes capacity to bind specifically with the nucleic acids of cells that no longer have intact membranes. The identification of these cells is then achieved by the red fluoresce of EthD-1 when viewed microscopically at excitation and emission wavelengths of 528-536nm and 617nm respectively. Conversely viable cells are evaluated through the membrane permeable calcein-AM which, upon entering the plasma membrane, is cleaved by intracellular esterase to fluoresce green under optical microscopy. Given that only cells with a functioning esterase enzyme are able to cleave calcein-AM it is preferentially selective to only fluoresce with viable (i.e. living) cells. The combination of calcein-AM with EthD-1 then serves as a simple method of simultaneously distinguishing between living and dead cells based on the observed fluorescent differentiation ^[96, 281-284].

Live/Dead[®] sample preparation

The Live/Dead[®] staining kit was employed to assess the viability of cells cultured on CorGlaes[®] Pure 107 disks over 24, 96 and 168 hours of incubation. Prior to cell culture the CorGlaes[®] Pure 107 disk samples were prepared by being quickly ground down and polished following the method described in section 5.2.7.1.

Live/Dead[®] staining protocol

For cell culture, polished disks were sterilised by immersing in a 70 vol% ethanol-water solution within a sterile laminar flow hood for sixty minutes. Samples were then rinsed a further three times with the 70 vol% ethanol-water solution and washed twice with HEPES saline solution. Sterile samples were then seeded in a 24-well plate at a cell concentration of 1×10^4 cells ml^{-1} at a surface area-to-volume ratio of $2.24 \text{ cm}^2 \text{ ml}^{-1}$ (SA:V) and incubated within a 5% CO_2 , 37°C incubator unit. Samples were cultured in triplicate ($n = 3$) for 24, 96 and 168 hours with Ø13x0.2mm Thermanox[®] coverslips (Thermo Fisher Scientific[™], USA) employed as a positive control. During incubation, the cell culture media was

replaced after 96 hours and at each culture period a Live/Dead[®] viability stain was performed following the steps outlined in Table 5.2.9.

Table 5.2.9. Steps describing the Live/Dead[®] stain of MG63 cells cultured on the surface of CorGlaes[®] Pure 107 disks.

| Step | Activity |
|------|--|
| 1 | Under sterile conditions a Live/Dead [®] stain was prepared by creating an EthD-1, calcein-AM and CDMEM solution at a 1:1:1000 volume ratio respectively to a total volume that ensured 2ml could be distributed into each sample well. |
| 2 | Under a laminar flow hood, the existing CDMEM in the culture plate was removed before introducing the Live/Dead [®] stain to each well and returning the culture plate to the incubator. |
| 3 | Culture plates were then removed after thirty minutes and the staining media extracted before samples were inverted onto glass coverslips and transferred to a Axiovert 200M microscope (Carl Zeiss, Germany) for image capturing. |

The expected pH of the CDMEM at each culture period of the Live/Dead[®] stain was recorded by immersing separate CorGlaes[®] Pure 107 disks over the corresponding incubation period in acellular CDMEM at a 2.24 cm² ml⁻¹ SA:V ratio. The samples were stored in a 5% CO₂ incubator at 37°C with the pH recorded using a HI 221 pH Meter (Hanna Instruments, USA) at 24, 96 and 168 hours of immersion. This was compared with a blank, sample free CDMEM control that was stored under identical conditions.

5.3 Results

5.3.1 XRD

The XRD trace of the CorGlaes[®] Pure 107 composition (Figure 5.3.1) displays a clear absence of any defined crystallisation peaks over the $2\theta = 5\text{-}85^\circ$ range with a broad spectrum halo peak centred at $2\theta \approx 23^\circ$.

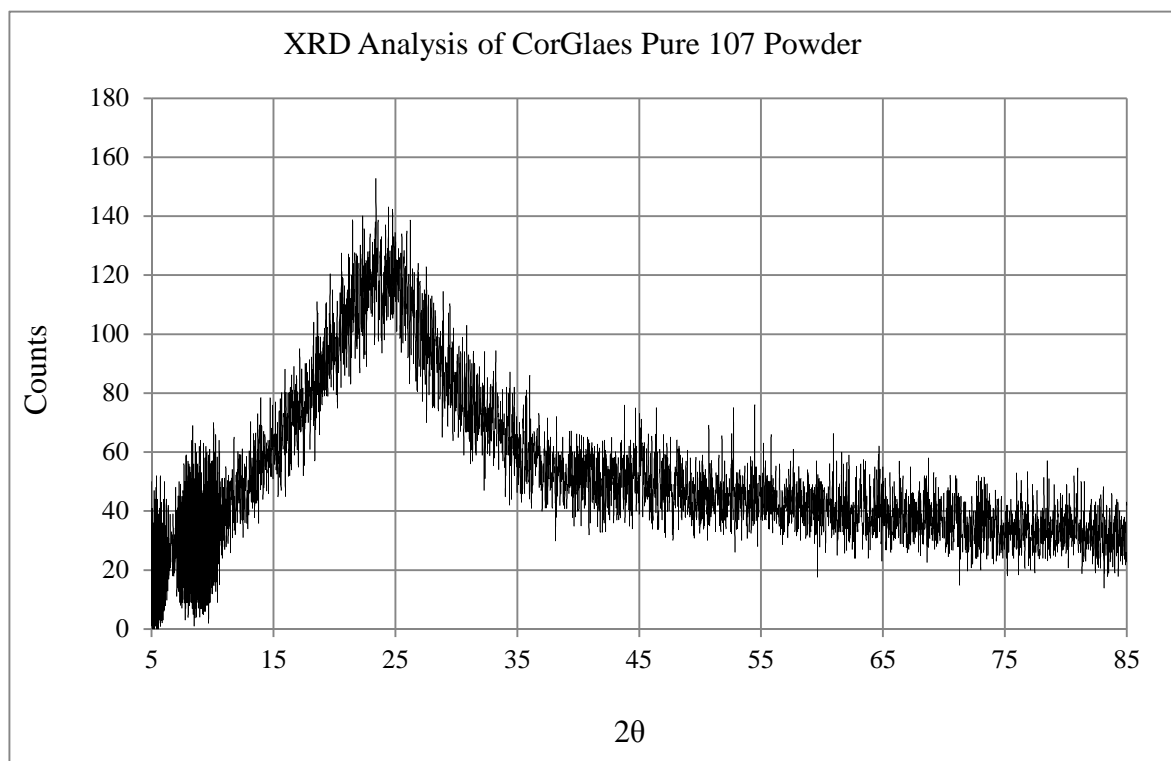


Figure 5.3.1 XRD trace of CorGlaes[®] Pure 107 composition of phosphate glass over $5\text{-}85^\circ$ 2θ with no crystallisation peaks and a broad halo centred at $2\theta \approx 23^\circ$.

5.3.2 FTIR

FTIR traces of the CorGlaes[®] Pure 107 glass over the complete mid-infrared spectrum ($4000\text{-}400\text{cm}^{-1}$) and $1400\text{-}400\text{cm}^{-1}$ region is shown in Figure 5.3.2. The position of these peaks was reflective of the CorGlaes[®] Pure 107 glass composition and based on the literature was assigned to the vibration of phosphate structural groups as listed in Table 5.3.1. The peaks at 3466cm^{-1} and 1664cm^{-1} were associated with the presence of moisture and thus not included in Table 5.3.1.

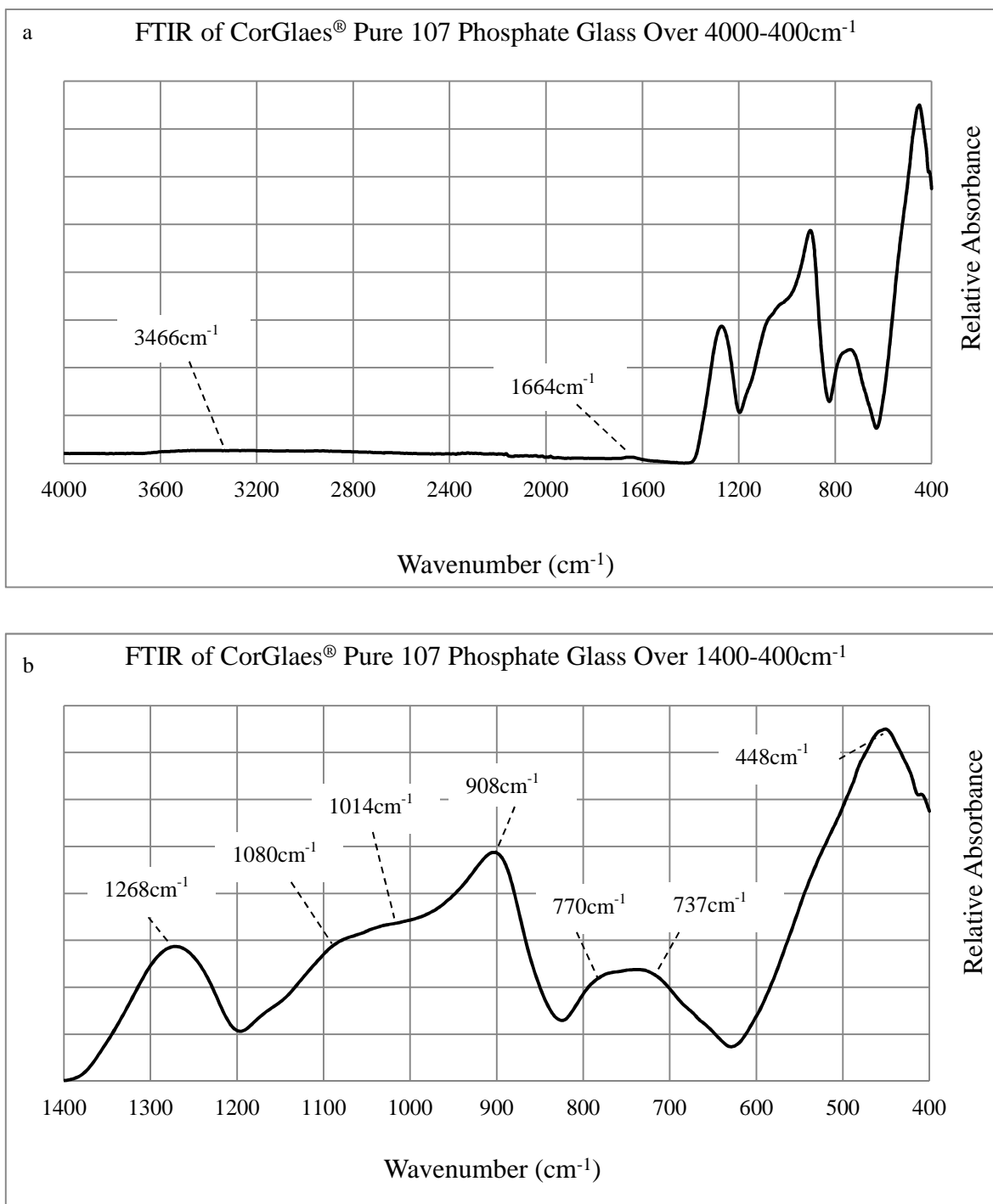


Figure 5.3.2. FTIR vibrational spectra of the CorGlaes® Pure 107 phosphate glass over a) The complete mid-IR range (4000-400 cm^{-1}) and b) The 1400-400 cm^{-1} wavenumber range showing absorption peaks and shoulders corresponding to the glass's structure with the wavenumber of identified spectral features labelled.

Table 5.3.1. Assignments of spectral features identified from the CorGlaes[®] Pure 107 FTIR spectrum over the 1400-400cm⁻¹ wavenumber range to the corresponding phosphate structural features.

| Feature | Wavenumber | Assignment |
|---------------|-------------------------|---|
| Peak | 1268cm ⁻¹ | P=O [ν_{as}] associated with Q ³ tetrahedra superposed with Q ² (PO ₂) ⁻ [ν_{as}] [190, 191, 285, 286] |
| Peak/Shoulder | 1080cm ⁻¹ | Q ² (PO ₂) ⁻ symmetric stretching [ν_s] [190, 191, 287] |
| Peak | 1014cm ⁻¹ | (P-O-P) asymmetric stretching [ν_{as}] (small metaphosphate rings) [159, 288] |
| Peak | 908cm ⁻¹ | (P-O-P) asymmetric stretching [ν_{as}] (chains) [159, 190, 191, 285, 286] |
| Peak | 770/737cm ⁻¹ | (P-O-P) symmetric stretching [ν_s] (rings) [182, 190, 286, 287] |
| Peak | 448cm ⁻¹ | Bending vibrations of bridging phosphorous δ (O-P-O) and/or δ (P=O) [288] |

5.3.3 DSC

The thermogram obtained from <3mm fragments of the CorGlaes[®] Pure 107 phosphate glass is shown in Figure 5.3.3. This trace displays a clear endothermic glass transition (T_g) however further exothermic (i.e. crystallisation peak) or endothermic (i.e. liquidus) events are obscured and are not obvious in the thermogram beyond $\approx 860^\circ\text{C}$. The level of obscurity in the thermogram (i.e. the radical deviation in the baseline) was greater than any found in the literature and prevented the identification of the crystallisation peak (T_p) as well as the liquidus temperature (T_{lq}).

This was believed to have arisen from influences to the testing equipment during the DSC thermal cycle and relates to nearby construction work that commenced mid-way through the DSC run. The resulting intense vibrations throughout the laboratory and testing equipment was then believed to have accounted for the clear T_g , but substantial deviation in the baseline after $\approx 860^\circ\text{C}$. Given the limited availability of the DSC equipment and relevance of the fibres to composite development, the thermal characterisation of this glass composition was repeated at a later date using CorGlaes[®] Pure 107 fibres.

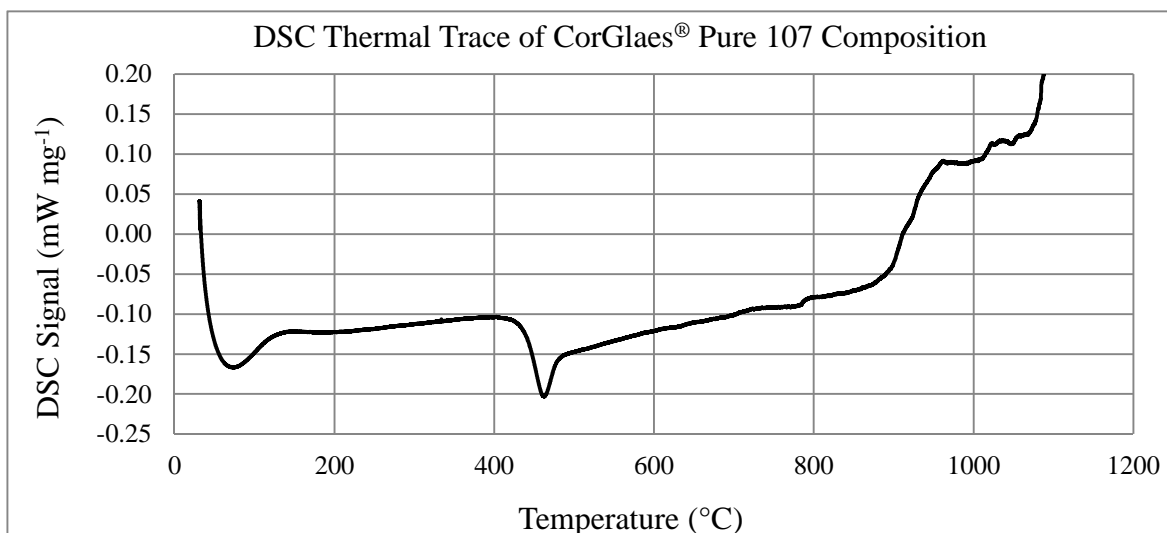


Figure 5.3.3. DSC trace of the CorGlaes® Pure 107 phosphate glass over the pre-programmed heating cycle with deviations in the baseline indicative of endo- and exothermic events.

Magnified sections of the DSC thermogram (Figure 5.3.4 and Figure 5.3.5) found the glass transition (T_g) and crystallisation onset (T_{oc}) temperatures to be 436°C and 784°C respectively by the intersection of tangents overlaid across the endo- or exothermic events. From Eqn 5.2.1 the CorGlaes® Pure 107 processing window (PW) was determined to be 348°C.

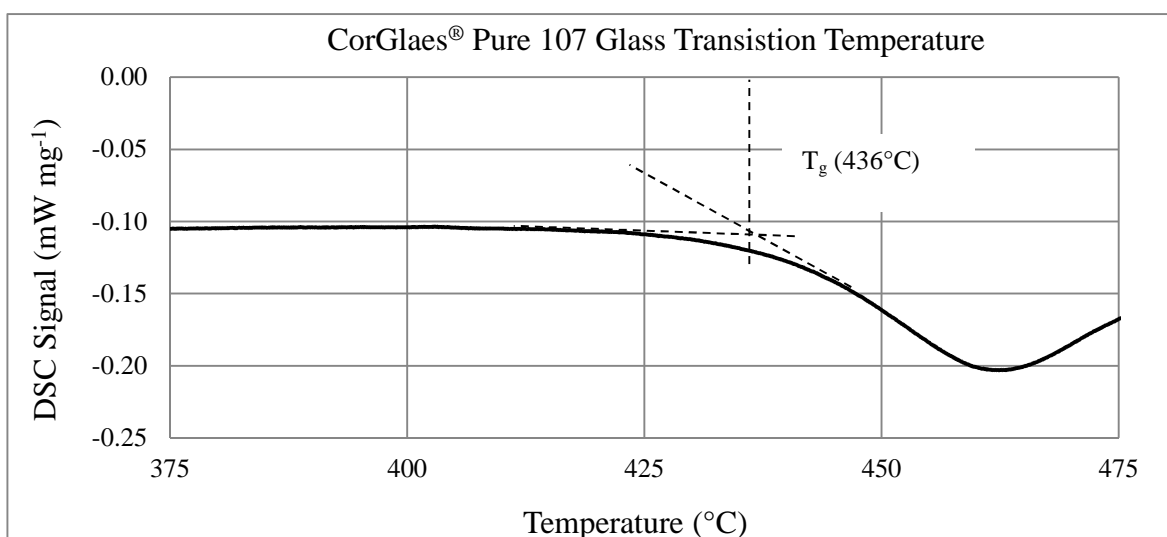


Figure 5.3.4. Magnified section of CorGlaes® Pure 107 DSC thermogram (Figure 5.3.3) showing the glass transition temperature at 436°C from the intersection of tangents.

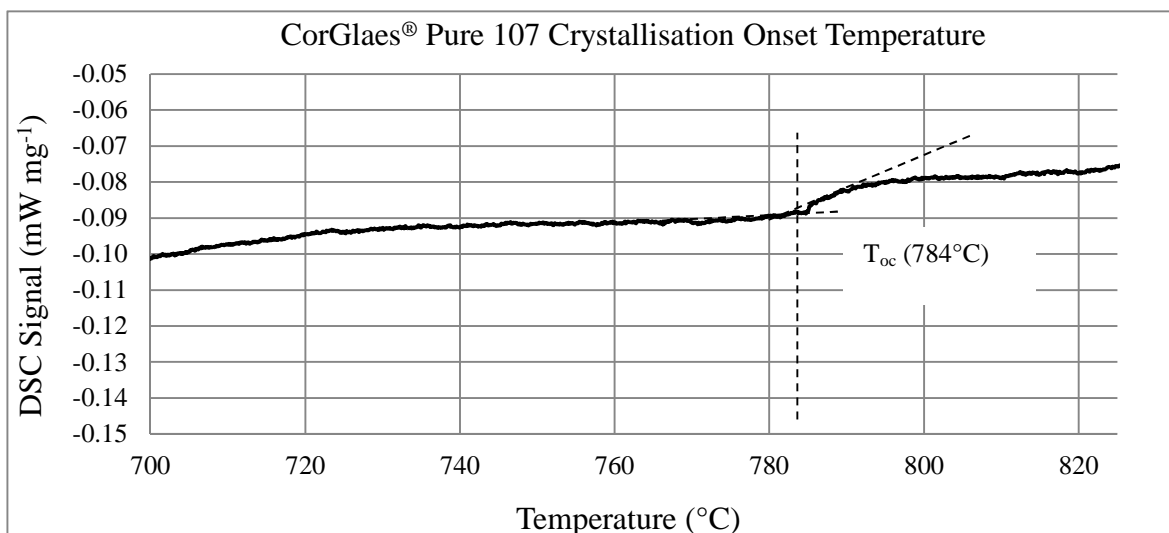


Figure 5.3.5 Magnified DSC thermogram of CorGlaes® Pure 107 (Figure 5.3.3) showing the crystallisation onset temperature from the intersection of tangents.

5.3.4 Density

The density of the CorGlaes® Pure 107 glass was determined to be 2.65 g cm^{-3} using Archimedes principle.

5.3.5 Flexural Strength and Elastic Modulus

The flexural strength and elastic modulus of the CorGlaes® Pure 107 glass was determined to be $64.29 \pm 27.11 \text{ MPa}$ and $33.62 \pm 2.00 \text{ GPa}$ respectively from the independent testing conducted by The Welding Institute (TWI) (Cambridge, UK).

5.3.6 Hardness and Fracture Toughness

The hardness and fracture toughness of the CorGlaes® Pure 107 glass using a 300g (2.94N) indentation load (Figure 5.3.6) were determined to be $3.98 \pm 0.17 \text{ GPa}$ and $0.48 \pm 0.05 \text{ MPa m}^{1/2}$ respectively.

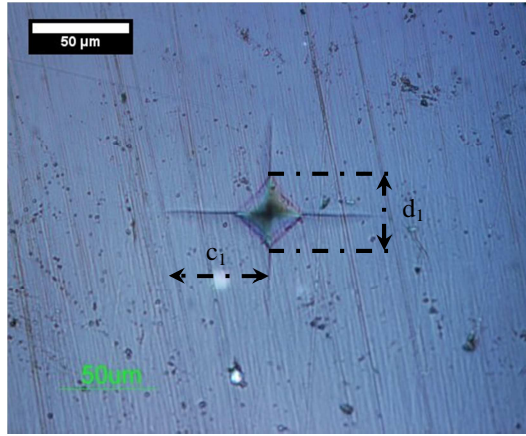


Figure 5.3.6. Optical image of CorGlaes[®] Pure 107 disk surface after Vickers micro indentation with a 300g load showing an indent diagonal (d_1) and crack length (c_1) emanating from indent site [scale bar = 50 μ m].

5.3.7 Dissolution

5.3.7.1 Dissolution Rate

The weight loss per unit area and media pH over the 1008 hour (six week) dissolution of CorGlaes[®] Pure 107 disks is shown in Figure 5.3.7. From an overlaid linear trendline passing through the origin the CorGlaes[®] Pure 107 dissolution rate was determined to be $0.004 \text{ mg cm}^{-2} \text{ hr}^{-1}$.

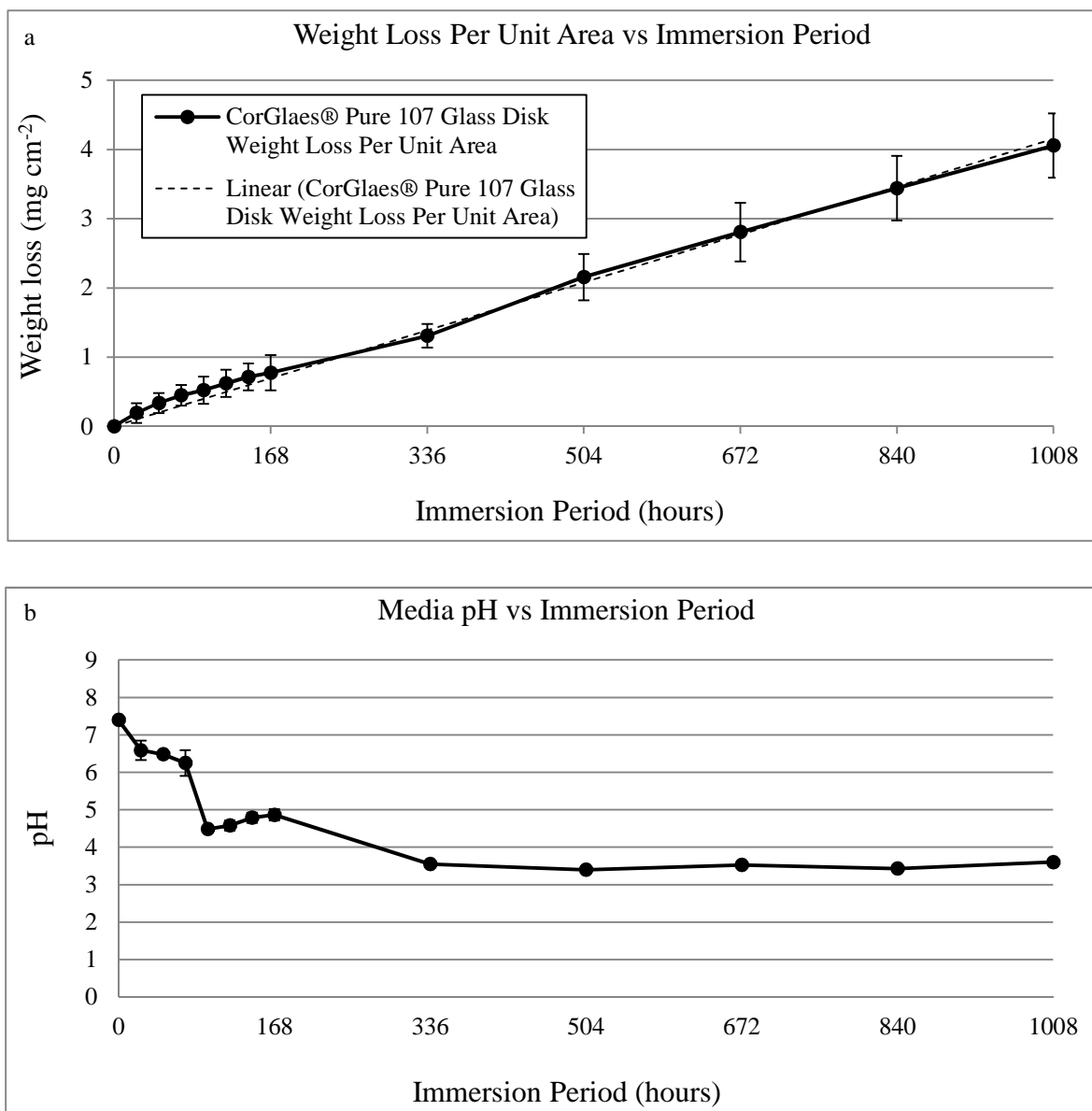


Figure 5.3.7. a) Weight loss during dissolution of CorGlaes[®] Pure 107 disks immersed in distilled water at 37°C with the overlaid trendline plotted through the origin indicative of the glass's dissolution rate and b) Extract pH of CorGlaes[®] Pure 107 disk dissolution media showing the formation of an acidic pH after 72 hours (standard deviation $\leq \pm 0.34$).

5.3.7.2 Ion Release

The daily and accumulative ionic concentrations of Ca^{2+} , Na^+ , Mg^{2+} and Zn^{2+} cations corresponding to the modifier oxides of the CorGlaes[®] Pure 107 composition as well as the PO_4^{3-} anion over the initial 168 hours of glass disk dissolution are shown in Figure 5.3.8.

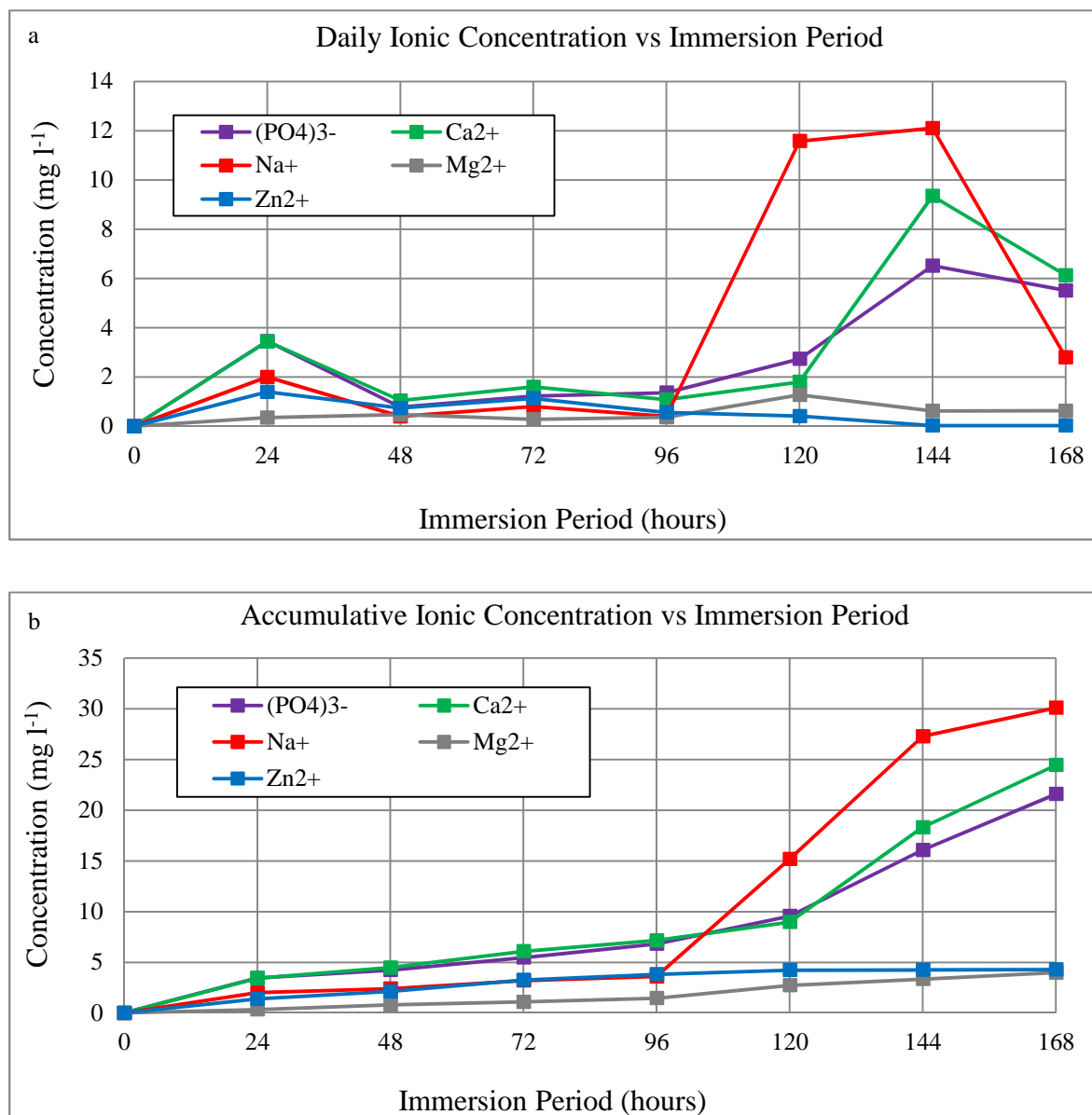


Figure 5.3.8 a) Daily ionic concentrations and b) Accumulative ionic concentrations in the immersion media over the first 168 hours of CorGlaes[®] Pure 107 disk dissolution in distilled water at 37°C.

5.3.8 Bioactivity

The FTIR spectra of the CorGlaes[®] Pure 107 glass across the 1400-400 cm^{-1} wavenumber range after the immersion of disk samples in c-SBF at 37°C for up to 336 hours is shown in Figure 5.3.9. The corresponding weight loss and media pH of the c-SBF over this period is shown in Figure 5.3.10. Due to the absence of a surface layer formation, Raman spectroscopy and SEM imaging were not performed.

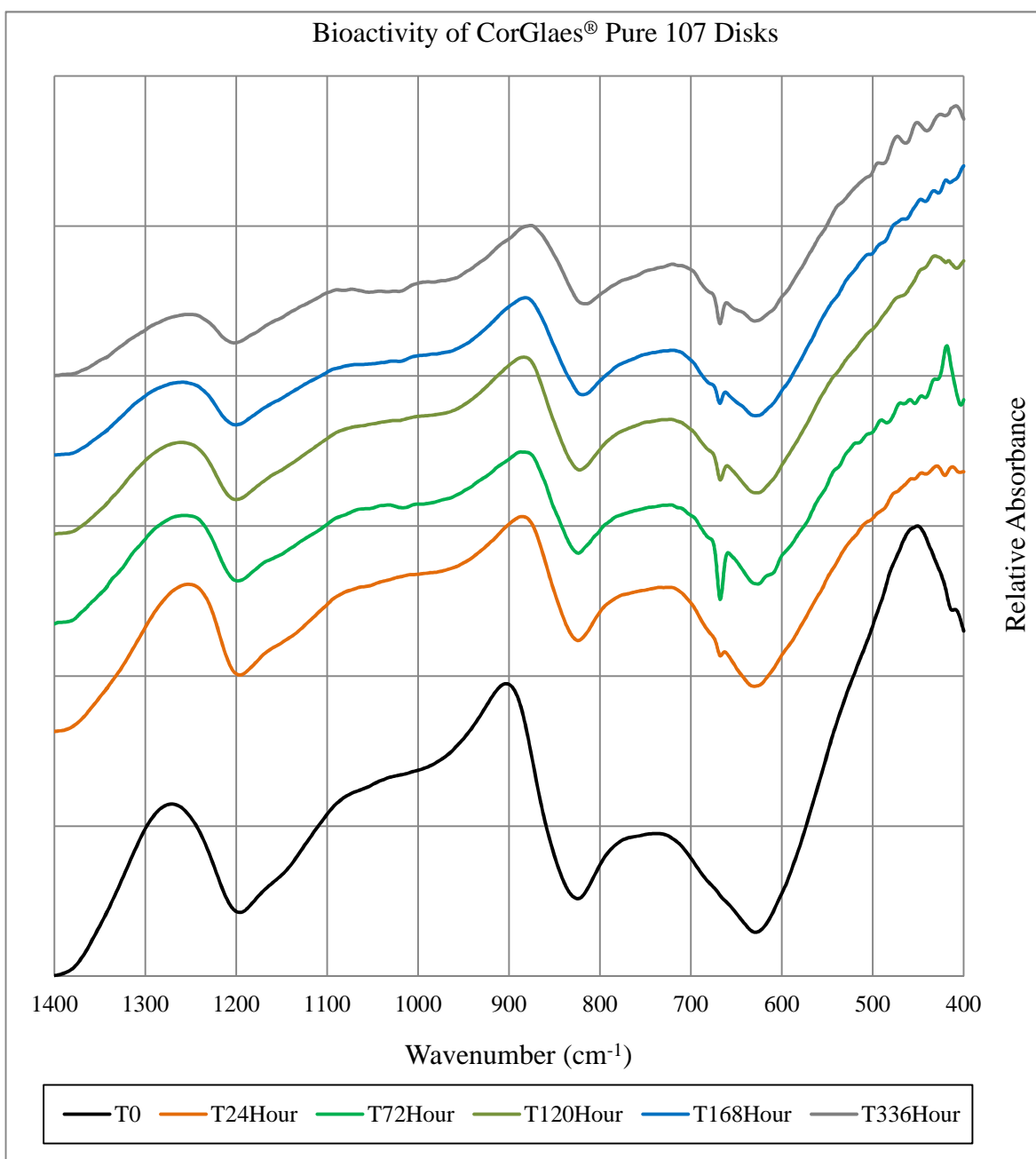


Figure 5.3.9. FTIR of CorGlaes[®] Pure 107 disk surfaces after immersion in c-SBF at 37°C for 24, 72, 120, 168 and 336 hours.

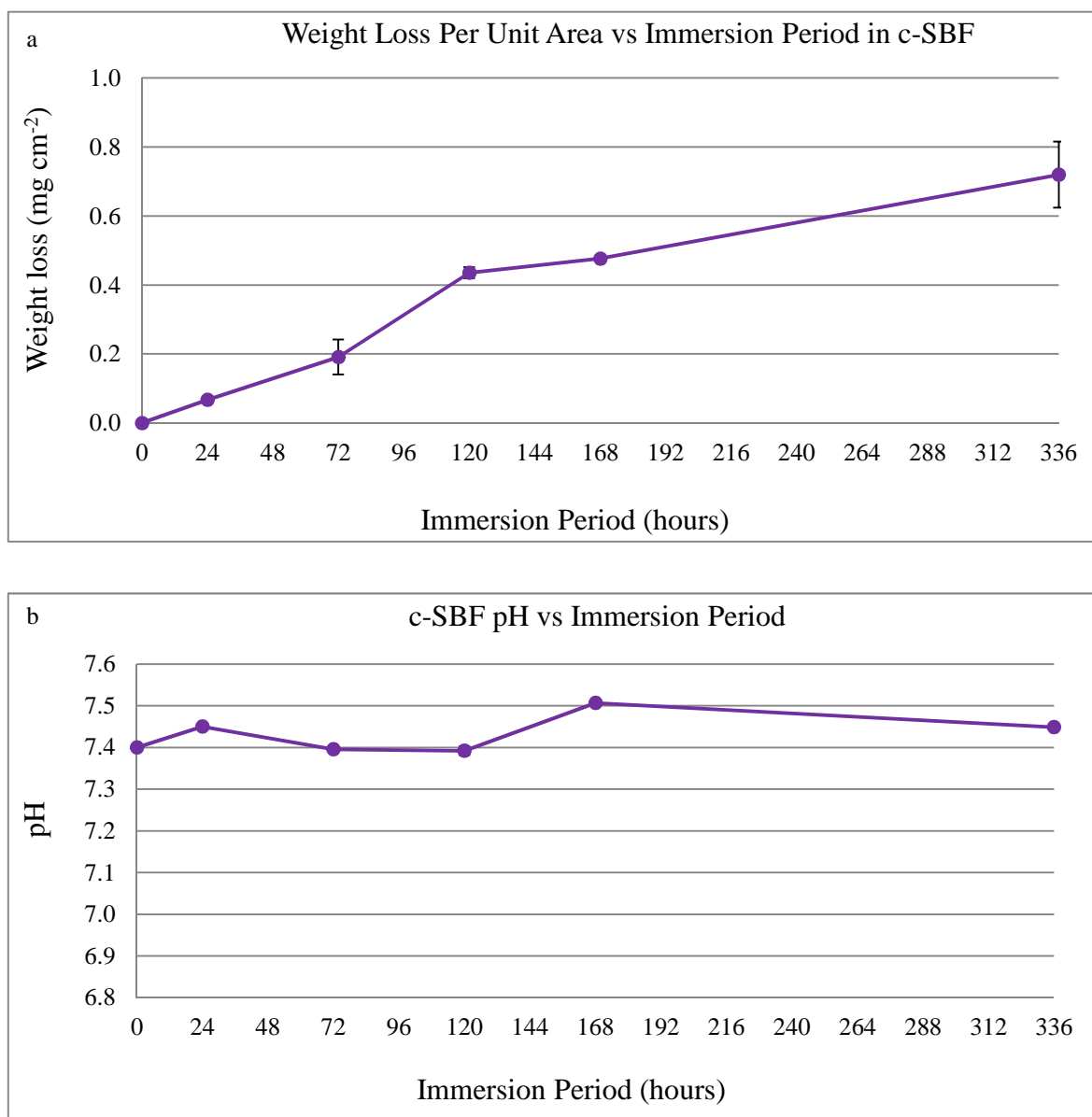


Figure 5.3.10. a) Weight loss during the immersion of CorGlaes[®] Pure 107 disks in c-SBF at 0.1 cm² ml⁻¹ and b) Extract pH of c-SBF media during bioactivity analysis of CorGlaes[®] Pure 107 disks (standard deviation $\leq \pm 0.01$).

5.3.9 Biocompatibility

5.3.9.1 MTT Assay

The viability of MG63 cells cultured for 24 hours in a range of CorGlaes[®] Pure 107 disk CDMEM extract concentrations collected after 24 and 96 hours of sample dissolution is compared with positive as well as negative control media in Figure 5.3.11. The statistical analysis (ANOVA) of the results found no significant difference ($p > 0.05$) between the immersion period or extract concentrations with the positive controls.

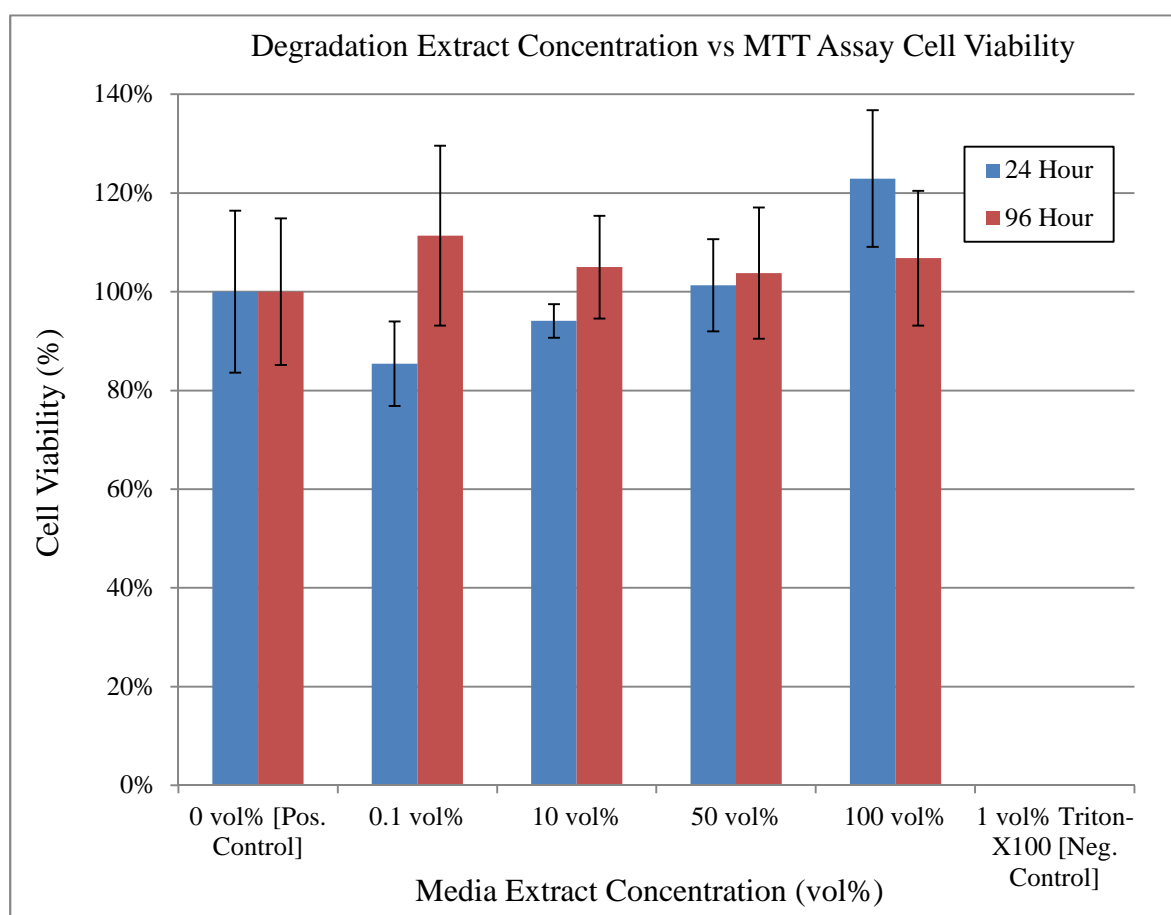


Figure 5.3.11. Viability of MG63 cells cultured in CorGlaes[®] Pure 107 disk extract media over 24 and 96 hours of dissolution and evaluated by MTT assay after 24 hours of incubation at 0.1, 10, 50, 100 vol% extract concentrations.

5.3.9.2 Live/Dead[®] Staining

Live/Dead[®] staining of MG63 cells seeded on Thermanox[®] coverslips and CorGlaes[®] Pure 107 disks after 24, 96 and 168 hours of culture is shown in Figure 5.3.12 with the corresponding media pH shown in Figure 5.3.13.

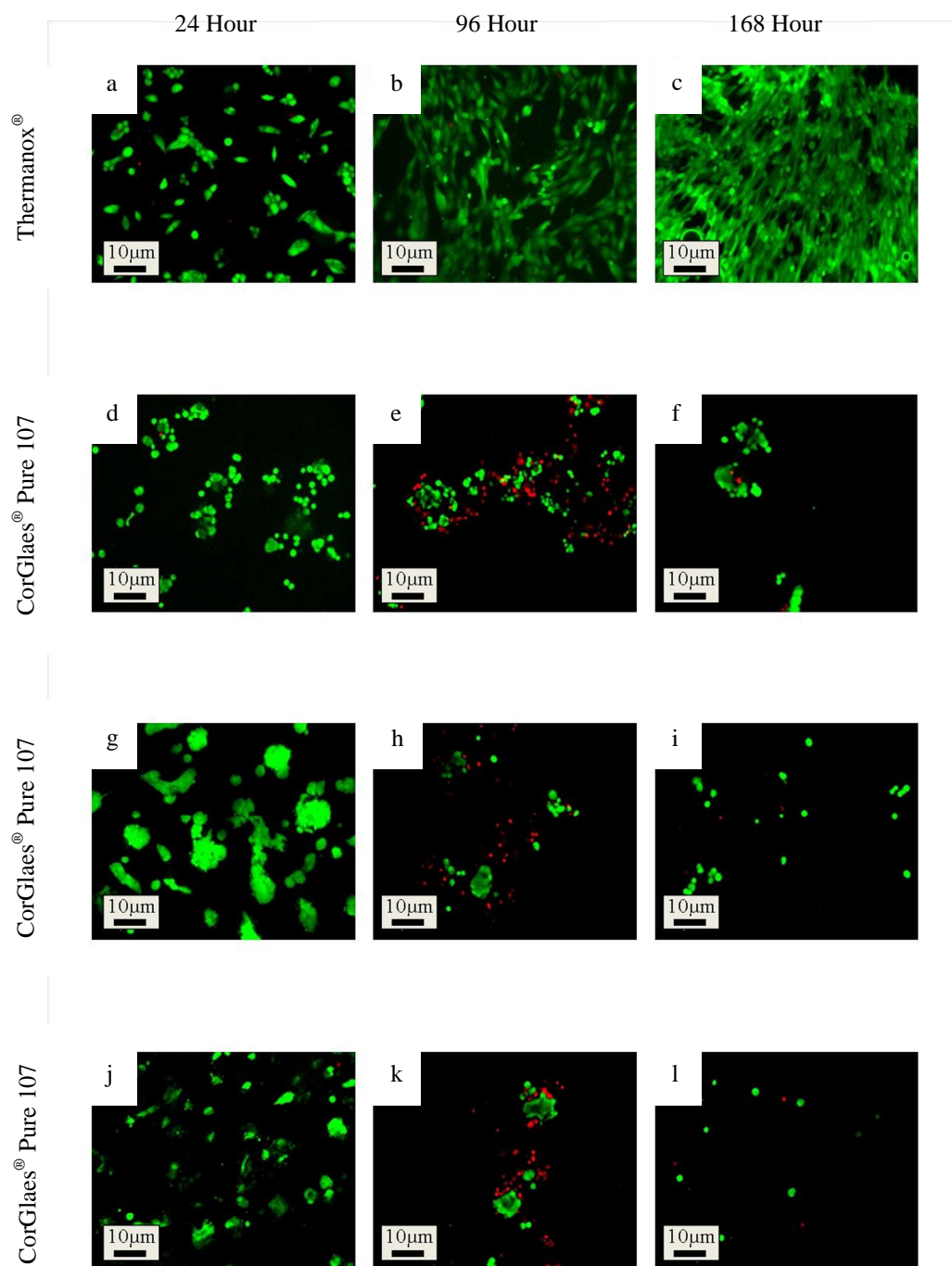


Figure 5.3.12. Live/Dead[®] cell viability staining of Thermanox[®] coverslip controls (a-c) and CorGlaes[®] Pure 107 disks (d-l) showing reduced MG63 cell viability when cultured on CorGlaes[®] Pure 107 disks with increasing incubation period compared to the cell spreading observed on the positive controls (Thermanox[®]) [All scale bars = 10 μm].

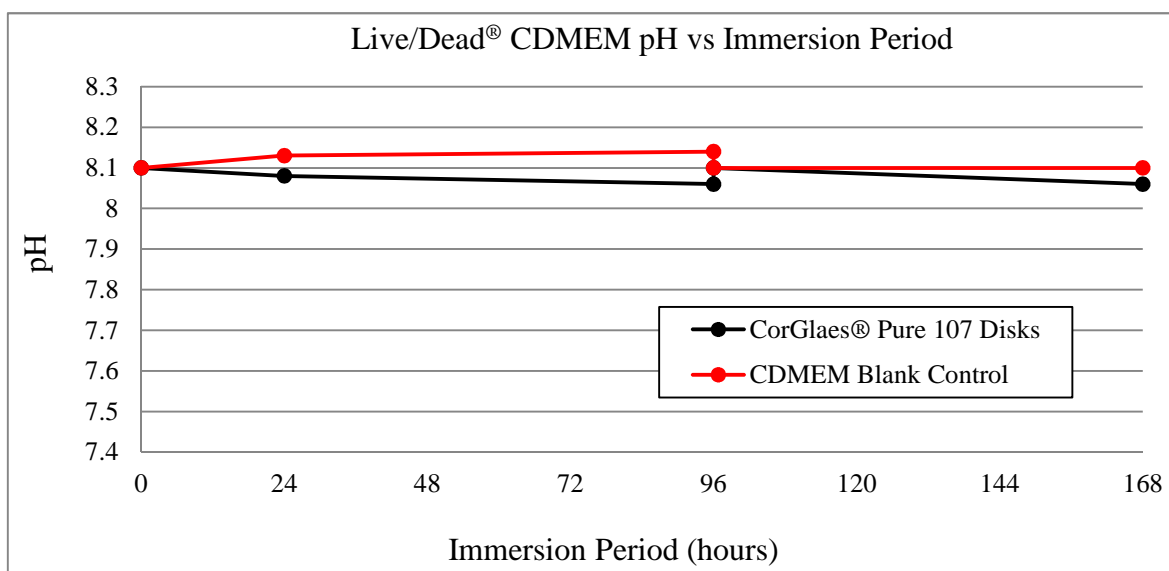


Figure 5.3.13. Comparison of CDMEM pH over the corresponding incubation period for Live/Dead® cell cytotoxicity testing of CorGlaes® Pure 107 disks compared to a blank CDMEM control (standard deviations $\leq \pm 0.01$) - the media change at 96 hours corresponding to the cell culture protocol is also included.

5.4 Discussion

Analysis of the CorGlaes[®] Pure 107 powder by XRD confirmed the amorphous structure of the glass due to the lack of any clear crystallisation peaks and was characteristic of the long range structural disorder found in glassy materials (section 3.4.3). The presence of a broad peak was in line with the literature and its location centred at $2\theta \approx 23^\circ$ was believed to correspond with the dominant crystalline phase that could be formed from the CorGlaes[®] Pure 107 composition (Figure 5.4.1) [232]. The position and shift in the location of an amorphous halo in an XRD trace is also considered as an indication of the degree of compactness in a glass's network [192].

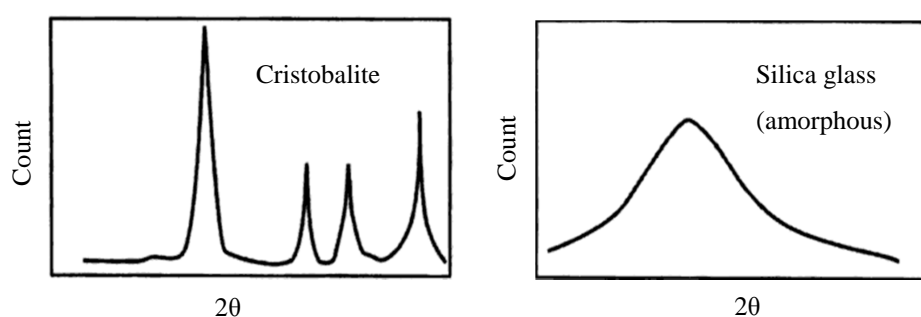


Figure 5.4.1. Illustration comparing the XRD results between a crystalline and amorphous material of the same composition highlighting the correspondence of sharp and broad peaks between both results [Modified from Suryanarayana & Norton (1998)].

The FTIR spectrum shown in Figure 5.3.2 was reflective of the CorGlaes[®] Pure 107 composition but was believed to be a convolution of various overlapping Gaussian components that prevented the complete identification of all the phosphate structural groups. This band overlapping was likely due to the glass's structural disorder from the presence of long P-O-P chains and rings in the Q^2 structural units that would permit additional vibrational modes and account for the generally broad nature of the absorption peaks (Moustafa & El-Egili, 1998). Furthermore the assignment of wavenumber peaks to specific phosphate groups (i.e. Q^3 , Q^2 , Q^1 , Q^0 units) is open to interpretation given the relative shifts in absorbance peaks produced between different glass compositions. This is due to changes in the structural features and bond strengths within the glass's network from the effects of its modifier oxides (section 3.4.3). Consequently, the phosphate structural groups are typically categorised over a range of wavenumbers (Moustafa & Eglili, 1998) [288].

From the results shown in Figure 5.3.2, the assignment of the absorption peaks to Q^3 and Q^2 phosphate groups (Table 5.3.1) based on the available literature appeared to confirm the ultraphosphate composition of the CorGlaes[®] Pure 107 glass. These assignments were also found to be in agreement with the generalised ranges described by Moustafa & Egili (1998) due to the vibration of Q^2 P-O-P chain and ring type structures at 737cm^{-1} , 770cm^{-1} , 908cm^{-1} and 1014cm^{-1} . However the assignment of bands at 1014cm^{-1} is challenged by its association with Q^3 P-O [ν_{as}] as reported by Lucacel et al. (2012) and thus despite agreeing with the consensus of data, some uncertainty remains in the current assignments. Further identification of the structural phosphate groups within the CorGlaes[®] Pure 107 composition could be achieved through deconvolution of the FTIR spectrum to resolve the broad peaks as demonstrated in Figure 5.4.2 [159, 182, 288].

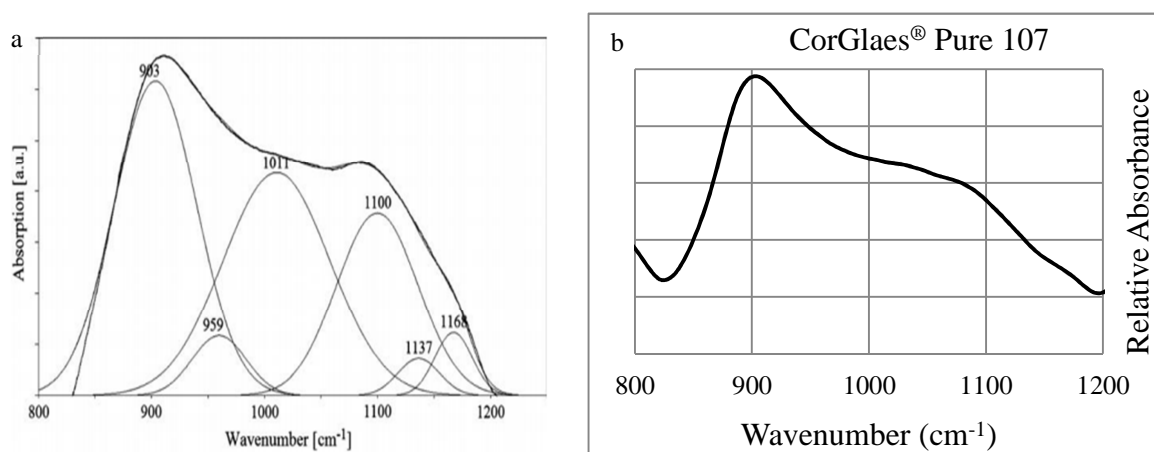


Figure 5.4.2. FTIR spectra showing a) The deconvolution of a phosphate glass FTIR spectrum over the $1200\text{-}800\text{cm}^{-1}$ range and b) An equivalent FTIR spectrum of the CorGlaes[®] Pure 107 composition illustrating the potential for similar band overlapping [Reproduced from Lucacel et al. (2009)].

The very broad but low intensity absorption peaks centred at $\approx 3466\text{cm}^{-1}$ and $\approx 1666\text{cm}^{-1}$ (Figure 5.3.2) were assigned to the absorption of atmospheric moisture across the glass surface as previously reported by Moustafa & Egili (1998), Lucacel et al. (2009) and Kiani et al. (2012) [159, 288, 289].

From the DSC thermogram (Figure 5.3.3), the CorGlaes[®] Pure 107 composition was revealed to possess a larger processing window (PW) compared to Bioglass[®] 45S5 or alternate PGs intended for biomedical applications (Table 5.4.1) due to its significantly higher T_{oc} . This parameter is closely related to the viscosity of the glass melt and was

considered to be a result of several contributing factors related to the CorGlaes[®] Pure 107 composition that included its structural arrangement as well as the selection and number of the modifier oxides (MOs).

Table 5.4.1. Comparison of the thermal properties and thermal processing windows (PWs) of different metaphosphate, polyphosphate and pyrophosphate glasses intended for biomedical applications.

| Material/Composition (mol%) | Thermal events (°C) | | |
|---|---------------------|-----------------|-----|
| | T _g | T _{oc} | PW |
| CorGlaes [®] Pure 107 | 436 | 784 | 348 |
| (P ₂ O ₅) ₅₀ -(CaO) _{33.75} -(MgO) _{11.25} -(TiO ₂) ₅ ^[192] | 522 | 742 | 220 |
| Bioglass [®] 45S5 ^[109] | 538 | 667 | 129 |
| (P ₂ O ₅) ₅₀ -(CaO) ₄₅ -(TiO ₂) ₅ ^[192] | 518 | 645 | 127 |
| (P ₂ O ₅) ₅₀ -(CaO) ₁₆ -(MgO) ₂₄ -(B ₂ O ₃) ₁₀ ^[184] | 552 | 669 | 117 |
| (P ₂ O ₅) ₄₅ -(CaO) ₁₆ -(Na ₂ O) ₅ -(MgO) ₂₄ -(B ₂ O ₃) ₁₀ ^[184] | 500 | 615 | 115 |
| (P ₂ O ₅) ₃₀ -(CaO) ₆₀ -(TiO ₂) ₁₀ ^[192] | 645 | 755 | 110 |
| (P ₂ O ₅) ₅₀ -(CaO) ₁₆ -(Na ₂ O) ₁₀ -(MgO) ₂₄ ^[184] | 452 | 538 | 86 |
| (P ₂ O ₅) ₄₅ -(CaO) ₁₆ -(Na ₂ O) ₁₅ -(MgO) ₂₄ ^[184] | 440 | 512 | 72 |

Phosphate content (P₂O₅ mol%) was previously reported by Ahmed et al. (2004) to alter a glass's thermal properties due to its effect on the structure and corresponding degree of disruption throughout the phosphate network. Accordingly ultraphosphate glasses are considered by Jones & Clare (2012) to possess a greater degree of thermal stability compared to meta- and polyphosphate compositions and correlates with the data shown in Table 5.4.1. This is due to the structure of ultraphosphate glasses consisting of a 3D phosphate network with the combined Q² phosphate chains and ring type structures further impeding the glass's reorganisation into an arranged crystalline state by becoming entangled and increasing the melt viscosity ^[109]. The quinary composition of the CorGlaes[®] Pure 107 glass would also have likely suppressed the onset of glass crystallisation by increasing the entropy of mixing and the subsequent energy barrier required for atomic rearrangement to form critical sized nuclei ^[109, 192, 205].

The inclusion of network modifier cations into the CorGlaes[®] Pure 107 composition with sufficiently large charge-to-size ratios was also believed to have influenced the glass's thermal stability. This is due to the expected strong ionic cross-linking in the phosphate network of the CorGlaes[®] Pure 107 structure from the inclusion of Mg^{2+} , Zn^{2+} and Ca^{2+} cations and their respective charge-to-size ratios (0.0232, 0.0227 and 0.0175). The CorGlaes[®] Pure 107 network structure would then be more capable of suppressing the onset of crystallisation and would be in line with previous results (Ahmed et al., 2004; Khor et al., 2011; Jones & Clare, 2012; Morikawa et al., 2013). However, previous studies have also shown how increased network stability is associated with a higher T_g due to the increased energy required to break the structural bonds which contradicts the comparatively low T_g found in the CorGlaes[®] Pure 107 results (Table 5.4.1). Yet this could be accounted for by the general decrease in T_g found in ultraphosphate glasses compared to metaphosphate compositions as reported by Ahmed et al. (2004) ^[109, 173, 187, 192].

Based on previous metaphosphate glass compositions studied by Morikawa (2013), the large CorGlaes[®] Pure 107 PW could also be attributed to a mixed cation effect between the Mg^{2+} and Ca^{2+} ions (Figure 5.4.3). This is believed to be related to the difference in polarity of the glass's chemical bonds as a result of the higher electronegativity of magnesium compared to calcium. If following this phenomenon, glasses would possess T_g and T_{oc} values that followed non-linear trends and deviated from the expected behaviour commonly reported for phosphate glass compositions ^[192].

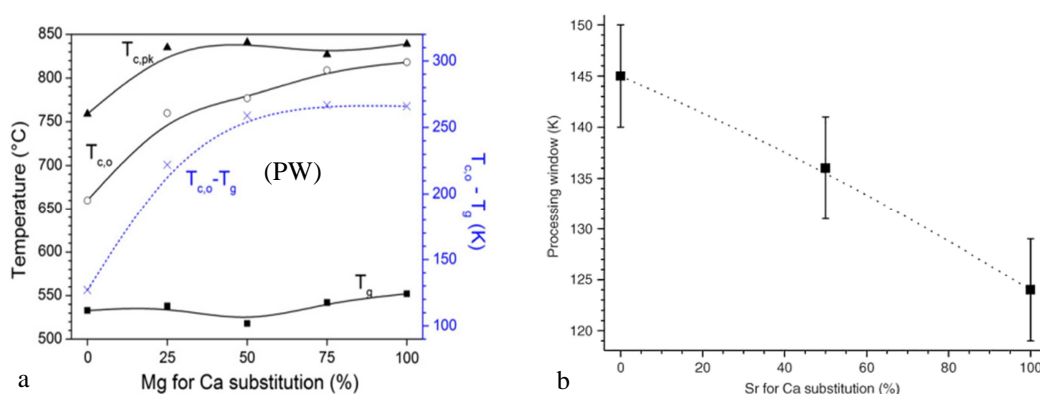


Figure 5.4.3. Variation in thermal properties (T_g , T_{oc} , PW) with the increasing substitution of a) Mg for Ca [Reproduced from Morikawa et al. (2013)] or b) Sr for Ca [Reproduced Jones & Clare (2012)] into phosphate glass compositions showing a clear difference between non-linear (i.e. mixed cation effects) and linear PW relationships respectively.

This mixed cation effect has previously seen significant increases in a glass's crystallisation temperature and subsequently large improvements in its processing window. It is however unclear what role ZnO may have played in any mixed cation effects given the lack of comparative data and the large effects that small compositional changes can make to a glass's crystallisation behaviour. Furthermore if potentially acting as an intermediate oxide, the MgO may have induced further thermal stability to CorGlaes[®] Pure 107 by entering the phosphate network backbone. Such behaviour has been observed previously in highly disrupted bioactive glasses where the Mg²⁺ cation has shifted from a network modifier to a network former after exceeding a so-called "critical concentration" (Jones & Clare, 2012). This was reported to have produced glasses with significantly wider PW values at compositions incorporating >20 mol% MgO [109]. However given that this threshold was deemed to be dependent upon the glass's composition and was conducted using a silicate based glass, it is unclear how this would translate to phosphate based glasses [109, 114, 187, 192, 205, 290].

The density of CorGlaes[®] Pure 107 glass was reflective of the accumulated atomic weights from the glass's components and atomic packing in its network which was related to its modifier cations and network structure. A comparison of the calculated density for the CorGlaes[®] Pure 107 glass showed it to be in line with other biomedical glasses (Figure 5.4.4) [109, 184, 187, 195, 291, 292].

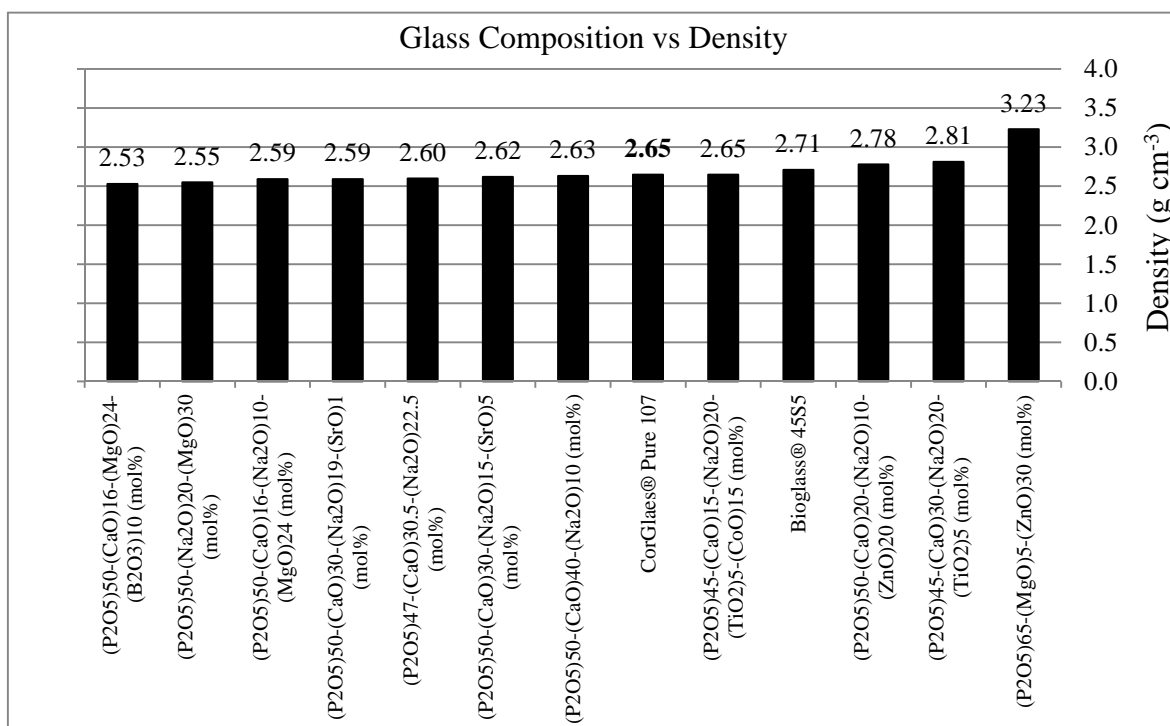


Figure 5.4.4. Comparison of CorGlaes® Pure 107 phosphate glass density with Bioglass® 45S5 and alternate ultra-, meta- and polyphosphate glass compositions intended for biomedical applications [Data from Abou Neel et al., 2008; Devi et al., 2010; Khor et al., 2011; Jones & Clare, 2012; Lee et al., 2013; Sharmin et al., 2014].

From the mechanical testing results, the CorGlaes® Pure 107 glass was found to display a higher flexural strength and a similar elastic modulus compared to Bioglass® 45S5 (Figure 5.4.5). The elastic modulus of CorGlaes® Pure 107 glass also appeared to be significantly higher than some alternative metaphosphate glass compositions and within the range generally stated for bone ^[53, 96, 293-295].

It is generally accepted that PGs possess a lower mechanical strength and elastic modulus compared to silicate glasses and that according to Rouxel (2007), the elastic moduli of an oxide glass is primarily governed by its atomic bond strengths and atomic packing density (C_g). The atomic packing density is defined by Rouxel (2007) as the ratio between the minimum theoretical volume occupied by the ions and the effective volume of the glass. This property can be used alongside the dissociation energies of the glass's modifier oxides to calculate the total bonding energy (U_m) using the method proposed by Makisma-Mackenzie. From this, the total bond energy (U_m) has been found to typically show a linear relation to the elastic modulus of a glass ($E = 2U_m$) with weak bonding, an expanded network and a high number of non-bridging oxygen's generally producing glasses with a relatively low elastic modulus. Consequently due to the flexibility in available glass

compositions, a range of elastic moduli from 10 to 200 GPa have been reported for oxide glasses. Furthermore given the relation between network bond strength and elastic moduli, authors such as Shelby (2005) have highlighted the general trend of increasing elastic modulus with increasing T_g [157, 296-298].

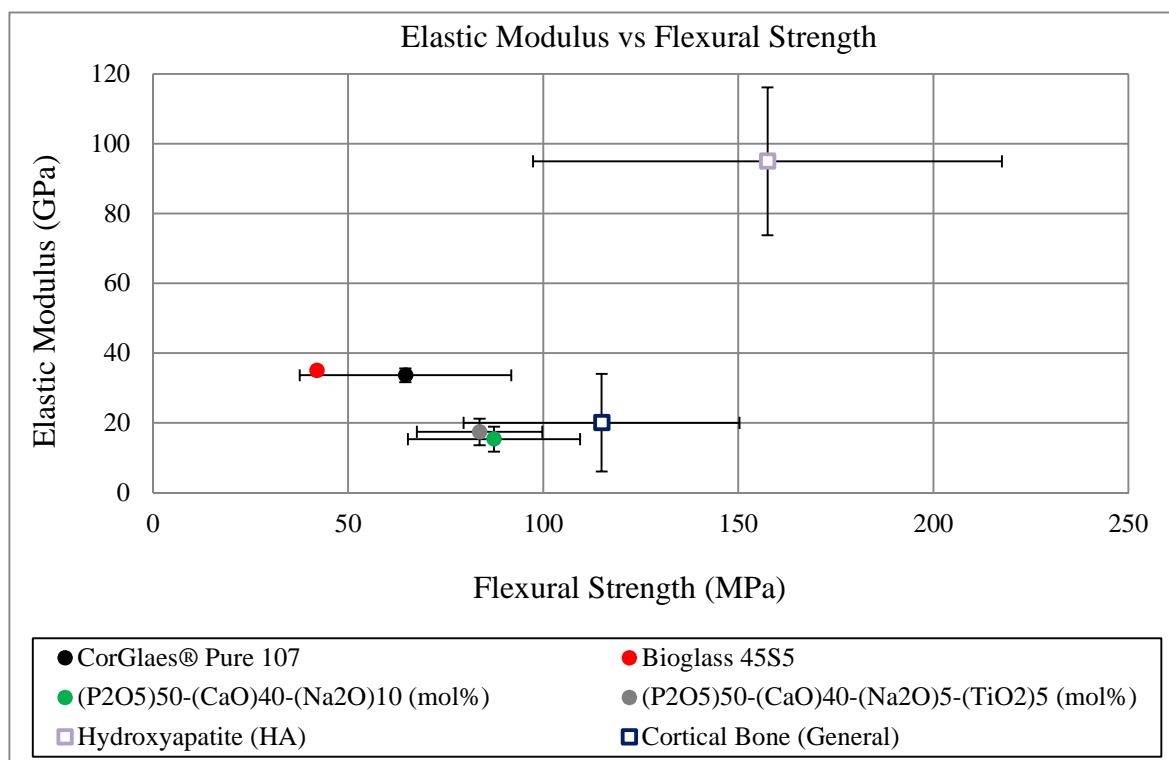


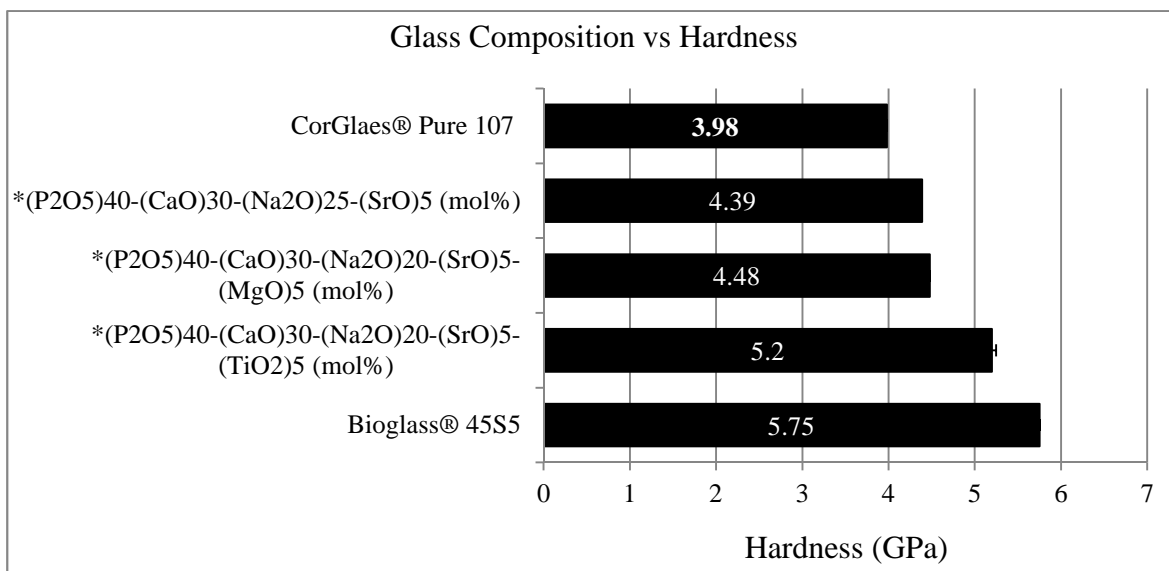
Figure 5.4.5. Comparison between the flexural strength and elastic modulus of the CorGlaes® Pure 107 glass with BioGlass® 45S5, cortical bone, hydroxyapatite along with alternate PG compositions intended for biomedical applications [Data from Thompson & Hench, 1998; Kokubo et al., 2003; Abou Neel et al., 2009; Ratner et al., 2012].

Accordingly, the comparatively high elastic modulus of the CorGlaes® Pure 107 composition (Figure 5.4.5) is associated with a combination of factors that include its selection of modifier cations as well as its quinary composition. This can be attributed to the anticipated high total network bonding energy (U_m) generated in the CorGlaes® Pure 107 glass network from the high charge-to-size ratio Mg^{2+} and Zn^{2+} cations. This is further complimented by the variation in ionic radii between the calcium (114 pm), magnesium (86 pm) as well as zinc (88 pm) modifier cations that, according to Rouxel (2007), would allow these ions to fill the interstitial sites within the glass network more effectively and increase the glass's C_g . This atomic packing density in the CorGlaes® Pure 107 glass structure is reflected by the density data shown in Figure 5.4.4 [173, 298]. Such features

would also appear to coincide with comments by Pukh et al. (2005) who discussed how the appropriate choice of modifier cations and degree of polymerisation in the network can produce phosphate glasses with elastic moduli close to or exceeding those displayed by silicate based glasses. Furthermore Rouxel (2007) also considers factors such as the coordination and molecular organisation (i.e. chains and ring structures) to have an impact on the elastic modulus of a glass. Such influences may help explain the minimal change in the elastic moduli reported between the two comparative PG compositions shown in Figure 5.4.5 despite the expected increase in U_m and number of modifier oxides through the substitution of Na_2O with TiO_2 . However any further interpretation of these results is limited by the lack of available data on the CorGlaes[®] Pure 107 composition as well as that of alternate biomedical PGs regarding their bulk elastic moduli [114, 157, 296, 297, 299-301].

The theoretical strengths of glasses are typically orders of magnitude greater than those found experimentally due to the presence of surface flaws across the sample that can act as stress concentrators. During mechanical loading, the highly localised stresses at these flaws are then able to exceed the theoretical strength of the glass to cause spontaneous crack growth and sample fracture as described by Griffith (Shelby, 2005). As a result, the inherent strength of a glass is typically considered to be irrelevant with regards to its practical value due to its reliance on the sample surface quality. Consequently the differences in flexural strengths and large standard deviations between the glass compositions shown in Figure 5.4.5 may be representative of the different levels of surface quality [157, 293].

Micro indentation techniques found the hardness of the CorGlaes[®] Pure 107 glass to be in line with the accepted range for PGs ($\approx 4\text{-}5$ GPa) and below that of Bioglass[®] 45S5 with a comparison between alternate biomedical glass compositions shown in Figure 5.4.6. The calculated fracture toughness was also found to be within the typical values reported by Ashizuka (1982) for metaphosphate glass compositions ($0.43\text{-}0.53$ MPa $\text{m}^{1/2}$) [109, 117, 172, 294, 302-306].



*Measured using a Berkovich tip indent (three sided diamond pyramid) at 400mN

Figure 5.4.6. Comparison of CorGlaes® Pure 107 glass hardness with different PG compositions and Bioglass® 45S5 [Data from Jones & Clare (2012) and Weiss et al. (2014)].

During Vicker's hardness testing, it is generally accepted that a glass will experience deformations and consequently indentation through a combination of compressive as well as shear stresses. These deformations are composed of elastic deformation (compression related), plastic flow (shear related) as well as densification (compression and shear related) phases when mechanically indented. Additionally the ratio of each deformation type is reported by Salama & El Batal (1994) to be dependent upon the glass's composition due to the corresponding glass structure. Yet due to the complex processes governing glass hardness, the underlying mechanisms are also considered by Salama & El Batal (1994) to be poorly understood ^[307, 308].

The hardness of a phosphate glass is however believed to be highly influenced by the ionic radii and the polarizability of the modifier cations (Salama & Batal, 1994; Weiss et al., 2014). Similar to the elastic modulus of an oxide glass, generally higher hardness values can be found in compositions with small ionic radii or high field strength cations due to the increased network compaction (C_g) and bond strengths in the network that increases its resistance to deformation (Shelby, 2005) ^[157, 172, 307].

Based on the limited comparative data, Figure 5.4.6 shows the hardness of the CorGlaes® Pure 107 glass to be lower than the alternate phosphate glass compositions. This could be accounted for by the presence of Q^1 phosphate units in the comparison polyphosphate

glasses (40 mol% P_2O_5) that could increase the atomic packing density (C_g) by acting as phosphate dimers (Ahmed et al. 2004). The inclusion of MgO or TiO_2 and the increased hardness would also appear to agree with the relationships governing glass hardness as described by Shelby (2005) due to the expected increase in U_m from their inclusion. The reduced hardness of the CorGlaes[®] Pure 107 glass would subsequently make samples more liable to surface damage which may explain the reduced flexural strength seen in Figure 5.4.5 due to the greater severity of the flaws or flaw population. However it should also be noted that a direct comparison between these compositions and the CorGlaes[®] Pure 107 glass is compromised by the differences in indentation technique, loading rate, indentation load and thermal history of the samples (i.e. annealing). Accordingly further dedicated work towards the compositional as well as thermal influences would be required to fully interpret the CorGlaes[®] Pure 107 Vickers hardness data [114, 145, 172, 190, 196, 307, 309].

Although glassy materials possess no crystalline structure, crack propagation is considered to behave similarly to that of a single crystal and as a result glasses generally display lower fracture toughness compared to polycrystalline materials. This is due to their homogeneity and lack of microstructure that permits cracks to travel freely without being retarded by the grain boundaries [303, 310]. The fracture toughness of glassy materials is considered by Inaba et al. (1999) to be directly related to its elastic modulus which, as discussed earlier, is dependent upon its U_m and C_g . Consequently a general trend of increasing fracture toughness with increasing elastic moduli has been previously observed by Weiss et al. (2014) and was attributed to the more rigid glass network obtained by the inclusion of Mg^{2+} or Ti^{4+} modifier cations (Figure 5.4.7) [172, 297].

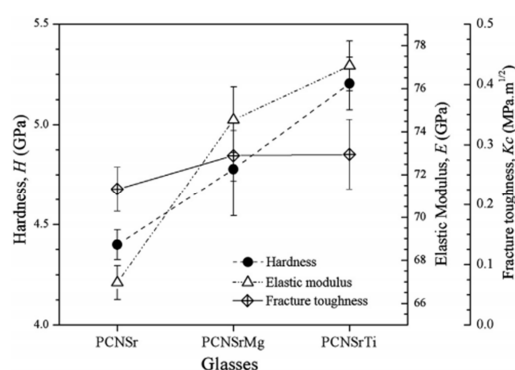


Figure 5.4.7. Increase in hardness, fracture toughness and elastic modulus with substitution of MgO or TiO_2 . Note: the elastic moduli reported here were determined from the hardness data and was excluded from the previous analysis that used three and four point bend techniques (Figure 5.4.5) [Reproduced from Weiss et al. (2014)].

A comparison between the fracture toughness of the CorGlaes[®] Pure 107 glass and those reported for Bioglass[®] 45S5 along with the biomedical PG compositions investigated by Weiss et al. (2014) is shown in Figure 5.4.8.

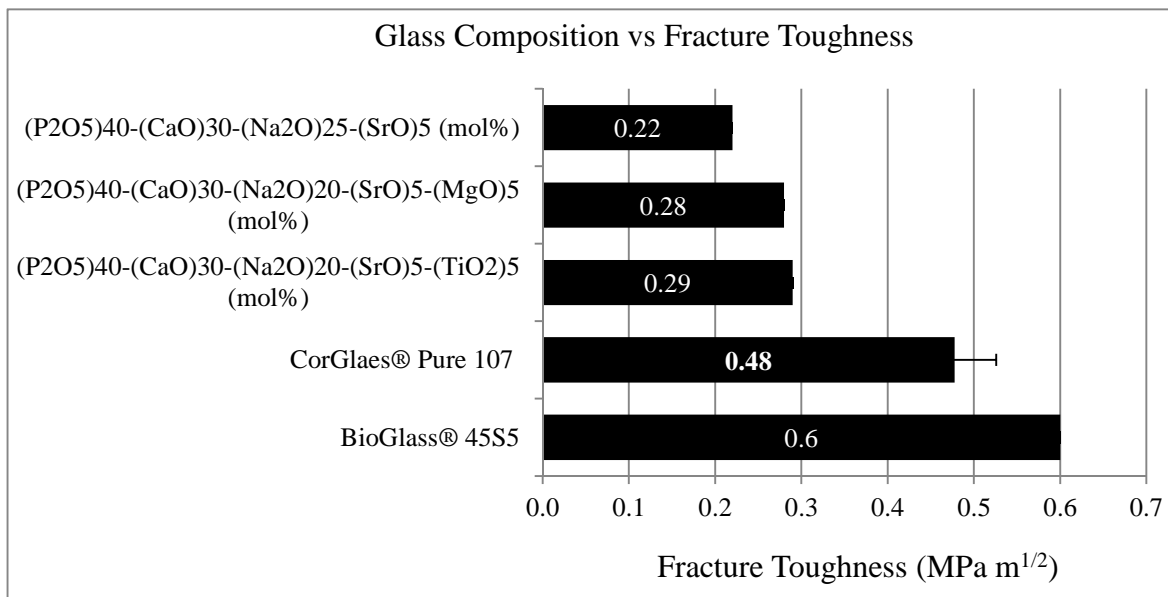


Figure 5.4.8. Comparison of CorGlaes[®] Pure 107 fracture toughness with Bioglass[®] 45S5 and alternate phosphate glass compositions [Data from Jones & Clare (2012) and Weiss et al. 2014].

However glass compositions which fail to adhere to these trends discussed by Inaba (1999) and Weiss et al. (2014) have also been reported with Ashizuka (1982) documenting abnormal variations in the fracture toughness of metaphosphate glasses containing MgO or ZnO. Furthermore Rao et al. (2014) believes that in contrast to Inaba et al. (1999), Kurkjian (2000) and Weiss et al. (2014), a more rigid structure reduces the fracture toughness of a glass due to its restrictions on the degree of plastic flow occurring during indentation. Given that Salama & El-Batal (1994) attributes an increased Vicker's hardness to a reduction in the ratio of plastic flow it is proposed that a trade-off between the hardness and fracture toughness could exist in certain phosphate glass compositions. This increased plastic flow would improve the glass's ability to relieve the stresses near the crack tip that are responsible for crack propagation. The results of the CorGlaes[®] Pure 107 glass shown in Figure 5.4.6 and Figure 5.4.8 would then appear to be in agreement with this proposal due to the superior fracture toughness of the CorGlaes[®] Pure 107 glass being offset by its reduced hardness. However a deeper investigation would be required in order to develop this concept further with regards to any other specific compositional influences

or trends. Furthermore the analysis presented here suffers from a lack of sufficient comparative data and conciseness in the experimental techniques adopted as previously highlighted in the analysis of the Vickers hardness results ^[172, 297, 307, 311, 312].

Immersion of the CorGlaes[®] Pure 107 disks in distilled water at 37°C (Figure 5.3.7) showed the dissolution rate to follow the two stage hydration and hydrolysis mechanisms as described by Bunker et al. (1984). This was apparent by the initially decreasing dissolution rate ($q \propto t^{1/2}$) over the first 168 hours (1 week) of immersion that was followed by a more linear profile ($q \propto t$). Given that the media was replaced every 24 hours over the first 168 hours, any accumulated ionic concentration effects believed responsible for the initially decreasing dissolution rate as proposed by Delahaye et al. (1998) were ruled out. From the plotted trend line through the origin, a dissolution rate (D_r) for the CorGlaes[®] Pure 107 composition was determined to be $4 \times 10^{-3} \text{ mg cm}^{-2} \text{ hr}^{-1}$ and was in line with the measured dissolution rate reported by Giltech Ltd. The ionic concentrations during sample immersion also showed the release of calcium, sodium, magnesium and zinc cationic species as expected from the known CorGlaes[®] Pure 107 compositional data ^[162, 164].

Correlating the results shown in Figure 5.3.7, the initial 24 hours saw the pH of the immersion media fall to ≈ 6.5 which was attributed to the formation of carbonic acid due to carbon dioxide being dissolved from the atmosphere into the media. However such pH values (i.e. $5.8 < \text{pH} < 6.5$) are still considered to be neutral in relation to phosphate glass dissolution kinetics by Delahaye et al. (1998). The decrease in pH after 72 hours was attributed to the release of various phosphate anions and their dissociation to form phosphoric acid (H_3PO_4) as reported by Ahmed et al. (2008, 2009) ^[164, 215, 218]. This initial release was believed to be from the annealed surface layer degrading across the disk samples as previously reported by Hayden et al. (2000), Cozien-Cazuc et al. (2008) and Lee et al. (2013) ^[183, 207, 313]. This is due to the ambient atmospheric moisture attacking the disk surface during the annealing process and cleaving the P-O-P chains. As a result the surfaces of annealed samples are considered to possess different properties compared to the bulk interior. This effect has previously been observed to occur over the first 24 to 72 hours of sample dissolution with Delahaye et al. (1998) commenting that during metaphosphate glass dissolution, an outer layer of phosphate chains is spalled from the glass surface without prior hydrolysis reactions ^[207]. The absence of any significant phosphate species being released into the media (Figure 5.3.8) from this outer surface layer dissolving may be due to the release of larger phosphate anionic species (e.g. $\text{P}_2\text{O}_7^{4-}$, $\text{P}_3\text{O}_9^{3-}$, $\text{P}_3\text{O}_{10}^{5-}$) that were not included in the analysis ^[179, 190, 314]. A gradual increase in pH was

also seen after 96 hours (Figure 5.3.7) and corresponded to a significant increase in Na^+ cation concentration in the immersion media (Figure 5.3.8). This was attributed to the consumption of H^+ ions in the media from the hydration reactions expected during phosphate glass dissolution as previously described in section 3.4.4. The apparent delay in this hydration reaction (i.e. its occurrence after 96 hours) and the associated changes to the ionic concentrations/pH was similar to previous studies reported by Novajara et al. (2011) and Lee et al. (2013) (Figure 5.4.9) [173, 183, 197].

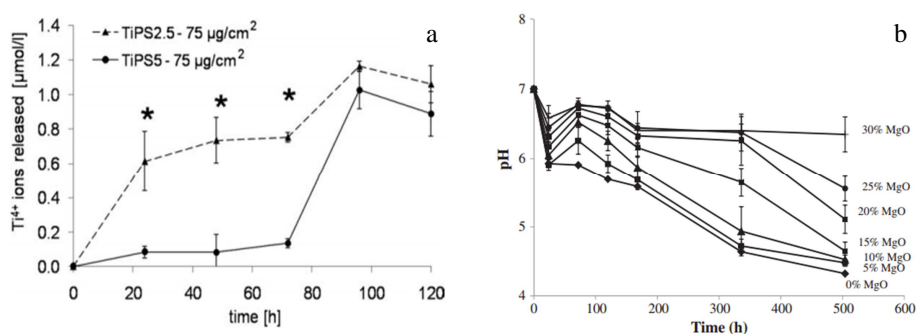


Figure 5.4.9. Dissolution of glass compositions showing a) Delayed release of Ti^{4+} ions from the glass with increasing concentration of TiO_2 (mol%) [Reproduced from Novajra et al. (2011)] and b) Changes in media pH during the dissolution of glass samples with increasing concentrations of MgO (mol%) [Reproduced Lee et al. (2013)].

The release of Na^+ was also coupled with an increase in Ca^{2+} and $(\text{PO}_4)^{3-}$ ion concentrations after 120 hours of immersion that was deemed to be reflective of the saturation and hydrolysis of the CorGlaes[®] Pure 107 glass's phosphate network. This is typically considered to signal the transition to a linear stage of phosphate glass dissolution and would appear to loosely correlate with the observed weight loss data (Figure 5.3.10) that showed increased linearity after 144 to 168 hours of immersion. Yet no significant increase in Zn^{2+} or Mg^{2+} release over the corresponding period was observed (Figure 5.3.11). This is despite the relatively high concentration of magnesium in the composition compared to zinc (based on comments by Giltech Ltd) which would imply that congruent dissolution did not occur (section 3.4.4). However, it could be proposed that the acidic environment generated by the CorGlaes[®] Pure 107 dissolution (pH \approx 4-4.8) may be producing the selective leaching of Zn^{2+} cations that has been shown by Khor et al. (2011) to effect the release rate of Mg^{2+} (Figure 5.4.10). However due the relatively short period over which the ion release data was recorded the non-congruent dissolution process seen

here may be due to some initial surface chemistry effects. Although further investigations would be required to expand on this and confirm ^[187].

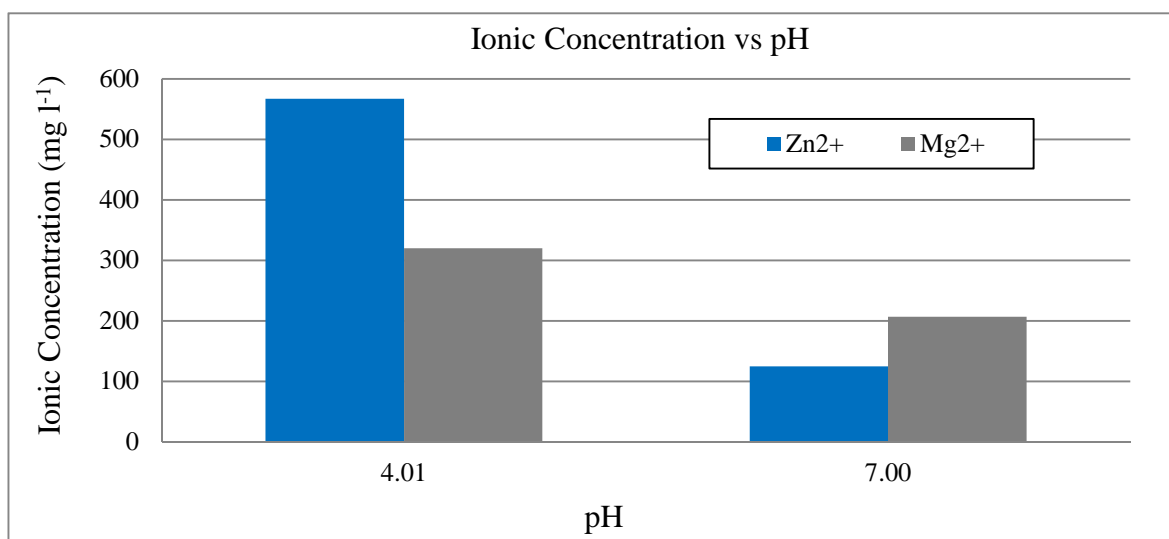


Figure 5.4.10. Variation in Zn²⁺ and Mg²⁺ ion release from a (P₂O₅)₅₅-(ZnO)₃₀-(MgO)₁₅ glass in different media pH buffer solutions (0.24-0.43 cm² ml⁻¹) at ambient temperature [Data from Khor et al. (2011)].

The drop and subsequent plateau of the media pH to ≈3.5 after 336 hours of immersion was attributed to the reduced exchange and replacement of the dissolution media which allowed increasing quantities of phosphate species to accumulate. This would have led to an increased concentration of phosphoric acid in the dissolution media and was in line with similar pH values recorded for ultraphosphate glasses by Ahmed et al. (2004). Yet this decrease in pH failed to exhibit any significant autocatalysis effects to the CorGlaes[®] Pure 107 dissolution rate that continued to progress linearly (Figure 5.3.7) ^[162, 173, 187, 315].

A comparison of the CorGlaes[®] Pure 107 dissolution rate with alternate ultra-, meta- and polyphosphate glass compositions under near identical test conditions is shown in Figure 5.4.11 ^[173, 175, 188, 190, 210, 316].

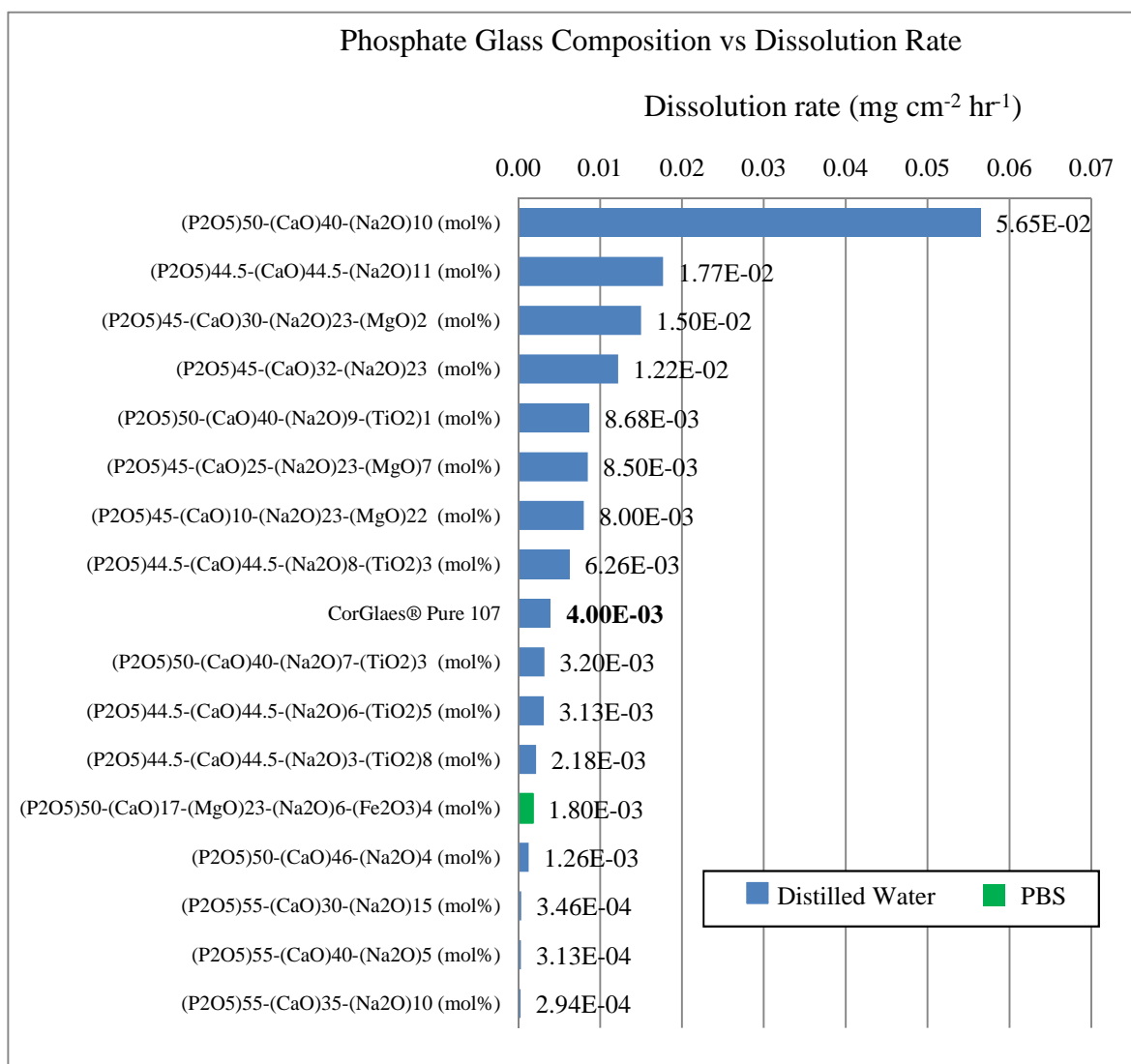


Figure 5.4.11. Comparison of CorGlaes® Pure 107 phosphate glass dissolution rate with a selection of different ultra-, meta- and polyphosphate glass compositions measured under near identical testing conditions in distilled water or PBS at 37°C [Data from Franks et al., 2002; Navarro et al., 2003; Ahmed et al., 2004; Skelton et al., 2007; Abou Neel et al., 2009; Hasan et al., 2012].

The comparison revealed the CorGlaes® Pure 107 glass to possess a mid-range dissolution rate which was related to its composition through the inclusion of Ca^{2+} , Mg^{2+} , Zn^{2+} cations as discussed in previous studies (Abou Neel et al., 2008, 2009; Khor et al., 2011; Lee et al., 2013). Furthermore the dissolution rate of the CorGlaes® Pure 107 glass was found to be within the limits deemed acceptable for permitting cell anchorage ($1.7 \times 10^{-2} \text{ mg cm}^{-2} \text{ hr}^{-1}$) but too rapid for cell proliferation ($3 \times 10^{-3} \text{ mg cm}^{-2} \text{ hr}^{-1}$) as identified from previous *in vitro* studies by Bitar et al. (2004) and Parsons et al. (2004) [178, 187].

The FTIR spectra of CorGlaes[®] Pure 107 samples shown in Figure 5.3.9 indicated that no surface layer had developed over the 336 hour (2 week) immersion period in c-SBF. These observations were in line with alternate PG compositions tested by Clement (1999) that failed to display any bioactivity after 72 hours of immersion in SBF. The marginal variations observed in the FTIR spectra were associated with a poor signal-to-noise ratio due to the sample surface quality (i.e. faces were not ground flat prior to testing) ^[273]. The pH of the c-SBF media over the corresponding immersion period was also found to remain neutral whilst the weight loss per unit area was significantly reduced compared to the equivalent period in distilled water (Figure 5.3.9).

The lack of bioactivity in the CorGlaes[®] Pure 107 glass was similar to the reported inability of calcium metaphosphate glasses to form an apatite surface layer during immersion in SBF by Kasuga (2005) and Devi et al. (2010). Based on this, the results obtained could be attributed to the low dissolution rate of the CorGlaes[®] Pure 107 glass and its subsequent effect on the dissolution-precipitation processes required for surface apatite formation (section 3.4.5). Owing to an ionic buffering effect, the dissolution of the CorGlaes[®] Pure 107 glass was found to have been significantly reduced (Figure 5.3.10) compared to that found in distilled water (Figure 5.3.7). This difference has been attributed by Uo et al. (1998) to the presence of Na⁺, Ca²⁺ and HPO₄²⁻ ions in the SBF media. As a result, reactions between the c-SBF and the glass surface could have been inhibited due to the lack of ionic constituents released from the CorGlaes[®] Pure 107 glass (e.g. Ca²⁺). This slow dissolution was thus likely to have prevented the formation of a calcium phosphate surface gel phase that is considered to be vital for initiating apatite nucleation according to Clement et al. (1999), Kasuga (2005) and Devi et al. (2010) ^[170, 176].

Additionally, PGs studied by Lucacel et al. (2012) have demonstrated the inhibitory effect of zinc on a glass's bioactivity due to its increased durability ^[182]. Consequently the CorGlaes[®] Pure 107 composition may be capable of forming a calcium phosphate apatite surface layer if the immersion period was increased beyond the tested 2 weeks. If combined with a reduced rate of c-SBF replacement, sufficient concentrations of ionic species may also be allowed to accumulate in the c-SBF. Prolonged immersion times such as those used by Clement (1999) have shown the development of calcium phosphate surface layers across meta- and polyphosphate glass compositions after 1344 hours (8 weeks) of immersion. However the CorGlaes[®] Pure 107 composition may also be displaying behaviour similar to that discussed by Kiani (2014) where titanium doped

phosphate glass compositions were found to only develop bioactive surface layers *in vivo* [170, 273, 289].

As demonstrated from previous studies (Salih et al., 2000; Bitar et al., 2004; Skelton et al., 2007), the dissolution rate of a phosphate glass will influence its osteogenic cell adhesion, proliferation, differentiation and cell viability. This is due to the associated ion release rates, pH changes as well as cell anchorage mechanisms (i.e. surface solubility) [175, 177, 178].

Initial biocompatibility testing of the CorGlaes[®] Pure 107 disks by MTT assay showed that no cytotoxic response was evoked during the culture of MG63 cells in glass dissolution extracts over the tested dissolution periods and across all concentrations (Figure 5.3.11). This was evident by the cell viability of all samples being maintained above the 70% threshold as specified by BS EN 10993-5:2009. These results indicated that the ion release rates and pH changes to the culture media were suitable for maintaining cell viability during *in vitro* cell culture experiments. A comparison across the extract concentrations obtained after 24 hours of sample dissolution showed a general increase in the average cell viability as the extract concentration increased. The increased viability could be attributed to the ions released from the glass as had been observed with alternate MTT results by Franks et al. (2002) who reported equivalent or increased cell growth due to the glass's dissolution by-products. This would then explain the general increase in average cell viability with increasing extract concentration due to the respective ionic concentrations in the CDMEM from the dissolution of CorGlaes[®] Pure 107 disks. However statistical analysis found no significant difference ($p > 0.05$) between the extract concentrations or immersion period with the positive controls on MG63 cell viability [188].

Images obtained during direct contact cell culture after 24 hours on Thermanox[®] and CorGlaes[®] Pure 107 samples showed live cells (green) across all samples with early signs of cell cytoplasmic flattening and spreading on the control coverslips (Figure 5.3.12a). The concentrated pockets of live MG63 cells on CorGlaes[®] Pure 107 samples was also suggestive of colonial clustering on the glass surfaces as reported by Lee et al. (2013). However a cytotoxic response in the CorGlaes[®] Pure 107 samples was then observed after 96 hours of culture with a significantly reduced cell population whilst the cell morphology remained round. This was coupled with the presence of dead cells (red) scattered across the sample surface (Figure 5.3.12e, h, k) and was contrasted by the development of polygonal shaped cell morphologies with filopodial extensions (indicative of cell spreading) on the Thermanox[®] coverslips after the equivalent culture period. The cell viability appeared to further decrease on CorGlaes[®] Pure 107 samples after 168 hours of culture (Figure 5.3.12f,

i, l) with further reductions to the number of viable cells (green). The absence of any large dead cell population despite the apparent cytotoxic response was attributed to the detachment of dead cells into the CDMEM during the culture or staining stages of CorGlaes[®] Pure 107 disk evaluation as previously observed by Abou Neel et al. (2008). Continual cell spreading and proliferation was found with the Thermanox[®] coverslips over the equivalent culture period with images showing a flat monolayer of highly confluent cells developing across the coverslip surface (Figure 5.3.12c) ^[195]. The pH results over the Live/Dead[®] culture period (Figure 5.3.13) also showed that the CDMEM pH remained above the cytotoxic limit of MG63 cells (pH 7.4) throughout the entire culture period ^[145, 195].

The combined results from the MTT assay and Live/Dead[®] images implied that either surface anchorage mechanisms or highly localised surface effects were responsible for the increasing cytotoxicity of the CorGlaes[®] Pure 107 disk samples. However it should be noted that the higher surface area-to-volume ratio (SA:V) used with the Live/Dead[®] protocol ($2.24 \text{ cm}^2 \text{ ml}^{-1}$) compared to the MTT assay ($1.25 \text{ cm}^2 \text{ ml}^{-1}$) may impede a correlation between the results of the two tests. This difference was due to the specifications of the MTT assay as dictated in BS EN 10993-5:2009 whilst no SA:V data regarding direct contact cultures on phosphate glass samples could be found from the consulted literature to establish consistency (Salih et al., 2000; Franks et al., 2002; Bitar et al., 2004; Abou Neel et al., 2007; Skelton et al., 2007; Abou Neel et al., 2008; Lee et al., 2013). As a result, cytotoxic effects due to an increased concentration of ions in the CDMEM from glass dissolution could not be completely ruled out ^[145, 165, 175, 177, 178, 188, 189, 195].

The pH data of the CDMEM culture media during the Live/Dead[®] staining was used to rule out any cytotoxicity arising from the acidic dissolution by-products of the CorGlaes[®] Pure 107 glass as had been observed during its immersion in distilled water. Dissolution of the disk sample surface and its associated restrictions to cell anchorage were also not considered. This was due to the results of Bitar et al. (2004) and Skelton et al. (2007) where the successful seeding and attachment of MG63 cells to annealed phosphate glass disks was achieved on samples with dissolution rates significantly higher ($5.65 \times 10^{-2} \text{ mg cm}^{-2} \text{ hr}^{-1}$) than the CorGlaes[®] Pure 107 glass ($4 \times 10^{-3} \text{ mg cm}^{-2} \text{ hr}^{-1}$) ^[195]. The lack of any acidic pH in the CDMEM also ruled out any acceleration to the CorGlaes[®] Pure 107 glass dissolution rate (via autocatalysis) which may have been expected given the higher SA:V ratio used in the Live/Dead[®] ($2.24 \text{ cm}^2 \text{ ml}^{-1}$) compared to the previous dissolution

experiments ($0.18 \text{ cm}^2 \text{ ml}^{-1}$). It was also likely that the CorGlaes[®] Pure 107 samples would have degraded at an even slower rate (i.e. $< 4 \times 10^{-3} \text{ mg cm}^{-2} \text{ hr}^{-1}$) in CDMEM based on the decreased PG D_r reported by Patel & Knowles (2006) when PG samples were immersed in cell culture media [206].

The resulting cytotoxic response observed in the Live/Dead[®] results of the CorGlaes[®] Pure 107 samples was consequently believed to be due to a highly localised acidic surface pH as reported by Salih et al. (2007) and Jones & Clare (2012). Such effects would not be detectable in the bulk media pH or MTT assay (due to the lack of direct cell contact with the sample surface). This proposal would then agree with the gradually increasing cytotoxicity observed across the MG63 culture period as the local surface pH gradually decreased to cytotoxic levels during sample dissolution. Alternatively the higher SA:V ratio of the Live/Dead[®] culture may be evoking a cytotoxic response from the gradual increase in ionic concentrations related to the glass's dissolution by-products. This could be related to the release and accumulation of Zn^{2+} ions in the CDMEM based on results of Abou Neel et al. (2008) with concentrations greater than 8ppm ($\approx 8 \text{ mg l}^{-1}$) found to be cytotoxic to MG63 cells. This is due to the release of lactate dehydrogenase from the cells and cell damage occurring via an oxidative stress mechanisms [195]. Furthermore rounded cell morphologies from the concentration of specific ions released via glass dissolution have also been reported by Bitar et al. (2004) and would correlate with the results found here. Based on the ion release profiles obtained at a significantly lower SA:V ratio ($0.18 \text{ cm}^2 \text{ ml}^{-1}$) in Figure 5.3.8 the time dependant accumulation of Zn^{2+} ions in the CDMEM from the CorGlaes[®] Pure 107 disk dissolution would be able to account for the observed decrease in cell viability despite the apparently suitable pH of the CDMEM. Integrating with the MTT results, it would then appear that this cytotoxic response was only achieved during its immersion at SA:V ratios $> 1.25 \text{ cm}^2 \text{ ml}^{-1}$. However the accuracy and applicability of these Live/Dead[®] results to an *in vivo* response is contested by the circulation of extracellular fluids and variation of the SA:V found *in vivo* compared to the static nature of the *in vitro* culture set up used here as discussed by Bitar et al. (2004) [109, 177, 178, 195].

5.5 Conclusions

Based on the previously reported advantages of calcium, magnesium and zinc for the regeneration of bone tissue (Table 3.4.3) it was anticipated that the unique CorGlaes[®] Pure 107 composition would prove advantageous as a potential orthopaedic biomaterial. Accordingly through a combination of multidisciplinary techniques the characterisation and comparison of the glass's mechanical, chemical and *in vitro* properties was assessed.

Analysis of the composition subsequently confirmed the ultraphosphate (FTIR) and amorphous state (XRD) of the glass whilst the significantly large processing window (348°C) made the composition highly suitable for fibre production. Mechanical testing of the composition also showed the elastic modulus of the CorGlaes[®] Pure 107 glass to be comparable to Bioglass[®] 45S5 whilst the density (2.65 g cm⁻³), hardness (3.98 ± 0.17 GPa) and fracture toughness (0.48 ± 0.05 MPa m^{1/2}) were in line with the reported literature regarding phosphate glasses. These properties were strongly related to the composition of the CorGlaes[®] Pure 107 glass that was also believed to have utilised advantageous mixed cation effects to achieve its material properties.

Dissolution of the CorGlaes[®] Pure 107 glass was found to be within the limits for cell adhesion with the acidic dissolution by-product attributed to the gradual formation of phosphoric acid that was expected from its ultraphosphate composition (55 mol% P₂O₅). This dissolution process corresponded with the release of cationic and anionic species relevant to the CorGlaes[®] Pure 107 composition but its mid-range dissolution rate (4×10⁻³ mg cm⁻² hr⁻¹) also resulted in a lack of calcium phosphate apatite formation on the sample surface. This lack of bioactivity was compounded by the cytotoxic response generated under the current testing conditions that was attributed to the accumulation of ionic species or localised surface pH effects during direct contact cell culture. Consequently based on the accumulated *in vitro* evidence, the CorGlaes[®] Pure 107 composition would appear unsuitable for *in vivo* applications but could be advantageous as a composite fibre reinforcing agent.

6 Characterisation of CorGlaes[®] Pure 107 Fibres

6.1 Outline

Characterisation of the CorGlaes[®] Pure 107 composition (chapter 5) had previously highlighted the suitability of this glass for post-processing fibre manufacturing due to its advantageous thermal properties (i.e. its large thermal processing window). Given that the unique properties of composite materials are derived from its constituent phases (section 3.2.3), the characterisation of CorGlaes[®] Pure 107 fibres was subsequently required. This was conducted through a range of testing techniques aimed at analysing the fibres structural, mechanical and dissolution properties as well as its bioactivity.

6.2 Materials and Methods

6.2.1 Fibre Manufacturing

CorGlaes[®] Pure 107 fibres were manufactured by Giltech Ltd using an in-house gravity fed melt spinning technique from a dedicated fibre production facility that consisted of a temperature controlled interchangeable ceramic clay bushing positioned above a $\text{Ø} = 0.637\text{m}$ stainless steel drum (Figure 6.2.1). During fibre production, these clay bushings could be vertically displaced from the surrounding resistance heating elements in order to further regulate the glass melt temperature and aid fibre manufacturing.

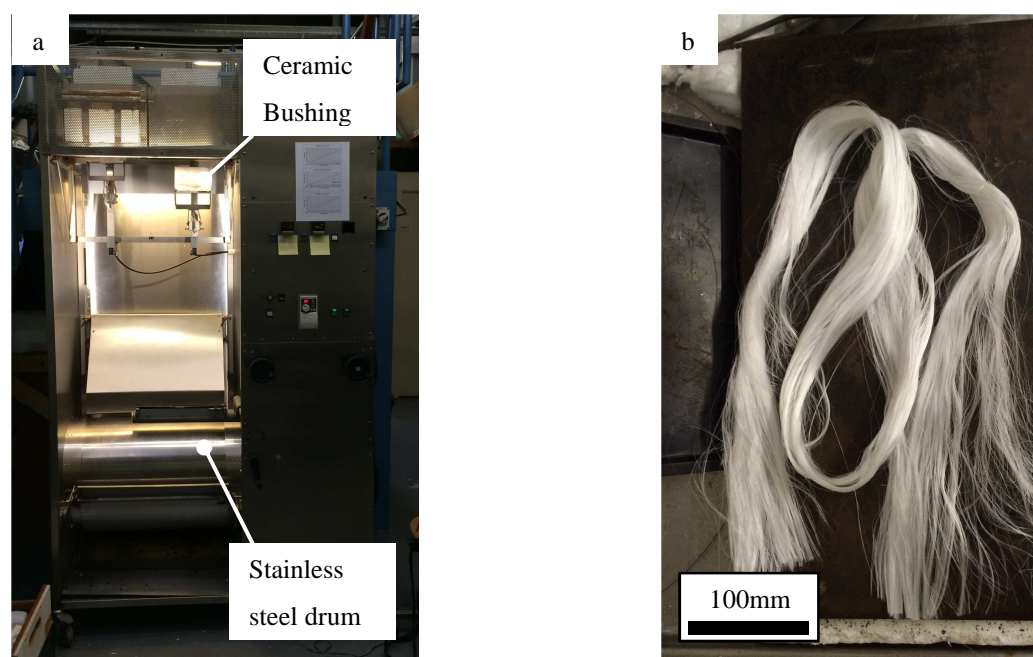


Figure 6.2.1. Images of a) Gravity fed melt spinning fibre manufacturing plant with ceramic bushing and stainless steel drum labelled and b) Image of CorGlaes[®] Pure 107 fibres [scale bar = 100mm].

For glass fibre production, $\approx 350\text{g}$ of CorGlaes[®] Pure 107 cullet fragments were heated to 1000°C at $1^{\circ}\text{C min}^{-1}$ and maintained at this state for 4 hours to produce a homogenous glass melt. The molten glass was then transferred to a clay bushing containing an array of $\text{Ø}2\text{mm}$ holes ($n = 50$) that was preheated to $680\text{-}690^{\circ}\text{C}$ in order to achieve the desired glass melt viscosity for fibre manufacturing (section 3.4.7.2). Under gravity, glass droplets travelled down through the bushing orifices and were subsequently drawn/collected around the drum (rotating at 250 rpm). Prior to fibre manufacturing, the drum was coated with a Knittol[®] lubricant (Selco, India) to preserve the integrity of the manufactured fibres (by

reducing fibre-to-fibre abrasion) and protect them from environmental moisture^[317]. Fibre production continued until the feed melt was depleted with the aligned CorGlaes[®] Pure 107 fibres removed from the static drum by cutting parallel with the drums long axis. The fibres (Figure 6.2.1) were then placed in PE bags and stored inside a desiccator without any annealing stages. Prior to all experimental work the CorGlaes[®] Pure 107 fibres were washed in Chloroform (VWR, USA) for 10 minutes in order to remove the Knittol[®] lubricant and dried inside a fume cabinet for 15 minutes at ambient temperature.

6.2.2 XRD and DSC

XRD was conducted on crushed CorGlaes[®] Pure 107 fibres according to the procedure described in section 5.2.2. Fibres were crushed using a pestle and mortar with XRD intended to assess the degree of crystallisation present in the manufactured fibres. DSC was performed on ≈ 10 mm length CorGlaes[®] Pure 107 fibres as described in section 5.2.4.

6.2.3 Raman Spectroscopy

Raman spectroscopy was performed on CorGlaes[®] Pure 107 fibres using a LabRAM HR (Horiba Jobin Yvon, France) with a Ventus 532 laser (Ventus, USA) over a $1400\text{-}100\text{cm}^{-1}$ wavenumber range. Spectra from the ≈ 20 mm length fibre samples were collected in triplicate ($n = 3$) from a 532.17nm laser line with a 10% OD objective and 600 grating over a 10 second accumulation period. Raman spectroscopy was performed at the School of Chemistry, University of Glasgow.

6.2.4 Fibre Diameter

The diameter of CorGlaes[®] Pure 107 fibres (under the current manufacturing conditions) was determined from an isolated tow of 20mm length fibres using a Sigma VP SEM (Carl Zeiss, Germany) according to Method C of BS ISO 11567:1995. Samples were prepared by backing the fibres onto card using aluminium tape before sputter-coating with a thin layer of gold (Agar Scientific, UK). Cross-sectional images were captured in SE and BSE modes using a 20kV accelerating voltage and measurements recorded using the equipment's Zeiss SmartSEM software. From the diameter of 30 samples ($n = 30$) the average cross-sectional area of the fibres was then calculated^[318]. SEM was performed at the School of Geographical and Earth Sciences, University of Glasgow.

6.2.5 Tensile Testing

Tensile testing of CorGlaes[®] Pure 107 fibres was conducted following ISO 11566:1996 using a Zwick/Roell Z2.0 (Zwick Roell, USA) tensile test machine with a 5N load cell operating at a crosshead speed of 1 mm min^{-1} [319]. Tensile test specimens were prepared by creating mounting frames with a 25mm gauge length from stationary card to the dimensions specified in BS ISO 11566:1996 (Figure 6.2.2). Individual fibres were isolated from an aligned fibre tow and fixed to the mounting frames using an epoxy adhesive (Loctite, Germany). Frames were then secured using grips to the testing equipment before the sidewalls of the frame were cut in order to isolate the fibre. Force-displacement data was then collected for 50 fibre samples ($n = 50$) using Zwick/Roell TestXpert[®] software [319].

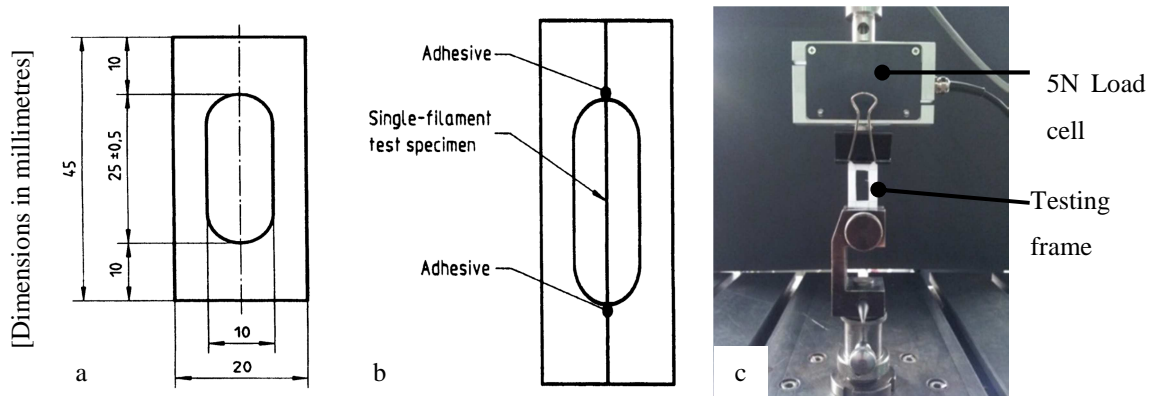


Figure 6.2.2. Illustration of sample housing frames employed in tensile testing of CorGlaes[®] Pure 107 fibres showing a) Housing frame dimensions b) Fixation of sample specimens [Reproduced from BS ISO 11566:1996] and c) Image of testing configuration showing a card housing prior to cutting of the support frame.

To account for influences from the load train and gripping system of the tensile testing set up, a correction coefficient (also known as the system compliance factor) was determined by tensile testing CorGlaes[®] Pure 107 fibres at 10mm, 20mm and 30mm specimen gauge lengths. Five samples ($n = 5$) were tested at each gauge length under identical testing conditions as those specified by BS ISO 11566:1996 and the force-displacement plots used to calculate the $\Delta L/\Delta F$ ratio (mm N^{-1}) for each gauge length. The system compliance factor (k) was then determined from plots of $\Delta L/\Delta F$ against the fibre gauge length using a linear regression of an applied trendline back to the ordinate value (i.e. zero gauge length) [319].

To calculate the tensile strength and tensile modulus of the CorGlaes[®] Pure 107 fibres the recorded force-displacement and dimensional data was applied to Eqn 6.2.1 and Eqn 6.2.2 respectively following Method B of ISO 11566:1996 [319].

$$\sigma_f = \frac{F_f}{A_f}$$

Eqn 6.2.1

where σ_f = fibre tensile strength (MPa), F_f = fibre maximum tensile force (N), A_f = fibre cross-sectional area (mm²)

$$E_f = \frac{\left(\frac{\Delta F_B}{A_f}\right) \left(\frac{L_f}{\Delta L_B}\right)}{1 - k \left(\frac{\Delta F_B}{\Delta L_B}\right)}$$

Eqn 6.2.2

where E_f = fibre tensile modulus (GPa), L_f = gauge length (mm), ΔF_B = difference in force corresponding to the selected strain limits (N), ΔL_B = difference in cross-head displacement corresponding to the selected strain limits (mm), k = system compliance (mm N⁻¹).

Note: An averaged value of the cross-sectional area was used in Eqn 6.2.1 and Eqn 6.2.2 from the dimensional data obtained in section 6.2.4 with the selection of strain limits based on the nominal strain at failure (ϵ_f) of the tested samples.

6.2.5.1 Weibull Analysis

The strength of a glass or brittle ceramic material is generally dependent upon its fracture toughness (K_{IC}) and critical flaw size (a). Thus the determination of a glass's mechanical performance requires knowledge of the flaw population that must be evaluated statistically. Weibull distribution statistics has commonly been used to characterise the statistical variation in fracture strength of a brittle material and is based on the 'weakest link theory' where the most significant flaw will control the overall strength of a material. However this critical flaw may not necessary be the largest and is also reliant on its specific location and orientation [218, 269, 320].

To account for the flaw size distribution present in the CorGlaes[®] Pure 107 glass fibres a determination of the flaw population throughout the experimental sample set was required. The Weibull distribution of statistical analysis was subsequently used to examine the scatter of flaw size distributions and fracture strengths through calculating the Weibull modulus (m). For analysis, the tensile testing data was sorted by increasing tensile strength and a Weibull distribution plot was constructed for the CorGlaes[®] Pure 107 fibres using Eqn 6.2.3 and Eqn 6.2.4 [269, 320].

$$P_F = \frac{(i-0.5)}{N}$$

Eqn 6.2.3

where P_F = probability of failure, $i = i^{\text{th}}$ tensile strength value, N = total number of specimens tested.

$$\ln\left(\ln\left(\frac{1}{1-P_F}\right)\right) = m(\ln \sigma) - m(\ln \sigma_0)$$

Eqn 6.2.4

where σ = Tensile strength (MPa), m = Weibull modulus, σ_0 = Normalising stress - considered by Ahmed et al. (2008) as the “stress at which 63.2% of the tested fibres had failed” or “the most probable strength expected from a fibre of gauge length L_0 ” by Hull & Clyne (1996) [120, 218].

6.2.5.2 Fibre Fracture Analysis

Given that the tensile strength of glass fibres are highly dependent upon their surface quality, the influence of surface flaw type and relative depth was also determined in relation to the experimentally measured tensile strengths of the CorGlaes[®] Pure 107 fibres. This was evaluated for the presence of either a straight edge or semi-circular surface flaw using Eqn 6.2.5 [317].

$$\sigma_f = \frac{1}{Y(c_{flaw}, R)} K_{IC} (\pi c_{flaw})^{-1/2}$$

Eqn 6.2.5

where c_{flaw} = flaw depth (nm), K_{IC} = fracture toughness (MPa m^{1/2}), $Y(c_{flaw}, R)$ = crack geometry constant dependant on flaw depth (c_{flaw}) and fibre radius (R) : 0.6366 for semi-circular flaws and 1.1260 for straight edge flaws ^[317].

Note: For Eqn 6.2.5, the fracture toughness previously determined in section 5.3.6 was applied (0.48 MPa m^{1/2}).

6.2.6 Silane Treated CorGlaes[®] Pure 107 Fibres

Surface modification of the CorGlaes[®] Pure 107 fibres was performed using a 10 wt.% concentration of a 3-aminopropyl-triethoxy (APS) sizing agent following the protocol originally outlined by Khan et al. (2011). These steps are summarised in Table 6.2.1 for treating a 1.5g batch of CorGlaes[®] Pure 107 fibres ^[228].

Table 6.2.1. Procedure for the silane treatment of fibres as described by Khan et al. (2011).

| Step | Activity |
|------|--|
| 1 | 90ml of ethanol (VWR, USA) was diluted with 10ml of distilled water to create a 90 vol% ethanol solution. |
| 2 | 9.6ml of 3-aminopropyl-triethoxy (Sigma-Aldrich, USA) was added to 100ml of the ethanol solution to create a 10 wt.% APS solution. |
| 3 | A 1.5g batch of fibres was immersed in 100ml of the 10 wt.% APS solution for 15 minutes inside a laminar fume hood. |
| 4 | Fibres were removed and washed in 50ml of ethanol under vacuum filtration with grade three filter paper (Whatman, UK) used in conjunction with a Büchner funnel. |
| 5 | Fibres were then placed in an air circulated oven for 24 hours at 120°C to cure the sizing agent. |

6.2.7 Fibre Dissolution Rate

The weight loss and media pH during the dissolution of the CorGlaes[®] Pure 107 fibres was determined in triplicate ($n = 3$) for each dissolution period over 24, 48, 72, 96 and 168 hours of immersion. This was performed using distilled water (DW), phosphate buffered saline (PBS), Dulbecco's Modified Eagle's Medium (DMEM), and corrected simulated body fluid (c-SBF) immersion media along with a set of APS treated CorGlaes[®] Pure 107 fibres in distilled water. The PBS was produced by dissolving a sachet of PBS (P5368-10PAK, Sigma-Aldrich, USA) into one litre of distilled water whilst the c-SBF was prepared as described in section 5.2.9.1. Bacterial growth in the DMEM was inhibited by the addition of sodium azide (Sigma-Aldrich, USA) to the DMEM at a concentration of 0.1 vol% prior to fibre immersion. The initial ionic concentrations of the c-SBF, DMEM and PBS are listed in Table 6.2.2 with the ionic conductivity of each media prior to sample dissolution measured using a HI-8733 conductivity meter (Hanna Instruments, USA).

Table 6.2.2. Ionic concentrations of acellular DMEM cell culture media, c-SBF and PBS [Data from Kokubo et al. (2003) and Lutišanová et al. (2011)].

| Media | Ionic concentration (mM) | | | | | | | |
|-------|--------------------------|----------------|------------------|------------------|-------------------------------|-----------------|--------------------------------|-------------------------------|
| | Na ⁺ | K ⁻ | Ca ²⁺ | Mg ²⁺ | HCO ₃ ⁻ | Cl ⁻ | HPO ₄ ²⁻ | SO ₄ ²⁻ |
| c-SBF | 142.0 | 5.0 | 2.5 | 1.5 | 4.2 | 147.8 | 1.0 | 0.5 |
| DMEM | 154.6 | 5.37 | 1.82 | 0.8 | 44.0 | 120.5 | 1.0 | 0.8 |
| PBS | 350 | 5.19 | - | - | - | 233 | 10 | - |

A dissolution sample consisted of a 200mg batch of 20mm length fibres that were stored inside a sealed 10ml glass vial giving a $14.4 \text{ cm}^2 \text{ ml}^{-1}$ surface area-to-volume ratio (SA:V). Each sample was stored in an individual glass vial and placed within a 37°C incubator unit with the sample weights recorded periodically using a $\pm 0.1 \text{ mg}$ Pioneer[™] analytical scale (Ohaus, USA). This was performed in tandem with measurements of the dissolution media pH using a HI 221 pH Meter (Hanna Instruments, USA). At each dissolution period, the immersion media was decanted and samples dried using an air circulated oven at 60°C for 4 hours. The dry weight loss was then determined by Eqn 6.2.6. and was plotted against the immersion period (hours) along with the solution pH. The media was not changed at any point with the exception of the DMEM that was replaced after 96 hours in order to mimic the protocols used during *in vitro* cell culture studies. ^[206].

$$\text{Percentage Weight Loss} = \frac{w_o - w_t}{w_o} * 100$$

Eqn 6.2.6

where w_o = initial sample weight (mg) and w_t = sample weight at time point t_x (mg)

The dissolution rate of the fibres normalised to the total theoretical surface area of each sample batch was determined using Eqn 6.2.7 from the weight loss measurements after 24 hours of dissolution. To calculate the total surface area in a 200mg fibre batch, each fibre was assumed to be of uniform length (20mm) and identical diameter (20.85 μ m) in order to calculate the surface area of a single pristine fibre. The total number of fibres per 200mg batch and the subsequent total surface area (cm²) was then calculated from the theoretical weight of single 20mm length, Ø20.85 μ m fibre ^[201, 207].

$$\text{Fibre dissolution rate} = \frac{\frac{w_o - w_t}{A}}{t}$$

Eqn 6.2.7

where A = sample surface area (cm²), t = time (i.e. immersion period – hours).

6.2.8 Fibre Bioactivity

The bioactivity of CorGlaes[®] Pure 107 fibres was assessed by individually immersing 26mg batches of 20mm length fibres in c-SBF at 1 cm² ml⁻¹ SA:V ratio inside polystyrene universal tubes and stored at 37°C within an incubator unit with the c-SBF prepared according to the method described in section 5.2.9.1. The media was not changed over the immersion period and samples were examined in triplicate ($n = 3$) for each incubation period of 0.5, 1, 3, 6, 12, 24, 48, 168 and 336 hours (2 weeks) before being extracted and rinsed in acetone (VWR, USA). Extracted fibres were then dried at 60°C inside an air circulated oven for 3 hours before being stored within a desiccator for further analysis. The c-SBF pH was also measured at each extraction point using a HI 221 pH Meter (Hanna Instruments, USA) with the bioactivity of the fibres characterised following the procedure outlined by the flow chart shown in Figure 5.2.2.

6.3 Results

6.3.1 XRD

The XRD profile of the CorGlaes[®] Pure 107 fibres is presented in Figure 6.3.1 and showed no clearly defined crystallisation peaks but a broad halo centred at $2\theta \approx 23^\circ$.

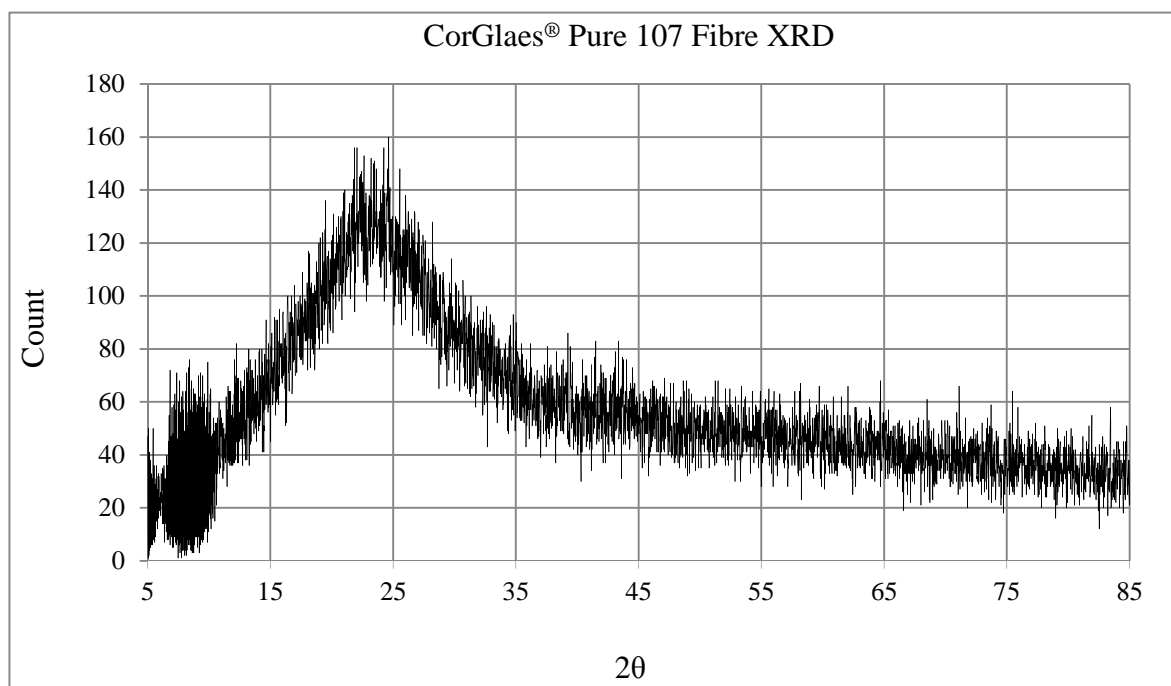


Figure 6.3.1. XRD profile of CorGlaes[®] Pure 107 fibres showing the amorphous structure of the fibres produced under the operating conditions specified in section 6.2.1.

6.3.2 DSC

The thermogram obtained from the DSC of CorGlaes[®] Pure 107 fibres over the predetermined thermal program is shown in Figure 6.3.2. Magnified sections of the thermogram highlighting the glass transition (T_g), crystallisation onset (T_{oc}) as well as the crystallisation peak (T_p) and liquidus temperature (T_{lq}) are shown in Figure 6.3.3, Figure 6.3.4 and Figure 6.3.5 respectively. These were determined from the intersection of tangents overlaid across the endo- or exothermic events and are listed in Table 6.3.1 alongside the PW that was calculated using Eqn 5.2.1.

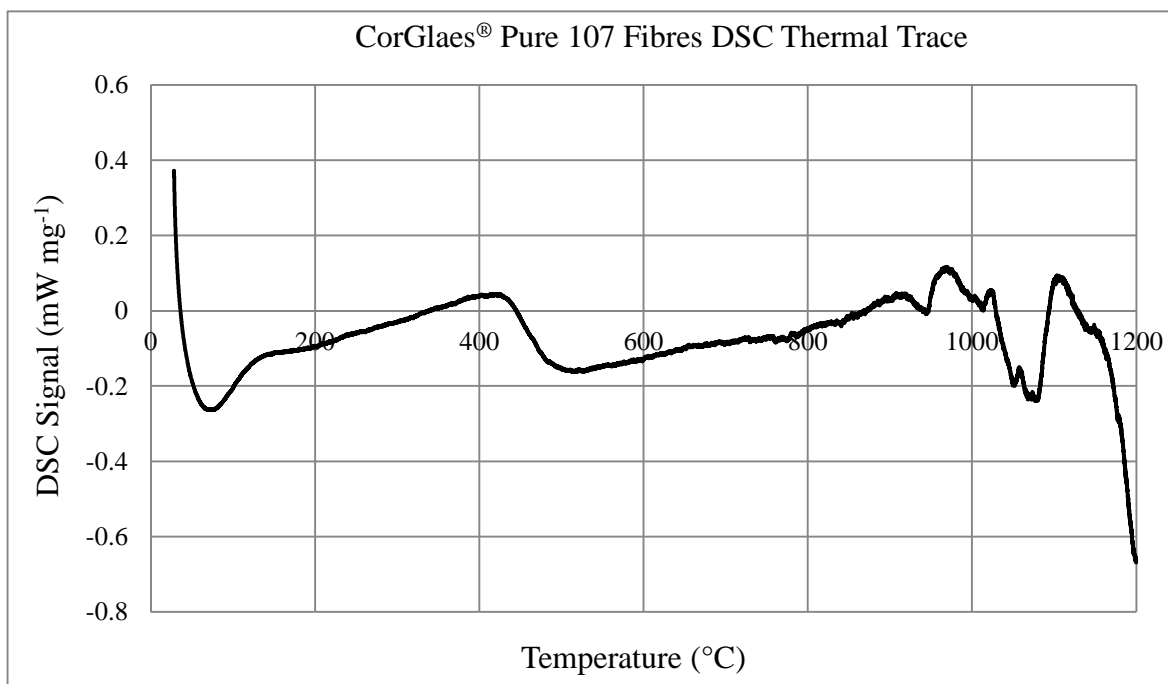


Figure 6.3.2. DSC thermogram of CorGlaes® Pure 107 fibres over a thermal cycle from 25°C to 1200°C.

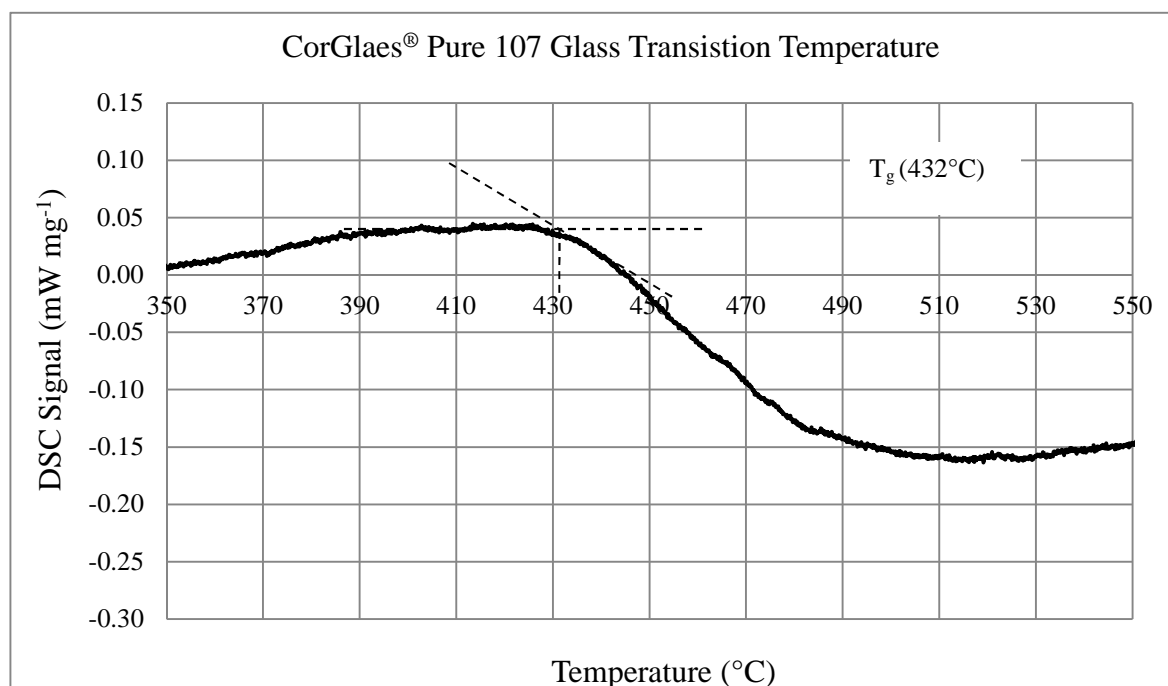


Figure 6.3.3. DSC thermogram of CorGlaes® Pure 107 fibres with the glass transition temperature identified as 432°C from the tangent intersection (Magnified section from Figure 6.3.2).

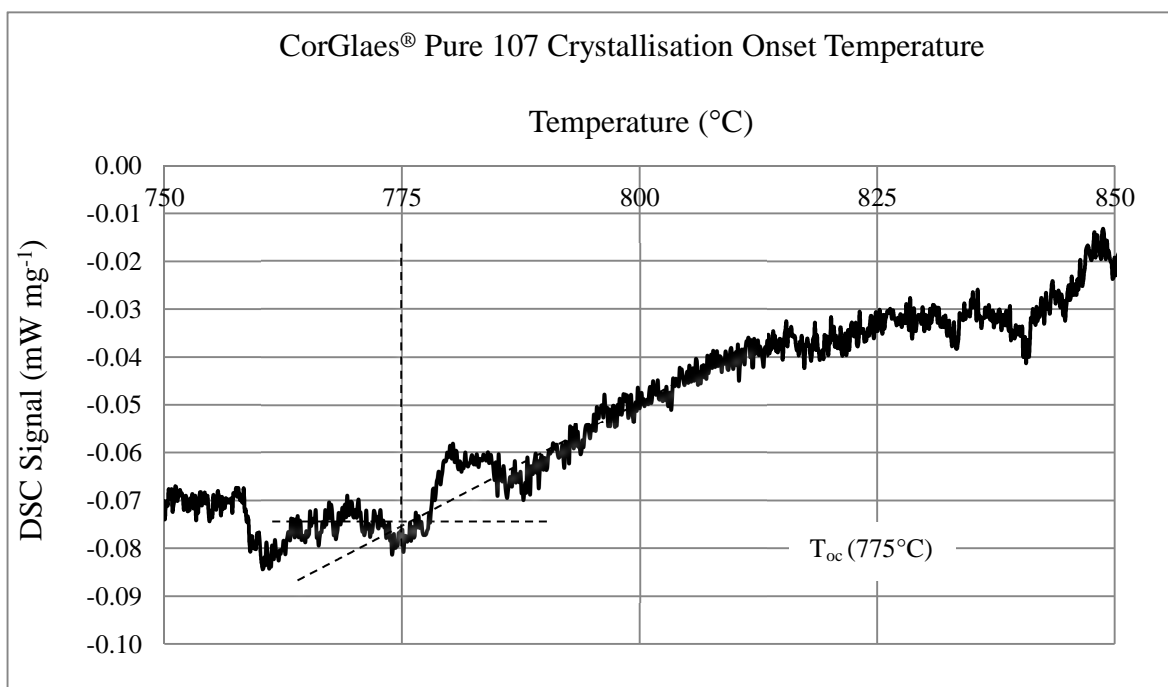


Figure 6.3.4. Crystallisation onset temperature of CorGlaes® Pure 107 fibres identified from the intersection of lines on the DSC thermogram (magnified section of Figure 6.3.2).

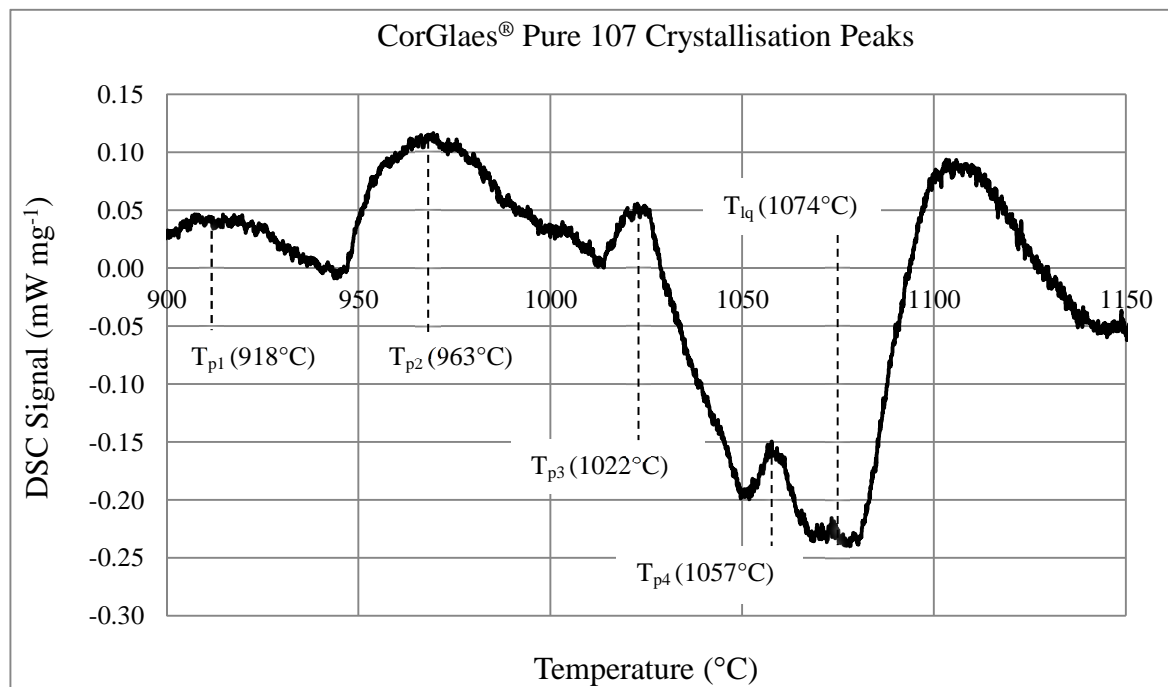


Figure 6.3.5. DSC thermogram of CorGlaes® Pure 107 fibres showing multiple crystallisation peaks and its liquidus temperature (magnified section of Figure 6.3.2).

Table 6.3.1. Thermal properties of CorGlaes[®] Pure 107 fibres.

| Thermal property | Temperature (°C) |
|--|------------------|
| Glass transition temperature (T_g) | 432 |
| Crystallisation onset temperature (T_{oc}) | 775 |
| Processing window (°C) | 343 |
| Crystallisation peak ¹ (T_{p1}) | 918 |
| Crystallisation peak ² (T_{p2}) | 963 |
| Crystallisation peak ³ (T_{p3}) | 1022 |
| Crystallisation peak ⁴ (T_{p4}) | 1057 |
| Liquidus temperature (T_{lq}) | 1074 |

6.3.3 Raman Spectroscopy

The Raman spectrum obtained from the CorGlaes[®] Pure 107 fibres is shown below in Figure 6.3.6 with the assignment of the spectral features to the associated phosphate structures listed in Table 6.3.2.

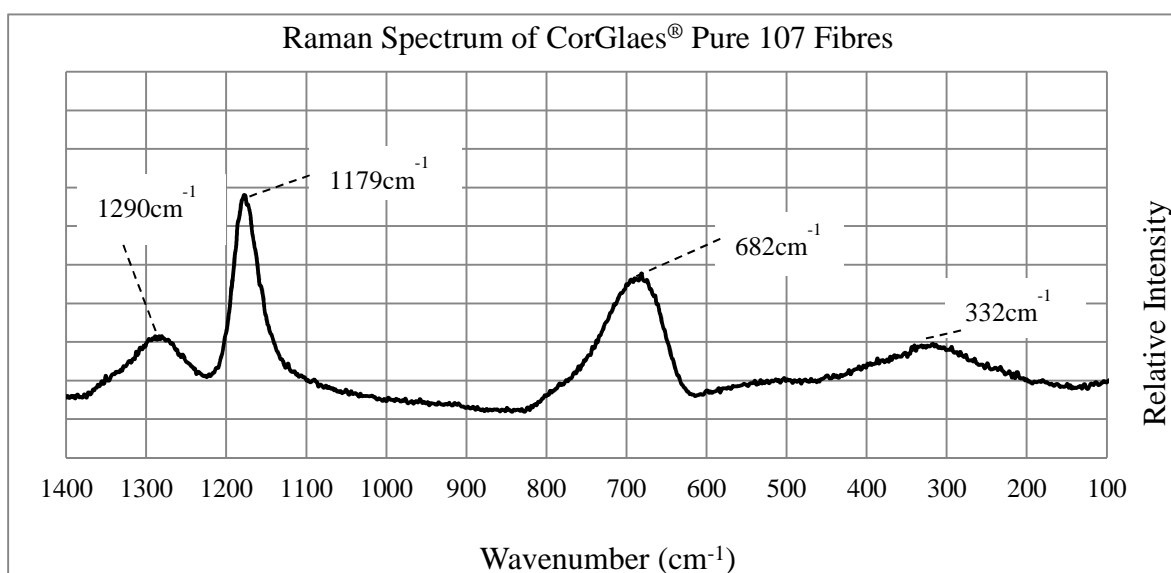


Figure 6.3.6 Raman spectrum of CorGlaes[®] Pure 107 fibres over the 1400-100 cm^{-1} wavenumber range with peaks corresponding to the structural features of the CorGlaes[®] Pure 107 composition.

Table 6.3.2. Assignments of spectral features identified in the Raman spectrum of the CorGlaes[®] Pure 107 fibres to the phosphate structural features.

| Feature | Wavenumber | Assignment |
|---------|----------------------|--|
| Peak | 1290cm ⁻¹ | (PO ₂) asymmetric [ν_{as}] [158] |
| Peak | 1179cm ⁻¹ | (PO ₂) symmetric [ν_s] [158] |
| Peak | 682cm ⁻¹ | (P-O-P) symmetric [ν_s] [158] |
| Peak | 332cm ⁻¹ | (P-O-P) bending vibration mode [287] |

6.3.4 Fibre Diameter

From the thirty samples ($n = 30$) the average diameter of the CorGlaes[®] Pure 107 fibres was determined to be $20.85 \pm 3.25\mu\text{m}$ with a range of 16.07 - 27.06 μm (Figure 6.3.7). These measurements lead to an average cross-sectional area (A_f) of 349.14 μm^2 for the CorGlaes[®] Pure 107 fibres under the current fibre plant manufacturing conditions (section 6.2.1).

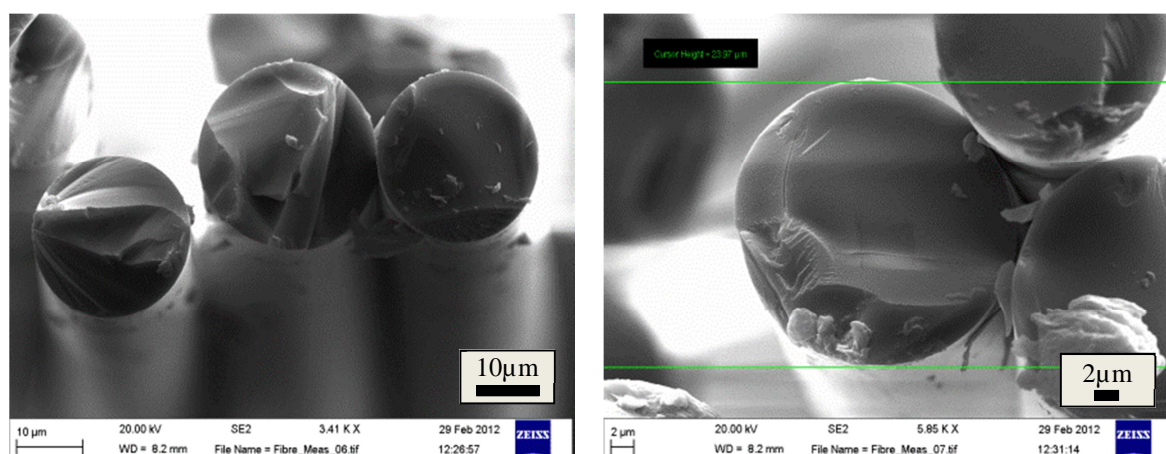


Figure 6.3.7. SEM images of CorGlaes[®] Pure 107 fibres with measurements of the diameters used to determine the average cross sectional area [scale bars = 10 μm , 2 μm].

6.3.5 Tensile Testing

A typical force-displacement and corresponding stress-strain plot for a tensile tested CorGlaes[®] Pure 107 fibre is shown in Figure 6.3.8 and from the results an average tensile strength and tensile modulus of 426 ± 143 MPa and 65.5 ± 20.8 GPa were found respectively. This was determined from the system compliance factor (k) of 0.4747 with the Weibull statistical model (Figure 6.3.9) producing a Weibull modulus (m) of 3.406 with a 525 MPa normalising stress (σ_0) (Figure 6.3.10).

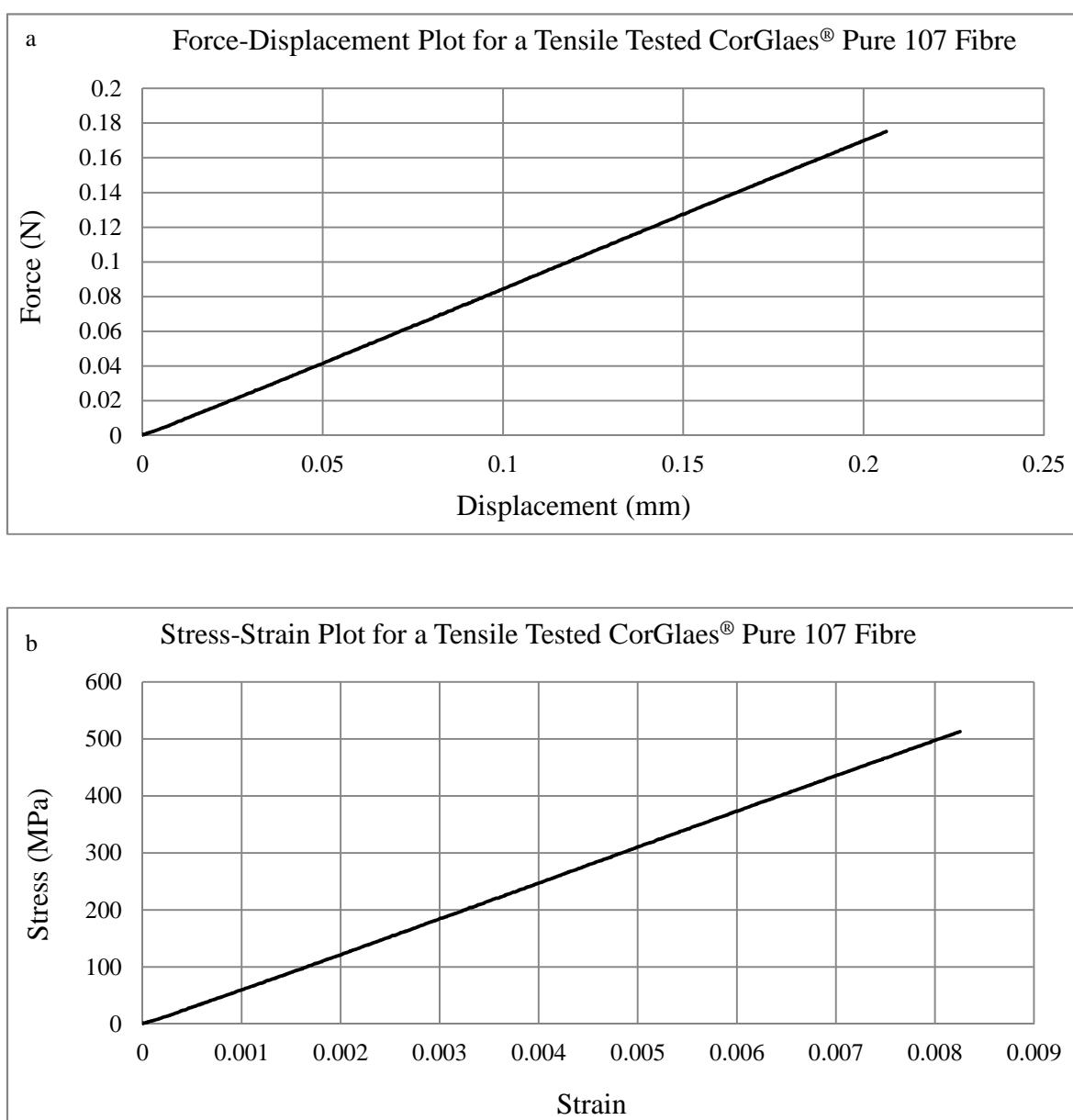


Figure 6.3.8. a) Force-displacement plot and b) Stress-strain plot of a tensile tested $\approx \text{Ø}20\mu\text{m}$ CorGlaes[®] Pure 107 fibre at a cross-head speed of 1mm s^{-1} .

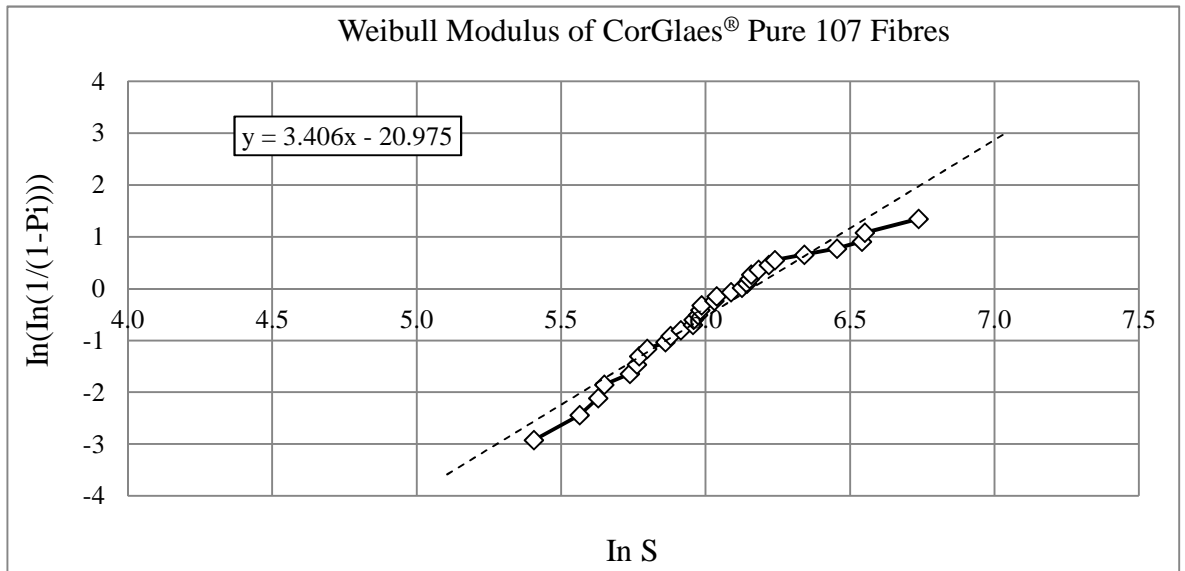


Figure 6.3.9. Determination of Weibull modulus (m) from CorGlaes® Pure 107 fibre tensile test data based on the gradient of the plotted trendline.

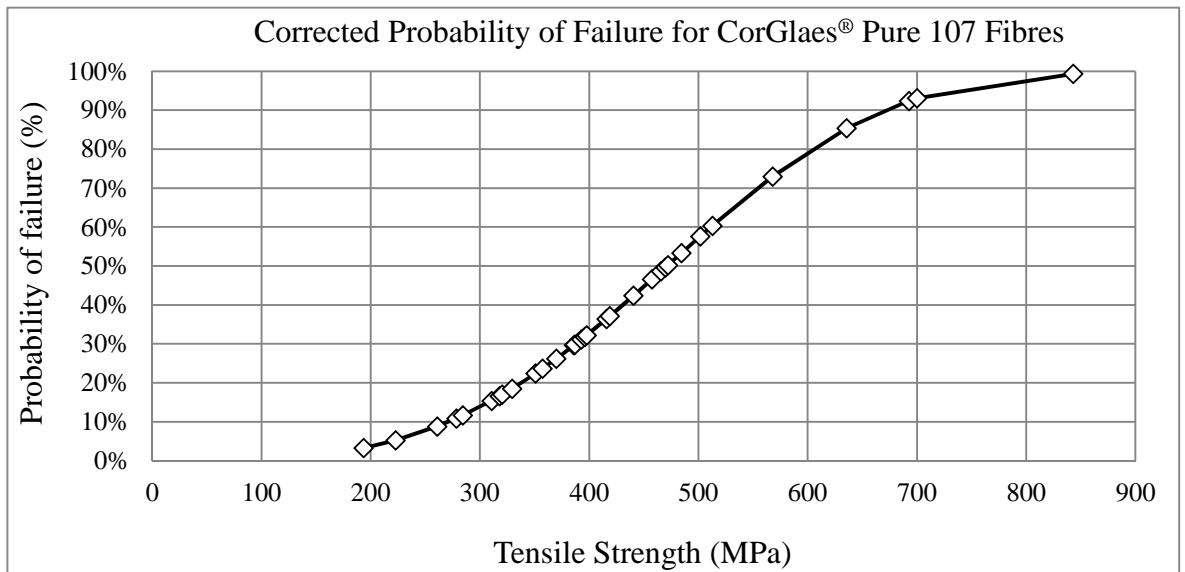


Figure 6.3.10. Corrected probability of failure based on the Weibull statistical analysis of the CorGlaes® Pure 107 fibre tensile test data.

The variation in CorGlaes® Pure 107 fibre tensile strength based on the presence of a semi-circular or straight cut surface flaw is shown in Figure 6.3.11 using the tensile test data from the fibres and the fracture toughness previously determined from the CorGlaes® Pure 107 disks (section 5.3.6).

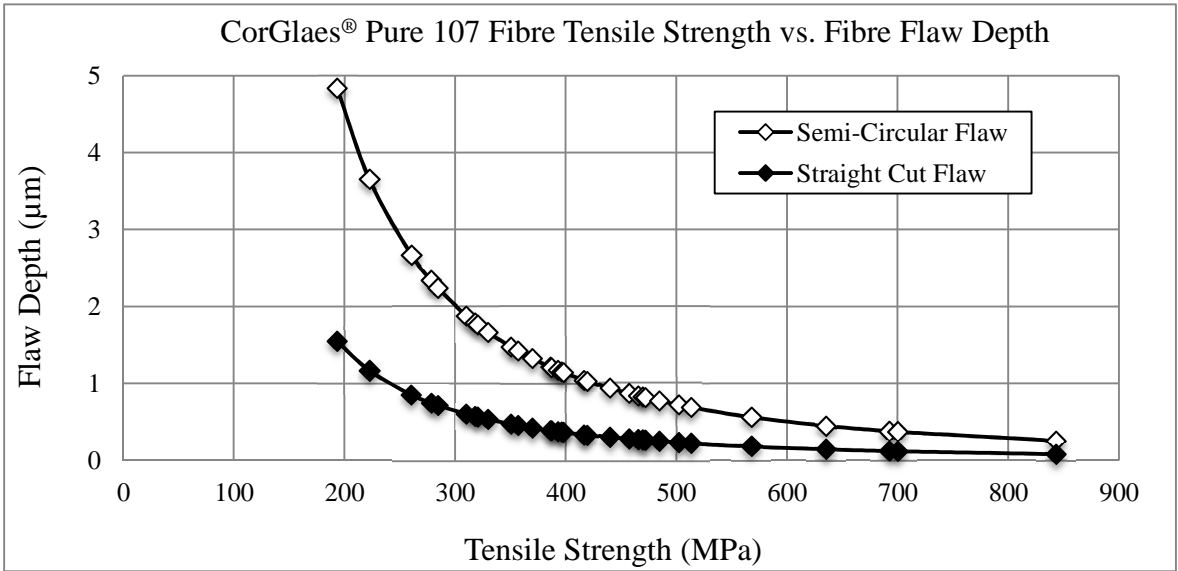


Figure 6.3.11. Variation in experimental CorGlaes® Pure 107 tensile strength with theoretically determined surface flaw type and depth.

6.3.6 Dissolution Rate

The dry weight loss and corresponding media pH over 24, 48, 72, 96 and 168 hours of CorGlaes[®] Pure 107 fibre dissolution is shown in Figure 6.3.12. The resulting dissolution rate of the CorGlaes[®] Pure 107 fibres over the first 24 hours of immersion with respect to the initial ionic conductivity of each immersion media is shown in Figure 6.3.13.

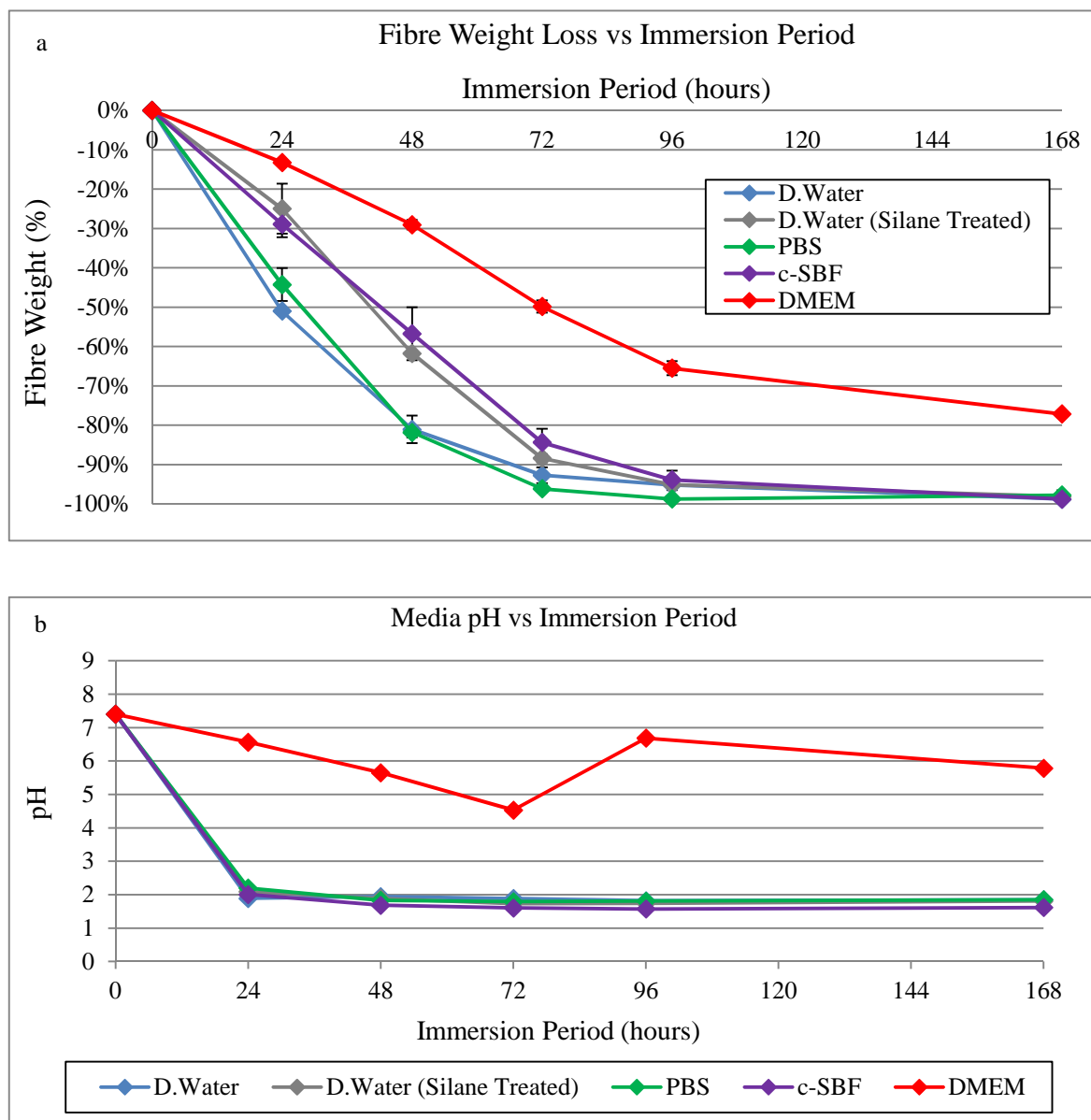


Figure 6.3.12. Comparison of CorGlaes[®] Pure 107 fibre dissolution up to 168 hours in various immersion media showing a) Dry weight loss over time and b) Media pH throughout the immersion period with the replacement of DMEM at 96 hours of immersion (standard deviation $\leq \pm 0.07$).

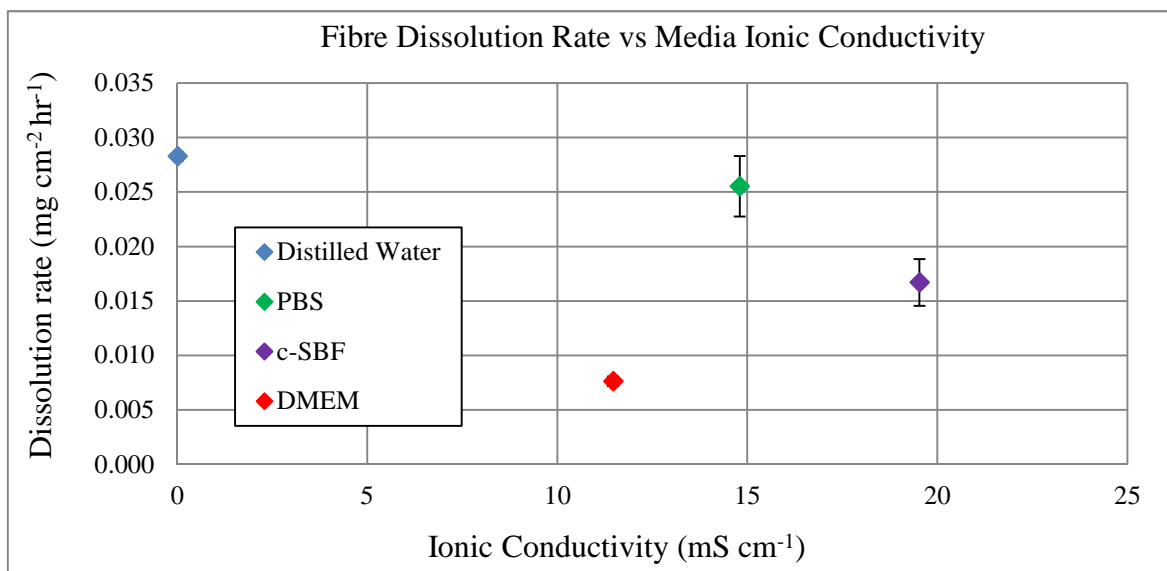


Figure 6.3.13. Comparison of CorGlaes[®] Pure 107 fibre dissolution rate against the initial ionic conductivity of the immersion media after 24 hours of immersion.

6.3.7 Fibre Bioactivity

The pH of the c-SBF during CorGlaes[®] Pure 107 fibre bioactivity testing is shown in Figure 6.3.14. The characterisation of fibre samples across the 336 hours was assessed by FTIR (Figure 6.3.15) and Raman (Figure 6.3.16) with the corresponding SEM images of the fibres shown in Figure 6.3.17 and Figure 6.3.18.

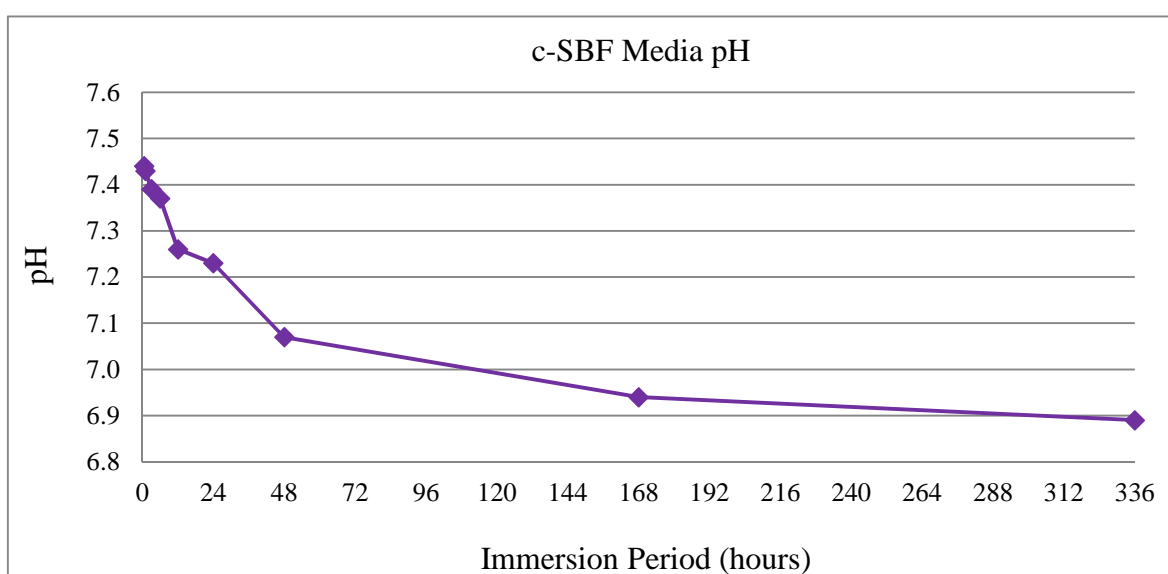


Figure 6.3.14. Media pH of c-SBF during bioactivity testing of CorGlaes[®] Pure 107 fibres over 336 hours of immersion showing the decrease in pH with prolonged immersion (standard deviation <math>< \pm 0.02</math>).

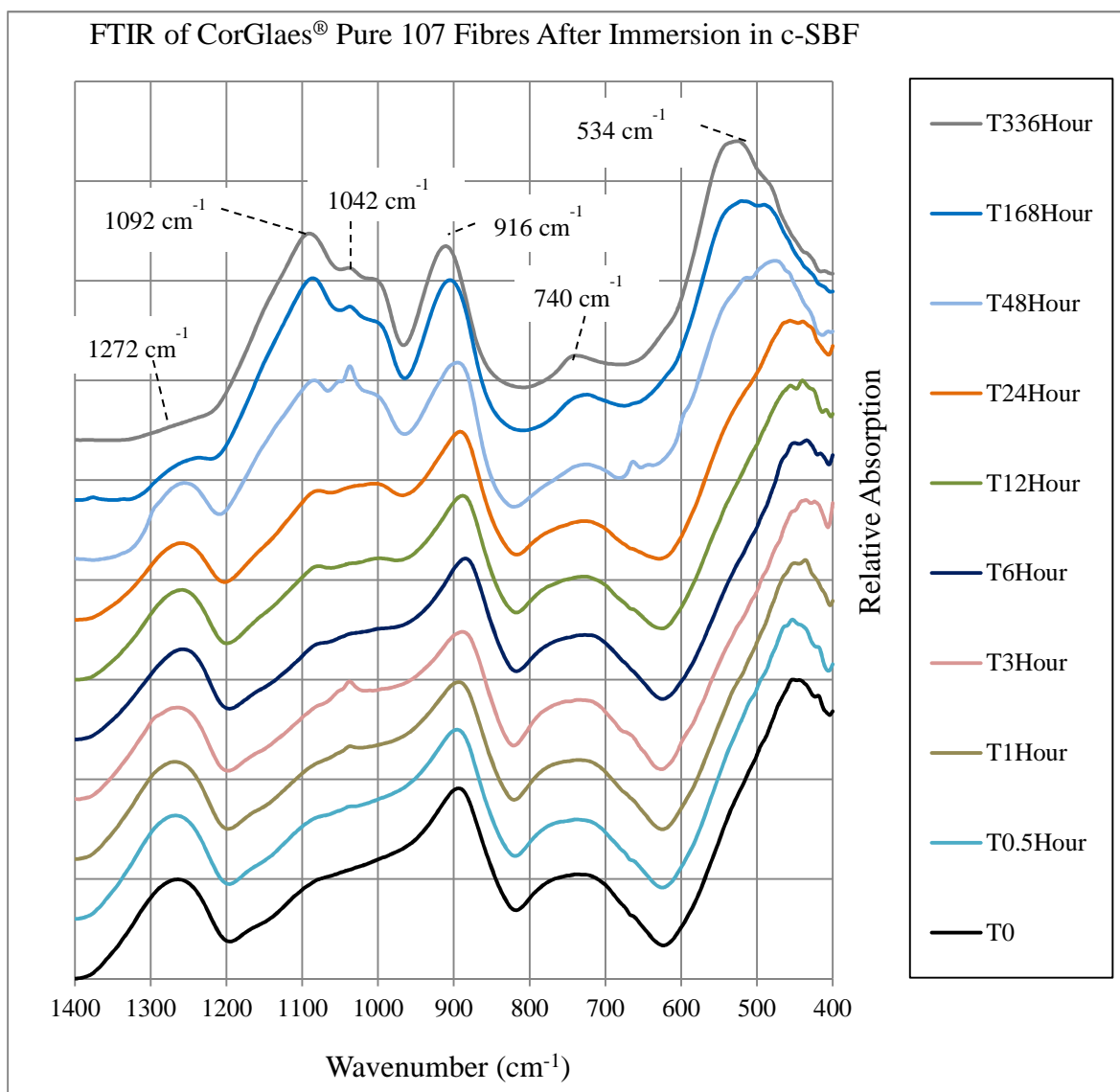


Figure 6.3.15. FTIR spectra of CorGlaes® Pure 107 fibres after immersion in c-SBF for up to 336 hours (2 weeks) with the formation and suppression of broad peaks over the immersion period labelled accordingly.

Immersion of CorGlaes® Pure 107 fibres in c-SBF showed changes from the initial $[T_0]$ FTIR and Raman spectra over the 336 hour (2 week) immersion period with a whitish precipitate gradually forming on the fibres and at the bottom of the vials. This appeared to indicate the precipitation of compounds out of solution due to the supersaturated conditions of the media and the ions released during glass fibre dissolution (Clement et al. 1999). The handling of fibres also became increasingly difficult after immersion periods greater than 48 hours due to their increased brittleness ^[273].

FTIR analysis of the fibres (Figure 6.3.15) showed a shift in the broad absorption peaks initially centred at 893cm^{-1} and $\approx 448\text{cm}^{-1}$ [T_0] to 916cm^{-1} and 534cm^{-1} respectively [$T_{336\text{Hour}}$] while a new broad peak spanning across 1200cm^{-1} to 1000cm^{-1} was also formed. This was coupled with the semi-suppression and complete suppression of the peaks at 1268cm^{-1} and 737cm^{-1} respectively [$T_{336\text{Hour}}$]. A shift in the Raman spectra was also observed but adequate results could only be collected from fibres after 336 hours of immersion due to fluorescence effects that produced poor signal-to-noise ratios. The Raman spectra (Figure 6.3.16) of samples after 336 hours of immersion showed the suppression of previous [T_0] peaks and the formation of broad peaks centred at 1042cm^{-1} , 957cm^{-1} , 750cm^{-1} and 356cm^{-1} . SEM analysis of the fibres revealed the simultaneous appearance of cracking and precipitate formation on the fibre surfaces as well as a change in the fibre morphology (Figure 6.3.17). This appeared to follow a transition from a smooth pristine surface [T_0] to one which showed surface cracking and peeling [$T_{6\text{Hour}}$ - $T_{48\text{Hour}}$] that eventually returned to a pristine surface with precipitate deposited across it. The immersion of fibres in c-SBF also saw a decrease in its pH from the 7.4 to ≈ 6.9 after 336 hours of immersion.

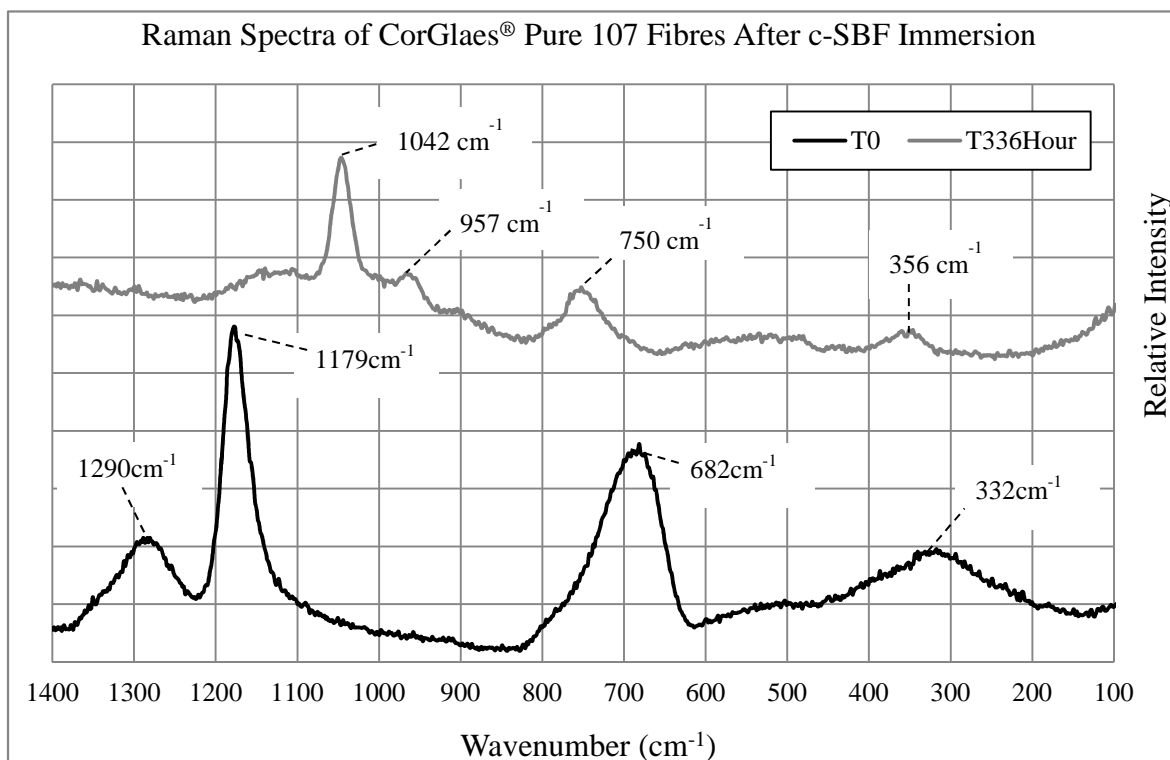


Figure 6.3.16. Comparison of Raman spectra obtained from CorGlaes® Pure 107 fibres prior to bioactivity testing [T_0] and after 336 hours of immersion [$T_{336\text{Hour}}$] in c-SBF at 37°C with the peaks labelled.

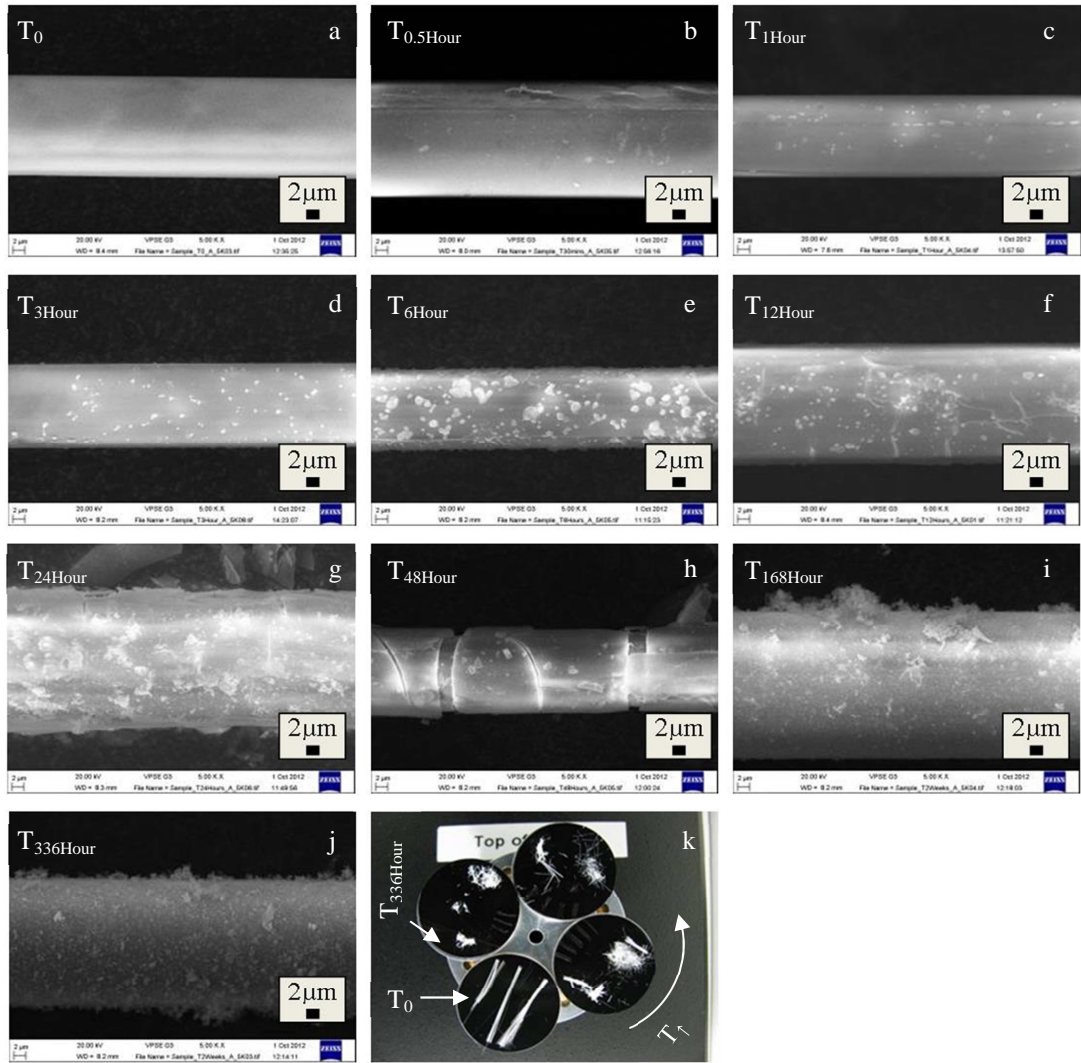


Figure 6.3.17. SEM Images of CorGlaes[®] Pure 107 fibres prior to bioactivity testing [T_0] and after immersion in c-SBF at various points over a 336 hour period showing the changes across the fibre surface at a) T_0 b) 0.5 c) 1 d) 3 e) 6 f) 12 g) 24 h) 48 i) 168 j) 336 hours of immersion [scale bar = $2\mu\text{m}$] and k) Image of CorGlaes[®] Pure 107 fibres on 25mm SEM mounting stubs after each immersion period in c-SBF prior to SEM imaging (moving counter-clockwise from T_0 as indicated) showing the decreasing amount of retrievable fibre with increasing immersion time from $T_0 \rightarrow T_{336\text{Hour}}$.

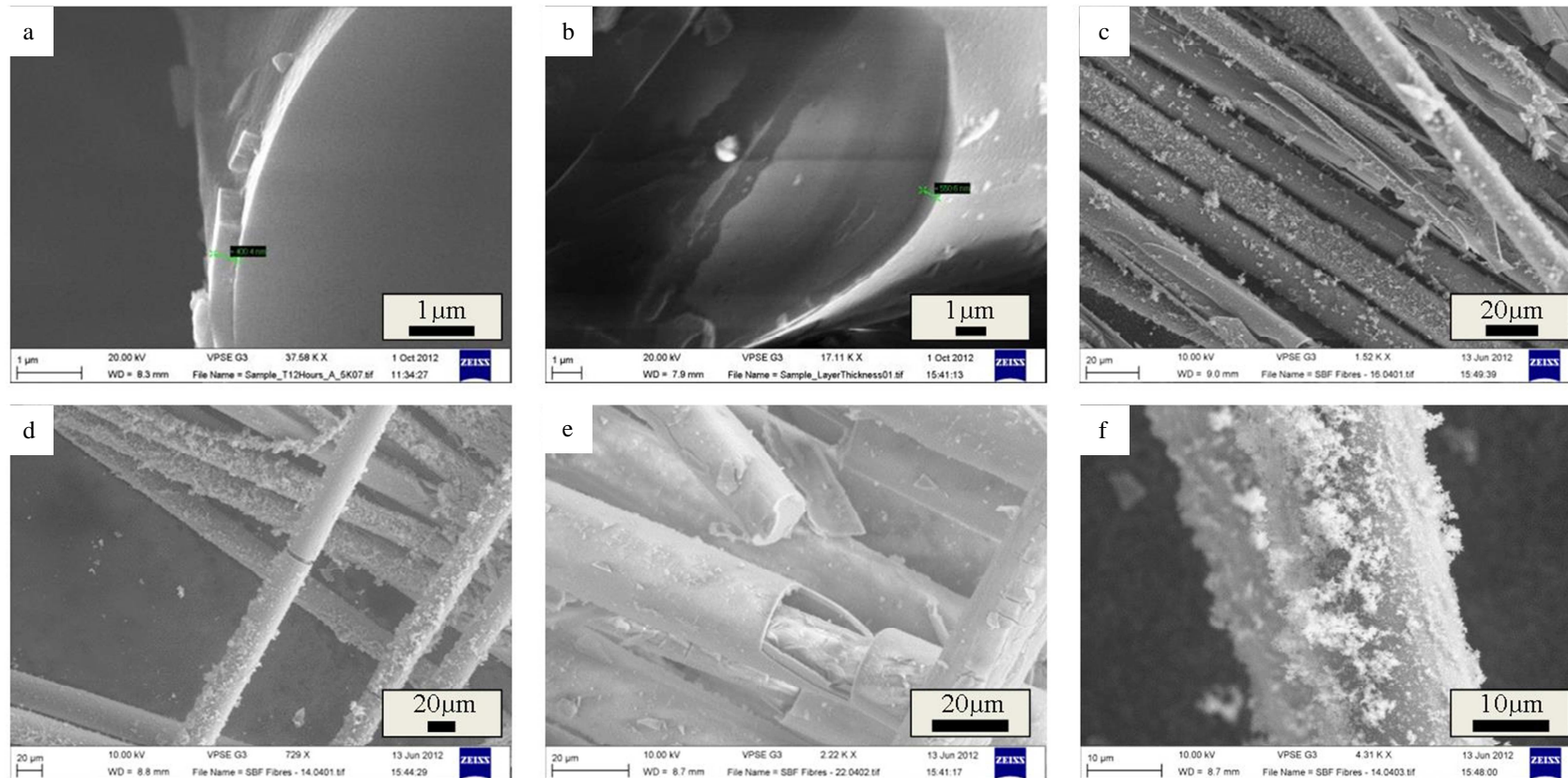


Figure 6.3.18. SEM images of CorGlaes® Pure 107 fibres after immersion in c-SBF a-b) Fibre cross-section showing an outer surface layer of 400.4 nm and 550.6nm thickness respectively after 12 hours of immersion [scale bar = 1μm] c-e) Surface precipitation and cracking on fibres after 168 hours of immersion [scale bar = 20μm] and f) Surface deposition onto fibres after 336 hours of immersion [scale bar = 10μm].

6.4 Discussion

The XRD profile of the CorGlaes[®] Pure 107 fibres confirmed their amorphous structure and long-range disorder as found in various other glass fibre compositions such as those investigated by Haque et al. (2013). This verified that no crystallisation had occurred during fibre manufacturing and that the glass feed temperatures (680-690°C) were suitable for fibre production. The absence of any crystallisation peaks also verified the general accuracy of the large processing window (PW) previously identified from the DSC thermogram of <3mm CorGlaes[®] Pure 107 fragments (section 5.3.3) [209].

A comparison between the DSC results of the $\approx\text{Ø}20\mu\text{m}$ CorGlaes[®] Pure 107 fibres and <3mm fragment samples (section 5.3.3) showed a clear difference in the two thermograms which was attributed to the improved operating conditions during sample testing. However the improved clarity in the thermal events could also be attributed to size effects between the tested samples. The nearly identical values for the glass transition (T_g) and crystallisation onset temperatures (T_{oc}) correlated well with those found from the monolith fragments with the fibre PW (343°C) closely matching that previously determined (348°C). The slight discrepancy in PW could be accounted for by user error in the data interpretation or size effects between samples due to the increased time required for the larger <3mm fragments to reach the furnace temperature. The improved clarity of the thermogram obtained from the CorGlaes[®] Pure 107 fibres also allowed the glass crystallisation peak temperatures as well as the glass liquidus temperature to be found [290].

The DSC thermogram shown in Figure 6.3.5 also identified the presence of multiple crystallisation peaks (T_{p1} , T_{p2} , T_{p3} , T_{p4}) in the DSC thermogram that were considered to represent the occurrence of surface and bulk crystallisation events as well the possibility of different crystalline phases. This was based on studies by Reynoso et al. (2003) with the broad (T_{p1}, T_{p2}) and sharp (T_{p3}, T_{p4}) crystallisation peaks seen in Figure 6.3.5 corresponding to surface and bulk crystallisation events respectively. The appearance of multiple crystallisation events are considered by Reynoso et al. (2003) to be highly sensitive to particle size effects and consequently may not have been apparent on the previous thermogram obtained from the <3mm fragments. This is due to the larger surface area of the fibres that allow a greater number of surface nucleation and growth events to occur during crystallisation that increases their signal strength in the DSC thermogram [321]. These results would also be in line with work reported by Jones & Clare (2012) where a DSC thermogram between a 1mm glass frit and fine glass powder of a $\text{P}_2\text{O}_5\text{-CaO-MgO-Na}_2\text{O-TiO}_2$ system showed the formation of two distinct crystalline phases in its powder

format only (Figure 6.4.1). These were later identified as calcium pyrophosphate ($\text{Ca}_2\text{P}_2\text{O}_7$) and a mixed calcium magnesium pyrophosphate (CaMgP_2O_7) crystallisation phase. Given the relative similarity between the compositional components of this glass with the CorGlaes[®] Pure 107 composition it would be anticipated that the crystalline phases in the CorGlaes[®] Pure 107 DSC thermogram may be similar [109, 321].

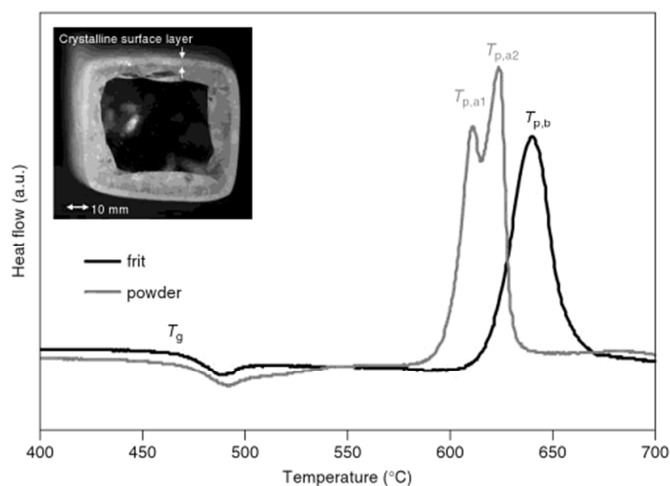


Figure 6.4.1. DSC thermogram of $\text{P}_2\text{O}_5\text{-CaO-MgO-Na}_2\text{O-TiO}_2$ glass system between 1mm glass frit and fine powder samples showing the formation of two crystalline phases/peaks in the glass powder corresponding to the formation of $\text{Ca}_2\text{P}_2\text{O}_7$ and CaMgP_2O_7 [Reproduced from Jones & Clare (2012)].

The occurrence of bulk crystalline phases (T_{p3} , T_{p4}) at temperatures above the 1000°C melt used by Giltech Ltd for the CorGlaes[®] Pure 107 glass was likely due to the decrease in melt viscosity. As discussed by Jones & Clare (2012), the tendency of a glass to crystallise is dependent upon its melt viscosity and as a result the increasing temperature would have allowed for the formation of crystalline phases due to the increased molecular mobility of the phosphate chains to reorganise into a crystalline state. The identification of the liquidus temperature at 1074°C would then indicate that a higher melt temperature ($>1074^\circ\text{C}$) should be considered for melt quenched applications when working with this glass composition. However given that no crystallisation was found in the XRD results of either the fibre or bulk forms (Figure 5.3.1) there is also sufficient counter evidence to support the current manufacturing methods [109, 249].

Along with the DSC and XRD, Raman spectroscopy of the CorGlaes[®] Pure 107 fibres identified Q^3 and Q^2 phosphate structural units that coordinated with its ultraphosphate

composition (55 mol% P₂O₅) as discussed by Brow (2000). This subsequently confirmed the accuracy of the previous FTIR results (section 5.3.2) ^[158].

The $20.85 \pm 3.25\mu\text{m}$ diameter of the CorGlaes[®] Pure 107 phosphate glass fibres (Figure 6.3.7) was in line with the typical 10-20 μm diameters used in synthetic fibre reinforced composites. A comparison with alternate studies also found the CorGlaes[®] Pure 107 fibre diameters to be in line with those used in the development of similar degradable PGF reinforced composites (Table 6.4.1) ^[322-324]. This is due to the high aspect ratios (i.e. fibre length to diameter ratio) of continuous fibres with the large surface area per unit volume allowing maximum stress transfer and reinforcement throughout the composite material (section 3.2.3). The results consequently indicated that the current manufacturing specifications (section 5.2.1) were highly suitable for the production of CorGlaes[®] Pure 107 fibres as a composite reinforcing phase ^[320, 322-324].

Table 6.4.1. Comparison of phosphate glass fibre diameters used as reinforcing agents in polymer composite devices intended for orthopaedic applications.

| Author | Fibre Diameter (μm) |
|--|----------------------------------|
| Onal et al. (2007) ^[325] | 18 |
| Ahmed et al. (2008) ^[215] | 20 - 25 |
| Ahmed et al. (2008) ^[218] | 20 - 25 |
| Mohammadi et al. (2011) ^[216] | 10 - 20 |
| Hasan et al. (2012) ^[221] | 20 ± 5 |
| Mohammadi et al. (2012) ^[169] | 10 - 20 |
| Haque et al. (2013) ^[209] | 15 - 25 |
| Sharmin et al. (2014) ^[211] | 20 |

A typical force-displacement plot from a tensile tested CorGlaes[®] Pure 107 fibre and its corresponding stress-strain plot (Figure 6.3.8) showed a lack of any significant plastic deformation prior to sample fracture that is characteristic of a brittle material. However from the fifty samples prepared ($n = 50$) only thirty-two data plots ($n = 32$) were used for further data analysis. This was due to the premature failure of fibre samples during testing and the sporadic occurrence of multiple fractures in a single sample that was evident by the

multiple deviations in the force-displacement plot (Figure 6.4.2). This was attributed to human error during sample preparation with data also excluded from specimens where fibre fracture had occurred in close proximity to the epoxy adhesive.

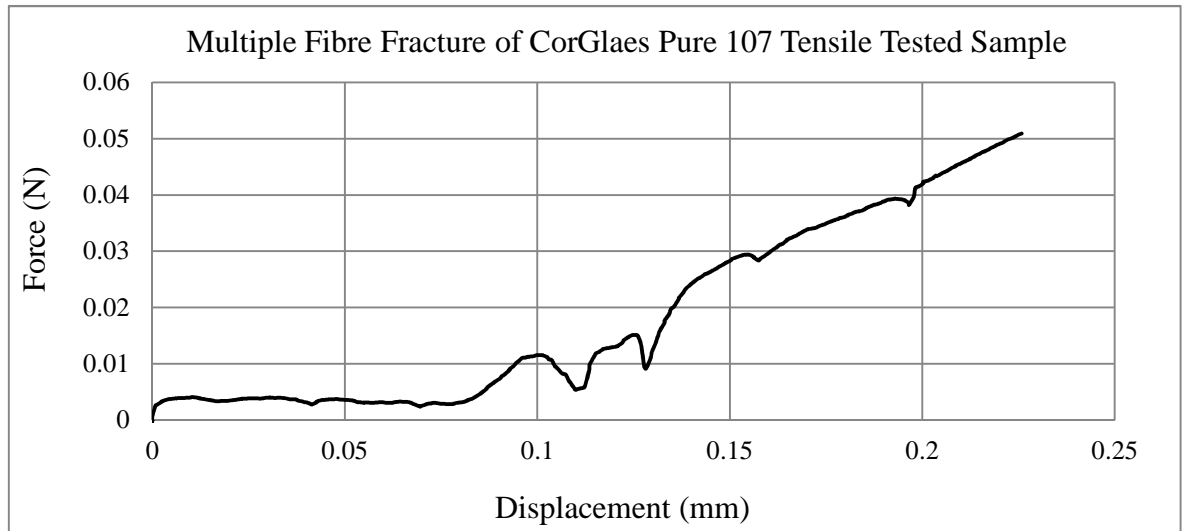


Figure 6.4.2. Force-displacement plot of a rejected tensile tested CorGlaes® Pure 107 fibre sample showing evidence of several fractures due to the presence of multiple fibres being accidentally secured to the housing card during sample preparation.

Compared to the bulk glass, the average tensile modulus of the CorGlaes® Pure 107 fibres was significantly higher and was in line with literature values. This was due to the fibre drawing process that preferentially selected the strong P-O-P bonds and installed a degree of molecular chain alignment along the fibres long axis (section 3.4.7.1). Such chain alignment contradicts the glass's natural isotropic structure (as found in glass monoliths) to produce fibres with anisotropic optical and mechanical properties (Murgatroyd et al., 1943; Ahmed et al., 2004; Sharmin et al., 2014). The average tensile modulus of the CorGlaes® Pure 107 fibres was also found to be in the upper range when compared with alternate PGF compositions that were intended for biomedical applications (e.g. composite reinforcement or cell transport vehicles) (Figure 6.4.3) ^[207, 209-211, 215].

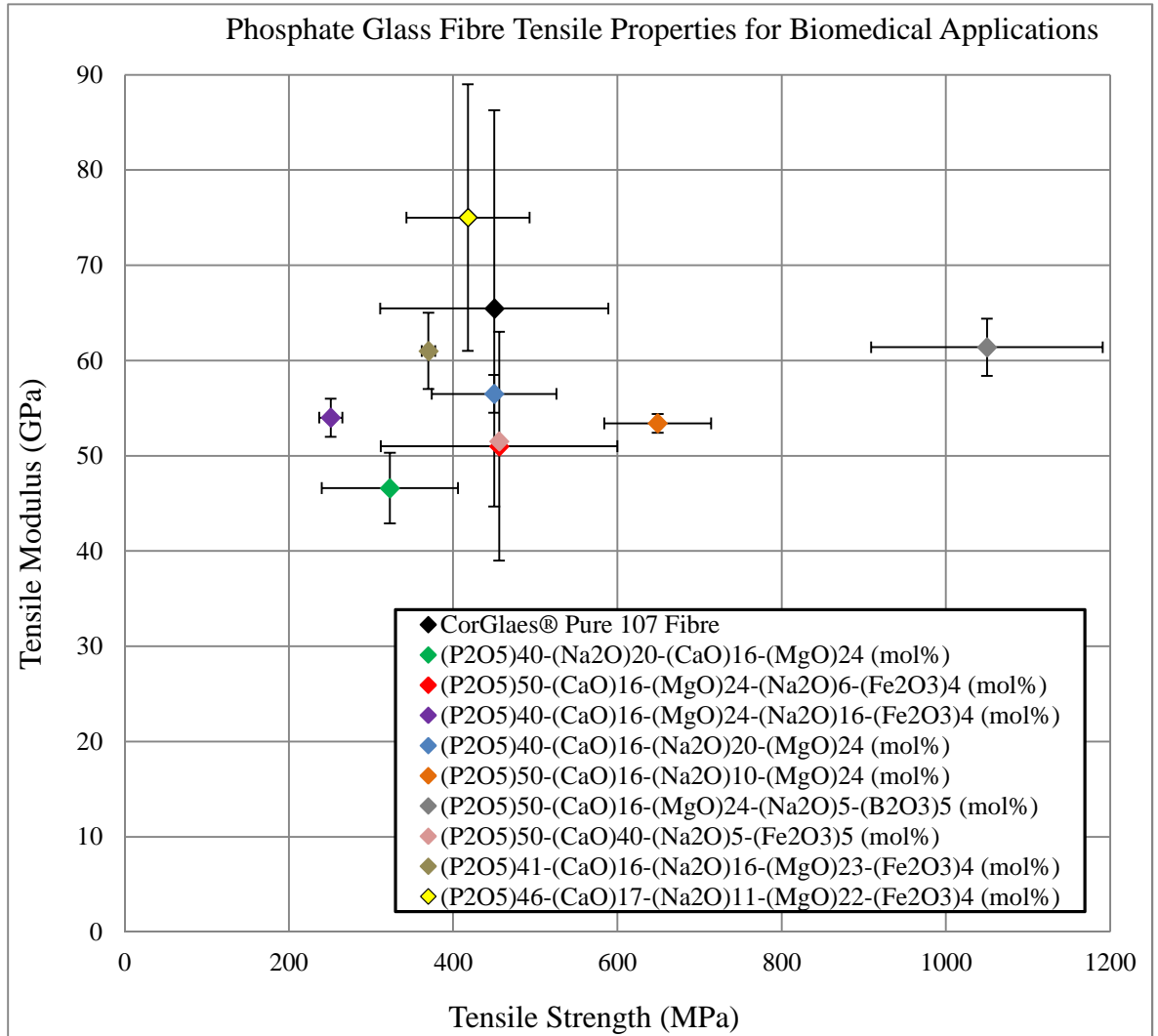


Figure 6.4.3 Comparison of CorGlaes[®] Pure 107 fibre tensile properties with alternate phosphate glass fibre compositions of similar $\approx 20\mu\text{m}$ diameter, tested according to ISO 11566:1996 [Data from Ahmed et al., 2008; Cozein-Cazuc et al., 2008; Hasan et al., 2012; Haque et al., 2013; Sharmin et al., 2014].

The tensile modulus of a phosphate glass fibre is considered by Sharmin et al. (2014) to be dependent upon the same influences as previously discussed for bulk phosphate glass monoliths (i.e. the network's cationic field strength and atomic packing density) (section 5.4). Furthermore the inherent tensile strength of phosphate glass fibres is believed to be regulated by the cross-link density and chain lengths of the phosphate backbone. The tensile strength of the CorGlaes[®] Pure 107 composition is then expected to benefit from the presence of magnesium and zinc if acting as intermediate oxides (section 3.4.3) which can potentially increase the glass's cross-link density or chain length by being incorporated into the glass's P-O-P backbone. Yet the large standard deviation in the tensile strength and tensile modulus of the CorGlaes[®] Pure 107 fibres has also made comparisons with

alternate glass fibre properties difficult. This was attributed to several factors related to the fibre manufacturing and test sample preparation processes ^[211].

Due to constrictions in the testing technique and severely limited number of successfully recovered fibre samples after fracture, an accurate correlation between the tensile test results and the precise sample fibre diameters could not be established. The averaged fibre diameter of 20.85 μm was then used for Eqn 6.2.1 as well as Eqn 6.2.2 and as a result deviations in the fibre diameter between samples could not be accounted for. Such variations would likely have arisen during fibre manufacturing from changes to the hydrostatic pressure in the glass melt and thus mass flow through the bushing nozzle as the melt volume was depleted as reported by Kobayashi et al. (2010). Consequently, fibre diameters obtained at the start of fibre manufacturing were likely to be greater than those at the end. This influence is demonstrated in Table 6.4.2 by the change in tensile modulus at the upper and lower range of the recorded CorGlaes[®] Pure 107 fibre diameters ^[229].

Table 6.4.2. Variation in tensile modulus (Eqn 6.2.2) with lower, average and upper range of fibre diameters (section 6.3.4) with the maximum tensile force (0.288N) recorded during the tensile testing of CorGlaes[®] Pure 107 fibres.

| Fibre Diameter (μm) | Fibre Cross-Sectional Area (mm^2) | Elastic Modulus (GPa) |
|----------------------------------|--|-----------------------|
| 16.07 | 2.03×10^{-4} | 151.9 |
| 20.85 | 3.41×10^{-4} | 90.3 |
| 27.06 | 5.75×10^{-4} | 53.6 |

The large error in the tensile strengths of the CorGlaes[®] Pure 107 fibres were to be expected however given the similar range reported in previous results (Figure 6.4.3). These were attributed to the introduction of Griffith flaws (i.e. surface defects) in the fibres that were likely generated during the manufacturing of the tensile testing samples (e.g. cutting and handling of the fibres). Yet the presence of such flaws are considered by De Diego et al. (2000) to be an accurate representation of the practical fibre properties due to the likely handling of fibres experienced during composite manufacturing. The results shown in Figure 6.3.11 consequently demonstrated how a straight edge or semi-circular flaw surface defect of increasing size ($\approx 0 \rightarrow 5\mu\text{m}$) had a detrimental effect on the tensile strengths of the

CorGlaes[®] Pure 107 fibres. This was in line with comments by Haque et al. (2013) who discussed the large number of studies dedicated to the ‘practical strength’ of oxide glasses due to the influence of surface quality on their mechanical performance^[207, 209, 326].

Accordingly the observed variation in tensile strength was accounted for by a Weibull distribution with the resulting Weibull modulus (m) providing a dimensionless measure of the strength distribution throughout the fibres. From this it was found that the CorGlaes[®] Pure 107 fibres gave a Weibull modulus of $m = 3.41$ for the tested sample set with a normalising stress (σ_0) of 525 MPa. The Weibull modulus value fell within the range reported for ceramic materials ($m = 2-15$) but was significantly lower than those typically found in commercial grade glass fibres ($m = 10-30$). A Weibull modulus <4 also indicated that the flaws present on CorGlaes[®] Pure 107 fibres were not evenly distributed throughout the material and suggested a degree of continuity. This could imply that the scatter in fibre tensile strengths was related to the specific handling of the fibres during sample preparation. The Weibull modulus was also found to be comparable to values reported during the tensile testing of $(P_2O_5)_{50}-(CaO)_{40}-(Na_2O)_5-(Fe_2O_3)_5$ (mol%) fibres ($m = 3.37$) by Ahmed et al. (2009) using the same testing method. Yet studies by Sharmin et al. (2014) have demonstrated the ability to produce PGFs with Weibull moduli (m) as high as 7.7-10.5 (Figure 6.4.4)^[211, 215, 218, 300, 327].

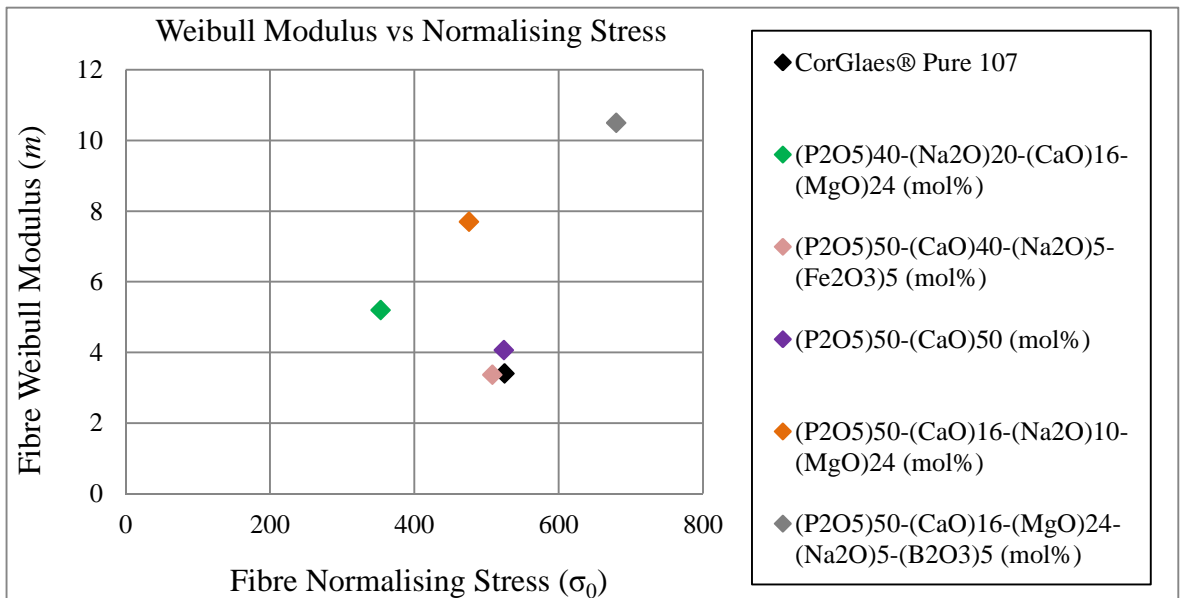


Figure 6.4.4. Comparison of CorGlaes[®] Pure 107 fibre Weibull modulus (m) and normalising stress (σ_0) with alternate PGF's tested according to ISO 11566:1996 [Data from Ahmed et al., 2008,2009; Cozien-Cazuc et al., 2008; Sharmin et al., 2014].

The dissolution of as made and surface treated CorGlaes[®] Pure 107 fibres in different media (Figure 6.3.13) showed distinct changes to the fibre dissolution rates over the initial 24 hours. Continued immersion over the entire 168 hour period also revealed the weight loss profile to be non-linear after 72 to 96 hours of dissolution following an inverse exponential curve. Fibres immersed in distilled water ($2.83 \times 10^{-2} \text{ mg cm}^{-2} \text{ hr}^{-1}$) and PBS ($2.55 \times 10^{-2} \text{ mg cm}^{-2} \text{ hr}^{-1}$) appeared to display comparable dissolution rates whilst similar rates were observed between samples immersed in c-SBF ($1.67 \times 10^{-2} \text{ mg cm}^{-2} \text{ hr}^{-1}$) and silane treated fibres ($1.44 \times 10^{-2} \text{ mg cm}^{-2} \text{ hr}^{-1}$) over the initial 24 hours. The dissolution of fibre samples in distilled water, c-SBF, PBS and silane treated fibres was also coupled with a universal drop and plateau in pH after 24 hours to ≈ 2 (Figure 6.3.12). This pH reduction was significantly lower than that previously recorded from the dissolution of CorGlaes[®] Pure 107 disks (section 5.3.7.1) and was attributed to the increased surface area-to-volume ratio with the fibres ($14.4 \text{ cm}^2 \text{ ml}^{-1}$) compared to the previous tests ($0.18 \text{ cm}^2 \text{ ml}^{-1}$). Due to the static test conditions, this led to a greater accumulation of phosphate species and concentration of phosphoric acid in the media. In contrast, fibres immersed in DMEM showed the slowest rates of fibre dissolution ($7.63 \times 10^{-3} \text{ mg cm}^{-2} \text{ hr}^{-1}$) that appeared to degrade in a linear fashion over a prolonged period compared to the other media. The pH also displayed a more gradual decrease reaching ≈ 4.5 at 72 hours and corresponded with a visible change in the media colour from red to yellow before it was replaced with fresh DMEM after 96 hours.

It is believed that PGFs will undergo the same dissolution mechanisms as their bulk monolith equivalent with the same compositional dependence. However phosphate glass fibres will typically degrade faster than the equivalent bulk sample as seen with the CorGlaes[®] Pure 107 composition and agrees with data reported by Ahmed et al. (2004). This is due to the increased surface area and different mechanical/thermal histories between each form (e.g. the rapid air quenching of the fibres). The reduced fibre dissolution rates in DMEM were also in line with the trends observed by Patel & Knowles (2006) but remained below the preferred dissolution rate of fibres intended for composite reinforcement ($2 \times 10^{-4} \text{ mg cm}^{-2} \text{ hr}^{-1}$) as suggested by Hasan et al. (2012) ^[194, 201, 205, 210].

It has been previously reported by Franks et al. (2000) that the ionic concentration of an immersion media can influence the rate of ionic diffusion from a phosphate glass (i.e. dissolution rate) ^[174]. Consequently it was believed that the initial ionic conductivity of each media would correspond with its ability to suppress the dissolution rate of the CorGlaes[®] Pure 107 fibres. However this trend was not strictly reflected in these results

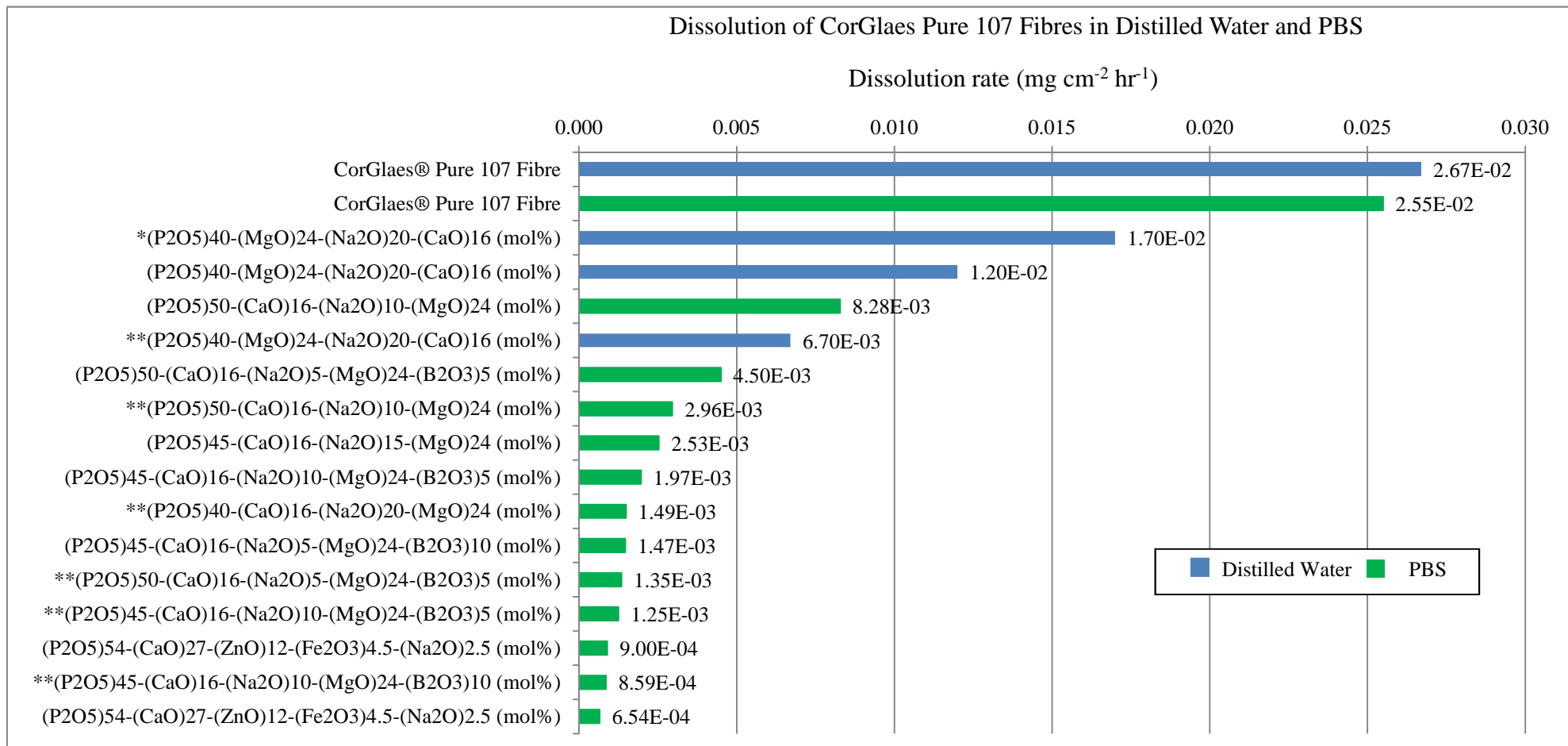
with similar dissolution rates observed in the distilled water ($\approx 0 \text{ mS cm}^{-1}$) and PBS (14.8 mS cm^{-1}). This contrasted previous results reported by Rinehart et al. (1999) who observed a reduced dissolution rate when PGFs were immersed in PBS compared to distilled water [270]. However this discrepancy between these results and those of Rinehart et al. (2009) could be accounted for by the difference in glass composition and testing conditions. Rinehart et al. (1999) used a 500ml circulating flow system ($\text{SA:V} = 0.15 \text{ cm}^2 \text{ ml}^{-1}$) while this study used a 10ml static environment ($\text{SA:V} = 14.4 \text{ cm}^2 \text{ ml}^{-1}$). As a result the influence of the dissolution by-products on the glass dissolution process (specifically any autocatalysis effects) would have been substantially more severe in the CorGlaes® Pure 107 experimental set up. The inhibitory effect of c-SBF on phosphate glass dissolution has been previously associated with the presence of Na^+ , Ca^{2+} and HPO_4^{2-} by Uo et al. (1998). However c-SBF also contains $\text{Mg}^{2+}/\text{Ca}^{2+}$ and as a result, the reduced rates observed in c-SBF (19.53 mS cm^{-1}) compared to PBS (14.8 mS cm^{-1}) may be due to the absence of these ions in the PBS composition used in this experimental method. Some visible precipitation within the c-SBF may have also influenced the weight loss measurements however no method of separating the precipitated phases could be employed without damaging the fibres (and further influencing the weight data) [176, 201]. The decreasing rate of fibre dissolution in the various media after 72 to 96 hours was assumed to be due to the ionic saturation of the media and correlated with 80-85% of the fibre weight being lost in all samples except DMEM. This decrease was attributed to the saturation of the media with the least soluble ionic species (corresponding to the glass's composition) as previously reported by Cozien-Cazuc et al. (2009) [201].

The improved durability of fibres degraded in DMEM media agreed with previous work by Patel & Knowles (2006) and was believed to be due to the presence of a sodium bicarbonate (NaHCO_3) pH buffering agent in the DMEM that retarded the decrease in media pH and autocatalysis effects during fibre dissolution [206]. This buffering agent subsequently accounted for the observed improvement in fibre durability compared to c-SBF despite their similar ionic composition (Table 6.2.2).

The progressive change in DMEM colour was due to the presence of a phenol red pH indicator in the media that will change from its native red (at neutral) to yellow in acidic conditions. Although bioactivity has been reported with bioactive glasses in DMEM by Lutišánová et al. (2011), no visible precipitates were found in the vials during fibre dissolution and thus any influence to the weight measurements were considered to be negligible. Silane surface treated fibres also showed a reduction in fibre dissolution rates

that were comparable to that displayed by c-SBF. Based on comments by Cozien-Cazuc et al. (2009) this was considered to indicate the successful bonding between the sizing agent and fibre surface with the reduction in fibre dissolution rates stemming from the formation of a hydrophobic surface layer that helped protect against water diffusion into the glass [206, 227, 328].

A comparison between the dissolution rate of the CorGlaes[®] Pure 107 fibres in distilled water and PBS with those reported in the literature for similar diameter PGFs showed the CorGlaes[®] Pure 107 fibres to possess a high dissolution rate (Figure 6.4.5). However a direct comparison is obscured by the high SA:V ratio used in the testing procedure of the CorGlaes[®] Pure 107 fibres ($14.4 \text{ cm}^2 \text{ ml}^{-1}$) compared to the average used in the majority of alternate methods ($\approx 7.3 \text{ cm}^2 \text{ ml}^{-1}$). As previously discussed by Mohammadi et al. (2012), the SA:V ratio will have a significant effect on fibre dissolution rate and would make the autocatalytic effects more severe for the CorGlaes[®] Pure 107 fibres. However given that high SA:V ratios would be encountered at the fibre-matrix interface in a composite material during its degradation, the dissolution rates and pH values measured here were considered to provide a better prediction of the fibres behaviour as a composite reinforcing agent. The use of annealing treatments has also been shown in various studies to reduce the dissolution rate of phosphate glass fibres compared to their as made state (section 3.4.7.3) and may be of interest for further processing of the CorGlaes[®] Pure 107 fibres [169, 201, 207, 209, 211, 270].



* Surface treated with a coupling agent

** Annealed

Figure 6.4.5. Comparison of CorGlaes® Pure 107 fibre dissolution rates in distilled water and PBS compared with alternate PGF compositions [Data from Rinehart et al., 1999; Cozien-Cazuc et al., 2009; Haque et al., 2013; Sharmin et al., 2014].

Inspection of the FTIR spectra after the immersion of CorGlaes[®] Pure 107 fibres in c-SBF found that these traces failed to correlate with the distinct wavenumber peaks of a crystalline apatite as reported in previous studies such as the silica based glass fibres investigated by Clupper et al. (2004). The lack of any sharp, well defined peaks in the FTIR spectra was indicative of an amorphous phase on the fibre surface and was initially interpreted as indicating a form of amorphous calcium phosphate (ACP, Ca/P = 1.5). This phase is considered to serve as a precursor to bone mineralisation and can spontaneously transform into crystalline apatite phases depending on the precipitation conditions (i.e. pH and Ca/P ratio). However approximate wavenumber values from the FTIR and Raman spectra failed to match with those documented for ACP and were believed to correspond with the precipitation of amorphous pyrophosphate salts (Leeuwen et al. 2012) [329-331]. These included calcium pyrophosphate ($\text{Ca}_2\text{P}_2\text{O}_7$) (Ca/P = 1), magnesium pyrophosphate ($\text{Mg}_2\text{P}_2\text{O}_7$) and zinc pyrophosphate ($\text{Zn}_2\text{P}_2\text{O}_7$) with the amorphous nature of these phases attributed to the rapid rate of precipitation from the super saturated c-SBF solution (Figure 6.4.6). Such compounds would also correlate with the ionic constituents of the CorGlaes[®] Pure 107 composition and have been previously reported to precipitate during PG dissolution by Franks et al. (2000) and Khor et al. (2011) [174, 187].

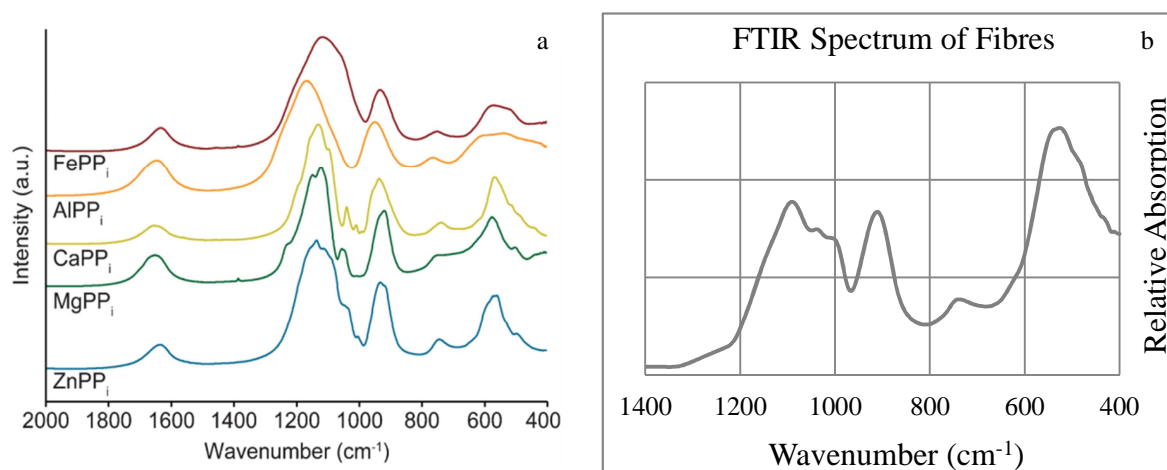


Figure 6.4.6. a) FTIR absorption spectra of various semi-amorphous metal pyrophosphate salts over 2000-400 cm^{-1} wavenumber range [Reproduced from Leeuwen et al. (2012)] and b) FTIR of CorGlaes[®] Pure 107 fibres after 336 hours of immersion in c-SBF (1400-400 cm^{-1}).

These phases are expected to form via hydrolysis mechanisms (as described in Eqn 6.4.1 for $\text{Zn}_2\text{P}_2\text{O}_7$) with the observed decrease in media pH over the immersion period resulting from the phosphoric acid (H_3PO_4) reaction by-product ^[187, 332].



Eqn 6.4.1

The application of pyrophosphates for bone regenerative applications has received limited attention and is considered to be relatively unexplored according to Grover et al. (2013). It has also been reported by Kasuga et al. (2005) that β -calcium pyrophosphate (β -CPP) can display bioactivity similar to that of hydroxyapatite (HA) and beta tricalcium phosphate (β -TCP). However pyrophosphate ions (P_2O_7)⁴⁻ are known to suppress HA crystallisation and have consequently also been discussed as a method of influencing and controlling bone mineralisation. This is due to the ability of alkaline phosphatase (an enzyme secreted by osteoblasts) to hydrolyse pyrophosphate ions and alleviate the inhibitory effects of pyrophosphate salts. *In vivo* mineralisation is then stimulated through the release and saturation of the surrounding extracellular fluids with orthophosphate units (PO_4)³⁻ ^[168, 333, 334].

Yet it is also possible that these precipitates may also have consisted of magnesium ($\text{Ca}_{2-x}\text{Mg}_x\text{P}_2\text{O}_7$) and zinc ($\text{Ca}_{2-x}\text{Zn}_x\text{P}_2\text{O}_7$) doped calcium pyrophosphate. However the precise identification of each respective amorphous phase from the available FTIR/Raman spectra is restricted due to the similar IR signals of these salts and associated band overlapping. Further identification could be conducted by post-annealing and repeated analysis via XRD and FTIR with deconvolution of the spectra to identify the crystalline phases as performed by Franks et al. (2000) and Khor et al. (2011) ^[330, 331, 335].

Yet despite the potential of these pyrophosphate salts for *in vivo* applications, the inability of the CorGlaes[®] Pure 107 glass composition to form a more ‘traditional’ bioactive apatite layer (i.e. HCA) across the fibres surface during *in vitro* test conditions was in line with the literature. The precipitation of these salts reflected the high dissolution rate of the CorGlaes[®] Pure 107 fibres when compared to the CorGlaes[®] Pure 107 disks and this rate is considered to directly influence the resulting calcium phosphate phase (Mohammadi et al. 2012). Furthermore the decrease in media pH produced from ultraphosphate glass

dissolution is believed to suppress apatite formation despite the large quantities of calcium and phosphate released into the media. However as stated in section 3.4.5, some PG compositions such as those investigated by Kiani et al. (2012) have demonstrated the ability to exhibit bioactivity *in vivo* despite failing to do so *in vitro*. This could be due to the *in vivo* circulation of the extracellular fluid helping to maintain a physiological pH in the surrounding environment and allowing for apatite nucleation on the glass surface compared to the static environment encountered *in vitro*. Consequently the CorGlaes[®] Pure 107 fibres may also be capable of displaying similar behaviour *in vivo* through improved regulation of the pH [100, 168, 170, 177, 273, 289]. However it should also be considered that when applied as a composite reinforcing agent, the altered fibre dissolution rates as well as the volume fraction of fibres employed (section 3.2.3.2) may lead to the development of alternate phases when such composites are immersed in c-SBF.

Lastly, the observed change in fibre morphology over the immersion period was attributed to the dissolution of the fibres and the subsequent cracking/peeling of an outer surface layer on the glass fibres. This change in morphology was in line with previous SEM images (Figure 6.4.7) observed during PGF dissolution by Rinehart et al. (1999) and Sharmin et al. (2014) with SEM images of the CorGlaes[®] Pure 107 fibres (Figure 6.3.18a,b) indicating a surface layer of $\approx 0.4\text{-}0.55\mu\text{m}$ [211].

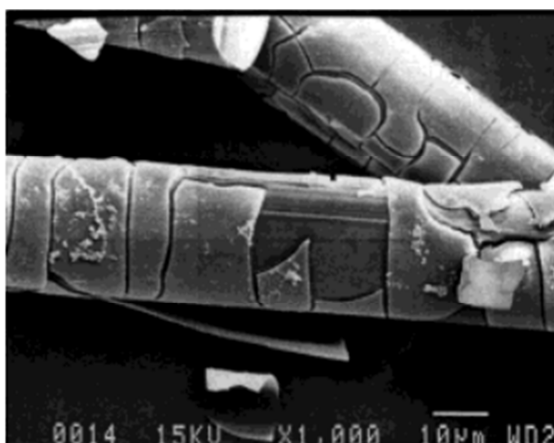


Figure 6.4.7. SEM image of phosphate glass fibres after 24 hours of immersion in PBS at 37°C showing significant cracking and peeling of the outer surface layer [Reproduced from Rinehart et al. (1999)].

6.5 Conclusions

Thermal analysis of the CorGlaes[®] Pure 107 fibres confirmed the high suitability of this novel PG composition for fibre production due to its high thermal stability. Tensile testing of the $\approx\text{Ø}20\mu\text{m}$ CorGlaes[®] Pure 107 fibres also confirmed their mechanical suitability as a composite reinforcing agent. However the susceptibility of the CorGlaes[®] Pure 107 fibres to autocatalytic effects gives them unsuitably high dissolution rates. The dissolution rate of the fibres was also found to vary between different media as well as after an APS surface treatment with the D_r strongly retarded through adequate control of the media pH. The fast dissolution rate of these fibres was responsible for the formation of pyrophosphate salts when immersed in c-SBF due the rapid ion release and decrease in c-SBF pH.

7 CorGlaes[®] Pure 107 Fibre Composites as Potential Cranioplasty Plates

7.1 Outline

Mechanical testing of the $\approx\text{Ø}20\mu\text{m}$ CorGlaes[®] Pure fibres (chapter 6) showed their suitability as a potential composite reinforcing agent. This was due to their tensile strength (426 ± 143 MPa) and tensile modulus (65.5 ± 20.8 GPa) being in line with previous PGF data obtained from the literature that were intended for similar applications. Consequently the characterisation of a CorGlaes[®] Pure 107 fibre reinforced composite material was conducted with the initial composite specifications based on the parameters and specifications (e.g. manufacturing method, volume fractions, matrix etc.) frequently employed in the literature (section 3.4.8).

7.2 Materials and Methods

7.2.1 CorGlaes[®] Pure 107 Glass Fibre Mats

Continuous fibre mats of unidirectionally aligned (UD) and randomly orientated continuous fibre (RCM) architectures for composite manufacturing were produced by manually expanding the melt spun CorGlaes[®] Pure 107 fibre tows (Figure 6.2.1). For UD mats, the tows were evenly expanded parallel to the fibre's primary axis whilst random fibre mats were generated by collectively drawing out fibres across a metal table tangential to their primary axis. This formed a loose fibrous structure that was then circumferentially collected around a hand driven mandril with the resulting expansion inducing random orientations throughout the fibres. The expanded mats were then removed from the mandrill before being cut and stored in PE bags (Figure 7.2.1) ^[122].

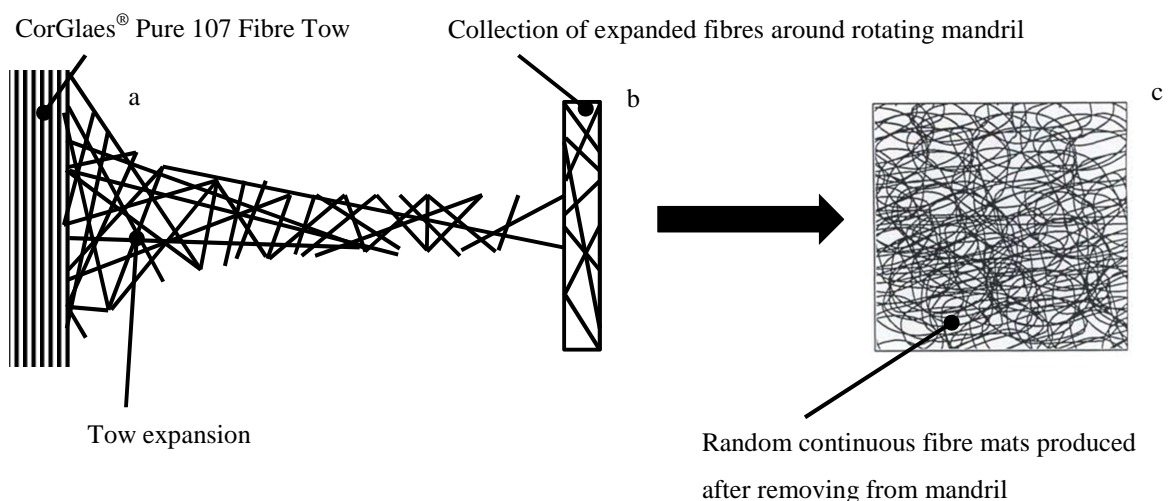


Figure 7.2.1. Illustration of manufacturing method for producing random continuous fibre mats (RCM) from a CorGlaes[®] Pure 107 fibre tow a) Expansion of fibres parallel to fibre tow b) Collection around a hand driven mandril and c) Cutting and removal from mandril into RCM mats [Modified from Mallick (1997) Composites Engineering Handbook].

7.2.2 Composite Precursors

7.2.2.1 Fibre Pre-Pregs

Polymer impregnated continuous CorGlaes[®] Pure 107 fibre mats (pre-pregs) were created by cutting the UD/RCM fibre mats into 130x80mm sections and preparing a low viscosity 3 w/v % 3001D PLA (NatureWorks[®], USA) solution using chloroform (VWR, USA) as

the polymer solvent. Fibre mats were then placed in metal foil trays (130x80x10mm) inside a fume cabinet and solvent cast with a pre-determined volume of the PLA solution to achieve a desired pre-preg (pp) fibre volume fraction (V_{f-pp}). The solvent cast pre-preg mats (Figure 7.2.2a-b) were then left for 12 hours to allow the solvent to completely evaporate before being removed from the trays and stored inside a desiccator.

To quantify the primary orientation and coherency in the fibre alignment of each mat architecture type, images of the fibre pre-pregs were analysed using ImageJ software (National Institutes of Health, USA). ImageJ is an open source Java based platform employed for image processing and analysis that was developed by the National Institutes of Health (NIH) and was used in conjunction with an additional OrientationJ plug-in. The analysis was performed on 5 images ($n = 5$) from each fibre mat type and compared with an idealised set of aligned or randomly orientated arrays. These were generated using MATLAB software (MathWorks[®], USA) and acted as control images (Figure 7.2.2).

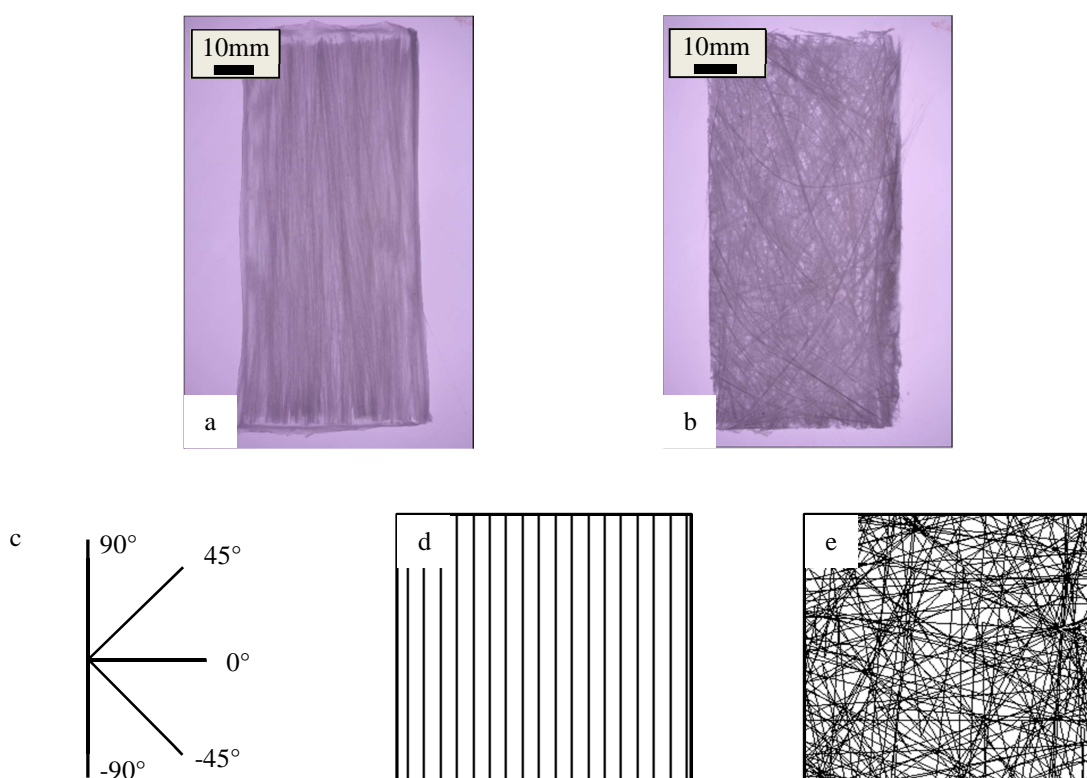


Figure 7.2.2. Back-lit illuminated images of a) 100x50mm section of UD solvent cast CorGlaes[®] Pure 107 fibre pre-preg [scale bar = 10mm] b) 100x50mm section RCM solvent cast CorGlaes[®] Pure 107 fibre pre-preg [scale bar = 10mm] c) Orientation axis used in OrientationJ results d) Unidirectional (UD) control image and e) Randomly orientated control image (generated by MATLAB).

7.2.2.2 Matrix Sheets

Matrix sheets of 0.1-0.2mm thickness were manufactured by compressing 9g of 3001D PLA granules (NatureWorks[®], USA) between two 305x305mm heated plates of a hydraulic compression moulding press (Mackey Bowley, England) at 200°C (Figure 7.2.3). The polymer granules were compressed under 1.5-2 MPa of pressure for 30 seconds before cooling to room temperature by passing water through both cooling plates. The PLA sheets were then cut into 130x80mm sections. To prevent polymer adhesion to the heated plates, intermediate layers of greaseproof paper were placed between the granules and the plates during manufacturing.



Figure 7.2.3. Compression moulding press used to produce PLA matrix sheets and CorGlaes[®] Pure 107 composites.

7.2.3 Composite Manufacturing

Continuous CorGlaes[®] Pure 107 fibre laminated composites were manufactured using a hand lay-up film stacking and compression moulding method with each CorGlaes[®] Pure 107 fibre pre-preg lamina ($n = 6$) stacked alternatively between 3001D PLA matrix sheets ($n = 7$) (Figure 7.2.4a-b). Compression moulded composites were created inside a 130x80mm stainless steel three-piece cavity mould (Figure 7.2.4c) using the compression moulding press (Figure 7.2.3) at 200°C for 15 minutes before being cooled to room temperature under 4 MPa pressure. To improve consistency in the composite thickness, metal shims were used in conjunction with the mould whilst a PTFE dry film lubricant (251-3794, RS Components, UK) was applied prior to composite manufacturing in order to ease removal of the sample from the mould (Figure 7.2.4d).

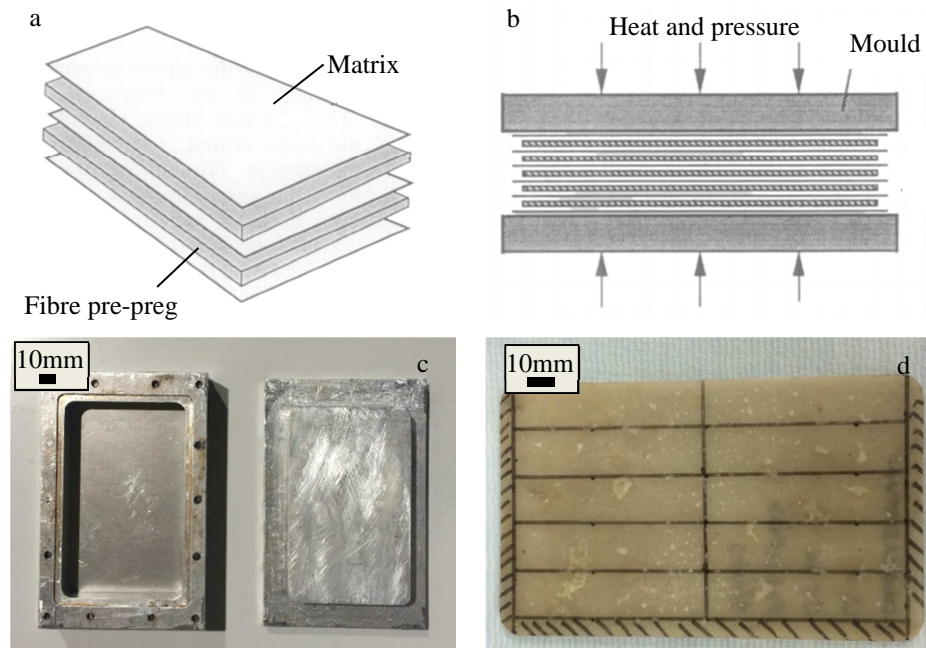


Figure 7.2.4. Illustration of a) Alternating film stacking technique with PLA matrix sheets and CorGlaes[®] Pure 107 fibre pre-pregs [Reproduced from Gibson & Månson (1992)] b) Sequential lay up of matrix films and fibre pre-pregs under heat and pressure inside the cavity mould [Reproduced from Gibson & Månson (1992)] c) 130x80mm stainless steel cavity mould used for composite manufacturing [scale bar = 10mm] and d) 130x80mm $0.2V_f$ RCM composite plate marked for further cutting stages of sample manufacturing [scale bar = 10mm].

Composites of different fibre volume fractions (V_f) and fibre architectures were subsequently manufactured based on the accumulative contributions from the polymer matrix and fibre pre-pregs that were calculated using Eqn 7.2.1 and Eqn 7.2.2. For aligned composites, UD lamina were alternatively stacked perpendicularly to the previous lamina to produce a symmetric cross-ply composite lay-up $[0/90/0/90/0/90]_T$ (where T denotes the total laminate stacking sequence). The predetermined fibre weight (w_f), fibre volume fraction (V_f) and manufacturing specifications for each composite configuration are shown in Table 7.2.1^[120, 122].

Positive control samples of 3001D PLA (NatureWorks[®], USA) were also manufactured by placing 30g of 3001D PLA polymer granules into the cavity mould inside the compression moulding press at 200°C for 10 minutes. The mould was then cooled to room temperature under 4 MPa pressure.

$$W_f = \frac{w_f}{w_c}$$

$$w_c = w_f + w_m$$

Eqn 7.2.1

where W_f = composite fibre weight fraction, w_c = composite weight (g), w_f = composite fibre weight (g), w_m = composite matrix weight (g).

$$V_f = \frac{(W_f/\rho_f)}{(W_f/\rho_f) + (W_m/\rho_m)}$$

Eqn 7.2.2

where V_f = composite fibre volume fraction, W_m = composite matrix weight fraction, ρ_f = fibre density (g cm^{-3}) [2.65 g cm^{-3}], ρ_m = matrix density (g cm^{-3}) [1.25 g cm^{-3}] [122].

Table 7.2.1. Manufacturing specifications of CorGlaes[®] Pure 107-PLA composites.

| | | CorGlaes [®] Pure 107 Pre-Preg (pp) | | PLA Matrix |
|---|-------|--|-------------------|----------------------|
| Composite | | 40ml 3 w/v % PLA solution | | 0.1-0.2mm sheets |
| Sample | V_f | Fibre weight per pp (g) | $V_{f\text{-pp}}$ | Weight per sheet (g) |
| ^a 0.01 V_f RCM | 0.01 | 0.1 | 1 | ≈2.9 |
| ^a 0.05 V_f RCM | 0.05 | 0.4 | 1 | ≈2.9 |
| ^b 0.1 V_f RCM | 0.1 | 0.8 | 0.5 | ≈2.4 |
| 0.2 V_f RCM | 0.2 | 2.5 | 0.5 | ≈2.9 |
| ^c 0.2 V_f [0/90] _{3S} | 0.2 | 2.5 | 0.5 | ≈2.9 |

^a No solvent casted pre-pregs (pp) were manufactured with the low V_f composites due to the difficulty in removing the resulting pre-pregs from the foils trays without significant sample damage.

^b 14ml of 3 w/v % PLA solution used to solvent cast 0.1 V_f composite pre-pregs.

^c [0/90]_{3S} represents the total stacking sequence ([0/90/0/90/0/90]_T) based upon its symmetry (s) and repetition ($n = 3$) of the [0/90] orientated cross-ply.

7.2.4 Mechanical Properties

The flexural strength (σ_{comp}) and elastic modulus (E_{comp}) of all CorGlaes[®] Pure 107-PLA composites and PLA control samples was assessed using a three-point bend method based on BS EN ISO 14125:1998. Testing specimens were cut from the 130x80mm composite plate (Figure 7.2.4d) to 60x15x2mm rectangular beams using a bandsaw in accordance with BS EN ISO 14125:1998. Due to the homogenous (RCM) or symmetrical ($[[0/90]_{3S}]$) nature of the CorGlaes[®] Pure 107-PLA composite lamina, no preferential orientation was selected during sample cutting with all specimens cut according to sample 'A' as shown in Figure 7.2.5a^[336].

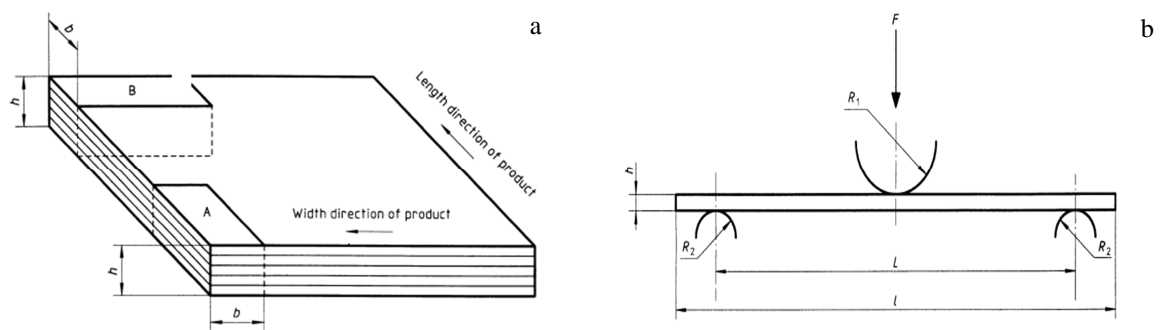


Figure 7.2.5. Illustration of a) Cutting specifications for samples cut along the length direction of the composite (A) and samples cut along the width direction of the composite (B) and b) 3-point bend testing arrangement used to test the CorGlaes[®] Pure 107-PLA composites and control samples [Reproduced from BS EN ISO 14125:1998].

Samples were then tested using a Zwick/Roell Z250 (Zwick Roell, USA) testing equipment with a 1kN load cell at a crosshead speed of 2mm min^{-1} in the testing arrangement illustrated by Figure 7.2.5b where the loading member radius (R_1) = 5mm, support member radius (R_2) = 2mm, support span (L) = 40mm, specimen span (l) = 60mm and specimen thickness (h) = 2mm. Force-displacement data was recorded using Zwick/Roell TestXpert[®] software with the mechanical properties of the specimens calculated using Eqn 7.2.3, Eqn 7.2.4 and Eqn 7.2.5 as described in Method A of BS EN ISO 14125:1998^[336]. Prior to testing, the width and thickness of each sample was measured at three different locations with digital callipers and used to calculate an averaged thickness (h) and width (b) for each specimen.

$$\sigma_{comp} = \frac{3FL}{2bh^2}$$

Eqn 7.2.3

where σ_{comp} = flexural strength (MPa), F = maximum load (N), L = specimen span (mm), h = specimen thickness (mm), b = specimen width (mm).

$$s' = \frac{\varepsilon_f' L^2}{6h} \quad s'' = \frac{\varepsilon_f'' L^2}{6h}$$

Eqn 7.2.4

where s' = beam mid-point deflection¹ (mm), s'' = beam mid-point deflection² (mm), ε_f' = flexural strain¹ (0.0005), ε_f'' = flexural strain² (0.0025).

$$E_{comp} = \frac{L^3}{4bh^3} \left(\frac{\Delta F}{\Delta s} \right)$$

Eqn 7.2.5

where E_{comp} = elastic modulus (MPa), ΔF = differential between F' and F'' from sample force-displacement plot corresponding to s' and s'' respectively (N), Δs = differential between deflections s' and s'' (mm).

A comparison between the experimental and theoretical elastic moduli was also conducted using the rule of mixtures (ROM) (Eqn 7.2.6). This model is based on the composite properties being the sum of each constituent with regards to their respective volume fractions. This can subsequently be used to predict the effective longitudinal (primary) or transverse elastic modulus in a laminate composite ^[219].

$$E_1 = n_0 n_1 E_f V_f + E_m (1 - V_f)$$

Eqn 7.2.6

where E_1 = elastic modulus (primary), n_0 = correction factor depending upon composite fibre orientation (0.375 for random in plane fibres and 0.5 for a balanced $0^\circ/90^\circ$ lay-up), n_1 = correction factor dependent upon fibre length (1 for fibres that are $\geq 10l_c$, where l_c is the critical fibre length), E_f = fibre modulus (GPa), E_m = matrix modulus (GPa), V_f = fibre volume fraction.

7.2.5 Degradation

7.2.5.1 Weight Loss and Mechanical Properties

Degradation of $0.2V_f$ RCM and $0.2V_f [0/90]_{3S}$ samples as well as a PLA control was carried out using distilled water on $60 \times 15 \times 2$ mm samples at a $0.21 \text{ cm}^2 \text{ ml}^{-1}$ SA:V ratio. Samples were stored individually within PP bottles and placed inside a 37°C incubator for up to 1008 hours (six weeks) before being evaluated in triplicate ($n = 3$) at each immersion period. Analysis of the degraded samples along with replacement of the immersion media was then conducted following the procedure outlined in Table 7.2.2.

Table 7.2.2. Immersion period and sample data during degradation of composite and control samples over 1008 hours in distilled water at 37°C .

| Immersion Period (hours) | Data | Measurement Points/Media Change |
|---|--|---|
| 2, 4, 6, 24, 48, 72, 96, 120, 144, 168 | *Wet weight Media pH | At each immersion period |
| 168, 336, 504, 672, 840, 1008 | Wet weight, Dry weight Media pH Flexural strength Elastic modulus | At each immersion period. Media changed at each immersion period and every 72 to 96 hours between measurements. |

*Composite wet weight over the first 144 hours only collected for $0.2V_f$ RCM composite and PLA control samples.

Due to the cutting procedure of the 130x80x2mm composite plate, samples were opened (i.e. exposed fibre faces) across 3 or 4 cross sectional faces. To ensure comparable results between samples, a 10 w/v % 3001D PLA solution was applied to the required composite faces so that only 3 cross-sections on all samples were exposed as shown in Figure 7.2.6.

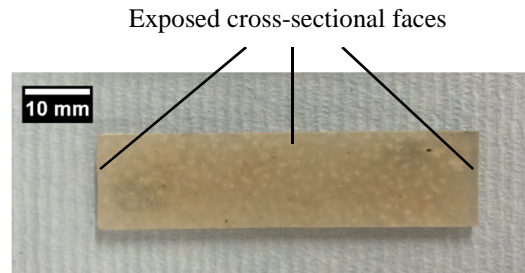


Figure 7.2.6. Image of 60x15x2mm 0.2V_f RCM composite sample used in degradation testing with the three exposed cross-sectional faces indicated [scale bar = 10mm].

During degradation, composite/control sample wet and dry weight as well as the degradation media pH were measured using a ± 0.1 mg PioneerTM analytical scale (Ohaus, USA) and HI 221 pH Meter (Hanna Instruments, USA) respectively. For dry weight measurements all samples were dried in an air circulated oven at 60°C for 12 hours prior to measurement with the sample wet weight and dry weight calculated using Eqn 7.2.7. These results were then plotted against the immersion period (hours).

$$\text{Change in Wet and Dry Weight} = \frac{w_0 - w_t}{w_0} * 100$$

Eqn 7.2.7

where w_0 = initial sample weight (mg) and w_t = sample wet/dry weight measured at time t_x (mg)

The flexural strength and elastic modulus of the degraded samples were subsequently evaluated using a three point bend method as outlined in section 7.2.4 using Eqn 7.2.3, Eqn 7.2.4 and Eqn 7.2.5 at each designated immersion period according to Table 7.2.2. SEM images of the 0.2V_f RCM composite as well as the PLA control fracture faces after

degradation and mechanical testing were captured using a Sigma VP SEM (Carl Zeiss, Germany) in SE and BSE modes at a 10kV accelerating voltage after coating the sample fracture sites with gold (Agar Scientific, UK) based on section 6.2.4. This was performed at the School of Geographical and Earth Sciences, University of Glasgow.

7.2.5.2 Ion Release

Ionic concentrations in the distilled water during the first 168 hours of 0.2V_f RCM composite degradation (section 7.2.5.1) were measured following the procedure outlined in section 5.2.8.2.

7.2.6 DMEM Degradation

Degradation of 0.2V_f RCM composites in acellular protein free DMEM (Sigma-Aldrich, USA) was conducted following the composite manufacturing and degradation methods as outlined in section 7.2.3 and section 7.2.5 respectively. Growth of bacteria and fungi in the DMEM was inhibited through the addition of sodium azide (Sigma-Aldrich, USA) to the DMEM at 0.1 vol% prior to composite degradation as previously described in section 6.2.7.

The precipitate formed on the degraded composite samples was examined by FTIR and XRD using the equipment and specifications outlined in section 5.2.3 and section 5.2.2 respectively. SEM images of the degraded composite fracture sites after mechanical testing was also conducted at a 5kV or 10kV accelerating voltage using a Hitachi S9000 SEM (Hitachi, Japan) after coating the fractured composite faces with gold (Agar Scientific, UK). This was conducted at the James Watt Nanofabrication Centre (JWNC), University of Glasgow.

7.2.7 Bioactivity

The bioactivity of 0.2V_f RCM composite samples was assessed by immersing 15x15x2mm samples in c-SBF for 24, 72, 120, 168 and 336 hours at a 0.1 cm² ml⁻¹ SA:V ratio. The c-SBF was prepared following the procedure outlined in section 5.2.9.1 with samples stored individually in inside PP bottles within a 37°C incubator. The c-SBF was not replaced over the immersion period and samples were assessed in triplicate ($n = 3$) by measuring the composite wet weight and media pH at each immersion period after washing the samples

in acetone (VWR, USA) to halt any further surface reactions as described in section 5.2.9.2. The results were then plotted against the immersion period (hours) with the sample planar and cross-sectional faces analysed by FTIR as described in section 5.2.9.2.

7.2.8 Biocompatibility

Prior to biocompatibility testing of the composite samples, *in vitro* cell culture and cell seeding was conducted following the method outlined in section 5.2.10.2.

The biocompatibility of 10x10x2mm 0.01V_f, 0.05V_f, 0.1V_f and 0.2V_f RCM composites was investigated by an initial MTT assay on MG63 cells following the methods described section 5.2.10.3 using 100 vol% extracts from each composite configuration after 24 and 96 hours of degradation. Samples were degraded at a 1.4 cm² ml⁻¹ SA:V in CDMEM with 10x10x2mm 3001D PLA samples used as a secondary positive control sample. The pH of the degradation media for each MTT assay was also measured from a sample of the extract using a HI 221 pH Meter (Hanna Instruments, USA). Cytotoxicity testing by MTT assay was also conducted on diluted extract concentrations (0.1, 10, 50 and 100 vol%) obtained from the degradation of 0.2V_f RCM composites after 24 and 96 hours in CDMEM based on the method previously performed in section 5.2.10.3.

After the MTT assay, biocompatible composite configurations were then to be evaluated by a direct contact cell culture and Live/Dead[®] staining (section 5.2.10.4) following the flow chart shown in Figure 5.2.3 at a 1.4 cm² ml⁻¹. This SA:V ratio was selected so that a better correlation between the MTT and Live/Dead[®] staining could be achieved.

Note: Although a 1.25 cm² ml⁻¹ SA:V ratio was intended for the composite MTT assay and Live/Dead[®] staining (section 5.2.10.3), significant lag in the pipette guns at the time of testing resulted in a 1.4 cm² ml⁻¹ SA:V ratio being used. To allow for comparisons between future results and across samples, a 1.4 cm² ml⁻¹ was consequently used in all future composite biocompatibility testing.

7.3 Results

7.3.1 Pre-Preg Orientation

The primary orientation and coherency in the computer generated control images as determined by the ImageJ[®] software is shown in Table 7.3.1 and compared with the average results for each fibre mat pre-preg architecture.

Table 7.3.1. Comparison of fibre anisotropy in UD and RCM fibre pre-pregs as defined by the primary orientation and coherency of their alignment using MATLAB control images and ImageJ[®] software.

| Sample | Primary Orientation (°) | Coherency (%) |
|--------------------------------|-------------------------|---------------|
| Parallel aligned control image | 90 | 100 |
| Random control image | 48 | 3 |
| Aligned pre-preg | 87 ± 2 | 83 ± 3 |
| Random pre-preg | 18 ± 9 | 30 ± 3 |

7.3.2 Mechanical Properties

Comparative stress-strain plots from a tensile tested CorGlaes[®] Pure 107 fibre (filler) as well as that obtained from the three point bend testing of a NatureWorks[®] 3001D PLA polymer control sample (matrix) and a $0.2V_f$ RCM composite are shown in Figure 7.3.1 with the respective failure stresses (σ_f/σ_m) and strains (ϵ_f/ϵ_m) overlaid. The flexural stress and elastic moduli of composites with increasing V_f alongside a PLA control is shown in Figure 7.3.2 with a complete description of each samples mechanical properties listed in Table A.1. of Appendix A. The elastic moduli of these composites is also compared with those predicted using the rule of mixtures model in Figure 7.3.3.

A comparison between the stress-strain plots obtained from the mechanical testing of $0.2V_f$ RCM and $0.2V_f [0/90]_{3S}$ composite architectures is shown in Figure 7.3.4.

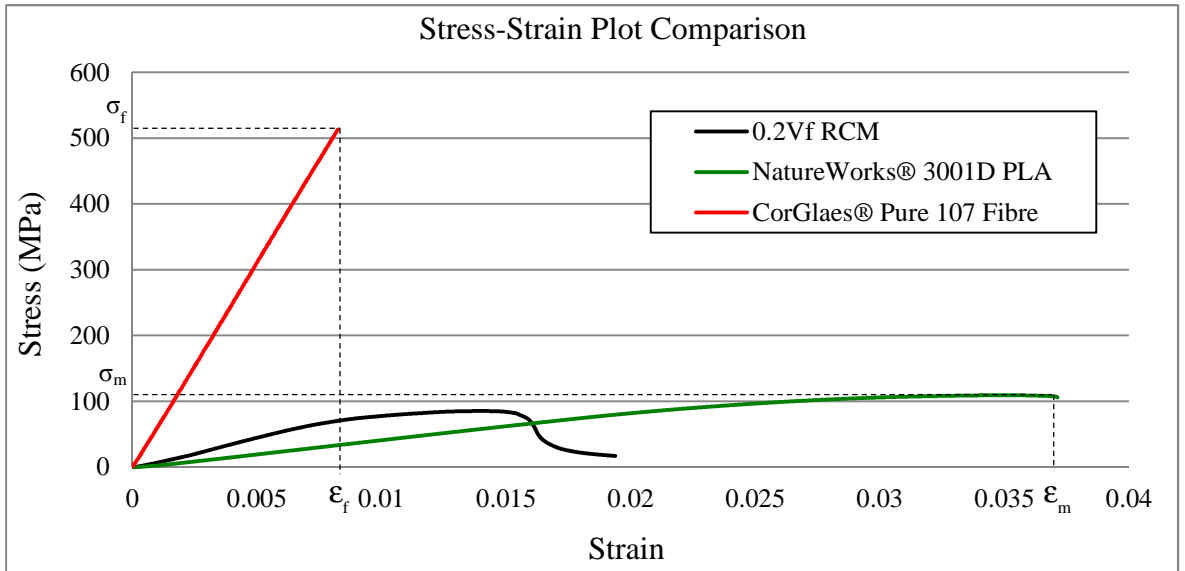


Figure 7.3.1. Stress-strain plots of CorGlaes® Pure 107 fibre (filler), NatureWorks® 3001D PLA polymer (matrix) and 0.2V_f RCM composite with the ultimate stress (σ_f/σ_m) and strain at failure (ϵ_f/ϵ_m) of each precursor phase indicated.

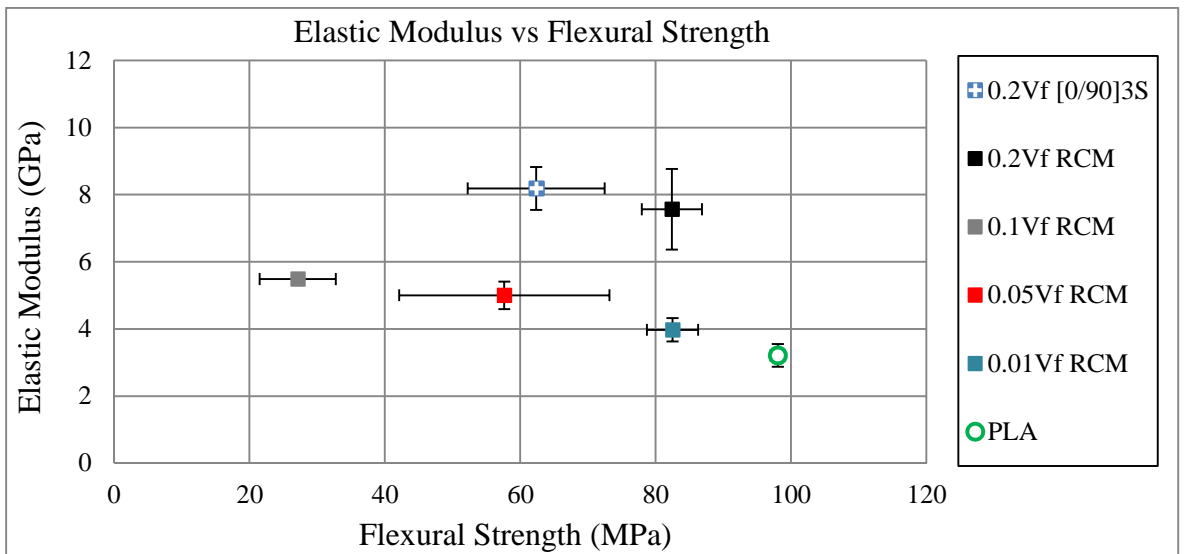


Figure 7.3.2. Variation in flexural strength and elastic modulus of CorGlaes® Pure 107 fibre-PLA composites with increasing fibre volume fraction (0→0.2V_f) and different fibre architectures (RCM and [0/90]_{3S}) alongside a PLA control.

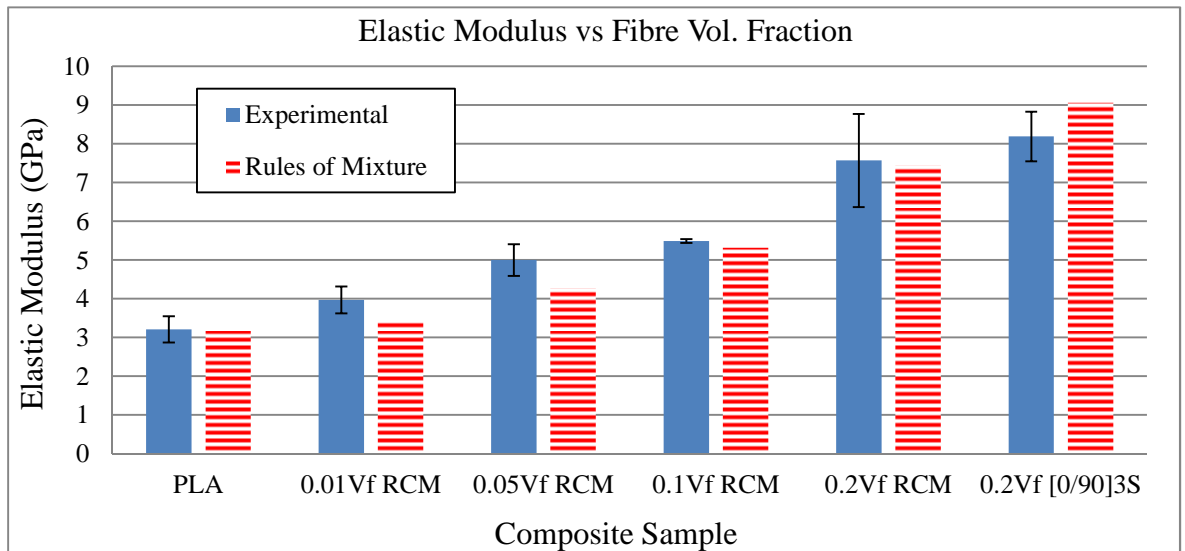


Figure 7.3.3. Comparison of experimental composite primary elastic modulus (E_1) with that predicted by the rule of mixtures model over different composite fibre volume fractions ($0 \rightarrow 0.2V_f$) and architectures (RCM, $[0/90]_{3S}$).

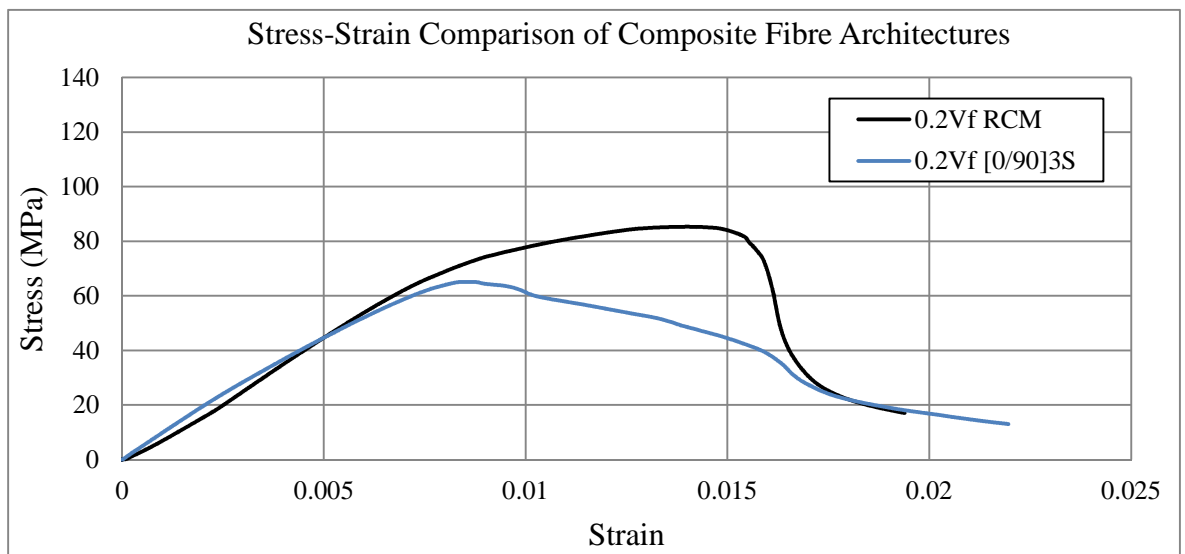


Figure 7.3.4. Comparison between stress-strain plots of $0.2V_f$ RCM and $0.2V_f [0/90]_{3S}$ composites obtained from three point bend testing according to BS EN ISO 14125:1998.

7.3.3 Degradation

7.3.3.1 Weight Loss and Mechanical Properties

The changes in wet and dry weight along with the media pH during degradation of the $0.2V_f$ RCM and $0.2V_f [0/90]_{3S}$ composites as well as a PLA control are shown in Figure 7.3.5 and Figure 7.3.6 respectively.

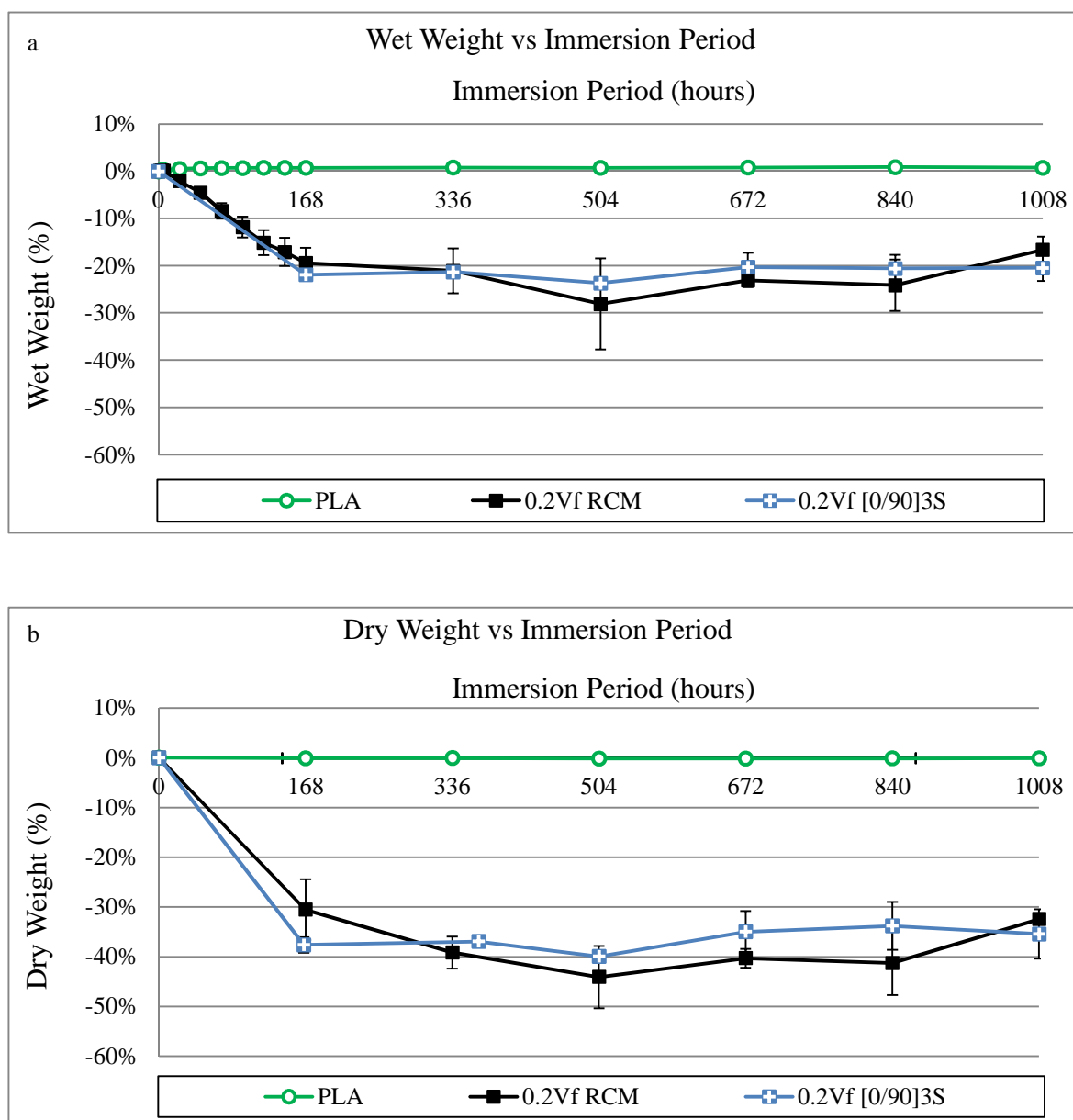


Figure 7.3.5. Degradation of $0.2V_f$ RCM and $0.2V_f [0/90]_{3S}$ composites in distilled water at 37°C along with a PLA control over 1008 hours (six weeks) showing a) Wet weight and b) Dry weight losses.

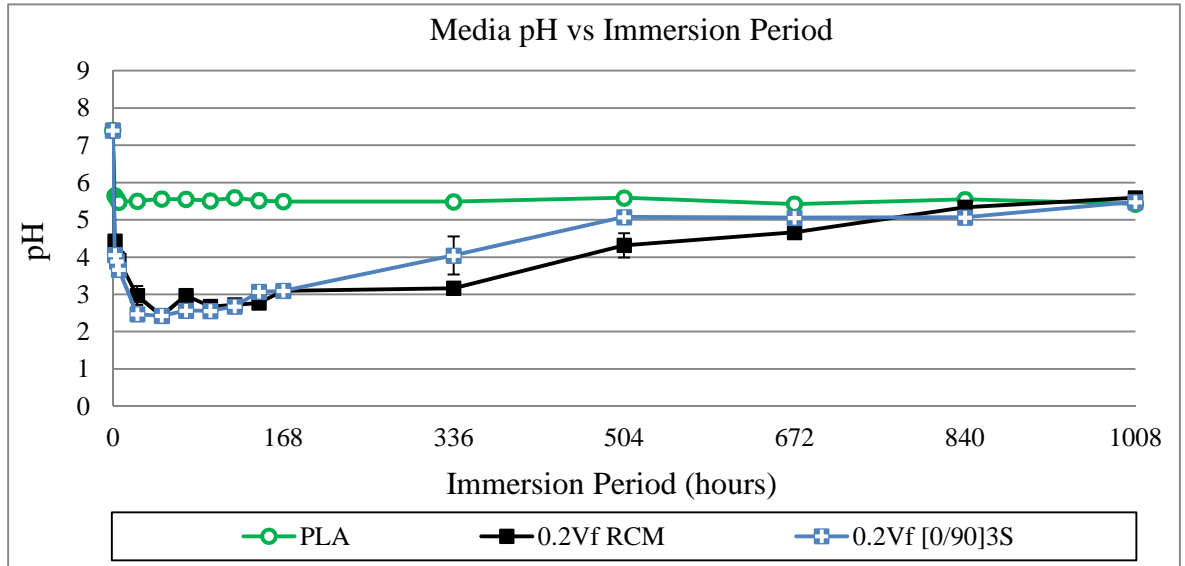


Figure 7.3.6. Media pH during 1008 hour (six week) degradation of 0.2V_f RCM and 0.2V_f [0/90]_{3S} composites along with a PLA control in distilled water at 37°C.

The flexural strength and elastic modulus of the corresponding samples after degradation in distilled water is shown in Figure 7.3.7 over 168 hour increments with SEM images of 0.2V_f RCM and PLA controls after the mechanical testing shown in Figure 7.3.8.

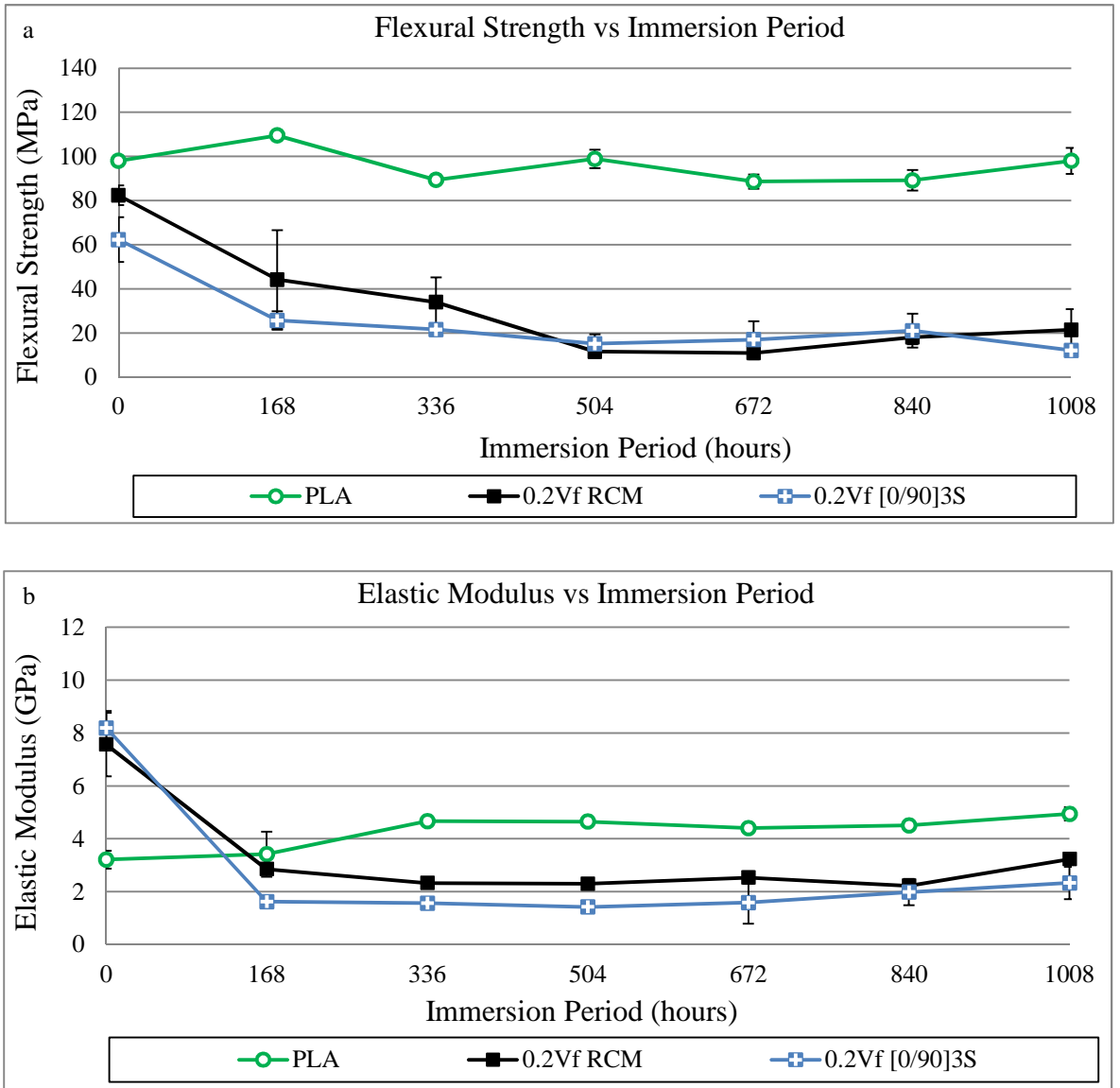


Figure 7.3.7. Comparison of a) Flexural strength and b) Elastic modulus during degradation of 0.2V_f RCM and 0.2V_f [0/90]_{3S} composites as well as a PLA control over 1008 hours (six weeks) in distilled water at 37°C.

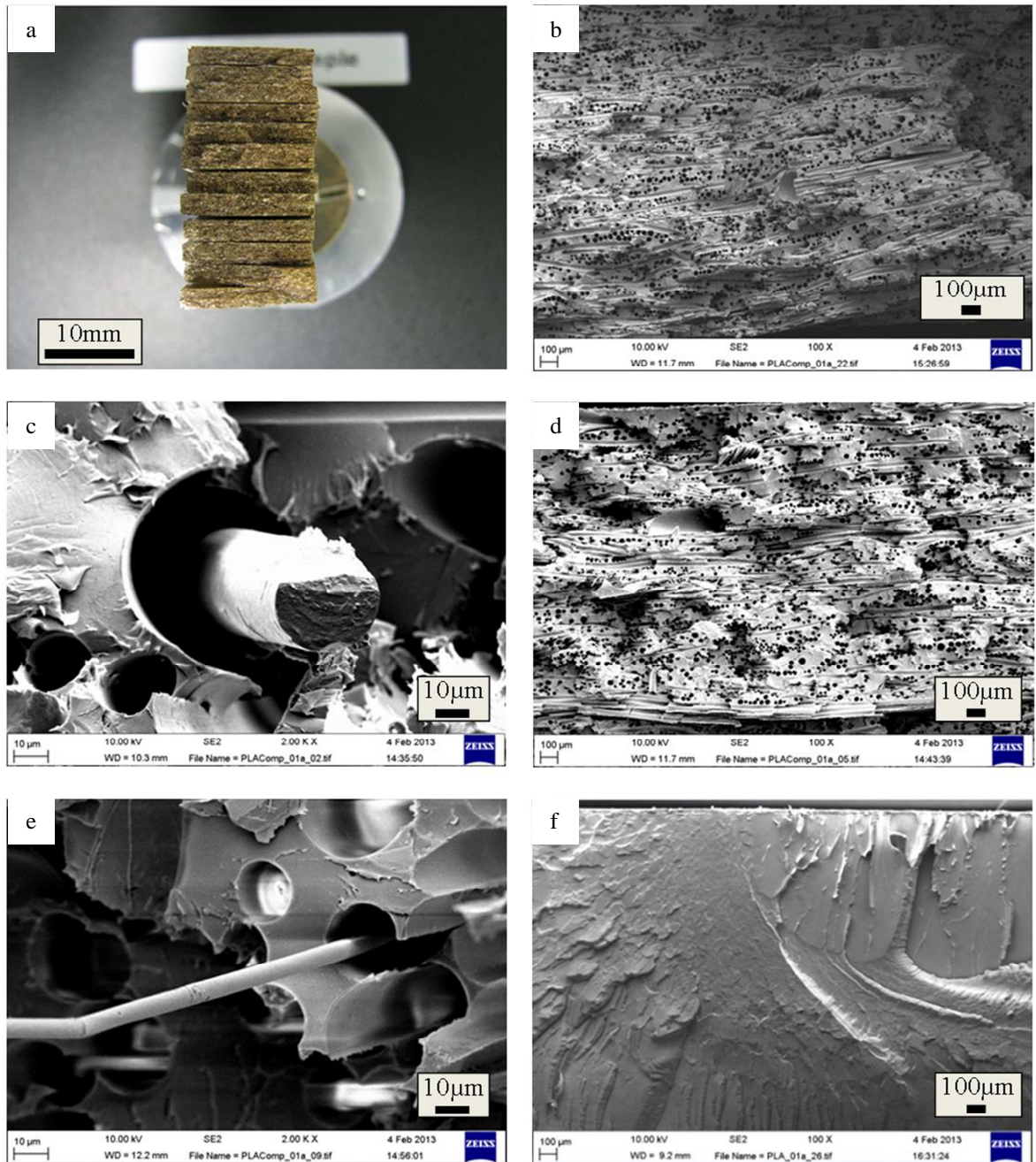


Figure 7.3.8. a) Fracture surfaces of degraded $0.2V_f$ RCM CorGlaes[®] Pure 107 composite samples after gold coating, SEM images of b) $0.2V_f$ RCM composite after 168 hours of degradation [scale bar = $100\mu\text{m}$] c) $0.2V_f$ RCM composite showing breakdown of fibre-matrix interface due to fibre dissolution after 168 hours [scale bar = $10\mu\text{m}$] d) $0.2V_f$ RCM composite after 336 hours of immersion [scale bar = $100\mu\text{m}$] e) $0.2V_f$ RCM composite after 504 hours of immersion [scale bar = $10\mu\text{m}$] f) PLA control fracture surfaces after 1008 hours of degradation [scale bar = $100\mu\text{m}$].

7.3.3.2 Ion Release

The daily and accumulative ionic concentrations of the immersion media over the first 168 hours of $0.2V_f$ RCM composite degradation are shown in Figure 7.3.9.

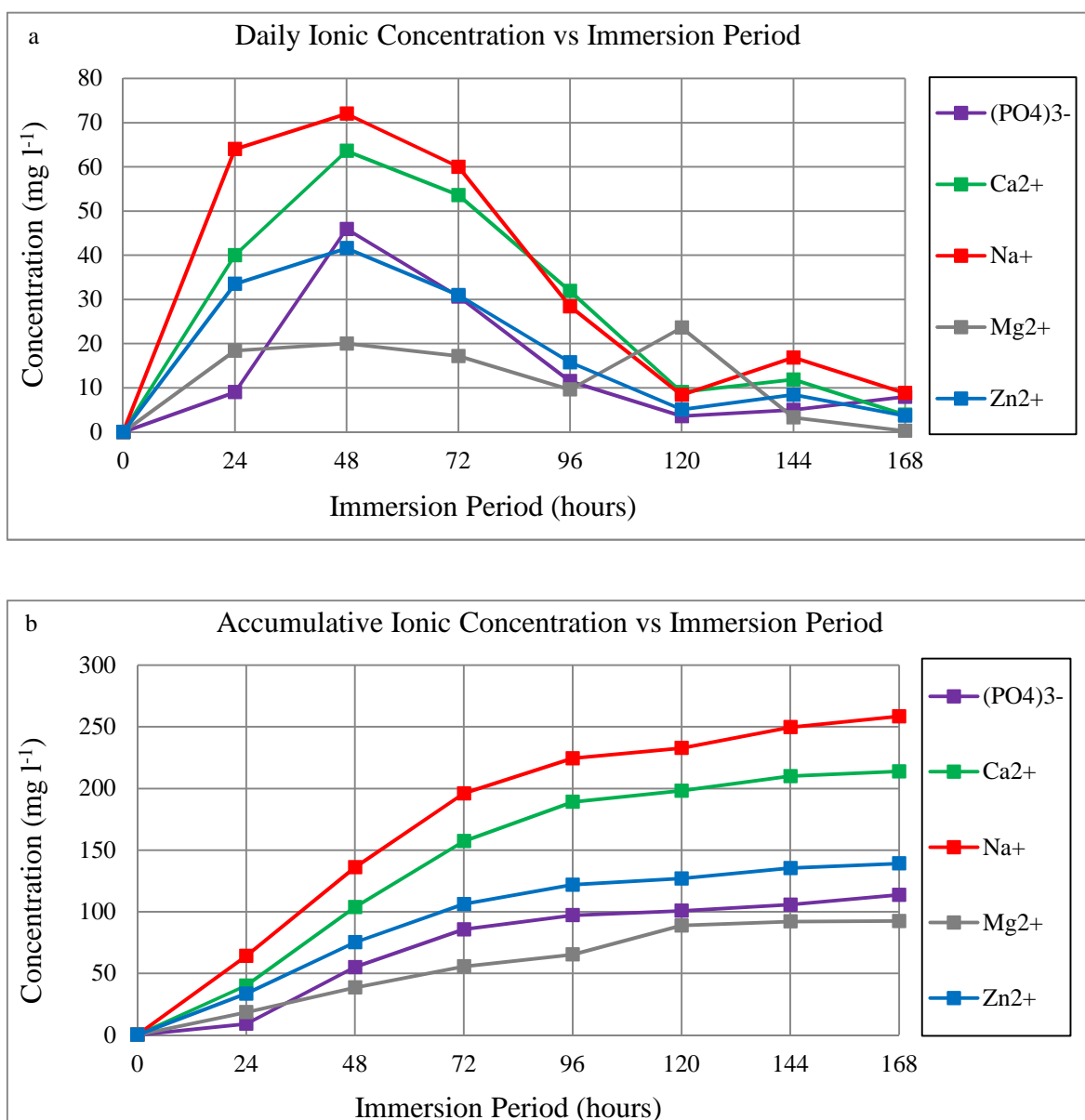


Figure 7.3.9. a) Daily ionic concentrations and b) Total accumulative ionic concentrations from $0.2V_f$ RCM composites over initial 168 hours of degradation in distilled water at $37^\circ C$.

7.3.4 DMEM Degradation

7.3.4.1 Weight Loss and Mechanical Properties

A comparison between the wet and dry weight during the degradation of 0.2V_f RCM composites in distilled water and acellular DMEM at 37°C is shown in Figure 7.3.10. Further comparisons between the media pH as well as the flexural strength and elastic moduli of the composites across the same degradation period are also shown in Figure 7.3.11 and Figure 7.3.12 respectively.

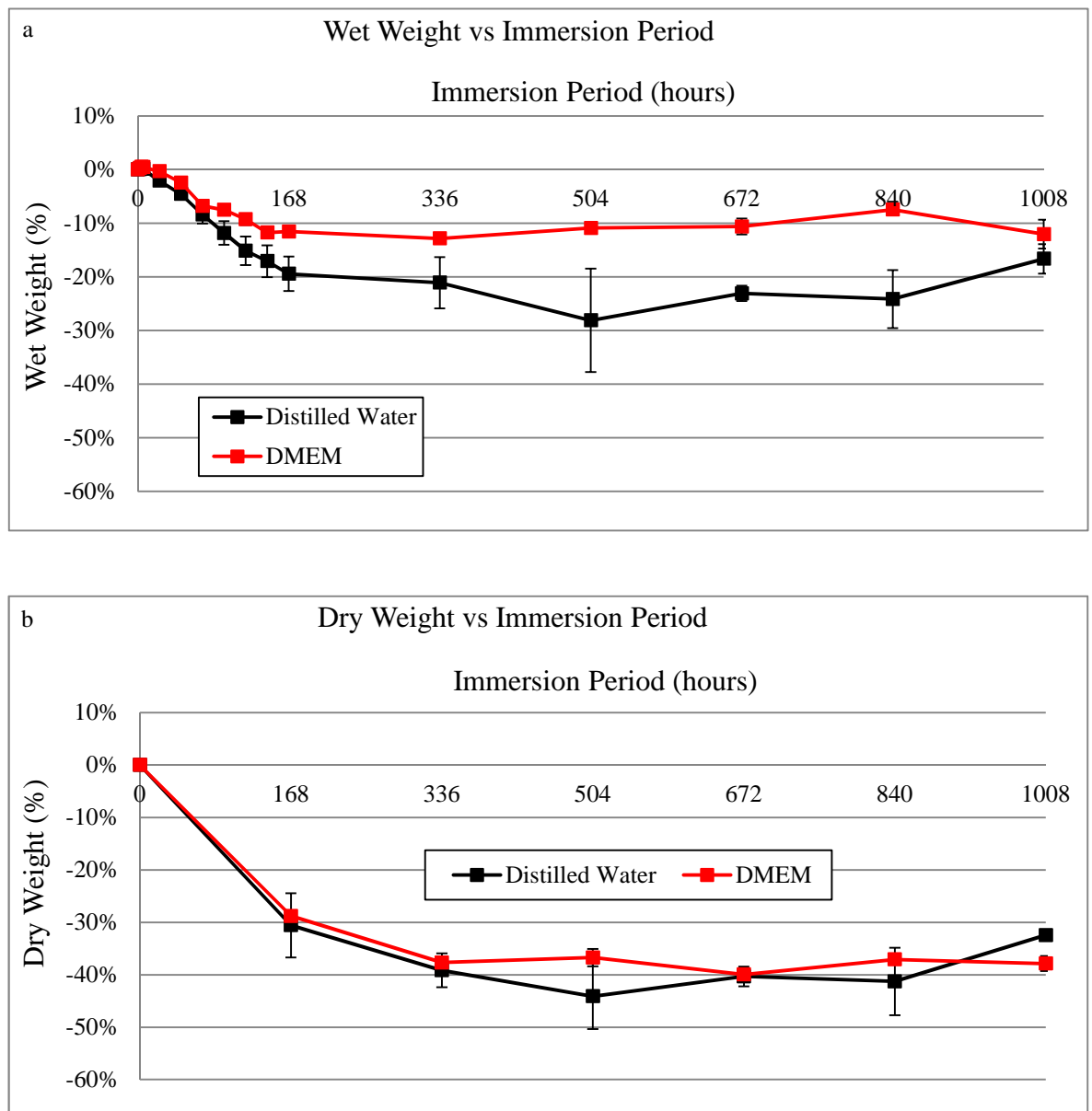


Figure 7.3.10. Comparison of a) Wet weight and b) Dry weight during degradation of 0.2V_f RCM composites in distilled water and DMEM over 1008 hours (six weeks) at 37°C.

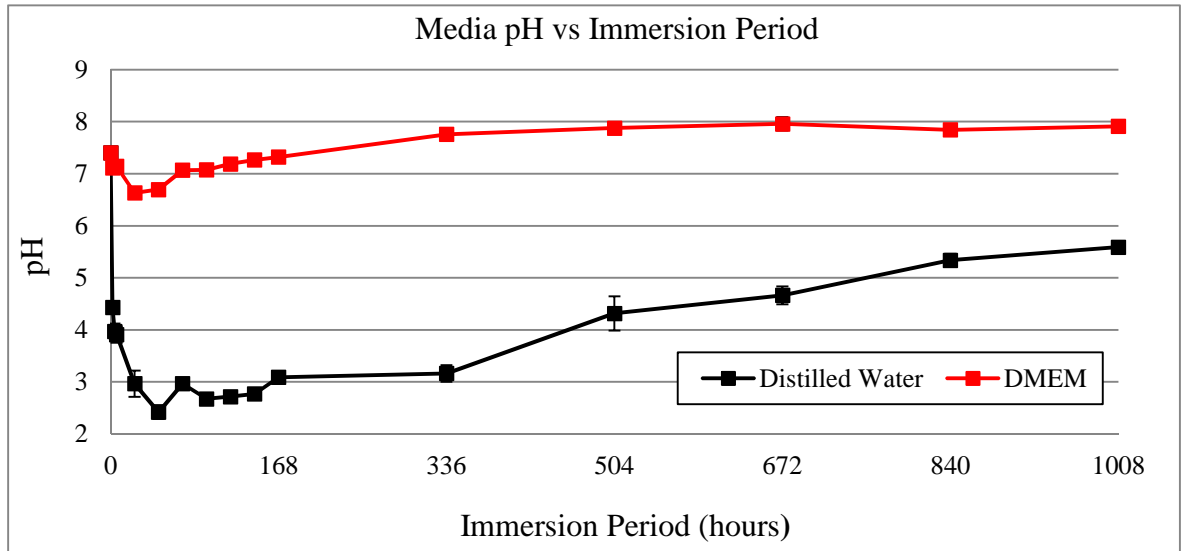


Figure 7.3.11. Comparison of media pH during $0.2V_f$ RCM composite degradation in distilled water and DMEM at 37°C over 1008 hours (standard deviation in DMEM $\leq \pm 0.06$).

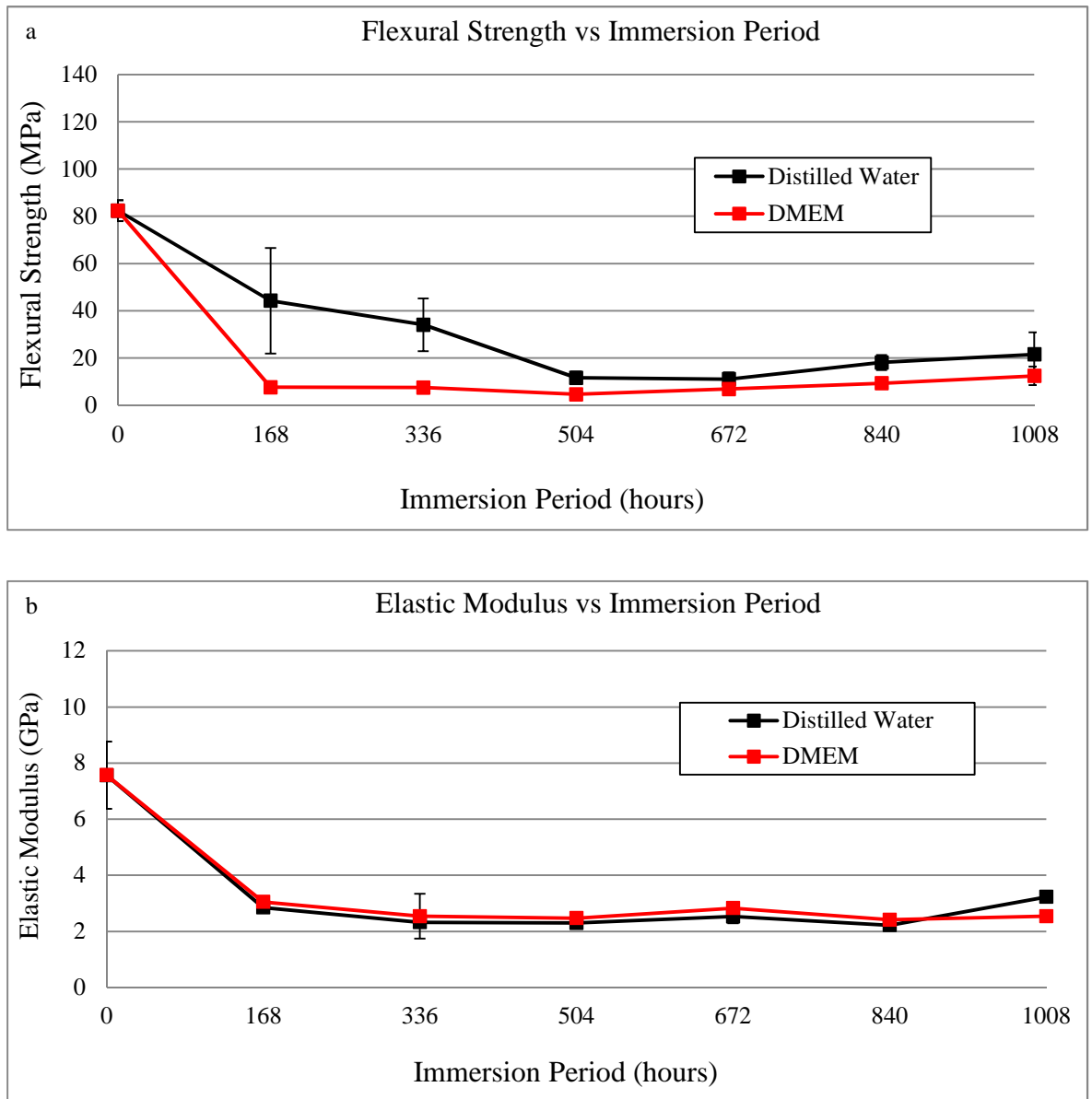


Figure 7.3.12. Comparison of a) 0.2V_f RCM composite flexural strength (standard deviation in DMEM $\leq \pm 4$ MPa) and b) 0.2V_f RCM composite elastic modulus during sample degradation in distilled water and DMEM over 1008 hours of degradation (standard deviation in DMEM $\leq \pm 0.8$ GPa).

7.3.4.2 Ion Release

The daily and accumulative ionic concentrations in the DMEM media during 0.2V_f RCM composite degradation is shown in Figure 7.3.13. The sodium (Na⁺) ionic concentration is shown separately from these results due to the significantly higher values that were observed which remained at ≈5000 mg l⁻¹ over the majority of the 168 hours (Figure 7.3.14).

Note: the DMEM ionic concentrations were not normalised with respect to its initial ionic constituents.

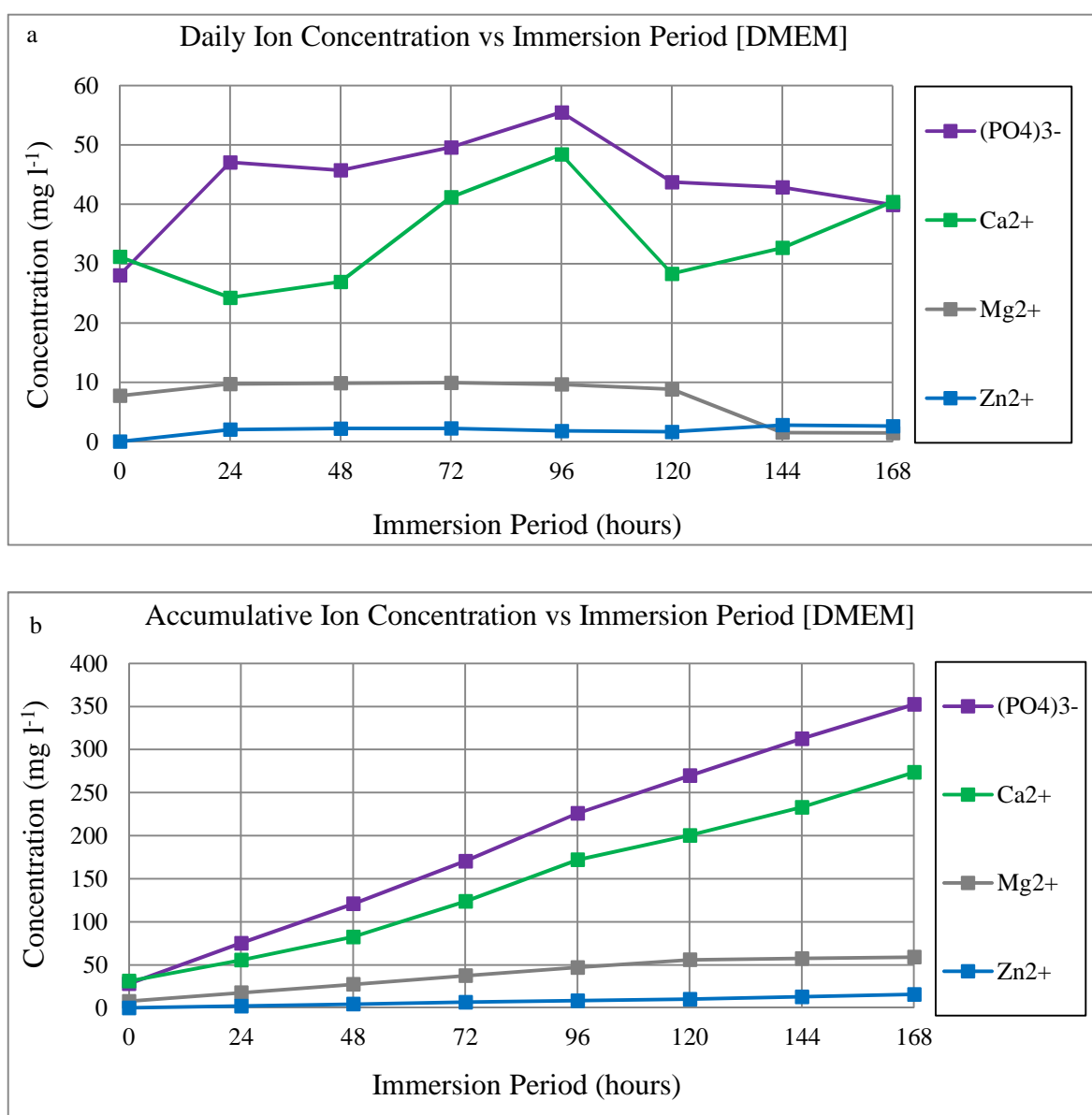


Figure 7.3.13. a) Daily ion release from 0.2V_f RCM composite during degradation in DMEM and b) Accumulative ion release from 0.2V_f RCM composite during degradation in DMEM over initial 168 hours.

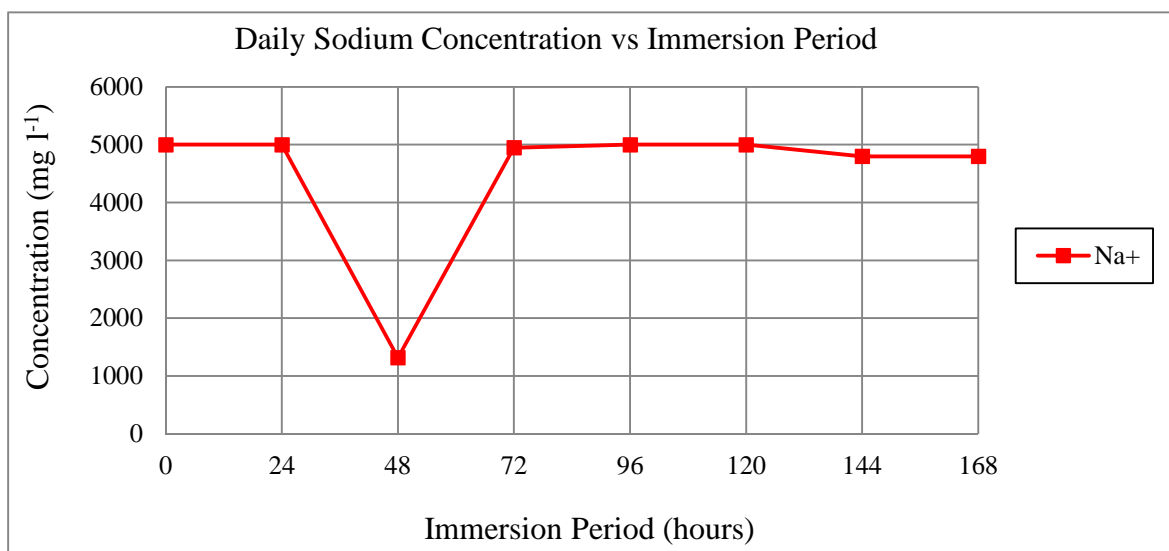


Figure 7.3.14. Daily sodium ionic concentration in DMEM during degradation of 0.2V_f RCM composite degradation over 168 hours.

During degradation of the 0.2 V_f RCM composite in DMEM it was observed that a white precipitate formed rapidly over the sample surface (Figure 7.3.15a) with larger fragments accumulating at the bottom of the vials. SEM analysis (Figure 7.3.15b-d) of fractured composites after DMEM degradation and mechanical testing also showed this precipitate to have formed within the pore voids created by the dissolution of the CorGlaes[®] Pure 107 fibres. Analysis of this precipitate by FTIR and its subsequent comparison with the CorGlaes[®] Pure 107 glass composition and CorGlaes[®] Pure 107 fibres after 336 hours of immersion in c-SBF is shown in Figure 7.3.16. An XRD trace of this precipitate is also shown in Figure 7.3.17.

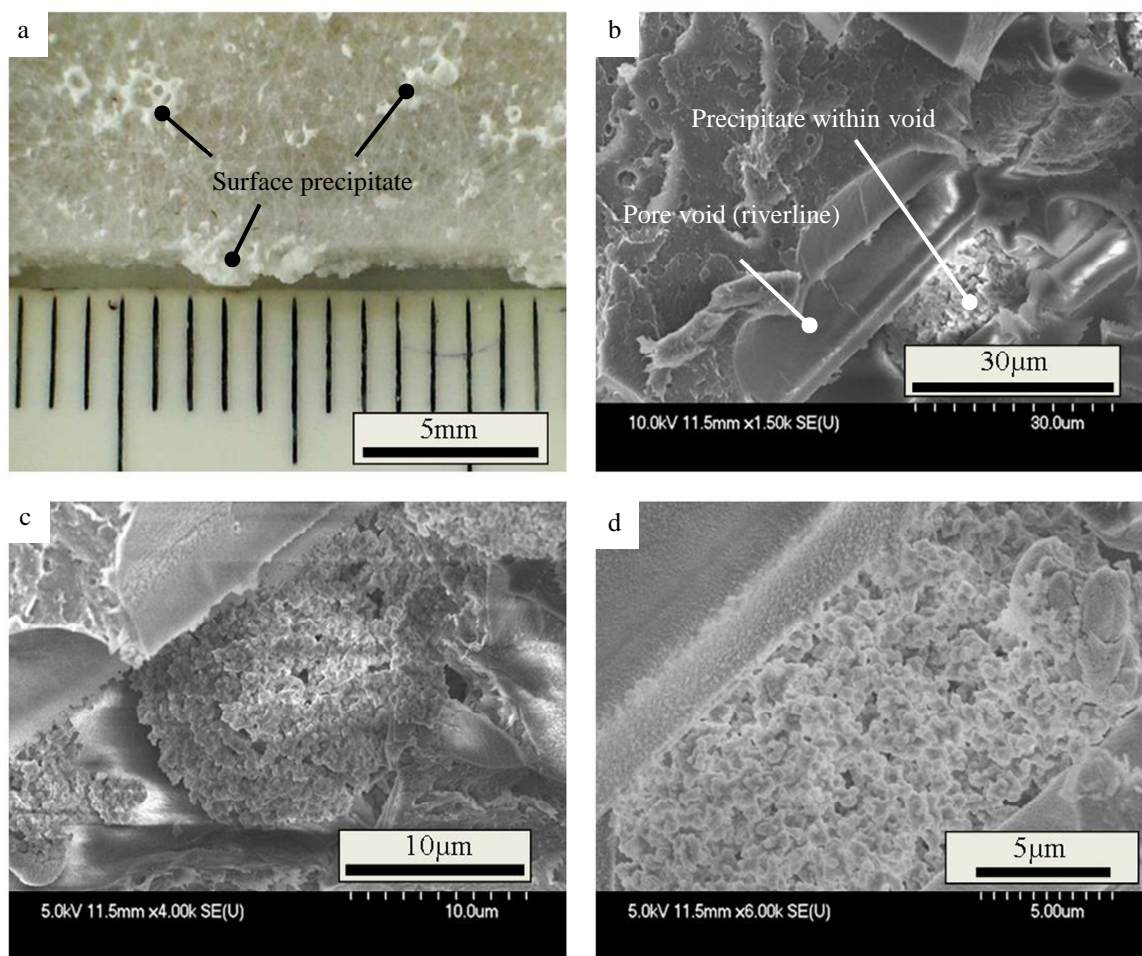


Figure 7.3.15. a) Surface image of the $0.2V_f$ RCM composite after 366 hours of degradation in DMEM [scale bar = 5mm] and b-d) SEM images of $0.2V_f$ RCM composite fracture sites after 336 hours of degradation in DMEM showing the formation of precipitants within the voids created by fibre dissolution [scale bars = $30\mu\text{m}$, $10\mu\text{m}$ and $5\mu\text{m}$].

Analysis of the FTIR spectra revealed that the precipitates formed possessed a structure similar to the deposits analysed during the previous bioactivity testing of the CorGlaes[®] Pure 107 fibres (section 6.3.7). This was evident by the appearance of a broad peak across $1200\text{-}1000\text{cm}^{-1}$ as well as across the $546\text{-}470\text{cm}^{-1}$ wavenumber range (Figure 7.3.16). The lack of any crystalline structure in the XRD trace also indicated that the precipitated phase possessed an amorphous structure with a broad weak halo centred at $2\theta \approx 30^\circ$ (Figure 7.3.17).

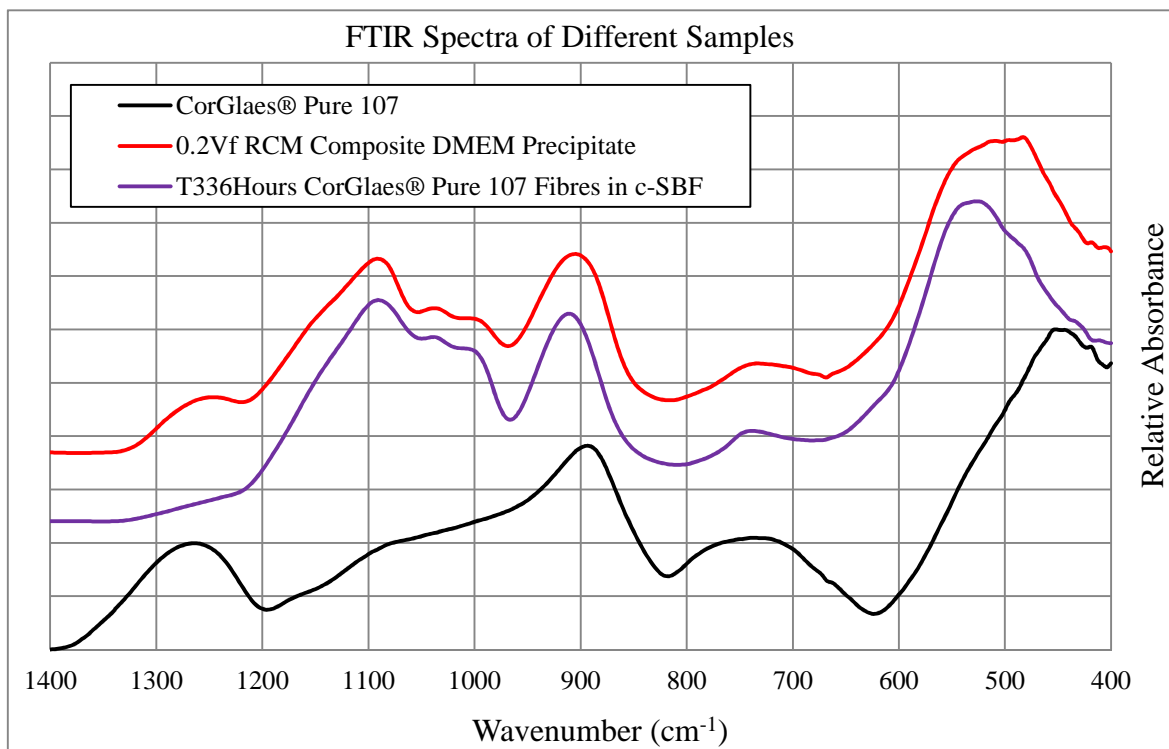


Figure 7.3.16. Comparison of FTIR spectra obtained from the precipitate formed during degradation of the 0.2V_f RCM composite in DMEM with the CorGlaes® Pure 107 composition and that obtained during bioactivity testing of CorGlaes® Pure 107 fibres after 336 hours of immersion in c-SBF.

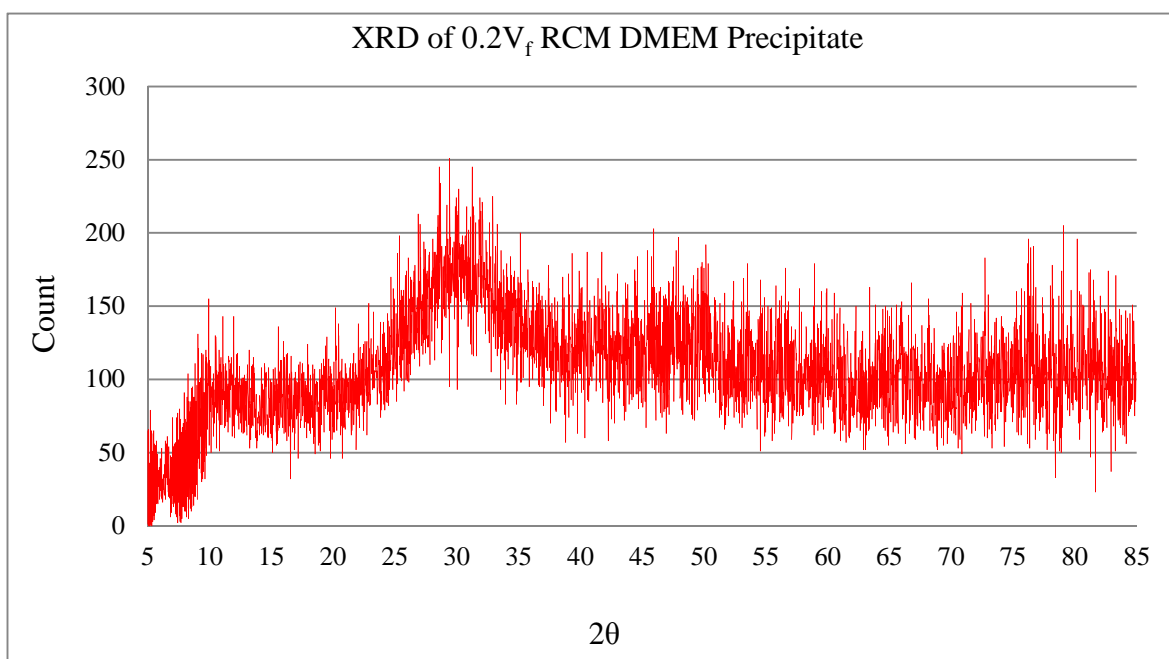


Figure 7.3.17. XRD trace of surface precipitate formed after 336 hours of 0.2V_f RCM composite degradation in DMEM showing an amorphous structure and halo at 2θ ≈ 30°.

7.3.5 Bioactivity

Images of 15x15x2mm 0.2V_f RCM composite samples after each immersion period in c-SBF is shown in Figure 7.3.18. The corresponding wet weight and c-SBF pH compared to that previously recorded during 0.2V_f RCM composite degradation in distilled water and DMEM are shown in Figure 7.3.19 and Figure 7.3.20 respectively.

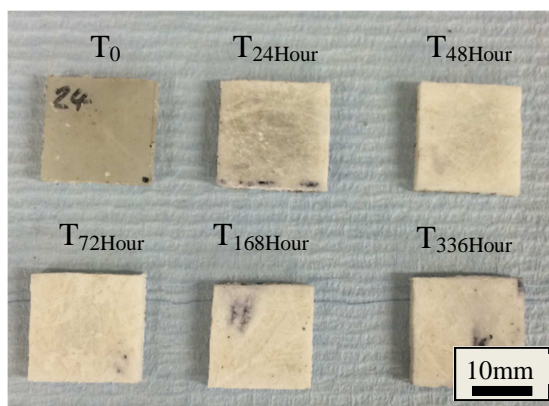


Figure 7.3.18. Images of 15x15x2mm 0.2V_f RCM composite samples over various immersion periods in c-SBF showing the formation of a surface precipitate with prolonged duration in c-SBF [scale bar = 10mm].

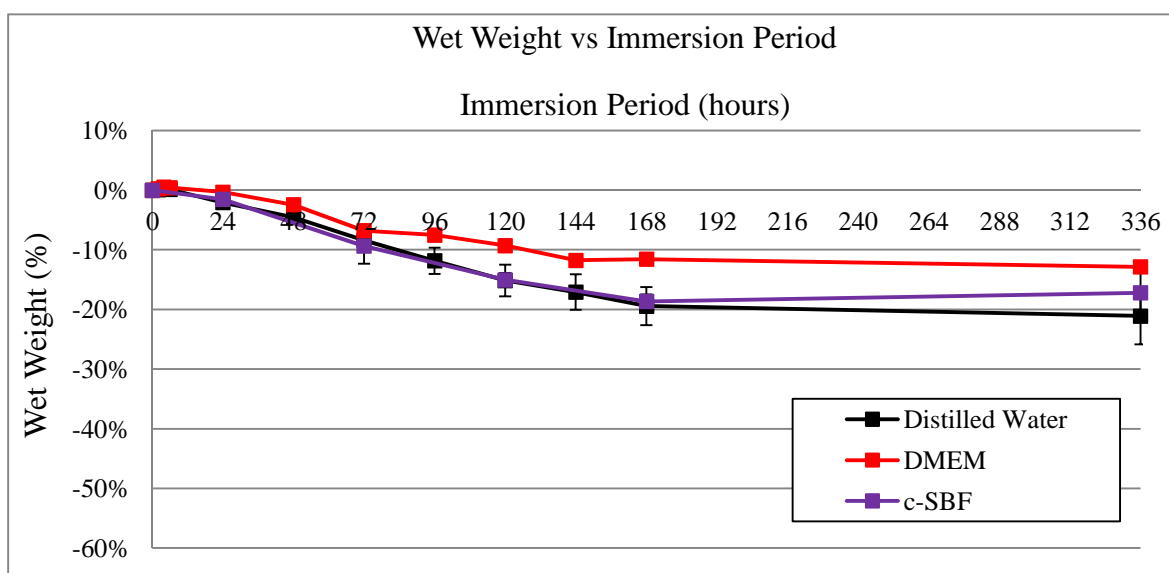


Figure 7.3.19. Comparison of 0.2V_f RCM composite wet weight during degradation in distilled water (SA:V = 0.21 cm² ml⁻¹), DMEM (SA:V = 0.21 cm² ml⁻¹) and c-SBF (SA:V = 0.1 cm² ml⁻¹).

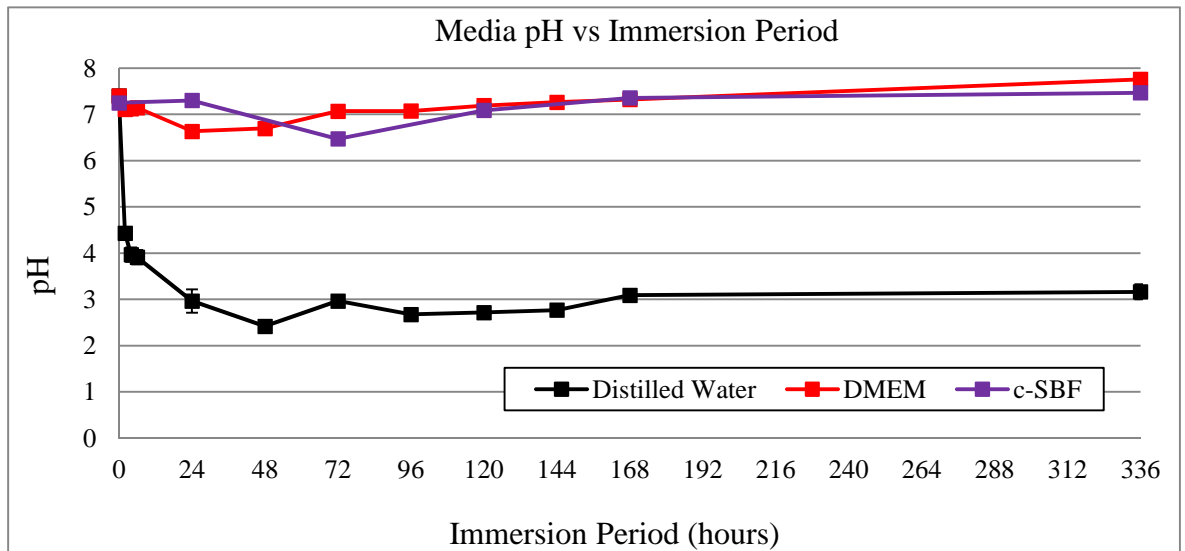


Figure 7.3.20. Comparison of media pH during degradation of $0.2V_f$ RCM composite in distilled water ($SA:V = 0.21 \text{ cm}^2 \text{ ml}^{-1}$), DMEM ($SA:V = 0.21 \text{ cm}^2 \text{ ml}^{-1}$) and c-SBF ($SA:V = 0.1 \text{ cm}^2 \text{ ml}^{-1}$).

The FTIR spectra of composite planar surfaces at each immersion period in c-SBF across the complete ($4000\text{-}400\text{cm}^{-1}$) and $1400\text{-}400\text{cm}^{-1}$ region of the spectra is shown in Figure 7.3.21. Compared with the initial composite surface FTIR spectrum, the results showed the formation of new peaks at 896cm^{-1} and $\approx 512\text{cm}^{-1}$ after 24 hours whilst continued immersion showed the gradual suppression in the intensity of peaks ranging from $1720\text{-}990\text{cm}^{-1}$. The shifting in peaks was also observed with increasing immersion time as the broad peak centred at 512cm^{-1} after 24 hours changed to 474cm^{-1} after 336 hours of immersion. FTIR spectra of the composite cross-sections were found to be identical to those collected from the planar faces.

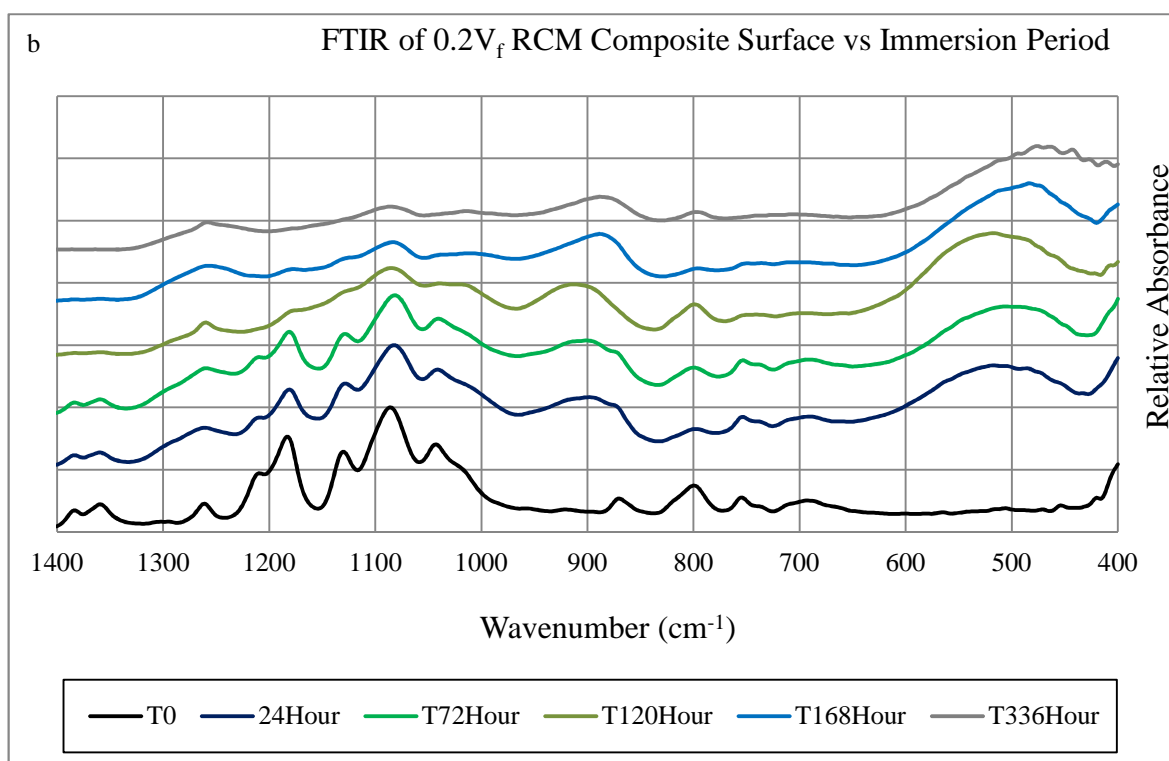
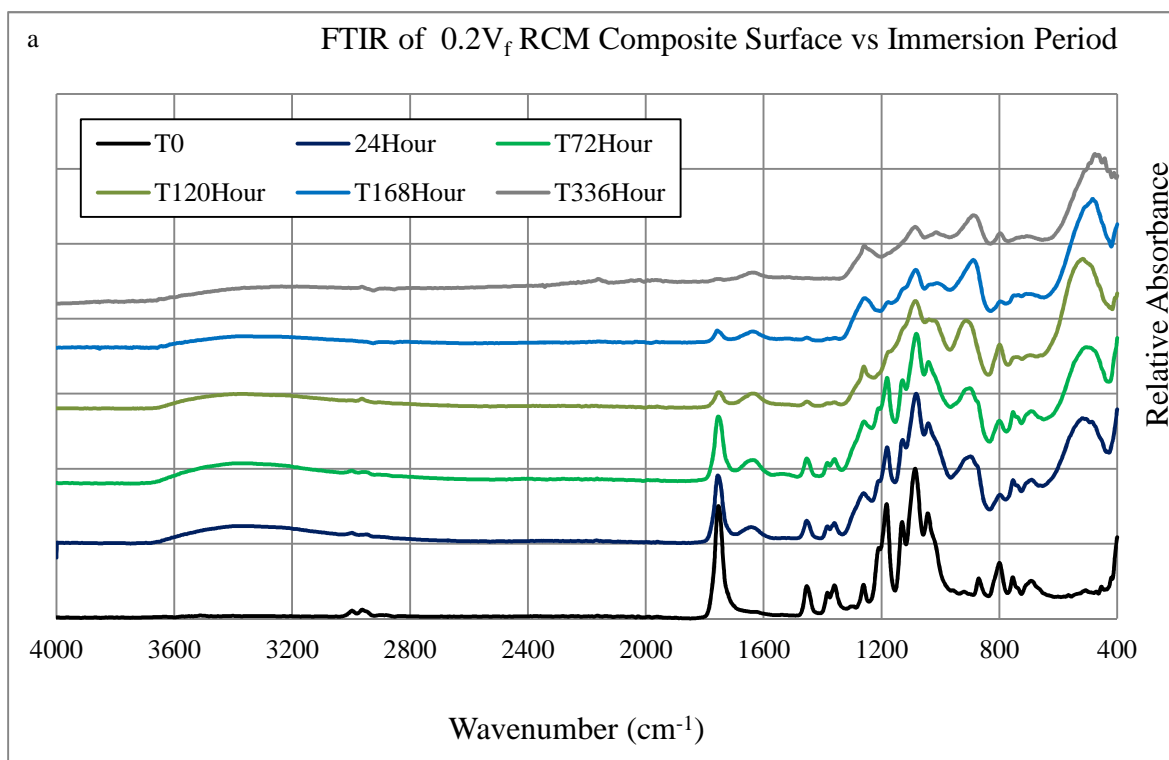


Figure 7.3.21. FTIR spectra of composite planar faces after immersion in c-SBF for up to 336 hours over a) $4000\text{-}400\text{cm}^{-1}$ and b) $1400\text{-}400\text{cm}^{-1}$ wavenumber ranges.

7.3.6 Biocompatibility

The MTT assay of MG63 cell viability using extracts from RCM composites with increasing fibre volume fraction and a PLA polymer control after 24 and 96 hours of degradation is shown in Figure 7.3.22 with the correlating media pH shown in Figure 7.3.23. Similarly, the MTT assay of degraded extracts from a 0.2V_f RCM composite at various concentrations (0.1, 10, 50, 100 vol%) after 24 and 96 hours of degradation in CDMEM is shown in Figure 7.3.24. Analysis of this data found a statistically significant difference between the fibre volume fractions ($p < 0.05$) (Figure 7.3.22) as well as the 0.2V_f extract concentrations on the cell viability compared to the positive controls (Figure 7.3.24) ($p < 0.05$).

Due to the observed cytotoxicity found in the MTT results, no direct contact cell culture and Live/Dead[®] staining was performed.

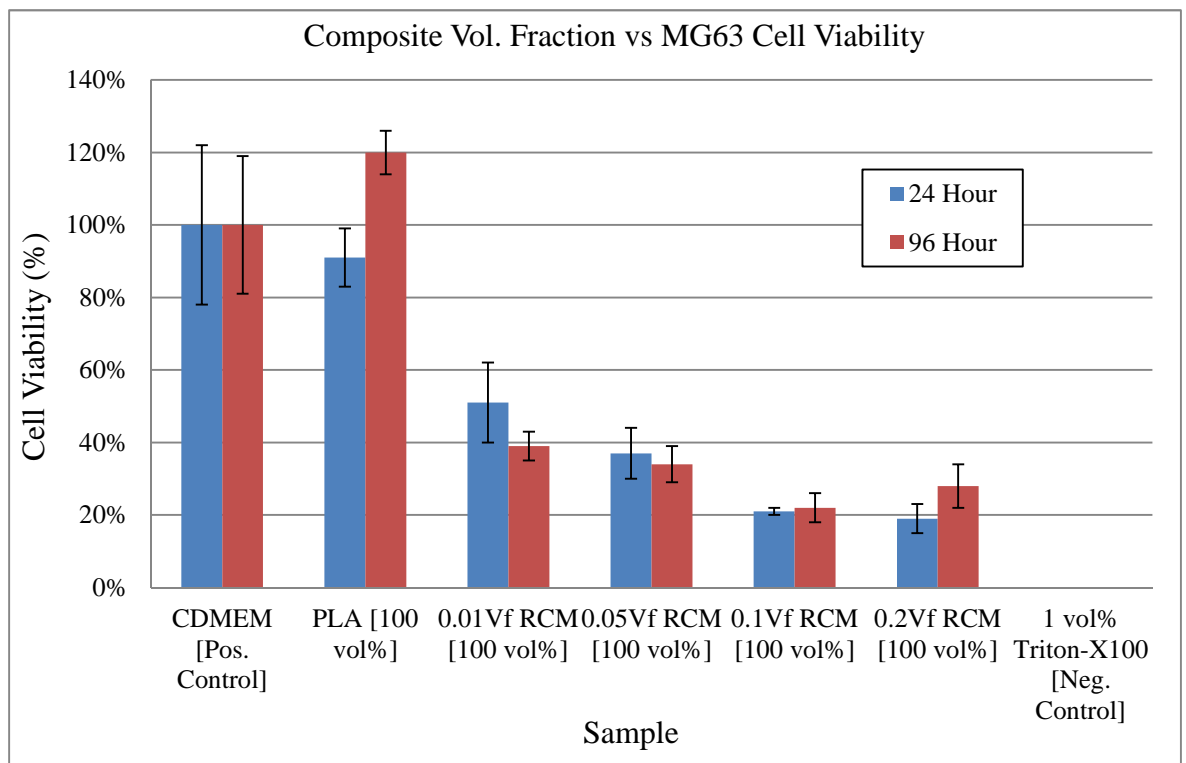


Figure 7.3.22. Comparison of degradation media cytotoxicity from NatureWorks[®] 3001D PLA and CorGlaes[®] Pure 107 fibre-PLA composites with increasing fibre volume fraction (0→0.2V_f) on MG63 cell viability using MTT assay.

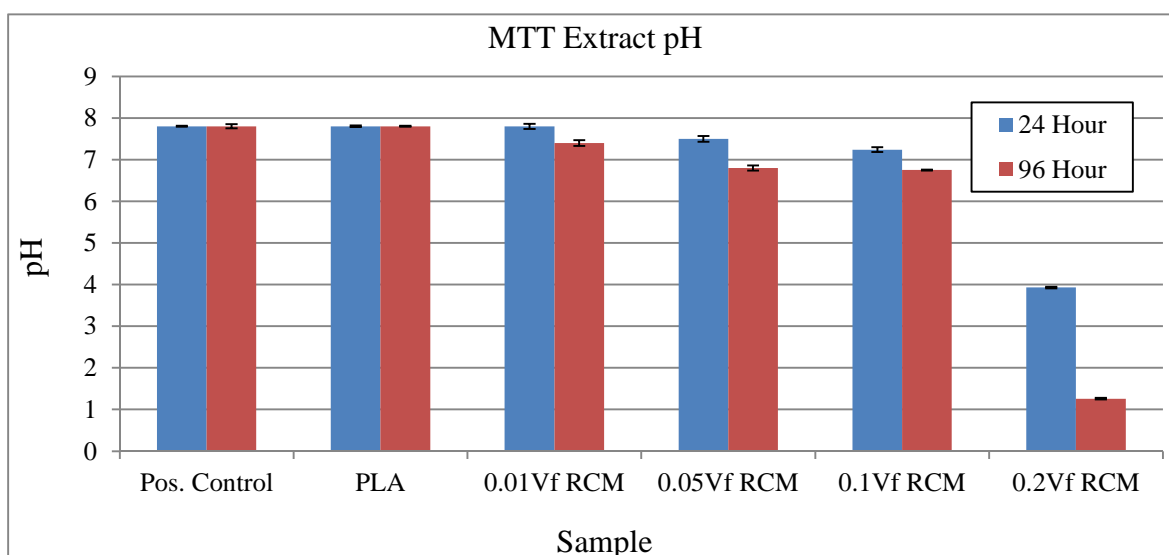


Figure 7.3.23. Media extract pH from composite samples and positive controls after 24 and 96 hours of degradation used in MTT assay.

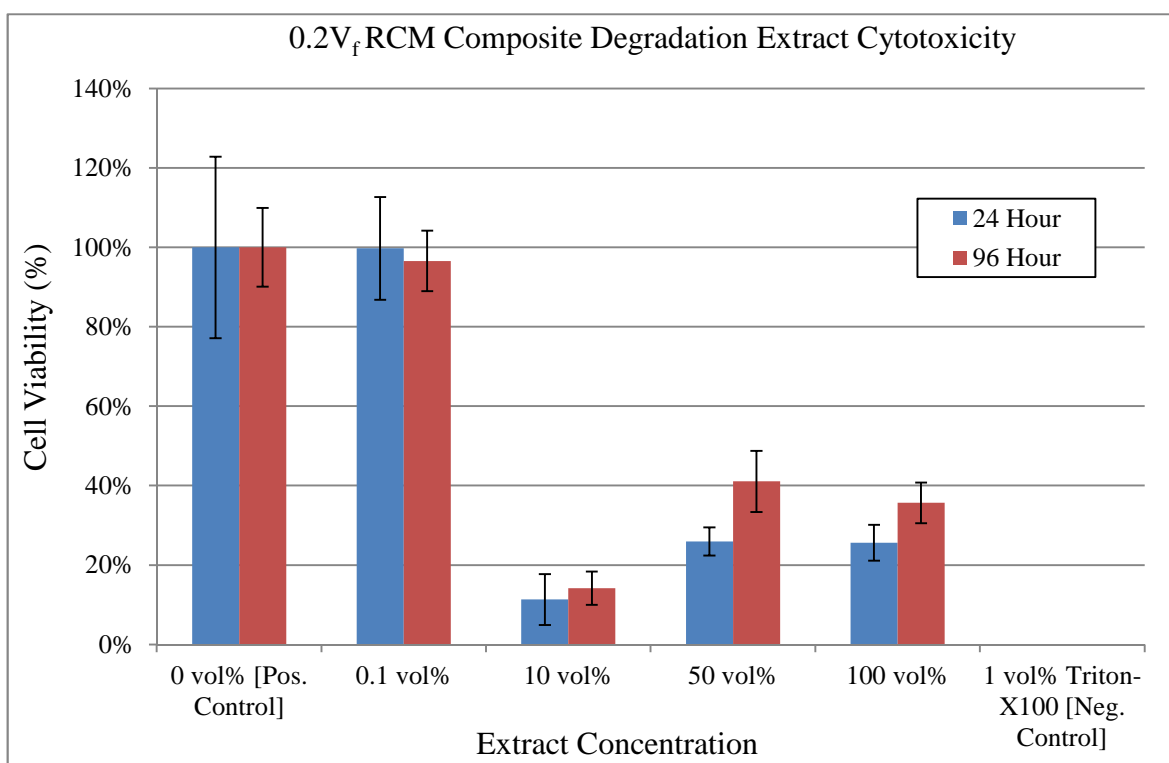


Figure 7.3.24. Degradation extract concentration from 0.2V_f RCM CorGlaes[®] Pure 107 composite on MG63 cell viability using MTT assay after 24 and 96 hours of degradation.

7.4 Discussion

Analysis of the OrientationJ[®] results (Table 7.3.1) obtained from unidirectional (UD) and random continuous fibre mat (RCM) pre-pregs showed a high degree of coherency (83%) in the orientation of the UD fibre mats that was close to those obtained from the aligned control images (100%). However the RCM pre-pregs also showed a degree of coherency (30%) in their primary orientation that was substantially higher than the idealised random control image (3%). This was attributed to the manual expansion method employed when manipulating the CorGlaes[®] Pure 107 fibres into randomly orientated mats and the attenuation around the hand driven mandrill that, as the results have shown, appeared to impart some preferential orientation in the RCM pre-preg mats.

Mechanical testing of the CorGlaes[®] Pure 107 fibre composites at different fibre volume fractions and architectures showed the expected increase in elastic modulus with increasing fibre volume fraction (V_f) compared to the PLA control (Ahmed et al., 2008; Mohammadi et al., 2012). The tensile fractures observed at the outermost layer of the composites during mechanical testing and absence of delamination also indicated that successful bonding between the composite lamina had occurred during sample manufacturing. The increased strain to failure and plastic deformation of the PLA control (ϵ_m) compared to the CorGlaes[®] Pure 107 fibre (ϵ_f) was also expected with the use of a polymer matrix ($\epsilon_m > \epsilon_f$) (Figure 7.3.1). However despite the increase in modulus, a reduction in the flexural strength was found in all composite samples below the neat PLA control (Figure 7.3.2). This could be attributed to several factors such as the inclusion of flaws into the matrix through fibre introduction, localised deviations in the composite V_f , fibre handling and subsequent fibre damage during composite manufacturing as well as the quality of fibre-matrix interface. This is related to the infiltration of the polymer resin into the reinforcing fibres (since solvent casting was not performed for $0.01V_f$ and $0.05V_f$ samples) ^[169, 215].

A comparison between the $0.2V_f$ RCM and $0.2V_f [0/90]_{3S}$ samples showed a distinct contrast in their mechanical properties and failure behaviour (Figure 7.3.4). This was evident by the increased flexural strength and plastic deformation found in the $0.2V_f$ RCM composites that was attributed to the difference in fibre architecture between samples. The area under the respective stress-strain plots also showed that the energy absorbed by the RCM composite configuration was greater than the $[0/90]_{3S}$ architecture, but remained below the PLA control (Table 7.4.1).

Table 7.4.1. Comparison of average sample toughness based on the area under the stress-strain plots recorded for each type of composite and control sample shown in Figure 7.3.4.

| Sample | Toughness (J m^{-3}) |
|----------------------|---------------------------------|
| PLA Control | 2.48 ± 0.06 |
| $0.2V_f$ RCM | 1.01 ± 0.01 |
| $0.2V_f [0/90]_{3S}$ | 0.69 ± 0.11 |

Accordingly, the increased flexural strength was believed to be due to the improved polymer infiltration of the RCM mats and subsequent improvement to the fibre-matrix interface compared to the aligned pre-preg lamina. Meanwhile the increased plastic deformation and toughness of the $0.2V_f$ RCM samples was attributed to their random, interlocking 2D architectures that were expected to possess localised areas of overlapping fibre intersections similar to those encountered in braided or woven fibre mats. These features are considered by Karbhari & Strassler (2007) to be capable of locally entrapping microcracks and serve as crack arrestors during composite fracture, but would also have likely had an effect on the frictional slippage occurring during fibre-pull out (section 3.2.3.1). The ability of these fibre intersections to distribute external stresses over a larger substrate area is also believed to result in an increased strain energy absorption which would correlate with the results shown in Table 7.4.1. In contrast, the parallel aligned fibres of the $[0/90]_{3S}$ lamina can allow unconstrained microcracking and splitting of the matrix to occur between fibres if they are not aligned perfectly parallel to the loading direction (Karbhari & Strassler, 2007). This would then corroborate with the observed fibre wrinkling/waviness and the imperfect fibre alignment (83%) identified from the OrientationJ results for the aligned CorGlaes[®] Pure 107 pre-pregs that was incurred from the hand lay-up method employed in composite manufacturing^[219, 337, 338].

These experimental values also appeared to correlate with those predicted by the rule of mixtures model for the different fibre volume fractions and architectures in the manufactured composites (Figure 7.3.3). The increased elastic moduli values obtained experimentally for the RCM composites was attributed to the unwanted degree of coherency found in the RCM architecture (Table 7.3.1) as well as the potential extrusion of materials from the mould (Figure 7.4.1). The extrusion of small quantities of polymer matrix during composite manufacturing would have subsequently raised the volume

fraction of the composite above the predetermined V_f . However this increase was considered to be marginal given that the extrusion of 0.07-1.66g of polymer matrix was calculated to only increase the composite volume fraction from the target $0.2V_f$ to $0.21V_f$.

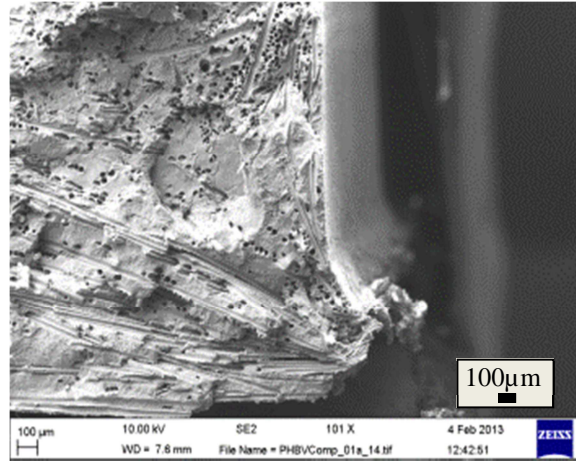


Figure 7.4.1. SEM of a degraded $0.2V_f$ RCM composite with the riverlines created from fibre degradation illustrating the shift in fibre dispersion due to the extrusion of the polymer matrix from the mould during manufacturing [scale bar = $100\mu\text{m}$].

Based on this, the increased experimental values shown for all RCM composites was believed to be due to the degree of anisotropy in the RCM composite architecture that could have been unexpectedly preferentially aligned parallel to the primary loading axis. This would have then conflicted with the correction factor (n_o) used in the rule of mixtures model (Eqn 7.2.6) that assumed a perfectly even and randomised distribution of 2D fibre orientations throughout each composite lamina. This would subsequently be in line with the increased experimental data observed by Ahmed et al. (2011) where instances of unwanted preferential orientation in composite samples were unable to be accounted for by the fibre orientation correction factor (n_o)^[219]. Meanwhile the decrease in experimental elastic modulus for the $0.2V_f$ $[0/90]_{3S}$ composites compared to the predicted values was attributed to the idealisations applied in the rule of mixtures which would not hold true in practical samples. These included the uniform filler distribution, absence of voids, perfect fibre-matrix interface and that both phases act in a linearly elastic manner (Ahmed et al. 2011)^[219].

Additionally, comparisons also showed that both the $0.2V_f$ RCM and $0.2V_f$ $[0/90]_{3S}$ composite samples possessed mechanical properties within the lower range of those

reported for the parietal bones by Motherway et al. (2009). However given its improved toughness and increased flexural strength, the $0.2V_f$ RCM composite was deemed more suitable for the target application as part of a cranioplasty plate implant device (Figure 7.4.2) ^[339, 340].

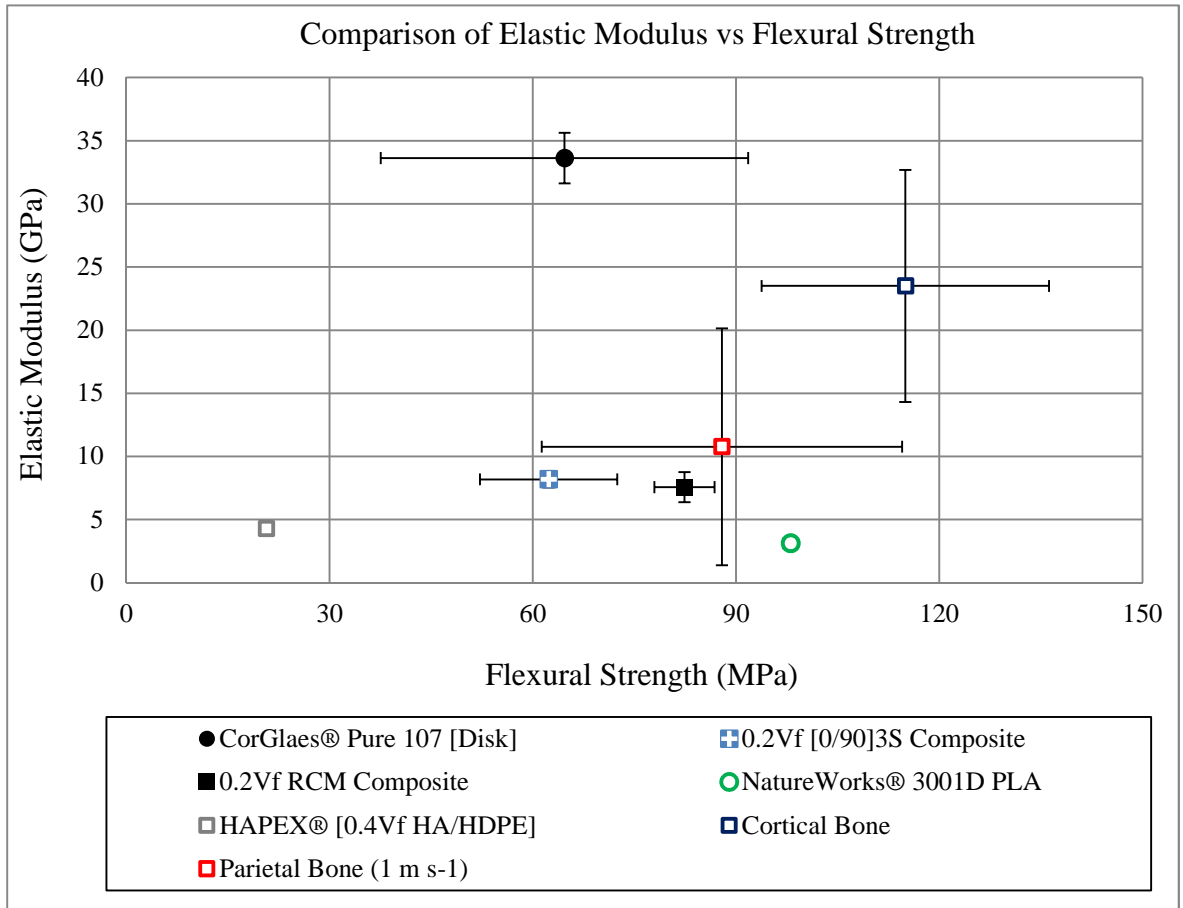


Figure 7.4.2. Comparison of $0.2V_f$ and $0.2V_f [0/90]_{3S}$ composite mechanical properties with the composite precursor materials, cortical/parietal bone and HAPEX® [Data from Motherway et al., 2009; Ratner, 2012; Tjong, 2012].

A comparison with the alternate phosphate glass fibre composites investigated in the literature (Figure 7.4.3) showed that the mechanical properties of the $0.2V_f$ CorGlaes® Pure 107 composites were within the expected values given the variation in fibre architecture, matrix/filler properties and fibre volume fractions in the comparative data. This is demonstrated by the general trend of increasing mechanical properties with increasing fibre volume fraction as well increasing properties between different composite architectures (chopped < orientated < unidirectional fibres) as discussed in section 3.2.3 ^[215, 219, 222, 223, 341].

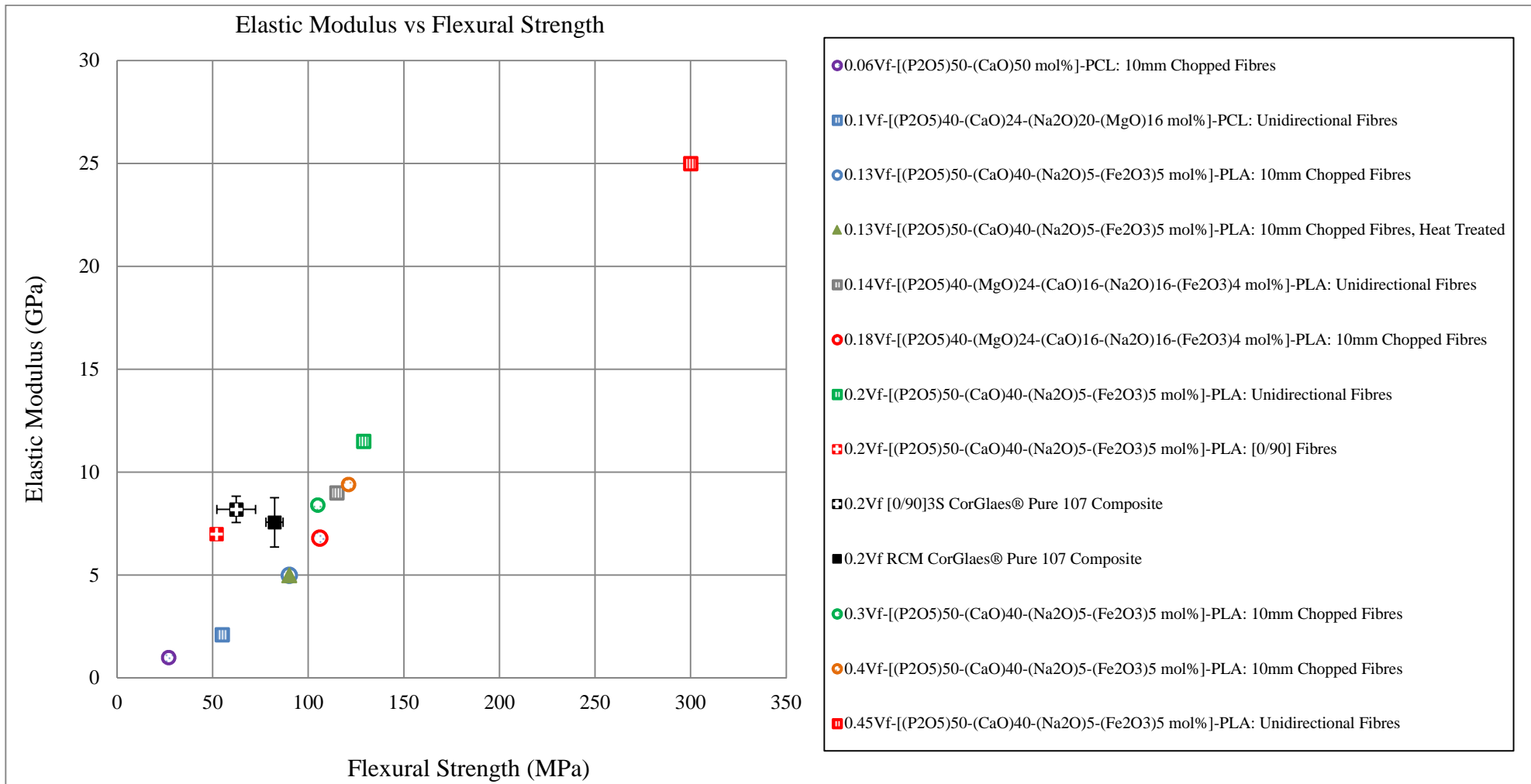


Figure 7.4.3. Comparison of PGF composites mechanical properties with 0.2V_f RCM and 0.2V_f [0/90]_{3S} CorGlaes[®] Pure 107 composites – arranged by increasing V_f [Data from Ahmed et al., 2008; Khan et al., 2010; Ahmed et al., 2011; Felfel et al., 2012; Han et al., 2013].

Degradation of the $0.2V_f$ RCM composites and PLA control showed an initial increase in the wet weight ($\approx 0.2\%$) after 4 hours of immersion (Figure 7.4.4). This was associated with the diffusion of degradation media into the PLA polymer matrix and was in line with previous results as reported by Onal et al. (2007) and Ahmed et al. (2011) ^[219, 325].

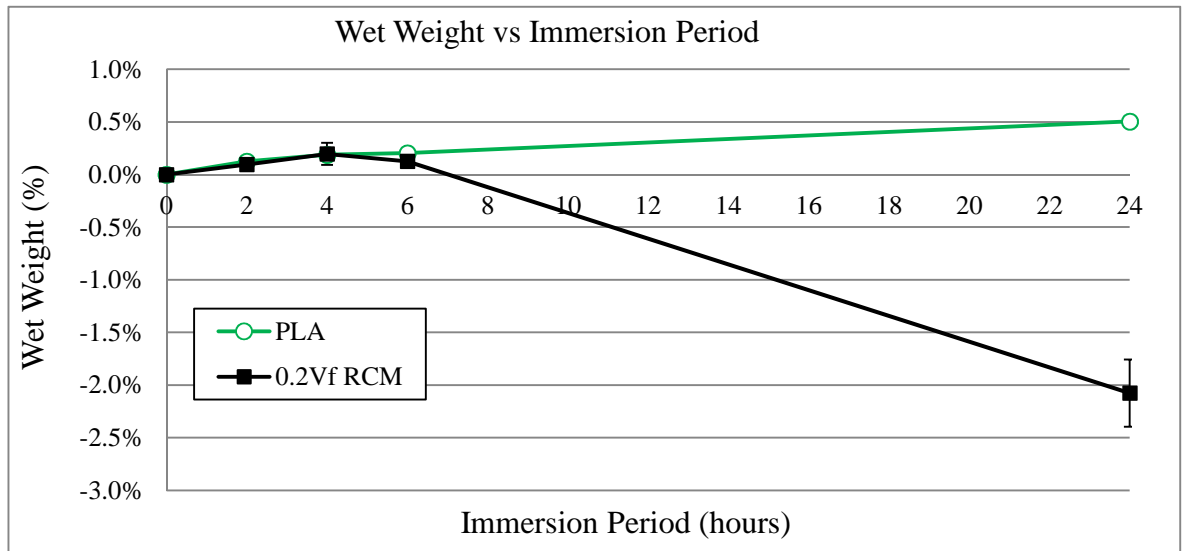


Figure 7.4.4. Comparison of $0.2V_f$ RCM composite and PLA control wet weight over initial 24 hours of degradation showing equal rates of media uptake in both samples after 4 hours of degradation.

However after 4 hours, the $0.2V_f$ RCM composite showed a steady decrease in its wet weight that was attributed to the dissolution of the CorGlaes[®] Pure 107 fibres when compared to the PLA control which continued to slowly increase. The reduction in composite wet weight continued until it appeared to plateau at approximately -20% to -25% after 168 hours of degradation (Figure 7.3.5). This plateau was interpreted as signalling the near complete dissolution of the CorGlaes[®] Pure 107 fibres and was contrasted by the PLA control that appeared to become saturated after 72 to 96 hours at an increased wet weight of $\approx 0.7\%$. Such time scales of polymer saturation and fibre dissolution were found to be in line with previous studies such as those conducted by Ahmed et al. (2011), Felfel et al. (2012) and Han et al. (2013). The correlating dry weight of all composite samples mirrored this trend but showed a greater dry weight loss compared to the equivalent wet weight (Figure 7.4.5). This was accounted for by the voids generated in the composite from fibre dissolution (Figure 7.3.8b-e) that could act as

reservoirs for the immersion media during sample weight measurements prior to drying as discussed by Ahmed et al. (2008) ^[215, 219, 222, 223].

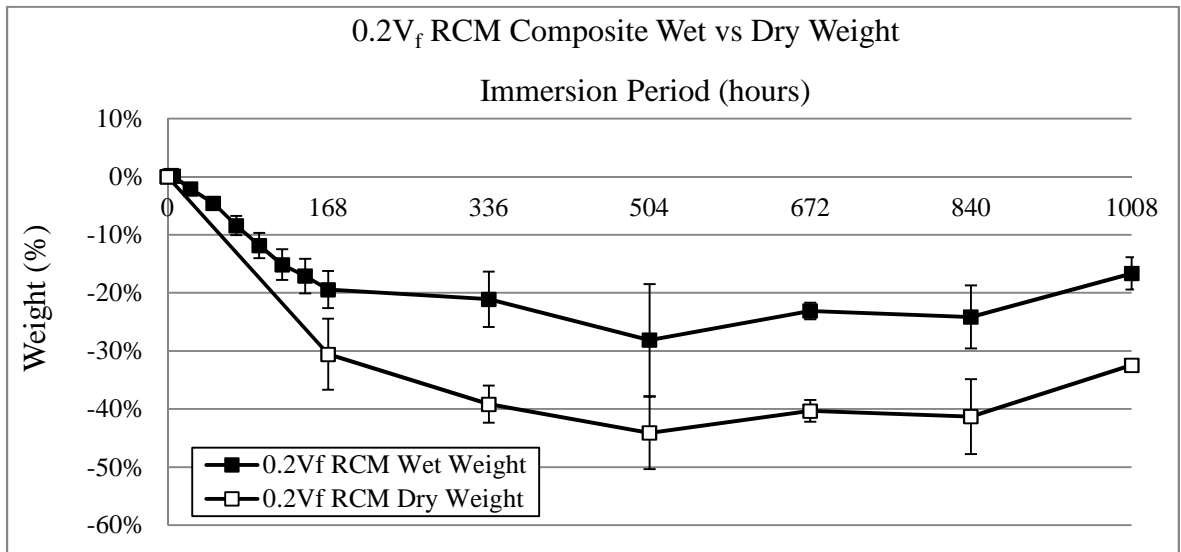


Figure 7.4.5. Comparison of 0.2V_f RCM composite wet and dry weight over 1008 hours of immersion in distilled water at 37°C.

As anticipated, the dry weight of the PLA control remained constant throughout the degradation period due to the relative time frame of the study and correlated with previous results reported by Ahmed et al. (2011). However it should also be recognised that the increased SA:V created by the internal porosity in the composite PLA matrix (due to fibre dissolution) may have increased hydrolytic polymer degradation in the composites compared to the PLA control (Ahmed et al. 2008) ^[219, 222, 223].

The dissolution of the reinforcing CorGlaes[®] Pure 107 fibres was coupled with a reduction in pH that was attributed to the formation of phosphoric acid (H₃PO₄). This was due to the rapid dissolution of the composite reinforcing fibres and was found to agree with the acidic pH reported by Ahmed et al. (2008, 2009, 2011) and Han et al. (2013) during the degradation of similar PGF composite configurations. The dissolution of these fibres is considered by Han et al. (2013) to occur via the same mechanisms as those reported for isolated fibres or bulk monolith samples and would appear to correlate with the low pH found during the previous dissolution testing of isolated CorGlaes[®] Pure 107 fibres (section 6.3.6).

The accumulation of the fibres dissolution species consequently led to a drop in media pH over the initial 24 hours to ≈ 2.5 despite frequent media replacement over the first 168 hours of degradation [169, 229]. As the degradation continued, the results showed this pH to gradually return to its initial values after 672 to 840 hours (4-5 weeks) and indicated that complete dissolution of any small fibre remnants had occurred. It should also be mentioned that it is unknown how significant an impact the surrounding phosphoric acid would have had on the rate of polymer matrix degradation due to its catalytic effect on the PLA degradation rate (section 3.2.2.3) (Ahmed et al. 2011). In contrast the pH of the PLA control media remained close to neutral (≈ 5.5) throughout the entire degradation period with the initial decrease in pH attributed to atmospheric influences and the generation of carbonic acid as discussed in section 5.3.7.1 [215, 218, 219, 223].

The weight loss stemming from the rapid dissolution of the CorGlaes[®] Pure 107 fibres over the first 168 hours also correlated with the rapid release of ions into the media (Figure 7.4.6). This was demonstrated by the daily ionic concentrations measured from the 0.2V_f RCM composite over this period that echoed similar results reported by Mohammadi et al. (2012) [169].

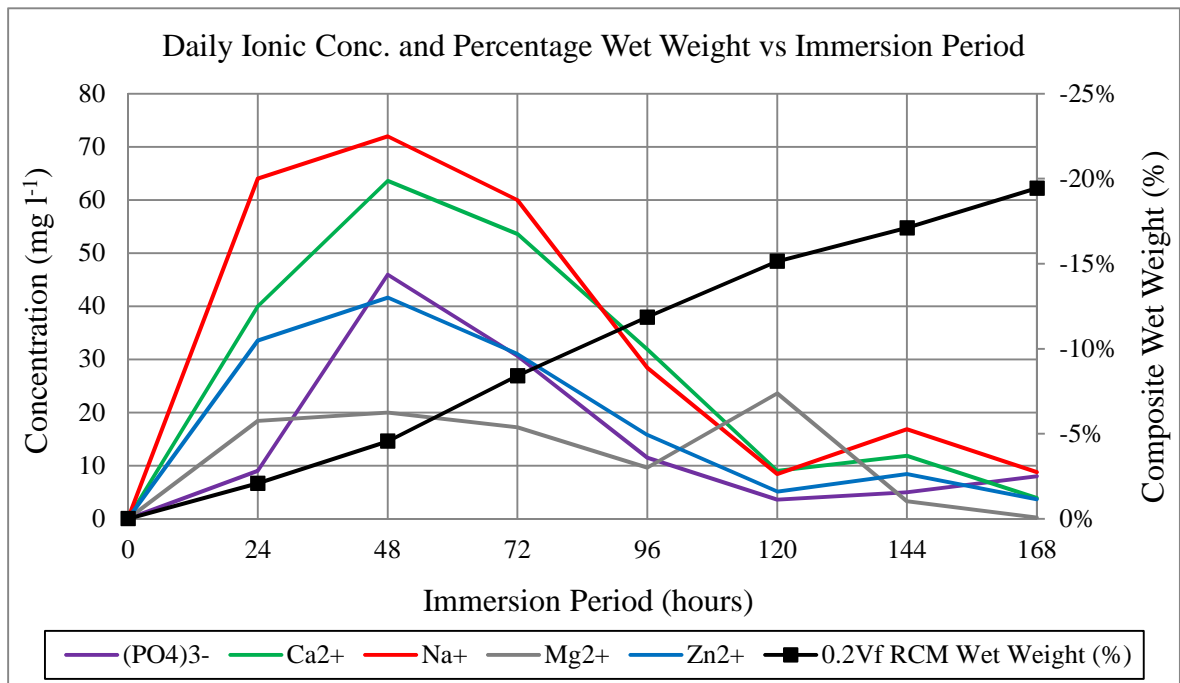


Figure 7.4.6. Correlation between the daily ionic concentrations of the degradation media and the 0.2V_f RCM composite wet weight over the initial 168 hours of immersion showing reductions in the ions released from the composite as the majority of the CorGlaes[®] Pure 107 fibres degraded.

The $0.2V_f$ RCM data (Figure 7.4.6) shows that the initially high rate of ion release quickly slowed after 48 to 72 hours as a result of the decreasing fibre content remaining within the composite. The near complete dissolution of the CorGlaes[®] Pure 107 fibres over this 168 hour period was also reflected by the non-linear curves seen in the accumulative ionic concentrations of the degradation media which began to plateau after 96-120 hours (Figure 7.3.9b) ^[169].

Mechanical testing of all composite samples showed that a rapid decrease in the flexural strength (-46% RCM, -58% [0/90]_{3S}) and modulus (-62% RCM, -80% [0/90]_{3S}) had occurred after 168 hours of degradation which fell below those of the PLA control samples. This was attributed to the break-down of the fibre-matrix interface via the ingress of moisture and dissolution of the reinforcing fibres (Ahmed et al. 2011). The rate at which this deterioration occurred was attributed to the large SA:V at the fibre matrix interface and the autocatalysis effects generated by the highly acidic media (Han et al. 2013) as previously seen during the dissolution of isolated CorGlaes[®] Pure 107 fibres (section 6.3.6). The fibre-matrix interface was also expected to have been severely disrupted by the capillary action of moisture along the interface (i.e. wicking) (Figure 7.4.7). However other factors such as the hydrophilicity of the PLA matrix and catalysis of the PLA hydrolysis reactions from the surrounding phosphoric acid were also expected to have influenced the interface breakdown and the resulting mechanical properties of the composites (Ahmed et al. 2008) ^[215, 218, 229].

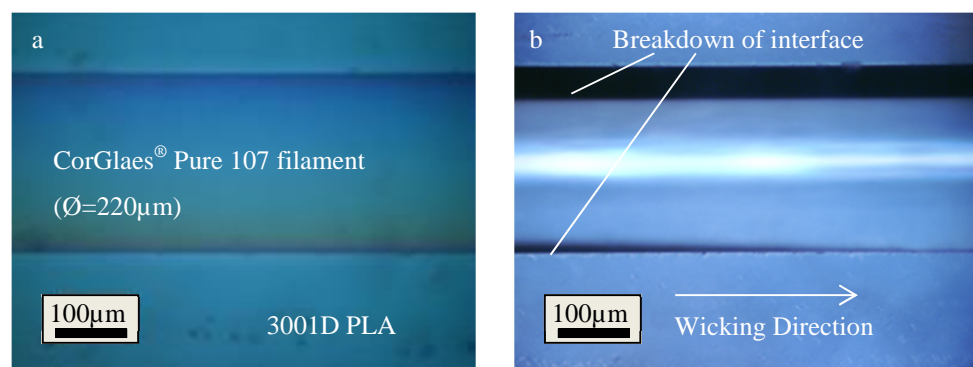


Figure 7.4.7. Optical microscope images of a $\sim\text{Ø}220\mu\text{m}$ CorGlaes[®] Pure 107 filament bonded to a glass coverslip with 3001D PLA and immersed in distilled water at 37°C showing a) Fibre-matrix interface at T_0 and b) Breakdown of the fibre-matrix interface after 336 hours of immersion due to the wicking of moisture along the fibre-matrix interface [scale bar = $100\mu\text{m}$].

The mechanical properties of the PLA were also seen to change over the degradation period with fluctuations in the flexural strength and an increase in elastic modulus observed during degradation. The variation in the polymer flexural strength was attributed to the presence of defects within the sample that would have accounted for the irregularity seen between samples in Figure 7.3.7. The observed increase in elastic modulus of the PLA control however was believed to be due to the higher degradation rate of the amorphous phase in the semi-crystalline PLA polymer. The expected increase in polymer crystallinity over the degradation period would then account for the increase in elastic modulus from 3.21 ± 0.34 GPa to 4.67 ± 0.12 GPa that was observed after 336 hours of immersion and is recognised to occur in semi-crystalline bioresorbable polymers. Such results would correlate with those reported by Felfel et al. (2010) where an increase from 26% to 44% in polymer crystallinity was measured after 300 hours during the degradation of NatureWorks® 3251-D PLA samples in distilled water. A slight change in the opaqueness of the 3001D PLA control was also observed during sample degradation and was believed to have been due to the recrystallization of the preferentially degraded amorphous phase [222, 342].

After 1008 hours of degradation it was found that the average flexural strength and elastic modulus of the $0.2V_f [0-90]_{3S}$ composites were lower (12.17 ± 0.56 MPa, 2.33 ± 0.61 GPa respectively) than the equivalent $0.2V_f$ RCM architecture (21.51 ± 9.38 MPa, 3.23 ± 0.17 GPa respectively). Furthermore compared to the equivalent PLA control, both degraded composites showed increased plastic deformation during testing (Figure 7.4.8). These differences in composite mechanical properties and failure modes were likely due to the difference in porous architectures created during CorGlaes® Pure 107 fibre dissolution and their relative ability to impede crack propagation compared to the PLA control. The tailoring of porous architectures via fibre dissolution in such composites has previously been discussed by Ahmed et al. (2008) with regards to meeting specific clinical needs. Yet the architecture has also been demonstrated here to have important mechanical considerations after complete fibre dissolution has occurred given that the resulting pore diameters ($\approx \emptyset 20\mu\text{m}$) were below those deemed acceptable for bone cellular ingrowth ($>300\mu\text{m}$). Stress-strain plots of the PLA control also showed a reduced strain at failure after 1008 hours compared to the initial $[T_0]$ values and correlated with the increased crystallinity of the polymer during its degradation as previously discussed [215, 342, 343].

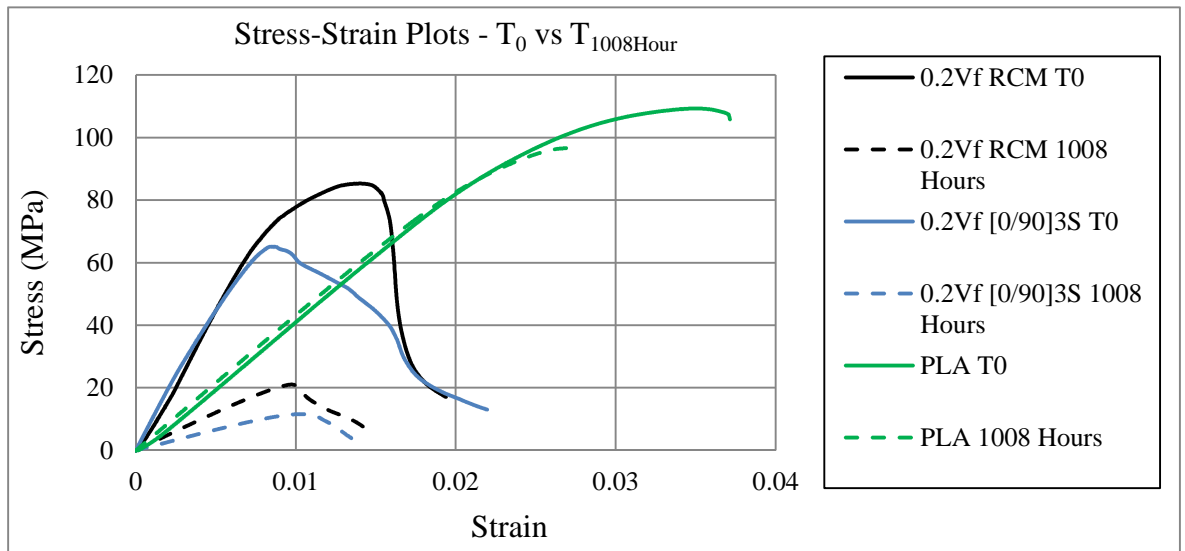


Figure 7.4.8. Comparison of stress-strain plots from initial (T_0) composite/control samples and after 1008 hours (six weeks) of degradation in distilled water at 37°C .

However despite the difference in initial composite mechanical properties between the two fibre architectures, the immersion of samples in distilled water revealed similar rates of fibre dissolution and subsequent loss of composite mechanical properties. This indicated that the RCM fibre architecture offered no advantage with regards to increasing composite durability. This was likely due to the continuous nature of both reinforcing phases when compared to the reduced dissolution rates found in chopped fibre composites by Ahmed et al. (2011) via the inhibitory effect of a discontinuous fibre phase on the wicking of moisture along the fibre-matrix interface (section 3.4.8). The increased rate at which the media pH returned to its initial values in the $[0/90]_{3S}$ composite (Figure 7.3.6) could also be reflective of the media's increased mobility into the composite interior with this type of fibre architecture. This increased mobility may have implications *in vivo* with regards to drug release or cell ingrowth and nutrient transport between such architectures should suitable pore sizes ($>300\mu\text{m}$) be produced. As a result, the arrays of alternating parallel fibres would appear to have completely degraded at a slightly faster rate than those used in the $0.2V_f$ RCM composite. This may then explain the difference in flexural strength between the two composite samples after 168 to 336 hours of degradation (Figure 7.3.7). However despite these considerations, the mechanical testing of degraded samples highlighted that the current rate of CorGlaes[®] Pure 107 fibre dissolution rendered these composites unable to match the targeted design specification of retaining at least 80% of their flexural strength and elastic modulus after 1008 hours (six weeks) of degradation (section 3.2.3.2) ^[219]. This was evident by the degradation data that showed a severe

reduction in the mechanical properties of both composites after the first 168 hours of degradation (Figure 7.4.9).

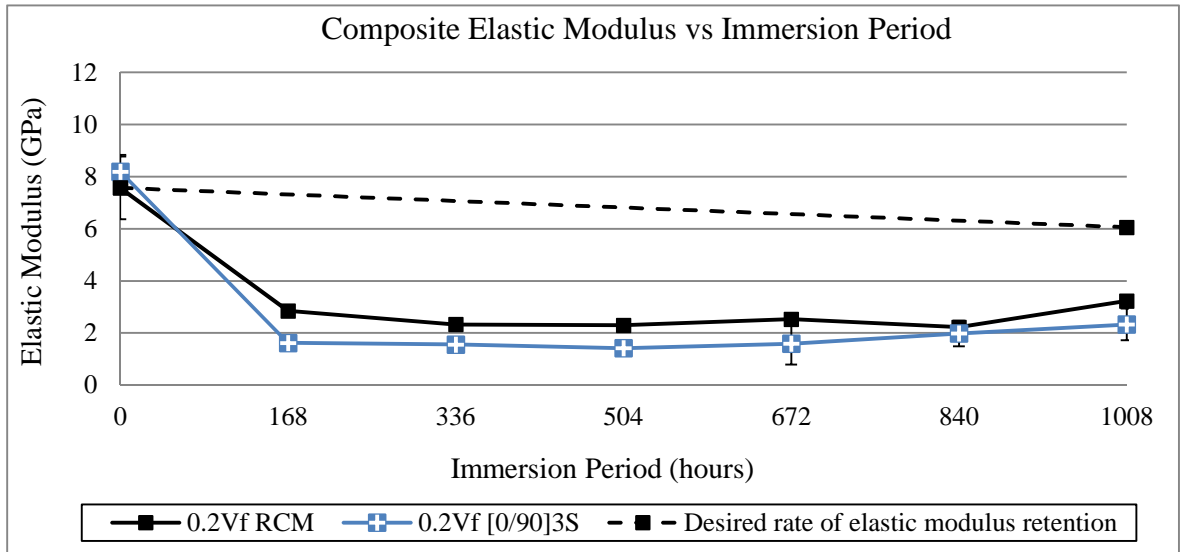


Figure 7.4.9. Comparison of $0.2V_f$ composite degradation with the targeted degradation rate of the composite elastic modulus.

It should be noted that the mechanical testing of dry samples may produce different mechanical properties compared to the testing of wet samples which is considered by Felfel et al. (2012) to be a better representation of *in vivo* performance. However the testing of dry samples was selected in this analysis due to the uncertain availability of the testing equipment with regards to specific sample immersion periods^[222].

Despite the reductions in CorGlaes[®] Pure 107 fibre dissolution rates previously observed in DMEM (section 6.3.6), the DMEM degradation of $0.2V_f$ RCM composite samples failed to show any increase in mechanical durability. This was evident by the near identical rate of dry weight loss (-28%) and reduction in the composite modulus (-59%) observed after 168 hours of degradation despite the pH of the DMEM appearing to be substantially buffered. However, the localised yellow discolouration of the DMEM in the immediate vicinity of the composites indicated that highly localised pH effects were occurring (Figure 7.4.10). This would have been due to the rapid dissolution of the CorGlaes[®] Pure 107 fibres that, based on the composite weight loss data, appeared to occur at the same rate as that experienced during composite degradation in distilled water. The rapid dissolution of the reinforcing fibres despite the presence of a pH buffer highlighted the influence of the high SA:V ratio at the fibre-matrix interface on composite degradation.

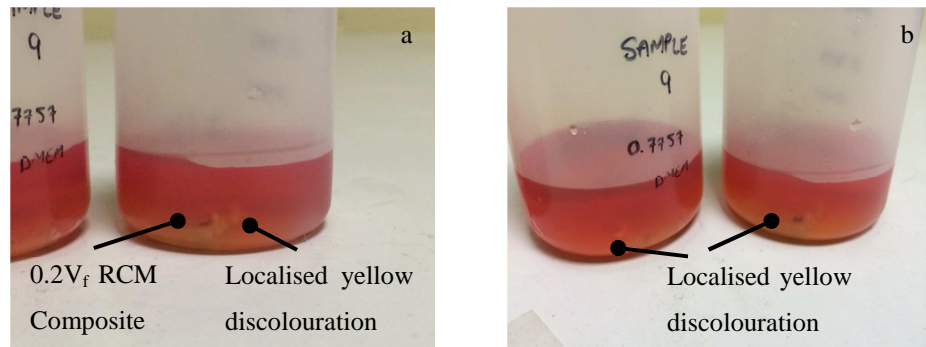


Figure 7.4.10. Degradation of a 15x15x2 mm 0.2V_f RCM composite samples in 0.1 vol% sodium azide-DMEM (SA:V = 0.21 cm² ml⁻¹) with the localised yellow discolouration of the media after 48 hours of degradation signalling an acidic environment surrounding the sample.

Further comparisons between the degradation of composites in DMEM and distilled water showed the same initial trend in media uptake due to polymer absorption prior to the decrease in wet weight from dissolution of the reinforcing fibres. However the overall decrease and plateau in wet weight was significantly reduced (-12%) compared to that recorded in distilled water (-20%) after 168 hours. This was believed to be due to the formation of a visible whitish precipitate across the composite sample surface that was apparent after 24 hours of immersion. These precipitates continued to form over the first week (168 hours) of immersion with SEM images of the degraded composites fracture faces (after mechanical testing) also showing that the precipitate had formed sporadically within the pores generated by fibre dissolution (Figure 7.3.15). However the majority of these surface deposits separated from the composite surface during sample drying and consequently led to similar dry weight measurements being obtained when compared to those previously recorded in distilled water.

As with the samples degraded in distilled water, a rapid deterioration in the composite mechanical properties was observed after 168 hours of degradation that was attributed to fibre dissolution as previously discussed. However mechanical testing of the composites also showed that despite possessing a near equivalent elastic moduli to that found after degradation in distilled water, the flexural strength and failure mechanisms varied between the different media. Consequently when degraded in DMEM, the samples appeared to display a brittle failure mode compared to the more ductile failure previously observed from 0.2V_f RCM composites over the equivalent immersion period in distilled water (Figure 7.4.11).

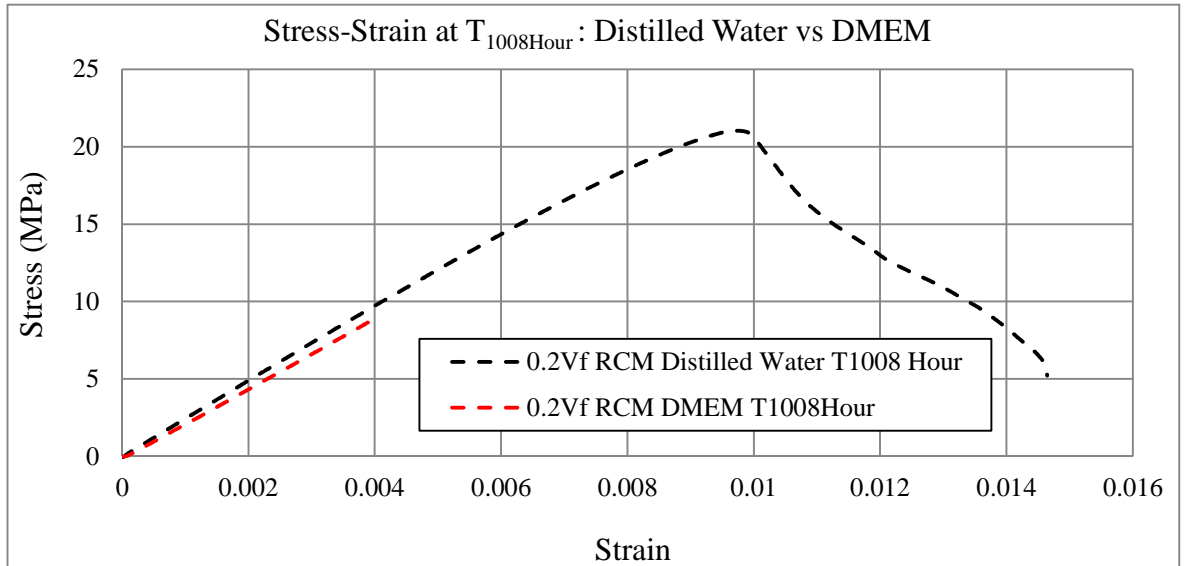


Figure 7.4.11. Comparison of stress-strain plots for $0.2V_f$ RCM composites after 1008 hours of degradation in distilled water and DMEM.

Work by Peña et al. (2006) has shown that polymers such as PCL will degrade at a faster rate in DMEM compared to PBS and that the influence of media with high molecular concentrations such as DMEM must be considered when evaluating material degradation. Furthermore Peña et al. (2006) also states that few studies have examined such effects with regards to material degradation in fluids more closely resembling biological media. Inspection of the stress-strain data obtained during CorGlaes[®] Pure 107 composite degradation indicated that the transition to a brittle failure mode appeared to occur within the first 168 hours of degradation. This would then imply that the observed failure behaviour of the remaining porous PLA matrix was strongly related to the interactions occurring between the dissolution of the CorGlaes[®] Pure 107 fibres and the DMEM. The rapid nature of this transition was also within a much smaller time frame than the 18 month study conducted by Peña et al. (2006). However due to restrictions on the available volume of DMEM no PLA controls were degraded for comparison. Further analysis is also restricted by the lack of comparative results in the literature examining the mechanical degradation of PGF composites in DMEM^[344].

Analysis of the precipitate formed during $0.2V_f$ RCM composite degradation in DMEM by FTIR and XRD (after drying the composite at 60°C for 12 hours) showed the material to possess an amorphous structure. Furthermore the FTIR spectrum of the precipitate was found to closely match that previously obtained during bioactivity testing of the CorGlaes[®] Pure 107 fibres in c-SBF. This appeared to indicate that the rapid dissolution of the composite reinforcing fibres and saturation of the DMEM had resulted in the precipitation

of various pyrophosphate salts as previously found in section 6.3.7. The precipitation of these salts was likely due to the similar ionic constituents/concentrations (Table 6.2.2) and media pH between the DMEM and c-SBF. A comparison between the accumulated ionic concentrations in the DMEM and distilled water during $0.2V_f$ RCM composite degradation also showed the DMEM to possess a significantly lower concentration of Mg^{2+} and Zn^{2+} ions (Figure 7.4.12). This is despite the composite weight data indicating similar rates of fibre dissolution in both media.

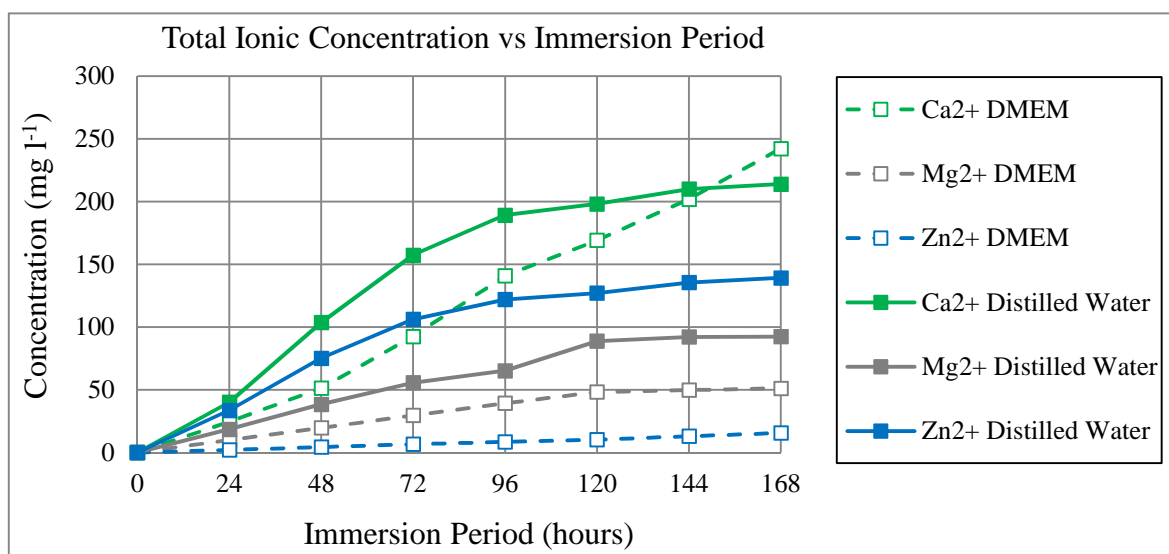


Figure 7.4.12. Comparison of Ca^{2+} , Mg^{2+} and Zn^{2+} accumulative ionic concentrations during the degradation of the $0.2V_f$ RCM composites in DMEM and distilled water (DMEM normalised with respect to its initial ionic concentrations before composite degradation i.e. T_0).

Combined with the XRD trace, the comparison between the ionic concentrations of each respective media (Figure 7.4.12) reinforces the proposed formation and deposition of amorphous pyrophosphate salts relevant to the CorGlaes[®] Pure 107 composition (section 6.4). Such results would also correlate with the general low solubility product constants (k_{sp}) of magnesium phosphate ($k_{sp} = 1 \times 10^{-24}$ at $25^\circ C$) and zinc phosphate ($k_{sp} = 9 \times 10^{-33}$ at $25^\circ C$) salts [345, 346]. The significantly higher Na^+ ionic concentrations found in the DMEM results (Figure 7.3.14) could not be accounted for but were believed to be due to interference from the DMEM during the analysis of the media.

Bioactivity testing of the $0.2V_f$ RCM samples showed the fibre dissolution to occur at a similar rate as that recorded during composite degradation in distilled water. This was

apparent by the near identical rate of decreasing wet weight when compared over the equivalent degradation period (Figure 7.3.19). However in contrast to the distilled water, the pH of the c-SBF during composite degradation was shown to be sustainably buffered and remained above 6.4 for the entire immersion period. This deviation in pH despite the similar rates of fibre dissolution could be accounted for however when considering the local and bulk SA:V ratios as well as the initial media ionic constituents/concentrations between the two experimental methods. Consequently the identically high SA:V at the fibre-matrix interface in both samples would account for the similar rates of rapid fibre dissolution. However the difference in bulk SA:V ratio between the mechanically degraded ($0.21 \text{ cm}^2 \text{ ml}^{-1}$) and bioactivity tested ($0.1 \text{ cm}^2 \text{ ml}^{-1}$) conditions along with the pH buffering and or precipitation of phosphate groups out of solution would then account for the deviation in bulk media pH for each respective immersion media

The immersion of composite samples was also coupled with the formation of a white precipitate on the planar and cross-sectional surfaces of the composite after 24 hours (Figure 7.3.18). As the immersion time increased it was observed that this surface layer gradually continued to be deposited. These visual observations were found to correlate well with the FTIR spectra obtained from the samples. This data showed the formation of new peaks after 24 hours of immersion whilst the initial peak wavenumbers at 1745 cm^{-1} and $1250\text{-}1050 \text{ cm}^{-1}$ (corresponding to the C=O, C-O and C-O-C stretching vibrations of the PLA polymer matrix) were gradually suppressed. These were subsequently replaced by the formation of broad amorphous peaks from the precipitate that appeared to be similar to the spectra encountered during $0.2V_f$ DMEM degradation and after the immersion of CorGlaes[®] Pure 107 fibres in c-SBF (Figure 7.4.13) ^[216].

Consequently the obtained FTIR spectra after $0.2V_f$ RCM bioactivity testing was attributed to the similar deposition of pyrophosphate salts as encountered in previous testing due to the rapid dissolution of the CorGlaes[®] Pure 107 fibres (section 6.3.7). Previous bioactivity studies on $0.18V_f$ PGF composites by Mohammadi et al. (2012) had established the precipitation of brushite ($\text{CaHPO}_4 \cdot 2\text{H}_2\text{O}$) across the composite surface after 336 hours (two weeks) of immersion. This stemmed from the acidic pH created by the fibre dissolution in SBF with Mohammadi et al. (2012) discussing how the rate of fibre dissolution and corresponding ion release rates had a significant effect on apatite precipitation ^[169].

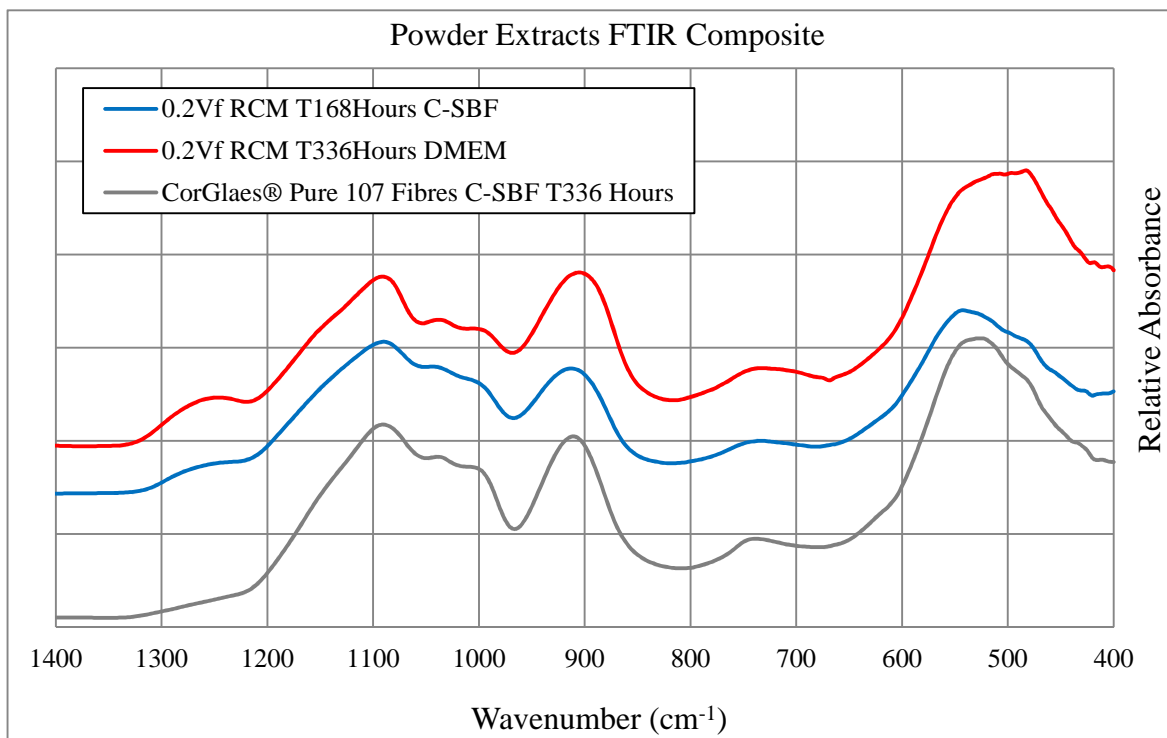


Figure 7.4.13. Comparison of FTIR spectra obtained from precipitates during immersion of composites in c-SBF and DMEM as well as CorGlaes[®] Pure 107 fibres in c-SBF.

Accordingly, the higher SA:V ratio at the fibre-matrix interface would be expected to produce an increased rate of fibre dissolution compared to that encountered during isolated CorGlaes[®] Pure 107 fibre bioactivity testing (section 6.3.7). Combined with the difference in bulk SA:V ratios between the c-SBF studies ($0.1 \text{ cm}^2 \text{ ml}^{-1}$) and mechanical degradation of the $0.2V_f$ RCM composites in DMEM ($0.21 \text{ cm}^2 \text{ ml}^{-1}$) such factors may then explain the deviation in FTIR spectra between the different samples and testing regimes. This is further reflected by the data shown in Figure 7.4.13 with a low intensity broad peak at $\approx 1256 \text{ cm}^{-1}$ appearing more prominently in precipitates obtained during PGF composite immersion and could indicate a difference in the phase composition or structure of the precipitate based on the rate of fibre dissolution^[216]. However, further investigation via annealing and deconvolution of the FTIR spectra would be required to further expand upon this due to the ambiguous nature of their amorphous structure and likely band overlapping in the spectra as previously discussed in section 6.4.

Furthermore, the inspection of both planar and cross-sectional faces was aimed at identifying any HCA formation at the exposed fibre cross-sections of the composite given the “halo” regions of HCA deposition that can form in the surrounding areas of the composites exposed fibres when immersed in SBF according to Vallittu et al. (2015)^[5].

Degradation of PLA and $0.01V_f \rightarrow 0.2V_f$ RCM composites in CDMEM for the MTT assay found that visible precipitates were formed in the media during $0.1V_f$ and $0.2V_f$ composite degradation due to the ionic saturation of the media as previously discussed. Biocompatibility testing of the sample extracts by MTT assay on MG63 cells subsequently showed that all composite viability results were below the 70% threshold stated by BS EN 10993-5:2009 and that a trend of increasing cytotoxicity was observed with increasing composite fibre volume fraction. This was attributed to the rapid dissolution of the CorGlaes[®] Pure 107 fibres and the associated changes to the media pH as well as the ionic concentrations in the CDMEM with different fibre volume fractions. The cytotoxicity from media extracts where pH levels were within the tolerable limits for MG63 cells (i.e. $\text{pH} \geq 7.4$) was believed to be due to the release and accumulation of Zn^{2+} ions as previously discussed in section 5.4. The variation in fibre volume fraction and subsequent Zn^{2+} concentration in the CDMEM extracts would then account for the increasing cell viability with decreasing V_f . Furthermore the time dependant accumulation of Zn^{2+} cations would also corroborate with the decreasing cell viability after prolonged degradation times (i.e. 96 hours) in the $0.01V_f$ and $0.05V_f$ samples (as previously observed during the Live/Dead[®] staining of CorGlaes[®] Pure 107 disks). In contrast, the high cell viability of MG63 cells cultured in the extracts obtained during 3001D PLA degradation confirmed its biocompatibility and that the cytotoxic response of the composites was directly related to the CorGlaes[®] Pure 107 fibres [280].

The MTT assay of the diluted extracts collected after 24 and 96 hours of $0.2V_f$ RCM composite degradation showed the media extracts to be highly cytotoxic to MG63 cells at 10, 50 and 100 vol% concentrations. As with the previous results, the poor viability of the MG63 cells was attributed to the acidic pH of the CDMEM at high extract concentrations or the accumulation of Zn^{2+} ions towards cytotoxic levels. The variation in CDMEM pH was apparent by the phenol red pH indicator in the CDMEM that caused a visible transition in the media from yellow to red as the dilution increased and the pH was raised towards neutral (Figure 7.4.14).

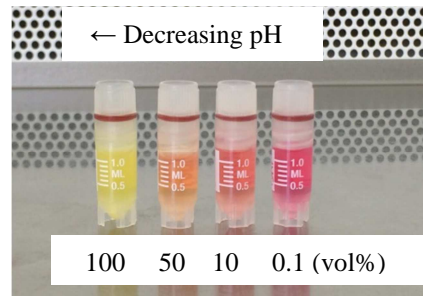


Figure 7.4.14. Variation in $0.2V_f$ RCM CorGlaes Pure 107 composite CDMEM degradation media extract after 96 hours at different concentrations (vol%) with the yellow discolouration indicating a highly acidic media.

However it was also observed in Figure 7.3.24 that despite being below the viability threshold, an increase in cell viability was observed with increasing extract concentration that contradicted the observed trends and proposed theories of the previous results (i.e. V_f decreases, cell viability increases). A repeat of the MTT assay procedure with acellular CDMEM using the same extract dilutions (i.e. $0.1 \rightarrow 100$ vol%) revealed that the composite degradation by-products or possible precipitates may be interfering with the MTT assay due to the presence of false positives being generated. This was apparent by the increase in cell viability recorded with increasing extract concentration despite the absence of any cells in the media (Figure 7.4.15). However the precise mechanisms regarding this interference effect were not explored and would require further dedicated investigations.

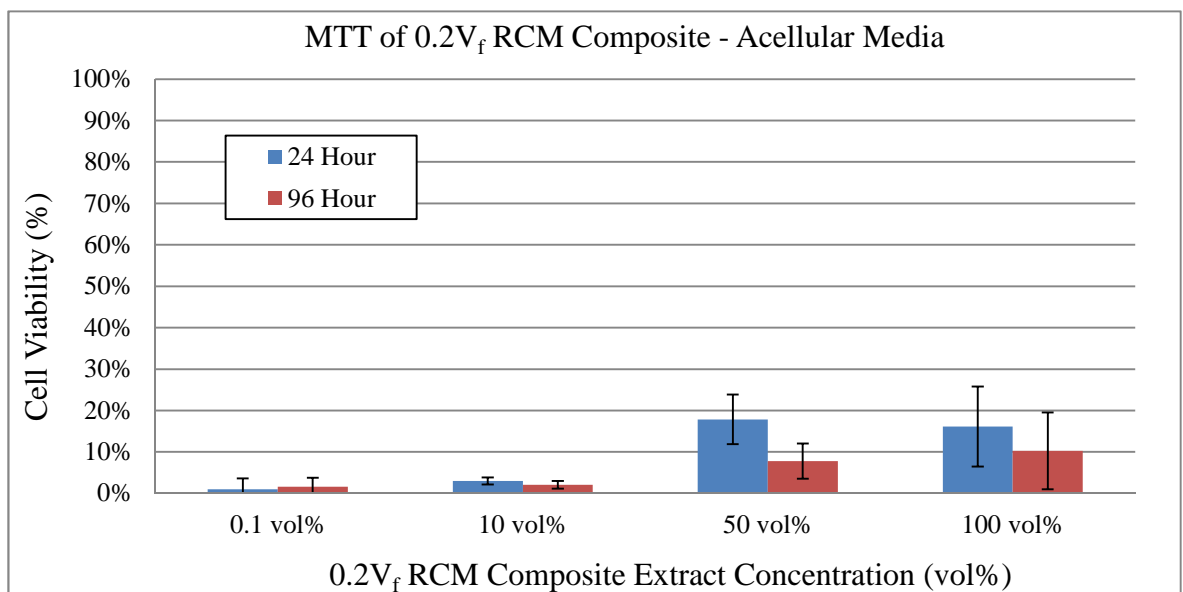


Figure 7.4.15. Effect of $0.2V_f$ RCM composite extract on the MTT results collected in acellular media showing false positive readings generated by possible influences from the dissolution of the reinforcing fibres.

7.5 Conclusions

The introduction of CorGlaes[®] Pure 107 fibres into a PLA polymer matrix showed the expected increase in elastic modulus with an increasing fibre volume fraction that closely matched the values predicted by the rule of mixtures. Furthermore the flexural strength (σ_{comp}) and elastic modulus (E_{comp}) of $0.2V_f$ RCM composites ($\sigma_{\text{comp}} = 82.39 \pm 4.46$ MPa, $E_{\text{comp}} = 7.57 \pm 1.20$ GPa) were found to be within the range reported by Motherway et al. (2009) for parietal bone. This random fibre architecture (RCM) showed an increase in flexural strength and energy absorption compared to the $[0/90]_{3S}$ laminate design that was also investigated. However despite showing initial promise, the current $0.2V_f$ CorGlaes[®] Pure 107-PLA composite configurations were unable to sustain an adequate flexural strength or elastic modulus over the required six week degradation period to meet the design parameters outlined in section 2.1. This was due to the susceptibility of these fibres to autocatalysis effects and the large SA:V ratios encountered at the fibre-matrix interface of the CorGlaes[®] Pure 107 fibre composites. Degradation of the $0.2V_f$ RCM composites within media typically used during *in vitro* cell culture (DMEM) revealed that a similarly rapid rate of composite fibre dissolution had occurred despite the previous results found in section 6.3.6. This was again attributed to the proposed autocatalytic effects which were believed to be highly localised to the composite samples given the ability of the DMEM to buffer the bulk media pH during $0.2V_f$ RCM degradation compared to distilled water^[46].

This high fibre dissolution rate also resulted in the deposition of pyrophosphate salts across the surface of the composite when immersed in c-SBF as previously found during the CorGlaes[®] Pure 107 fibre bioactivity experiments. Unfortunately the rapid dissolution of the composite fibres also rendered the current composite configurations cytotoxic to MG63 cells across all the tested fibre volume fractions ($0.01V_f \rightarrow 0.2V_f$). This was due to the related pH changes at high V_f (i.e. $0.2V_f$) or rapid release rate of ions (specifically Zn^{2+}) into the culture media ($0.01V_f \rightarrow 0.1V_f$) towards cytotoxic levels ($\approx 8 \text{ mg l}^{-1}$).

8 Modified CorGlaes[®] Pure 107 Fibre Composite

8.1 Outline

The previous characterisation of a 0.2V_f RCM CorGlaes[®] Pure 107 composite (chapter 7) demonstrated that this material configuration was capable of achieving flexural strengths and elastic moduli similar to those reported for the parietal bones of the skull [46]. However the immersion of these samples in distilled water or DMEM showed that they were unable to meet the design criteria of retaining at least 80% of their mechanical properties after 6 weeks of degradation. This result was attributed to the rapid dissolution of the reinforcing fibres and the breakdown of the fibre-matrix interface due to the low pH acidic environment and resulting autocatalysis effects that were initiated after immersion of the composite samples. The rapid dissolution of the fibres and the associated pH changes as well as the high ion release rates were also responsible for the observed composite cytotoxicity [339].

The silane treatment of silica and phosphate based glass fibres has been shown in previous studies to improve the initial mechanical properties of the resulting composites as well as its mechanical integrity during degradation (Khan et al., 2011, Hasan et al., 2012) (section 3.4.9) [221, 228]. Given the previous reduction in dissolution rate recorded for CorGlaes[®] Pure 107 fibres after silane treatment (section 6.3.6), APS treated CorGlaes[®] Pure 107 fibres were investigated as a composite reinforcing agent with regards to improving its mechanical properties during prolonged periods of degradation.

Yet previous studies such as those by Agrawal & Athanasiou (1997) as well as Schiller & Epple (2003) have also shown how different calcium phosphate salts have been able to buffer the media pH and retard autocatalytic effects during PLA-PGA polymer degradation. Such neutralising buffers have also been investigated by Kobayashi et al. (2010) where the addition of a calcium carbonate (CaCO₃) filler was shown to successfully buffer the media pH during the degradation of an ultraphosphate glass fibre composite. Such hybrid composite configurations (i.e. joint fibre-particle filler phases) could be easily manufactured through the existing compression moulding processes via modifications to the pre-preg or matrix sheet precursor stages (Shen et al. 2009). Based on this, it was believed that the incorporation of a secondary calcium phosphate particulate filler phase into a CorGlaes[®] Pure 107 composite configuration might successfully counteract the acidic by-products of the CorGlaes[®] Pure 107 fibre dissolution and neutralise the detrimental autocatalytic effects – increasing composite mechanical durability [229, 347-350].

8.2 Materials and Methods

8.2.1 Silane Treated CorGlaes[®] Pure 107 Composites

The initial and degenerative properties of a 0.2V_f RCM composite using CorGlaes[®] Pure 107 fibres treated with a 3-aminopropyl-triethoxy (APS) sizing agent was conducted based on the silane treatment protocol described in section 6.2.6. Subsequent composite manufacturing, mechanical testing and degradation of the APS composites was performed using the methods outlined in section 7.2.3, 7.2.4 and 7.2.5 respectively that had been previously used to produce and characterise composite samples. However no fibre pre-preg stage was used during the manufacturing of these 0.2V_f RCM-APS composites in order to prevent the APS surface treatment from potentially being affected.

8.2.2 CorGlaes[®] Pure 107 Fibre-Particle Hybrid Composites

Due to the availability and its widespread application in biomaterials, hydroxyapatite (HA) was selected as the calcium phosphate particulate filler phase for hybrid composite development. Given its pH dependant solubility (pH↓, k_{sp}↑) the HA filler was anticipated to provide a self-regulating method of buffering the media pH (Kolarik & Priestley, 2006) following the relationship described in Figure 8.2.1 [348, 351].

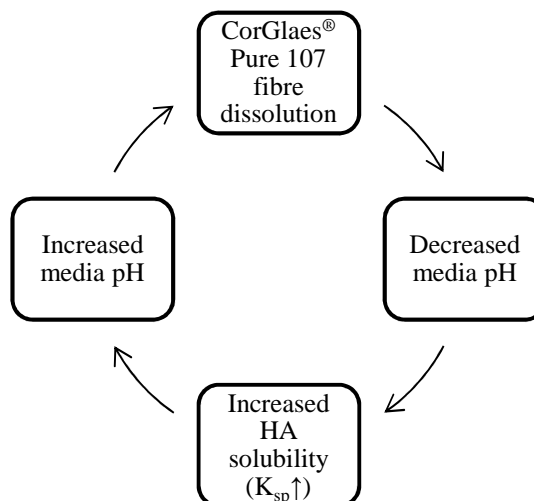


Figure 8.2.1. Cyclic relationship between the CorGlaes[®] Pure 107 fibre dissolution and the HA buffering effect on the surrounding media pH.

Hybrid composites of different fibre (V_f) and HA (V_{HA}) volume fractions were created by incorporating a secondary HA filler phase of sintering grade, 4µm hydroxyapatite particles

(P218R, Plasma Biotol, UK) into the pre-preg and matrix precursors of a CorGlaes[®] Pure 107 fibre-PLA composite. The manufacturing of these samples was based on the laminate compression moulding method previously outlined in section 7.2.2 and 7.2.3 with the respective weight and volume fractions of each composite phase calculated based on Eqn 8.2.1 and Eqn 8.2.2.

$$W_{HA} = \frac{w_{HA}}{w_{HA} + w_f + w_m}$$

$$w_c = w_{HA} + w_f + w_m$$

Eqn 8.2.1

where W_{HA} = composite HA weight fraction, w_{HA} = composite HA weight (g), w_f = composite fibre weight (g), w_m = composite matrix weight (g), w_c = composite weight (g)

$$V_{HA} = \frac{(W_{HA}/\rho_{HA})}{(W_{HA}/\rho_{HA}) + (W_f/\rho_f) + (W_m/\rho_m)}$$

Eqn 8.2.2

where V_{HA} = composite HA volume fraction, W_f = composite fibre weight fraction, W_m = composite matrix weight fraction, ρ_{HA} = HA density (g cm⁻³) [3.156 g cm⁻³], ρ_f = fibre density (g cm⁻³) [2.65 g cm⁻³], ρ_m = matrix density (g cm⁻³) [1.25 g cm⁻³].

8.2.3 Hybrid Composite Precursors

8.2.3.1 Fibre Pre-Pregs

Modified CorGlaes[®] Pure 107 fibre-pregs with a secondary HA phase (V_{HA-pp}) were manufactured through the inclusion of HA particles into a 3 w/v % PLA solution that used chloroform (VWR, USA) as the polymer solvent. The HA-PLA slurry was then magnetically stirred for 60 minutes before being placed in an Ultra 8000 ultrasonic bath (James Products Limited, UK) for three minutes. CorGlaes[®] Pure 107 fibres were then solvent cast with the HA-PLA slurry based on the method described in section 7.2.3.

8.2.3.2 Matrix Sheets

The manufacture of homogeneously distributed 0.3-0.4mm thick HA-PLA matrix sheets was performed through a solvent casting method using a 10 w/v % PLA solution with chloroform as the polymer solvent. Slurries of HA-PLA were created by adding HA particles to the polymer solution ($V_{\text{HA-m}}$) which was then magnetically stirred for 120 minutes before being placed in an Ultra 8000 ultrasonic bath (James Products Limited, UK) and ultrasonicated for three minutes. The slurry was then magnetically stirred for an additional 15 minutes before being returned to the ultrasonic bath for a final three minutes of ultrasonication. After the mixing stages, the slurry was poured into Ø150mm glass petri dishes (40ml per dish) inside a fume cabinet and left for 24 hours to allow the chloroform solvent to completely evaporate (Figure 8.2.2). The cast HA-PLA sheets were then cut into rectangular sections to make 180x30mm matrix sheets.

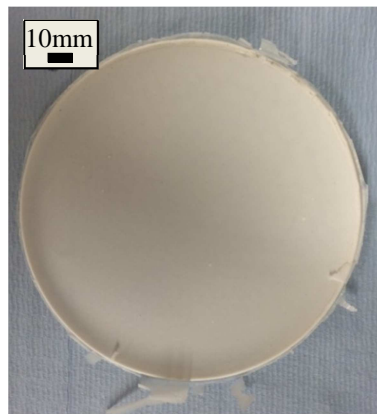


Figure 8.2.2. Image of a solvent cast Ø150mm $0.2V_{\text{HA}}$ -PLA matrix sheet obtained from a 10 w/v % solution of a HA-PLA slurry after 24 hours of solvent evaporating in a fume cabinet [scale bar = 10mm].

8.2.4 Hybrid Composite Manufacturing

Using the modified fibre pre-pregs and HA-PLA matrix sheets, hybrid composite samples were manufactured following the hand lay-up film stacking and compression moulding process described in section 7.2.3.

Where necessary, HA-PLA composite samples were manufactured to act as controls by compression moulding HA-PLA matrix sheets inside the 130x80mm stainless steel cavity mould at 200°C for a ten minute curing period. The mould was then cooled to room temperature under 4 MPa pressure.

8.2.5 Development of CorGlaes® Pure 107 Hybrid Composites

Characterisation of different hybrid composite configurations was conducted following a mechanical and biocompatible optimisation pathway as described by the flow chart shown in Figure 8.2.3.

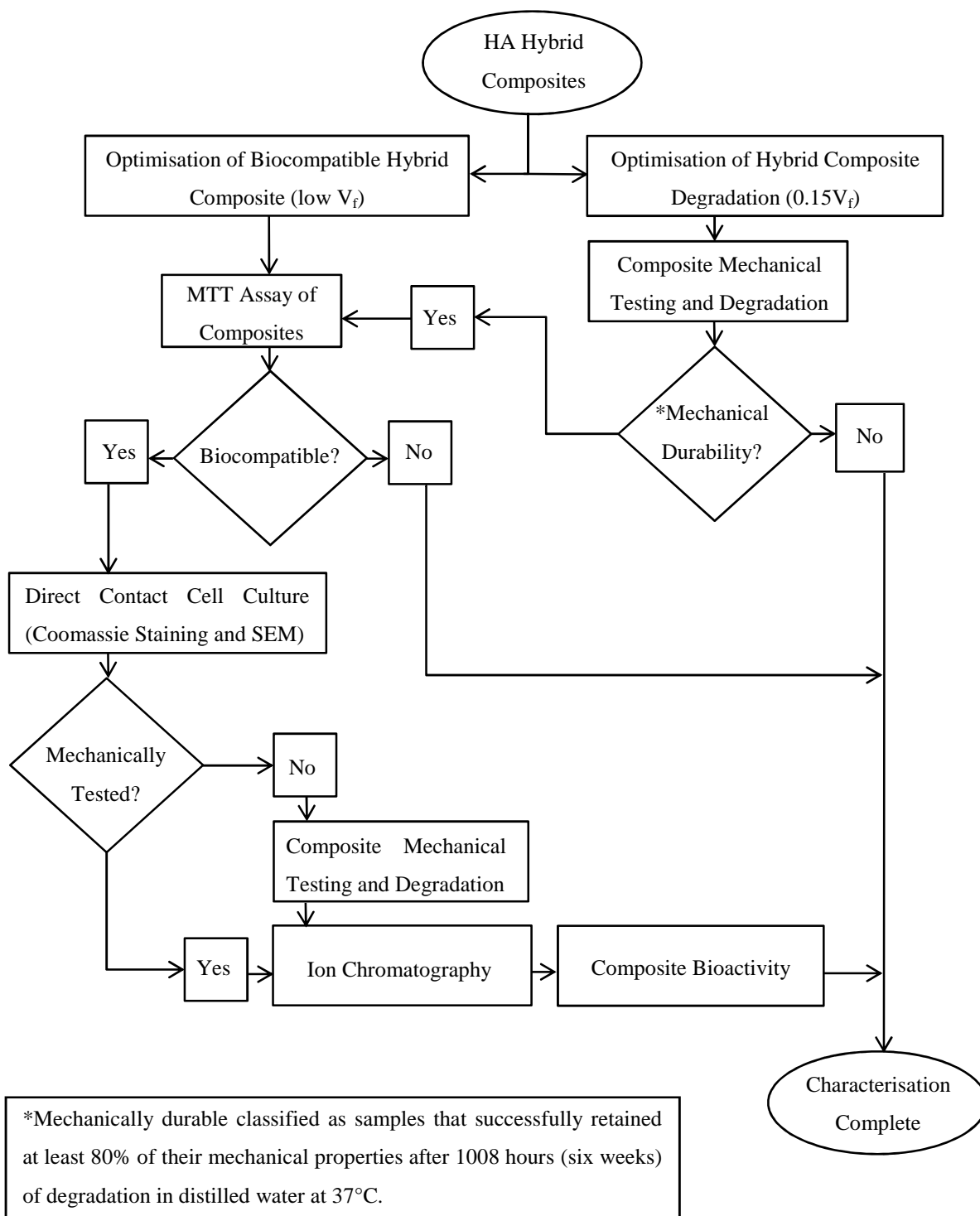


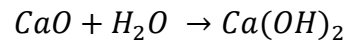
Figure 8.2.3. Process flow chart for development of CorGlaes® Pure 107 fibre HA filler hybrid composites.

The analysis of direct contact cultures after seeding cells on composite and control samples was assessed by Coomassie Brilliant Blue staining and SEM imaging due to the autofluorescence of the PLA that prevented Live/Dead[®] staining from being performed.

8.2.5.1 Optimisation of Hybrid Composite Degradation

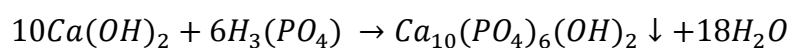
Based on the data obtained from previous composite samples (chapter 7), V_f - V_{HA} hybrid composites with increasing volume fractions of HA (V_{HA}) were manufactured. To examine the effects of HA distribution on the pH buffering and sample mechanical properties, composites with a homogenous distribution of HA ($V_{HA-pp} \approx V_{HA-m}$) were compared with an equivalent hybrid where the HA was primarily distributed within the fibre pre-pregs (i.e. non-homogenous distribution, $V_{HA-pp} > V_{HA-m}$).

Additionally the commercial manufacturing of HA via precipitation techniques can lead to calcium oxide (CaO) becoming entrapped within the HA and as a result these particles typically undergo an annealing stage to remove any remaining CaO contaminants. This is due to the highly alkaline (and consequently cytotoxic) calcium hydroxide ($Ca(OH)_2$) that can form when the CaO reacts with water as described by Eqn 8.2.3 ^[352, 353].



Eqn 8.2.3

However it was proposed that the inclusion of a CaO defective HA particulate filler should also be investigated within a hybrid composite configuration. This was due to the highly basic nature of the $Ca(OH)_2$ reaction products that could help neutralise the phosphoric acid (H_3PO_4) created by CorGlaes[®] Pure 107 fibre dissolution. Based on the reaction shown in Eqn 8.2.4, the application of a CaO defective HA could also lead to the precipitation and deposition of HA on the composite as it neutralised the phosphoric acid ^[354].



Eqn 8.2.4

Consequently a request was made to Plasma Biotol (Derbyshire, UK) that a specialised batch of HA be supplied without the final post-processing annealing stage. This resulted in the shipment of 4 μ m sintering grade 1% by mass CaO defective HA particles (Plasma Biotol, UK) that was used to generate CorGlaes[®] Pure 107 fibre HA_(CaO) hybrid composites.

Due to the difficulty in maintaining hybrid composites at a 0.2V_f as the volume fraction of HA increased (V_{HA}), hybrid composites were manufactured at a reduced fibre volume fraction (0.15V_f). This alteration was deemed acceptable for the purposes of sample comparison with the previous 0.2V_f RCM data and was acknowledged when analysing the results. The specifications for each constituent phase of the respective hybrid composite configurations and a 0.2V_{HA} fibre-free PLA composite control is shown below in Table 8.2.1 and Table 8.2.2. Such quantities were scaled up for the manufacturing of multiple specimens as required for sample characterisation.

Table 8.2.1. Specifications for precursor materials used in the manufacture of CorGlaes[®] Pure 107 hybrid composites with HA filler.

| ^a Composite | Fibre Pre-Preg ($n = 1$) (pp) | | Matrix sheet ($n = 1$) | | |
|--|---------------------------------|--------|---------------------------------------|----------------------|-------------------|
| | 40ml 3 w/v % PLA | | V _{f-pp} -V _{HA-pp} | 40ml 10 w/v % PLA | V _{HA-m} |
| | Fibre (g) | HA (g) | | HA (g) | |
| ^b 0.15V _f -0.1V _{HA(NHD)} | 2.5 | 1.25 | 0.41-0.17 | 1.1 | 0.1 |
| 0.15V _f -0.2V _{HA} | 2.5 | 1.25 | 0.41-0.17 | 2.6 | 0.2 |
| ^b 0.15V _f -0.2V _{HA(NHD)} | 2.5 | 3 | 0.33-0.33 | 0.8 | 0.07 |
| ^b 0.15V _f -0.2V _{HA(CaO)} | 2.5 | 3 | 0.33-0.33 | 0.8 | 0.07 |
| 0.2V _{HA} | 0 | 0 | 0 | 2.6 | 0.2 |

^a Sample names designate the accumulative volume fractions of fibres (V_f) and HA (V_{HA}) in the composite.

^b Designates samples where a non-homogenous distribution (NHD) of HA (V_{HA-pp} \neq V_{HA-m}) is present.

Table 8.2.2. Specifications for pre-preg and matrix phases of CorGlaes[®] Pure 107 composites with HA filler.

| ^a Composite | Fibre Pre-Preg | | HA-PLA Matrix Sheet | |
|--|----------------|-----------------------|---------------------|---------------------|
| | Weight (g) | Pre-Preg (<i>n</i>) | Weight (g) | Matrix (<i>n</i>) |
| ^b 0.15V _f -0.1V _{HA(NHD)} | ≈4.4 | 5 | ≈5 | 6 |
| 0.15V _f -0.2V _{HA} | ≈4.4 | 5 | ≈5 | 6 |
| ^b 0.15V _f -0.2V _{HA(NHD)} | ≈6.5 | 5 | ≈4.5 | 6 |
| ^b 0.15V _f -0.2V _{HA(CaO)} | ≈6.5 | 5 | ≈4.5 | 6 |
| 0.2V _{HA} | 0 | 0 | ≈5 | 9 |

^a Sample names designate the accumulative volume fractions of fibres (V_f) and HA (V_{HA}) in the composite.

^b Designates samples where a non-homogenous distribution (NHD) of HA (V_{HA-pp} ≠ V_{HA-m}) is present.

8.2.5.2 Optimisation of Biocompatible Hybrid Composites

Based on the MTT results found in section 7.3.6, 0.01V_f and 0.05V_f RCM CorGlaes[®] Pure 107 fibre PLA hybrid composites were assessed using composite samples with an increasing volume fraction of HA (V_{HA}) homogeneously distributed throughout the matrix phase (V_{HA-m}) along with a 0.2V_{HA} control.

To compare the effect of calcium phosphate filler solubility on composite biocompatibility, a 0.05V_f hybrid composite was manufactured using β -TCP as the secondary filler phase. This was due to the increased solubility of β -TCP ($K_{sp} = 10^{-28.9}$ at 25°C) compared to HA ($K_{sp} = 10^{-116.8}$ at 25°C) (Figure 8.2.4) and its widespread application in biomaterials. These samples were manufactured following the methods described in section 8.2.3.1, 8.2.3.2 and 8.2.4 using 4 μ m β -TCP particles (P228S, Plasma Biotol, UK) [100].

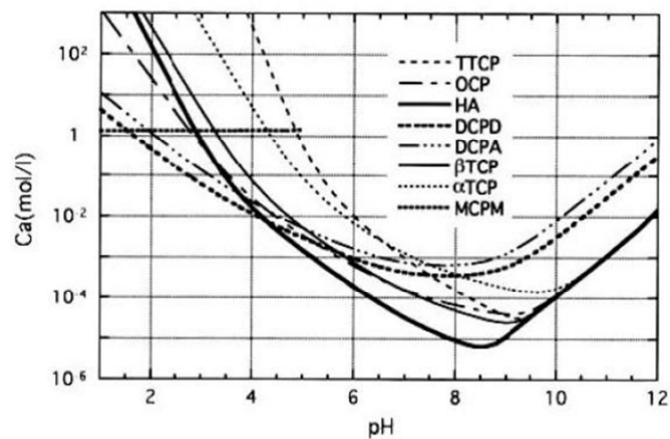


Figure 8.2.4. Variation in different calcium phosphate compound solubility with pH (solubility expressed as Ca concentration) [Reproduced from Dorozhkin (2013) Self-Setting Calcium Orthophosphate Cements].

The manufacturing specifications along with the weight and volume fractions of all precursor and composite samples is described below in Table 8.2.3 and Table 8.2.4. As specified in section 7.2.3, the low V_f of the composites prevented any solvent casting pre-preg stage due to the damage incurred when attempting to remove the samples from the foil trays.

Unfortunately the 130x80mm mould used in the manufacturing of previous composites was damaged and whilst being repaired a substitute 70x30mm three-piece cavity mould was used to manufacture the samples outlined in Table 8.2.3 and Table 8.2.4.

Table 8.2.3. Specifications for fibre pre-pregs and matrix precursor materials used for the manufacturing of CorGlaes[®] Pure 107 hybrid composites.

| Composite | Fibre Pre-Preg ($n = 1$) (pp) | | | Matrix sheet ($n = 1$) | |
|----------------------|---------------------------------|--------|----------------------|--------------------------|------------|
| | | | | 40ml 10 w/v % PLA | V_{HA-m} |
| | Fibre (g) | HA (g) | $V_{f-pp}-V_{HA-pp}$ | HA (g) | |
| $0.01V_f$ | 0.04 | 0 | 1-0 | 0 | 0 |
| $0.01V_f-0.1V_{HA}$ | 0.04 | 0 | 1-0 | 1.1 | 0.1 |
| $0.01V_f-0.2V_{HA}$ | 0.04 | 0 | 1-0 | 2.6 | 0.2 |
| $0.05V_f$ | 0.15 | 0 | 1-0 | 0 | 0 |
| $0.05V_f-0.1V_{HA}$ | 0.15 | 0 | 1-0 | 1.1 | 0.1 |
| $0.05V_f-0.2V_{HA}$ | 0.15 | 0 | 1-0 | 2.6 | 0.2 |
| $0.2V_{HA}$ | 0 | 0 | 0 | 2.6 | 0.2 |
| $0.05V_f-0.2V_{TCP}$ | 0.15 | 0 | 1-0 | 2.6 | 0.2 |

Table 8.2.4. Weight and number of precursor sheets used in the manufacture of CorGlaes[®] Pure 107 composites.

| Composite | CorGlaes [®] Pure 107 Fibre | | Matrix Sheets | |
|----------------------|--------------------------------------|------------------|---------------|----------------|
| | Weight (g) | Pre-Preg (n) | Weight (g) | Matrix (n) |
| $0.01V_f$ | 0.04 | 5 | 1.2 | 6 |
| $0.01V_f-0.1V_{HA}$ | 0.04 | 4 | 1.4 | 5 |
| $0.01V_f-0.2V_{HA}$ | 0.04 | 4 | 1.4 | 5 |
| $0.05V_f$ | 0.15 | 5 | 1.2 | 6 |
| $0.05V_f-0.1V_{HA}$ | 0.15 | 4 | 1.2 | 5 |
| $0.05V_f-0.2V_{HA}$ | 0.15 | 4 | 1.2 | 5 |
| $0.2V_{HA}$ | 0 | 0 | 1.2 | 9 |
| $0.05V_f-0.2V_{TCP}$ | 0.15 | 4 | 1.2 | 5 |

8.2.6 Mechanical Testing and Degradation

The mechanical testing and degradation of CorGlaes[®] Pure 107 hybrid composites (Figure 8.2.5) and control samples was conducted following the procedure outlined in section 7.2.4 and 7.2.5 respectively.

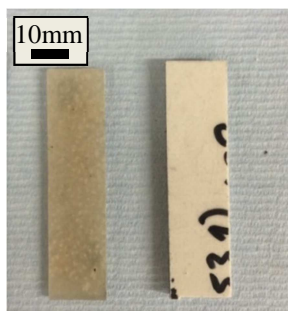


Figure 8.2.5. Image of a 60x15x2mm 0.2V_f RCM composite (left) and 0.15V_f-0.2V_{HA} hybrid composite (right) showing the change in colour of the hybrid sample due to the inclusion of hydroxyapatite (HA) particles into the pre-preg and matrix phases.

8.2.7 Biocompatibility of CorGlaes[®] Pure 107 Hybrid Composites

The procedures for cytotoxicity testing and preparing precursor solutions for cell culture were conducted following the instructions and recipes at the Centre for Cell Engineering (CCE), University of Glasgow.

Prior to biocompatibility testing, the *in vitro* cell culture and seeding of samples was performed following the method described in section 5.2.10.2.

8.2.7.1 Cell Culture Precursor Solutions

Cell culture fixative

A fixative solution for cells after cell culture was prepared following the recipe and chemical agents listed in Table 8.2.5. This solution was intended to preserve the dead cells in a condition as close as possible to their living state for visual analysis.

Table 8.2.5. Reagent chemicals involved in preparation of CCE cell fixative solution.

| Reagent | Quantity |
|--|----------|
| Phosphate buffered saline (PBS) (section 5.2.10.1) | 90ml |
| Formaldehyde (Sigma-Aldrich, USA) | 10ml |
| Sucrose (Sigma-Aldrich, USA) | 2g |

Fixative for SEM inspection

For SEM imaging, cultured cells were fixed with a solution containing 1.5% glutaraldehyde and 0.1M sodium cacodylate. This was created by mixing 1.2ml of a 25% glutaraldehyde solution with a 18.8ml sodium cacodylate buffer.

8.2.7.2 MTT Assay

The biocompatibility of the CorGlaes[®] Pure 107 hybrid composites and control materials was assessed by MTT assay using MG63 cells following the procedure outlined in section 7.2.8 for extracts obtained after 24 and 96 hours of degradation.

8.2.7.3 Coomassie Brilliant Blue

The Coomassie Brilliant Blue staining method is an inexpensive and easily processable technique for visualising proteins by binding them with a triphenylmethane dye. Two distinct classifications of the Coomassie Brilliant Blue dye are available and are based upon a methanol (G-250) or methanol-water (R-250) based recipe to produce blue-violet stains with either a reddish (R-250) or greenish tint (G-250) ^[355, 356].

Coomassie Brilliant Blue dye

The Coomassie dye (R-250) used for *in vitro* testing was prepared following the recipe outlined in Table 8.2.6. The stain was then passed through filter paper and stored at ambient temperature.

Table 8.2.6. Reagent chemicals used in the preparation of the Coomassie stain

| Reagent | Quantity |
|--------------------------------|----------|
| Methanol | 225ml |
| Acetic Acid | 50ml |
| Coomassie Brilliant Blue R-250 | 1.25 |
| Deionised Water | 225ml |

Coomassie Brilliant Blue protocol

Protein staining of cells cultured on CorGlaes[®] Pure 107 composite samples was performed using a Coomassie Brilliant Blue dye (R-250) on 10x10x2mm composite samples cultured with MG63 cells over 24, 96 and 168 hours of incubation in a 24-well plate. To correlate with the MTT assay results, composite samples were seeded at a cell density of 1×10^4 cells ml^{-1} at a $1.4 \text{ cm}^2 \text{ ml}^{-1}$ SA:V with Thermanox[®] coverslips (Thermo Fisher Scientific[™], USA) used as positive controls alongside additional suitable sample controls. Samples were cultured in 5% CO_2 at 37°C inside an incubator with the CDMEM media replaced after 96 hours. Coomassie staining of samples was then performed in triplicate ($n = 3$) for each culture period following the steps outlined in Table 8.2.7.

Table 8.2.7. Procedure for Coomassie staining of cells cultured on CorGlaes[®] Pure 107 composite samples.

| Step | Description |
|------|---|
| 1 | The culture plates were removed from the incubator and the CDMEM aspirated before samples were immersed in the fixative solution (Table 8.2.5) for fifteen minutes. |
| 2 | The fixative was removed and the samples washed three times with sterile PBS. |
| 3 | The Coomassie staining solution was then added to all samples for fifteen minutes before samples were washed five times with sterile PBS. Images were then captured using an Eclipse ME600 optical microscope (Nikon, Japan). |

8.2.7.4 SEM Imaging

Visual examination of MG63 cells cultured on composite and control samples by SEM was performed using a Sigma VP SEM (Carl Zeiss, Germany) SEM at 10kV accelerating voltage at the School of Geographical and Earth Sciences, University of Glasgow. The inspection of cultured cells was performed after seeding samples in triplicate ($n = 3$) at a cell density of 1×10^4 cells ml^{-1} at a $1.4 \text{ cm}^2 \text{ ml}^{-1}$ SA:V ratio and changing the CDMEM after 96 hours. Samples were then inspected after 24, 96 and 168 hours of incubation following the preparation steps outlined below with images captured using the Zeiss SmartSEM software package. Images were captured in triplicate ($n = 3$) for each sample across the different culture periods at x800 and x1500 magnifications.

SEM sample cell fixation

At each corresponding incubation period (24, 96, 168 hours) the culture plates were removed from the incubator and washed twice with sterile PBS before the SEM fixative was added to each sample inside a laminar flow fume cabinet. Plates were then wrapped in Parafilm M[®] (Sigma-Aldrich, USA) and placed inside a fridge at 4°C for one hour after which the fixative was removed and the samples were washed three times with a 0.1M sodium cacodylate buffer rinse. Sample plates were then wrapped in tin foil and returned to the fridge until SEM preparation.

SEM sample preparation

For SEM analysis, cell cultured samples were prepared by being removed from the fridge and washed with osmium tetroxide for one hour inside a fume hood before being rinsed three times with deionised water for ten minutes per rinse. Samples were then stained with 0.5% uranyl acetate, wrapped in foil and left for one hour. Following these steps the samples were sequentially dehydrated by being immersed for ten minutes with increasing concentrations of ethanol (30% → 50% → 70% → 90%). Samples were then rinsed four times with absolute ethanol for five minute periods before being washed twice in hexamethyldisilazane (HDMS) for five minute periods each. The samples were finally mounted onto aluminium stubs and sputter coated with gold (Agar Scientific, UK) for SEM imaging.

8.2.8 Ion Release

Analysis of the Ca^{2+} , Mg^{2+} , Zn^{2+} and Na^+ cations as well as the $(\text{PO}_4)^{3-}$ anion released from biocompatible CorGlaes[®] Pure 107 hybrid composites and suitable controls over the first 168 hours of sample degradation (see section 8.2.6) in distilled water was conducted following the procedure described in section 5.2.8.2.

8.2.9 Hybrid Composite Bioactivity

The bioactivity of biocompatible CorGlaes[®] Pure 107 hybrid composites was conducted following the procedure outlined in section 7.2.7. This was performed alongside a $0.2V_{\text{HA}}$ control and an equivalent HA-free CorGlaes[®] Pure 107 fibre composite (with the V_f matching that of the biocompatible hybrid composite).

8.3 Results

8.3.1 Silane Treated CorGlaes® Pure 107 Composites

8.3.1.1 Mechanical Properties

A comparison between the typical stress strain plots obtained from the previous 0.2V_f RCM and a silane treated 0.2V_f RCM composite (0.2V_f RCM-APS) is displayed in Figure 8.3.1 with the flexural strength and elastic moduli compared in Figure 8.3.2 [46].

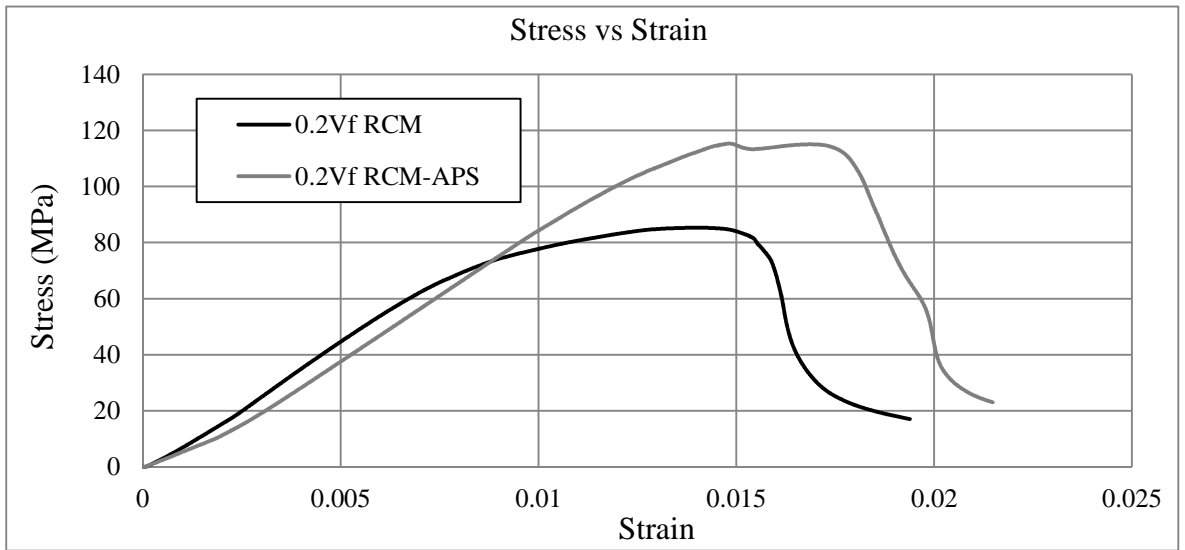


Figure 8.3.1. Typical stress-strain plots obtained from the mechanical testing of 0.2V_f RCM and 0.2V_f RCM-APS silane treated composites

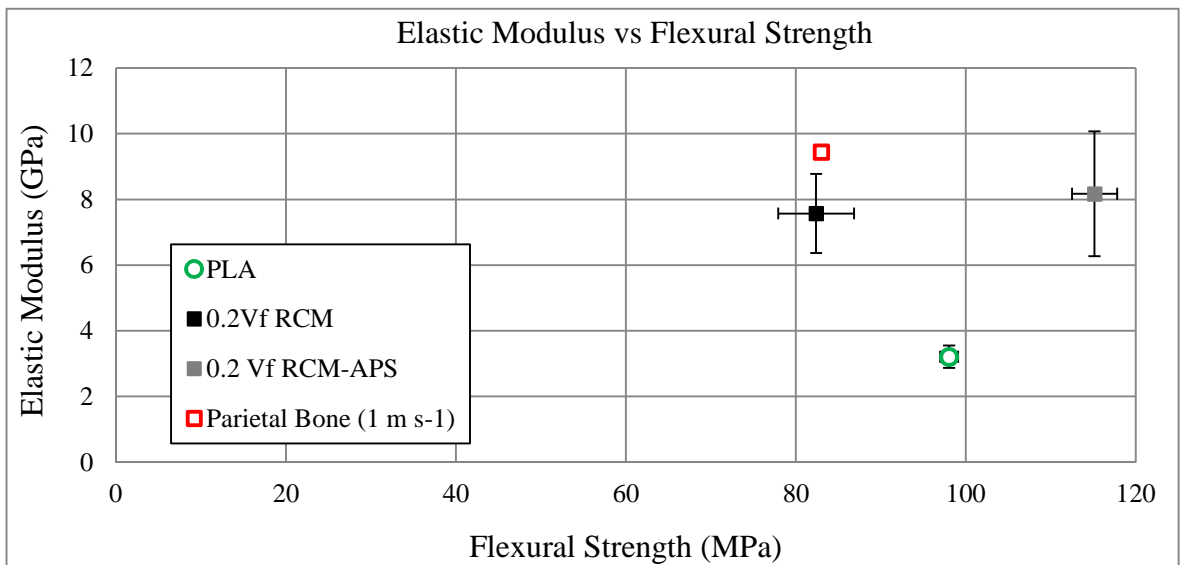


Figure 8.3.2. Comparison of 0.2V_f RCM-APS composite mechanical properties with the previous 0.2V_f RCM samples and parietal bone [Data from Motherway et al. (2009)]

8.3.1.2 Degradation

The wet/dry weight changes along with the media pH during the degradation of 0.2V_f RCM-APS composites is compared with the previous 0.2V_f RCM results over 1008 hours of immersion in Figure 8.3.3 and Figure 8.3.4. The retention of 0.2V_f RCM-APS sample mechanical properties over this degradation period is also compared in Figure 8.3.5.

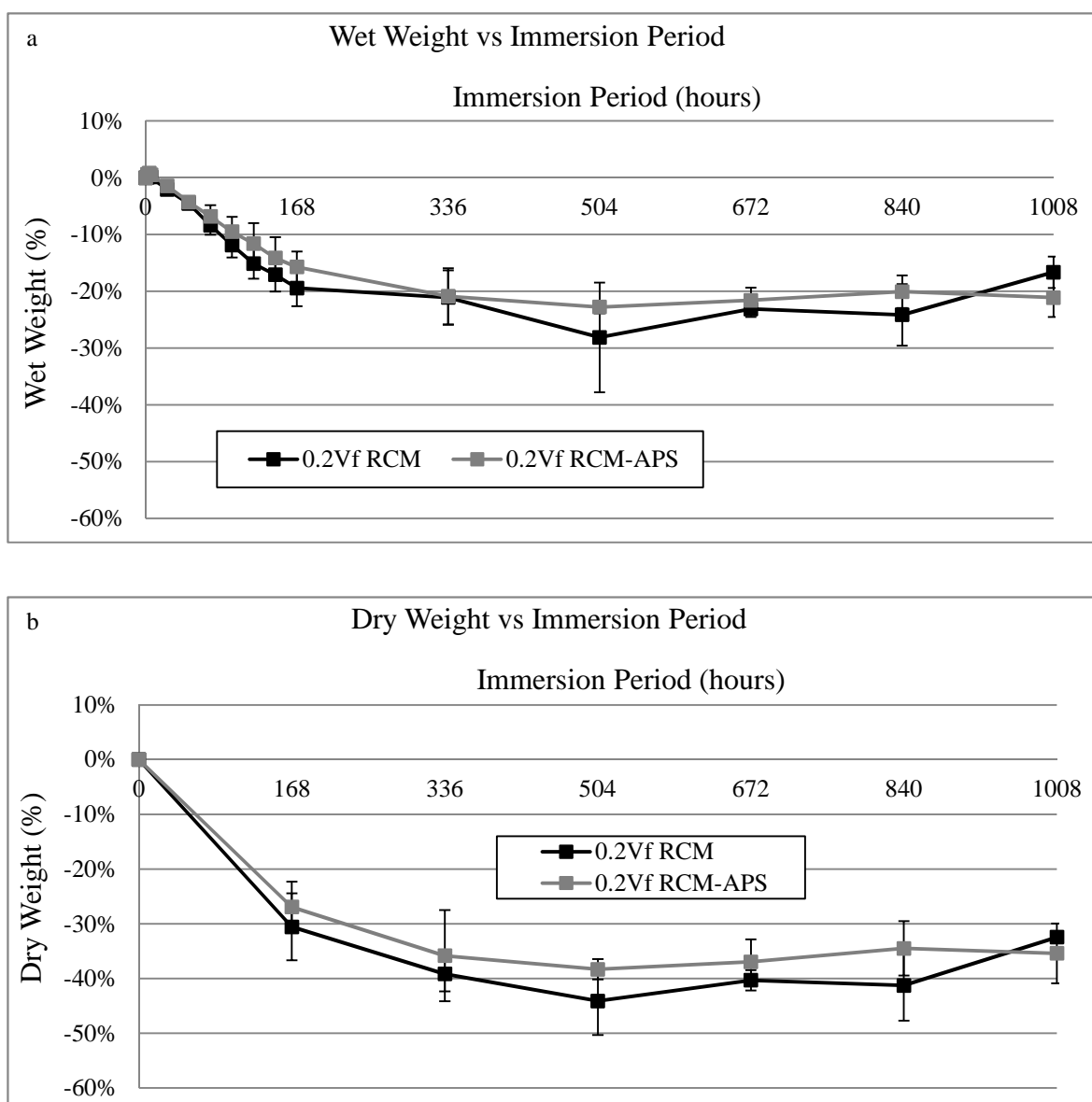


Figure 8.3.3. Comparison of silane treated 0.2V_f RCM-APS composites a) Wet weight and b) Dry weight with previous 0.2V_f RCM data over 1008 hours (six weeks) of degradation in distilled water at 37°C.

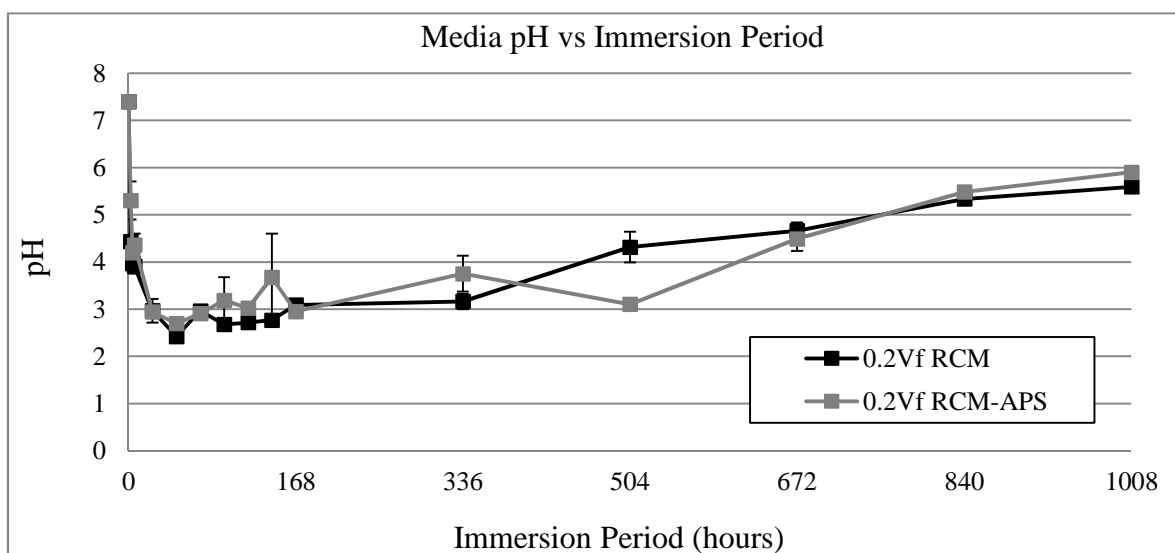


Figure 8.3.4. Media pH during degradation of silane treated 0.2V_f RCM-APS composite and 0.2V_f RCM samples for up to 1008 hours of immersion in distilled water at 37°C.

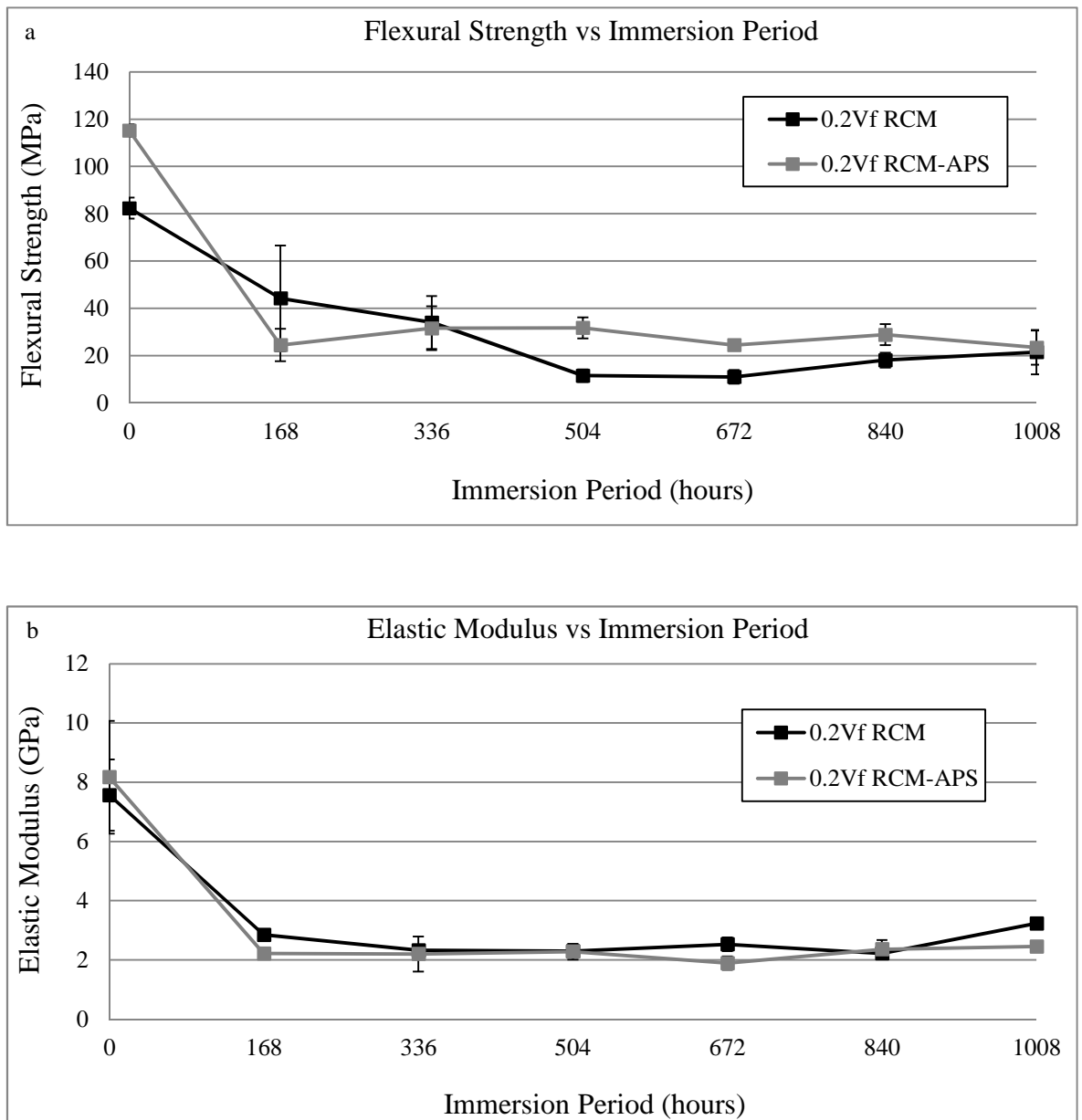


Figure 8.3.5. Comparison of silane treated 0.2V_f RCM-APS and 0.2V_f RCM composite a) Flexural strength and b) Elastic modulus during degradation in distilled water at 37°C for up to 1008 hours (six weeks).

8.3.2 Optimisation of Hybrid Composite Degradation

8.3.2.1 Mechanical Properties

The stress-strain plots recorded during the mechanical testing of $0.15V_f$ hybrid composites are compared with a $0.2V_{HA}$ control composite and previous $0.2V_f$ RCM data in Figure 8.3.6. The mechanical properties of these samples are compared in Figure 8.3.7.

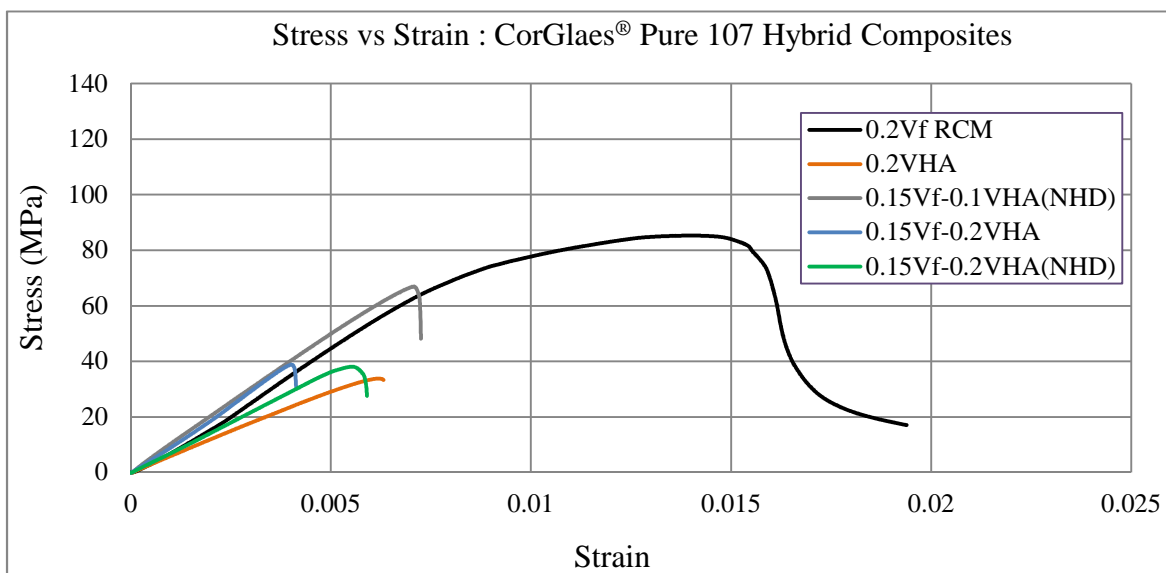


Figure 8.3.6. Comparison of stress-strain plots obtained from $0.2V_f$ RCM samples and $0.15V_fV_{HA}$ hybrid composites as well as a $0.2V_{HA}$ control.

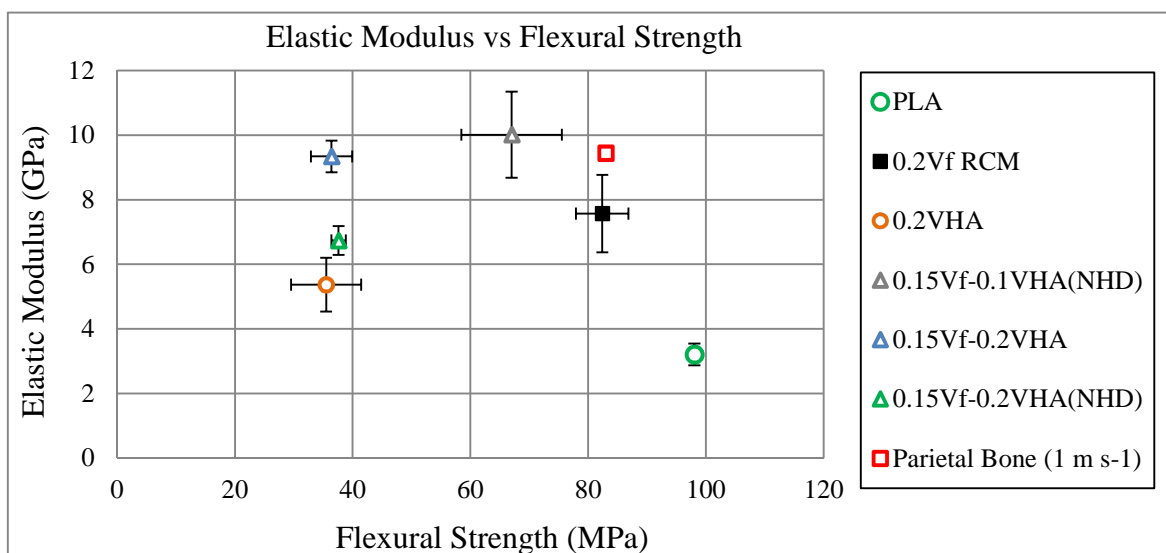


Figure 8.3.7. Comparison of flexural strength and elastic modulus of the different hybrid composite configurations shown in Figure 8.3.6 and control materials as well as parietal bone [Data from Motherway et al. (2009)].

A complete description of the hybrid composites and control sample mechanical properties are listed in Table A.2. of Appendix A.

Inspection of the fracture site after mechanical testing of a $0.15V_f-0.1V_{HA}$ hybrid composite sample is shown in Figure 8.3.8. This was conducted using a Hitachi S9000 SEM (Hitachi, Japan) at a 10kV accelerating voltage after coating the fracture faces with gold (Agar Scientific, UK) and was performed at the James Watt Nanofabrication Centre (JWNC), University of Glasgow.

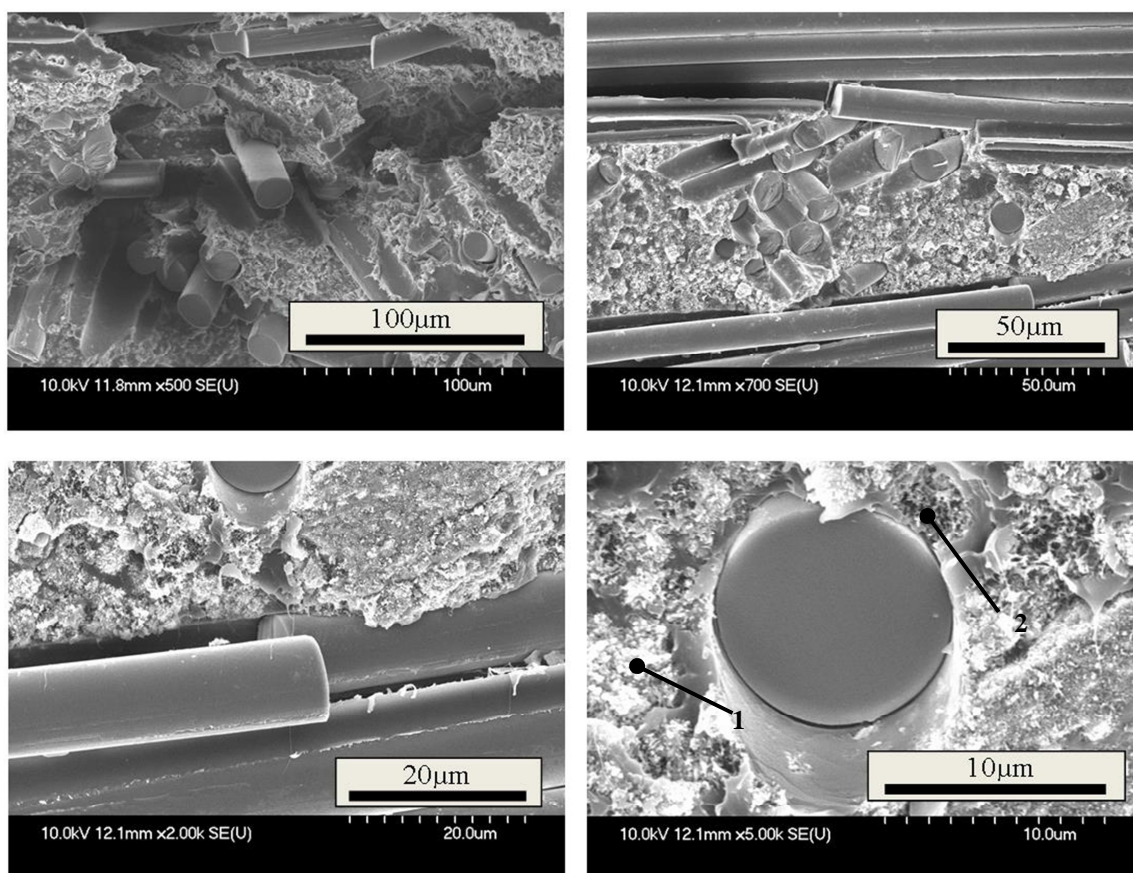


Figure 8.3.8. SEM images of mechanically tested $0.15V_f-0.1V_{HA(NHD)}$ composite fracture faces prior to degradation [i.e. T_0] with HA particles and the pull out of HA particles during mechanical testing shown by arrow 1 and 2 respectively [scale bar = 100 μ m, 50 μ m, 20 μ m, 10 μ m].

8.3.2.2 Degradation

A comparison of the different hybrid and control composites during their degradation in distilled water over 1008 hours is shown in Figure 8.3.9 as well as Figure 8.3.10 for the wet/dry weights and media pH respectively. The flexural strength and elastic modulus over this period is shown in Figure 8.3.11.

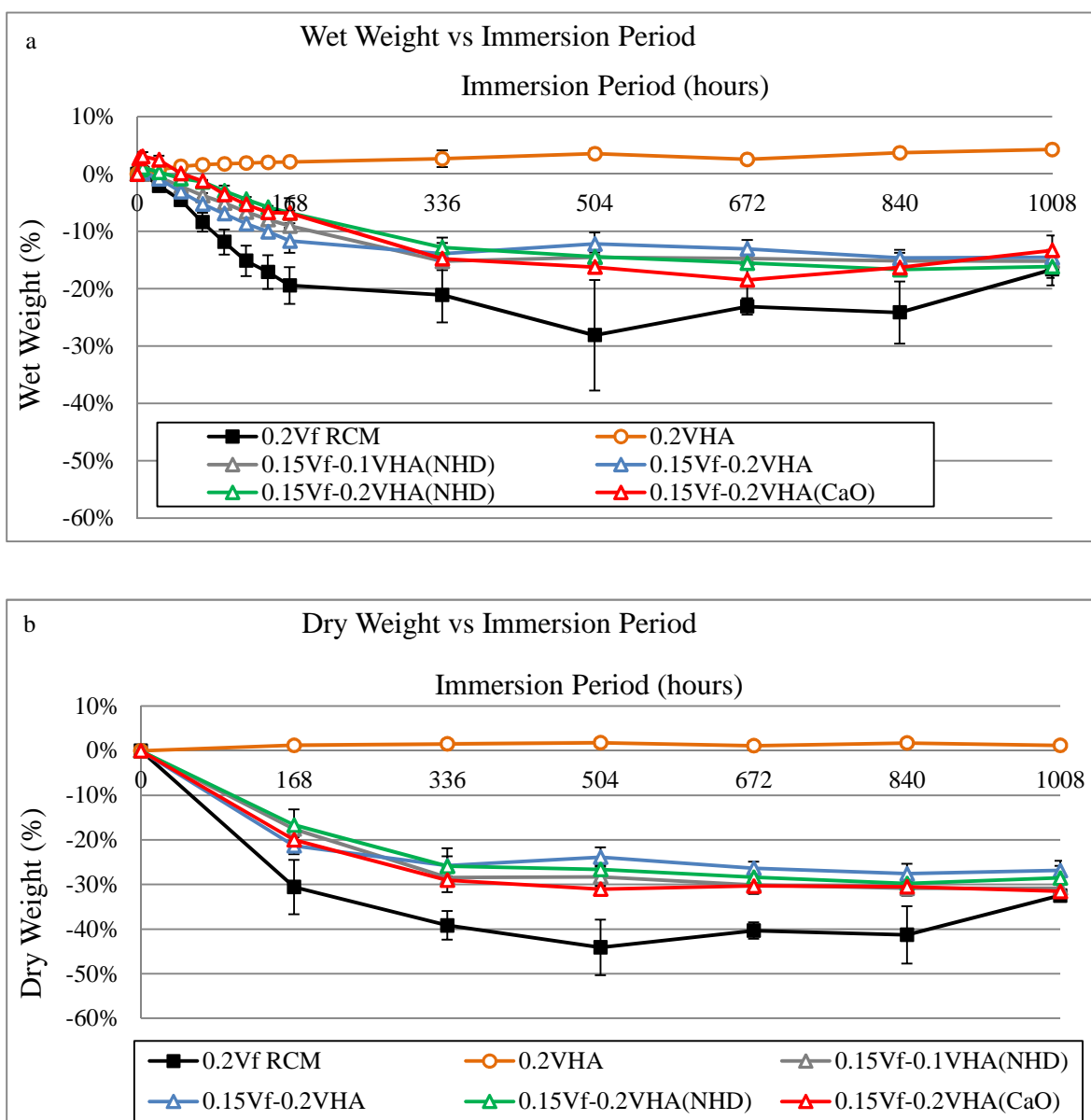


Figure 8.3.9. Comparison of a) Wet weight and b) Dry weight during the degradation of different hybrid composite configurations and control samples over 1008 hours of immersion in distilled water at 37°C.

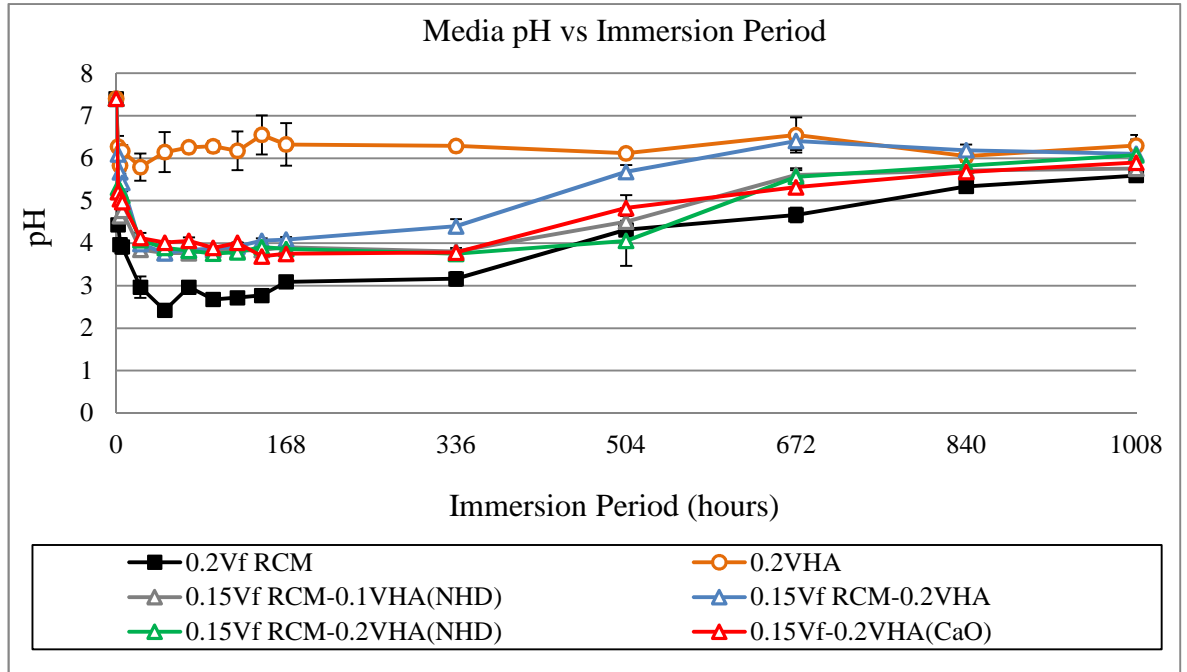


Figure 8.3.10. Comparison of media pH during degradation of hybrid composites and control samples over 1008 hours of immersion in distilled water at 37°C.

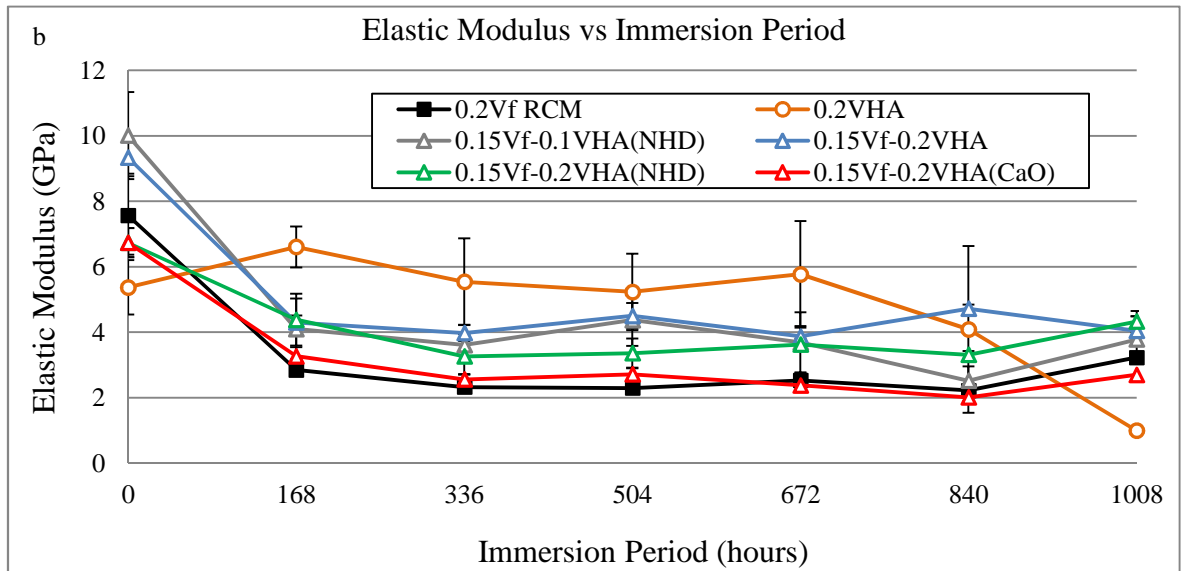
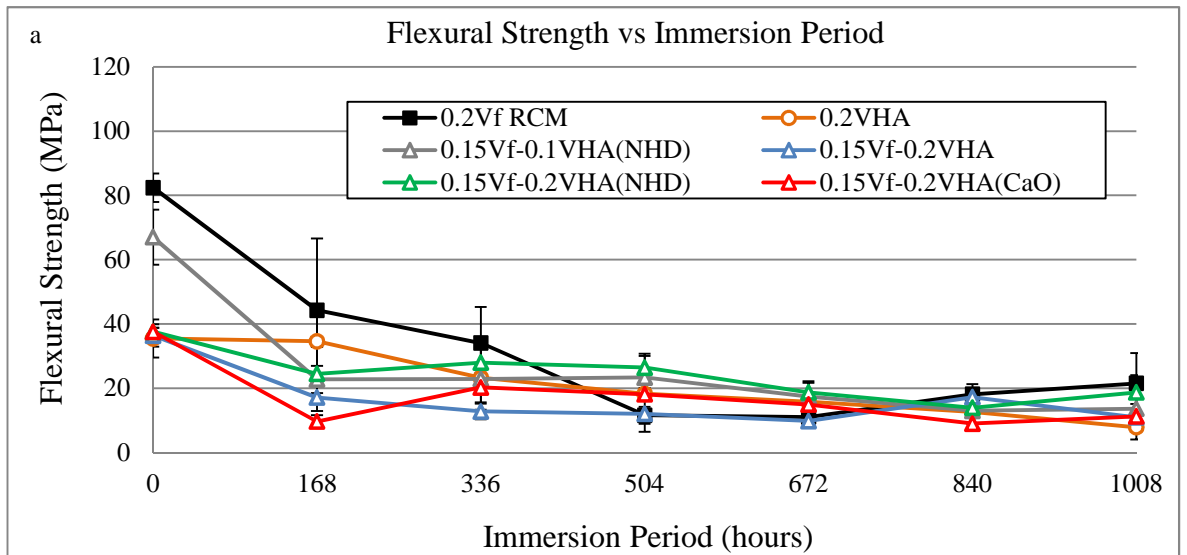


Figure 8.3.11. Comparison of hybrid and control composite samples a) Flexural strength and b) Elastic modulus during degradation in distilled water at 37°C over 1008 hours.

8.3.3 Optimisation of Biocompatible Hybrid Composites

8.3.3.1 MTT Assay

The MTT results from the extracts of different CorGlaes[®] Pure 107 hybrid composite configurations after 24 and 96 hours of degradation are shown in Figure 8.3.12. The data shows a generalised trend of increasing cell viability with increasing HA volume fraction in both $0.01V_f$ and $0.05V_f$ hybrid samples. Furthermore a statistically significant difference was found between the use of an HA or β -TCP filler on MG63 cell viability in the $0.05V_f$ hybrid composites ($p < 0.05$). The results also showed that the $0.2V_{HA}$ control sample displayed cell viabilities comparable to the CDMEM control. The pH of the media corresponding to these results is shown in Figure 8.3.13.

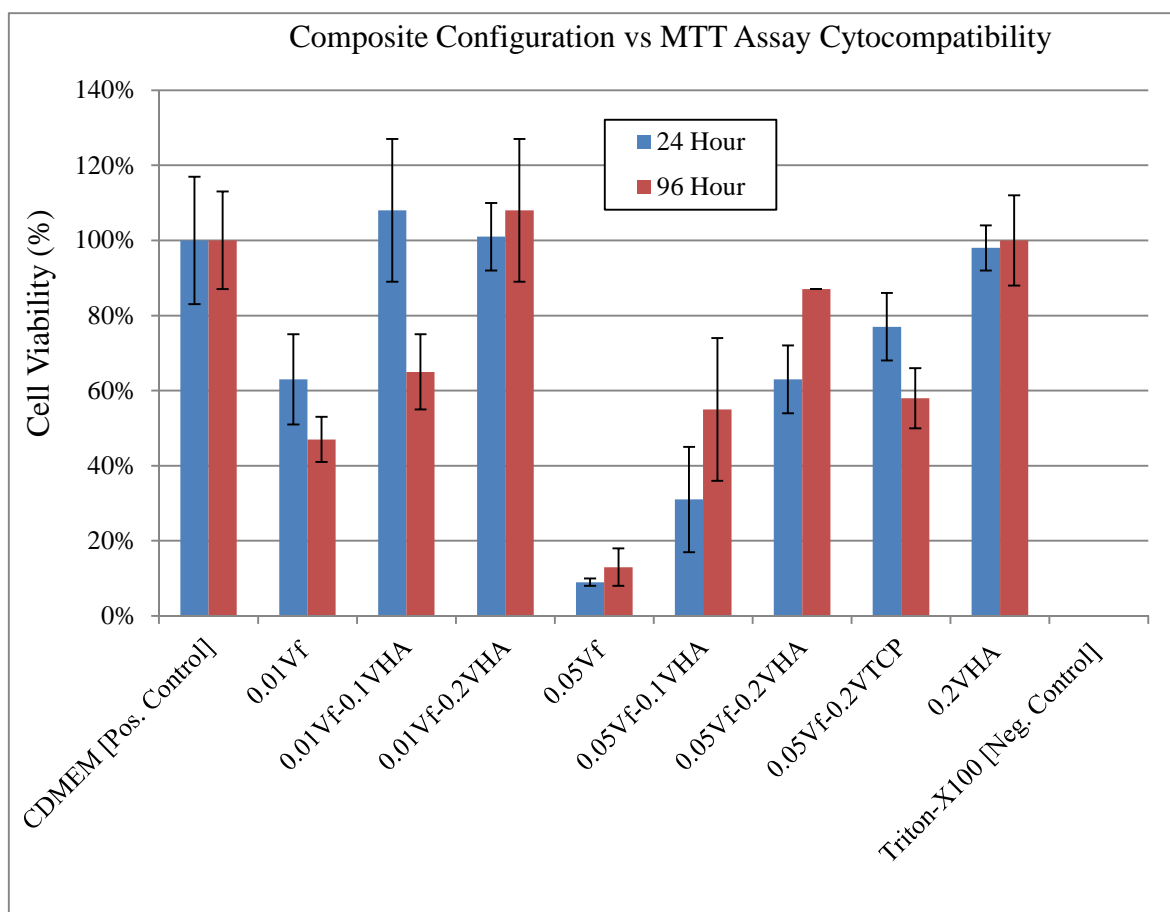


Figure 8.3.12. MTT assay of MG63 cell viability from the degradation extracts of composite materials containing $0.01V_f$ and $0.05V_f$ with $0V_{HA} \rightarrow 0.1V_{HA} \rightarrow 0.2V_{HA}$ filler volume fractions as well as a $0.05V_f-0.2V_{TCP}$ sample after 24 and 96 hours of degradation.

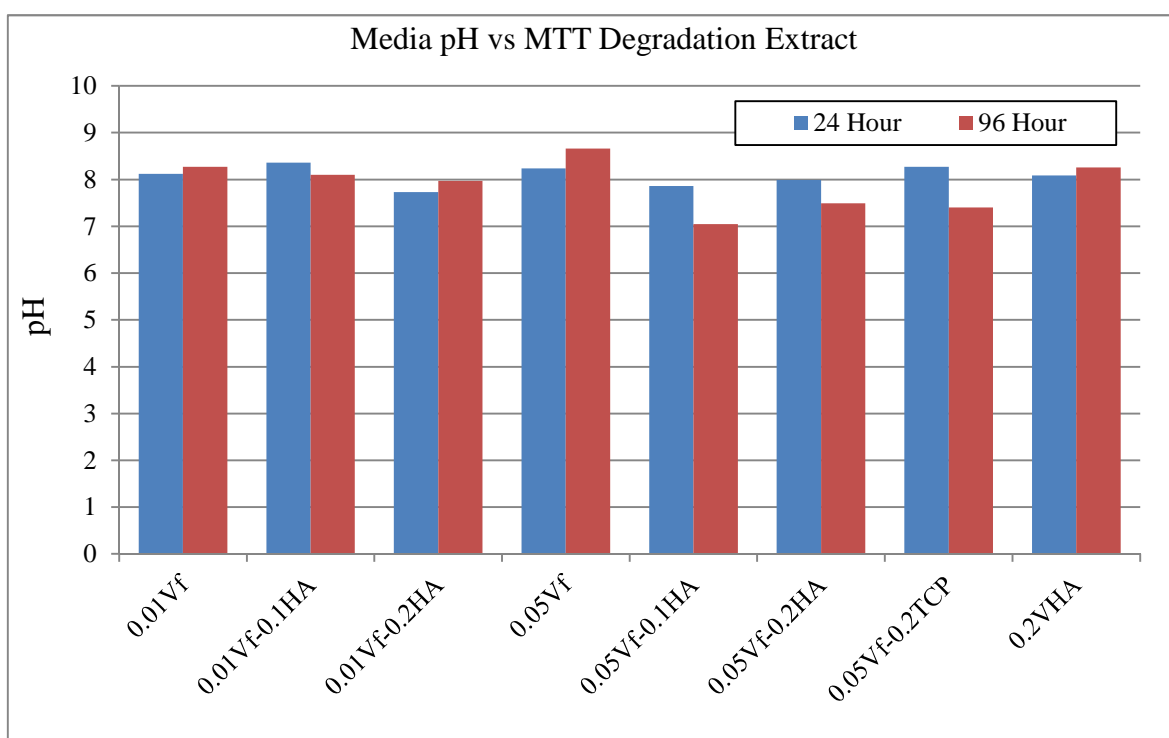


Figure 8.3.13. Comparison of media pH after 24 and 96 hours of different hybrid composite sample degradation in DMEM (standard deviations $< \pm 0.04$).

8.3.3.2 Coomassie Brilliant Blue

Given the biocompatibility of the $0.01V_f-0.2V_{HA}$ samples found by MTT assay (Figure 8.3.12), this composite configuration was subsequently investigated by direct contact cell culturing in accordance with the flow chart shown in Figure 8.2.3. This was conducted alongside the culture of MG63 cells on Thermanox[®] coverslips, neat PLA as well as $0.2V_{HA}$ and $0.01V_f$ composites to act as the further controls.

The Coomassie staining of the MG63 cells cultured on $0.01V_f-0.2V_{HA}$ hybrid composites along with the other samples listed after 24, 96 and 168 hours of incubation is shown in Figure 8.3.14, Figure 8.3.15 and Figure 8.3.16 respectively.

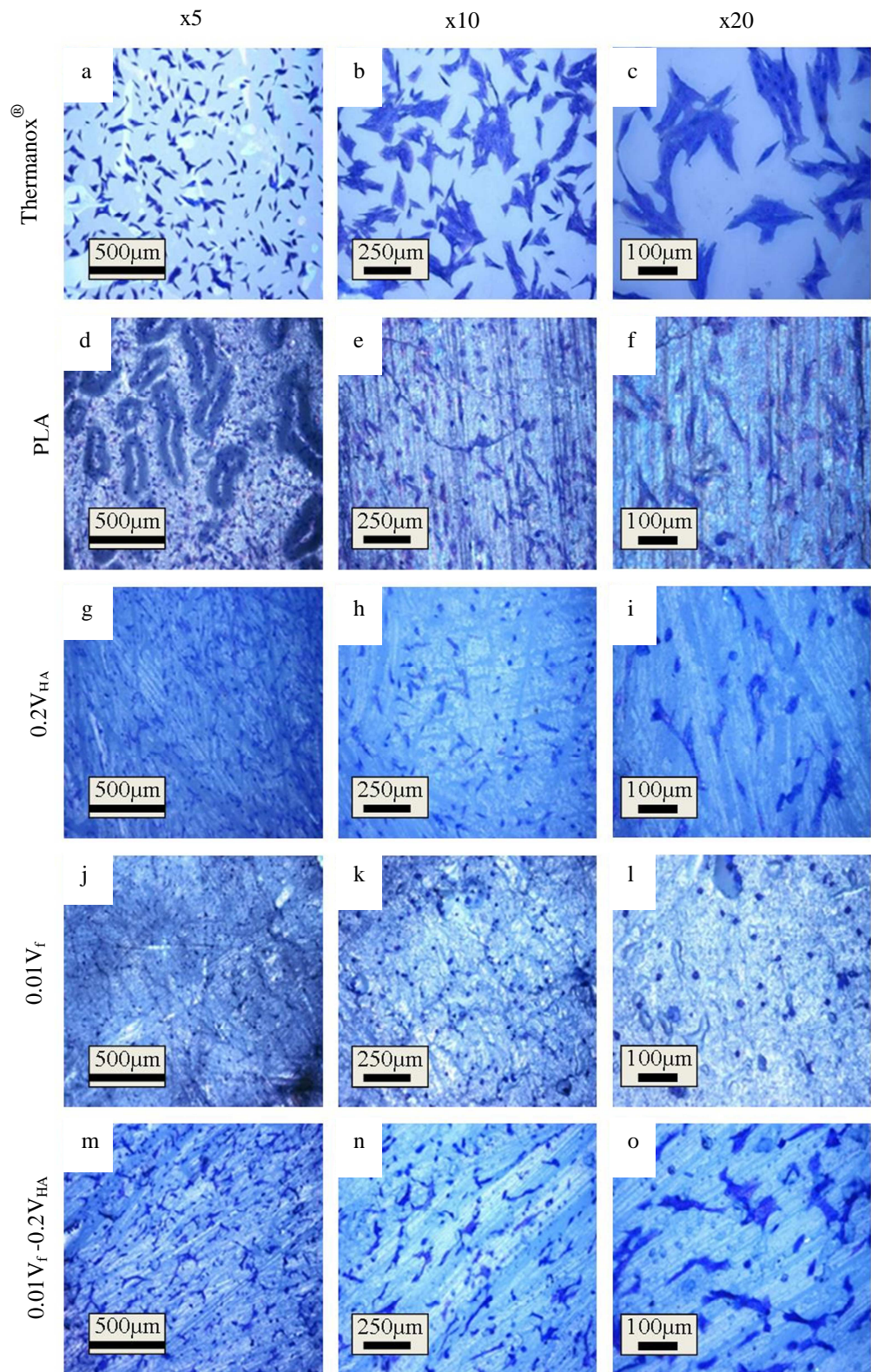


Figure 8.3.14. Coomassie staining of MG63 cells cultured after 24 hours for a-c) Thermanox[®] coverslips, d-f) PLA, g-i) 0.2V_{HA}, j-l) 0.01V_f and m-o) 0.01-0.2V_{HA} samples at x5, x10 and x20 magnifications [scale bars = 500 μm, 250 μm and 100 μm].

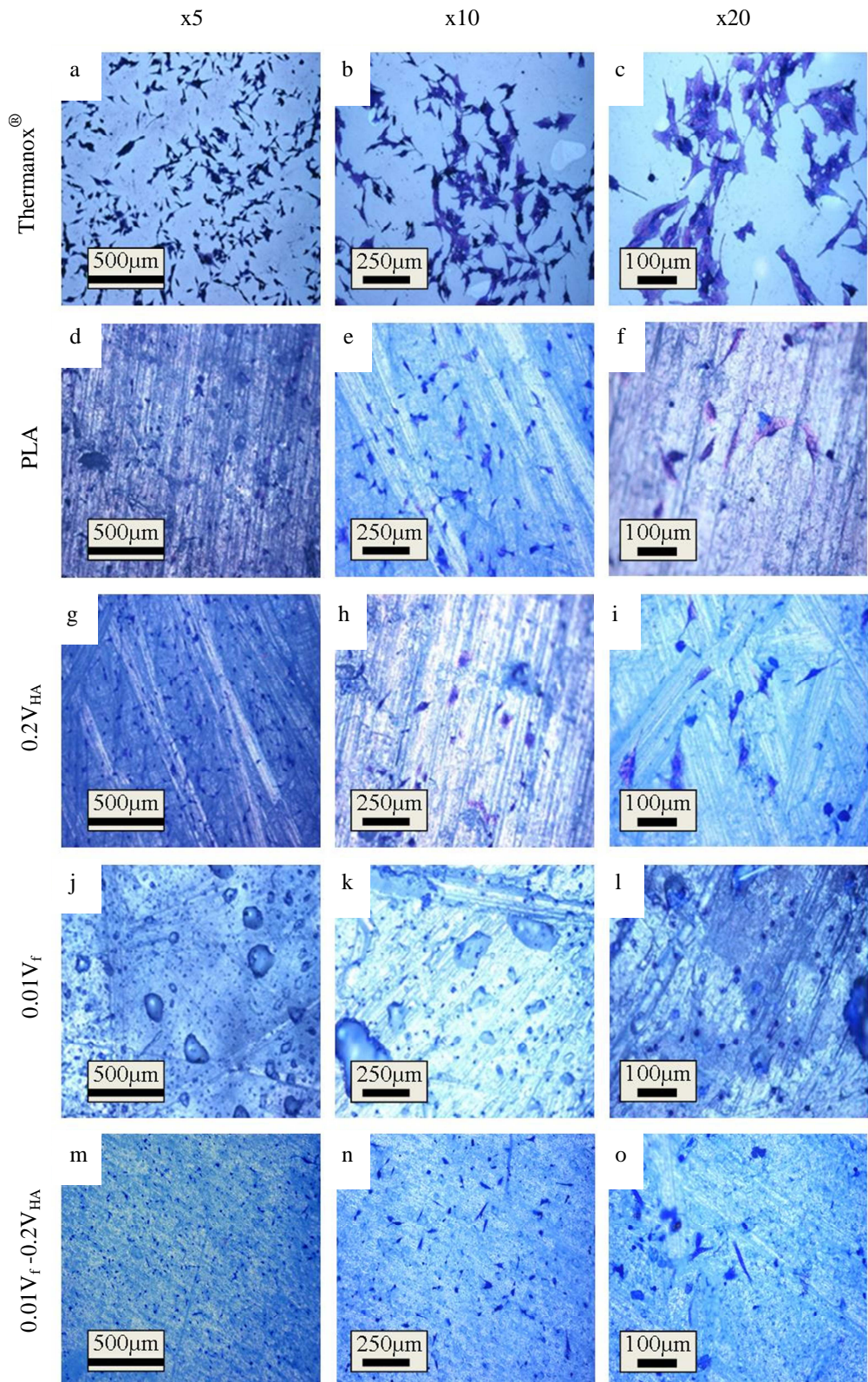


Figure 8.3.15. Coomassie staining of MG63 cells cultured after 96 hours on a-c) Thermanox[®] coverslips, d-f) PLA, g-i) $0.2V_{HA}$, j-l) $0.01V_f$ and m-o) $0.01-0.2V_{HA}$ samples at x5, x10 and x20 magnifications [scale bars = $500\mu\text{m}$, $250\mu\text{m}$ and $100\mu\text{m}$].

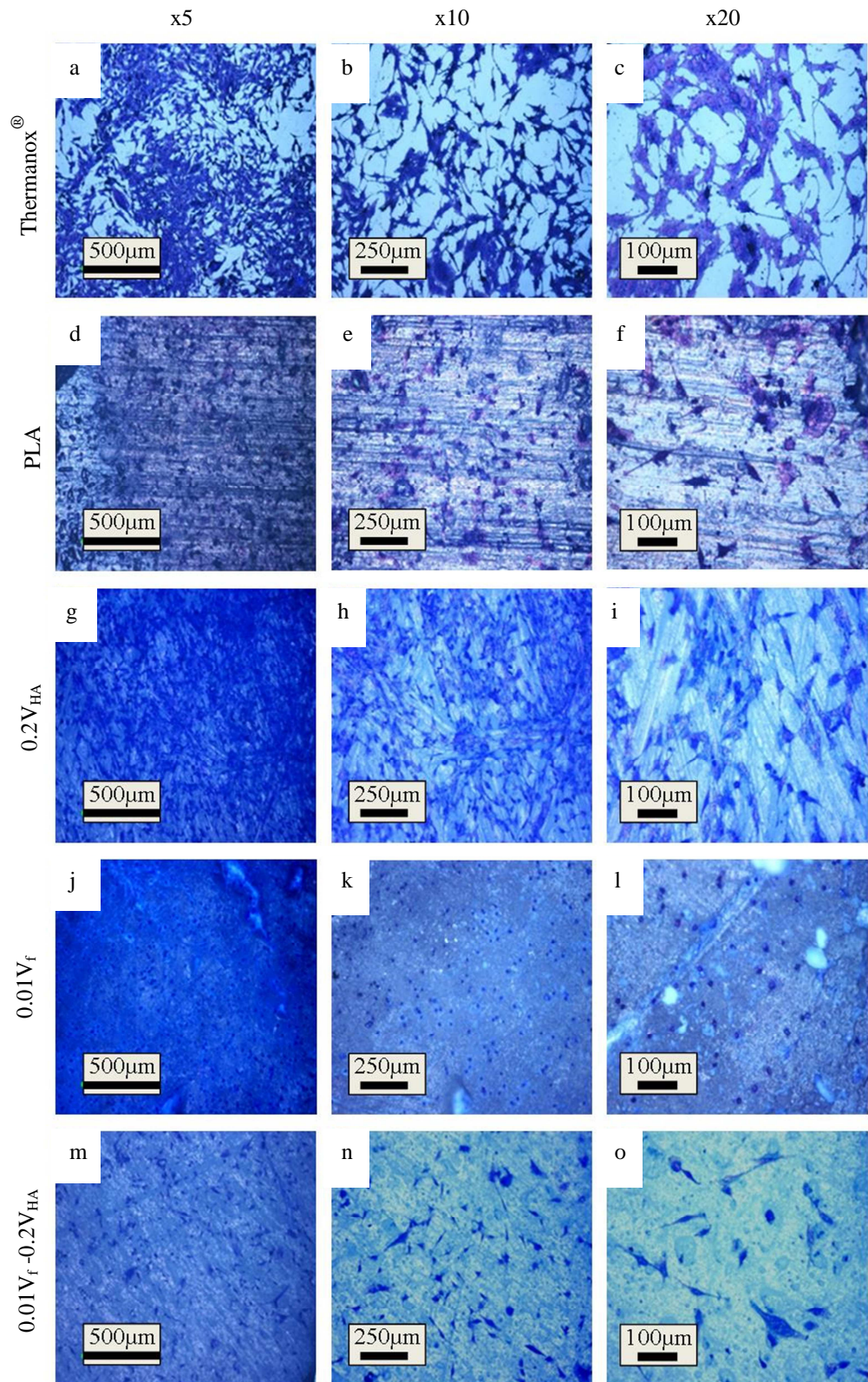


Figure 8.3.16. Coomassie staining of MG63 cells cultured after 168 hours on a-c) Thermanox[®] coverslips, d-f) PLA, g-i) $0.2V_{HA}$, j-l) $0.01V_f$ and m-o) $0.01-0.2V_{HA}$ samples at x5, x10 and x20 magnifications [scale bars = $500\mu\text{m}$, $250\mu\text{m}$ and $100\mu\text{m}$].

8.3.3.3 SEM Characterisation

Based on the Coomassie Brilliant Blue images of cultured MG63 cells (section 8.3.3.2), the seeding and culture of MG63 cells on neat PLA, 0.01V_f and 0.01V_f-0.2V_{HA} samples was analysed using SEM images. These were captured after 24, 96 and 168 hours of direct contact culture and are shown in Figure 8.3.17, Figure 8.3.18 and Figure 8.3.19 respectively at x800 and x1500 magnifications. A comparison between these samples after 168 hours of culture is also shown at x300 magnification in Figure 8.3.20.

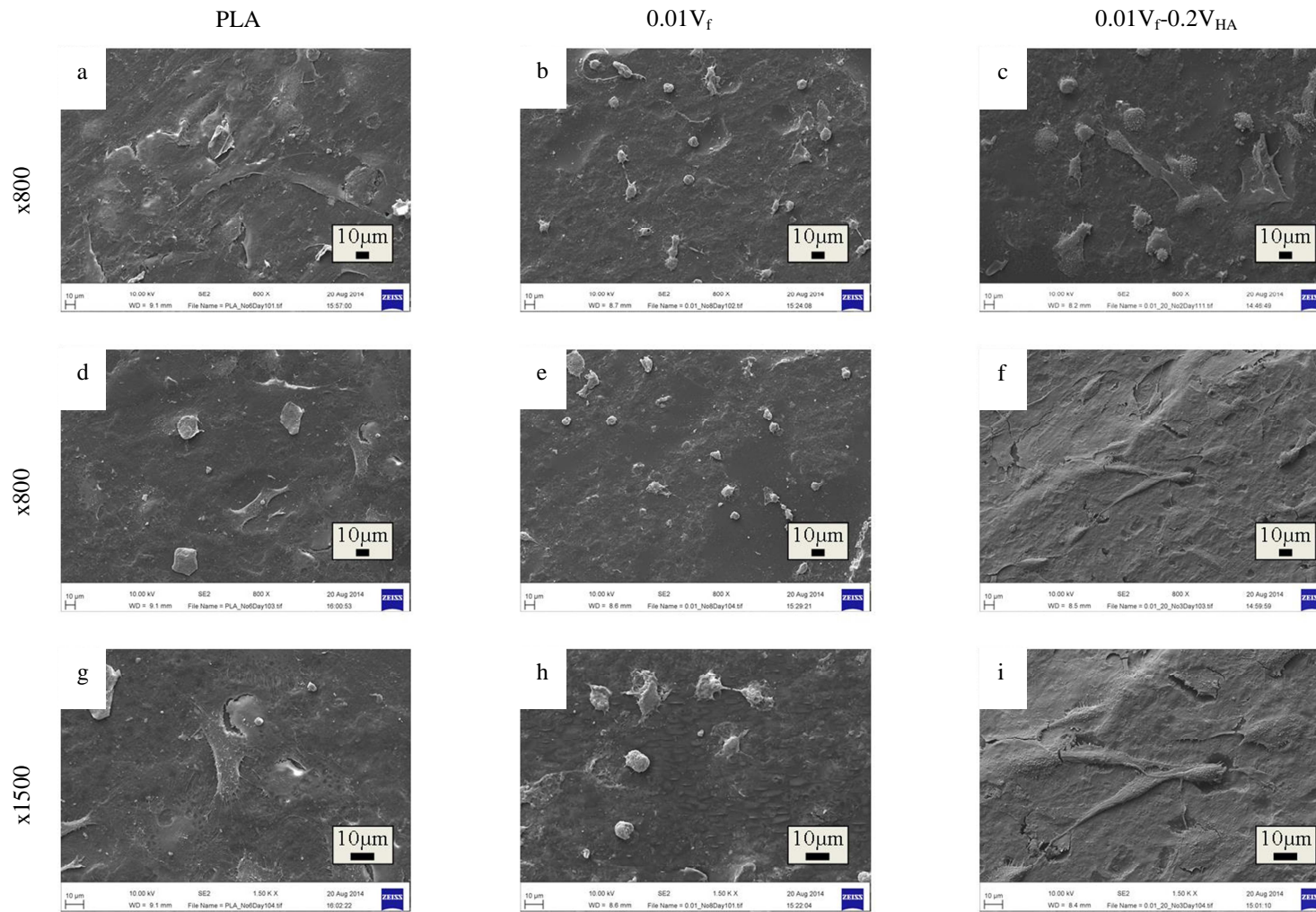


Figure 8.3.17. SEM images obtained after 24 hours of MG63 cells cultured on (a, d, g) PLA, (b, e, h) $0.01V_f$ and (c, f, i) $0.01V_f-0.2V_{HA}$ samples at x800 and x1500 magnification [scale bars = $10\mu\text{m}$].

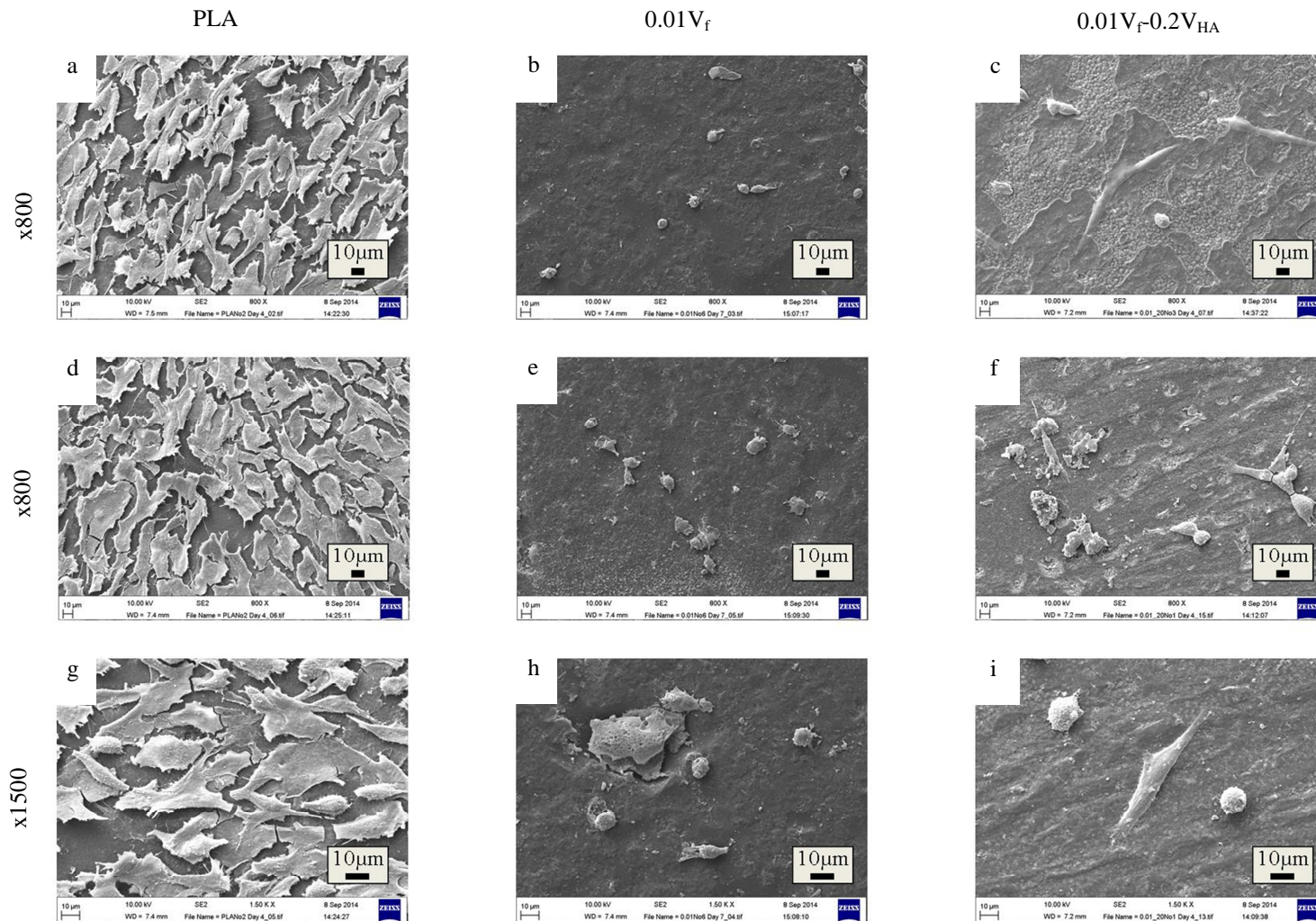


Figure 8.3.18. SEM images obtained after 96 hours of MG63 cells cultured on (a, d, g) PLA, (b, e, h) $0.01V_f$ and (c, f, i) $0.01V_f-0.2V_{HA}$ samples at x800 and x1500 magnification [scale bars = $10\mu\text{m}$].

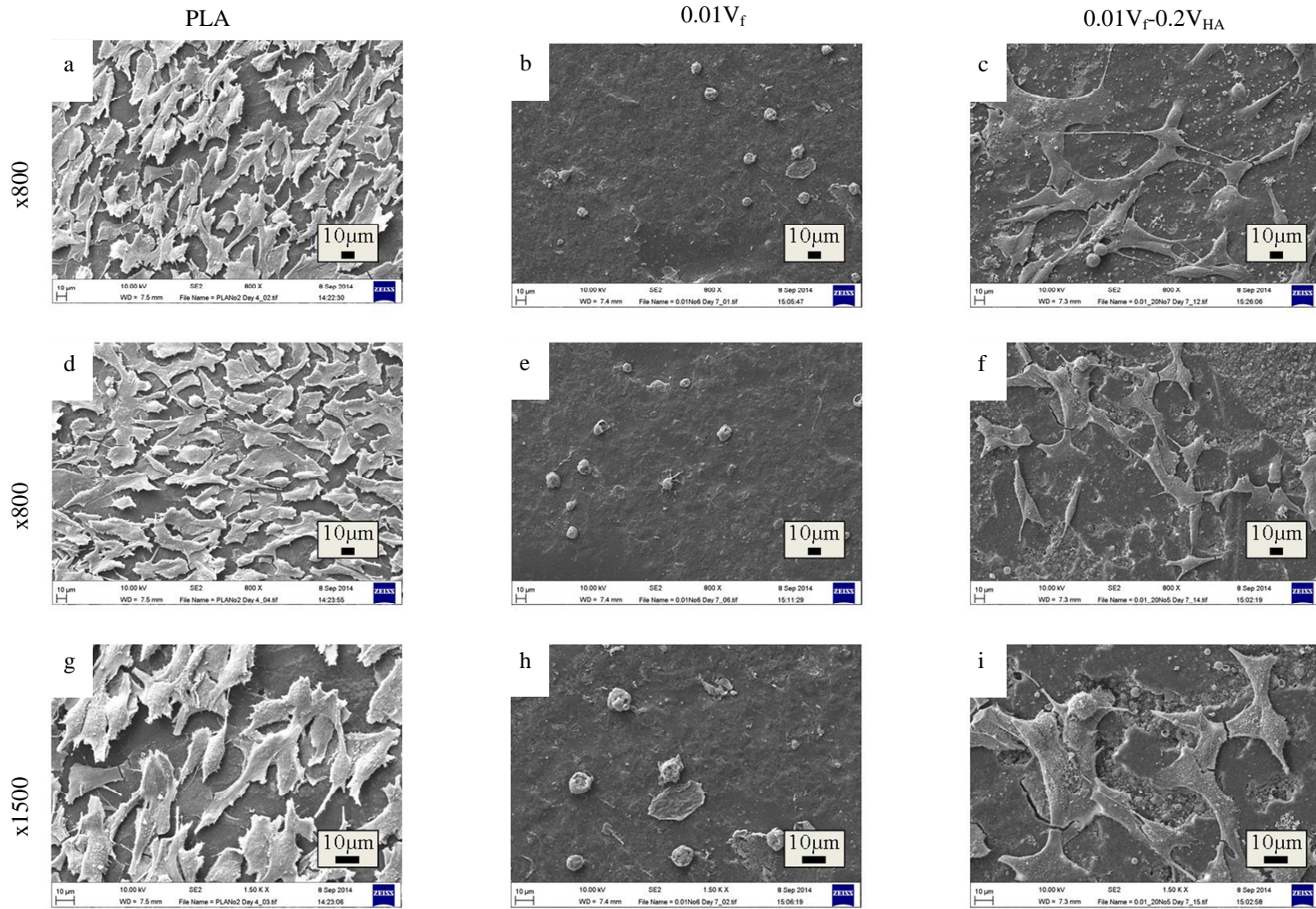


Figure 8.3.19. SEM images obtained after 168 hours of MG63 cells cultured on (a, d, g) PLA, (b, e, h) 0.01V_f and (c, f, i) 0.01V_f-0.2V_{HA} samples at x800 and x1500 magnification [scale bars = 10µm].

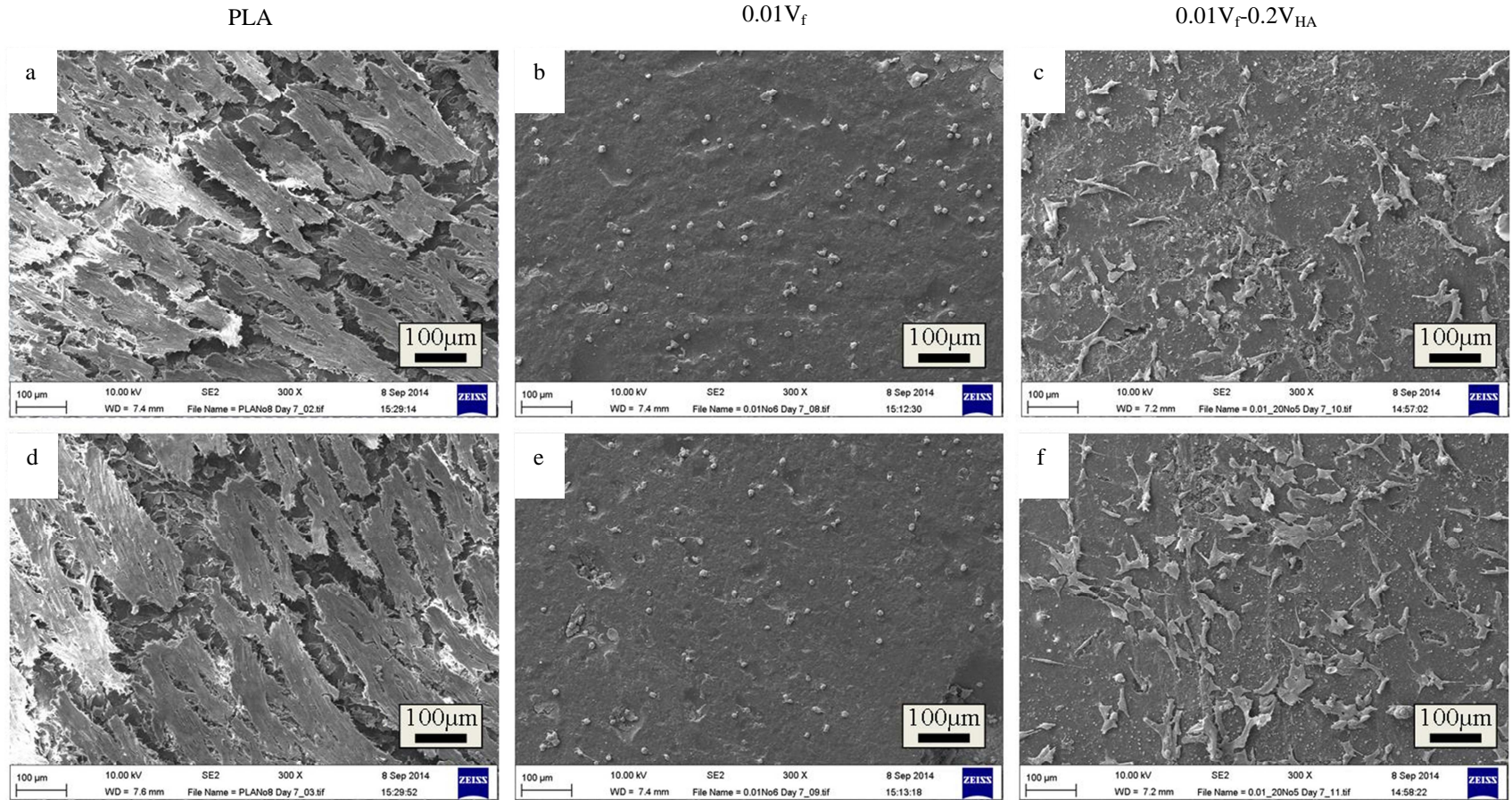


Figure 8.3.20. Comparison of MG63 cells cultured on (a,d) PLA, (b,e) $0.01V_f$ and (c,f) $0.01V_f-0.2V_{HA}$ after 168 hours of immersion at x300 magnification [scale bars = $100\mu\text{m}$].

8.3.3.4 Mechanical Properties

The stress-strain plots as well as the resulting mechanical properties of the biocompatible $0.01V_f-0.2V_{HA}$ hybrid composite are compared with $0.01V_f$ and $0.2V_{HA}$ samples in Figure 8.3.21 and Figure 8.3.22 respectively.

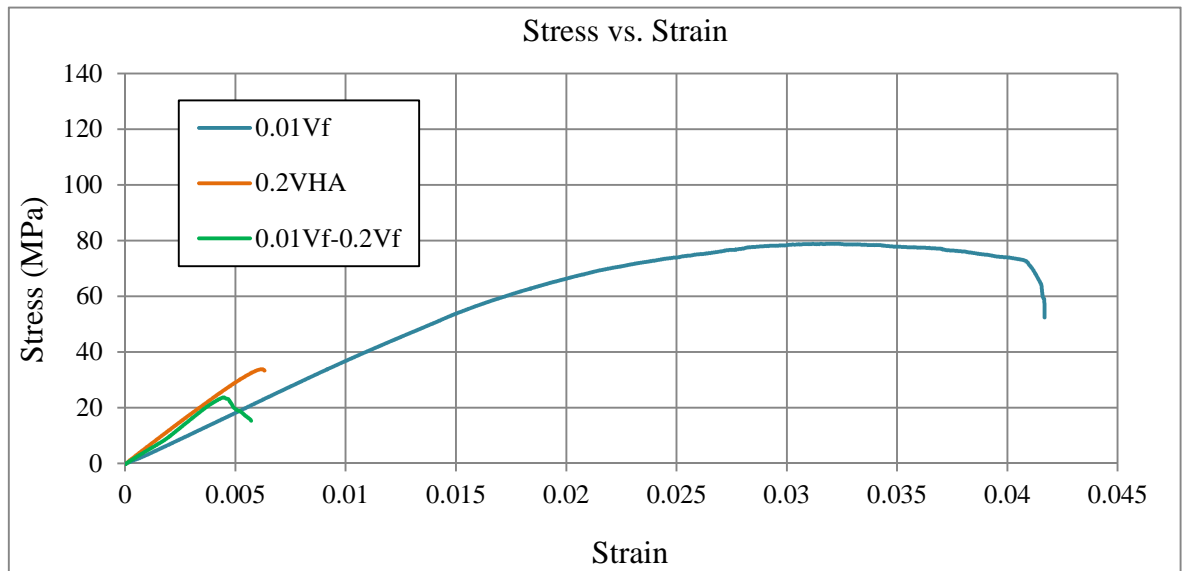


Figure 8.3.21. Stress-strain plots obtained from the three point bend testing of $0.01V_f-0.2V_{HA}$ hybrid samples as well as $0.01V_f$ and $0.2V_{HA}$ control samples.

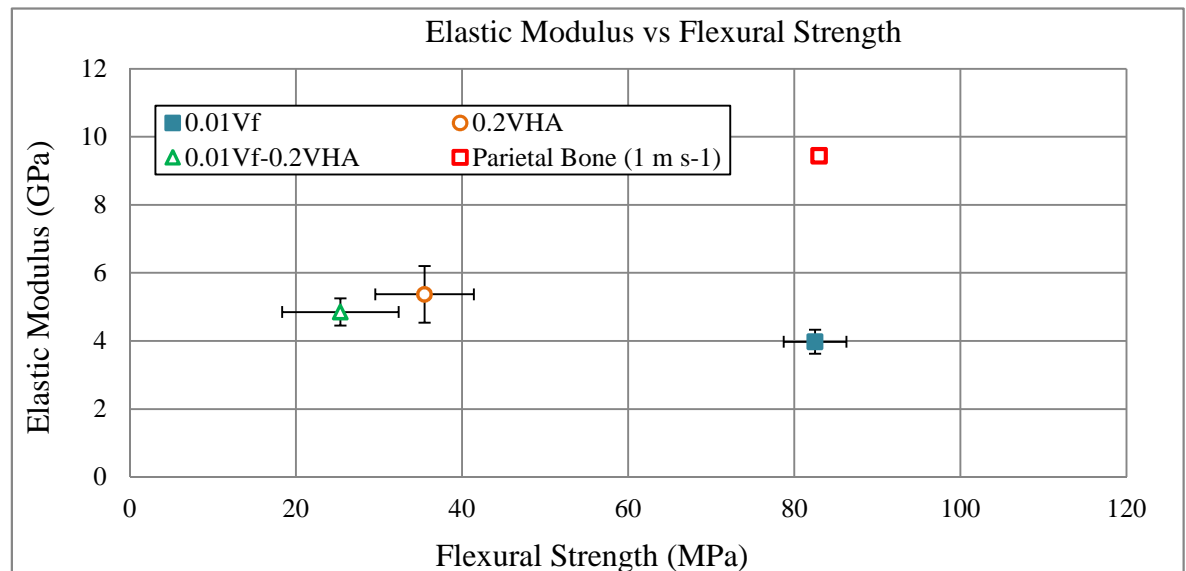


Figure 8.3.22. Comparison of flexural strength and elastic modulus of $0.01V_f-0.2V_{HA}$ hybrid composite with $0.01V_f$ and $0.2V_{HA}$ control samples as well as those recorded for the parietal bone [Data from Motherway et al. (2009)].

8.3.3.5 Degradation

The wet and dry weights during the degradation of $0.01V_f-0.2V_{HA}$ hybrid composites was subsequently compared with degradation data obtained from $0.01V_f$ and $0.2V_{HA}$ composite samples in Figure 8.3.23. Further comparisons between the media pH, flexural strength as well as the elastic modulus are shown in Figure 8.3.24 and Figure 8.3.25 respectively.

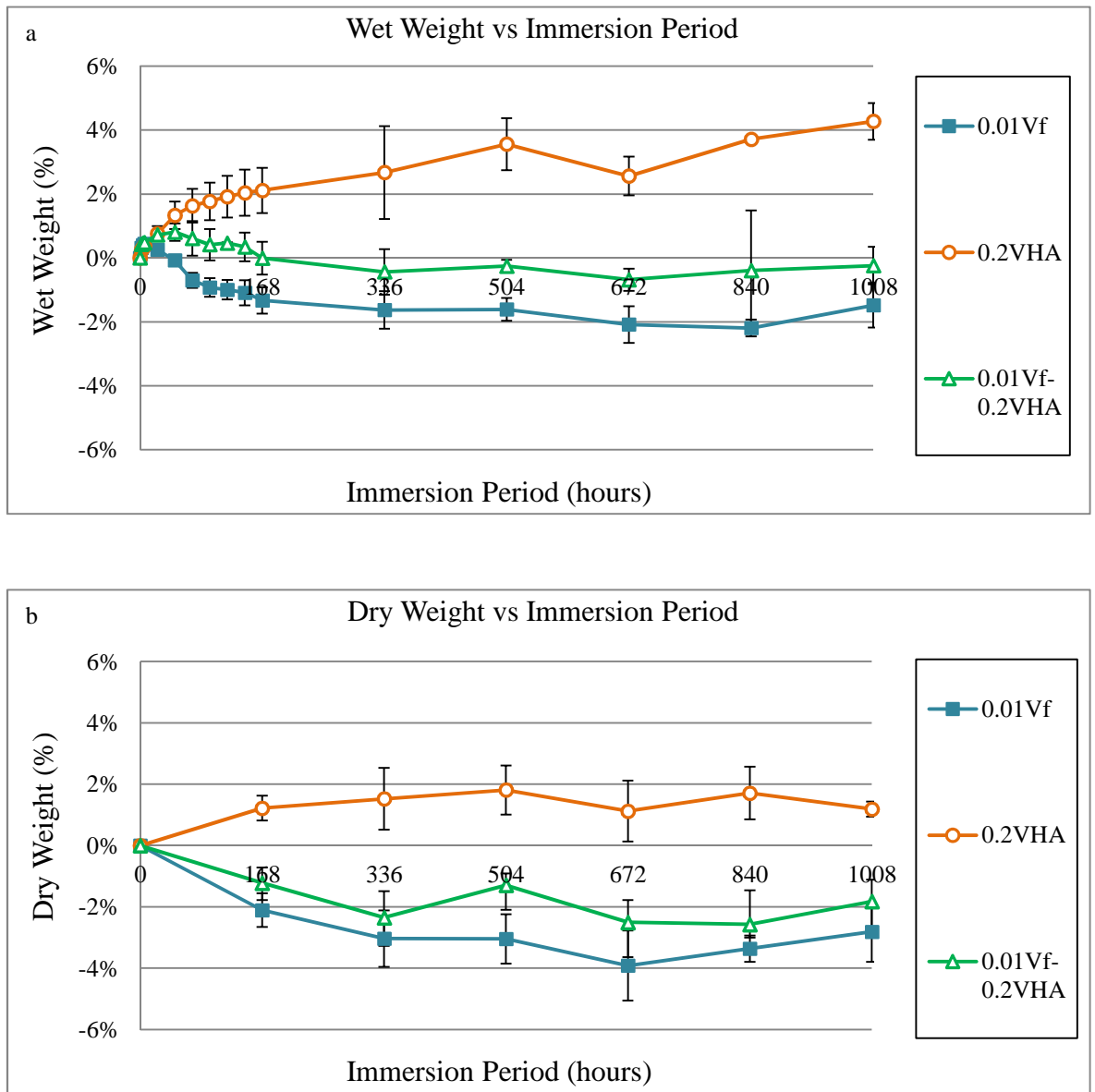


Figure 8.3.23. Comparison of a) Wet weight and b) Dry weight of $0.01V_f-0.2V_{HA}$, $0.01V_f$ and $0.2V_{HA}$ samples during 1008 hours of degradation in distilled water at 37°C .

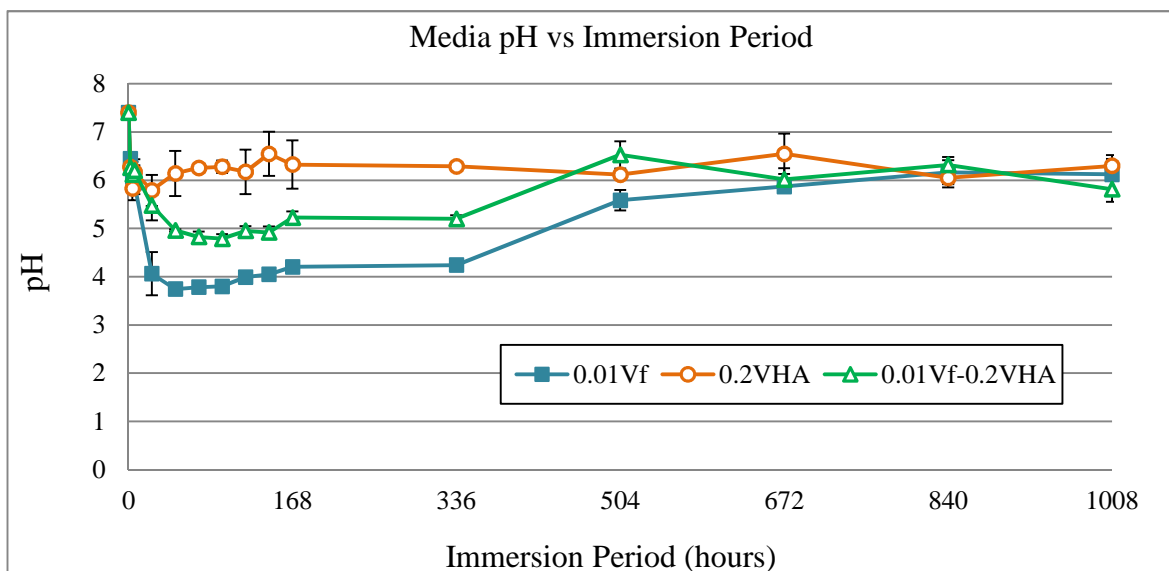


Figure 8.3.24. Comparison of media pH during the degradation of 0.01V_f-0.2V_{HA}, 0.01V_f and 0.2V_{HA} samples after 1008 hours of immersion in distilled water at 37°C.

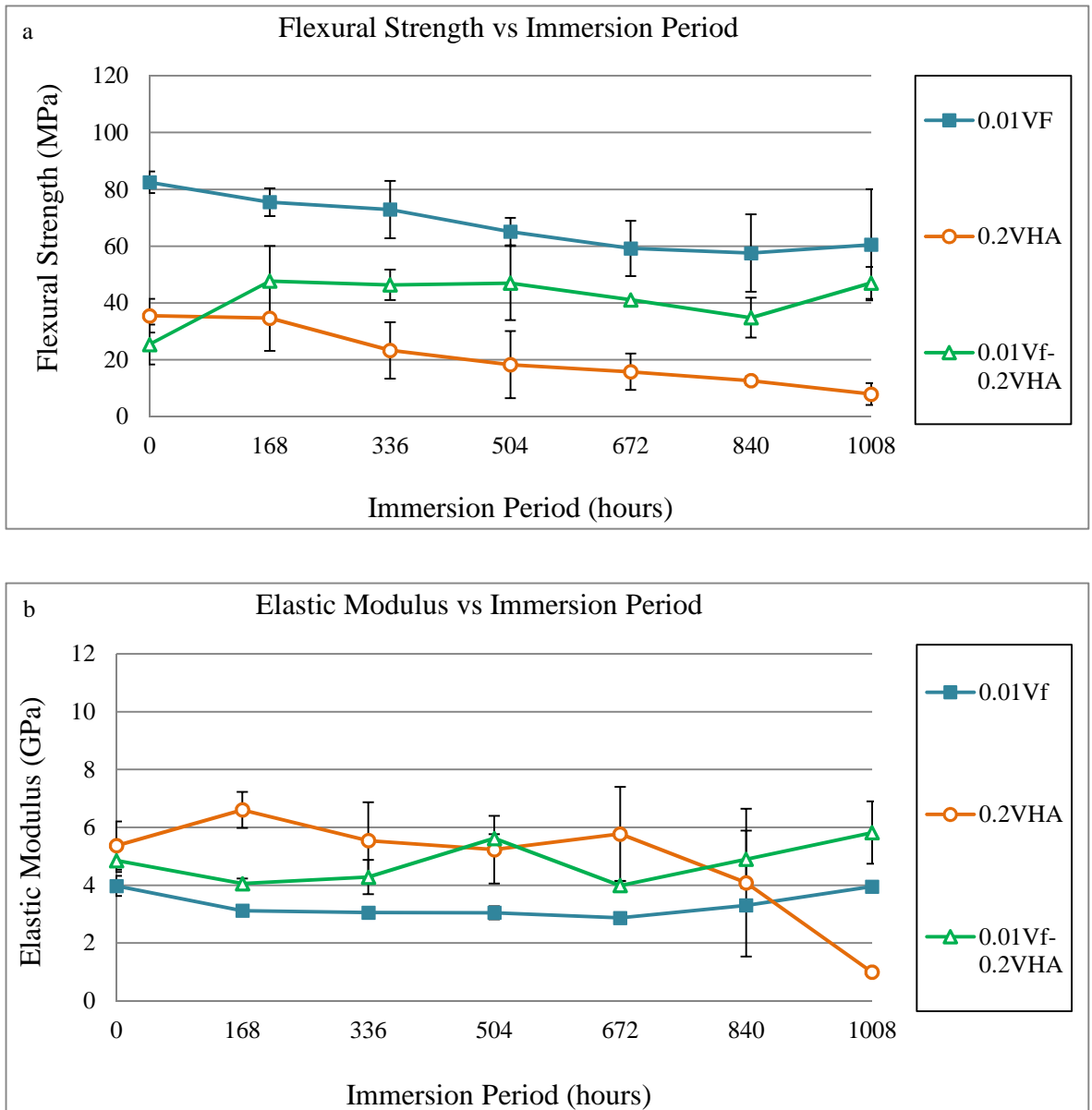


Figure 8.3.25. Comparison of a) Flexural strength and b) Elastic modulus of 0.01V_f-0.2V_{HA}, 0.01V_f and 0.2V_{HA} samples during 1008 hours of degradation in distilled water at 37°C.

8.3.3.6 Ion Release

The daily and accumulative ion release from the $0.01V_f$ and $0.01V_f-0.2V_{HA}$ composite samples is shown below in Figure 8.3.26 and Figure 8.3.27 over the initial 168 hours of degradation.

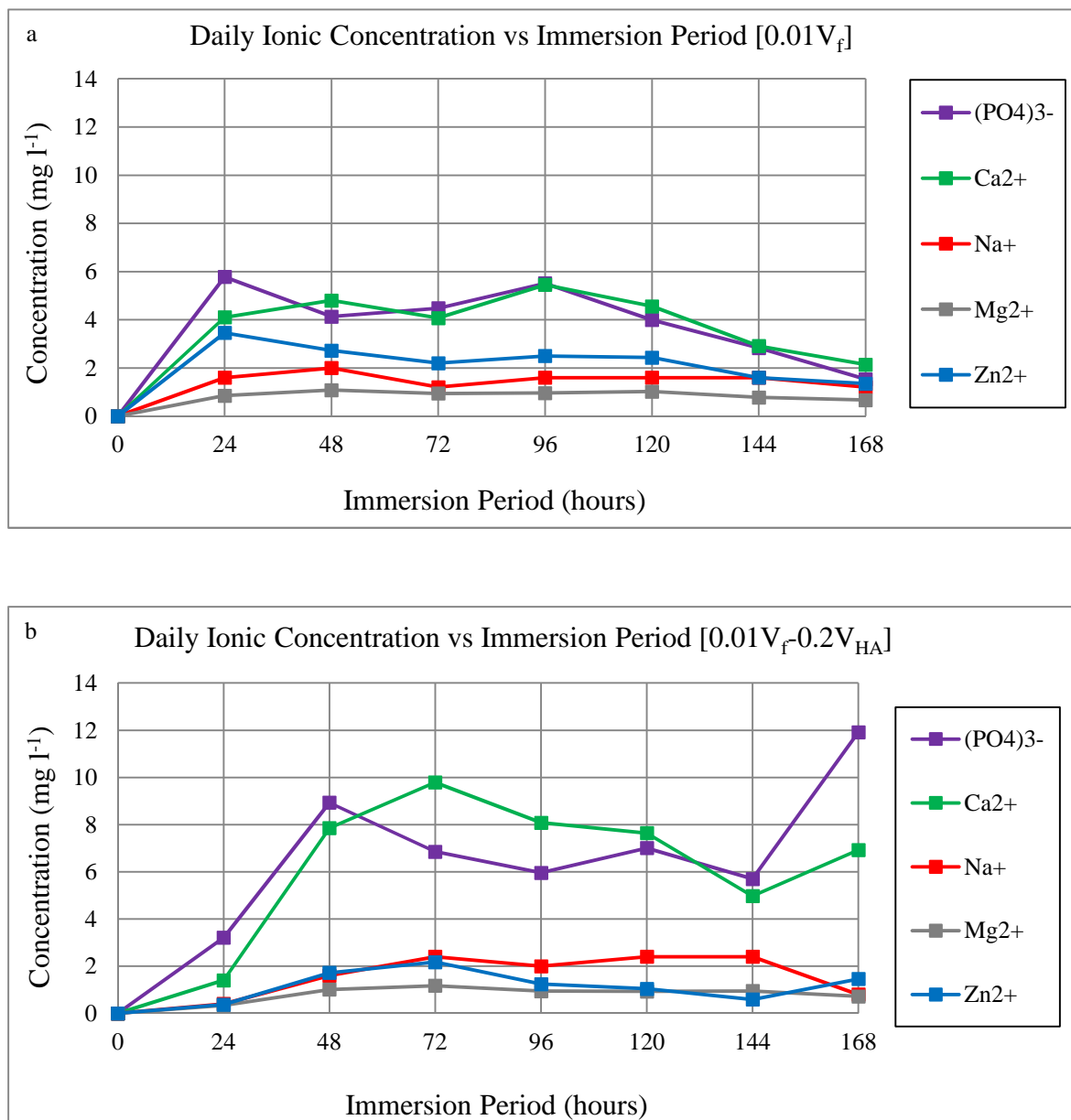


Figure 8.3.26. Comparison of daily ionic concentrations from a) $0.01V_f$ and b) $0.01V_f-0.2V_{HA}$ samples during the first 168 hours of degradation in distilled water.

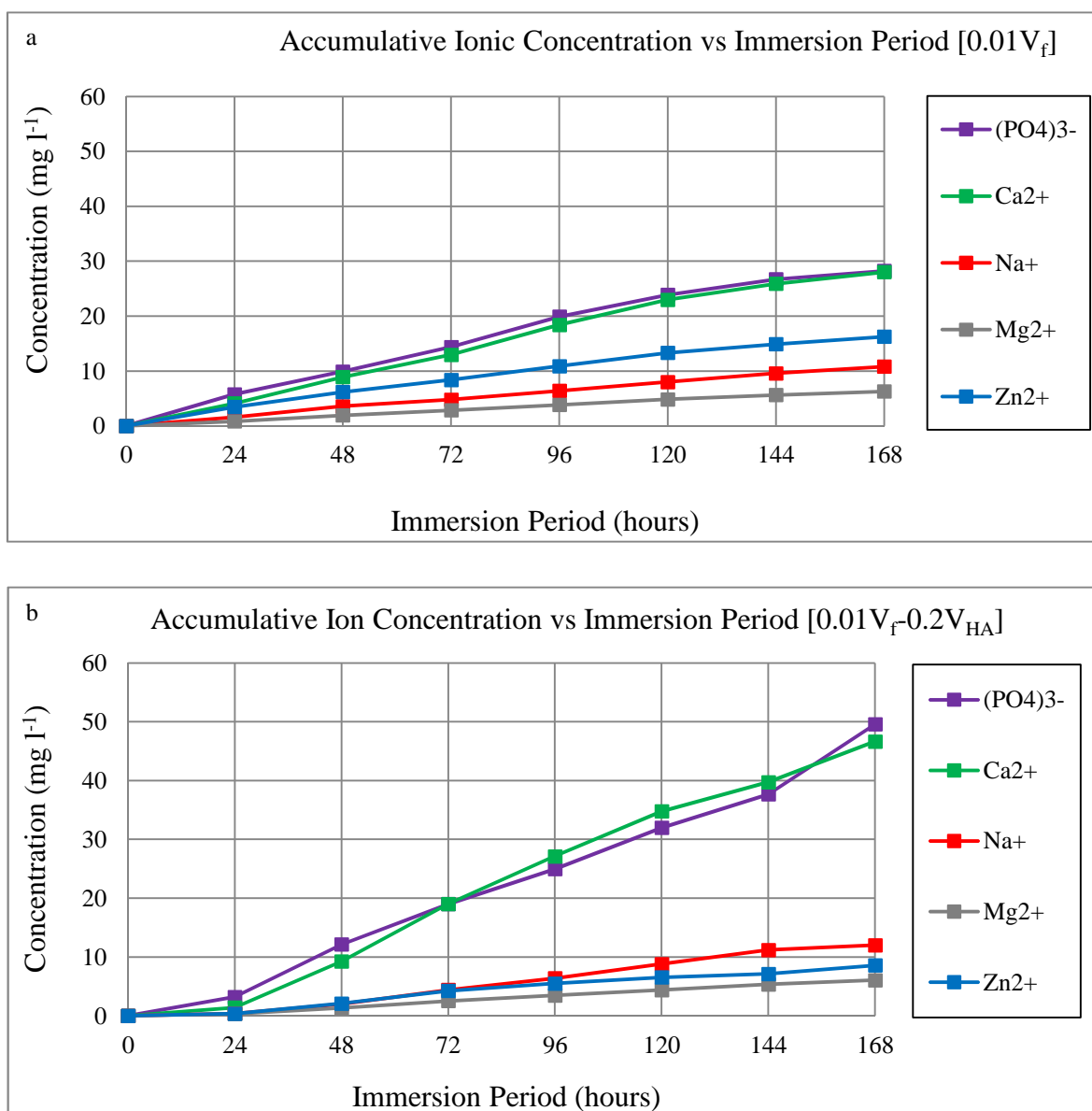


Figure 8.3.27. Comparison of the accumulative ionic media concentrations from a) $0.01V_f$ and b) $0.01V_f-0.2V_{HA}$ composites over the initial 168 hours of degradation in distilled water.

8.3.3.7 Bioactivity

The FTIR spectra obtained from the $0.01V_f$ and $0.01V_f-0.2V_{HA}$ composite planar surfaces are compared with that recorded from the $4\mu\text{m}$ hydroxyapatite (HA) particles (P218R, Plasma Biotol, UK) in Figure 8.3.28. The results showed that the HA filler was exposed on the hybrid composite surface by the presence of peaks at 962cm^{-1} , 633cm^{-1} , 604cm^{-1} and 562cm^{-1} that corresponded to the vibrational modes of the phosphate and hydroxyl groups in the HA. This observation was in line with previous results such as those described by Danoux et al. (2014) with overlapping of phosphate and polymer vibrational groups observed in the $0.01V_f-0.2V_{HA}$ hybrid composite spectrum^[357].

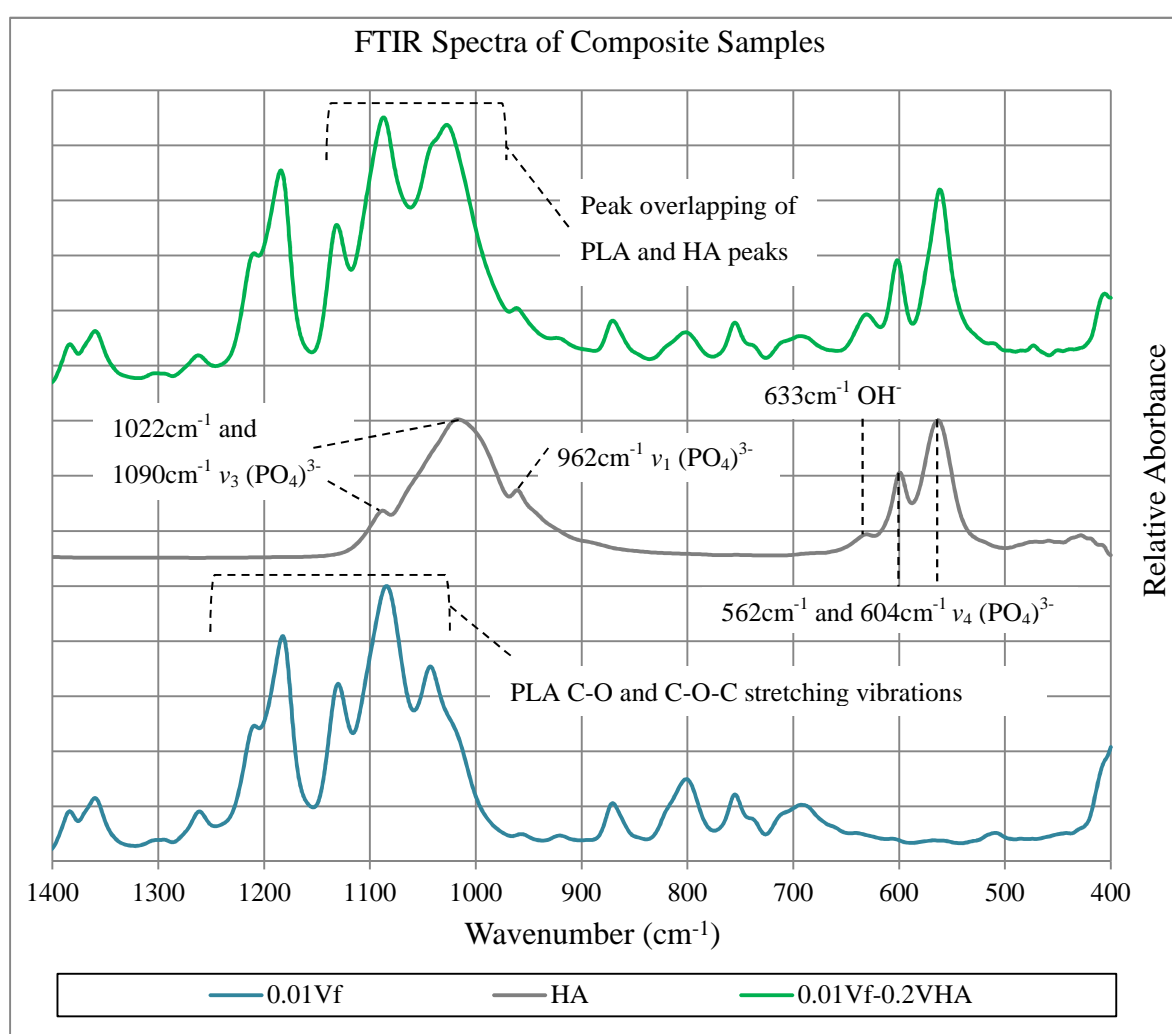


Figure 8.3.28. FTIR spectra obtained from the planar surfaces of a $0.01V_f$ composite, $4\mu\text{m}$ hydroxyapatite particles and a $0.01V_f-0.2V_{HA}$ hybrid composite over the $1400-400\text{cm}^{-1}$ wavenumber range showing the overlapping of HA and PLA bands in the hybrid composite spectrum.

The subsequent FTIR spectra after the immersion of $0.2V_{HA}$, $0.01V_f$ and $0.01V_f-0.2V_{HA}$ samples in c-SBF for up to 336 hours (2 weeks) is shown in Figure 8.3.29, Figure 8.3.30 and Figure 8.3.31 respectively.

The results showed that during the immersion of $0.2V_{HA}$ samples (Figure 8.3.29), the peak intensities of the HA bands at 562cm^{-1} and 604cm^{-1} varied between spectra with a general decrease at 168 and 336 hours of immersion. These spectra also appeared to show a peak shift from 1030cm^{-1} to 1044cm^{-1} after 120 hours of immersion with the suppression of peak intensities at 1264cm^{-1} and 800cm^{-1} seen after 24 hours. Meanwhile spectra obtained from the immersion of $0.01V_f$ composites (Figure 8.3.30) showed a change in the 1264cm^{-1} and 800cm^{-1} wavenumber peak intensities that appeared to increase in spectra obtained after 24 hours but then decrease with further immersion time. However, no other shift in peak wavenumber or intensity was observed from the $0.01V_f$ results.

The immersion of $0.01V_f-0.2V_{HA}$ samples in c-SBF (Figure 8.3.31) showed the same peak shifting (1030cm^{-1} to 1044cm^{-1}) as observed with the $0.2V_{HA}$ sample in spectra obtained after 72, 96 and 168 hours of immersion. The same variation in peak intensity at 604cm^{-1} and 562cm^{-1} was also observed with reduced intensities in spectra obtained after 72, 120 and 168 hours. Meanwhile a visual examination of the samples found that small deposits had formed on the cross-sections of one of the $0.01V_f-0.2V_{HA}$ samples after 336 hours of immersion.

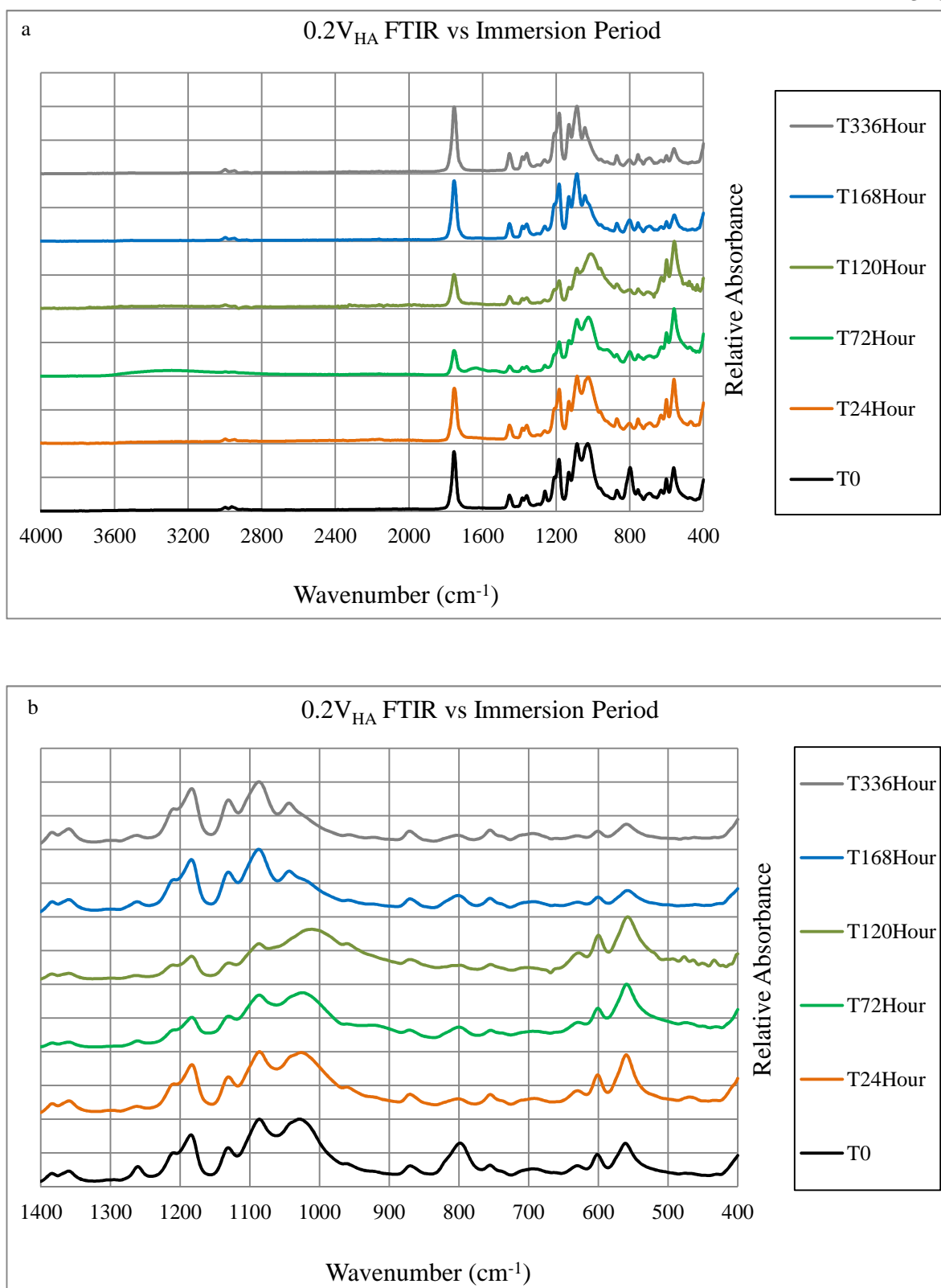


Figure 8.3.29. Comparison of FTIR spectra obtained after the immersion of 0.2V_{HA} composites in c-SBF for 24, 72, 120, 168 and 336 hours over the a) 4000-400cm⁻¹ and b) 1400-400cm⁻¹ wavenumber ranges.

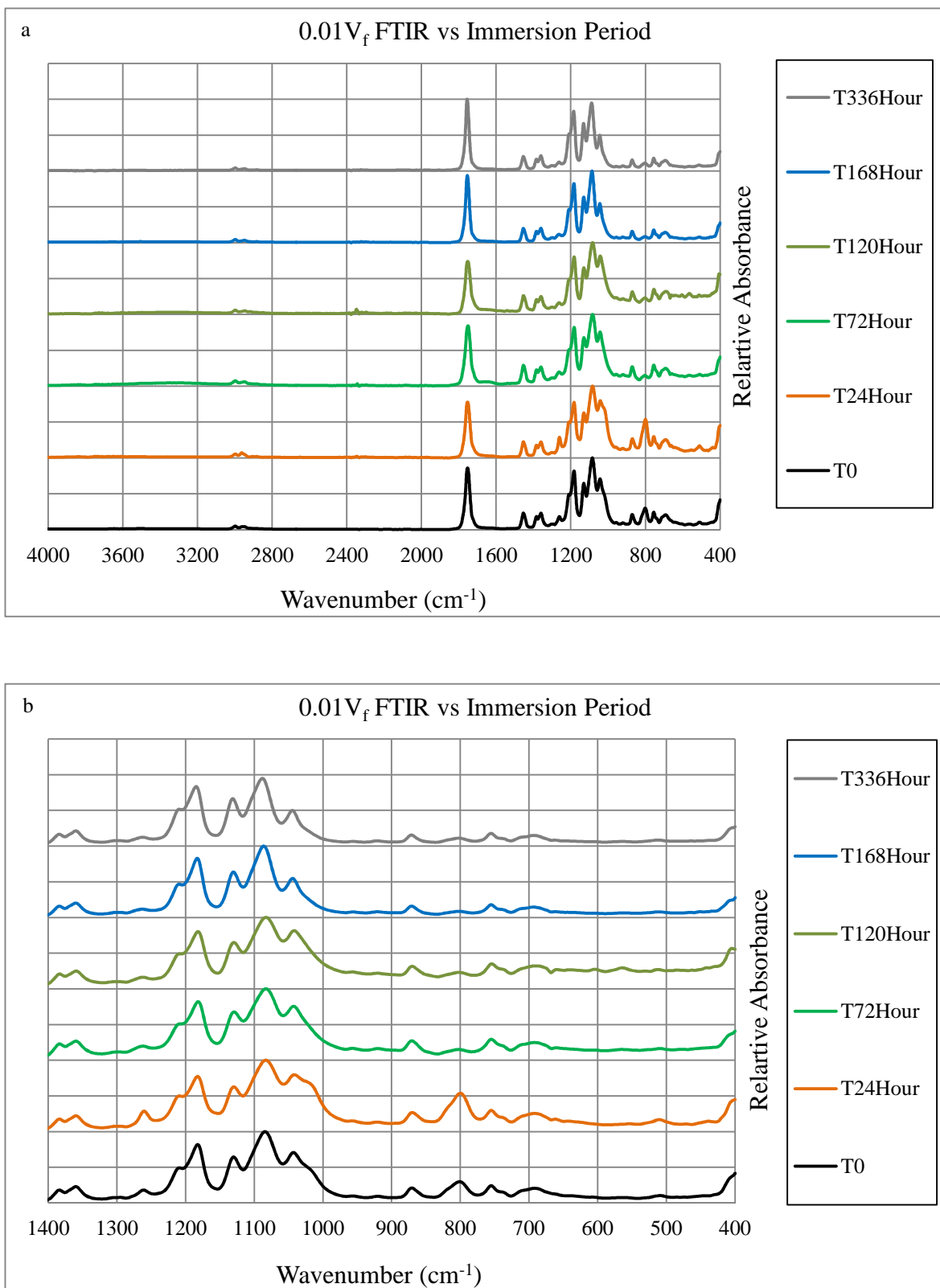


Figure 8.3.30. Comparison of FTIR spectra obtained after the immersion of 0.01V_f composites in c-SBF for 24, 72, 120, 168 and 336 hours over the a) 4000-400cm⁻¹ and b) 1400-400cm⁻¹ wavenumber ranges.

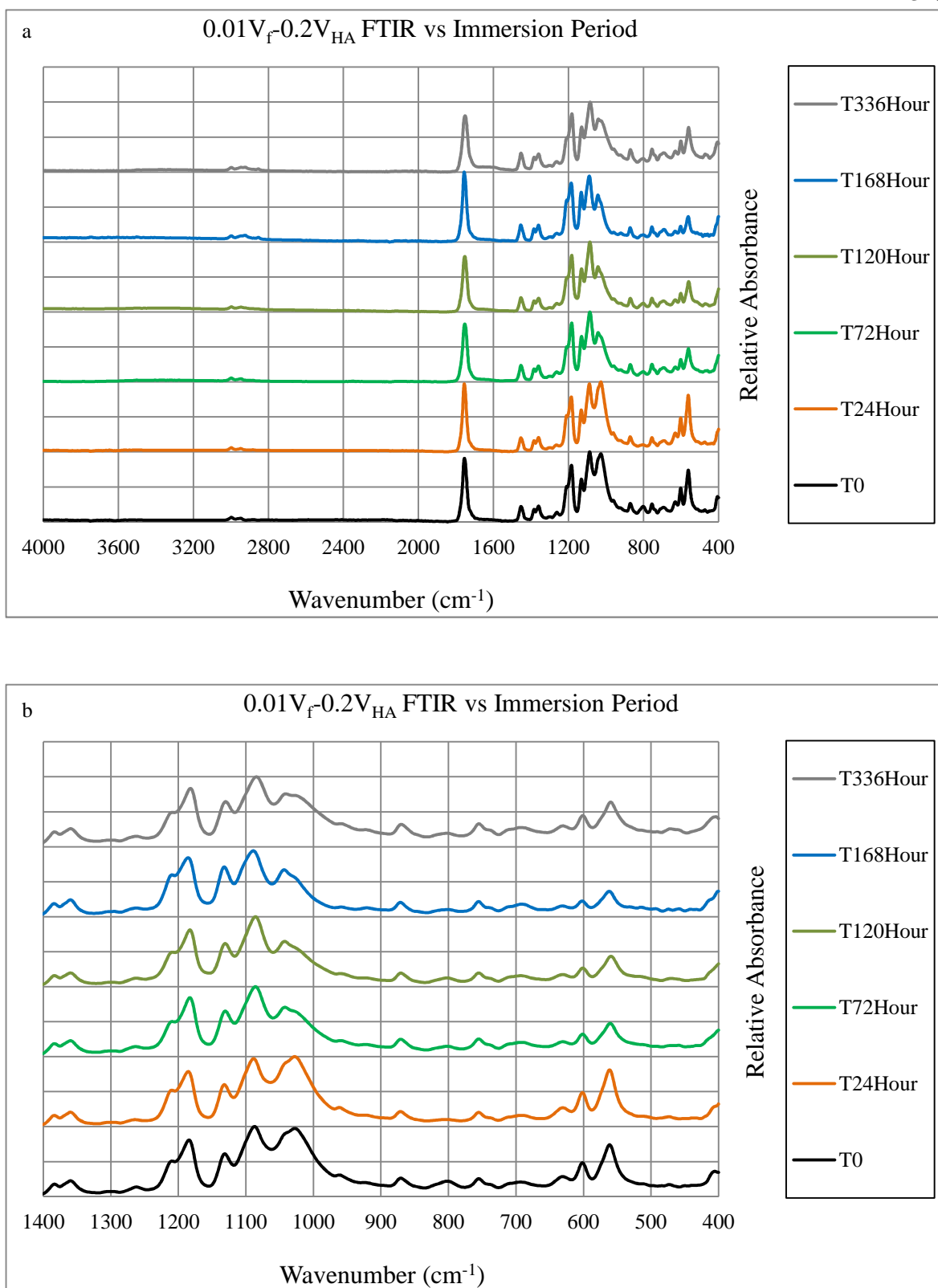


Figure 8.3.31. Comparison of FTIR spectra obtained after the immersion of 0.01V_f-0.2V_{HA} composites in c-SBF for 24, 72, 120, 168 and 336 hours over the a) 4000-400cm⁻¹ and b) 1400-400cm⁻¹ wavenumber ranges.

8.4 Discussion

Mechanical testing of the $0.2V_f$ RCM-APS samples showed that the silane treatment of CorGlaes[®] Pure 107 fibres produced composites with an increased average flexural strength (+39.7%), elastic modulus (+7.9 %) and toughness (+41.2%) compared to the non-treated $0.2V_f$ RCM samples. This result was reflected in the comparative stress-strain plots (Figure 8.3.1) with the improved flexural strength indicative of an improved interfacial shear bond strength (τ_b) between the fibre and matrix (section 3.4.9) through the use of an APS sizing agent.

These results were in line with those reported by Khan et al. (2011) who attributed the improved interfacial adhesion at the fibre-matrix interface to the reactions between the amine silane network on the APS treated fibre surfaces and the PLA matrix. Yet the improved composite mechanical properties may also be attributed to the partial healing of defects in the fibre surfaces by the APS treatment, as reported by Zinck et al. (2001) and Feih et al. (2005). Such mechanisms occur via the deposition, penetration and crosslinking of the sizing agent within the fibre surface defects (Figure 8.4.1). This can lead to the total removal or reduction in the severity of flaws that could have been introduced during the fibre handling stages of composite manufacture [221, 228, 317, 358].

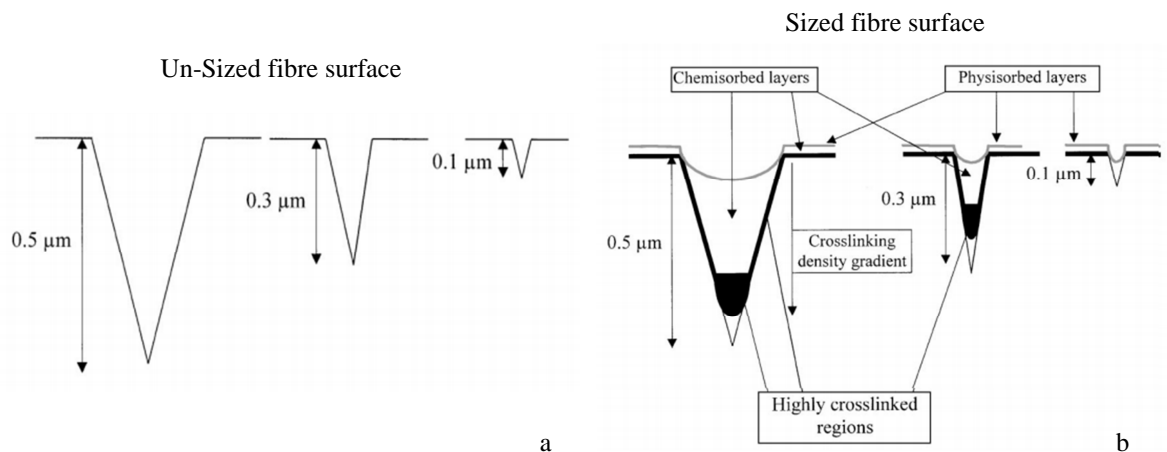


Figure 8.4.1. Comparison between a) Un-sized and b) Sized glass fibre surfaces showing the reduction in flaw size severity through the use of a silane surface treatment [Reproduced from Zinck et al. (2001)].

Yet despite the improved initial $[T_0]$ mechanical properties, the APS silane treatment provided no improvement to the composite integrity (i.e. mechanical property retention)

during sample degradation (Figure 8.3.5). This was evident by the rapid decrease in the wet and dry weight of the $0.2V_f$ RCM-APS samples that followed the same trends as previously observed during $0.2V_f$ RCM composite degradation (section 7.3.3.1) and contradicted previous results reported by Khan et al. (2011) and Hasan et al. (2013). However these differences could be accounted for by the polyphosphate composition (< 50 mol% P_2O_5) used in these studies. Such glass formulations would probably have possessed reduced dissolution rates that would also have made them less susceptible to autocatalytic effects compared to the CorGlaes[®] Pure 107 fibres (55 mol% P_2O_5) (due to their reduced P_2O_5 content). Consequently despite the polysiloxane fibre coating and increased interfacial hydrophobicity in the $0.2V_f$ RCM-APS samples, the CorGlaes[®] Pure 107 fibres remained highly susceptible to autocatalysis with the media pH decreasing to ≈ 2.9 after 24 hours of degradation. As expected from the rapid decrease in wet and dry weights (due to fibre dissolution), a large reduction in the flexural strength (-79%) and elastic modulus (-73%) of the $0.2V_f$ RCM-APS samples was observed after 168 hours of degradation [224, 228].

Analysis of the stress-strain plots obtained from the mechanical testing of the CorGlaes[®] Pure 107 fibre hybrid composites showed the failure behaviour of these samples shifted from an initial fibrous, ductile failure to a more brittle fracture mode with a reduced strain to failure (Figure 8.3.6). This transition was in line with previous results reported by Friedrich et al. (2005) as well as Kobayashi et al. (2010) and was attributed to the high modulus filler particles restricting the plastic deformation of the matrix (Liang, 2002) [229, 359-361].

Mechanical testing of hybrid samples also showed that the inclusion of a secondary HA filler phase (V_{HA-pp} , V_{HA-m}) led to changes in the elastic modulus (E_{comp}) which did not always correlate with the generally accepted increase in material stiffness expected from the inclusion of a secondary particulate filler to a glass fibre polymer composite [347, 359]. This was coupled with a reduction in flexural strength compared to the $0.2V_f$ RCM sample (Figure 8.3.7) with the resulting variations in the mechanical properties considered to be reflective of the different volume fractions (V_{HA}) and distributions of HA (V_{HA-pp} , V_{HA-m}) utilised in the hybrid composite configurations (Table 8.2.1).

From the results it was found that the greatest increase in elastic modulus (+22%) compared to the initial $0.2V_f$ RCM composite was achieved by the $0.15V_f-0.1V_{HA(NHD)}$ hybrid configuration (10.01 ± 1.33 GPa). This result contradicted the expected trend of increasing elastic moduli as the HA volume fraction was increased and/or a more homogenous distribution of HA ($V_{HA-pp} \approx V_{HA-m}$) was employed in the other samples. Such

results were attributed to the agglomeration of HA particles as the V_{HA} was increased that could have introduced areas of localised stress concentrators in the $0.15V_f-0.2V_{HA}$ samples compared to the $0.15V_f-0.1V_{HA(NHD)}$ composites. Such behaviour has been previously observed in the development of carbon fibre-HA hybrid composites as studied by Shen et al. (2009) where a decrease in elastic modulus was found to occur after the inclusion of 20 wt.% HA that was attributed to the poor dispersion of the HA particles ^[347, 360, 362].

The distribution/agglomeration of HA particles was also believed to have accounted for the lower elastic modulus of the $0.15V_f-0.2V_{HA(NHD)}$ (6.74 ± 0.45 GPa) composites compared to the $0.15V_f-0.2V_{HA}$ (9.34 ± 0.49 GPa) samples despite both possessing equal accumulative volume fractions of HA (V_{HA}). Consequently the reduced elastic modulus in the $0.15V_f-0.2V_{HA(NHD)}$ samples was attributed to the primary distribution of the HA throughout the CorGlaes[®] Pure 107 fibre pre-pregs ($0.33V_{HA-pp}$) compared to the $0.15V_f-0.2V_{HA}$ samples ($0.17V_{HA-pp}$). Based on the work of Shen et al. (2009), the higher V_{HA-pp} was thought to have formed localised stress concentrators and increased the probability of defects being introduced into the samples. The high pre-preg volume fraction of HA in the $0.15V_f-0.2V_{HA(NHD)}$ hybrid samples was also believed to have compromised the fibre-matrix interface by reducing the available surface area for fibre-matrix adhesion (Figure 8.4.2). This would then account for the reduction in flexural strength seen in the $0.15V_f-0.2V_{HA(NHD)}$ samples compared to the $0.15V_f-0.1V_{HA(NHD)}$ composites ^[347, 363].

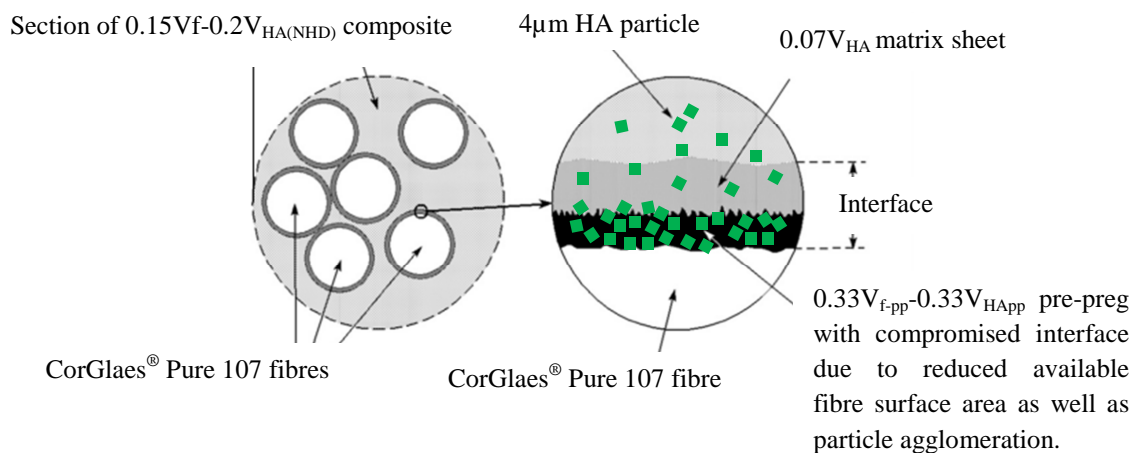


Figure 8.4.2. Illustration of the compromised fibre-matrix interface in the $0.15V_f-0.2V_{HA(NHD)}$ samples due to the high HA pre-preg volume fraction ($0.33V_{HA-pp}$) [Modified from Cech et al. (2013)].

The reduced flexural strength observed in the $0.15V_f-0.2V_{HA}$ composites was consequently attributed to the reduced melt flow index (MFI) of the HA-PLA matrix sheets ($0.2V_{HA-m}$) compared to the $0.15V_f-0.1V_{HA}$ samples ($0.1V_{HA-m}$) (Bregg et al. 2006). The reduced MFI would have likely affected the quality of the fibre-matrix interface during the manufacturing of the $0.15V_f-0.2V_{HA}$ samples due to its restriction on polymer infiltration into the reinforcing fibres (following Darcy's Law – section 3.2.3). Along with the factors discussed for the $0.15V_f-0.2V_{HA(NHD)}$ samples, these concepts would then be in agreement with the observed results where all $0.2V_{HA}$ hybrid samples were found to display similar flexural strengths to those exhibited by the fibre-free $0.2V_{HA}$ control. This subsequently highlighted the poor fibre-matrix interface that was generated as the V_{HA} was increased and/or the distribution of HA was altered (Bregg et al. 2006) ^[359, 360].

However based on points discussed by Bregg et al. (2009) and Shen et al. (2009), the reduction in flexural strength found in all hybrid samples (compared to the $0.2V_f$ RCM composite) could also have been influenced by the presence of cavities and microvoids at the HA-PLA interface. Such voids could have been incurred from the high specific surface area ($13.3 \text{ m}^2 \text{ g}^{-1}$) and subsequently reduced wetting of the non-sintered HA particles employed here compared to their sintered equivalent (specific surface area = $1.16 \text{ m}^2 \text{ g}^{-1}$) as reported by Joseph et al. (2002) as well as Zhang & Tanner (2008). Yet given the intention of the HA filler to act as a pH buffering agent, the increased specific surface area of the non-sintered HA used here was deemed more appropriate. Furthermore according to Wang et al. (2011), a weak interface could also have formed due to the contrast between the hydrophobic PLA matrix and hydrophilic HA filler ^[347, 360, 364-366].

As expected, the mechanical testing of the HA-PLA composites ($0.2V_{HA}$) showed that the incorporation of HA particles increased the elastic modulus (+67.3 %) and reduced the flexural strength (-63.8 %) compared to the neat PLA. This was coupled with a reduced strain at failure that was in line with the expected trends for microparticle reinforced composites where a weak interface is encountered (Friedrich et al., 2005; Fu et al., 2008). The reduced modulus of the $0.2V_{HA}$ particle composite ($5.37 \pm 0.83 \text{ GPa}$) compared to the hybrid samples also highlighted the contribution of the CorGlaes[®] Pure 107 fibres towards the hybrid composite elastic modulus despite the interface and agglomeration issues previously discussed ^[359, 367].

Degradation of the hybrid composites subsequently showed that a reduction followed by a plateau in the wet and dry weights occurred after 168 to 336 hours of degradation in all hybrid configurations. As previously discussed in section 7.4, the discrepancy between the

composite wet and dry weights was due to the ingress of media within the pores and voids generated from fibre dissolution. Additionally, the apparent reduction in wet and dry weight loss compared to the $0.2V_f$ RCM composite was due to the reduced volume (V_f) and weight fraction (W_f) of the CorGlaes[®] Pure 107 fibres ($\rho = 2.65 \text{ g cm}^{-3}$) in the hybrid composites due to the secondary HA filler phase ($\rho = 3.156 \text{ g cm}^{-3}$). Based on the percentage wet and dry weights of the $0.2V_{HA}$ samples, the decrease in hybrid composite weight was primarily due to CorGlaes[®] Pure 107 fibre dissolution. However, it is unknown what contribution to the weight loss that the dissolution of the secondary HA filler phase may have had on this data due to the absence of an acidic environment during $0.2V_{HA}$ sample degradation (Figure 8.3.10).

A comparison between the different hybrid configurations found that the HA volume fraction (V_{HA}) or HA phase distribution had no significant effect on the rate of weight loss (which was considered to represent fibre dissolution). Furthermore the degradation data also revealed that the inclusion of a 1% CaO defective HA filler had no effect on the mechanical integrity of the composite samples compared to the chemically pure HA. This may be due to the distribution of the CaO within the non-sintered particles that is believed to be less homogenous than its sintered equivalent (Personal Communication – Paul Steverson, Plasma Biotol, UK). Consequently if concentrated at the centre of the precipitated HA particles, the CaO may not have been able to efficiently interact with the acidic degradation media. However it may also be that the concentration of CaO was inadequate to sufficiently counteract the acidic pH and reduce the rate of fibre dissolution.

Compared to the $0.2V_{HA}$ samples, the decrease in hybrid sample weight was contrasted by the recorded increase in wet weight of the $0.2V_{HA}$ composites that was higher than that previously recorded from neat PLA samples (Figure 8.4.3). The increased water absorption observed in the $0.2V_{HA}$ composites was the result of several factors including the absorption of media by the HA particles (due to the HA hydroxyl groups affinity towards water). This increase in wet weight was also attributed to the incursion of media within the voids at the HA-PLA interface as previously reported by Tham et al. (2010) and Sultana et al. (2013) ^[92, 368]. However the increase in $0.2V_{HA}$ sample dry weight (Figure 8.3.9) could not be accounted for and was believed to be due to measurement error.

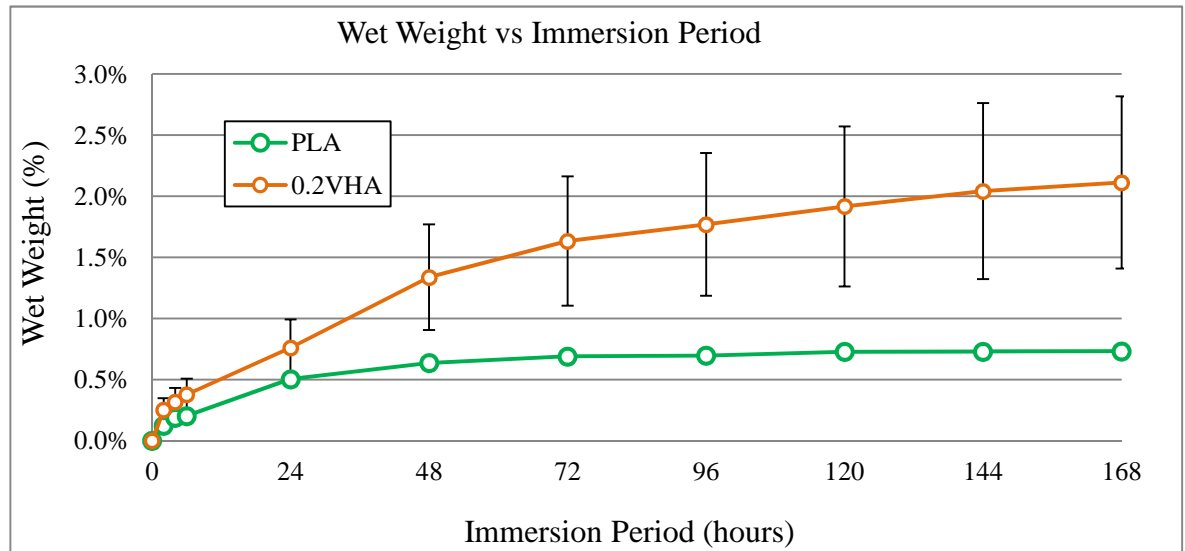


Figure 8.4.3. Wet weight of PLA and 0.2V_{HA} composite over initial 168 hours of immersion in distilled water at 37°C showing increased water absorption due to the presence of HA (standard deviation of PLA $\leq \pm 0.03\%$).

Although possessing a reduced V_f , the inclusion of HA into the composite configuration appeared to buffer and counteract the severity of acidic pH created by the dissolution of the CorGlaes[®] Pure 107 fibres compared to the data recorded during previous 0.2V_f RCM sample degradation (section 7.3). This was apparent over the initial 24 hours of degradation (Figure 8.4.4) with the degree of pH buffering also found to be influenced by the variation in V_{HA} , phase distribution and HA structure (i.e. 1% CaO) over the initial 6 hours of immersion. Accordingly during this period the results showed that the greatest pH buffering was found in the 0.15V_f-0.2V_{HA} hybrid composite configuration. However, after 24 hours, all hybrid samples appeared to reach a similar pH (≈ 4.1) but remained above the values previously recorded during 0.2V_f RCM sample degradation (≈ 2.9). This buffering effect of the HA filler was in line with the literature where calcium carbonate (CaCO₃) fillers had been shown by Kobayashi et al. (2010) to successfully buffer the pH of a short ultraphosphate glass fibre methacrylate-modified oligolactide hybrid composite ^[229]. However the respective fibre volume fraction (V_f) of this composite was not specified and only samples containing 20 wt.% CaCO₃ filler were investigated as they degraded in Tris buffer solution in contrast to the distilled water employed here.

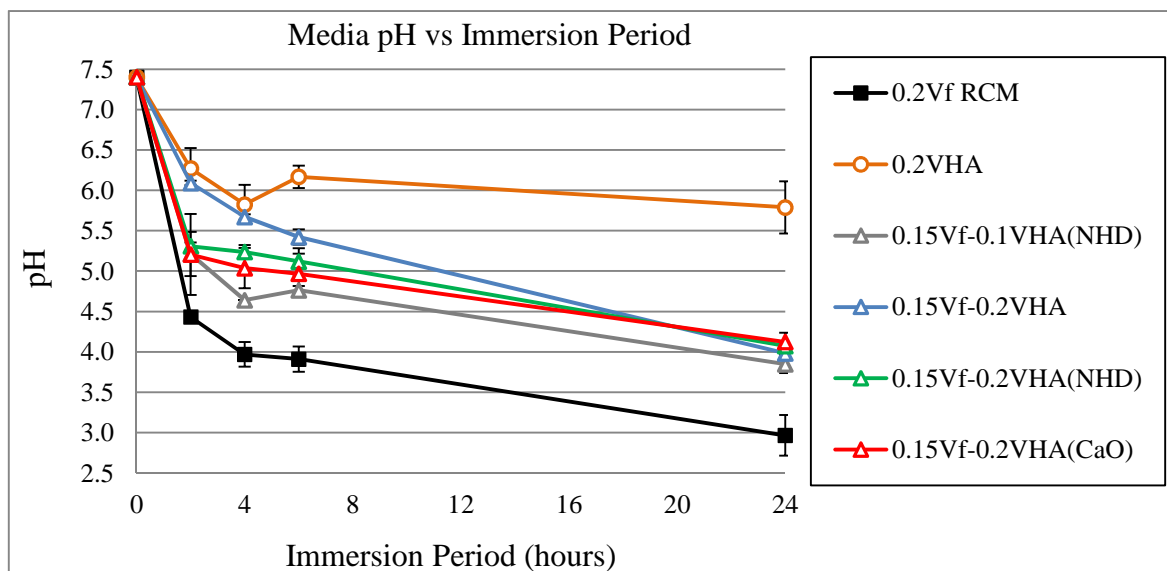


Figure 8.4.4. Comparison of media pH during the degradation of different composite configurations over the initial 24 hours of immersion in distilled water at 37°C.

Comparisons over the entire degradation period revealed that the 0.15V_f-0.2V_{HA} hybrid composites also appeared to accelerate the rate at which the pH returned to neutral (i.e. T₀) compared to the other hybrid composite configurations (Figure 8.3.10). This was believed to be due to its high HA volume fraction and homogenous distribution of the particles throughout the samples. Degradation of the 0.2V_{HA} samples also showed the HA to buffer the drop in pH previously observed from the formation of carbonic acid in the media when compared to the PLA control (Figure 8.4.5).

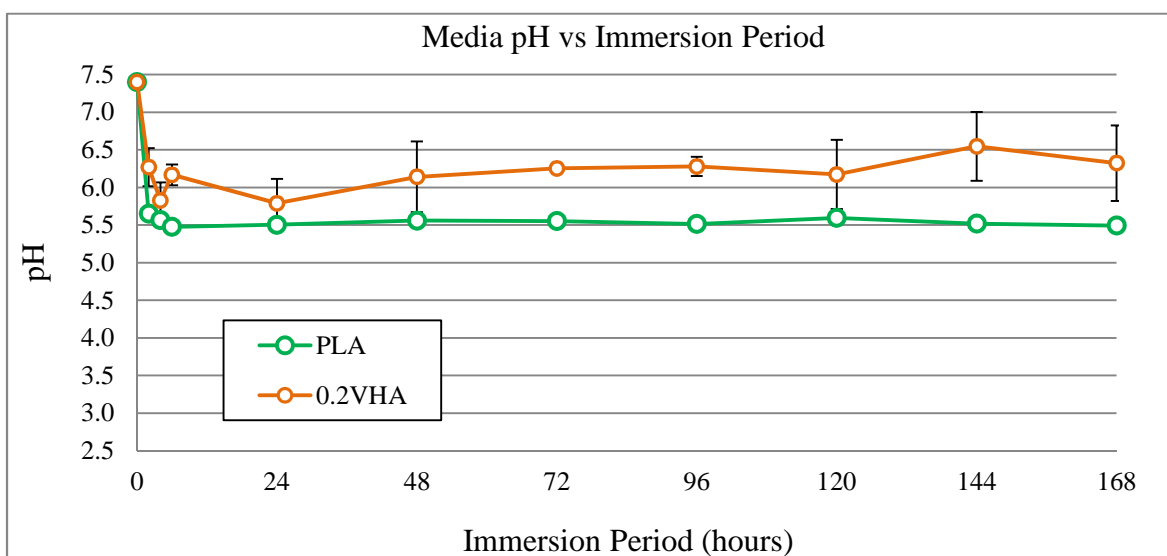


Figure 8.4.5. Comparison of media pH between 0.2V_{HA} and 3001D PLA samples over 168 hours of degradation in distilled water at 37°C.

As expected, the continued rapid rate of CorGlaes[®] Pure 107 fibre dissolution was coupled with a decrease, followed by an approximate plateau in both the flexural strength and elastic moduli of the hybrid composite samples after 168 hours of degradation. As previously observed with the 0.2V_f RCM composite, the drop in mechanical properties was attributed to the dissolution of the CorGlaes[®] Pure 107 fibres. A comparison with the hybrid samples also showed that the average flexural strength appeared to have decreased at an accelerated rate compared to the previous 0.2V_f RCM samples. This may have been due to the partial dissolution of the HA particles and breakdown of the HA-PLA interface as they buffered the degradation media along with the brittle failure mode of the hybrid samples.

Comparisons between the elastic moduli of different hybrid samples over the immersion period also showed the composites to have retained different post fibre dissolution mechanical properties depending on the hybrid configuration. Consequently, the generally highest post-fibre dissolution elastic modulus was found with the 0.15V_f-0.2V_{HA} hybrid composite that was believed to be due to its homogenous HA particle distribution (Bregg et al. 2006). This was particularly evident by the difference in elastic moduli found between the 0.15V_f-0.2V_{HA} samples (4.33 ± 0.32 GPa) compared to the 0.15V_f-0.2V_{HA(CaO)}} composites (2.70 ± 0.1 GPa) after 336 hours of immersion (when near complete fibre dissolution was expected to have occurred). Unfortunately, a lack of comparative data on the degradation of similar PGF hybrid composite materials restricts further analysis with no mechanical degradation data given by Kobayashi et al. (2010) during their immersion of PGF-CaCO₃ hybrid composites in Tris buffer solution^[229].

Degradation of 0.2V_{HA} composites showed a gradual decrease in composite flexural strength whilst the elastic modulus of the samples appeared relatively unchanged until a rapid decrease after 840 hours (5 weeks) of degradation. The gradual decrease in sample flexural strength was in line with results found by Russias et al. (2006) who tested 70-80 wt.% HA-PLA of composites. However due to the reduced HA content in the samples tested here this reduction in flexural strength was not as severe that as that recorded by Russias et al. (2006)^[135]. Based on this, the decrease in flexural strength was attributed to the weakening of the filamentous structures that bound the HA particles to the PLA matrix. This degradation mechanism at the HA-PLA interface would also have been expected to contribute to the continued decrease in the hybrid composites flexural strength that could be seen after 504 hours (3 weeks) of degradation despite the data indicating that near complete fibre dissolution had occurred after \approx 168 hours (Figure 8.3.11). The large

reduction in elastic modulus of the $0.2V_{HA}$ composite samples observed at 1008 hours could not be accounted for given that the resulting elastic modulus was significantly lower than the $0.15V_f-0.2V_{HA}$ hybrid composite samples after the equivalent degradation period (when taking fibre dissolution into account). This subsequently ruled out any mechanisms relating to the further breakdown of the HA-PLA interface in the $0.2V_{HA}$ composites after 1008 hours of immersion given the data obtained from the $0.15V_f-0.2V_{HA}$ samples.

However despite the beneficial pH effects from the secondary HA filler phase and ability of the DMEM solution to provide further pH buffering during *in vitro* degradation (section 7.3.4.1), no biocompatibility testing was performed on these hybrid composite configurations. This was due to the high dissolution rate of the CorGlaes[®] Pure 107 fibres, similar to that previously recorded from $0.2V_f$ RCM samples. Consequently despite the observed pH buffering, a high release rate of Zn^{2+} ions to cytotoxic levels was expected from the different hybrid composite configurations based on previous MTT data (section Figure 7.3.6).

From the MTT assay, the low volume fraction CorGlaes[®] Pure 107 fibre hybrid composites showed a trend of increasing cell viability as the HA volume fraction (V_{HA}) increased for both $0.01V_f$ and $0.05V_f$ hybrid configurations. However this trend was found to be independent of the CDMEM pH that was maintained above the 7.4 viability threshold for MG63 cells in nearly all samples. The irregular pH of 7.05 recorded from the $0.05V_f-0.1V_{HA}$ degradation extract after 96 hours (Figure 8.3.13) could not be accounted for given the higher pH of the HA-free $0.05V_f$ composites at an equivalent degradation period (Figure 7.3.23, Figure 8.3.13). As a result, this reading was subsequently attributed to measurement error due to the low volume of media available.

Given the suitability of the media pH, the increasing cell viability was believed to be due to the reduction in ion release rates (specifically the Zn^{2+} ion) from the composites due to the decreased rate of fibre dissolution. This was attributed to the localised pH buffering by the HA particles at the fibre-matrix interface. Such mechanisms would then correlate with the observed trends seen in Figure 8.3.12 where increasing HA volume fraction and subsequent decreases in fibre dissolution rate (via pH manipulation at the fibre-matrix interface) lead to greater cell viability in sample extracts. However of the different hybrid configurations investigated, only the $0.01V_f-0.2V_{HA}$ composite samples were found to possess an average cell viability above the 70% limit after 24 and 96 hours of degradation. This sample configuration was found to produce a statistically significant difference compared to the $0.01V_f$ samples ($p < 0.05$) and was comparable with the readings obtained

from the CDMEM controls ($p > 0.05$). The results also showed that despite a statistically significant difference ($p < 0.05$) in MG63 cell viability between the use of an HA and β -TCP filler, neither could produce biocompatible $0.05V_f$ hybrid samples (i.e. $>70\%$ viability) after 24 and 96 hours of degradation^[188].

The analysis of direct contact cultures by Coomassie staining on the biocompatible $0.01V_f$ - $0.2V_{HA}$ hybrid composite (identified by MTT assay) along with suitable controls showed that a degree of cell spreading occurred on all materials except the $0.01V_f$ composites after 24 hours of culture. Such results would appear to agree with the proposed suppression of ion release rates (via a reduced fibre dissolution rate) from the hybrid samples with cells cultured on the $0.01V_f$ composites maintaining rounded cell morphologies after 96 and 168 hours. This result consequently highlighted the severity of the CorGlaes[®] Pure 107 fibre cytotoxicity even at low composite fibre volume fractions and the deleterious cell response that can be evoked from the presence of zinc within a glass composition.

After 168 hours it was also apparent that a reduced cell population was present on both the $0.01V_f$ composite and the $0.01V_f$ hybrid material compared to the fibre-free controls. This indicated that some degree of cytotoxicity in the hybrid composites may still be present despite the inclusion of the HA filler. As expected, the PLA and $0.2V_{HA}$ composites alongside the Thermanox[®] control displayed a high degree of cell spreading that ruled out any alternative cytotoxic influences in the composite configurations.

The repetition and further analysis of this experiment using SEM images on $0.01V_f$ and $0.01V_f$ - $0.2V_{HA}$ hybrid samples alongside neat PLA was found to agree with the Coomassie staining and help verify the accuracy of the previous results. This was evident by the polygonal shaped cell spreading and filopodial extensions observed on the PLA controls as well as the $0.01V_f$ - $0.2V_{HA}$ hybrid composites that were in contrast to the mainly rounded cell morphology seen on the $0.01V_f$ composites after 24 hours of culture (Figure 8.3.17). Continued cell spreading was observed after 96 hours on the PLA samples but this cell population was also observed to be significantly higher than both the $0.01V_f$ and $0.01V_f$ - $0.2V_{HA}$ composites. However a comparison between the CorGlaes[®] Pure 107 composite samples did show that an increased degree of cell spreading was present in cells cultured on the $0.01V_f$ - $0.2V_{HA}$ hybrid samples (Figure 8.3.18c,f,i). In agreement with the Coomassie staining results, this difference in cell morphology was believed to be due to the difference in fibre dissolution rates and related concentration of Zn^{2+} within the media. The development of a multi-layered cell matrix was then seen to form over the PLA samples after 168 hours of culture whilst a high degree of cell spreading was also evident

on the $0.01V_f-0.2V_{HA}$ hybrids. This was contrasted by the $0.01V_f$ composites that maintained a rounded cell morphology (Figure 8.3.19b,e,h and Figure 8.3.20b,e,h).

Additionally, the SEM images of the hybrid sample surfaces after 168 hours of culture (Figure 8.3.19c,f,i and Figure 8.3.20c,f) showed the formation of surface damage that appeared to increase as the culture period progressed. Based on comments by Speidel & Iggowitzer (1998), this change in surface morphology was attributed to the accumulation of media within the pores and voids surrounding the hydroxyapatite particles. This can subsequently lead to the rupture and surface perforation of the sample when these particles are in close proximity to the surface. This would then appear to correlate with the observations and material configurations employed in the current study where surface damage was only observed in the hybrid composite samples due to the presence of hydroxyapatite particles ^[369]. This would also seem to be in line with the previously discussed mechanisms regarding the breakdown of the PLA-HA interface during sample degradation.

SEM images also identified small $\approx 0.5-4\mu\text{m}$ spherical particles after 168 hours of culture at the periphery and within the surface cavity's formed during cell culture on the $0.01V_f-0.2V_{HA}$ samples. However their presence or morphology could not be accounted for from the existing data (Figure 8.4.6). Given their absence from the $0.01V_f$ or PLA samples and lack of correlating literature, it was assumed that the formation of these particles was related to the interactions between the HA, CDMEM and the CorGlaes[®] Pure 107 fibres - however further investigation is required to fully account for these features.

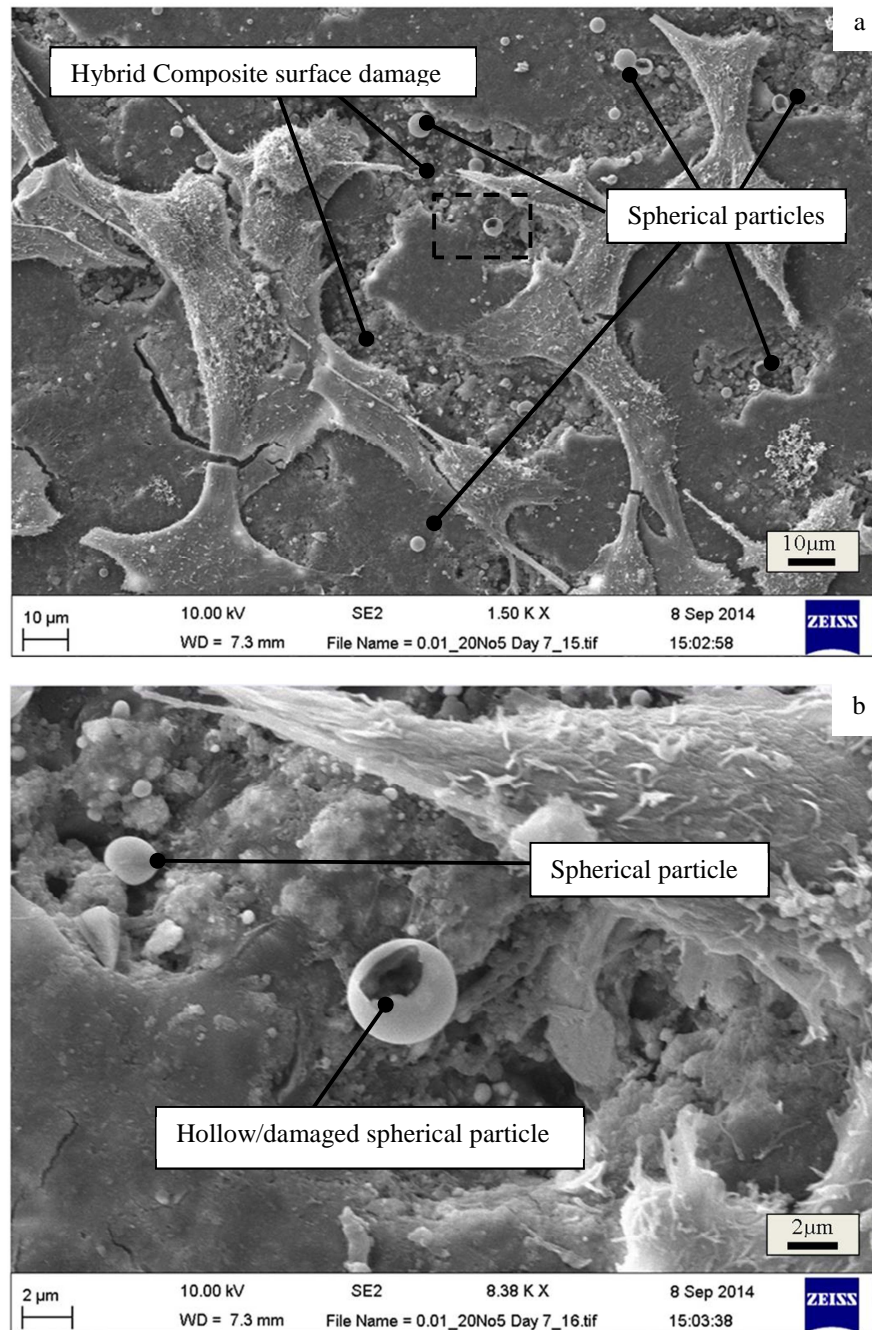


Figure 8.4.6. SEM images after 168 hours MG63 cell culture on $0.01V_f-0.2V_{HA}$ hybrid composites with a) The appearance of surface damage and spherical particles labelled [scale bar = $10\mu\text{m}$] and b) Magnified section of isolated area showing hollow/damaged nature of selected particle [scale bar = $2\mu\text{m}$].

Mechanical testing of the biocompatible $0.01V_f-0.2V_{HA}$ hybrid composite configuration showed the expected decrease in flexural strength, increase in elastic modulus and transition to a brittle failure mode through the inclusion of the $0.2V_{HA}$ filler compared to the $0.01V_f$ composite. However in contrast to the earlier results, the inclusion of CorGlaes[®] Pure 107 fibres produced hybrid composites with a reduced flexural strength and elastic

modulus compared to the $0.2V_{HA}$ composites. This behaviour was attributed to the absence of a fibre pre-preg solvent casting stage during composite manufacturing and the resulting poor polymer infiltration into the CorGlaes[®] Pure 107 fibres (due to the previously discussed changes to the polymer MFI at $0.2V_{HA-m}$). As a result, the quality of the fibre-matrix interface may have been compromised and created flaws or voids throughout the material. Furthermore the increased handling required to isolate the low quantity of fibres required for each composite lamina (due to the use of the smaller 70x30mm mould) would also have likely contributed to the poor mechanical properties of the $0.01V_f-0.2V_{HA}$ samples given the likely increase in fibre damage incurred.

The degradation of $0.01V_f$ and $0.01V_f-0.2V_{HA}$ samples was compared with the previously obtained $0.2V_{HA}$ degradation data. The results showed that a reduction in both the wet and dry weights occurred in the $0.01V_f$ and $0.01V_f-0.2V_{HA}$ composites due to the dissolution of the CorGlaes[®] Pure 107 fibres. It was also observed that the inclusion of the HA filler phase in the $0.01V_f-0.2V_{HA}$ hybrid composites resulted in the wet weight change from fibre dissolution being significantly masked. This was due to the large difference between the V_f and V_{HA} content and the associated water absorption from the presence of HA particles over the first 168 hours of immersion (Figure 8.4.7) as previously discussed.

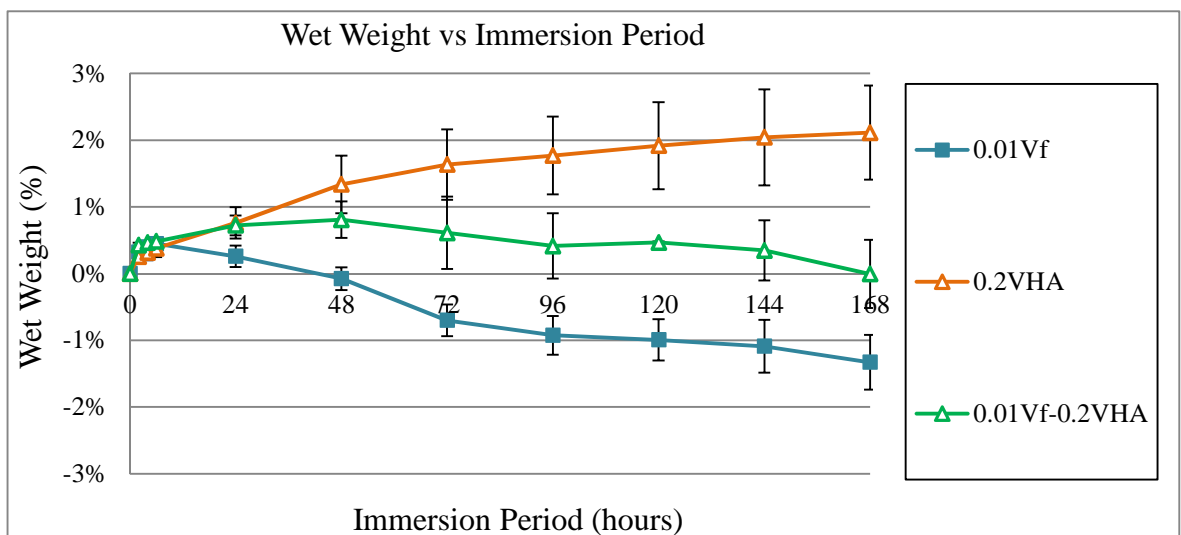


Figure 8.4.7. Comparison between sample wet weight over first 168 hours of degradation between $0.01V_f$, $0.01V_f-0.2V_{HA}$ and $0.2V_{HA}$ samples with the inclusion of HA in the hybrid composite samples obscuring the decrease in wet weight through fibre dissolution.

Accordingly, no comment can be made on the effects of the HA filler on the rate of CorGlaes[®] Pure 107 fibre dissolution rates using the wet weight data due to the absorption of moisture and small volume of fibres used. The same variation in composite wet/dry weights was observed (due to water ingress throughout the pores created by the degraded fibres as well as media absorption) and was in line with the previous results. The low fibre volume of these samples was also responsible for the significantly reduced weight loss compared to the previous $0.2V_f$ RCM or $0.15V_f$ hybrid samples.

Analysis of the dry weight data showed the expected decrease due to CorGlaes[®] Pure 107 fibre dissolution over the first 168-336 hours of immersion. This weight loss was then seen to plateau at $\approx 3.5\%$ and $\approx 2\%$ for the $0.01V_f$ and $0.01V_f-0.2V_{HA}$ samples respectively with the offset attributed to the reduced weight fraction (W_f) of the fibres due to the secondary HA filler phase. As before, no estimation as to the extent of HA dissolution in the hybrid composites during this degradation period could be assessed from the current data that may have also contributed to the weight loss results. The pH data obtained during sample degradation also showed the expected reduction in pH from the dissolution of the CorGlaes[®] Pure 107 fibres. However due to the decreased fibre volume fraction and associated reduction in phosphate species released into the media, the acidic pH did not reach the same severity in the $0.01V_f$ composites (≈ 4.0) as previously recorded during $0.2V_f$ RCM sample degradation (≈ 2.5). Similar to the previous data, the inclusion of HA was seen to raise the pH of the media during $0.01V_f-0.2V_{HA}$ sample degradation (≈ 5.0) but due to the difference in V_f , the pH was buffered to a greater extent compared to the $0.15V_f-0.2V_{HA}$ hybrid composite configuration (≈ 4.0).

The immersion of $0.01V_f$ samples also saw a gradual decrease in the average flexural strength of the composites that appeared to plateau after three weeks (504 hours) of degradation with a reduction and plateau in the elastic modulus occurring after 168 hours (1 week). Based on the previous data, the decrease in mechanical properties was attributed to the dissolution of the CorGlaes[®] Pure 107 fibres. The reduced fibre volume fraction in these composites also caused the overall decrease in flexural strength (-8.6 %) and elastic modulus (-21.5%) to be significantly lower than the $0.2V_f$ RCM samples when compared after 168 hours of degradation. This was due to the reduced reinforcement provided by the CorGlaes[®] Pure 107 fibres at $0.01V_f$ compared to $0.2V_f$ (section 3.2.3.1). Additionally, the increased variability in both the flexural strength and elastic modulus of the $0.01V_f$ composites during degradation was considered to be reflective of the increased difficulty in establishing a uniform distribution of fibres throughout the matrix. This was due to the low

quantity of CorGlaes[®] Pure 107 fibres in each lamina of the $0.01V_f$ composite compared to the $0.2V_f$ RCM samples.

The variation in $0.01V_f$ - $0.2V_{HA}$ sample mechanical properties over the 1008 hour degradation period was believed to be due to the reduced dependency of the composites on the CorGlaes[®] Pure 107 fibres for mechanical reinforcement (due to the large difference between the V_f and V_{HA}). As a result, the dissolution of these fibres appeared to have a negligible effect on the sample mechanical properties with the variation in mechanical properties seen between samples attributed to the unwanted non-homogenous distribution of the HA particles. However this variation may also have been influenced by the dissolution of the HA during pH buffering of the degradation media. Consequently these hybrid composites failed to display the same clear decline and plateau in mechanical properties as previously recorded for the $0.15V_f$ hybrid samples.

Furthermore, the inclusion of HA appeared to maintain the elastic modulus of the hybrid composite above that of the $0.01V_f$ sample throughout the entire immersion period but was below that of the $0.2V_{HA}$ control. This was likely due to the internal porosity created from fibre dissolution as well as the previously mentioned breakdown of the HA-PLA interface via buffering of the media pH. However it was observed that that the elastic modulus of the $0.01V_f$ and $0.01V_f$ - $0.2V_{HA}$ samples was superior to that of the $0.2V_{HA}$ control when compared after 1008 hours of immersion. This subsequently cast further doubt on the accuracy of this result (i.e. the sudden drop in elastic modulus for the $0.2V_{HA}$ sample at 1008 hours) as discussed earlier.

A comparison between the ionic release rates during the initial 168 hours of $0.01V_f$ and $0.01V_f$ - $0.2V_{HA}$ sample degradation revealed a marked difference in the daily and accumulative ionic concentrations (Figure 8.3.26 and Figure 8.3.27). This was apparent by the increased concentrations of $(PO_4)^{3-}$ and Ca^{2+} ions in the $0.01V_f$ - $0.2V_{HA}$ degradation media compared to the $0.01V_f$ samples (Figure 8.4.8). The increased concentration of these ions was to be expected given the Ca^{2+} and $(PO_4)^{3-}$ products that occur from HA dissolution (Vallittu, 2012) ^[370]. This would then correlate with the dissolution of the secondary HA phase as a result of the phosphoric acid generated during fibre dissolution and the subsequent pH buffering that was recorded during $0.01V_f$ - $0.2V_{HA}$ sample degradation (Figure 8.3.24). Inspection of the accumulative ionic concentrations from both samples also revealed that similar concentrations of Mg^{2+} ($\approx 6 \text{ mg l}^{-1}$) and Na^+ ions ($\approx 11 \text{ mg l}^{-1}$) were released from the fibres into the media after 168 hours (Figure 8.3.27). This would then imply that similar fibre volume fractions as well as fibre dissolution rates were

present in each composite type despite the inclusion of HA into the hybrid composite configuration. This then challenges the notion that a reduced fibre dissolution rate was responsible for the previously found increase in biocompatibility of the hybrid composite samples (Figure 8.3.12).

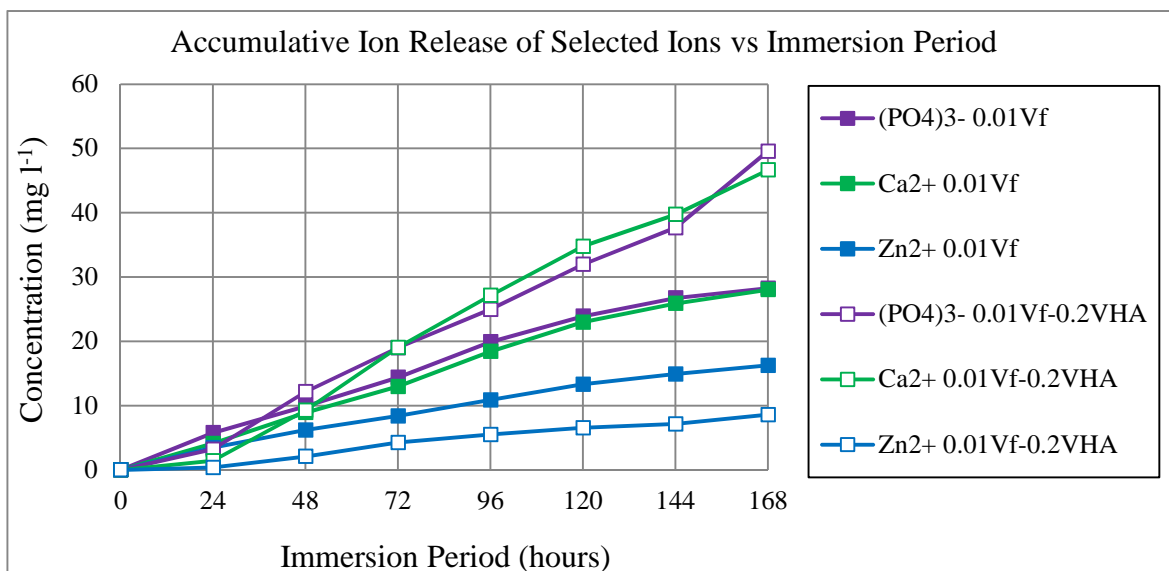


Figure 8.4.8. Comparison between the accumulative ion release from 0.01V_f and 0.01V_f-0.2V_{HA} composites over the initial 168 hours of degradation showing a marked decrease in the total concentration of Zn²⁺ and increase in (PO₄)³⁻ and Ca²⁺ ions release from the 0.01V_f-0.2V_{HA} hybrid composite.

However these results could be accounted for when considering the difference in Zn²⁺ ions accumulated after 168 hours between the 0.01V_f (16.3 mg l⁻¹) and 0.01V_f-0.2V_{HA} (8.6 mg l⁻¹) samples (Figure 8.4.8). Since it has already been established that excess Zn²⁺ (↑~8 mg l⁻¹) and a low pH (< 7.4) can be cytotoxic to MG63 cells, the inclusion of HA was subsequently expected to limit these factors by buffering the pH and limiting the autocatalysis effects. As discussed in section 3.4.6.2, dissolution studies by Khor et al. (2011) have highlighted the preferential leaching of Zn²⁺ ions when PG samples were degraded in low pH, acidic conditions. Based on the collected data, it is proposed that an elevation in pH at the fibre-matrix interface was generated by the inclusion of a secondary HA filler phase that consequently limited the preferential leaching of Zn²⁺ ions from the CorGlaes[®] Pure 107 fibres compared to the 0.01V_f samples (Figure 8.4.9). This would have then have restricted the rate at which the Zn²⁺ ions could accumulate towards cytotoxic levels within the 0.01V_f-0.2V_{HA} sample degradation media [187].

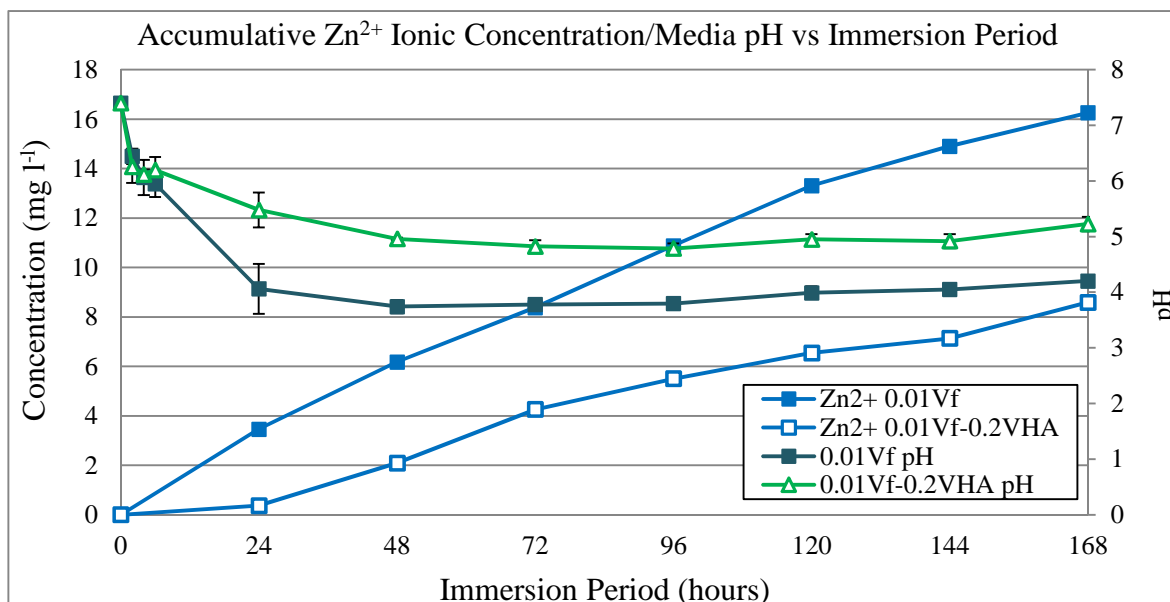


Figure 8.4.9. Comparison of Zn^{2+} accumulative ionic release and media pH against the immersion period for $0.01V_f$ and $0.01V_f-0.2V_{HA}$ samples

This concept would then correlate with the MTT and direct contact culture results where only the $0.01V_f$ samples appeared to be cytotoxic despite ion release data implying that the CorGlaes[®] Pure 107 fibres in both samples were degrading at similar rates. Consequently this difference in Zn^{2+} release and rates at which this ion could accumulate to cytotoxic levels would explain the difference in cell population/morphology between the $0.01V_f$ and $0.01V_f-0.2V_{HA}$ composites as well as when compared to the PLA control (Figure 8.3.20).

To elaborate, during the *in vitro* culture of samples it was likely that the rate of Zn^{2+} release from the $0.01V_f$ samples (via fibre dissolution) exceeded the MG63 cytotoxic limits before the media was replaced after 96 hours. This consequently produced the rounded cell morphology and declining cell population that was observed in both Coomassie and SEM images. In contrast, the reduced rate of Zn^{2+} ion release from the $0.01V_f-0.2V_{HA}$ hybrids in conjunction with the replacement of the media at 96 hours prevented such a severe reduction in cell viability. Based on the SEM and Coomassie staining images, this would then account for the reduced cell population and mixed morphology (i.e. round/spread) seen in cells after 96 hours of culture (Figure 8.3.18) on the $0.01V_f-0.2V_{HA}$ samples as the Zn^{2+} ions began to reach cytotoxic levels before the culture media was replaced.

Furthermore, since earlier results had indicated that the DMEM media had no retarding effects on the CorGlaes[®] Pure 107 fibre dissolution rate when utilised as a composite reinforcing agent (section 7.3.4), the evidence for this concept based on the ion release data

during sample degradation in distilled water was deemed valid. However it should also be noted that the biocompatibility testing (i.e. MTT, direct contact culture) was performed at a higher SA:V ratio ($1.4 \text{ cm}^2 \text{ ml}^{-1}$) than that employed during mechanical degradation ($0.21 \text{ cm}^2 \text{ ml}^{-1}$). As a result, the ionic concentrations shown in Figure 8.3.26 and Figure 8.3.27 are expected to be lower than those encountered during the *in vitro* cell culture experiments. Yet this does not affect the general principle regarding the selective Zn^{2+} ion release as proposed here.

Analysis of the FTIR spectra (section 8.3.3.7) obtained from the planar sample surfaces after immersion in c-SBF showed variations and shifts in the peak wavenumber/intensities of the $0.2V_{\text{HA}}$ composites (Figure 8.3.29) with the band at $\approx 1030 \text{ cm}^{-1}$ (T_0) shifting to 1044 cm^{-1} . It was also apparent that the intensity of the peaks at 604 cm^{-1} and 562 cm^{-1} varied between spectra which, due to the $0.5\text{-}5 \mu\text{m}$ penetration depth of the FTIR-ATR equipment, was attributed to the exposure of HA particles on the hybrid composite surface as discussed by Persson et al. (2014) ^[371]. As a result, areas with a low concentration of HA particles exposed or in reduced proximity to the composite surface had a reduced HA signal intensity and a decrease in peak band overlapping. This then made the 1044 cm^{-1} peak (PLA, $\text{C}=\text{CH}_3$ vibration) more prominent and would then account for the apparent peak shifting (i.e. 1030 cm^{-1} (T_0) \leftrightarrow 1044 cm^{-1}) observed between the spectra obtained from the $0.2V_{\text{HA}}$ samples across the immersion period. These results highlighted the variation in HA distribution across the sample surfaces with the sample areas chosen at random by the user. This would also seem to correlate with the non-uniform distributions and particle agglomeration effects that were previously discussed during the mechanical characterisation of the hybrid composites. Such variations in HA surface exposure were also believed to have accounted for the similar peak transitions observed in the $0.01V_{\text{f}}$ - $0.2V_{\text{HA}}$ hybrid composite (Figure 8.3.31) spectra. Meanwhile the absence of HA accounted for the lack of any similar shifts being observed in the $0.01V_{\text{f}}$ spectra (Figure 8.3.30) ^[371].

It was also observed that peaks at 1264 cm^{-1} and 800 cm^{-1} on the $0.2V_{\text{HA}}$ and $0.01V_{\text{f}}$ samples showed a marked decrease after 24-72 hours (Figure 8.3.29 and Figure 8.3.30). Based on the FTIR analysis of polymer degradation by Partini & Pantani (2007), any changes in these peak intensities through hydrolytic degradation were ruled out ^[372]. Consequently this observation was believed to be due to the PTFE lubricant applied during composite manufacturing or other contaminant (e.g. from the cutting stages of specimen preparation) that had not been completely removed prior to c-SBF immersion. This would then account for the early decline in the intensity of these peaks shortly after immersion and why such

strong peaks were not detected on all samples. Examining previous results it was also seen that the same peak variations were observed during $0.2V_f$ RCM bioactivity testing (Figure 7.3.21). However further investigation is required to confirm.

The FTIR analysis of minute surface deposits removed from the $0.01V_f$ - $0.2V_{HA}$ sample cross-sections (collected after 336 hours of immersion) found these to match the previous pyrophosphate salts found during $0.2V_f$ RCM composite bioactivity testing (Figure 8.4.10). Yet the visible formation of these salts was negligible and were only found on a single sample from the three analysed by FTIR after 336 hours compared to the rapid formation found on all $0.2V_f$ RCM samples. The small quantity of these compounds was attributed to the significantly lower V_f of CorGlaes[®] Pure 107 fibres in the hybrid composite configuration and thus reduced concentrations of ions released into the media as a result. The appearance of this precipitate at the sample cross-section was also in line with the cross-sectional “halo” regions of bioactive PGF composite materials as discussed by Vallittu et al. (2015)^[5]. The inconsistent formation of these compounds was believed to be due to an unwanted/localised increase in the fibre volume fraction within specific samples. This would then account for the absence of any similar pyrophosphate salt precipitates found during the FTIR analysis of the $0.01V_f$ composite cross-sections after immersion.

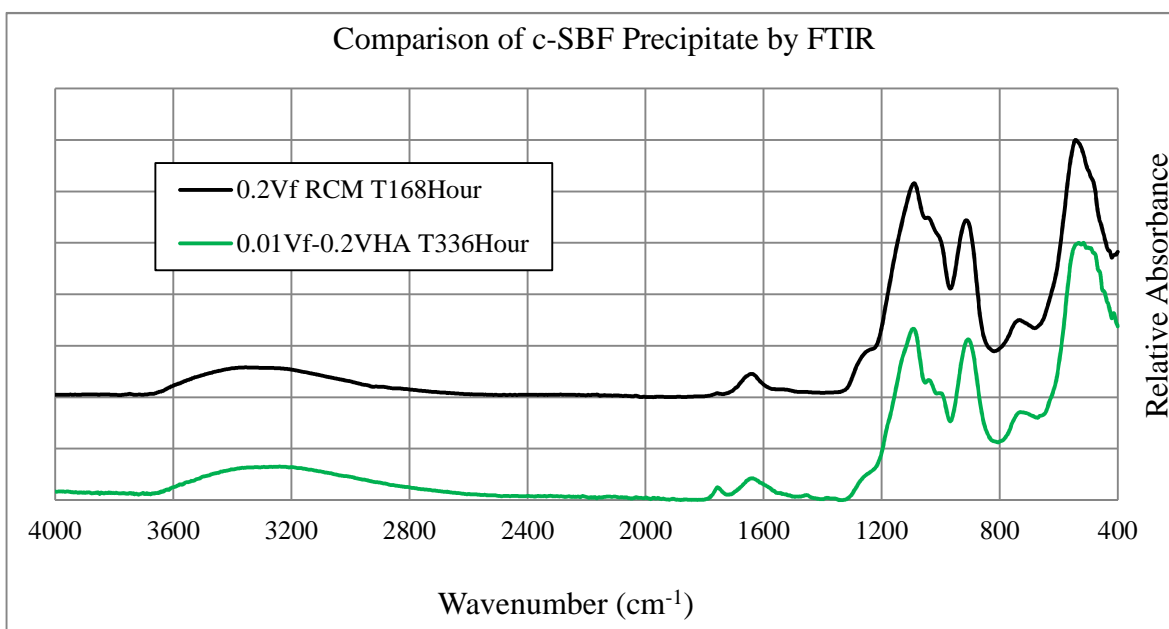


Figure 8.4.10. Comparison of precipitates from $0.01V_f$ - $0.2V_{HA}$ and $0.2V_f$ RCM composites after immersion in c-SBF over the 4000 - 400cm^{-1} wavenumber range.

8.5 Conclusions

Modifications to the previous 0.2V_f RCM CorGlaes[®] Pure 107 composite configuration showed that the use of silane treatments or a secondary filler phase had different influences on the composites mechanical behaviour. This was evident by the increase in initial flexural strength (+39.7%), elastic modulus (+7.9%) and toughness (+41.2%) observed when the CorGlaes[®] Pure 107 fibres were treated with an APS sizing agent due to the improved interfacial bonding at the fibre-matrix interface. However the application of this surface treatment provided no improvement to composite durability as a result of the severe autocatalysis effects caused by the fibre's acidic pH dissolution by-products.

The investigation into different 0.15V_f PGF hybrid composite configurations revealed that the inclusion of a hydroxyapatite (HA) particle filler phase was capable of producing materials with an increased elastic modulus compared to the previous 0.2V_f RCM samples. Furthermore the inclusion of HA caused the failure mode of these composites to change from a ductile to brittle fracture mode. The configuration of the hybrid composites was also found to influence the initial mechanical properties with the greatest increase in elastic modulus (+22%) compared to the 0.2V_f RCM samples found from the inclusion of a non-homogeneously distributed 0.1 volume fraction of HA. However mechanical testing of the investigated hybrid composite configurations also revealed that particle agglomeration at higher HA volume fractions compromised the mechanical properties of the hybrid samples.

The subsequent degradation of these samples found that despite the media pH being buffered (compared to the 0.2V_f RCM samples) that the apparent rate of fibre dissolution remained unchanged. Therefore, it was anticipated that due to the high ion release rates all hybrid composite samples would continue to be cytotoxic due to the high concentrations of Zn²⁺ ions that would have been released into the media during *in vitro* testing.

Alternatively, the focus on developing biocompatible hybrid composites through the incorporation of HA into low V_f samples found that the addition of 0.2V_{HA} into a 0.01V_f sample produced biocompatible materials when assessed by MTT assay. Such results were subsequently confirmed through the analysis of MG63 cells by Coomassie Brilliant Blue staining and SEM after direct contact culturing on composite samples. Although this behaviour was initially attributed to a reduced fibre dissolution rate, degradation of the corresponding sample configurations and controls indicated that the buffered media pH (via the addition of HA) had influenced the selective leaching of the Zn²⁺. However due to the smaller fibre volume fraction, the CorGlaes[®] Pure 107 fibres had a reduced impact on the initial and degenerative mechanical properties during sample degradation in distilled

water. The low V_f of the samples did produce sporadic deposits of pyrophosphate salt deposition during c-SBF bioactivity testing but the FTIR spectra also revealed the presence of HA on the composite surface from the existing secondary filler phase.

Consequently based on the accumulated hybrid composite data, the specific application of the CorGlaes[®] Pure 107 fibres appears to be confined to possibly providing advantageous stimulatory effects *in vivo* (via ion release) rather than as the primary reinforcing agent of a biodegradable composite. The results have also indicated the potential for the development of novel hybrid composite designs to be investigated.

9 Discussion

Despite the extensive range of possible phosphate glass compositions, their application in biomedical devices is limited by the need to achieve glass artefacts (i.e. monoliths, fibres etc.) with suitable dissolution rates, mechanical properties and potential bioactivity whilst being composed of metabolically acceptable constituents. Consequently review articles of biomedical phosphate glasses (e.g. Knowles, 2003; Abou Neel et al., 2009) have demonstrated the balance between achieving mechanically and biologically advantageous glass systems whilst maintaining good processability^[160, 213]. As observed in section 3.4.6.1 and 3.4.6.2, the development of these glasses has typically been conducted through a cross-compositional analysis where a selected modifier oxide concentration has been varied (e.g. 0→10 mol%) in order to assess its effect on a glass's properties. Consequently the characterisation is performed using a comparative analysis across these variations. However, given that this project was restricted to the CorGlaes[®] Pure 107 glass and that limited compositional data was available, the characterisation performed here was based on a broad examination of the relevant literature. This may have subsequently affected the accuracy and depth of the CorGlaes[®] Pure 107 glass analysis. Yet by following this method to characterise its bulk and fibre formats, a broad review (not been previously reported) of different biomedical PG properties has been produced.

Based on the available literature, it is believed that no previous investigations have examined a quinary glass composition similar to CorGlaes[®] Pure 107. Given the relevance of its constituency ions to the physiological roles in bone growth (i.e. $(\text{PO}_4)^{3-}$, Ca^{2+} , Mg^{2+} and Zn^{2+} - Table 3.4.3) the CorGlaes[®] Pure 107 composition was believed to be a suitable candidate for potential bone tissue regenerative applications. However characterisation of the CorGlaes[®] Pure 107 disks (chapter 5) revealed that its good flexural strength, elastic modulus (comparable to that of Bioglass[®] 45S5) and high thermal stability (PW) were offset by its poor biocompatibility. Combined with the previous data reported by Abou Neel et al. (2008), the CorGlaes[®] Pure 107 results highlighted concerns over localised acidity as well as the suitability of zinc in biomedical phosphate glass compositions. This is despite its advantages as a modifier oxide (i.e. its charge-to-size ratio) and potential stimulatory effects *in vivo*^[195]. However, this basis must also be considered with regards to the P_2O_5 concentration which made the CorGlaes[®] Pure 107 glass inherently prone to autocatalysis effects that ultimately influenced the ion release rates from the samples (i.e. composites). The effect of pH is further emphasised in these results when considering the selective leaching of Zn^{2+} ions from PGs in acidic media as reported by Khor et al. (2011). This subsequently supports the development of low P_2O_5

polyphosphate glass compositions (i.e. < 50 mol% P₂O₅) such as those recently investigated by Sharmin et al. (2014) where B₂O₃ was substituted into the glass formulation ^[187, 211]. The results presented here have also provided further insight into the applicability of glass compositions that utilise mixed ion effects to achieve enhanced properties outside the expected trends as evident by the PW recorded for the CoreGlaes[®] Pure 107 glass.

The production and characterisation of CorGlaes[®] Pure 107 fibres (chapter 6) has also highlighted the sensitivity of these materials to surface flaw type/size that can be produced during the necessary handling stages. Based on this, the comparison of fibre tensile properties are subsequently susceptible to variations based on the handling of fibres between different studies. Yet this can also be affected by fluctuations in the fibre diameter that could occur during PGF manufacturing. Meanwhile the novel study on the influence of different media on the CorGlaes[®] Pure 107 fibres has demonstrated the variability in fibre dissolution rates across different interdisciplinary techniques (e.g. cell culture, bioactivity and mechanical degradation). Consequently these results raise considerations when relating mechanical properties or dissolution rates to *in vitro* data and is particularly relevant when intending to use PGFs as a single implant construct (i.e. implants composed purely of fibres) such as the cell delivery vehicles previously studied by Ahmed et al. (2004) and Bitar et al. (2005) ^[178, 194].

When used as a composite reinforcing agent, the initial results (chapter 7) showed the benefits of a random continuous mat (RCM) CorGlaes[®] Pure 107 fibre architecture which, based on the available literature, had not been previously investigated for PGF composite biomaterials. These advantages were due to the observed improvements in material toughness found in the laminate RCM composites as a result of fibre pull-out mechanisms and improved polymer infiltration into the RCM fibre constructs. The RCM architecture may then be more favourable in specific composite applications compared to the unidirectional (UD), [0/90] cross-plys or random chopped fibre filler phases previously investigated (e.g. Ahmed et al., 2009; Ahmed et al., 2011) ^[218, 219]. Based on the results by Han et al. (2013), this RCM architecture may also be more favourable compared to UD fibres for composite implant devices where intra-operative screw holes are required prior to implantation ^[223]. This is due to the increased damage that UD composites can incur compared to random chopped fibre mats when screw holes are introduced via drilling techniques.

Mechanical testing of the 0.2V_f RCM composites also found that the flexural strengths and elastic moduli of these CorGlaes[®] Pure 107 composite configurations were within the range of those reported for parietal bone. This result implied that degradable PGF-composites have potential for the proposed cranioplasty applications as discussed in chapter 2. Additionally, the elastic moduli of these samples were also seen to correlate with those predicted by the rule of mixtures (ROM) for both fibre architectures investigated. However these properties could potentially be further increased through modifications to the manufacturing method aimed at improving polymer impregnation into the fibres (such as vacuum forming techniques). Unfortunately due to autocatalysis effects, the 0.2V_f CorGlaes[®] Pure 107 composites failed to retain at least 80% of their initial mechanical properties over the six week degradation period as set out by the initial design criteria in section 2.1.

These autocatalytic effects have been observed in other PGF-composite materials (Ahmed et al., 2009, 2011; Han et al., 2013) and highlighted the balance between achieving glass fibres with good processability whilst possessing slow dissolution rates. This is particularly relevant to the P₂O₅ content which at high concentrations allows for PGFs to be easily produced but is hampered by their resultant susceptibility to autocatalysis effects due to the increased amount of phosphate species released into the media. Alternatively low P₂O₅ glasses (e.g. polyphosphate glasses) are less prone to autocatalysis but are typically harder to manufacture into fibres and are more likely to crystallise. Such features consequently reinforce earlier sentiments that the wide range of potential PG compositions is ultimately restricted by their practicality. Furthermore, the continued use of PLA as a matrix component in the development of PGF composites would seem disadvantageous given its acidic degradation by-products and importance of the fibre-matrix interface to maintaining adequate composite mechanical properties ^[218, 219, 223].

Continuing from the previous CorGlaes[®] Pure 107 fibre dissolution data in section 6.3.6, the translation between mechanical and cell culture environments on composite samples was also investigated due to the absence of any ionic influences during composite degradation in distilled water. The correlation and discrepancies between composite degradation behaviour in each media (i.e. weight loss, media pH) showed how the high surface area-to-volume ratios (SA:V) at the fibre-matrix interface can be detrimental to the reinforcing fibres dissolution rate. As a result, the relevance of a PGF's dissolution rate is obscured when it is to be applied in a composite system given the increased influence of its dissolution by-products. This high rate of fibre dissolution was also responsible for the

cytotoxicity found across all fibre volume fractions (V_f) investigated. Such results consequently reinforced the importance of considering the pH changes and ion release rates (i.e. cytotoxicity limits) but also showed how these factors can interact with each other.

The development of PGF polymer composite materials has typically examined different glass compositions in a two phase, matrix-filler design (e.g. Ahmed et al., 2008; Brauer et al., 2008; Parsons et al., 2009; Khan et al., 2010; Ahmed et al., 2011) ^[212, 215, 217, 228]. Yet the versatility in available glass compositions can be restricted by the design requirements of biomedical glasses as well as the radical, sometimes detrimental, changes to the properties of a glass that can be caused from small compositional variations (Hench, 2013) ^[76]. Furthermore given that no single bioactive material is considered by Hench (2013) to be optimal for all applications, there is a need to develop a range of different glass compositions. Such sentiments are also in line with the need for application specific glass dissolution rates as discussed by Hasan et al. (2012) ^[210]. Consequently the investigation of different hybrid PGF composite configurations based on this concept was intended to allow for further design versatility in composite properties without relying on compositional changes to the reinforcing PGFs.

Given the limitation to using only the CorGlaes[®] Pure 107 glass, the hybrid composites developed in this study were intended to improve the mechanical integrity of the composite material during its degradation by counteracting the fibre's autocatalytic effects. The investigation of different hybrid composite designs was also aimed at establishing an optimised hybrid configuration based on the ability of calcium phosphates to buffer an acidic pH. Given the absence of design variation as well as a lack of data on the mechanical degradation or *in vitro* cell culture results in previous work it was believed that the results collected here could be utilised for future hybrid composite designs ^[229].

The characterisation of different hybrid samples (chapter 8) subsequently showed that despite variations in the initial mechanical properties and apparent pH buffering of the degradation media, no significant improvements in composite mechanical durability were achieved in any of the mechanically optimised hybrid sample configurations. These samples are expected to have remained cytotoxic due to the rate of Zn^{2+} ion release with further increases to the HA volume fraction (V_{HA}) restricted by the HA particles effects on the polymer melt flow and subsequent polymer infiltration into the fibres. The transition of the composites initial (i.e. HA-free) fibrous, ductile failure behaviour to a brittle failure

mode would also cast doubt on the suitability of fibre-particle hybrid composite configurations for cranioplasty plate applications (Brauer et al. 2008) ^[217].

Alternatively the increasing biocompatibility found in low V_f hybrid composites ($0.01V_f/0.05V_f$) with increasing HA volume fraction (V_{HA}) demonstrated the severity of the acidic pH and inability of the HA to adequately buffer the degradation media in higher V_f composites (i.e. $0.15V_f$). However, it was shown that hybrid composite designs could be used to render previously cytotoxic low V_f composites as biocompatible. Although due to the low V_f required to achieve hybrid biocompatibility, the CorGlaes[®] Pure 107 fibres were ultimately reduced to providing an *in vivo* stimulus as oppose to their intended function as a reinforcing agent.

With these results the CorGlaes[®] Pure 107 fibres would appear to be unsuitable for the proposed cranioplasty plate material. However the development of PGF-composites with suitable mechanical properties (prior to degradation) did prove the initial viability of the concept.

In line with comments by Hasan et al. (2012) and Hench (2013), it would appear that the functionality of a PGF-composite cranioplasty plate could not be fulfilled by a single PGF composition alone ^[76, 210]. This is due to the conflicting design requirements in PGF composites where high fibre dissolution rates (and associated ion release rates) would be advantageous for suppressing bacterial infections as well as eliciting early bioactive or osteoinductive responses *in vivo* (section 3.4.5). However this would also likely compromise the mechanical durability of the device after implantation (due to the rapid dissolution of the mechanically reinforcing fibres). Consequently hybrid composite designs may allow for such dual functionality to be achieved through the use of different constituent components (i.e. multiple PGF compositions). Based on the data obtained from the CorGlaes[®] Pure 107 hybrid composites, a dual fibre system of fast (bioactive/antimicrobial) and slow (mechanically reinforcing) dissolution rate PGFs would appear to be the preferable option. This is primarily due to the increased brittleness found in fibre-particle hybrid systems that could jeopardise the ability of the implant to adequately protect the underlying cerebral tissue. As a result, the inclusion of bioactive particles (such as HA or alternate bioactive glass compositions) would be less favourable.

10 Conclusions

- Structural analysis of the CorGlaes[®] Pure 107 composition confirmed its amorphous, ultraphosphate structure whilst its thermal properties (i.e. large PW) made it highly suitable for fibre manufacturing.
- The CorGlaes[®] Pure 107 glass exhibited a superior flexural strength and similar elastic moduli to that reported for Bioglass[®] 45S5 with the density, hardness and fracture toughness within the expected range for PGs.
- The CorGlaes[®] Pure 107 annealed disks possessed a dissolution rate of $4 \times 10^{-3} \text{ mg cm}^{-2} \text{ hr}^{-1}$.
- Despite dissolution extracts being biocompatible, the glass composition was cytotoxic to MG63 cells during direct contact cell culture.
- Mechanical testing of $\text{Ø} \approx 20 \mu\text{m}$ CorGlaes[®] Pure 107 fibres showed the tensile strength ($462 \pm 143 \text{ MPa}$) and tensile modulus ($65.5 \pm 20.8 \text{ GPa}$) to be similar to those reported for other PGF systems.
- As an isolated element, the fibre dissolution rate was affected by the different media typically used in biomaterial characterisation.
- The immersion of fibres in c-SBF resulted in the deposition of different pyrophosphate salts relative to the CorGlaes[®] Pure 107 composition.
- The incorporation of CorGlaes[®] Pure 107 fibres into a PLA matrix showed the expected increase in elastic moduli that closely matched those predicted by the rule of mixtures.
- $0.2V_f$ CorGlaes[®] Pure 107 fibre composite configurations of RCM and $[0/90]_{3S}$ fibre architectures possessed mechanical properties within the range of those reported for the parietal bones of the skull.
- RCM fibre mat architectures were found to be advantageous for developing cranioplasty plates due to their improved toughness and flexural strength compared to $[0/90]_{3S}$ cross-ply composite configurations.
- $0.2V_f$ RCM and $0.2V_f [0/90]_{3S}$ composites failed to retain at least 80% of their mechanical properties during six weeks of degradation in distilled water or DMEM - where pyrophosphate salt deposition was also observed.

- Pyrophosphate salt deposition was also recorded during the immersion of $0.2V_f$ RCM composites in c-SBF.
- A cytotoxic response from composite degradation extracts was found across $0.01V_f$, $0.05V_f$, $0.1V_f$ and $0.2V_f$ samples after 24 and 96 hours of degradation with MG63 cells when assessed by MTT assay.
- Silane treatment of CorGlaes[®] Pure 107 fibres produced composites with increased mechanical properties but this failed to sufficiently retard the loss of mechanical properties during sample degradation.
- The distribution and volume fraction of hydroxyapatite (HA) in $0.15V_f$ RCM hybrid composites had a strong influence on composite mechanical properties where the maximum increase in elastic modulus was recorded after the introduction of $0.1V_{HA}$ that was non-homogenously distributed throughout the sample.
- All hybrid composite variations buffered the degradation media pH but failed to adequately reduce the fibre dissolution rates and consequently the loss in mechanical properties during sample degradation in distilled water at 37°C .
- The cell viability from composite degradation extracts showed an increasing degree of biocompatibility as the HA volume fraction increased ($0V_{HA} \rightarrow 0.1V_{HA} \rightarrow 0.2V_{HA}$) in $0.01V_f$ and $0.05V_f$ composite samples when assessed by MTT assay.
- Despite the statistically significant difference in the MTT assay results, the increased solubility of a β -TCP filler phase (compared to HA) was unable to produce biocompatible $0.05V_f$ composites.
- Only a $0.01V_f$ - $0.2V_{HA}$ composite configuration was found to be biocompatible, but the resulting mechanical properties were considerably reduced compared to the $0.2V_f$ RCM samples and below those of the parietal bones.
- CorGlaes[®] Pure 107 fibres are unsuitable as a composite reinforcing agent but PGF composites show potential as part of a cranioplasty plate material.
- Hybrid PGF-composites using multiple glass fibre compositions are an attractive option for future implant designs that require an immediate *in vivo* response and long term mechanical properties.

11 Future Work

Although the fundamental application of PGF composites as part of a cranioplasty plate material has been proven mechanically, the continued development of these materials should focus on:

- a) The evolution of glass compositions tailored towards cranioplasty composite applications with reduced dissolution rates that are able to maintain a neutral media pH during their dissolution despite the high surface area-to-volume ratios at the fibre-matrix interface.
- b) Manufacturing of fibre pre-pregs using vacuum forming techniques for potentially improving composite mechanical properties (due to the improved polymer infiltration into the fibres).
- c) The development of continuous fibre spools from PGF manufacturing techniques that would allow these materials to be incorporated into fibre pre-impregnation equipment. This would eliminate the manual handling stages of composite production that can compromise fibre integrity and would allow for composites with increased mechanical properties due to the improved packing density of the fibres and consequently increased V_f .
- d) The development of woven PGF constructs (as are available with conventional glass fibres) that would allow for the development of composite materials with more adaptable mechanical properties.
- e) Impact testing of PGF composite configurations prior to and after sample degradation to further assesses their suitability as a cranioplasty plate component.
- f) Investigation into the potential of phosphate glass platelets as a reinforcing agent in general fracture fixation plates due to their high aspect ratios compared to particles. This could potentially allow for the manufacturing of composites with improved mechanical properties (compared to particles) whilst the discontinuous nature of the reinforcing phase would decrease the rate of fluid wicking throughout the interface.

However, the concept of hybrid PGF composites should also be developed and includes:

- a) Hybrid composites incorporating different PGF compositions that could contain low dissolution rate, high modulus fibres (as the main reinforcing agent) with a secondary phase of high dissolution rate fibres intended to generate a rapid bioactive/osteoinductive response or a controlled release of ions aimed at infectious prevention (e.g. silver, Ag^+).
- b) Laminated hybrid composites utilising PGF and degradable magnesium fibres where high mechanical properties and long term durability are required alongside a physiological stimulus provided by the *in vivo* dissolution of the PGFs.

Appendix A

Table A.1. Mechanical properties of the different composite configurations manufactured in chapter 7.

| Sample | Flexural Strength (MPa) | Elastic Modulus (GPa) |
|--|-------------------------|-----------------------|
| NatureWorks [®] 3001D PLA | 98.04 ± 1.06 | 3.21 ± 0.34 |
| 0.01V _f RCM | 82.50 ± 3.77 | 3.97 ± 0.35 |
| 0.05V _f RCM | 57.64 ± 15.55 | 5.00 ± 0.41 |
| 0.1V _f RCM | 27.12 ± 5.62 | 5.49 ± 0.05 |
| 0.2V _f RCM | 82.39 ± 4.46 | 7.57 ± 1.20 |
| 0.2V _f RCM [0/90] _{3S} | 62.35 ± 10.14 | 8.19 ± 0.64 |

Table A.2. Mechanical properties of the different modified composite configurations manufactured in chapter 8.

| Sample | Flexural Strength (MPa) | Elastic Modulus (GPa) |
|---|-------------------------|-----------------------|
| 0.2V _f RCM-APS | 115.15 ± 2.65 | 8.17 ± 1.90 |
| 0.2V _{HA} | 35.49 ± 5.94 | 5.37 ± 0.83 |
| 0.15V _f -0.1V _{HA(NHD)} | 67.00 ± 8.55 | 10.01 ± 1.33 |
| 0.15V _f -0.2V _{HA} | 36.41 ± 3.53 | 9.34 ± 0.49 |
| 0.15V _f -0.2V _{HA(NHD)} | 37.61 ± 1.23 | 6.74 ± 0.45 |
| 0.01V _f -0.2V _{HA} | 25.36 ± 7.00 | 4.85 ± 0.4 |

References

1. Giltech. *Giltech - Medical Advancement*. 2015 [05/02/2015]; Available from: <http://www.giltech.biz/>.
2. Spetzger, U., V. Vougioukas, and J. Schipper, *Materials and techniques for osseous skull reconstruction*. Minimally Invasive Therapy & Allied Technologies, 2010. **19**(2): p. 110-121.
3. O'Keefe, A.B., T. Lawrence, and S. Bojanic, *Oxford craniotomy infections database: A cost analysis of craniotomy infection*. British Journal of Neurosurgery, 2012. **26**(2): p. 265-269.
4. Aitasalo, K.M.J., J.M. Piitulainen, J. Rekola, and P.K. Vallittu, *Craniofacial bone reconstruction with bioactive fiber-reinforced composite implant*. Head & Neck, 2014. **36**(5): p. 722-728.
5. Vallittu, P.K., T.O. Närhi, and L. Hupa, *Fiber glass–bioactive glass composite for bone replacing and bone anchoring implants*. Dental Materials, 2015.
6. Nganga, S., D. Zhang, N. Moritz, P.K. Vallittu, and L. Hupa, *Multi-layer porous fiber-reinforced composites for implants: In vitro calcium phosphate formation in the presence of bioactive glass*. Dental Materials, 2012. **28**(11): p. 1134-1145.
7. Mustafa, Z. and K.E. Tanner, *Composites for Hard Tissue Repair*, in *Wiley Encyclopedia of Composites*, L. Nicolais and A. Borzacchiello, Editors. 2011, John Wiley & Sons, Inc.
8. Al-Obaid, Y.F., F.N. Bangash, and T. Bangash, *Trauma - An Engineering Analysis: With Medical Case Studies Investigation*. 2007: Springer.
9. Pietrzak, W.S. and B.L. Eppley, *Resorbable polymer fixation for craniomaxillofacial surgery: Development and engineering paradigms*. Journal of Craniofacial Surgery, 2000. **11**(6): p. 575-585.
10. Poitout, D.G., *Biomechanics and Biomaterials in Orthopedics*. 2004: Springer.
11. An, Y.H. and R.A. Draughn, *Mechanical Testing of Bone and the Bone-Implant Interface*. 1999: Taylor & Francis.
12. Planell, J.A., S.M. Best, D. Lacroix, and A. Merolli, *Bone Repair Biomaterials*. 2009: Elsevier Science.
13. Hamill, J. and K.M. Knutzen, *Biomechanical Basis of Human Movement*. 2006: Lippincott Williams & Wilkins.
14. Belinha, J., *Meshless Methods in Biomechanics: Bone Tissue Remodelling Analysis*. 2014: Springer.
15. Neira, M.I.S., *An efficient approach to the synthesis of a calcium phosphate bone-cement and its reinforcement by hydroxyapatite crystals of various particle morphologies*. 2011: Universidade de Santiago de Compostela, Servizo de Publicacións e Intercambio Científico.
16. Khurana, J.S., E.F. McCarthy, and P.J. Zhang, *Essentials in Bone and Soft-Tissue Pathology*. 2010: Springer.
17. Hollinger, J.O., T.A. Einhorn, B. Doll, and C. Sfeir, *Bone Tissue Engineering*. 2004: Taylor & Francis.
18. Qin, Q.H., *Mechanics of Cellular Bone Remodeling: Coupled Thermal, Electrical, and Mechanical Field Effects*. 2013: Taylor & Francis.
19. Cowin, S.C. and S.B. Doty, *Tissue Mechanics*. 2007: Springer.
20. Kardamakis, D., V. Vassiliou, and E. Chow, *Bone Metastases: A translational and clinical approach*. 2009: Springer.
21. Steinhoff, G., *Regenerative Medicine: From Protocol to Patient*. 2013: Springer Netherlands.
22. Hadjidakis, D.J. and I.I. Androulakis, *Bone Remodeling*. Annals of the New York Academy of Sciences, 2006. **1092**(1): p. 385-396.

23. Lanham-New, S.A., I.A. Macdonald, and H.M. Roche, *Nutrition and Metabolism*. 2011: Wiley.
24. Boccaccini, A.R. and J. Gough, *Tissue Engineering Using Ceramics and Polymers*. 2007: Elsevier Science.
25. Brickley, M. and R. Ives, *The Bioarchaeology of Metabolic Bone Disease*. 2010: Elsevier Science.
26. Currey, J.D., *The structure and mechanics of bone*. *Journal of Materials Science*, 2012. **47**(1): p. 41-54.
27. Weiner, S. and H.D. Wagner, *The material bone: Structure mechanical function relations*. *Annual Review of Materials Science*, 1998. **28**: p. 271-298.
28. Rho, J.-Y., L. Kuhn-Spearing, and P. Zioupos, *Mechanical properties and the hierarchical structure of bone*. *Medical Engineering & Physics*, 1998. **20**(2): p. 92-102.
29. Rogers, K., *Bone and Muscle: Structure, Force, and Motion*. 2010: Britannica Educational Pub.
30. Narayan, R., *Biomedical Materials*. 2009: Springer.
31. Khurana, J.S., *Bone Pathology*. 2009: Humana Press.
32. Patton, K.T., *Survival Guide for Anatomy & Physiology*. 2013: Elsevier Health Sciences.
33. Burr, D.B. and M.R. Allen, *Basic and Applied Bone Biology*. 2013: Elsevier Science.
34. Giraud-Guille, M.M., *Twisted plywood architecture of collagen fibrils in human compact bone osteons*. *Calcified Tissue International*, 1988. **42**(3): p. 167-180.
35. Adler, C.P., *Bone Diseases: Macroscopic, Histological, and Radiological Diagnosis of Structural Changes in the Skeleton*. 2000: Springer.
36. Marotti, G., M.A. Muglia, and C. Palumbo, *Collagen texture and osteocyte distribution in lamellar bone*. *Ital J Anat Embryol*, 1995. **100**(Suppl 1): p. 95-102.
37. Martin, R.B., D.B. Burr, and N.A. Sharkey, *Skeletal Tissue Mechanics*. 1998: U.S. Government Printing Office.
38. Currey, J.D., *Bones: Structure and Mechanics*. 2013: Princeton University Press.
39. Roesler, J., H. Harders, and M. Baeker, *Mechanical Behaviour of Engineering Materials: Metals, Ceramics, Polymers, and Composites*. 2007: Springer.
40. Olszta, M.J., X. Cheng, S.S. Jee, R. Kumar, Y.-Y. Kim, M.J. Kaufman, E.P. Douglas, and L.B. Gower, *Bone structure and formation: A new perspective*. *Materials Science and Engineering: R: Reports*, 2007. **58**(3-5): p. 77-116.
41. Hancox, N.M., *Biology of Bone*. 1972: University Press.
42. Martini, F., *Anatomy and Physiology 2007 Edition*. 2007: Rex Bookstore, Inc.
43. Kulkarni, N.V., *Clinical Anatomy: (a Problem Solving Approach)*. 2011: Jaypee Brothers Medical Pub.
44. Rice, D.P., *Craniofacial Sutures: Development, Disease and Treatment*. 2008: Karger.
45. Schlossberg, L. and G.D. Zuidema, *The Johns Hopkins Atlas of Human Functional Anatomy*. 1997: Johns Hopkins University Press.
46. Motherway, J.A., P. Verschueren, G. Van der Perre, J. Vander Sloten, and M.D. Gilchrist, *The mechanical properties of cranial bone: The effect of loading rate and cranial sampling position*. *Journal of Biomechanics*, 2009. **42**(13): p. 2129-2135.
47. Gallucci, M., S. Capoccia, and A. Catalucci, *Radiographic Atlas of Skull and Brain Anatomy*. 2007: Springer Berlin Heidelberg.
48. Orchard, G. and B. Nation, *Cell Structure & Function*. 2014: OUP Oxford.
49. Winkelstein, B.A., *Orthopaedic Biomechanics*. 2012: Taylor & Francis.

50. Peterson, J. and P.C. Dechow, *Material properties of the human cranial vault and zygoma*. The Anatomical Record Part A: Discoveries in Molecular, Cellular, and Evolutionary Biology, 2003. **274A**(1): p. 785-797.
51. Deeks, A.J. and H. Hao, *Developments in Mechanics of Structures & Materials: Proceedings of the 18th Australasian Conference on the Mechanics of Structures and Materials, Perth, Australia, 1-3 December 2004, Two Volume Set*. 2004: Taylor & Francis.
52. Wang, X., J.S. Nyman, and M. Reyes, *Fundamental Biomechanics in Bone Tissue Engineering*. 2009: Morgan & Claypool Publishers.
53. Kokubo, T., H.-M. Kim, and M. Kawashita, *Novel bioactive materials with different mechanical properties*. Biomaterials, 2003. **24**(13): p. 2161-2175.
54. Noailly, J., L. Ambrosio, K. Elizabeth Tanner, J. Planell, and D. Lacroix, *In silico evaluation of a new composite disc substitute with a L3–L5 lumbar spine finite element model*. European Spine Journal, 2012. **21**(5): p. 675-687.
55. Black, J. and G. Hastings, *Handbook of Biomaterial Properties*. 1998: Springer US.
56. Nahum, A.M. and J. Melvin, *Accidental Injury: Biomechanics and Prevention*. 2002: Springer.
57. Bronner, F., M.C. Farach-Carson, and H.I. Roach, *Bone and Development*. 2010: Springer-Verlag.
58. Davis, M.T., A.M. Loyd, H.-y.H. Shen, M.H. Mulroy, R.W. Nightingale, B.S. Myers, and C.D. Bass, *The mechanical and morphological properties of 6 year-old cranial bone*. Journal of Biomechanics, 2012. **45**(15): p. 2493-2498.
59. Demetriades, D. and E. Newton, *Color Atlas of Emergency Trauma*. 2011: Cambridge University Press.
60. Oestern, H.J., O. Trentz, and S. Uranues, *Head, Thoracic, Abdominal, and Vascular Injuries: Trauma Surgery I*. 2011: Springer.
61. Behari, J., *Biophysical Bone Behavior: Principles and Applications*. 2009: Wiley.
62. Kingsnorth, A. and D. Bowley, *Fundamentals of Surgical Practice: A Preparation Guide for the Intercollegiate MRCS Examination*. 2011: Cambridge University Press.
63. Thaller, S. and W.S. McDonald, *Facial Trauma*. 2004: Taylor & Francis.
64. Porth, C., *Essentials of Pathophysiology: Concepts of Altered Health States*. 2011: Wolters Kluwer/Lippincott Williams & Wilkins.
65. Heber-Katz, E. and D.L. Stocum, *New Perspectives in Regeneration*. 2013: Springer.
66. Atala, A. and J. Allickson, *Translational Regenerative Medicine*. 2014: Elsevier Science.
67. Victoria, G., B. Petrisor, B. Drew, and D. Dick, *Bone stimulation for fracture healing: Whats all the fuss*. Indian Journal of Orthopaedics, 2009. **43**(2): p. 117-120.
68. Albrektsson, T. and C. Johansson, *Osteoinduction, osteoconduction and osseointegration*. European Spine Journal, 2001. **10**: p. S96-S101.
69. Kolk, A., J. Handschel, W. Drescher, D. Rothamel, F. Kloss, M. Blessmann, M. Heiland, K.-D. Wolff, and R. Smeets, *Current trends and future perspectives of bone substitute materials – From space holders to innovative biomaterials*. Journal of Cranio-Maxillofacial Surgery, 2012. **40**(8): p. 706-718.
70. Ricciardi, B.F. and M.P. Bostrom, *Bone graft substitutes: Claims and credibility*. Seminars in Arthroplasty, 2013. **24**(2): p. 119-123.
71. Damien, C.J. and J.R. Parsons, *Bone graft and bone graft substitutes: A review of current technology and applications*. Journal of Applied Biomaterials, 1991. **2**(3): p. 187-208.

72. Calori, G.M., E. Mazza, M. Colombo, and C. Ripamonti, *The use of bone-graft substitutes in large bone defects: Any specific needs?* Injury, 2011. **42, Supplement 2**: p. S56-S63.
73. Blokhuis, T.J. and J.J.C. Arts, *Bioactive and osteoinductive bone graft substitutes: Definitions, facts and myths.* Injury, 2011. **42, Supplement 2**: p. S26-S29.
74. Giannoudis, P.V., H. Dinopoulos, and E. Tsiridis, *Bone substitutes: An update.* Injury, 2005. **36, Supplement 3**: p. S20-S27.
75. Boutrand, J.P., *Biocompatibility and Performance of Medical Devices.* 2012: Elsevier Science.
76. Hench, L.L., *An Introduction to Bioceramics Second Edition.* 2013: World Scientific.
77. Polak, J.M., L.L. Hench, and P. Kemp, *Future Strategies for Tissue and Organ Replacement.* 2002: Imperial College Press.
78. Hench, L. and J. Jones, *Biomaterials, Artificial Organs and Tissue Engineering.* 2005: Elsevier Science.
79. Yaszemski, M.J., *Biomaterials in Orthopedics.* 2003: Taylor & Francis.
80. Mow, V.C. and R. Huijskes, *Basic Orthopaedic Biomechanics & Mechano-biology.* 2005: Lippincott Williams & Wilkins.
81. Rodríguez-González, F.Á., *Biomaterials In Orthopaedic Surgery.* 2009: ASM International.
82. Hollinger, J.O., *An Introduction to Biomaterials, Second Edition.* 2011: Taylor & Francis.
83. Wuisman, P.I.J.M. and T.M. Smit, *Degradable Polymers for Skeletal Implants.* 2009: Nova Science Publishers.
84. Atala, A. and D.J. Mooney, *Synthetic Biodegradable Polymer Scaffolds.* 1997: Birkhäuser Boston.
85. Eglin, D. and M. Alini, *Degradable Polymeric Materials for Osteosynthesis: Tutorial.* European Cells & Materials, 2008. **16**: p. 80-91.
86. Chen, Q., C. Zhu, and G. Thouas, *Progress and challenges in biomaterials used for bone tissue engineering: bioactive glasses and elastomeric composites.* Progress in Biomaterials, 2012. **1(1)**: p. 2.
87. Sultana, N., *Biodegradable Polymer-Based Scaffolds for Bone Tissue Engineering.* 2012: Springer.
88. Dumitriu, S., *Polymeric Biomaterials, Revised and Expanded.* 2001: CRC Press.
89. Dawes, E.A., *Polyhydroxybutyrate - An Intriguing Bio-polymer.* Bioscience Reports, 1988. **8(6)**: p. 537-547.
90. Knowles, J.C., *Development of a Natural Degradable Polymer for Orthopedic Use.* Journal of Medical Engineering & Technology, 1993. **17(4)**: p. 129-137.
91. Yaszemski, M.J., D.J. Trantolo, K.U. Lewandrowski, V. Hasirci, D.E. Altobelli, and D.L. Wise, *Tissue Engineering And Novel Delivery Systems.* 2003: Taylor & Francis.
92. Sultana, N. and T.H. Khan, *In Vitro Degradation of PHBV Scaffolds and nHA/PHBV Composite Scaffolds Containing Hydroxyapatite Nanoparticles for Bone Tissue Engineering.* Journal of Nanomaterials, 2012.
93. Köse, G.T., F. Korkusuz, P. Korkusuz, N. Purali, A. Özkul, and V. Hasirci, *Bone generation on PHBV matrices: an in vitro study.* Biomaterials, 2003. **24(27)**: p. 4999-5007.
94. Van de Velde, K. and P. Kiekens, *Biopolymers: overview of several properties and consequences on their applications.* Polymer Testing, 2002. **21(4)**: p. 433-442.
95. Domb, A.J. and N. Kumar, *Biodegradable Polymers in Clinical Use and Clinical Development.* 2011: Wiley.

96. Ratner, B.D., A.S. Hoffman, F.J. Schoen, and J.E. Lemons, *Biomaterials Science: An Introduction to Materials in Medicine*. 2012: Elsevier Science.
97. Santin, M. and G.J. Phillips, *Biomimetic, Bioresponsive, and Bioactive Materials: An Introduction to Integrating Materials with Tissues*. 2012: Wiley.
98. Putlyaev, V.I. and T.V. Safronova, *A new generation of calcium phosphate biomaterials: The role of phase and chemical compositions*. *Glass and Ceramics*, 2006. **63**(3-4): p. 99-102.
99. Sakka, S., F.B. Ayed, and J. Bouaziz, *Mechanical Properties of Biomaterials Based on Calcium Phosphates and Bioinert Oxides for Applications in Biomedicine*. 2013: INTECH Open Access Publisher.
100. Ben-Nissan, B., *Advances in Calcium Phosphate Biomaterials*. 2014: Springer.
101. Bohner, M., *Resorbable biomaterials as bone graft substitutes*. *Materials Today*, 2010. **13**(1-2): p. 24-30.
102. Kokubo, T., *Bioceramics and their Clinical Applications*. 2008: Elsevier Science.
103. Boccaccini, A.R. and P.X. Ma, *Tissue Engineering Using Ceramics and Polymers*. 2014: Elsevier Science.
104. Deb, S., *Orthopaedic Bone Cements*. 2008: Elsevier Science.
105. Ambrosio, L., *Biomedical Composites*. 2009: Elsevier Science.
106. Vaishya, R., M. Chauhan, and A. Vaish, *Bone cement*. *Journal of Clinical Orthopaedics & Trauma*. **4**(4): p. 157-163.
107. Chirila, T. and D. Harkin, *Biomaterials and Regenerative Medicine in Ophthalmology*. 2009: Elsevier Science.
108. Tanner, K.E. and M.J. Dalby, *Guest Editorial*. *Proceedings of the Institution of Mechanical Engineers, Part H: Journal of Engineering in Medicine*, 2010. **224**(12): p. i-iv.
109. Jones, J. and A. Clare, *Bio-Glasses: An Introduction*. 2012: Wiley.
110. Rahaman, M.N., D.E. Day, B. Sonny Bal, Q. Fu, S.B. Jung, L.F. Bonewald, and A.P. Tomsia, *Bioactive glass in tissue engineering*. *Acta Biomaterialia*, 2011. **7**(6): p. 2355-2373.
111. Jones, J.R., *Review of bioactive glass: From Hench to hybrids*. *Acta Biomaterialia*, 2013. **9**(1): p. 4457-4486.
112. Jones, J.R., S. Lin, S. Yue, P.D. Lee, J.V. Hanna, M.E. Smith, and R.J. Newport, *Bioactive glass scaffolds for bone regeneration and their hierarchical characterisation*. *Proceedings of the Institution of Mechanical Engineers, Part H: Journal of Engineering in Medicine*, 2010. **224**(12): p. 1373-1387.
113. Hench, L.L., *New Materials and Technologies for Healthcare*. 2012: Imperial College Press.
114. Tylkowski, M. and D.S. Brauer, *Mixed alkali effects in Bioglass® 45S5*. *Journal of Non-Crystalline Solids*, 2013. **376**: p. 175-181.
115. Nicholson, J.W., *The Chemistry of Medical and Dental Materials*. 2002: Royal Society of Chemistry.
116. Carter, C.B. and G. Norton, *Ceramic Materials: Science and Engineering*. 2013: Springer.
117. Holand, W. and G.H. Beall, *Glass Ceramic Technology*. 2012: Wiley.
118. Thomas, S., K. Joseph, S.K. Malhotra, K. Goda, and S. Sreekala, *Polymer Composites, Macro- and Microcomposites*. 2012: Wiley.
119. Balasubramanian, M., *Composite Materials and Processing*. Illustrated ed. 2013: CRC Press.
120. Hull, D. and T.W. Clyne, *An Introduction to Composite Materials*. 1996: Cambridge University Press.
121. Chawla, K.K., *Composite Materials: Science and Engineering*. 2012: Springer.
122. Mallick, P.K., *Composites Engineering Handbook*. 1997: Taylor & Francis.

123. Gürdal, Z., R.T. Haftka, and P. Hajela, *Design and Optimization of Laminated Composite Materials*. 1999: Wiley.
124. Gibson, R.F., *Principles of Composite Material Mechanics, Second Edition*. 2007: CRC Press.
125. Hollaway, L., *Polymers and Polymer Composites in Construction*. 1990: T. Telford.
126. Campbell, F.C., *Structural Composite Materials*. 2010: ASM International.
127. Kim, J.K. and Y.W. Mai, *Engineered Interfaces in Fiber Reinforced Composites*. 1998: Elsevier Science.
128. Fu, S.Y., B. Lauke, and Y.W. Mai, *Science and Engineering of Short Fibre Reinforced Polymers Composites*. 2009: Woodhead Publishing.
129. Ramakrishna, S., J. Mayer, E. Wintermantel, and K.W. Leong, *Biomedical applications of polymer-composite materials: a review*. *Composites Science and Technology*, 2001. **61**(9): p. 1189-1224.
130. Rezwan, K., Q.Z. Chen, J.J. Blaker, and A.R. Boccaccini, *Biodegradable and bioactive porous polymer/inorganic composite scaffolds for bone tissue engineering*. *Biomaterials*, 2006. **27**(18): p. 3413-3431.
131. Tanner, K.E., *Bioactive composites for bone tissue engineering*. *Proceedings of the Institution of Mechanical Engineers, Part H: Journal of Engineering in Medicine*, 2010. **224**(12): p. 1359-1372.
132. Dalby, M.J., M.V. Kayser, W. Bonfield, and L. Di Silvio, *Initial attachment of osteoblasts to an optimised HAPEX™ topography*. *Biomaterials*, 2002. **23**(3): p. 681-690.
133. Tjong, S.C., *Advances in Biomedical Sciences and Engineering*. 2009: Bentham Science Publishers.
134. Rezwan, K., Q. Chen, J. Blaker, and A. Boccaccini, *Biodegradable and bioactive porous polymer/inorganic composite scaffolds for bone tissue engineering*. *Biomaterials*, 2006. **27**: p. 3413 - 3431.
135. Russias, J., E. Saiz, R.K. Nalla, K. Gryn, R.O. Ritchie, and A.P. Tomsia, *Fabrication and mechanical properties of PLA/HA composites: A study of in vitro degradation*. *Materials Science and Engineering: C*, 2006. **26**(8): p. 1289-1295.
136. Zhou, Z., Q. Yi, X. Liu, L. Liu, and Q. Liu, *In vitro degradation behaviors of Poly-L-lactide/bioactive glass composite materials in phosphate-buffered solution*. *Polymer Bulletin*, 2009. **63**(4): p. 575-586.
137. Felfel, R.M., I. Ahmed, A.J. Parsons, and C.D. Rudd, *Bioresorbable composite screws manufactured via forging process: Pull-out, shear, flexural and degradation characteristics*. *Journal of the Mechanical Behavior of Biomedical Materials*, 2013. **18**: p. 108-122.
138. Charles, L.F., E.R. Kramer, M.T. Shaw, J.R. Olson, and M. Wei, *Self-reinforced composites of hydroxyapatite-coated PLLA fibers: Fabrication and mechanical characterization*. *Journal of the Mechanical Behavior of Biomedical Materials*, 2013. **17**: p. 269-277.
139. Suzuki, S. and Y. Ikada, *Biomaterials for Surgical Operation*. 2011: Humana Press.
140. Redfern, R.M., Pulhorn, H., *Cranioplasty*. *Advances in Clinical Neuroscience and Rehabilitation*, 2007. **7**(5): p. 32-34.
141. Mukherjee, S., B. Thakur, I. Haq, S. Hettige, and A.J. Martin, *Complications of titanium cranioplasty-a retrospective analysis of 174 patients*. *Acta Neurochirurgica*, 2014. **156**(5): p. 989-998.
142. Thavarajah, D., P.D. Lacy, A. Hussien, and A. Sugar, *The minimum time for cranioplasty insertion from craniectomy is six months to reduce risk of infection- a case series of 82 patients*. *British Journal of Neurosurgery*, 2012. **26**(1): p. 78-80.

143. Harris, D.A., A.J. Fong, E.P. Buchanan, L. Monson, D. Khechoyan, and S. Lam, *History of synthetic materials in alloplastic cranioplasty*. Neurosurgical Focus, 2014. **36**(4).
144. Massera, J., I. Ahmed, L. Petit, V. Aallos, and L. Hupa, *Phosphate-based glass fiber vs. bulk glass: Change in fiber optical response to probe in vitro glass reactivity*. Materials Science and Engineering: C, 2014. **37**: p. 251-257.
145. Lee, I.-H., H.-s. Yu, N.J. Lakhkar, H.-W. Kim, M.-S. Gong, J.C. Knowles, and I.B. Wall, *Development, characterisation and biocompatibility testing of a cobalt-containing titanium phosphate-based glass for engineering of vascularized hard tissues*. Materials Science and Engineering: C, 2013. **33**(4): p. 2104-2112.
146. Haynes, W.M., *CRC Handbook of Chemistry and Physics, 93rd Edition*. 2012: Taylor & Francis.
147. Liu, J.K., O.N. Gottfried, C.D. Cole, W.R. Dougherty, and W.T. Couldwell, *Porous polyethylene implant for cranioplasty and skull base reconstruction*. Neurosurgical focus, 2004. **16**(3): p. ECP1.
148. Bronzino, J.D. and D.R. Peterson, *Tissue Engineering and Artificial Organs*. 2006: Taylor & Francis.
149. Stefani, R., G. Esposito, B. Zanotti, C. Iaccarino, M.M. Fontanella, and F. Servadei, *Use of "custom made" porous hydroxyapatite implants for cranioplasty: postoperative analysis of complications in 1549 patients*. Surgical Neurology International, 2013. **4**: p. 12.
150. Matic, D.B. and P.N. Manson, *Biomechanical analysis of hydroxyapatite cement cranioplasty*. Journal of Craniofacial Surgery, 2004. **15**(3): p. 415-422.
151. Elshahat, A., M.A. Shermak, N. Inoue, E.Y.S. Chao, and P. Manson, *The use of Novabone and Norian in cranioplasty: a comparative study*. Vol. 15. 2004. 483-9.
152. Saringer, W., I. Nöbauer-Huhmann, and E. Knosp, *Cranioplasty with Individual Carbon Fibre Reinforced Polymere (CFRP) Medical Grade Implants Based on CAD/CAM Technique*. Acta Neurochirurgica, 2002. **144**(11): p. 1193-1203.
153. Tuusa, S.M.R., M.J. Peltola, T. Tirri, M.A. Puska, M. Røyttä, H. Aho, J. Sandholm, L.V.J. Lassila, and P.K. Vallittu, *Reconstruction of critical size calvarial bone defects in rabbits with glass-fiber-reinforced composite with bioactive glass granule coating*. Journal of Biomedical Materials Research Part B: Applied Biomaterials, 2008. **84B**(2): p. 510-519.
154. Piitulainen, J., J. Posti, K.J. Aitasalo, V. Vuorinen, P. Vallittu, and W. Serlo, *Paediatric cranial defect reconstruction using bioactive fibre-reinforced composite implant: early outcomes*. Acta Neurochirurgica, 2015: p. 1-7.
155. Zhang, Y. and K.E. Tanner, *Impact behavior of hydroxyapatite reinforced polyethylene composites*. Journal of Materials Science: Materials in Medicine, 2003. **14**(1): p. 63-68.
156. Hill, C.S., A.M.V. Luoma, S.R. Wilson, and N. Kitchen, *Titanium cranioplasty and the prediction of complications*. British Journal of Neurosurgery, 2012. **26**(6): p. 832-837.
157. Shelby, J.E., *Introduction to Glass Science and Technology*. 2005: Royal Society of Chemistry.
158. Brow, R.K., *Review: the structure of simple phosphate glasses*. Journal of Non-Crystalline Solids, 2000. **263**(1-4): p. 1-28.
159. Ciceo Lucacel, R., A.O. Hulpus, V. Simon, and I. Ardelean, *Structural characterization of phosphate glasses doped with silver*. Journal of Non-Crystalline Solids, 2009. **355**(7): p. 425-429.
160. Abou Neel, E.A., D.M. Pickup, S.P. Valappil, R.J. Newport, and J.C. Knowles, *Bioactive functional materials: a perspective on phosphate-based glasses*. Journal of Materials Chemistry, 2009. **19**(6): p. 690-701.

161. Shannon, R.D., *Revised effective ionic radii and systematic studies of interatomic distances in halides and chalcogenides*. Acta Crystallographica Section A, 1976. **32**(5): p. 751-767.
162. Bunker, B.C., G.W. Arnold, and J.A. Wilder, *Phosphate glass dissolution in aqueous solutions*. Journal of Non-Crystalline Solids, 1984. **64**(3): p. 291-316.
163. Gao, H., T. Tan, and D. Wang, *Dissolution mechanism and release kinetics of phosphate controlled release glasses in aqueous medium*. Journal of Controlled Release, 2004. **96**(1): p. 29-36.
164. Delahaye, F., L. Montagne, G. Palavit, J. Claude Touray, and P. Baillif, *Acid dissolution of sodium-calcium metaphosphate glasses*. Journal of Non-Crystalline Solids, 1998. **242**(1): p. 25-32.
165. Abou Neel, E.A., T. Mizoguchi, M. Ito, M. Bitar, V. Salih, and J.C. Knowles, *In vitro bioactivity and gene expression by cells cultured on titanium dioxide doped phosphate-based glasses*. Biomaterials, 2007. **28**(19): p. 2967-2977.
166. Hench, L.L., *Bioactive materials: The potential for tissue regeneration*. Journal of Biomedical Materials Research, 1998. **41**(4): p. 511-518.
167. Kaur, G., O.P. Pandey, K. Singh, D. Homa, B. Scott, and G. Pickrell, *A review of bioactive glasses: Their structure, properties, fabrication and apatite formation*. Journal of Biomedical Materials Research Part A, 2014. **102**(1): p. 254-274.
168. Kasuga, T., *Bioactive calcium pyrophosphate glasses and glass-ceramics*. Acta Biomaterialia, 2005. **1**(1): p. 55-64.
169. Mohammadi, M.S., I. Ahmed, N. Muja, S. Almeida, C.D. Rudd, M.N. Bureau, and S.N. Nazhat, *Effect of Si and Fe doping on calcium phosphate glass fibre reinforced polycaprolactone bone analogous composites*. Acta Biomaterialia, 2012. **8**(4): p. 1616-1626.
170. Gayathri Devi, A.V., V. Rajendran, and N. Rajendran, *Structure, solubility and bioactivity in TiO₂-doped phosphate-based bioglasses and glass-ceramics*. Materials Chemistry and Physics, 2010. **124**(1): p. 312-318.
171. Karsenty, G., *Role of Cbfa1 in osteoblast differentiation and function*. Seminars in Cell & Developmental Biology, 2000. **11**(5): p. 343-346.
172. Weiss, D.S.L., R.D. Torres, S. Buchner, S. Blunk, and P. Soares, *Effect of Ti and Mg dopants on the mechanical properties, solubility, and bioactivity in vitro of a Sr-containing phosphate based glass*. Journal of Non-Crystalline Solids, 2014. **386**: p. 34-38.
173. Ahmed, I., M. Lewis, I. Olsen, and J.C. Knowles, *Phosphate glasses for tissue engineering: Part I. Processing and characterisation of a ternary-based P₂O₅-CaO-Na₂O glass system*. Biomaterials, 2004. **25**(3): p. 491-499.
174. Franks, K., I. Abrahams, and J.C. Knowles, *Development of soluble glasses for biomedical use Part I: In vitro solubility measurement*. Journal of Materials Science-Materials in Medicine, 2000. **11**(10): p. 609-614.
175. Skelton, K.L., J.V. Glenn, S.A. Clarke, G. Georgiou, S.P. Valappil, J.C. Knowles, S.N. Nazhat, and G.R. Jordan, *Effect of ternary phosphate-based glass compositions on osteoblast and osteoblast-like proliferation, differentiation and death in vitro*. Acta Biomaterialia, 2007. **3**(4): p. 563-572.
176. Uo, M., M. Mizuno, Y. Kuboki, A. Makishima, and F. Watari, *Properties and cytotoxicity of water soluble Na₂O-CaO-P₂O₅ glasses*. Biomaterials, 1998. **19**(24): p. 2277-2284.
177. Salih, V., K. Franks, M. James, G.W. Hastings, J.C. Knowles, and I. Olsen, *Development of soluble glasses for biomedical use Part II: The biological response of human osteoblast cell lines to phosphate-based soluble glasses*. Journal of Materials Science-Materials in Medicine, 2000. **11**(10): p. 615-620.

178. Bitar, M., V. Salih, V. Mudera, J.C. Knowles, and M.P. Lewis, *Soluble phosphate glasses: in vitro studies using human cells of hard and soft tissue origin*. *Biomaterials*, 2004. **25**(12): p. 2283-2292.
179. Ahmed, I., M.P. Lewis, S.N. Nazhat, and J.C. Knowles, *Quantification of Anion and Cation Release from a Range of Ternary Phosphate-based Glasses with Fixed 45 mol% P₂O₅*. *Journal of Biomaterials Applications*, 2005. **20**(1): p. 65-80.
180. Abou Neel, E.A., I. Ahmed, J.J. Blaker, A. Bismarck, A.R. Boccaccini, M.P. Lewis, S.N. Nazhat, and J.C. Knowles, *Effect of iron on the surface, degradation and ion release properties of phosphate-based glass fibres*. *Acta Biomaterialia*, 2005. **1**(5): p. 553-563.
181. Knowles, J.C., K. Franks, and I. Abrahams, *Investigation of the solubility and ion release in the glass system K₂O-Na₂O-CaO-P₂O₅*. *Biomaterials*, 2001. **22**(23): p. 3091-3096.
182. Lucacel, R.C., O. Ponta, and V. Simon, *Short-range structure and in vitro behavior of ZnO-CaO-P₂O₅ bioglasses*. *Journal of Non-Crystalline Solids*, 2012. **358**(20): p. 2803-2809.
183. Lee, I.-H., S.-H. Shin, F. Foroutan, N.J. Lakhkar, M.-S. Gong, and J.C. Knowles, *Effects of magnesium content on the physical, chemical and degradation properties in a MgO-CaO-Na₂O-P₂O₅ glass system*. *Journal of Non-Crystalline Solids*, 2013. **363**: p. 57-63.
184. Sharmin, N., M.S. Hasan, A.J. Parsons, D. Furniss, C.A. Scotchford, I. Ahmed, and C.D. Rudd, *Effect of Boron Addition on the Thermal, Degradation, and Cytocompatibility Properties of Phosphate-Based Glasses*. *Biomed Research International*, 2013.
185. Lakhkar, N.J., I.-H. Lee, H.-W. Kim, V. Salih, I.B. Wall, and J.C. Knowles, *Bone formation controlled by biologically relevant inorganic ions: Role and controlled delivery from phosphate-based glasses*. *Advanced Drug Delivery Reviews*, 2013. **65**(4): p. 405-420.
186. Hoppe, A., N.S. Güldal, and A.R. Boccaccini, *A review of the biological response to ionic dissolution products from bioactive glasses and glass-ceramics*. *Biomaterials*, 2011. **32**(11): p. 2757-2774.
187. Khor, S.F., Z.A. Talib, W.M. Daud, and H.A.A. Sidek, *Degradation study on ternary zinc magnesium phosphate glasses*. *Journal of Materials Science*, 2011. **46**(24): p. 7895-7900.
188. Franks, K., V. Salih, J.C. Knowles, and I. Olsen, *The effect of MgO on the solubility behavior and cell proliferation in a quaternary soluble phosphate based glass system*. *Journal of Materials Science-Materials in Medicine*, 2002. **13**(6): p. 549-556.
189. Salih, V., A. Patel, and J.C. Knowles, *Zinc-containing phosphate-based glasses for tissue engineering*. *Biomedical Materials*, 2007. **2**(1): p. 11-20.
190. Abou Neel, E.A., W. Chrzanowski, S.P. Valappil, L.A. O'Dell, D.M. Pickup, M.E. Smith, R.J. Newport, and J.C. Knowles, *Doping of a high calcium oxide metaphosphate glass with titanium dioxide*. *Journal of Non-Crystalline Solids*, 2009. **355**(16-17): p. 991-1000.
191. Abou Neel, E.A., W. Chrzanowski, D.M. Pickup, L.A. O'Dell, N.J. Mordan, R.J. Newport, M.E. Smith, and J.C. Knowles, *Structure and properties of strontium-doped phosphate-based glasses*. *Journal of the Royal Society Interface*, 2009. **6**(34): p. 435-446.
192. Morikawa, H., S. Lee, T. Kasuga, and D.S. Brauer, *Effects of magnesium for calcium substitution in P₂O₅-CaO-TiO₂ glasses*. *Journal of Non-Crystalline Solids*, 2013. **380**: p. 53-59.

193. Parsons, A.J., M. Evans, C.D. Rudd, and C.A. Scotchford, *Synthesis and degradation of sodium iron phosphate glasses and their in vitro cell response*. Journal of Biomedical Materials Research Part A, 2004. **71A**(2): p. 283-291.
194. Ahmed, I., C.A. Collins, M.P. Lewis, I. Olsen, and J.C. Knowles, *Processing, characterisation and biocompatibility of iron-phosphate glass fibres for tissue engineering*. Biomaterials, 2004. **25**(16): p. 3223-3232.
195. Abou Neel, E., L. O'Dell, M. Smith, and J. Knowles, *Processing, characterisation, and biocompatibility of zinc modified metaphosphate based glasses for biomedical applications*. Journal of Materials Science: Materials in Medicine, 2008. **19**(4): p. 1669-1679.
196. Marikani, A., A. Maheswaran, M. Premanathan, and L. Amalraj, *Synthesis and characterization of calcium phosphate based bioactive quaternary P_2O_5 -CaO- Na_2O - K_2O glasses*. Journal of Non-Crystalline Solids, 2008. **354**(33): p. 3929-3934.
197. Novajra, G., C. Vitale-Brovarone, J.C. Knowles, G. Maina, V. Aina, D. Ghigo, and L. Bergandi, *Effects of TiO_2 -containing phosphate glasses on solubility and in vitro biocompatibility*. Journal of Biomedical Materials Research Part A, 2011. **99A**(2): p. 295-306.
198. Valappil, S.P., J.C. Knowles, and M. Wilson, *Effect of silver-doped phosphate-based glasses on bacterial biofilm growth*. Applied and Environmental Microbiology, 2008. **74**(16): p. 5228-5230.
199. Ahmed, I., D. Ready, M. Wilson, and J.C. Knowles, *Antimicrobial effect of silver-doped phosphate-based glasses*. Journal of Biomedical Materials Research Part A, 2006. **79A**(3): p. 618-626.
200. Stockhorst, H. and R. Brückner, *Structure sensitive measurements on phosphate glass fibers*. Journal of Non-Crystalline Solids, 1986. **85**(1-2): p. 105-126.
201. Cozien-Cazuc, S., A.J. Parsons, G.S. Walker, I.A. Jones, and C.D. Rudd, *Real-time dissolution of $P_{40}Na_{20}Ca_{16}Mg_{24}$ phosphate glass fibers*. Journal of Non-Crystalline Solids, 2009. **355**(50-51): p. 2514-2521.
202. Wallenberger, F., *Commercial and Experimental Glass Fibers*, in *Fiberglass and Glass Technology*, F.T. Wallenberger and P.A. Bingham, Editors. 2010, Springer US. p. 3-90.
203. Kostikov, V.I. and V.I. Kostikov, *Fibre Science and Technology*. 1995: Springer.
204. Alekseeva, T., E.A. Abou Neel, J.C. Knowles, and R.A. Brown, *Development of Conical Soluble Phosphate Glass Fibers for Directional Tissue Growth*. Journal of Biomaterials Applications, 2012. **26**(6): p. 733-744.
205. Ahmed, I., M. Lewis, I. Olsen, and J.C. Knowles, *Phosphate glasses for tissue engineering: Part 2. Processing and characterisation of a ternary-based P_2O_5 -CaO- Na_2O glass fibre system*. Biomaterials, 2004. **25**(3): p. 501-507.
206. Patel, A. and J.C. Knowles, *Investigation of silica-iron-phosphate glasses for tissue engineering*. Journal of Materials Science: Materials in Medicine, 2006. **17**(10): p. 937-944.
207. Cozien-Cazuc, S., A.J. Parsons, G.S. Walker, I.A. Jones, and C.D. Rudd, *Effects of aqueous aging on the mechanical properties of $P_{40}Na_{20}Ca_{16}Mg_{24}$ phosphate glass fibres*. Journal of Materials Science, 2008. **43**(14): p. 4834-4839.
208. Liu, X.L., D.M. Grant, A.J. Parsons, L.T. Harper, C.D. Rudd, and I. Ahmed, *Magnesium Coated Bioresorbable Phosphate Glass Fibres: Investigation of the Interface between Fibre and Polyester Matrices*. Biomed Research International, 2013.
209. Haque, P., I. Ahmed, A. Parsons, R. Felfel, G. Walker, and C. Rudd, *Degradation properties and microstructural analysis of $40P_2O_5$ - $24MgO$ - $16CaO$ - $16Na_2O$*

- 4Fe₂O₃ phosphate glass fibres*. Journal of Non-Crystalline Solids, 2013. **375**: p. 99-109.
210. Hasan, M.S., I. Ahmed, A.J. Parsons, G.S. Walker, and C.A. Scotchford, *Material characterisation and cytocompatibility assessment of quinary phosphate glasses*. Journal of Materials Science: Materials in Medicine, 2012. **23**(10): p. 2531-2541.
211. Sharmin, N., A.J. Parsons, C.D. Rudd, and I. Ahmed, *Effect of boron oxide addition on fibre drawing, mechanical properties and dissolution behaviour of phosphate-based glass fibres with fixed 40, 45 and 50 mol% P₂O₅*. Journal of Biomaterials Applications, 2014.
212. Parsons, A.J., I. Ahmed, P. Haque, B. Fitzpatrick, M.I.K. Niazi, G.S. Walker, and C.D. Rudd, *Phosphate Glass Fibre Composites for Bone Repair*. Journal of Bionic Engineering, 2009. **6**(4): p. 318-323.
213. Knowles, J.C., *Phosphate based glasses for biomedical applications*. Journal of Materials Chemistry, 2003. **13**(10): p. 2395-2401.
214. Felfel, R.M., I. Ahmed, A.J. Parsons, G. Palmer, V. Sottile, and C.D. Rudd, *Cytocompatibility, degradation, mechanical property retention and ion release profiles for phosphate glass fibre reinforced composite rods*. Materials Science and Engineering: C, 2013. **33**(4): p. 1914-1924.
215. Ahmed, I., A.J. Parsons, G. Palmer, J.C. Knowles, G.S. Walker, and C.D. Rudd, *Weight loss, ion release and initial mechanical properties of a binary calcium phosphate glass fibre/PCL composite*. Acta Biomaterialia, 2008. **4**(5): p. 1307-1314.
216. Mohammadi, M.S., I. Ahmed, N. Muja, C.D. Rudd, M.N. Bureau, and S.N. Nazhat, *Effect of phosphate-based glass fibre surface properties on thermally produced poly(lactic acid) matrix composites*. Journal of Materials Science-Materials in Medicine, 2011. **22**(12): p. 2659-2672.
217. Brauer, D., C. Rüssel, S. Vogt, J. Weisser, and M. Schnabelrauch, *Degradable phosphate glass fiber reinforced polymer matrices: mechanical properties and cell response*. Journal of Materials Science: Materials in Medicine, 2008. **19**(1): p. 121-127.
218. Ahmed, I., P.S. Cronin, E.A. Abou Neel, A.J. Parsons, J.C. Knowles, and C.D. Rudd, *Retention of Mechanical Properties and Cytocompatibility of a Phosphate-Based Glass Fiber/Polylactic Acid Composite*. Journal of Biomedical Materials Research Part B-Applied Biomaterials, 2009. **89B**(1): p. 18-27.
219. Ahmed, I., I.A. Jones, A.J. Parsons, J. Bernard, J. Farmer, C.A. Scotchford, G.S. Walker, and C.D. Rudd, *Composites for bone repair: phosphate glass fibre reinforced PLA with varying fibre architecture*. Journal of Materials Science: Materials in Medicine, 2011. **22**(8): p. 1825-1834.
220. Haque, P., A.J. Parsons, I.A. Barker, I. Ahmed, D.J. Irvine, G.S. Walker, and C.D. Rudd, *Interfacial properties of phosphate glass fibres/PLA composites: Effect of the end functionalities of oligomeric PLA coupling agents*. Composites Science and Technology, 2010. **70**(13): p. 1854-1860.
221. Hasan, M.S., I. Ahmed, A. Parsons, G. Walker, and C. Scotchford, *Cytocompatibility and Mechanical Properties of Short Phosphate Glass Fibre Reinforced Polylactic Acid (PLA) Composites: Effect of Coupling Agent Mediated Interface*. Journal of Functional Biomaterials, 2012. **3**(4).
222. Felfel, R.M., I. Ahmed, A.J. Parsons, P. Haque, G.S. Walker, and C.D. Rudd, *Investigation of Crystallinity, Molecular Weight Change, and Mechanical Properties of PLA/PBG Bioresorbable Composites as Bone Fracture Fixation Plates*. Journal of Biomaterials Applications, 2012. **26**(7): p. 765-789.

223. Han, N., I. Ahmed, A.J. Parsons, L. Harper, C.A. Scotchford, B.E. Scammell, and C.D. Rudd, *Influence of screw holes and gamma sterilization on properties of phosphate glass fiber-reinforced composite bone plates*. Journal of Biomaterials Applications, 2013. **27**(8): p. 990-1002.
224. Hasan, M.S., I. Ahmed, A.J. Parsons, G.S. Walker, and C.A. Scotchford, *The influence of coupling agents on mechanical property retention and long-term cytocompatibility of phosphate glass fibre reinforced PLA composites*. Journal of the Mechanical Behavior of Biomedical Materials, 2013. **28**: p. 1-14.
225. Liu, X., M.S. Hasan, D.M. Grant, L.T. Harper, A.J. Parsons, G. Palmer, C.D. Rudd, and I. Ahmed, *Mechanical, degradation and cytocompatibility properties of magnesium coated phosphate glass fibre reinforced polycaprolactone composites*. Journal of Biomaterials Applications, 2014. **29**(5): p. 675-687.
226. Hasan, M.S., I. Ahmed, A.J. Parsons, C.D. Rudd, G.S. Walker, and C.A. Scotchford, *Investigating the use of coupling agents to improve the interfacial properties between a resorbable phosphate glass and polylactic acid matrix*. Journal of Biomaterials Applications, 2013. **28**(3): p. 354-366.
227. Hasan, M.S., I. Ahmed, A.J. Parsons, G.S. Walker, and C.A. Scotchford, *Cytocompatibility assessment of chemical surface treatments for phosphate glass to improve adhesion between glass and polyester*. Journal of Biomedical Materials Research Part A, 2013. **101**(11): p. 3301-3310.
228. Khan, R.A., A.J. Parsons, I.A. Jones, G.S. Walker, and C.D. Rudd, *Effectiveness of 3-Aminopropyl-Triethoxy-Silane as a Coupling Agent for Phosphate Glass Fiber-Reinforced Poly(caprolactone)-based Composites for Fracture Fixation Devices*. Journal of Thermoplastic Composite Materials, 2011. **24**(4): p. 517-534.
229. Kobayashi, H.Y.L.S., D.S. Brauer, and C. Rüssel, *Mechanical properties of a degradable phosphate glass fibre reinforced polymer composite for internal fracture fixation*. Materials Science and Engineering: C, 2010. **30**(7): p. 1003-1007.
230. Mittemeijer, E.J., *Fundamentals of Materials Science: The Microstructure–Property Relationship Using Metals as Model Systems*. 2010: Springer.
231. Smith, F., *Industrial Applications of X-Ray Diffraction*. 1999: Taylor & Francis.
232. Suryanarayana, C. and G. Norton, *X-Ray Diffraction: A Practical Approach*. 1998: Springer.
233. Guo, Z. and L. Tan, *Fundamentals and Applications of Nanomaterials*. 2009: Artech House, Incorporated.
234. Stuart, B.H., *Infrared Spectroscopy: Fundamentals and Applications*. 2004: Wiley.
235. Anderson, R.J., D.J. Bendell, P.W. Groundwater, and R.S.o. Chemistry, *Organic Spectroscopic Analysis*. 2004: Royal Society of Chemistry.
236. Colorado, U.o. *The Electromagnetic Spectrum 15 Infrared Spectroscopy: Theory*. 2002 [cited 2013 30.12.13]; Available from: <http://orgchem.colorado.edu/Spectroscopy/irtutor/IRtheory.pdf>.
237. Larkin, P., *Infrared and Raman Spectroscopy; Principles and Spectral Interpretation*. 2011: Elsevier Science.
238. Smith, B.C., *Fundamentals of Fourier Transform Infrared Spectroscopy, Second Edition*. 2011: Taylor & Francis.
239. Lewis, I.R. and H. Edwards, *Handbook of Raman Spectroscopy: From the Research Laboratory to the Process Line*. 2001: Taylor & Francis.
240. Chalmers, J.M., H.G.M. Edwards, and M.D. Hargreaves, *Infrared and Raman Spectroscopy in Forensic Science*. 2012: Wiley.
241. Ferraro, J.R., *Introductory Raman Spectroscopy*. 2003: Elsevier Science.
242. McCreery, R.L., *Raman Spectroscopy for Chemical Analysis*. 2005: Wiley.

243. Reading, M. and D.J. Hourston, *Modulated Temperature Differential Scanning Calorimetry: Theoretical and Practical Applications in Polymer Characterisation*. 2006: Springer.
244. Höhne, G., W. Hemminger, and H.J. Flammersheim, *Differential Scanning Calorimetry*. 2003: Springer.
245. Brown, E., *Introduction to Thermal Analysis: Techniques and Applications*. 2001: Springer.
246. Brown, M.E. and P.K. Gallagher, *Handbook of Thermal Analysis and Calorimetry: Recent Advances, Techniques and Applications*. 2011: Elsevier Science.
247. Haines, P.J., *Principles of Thermal Analysis and Calorimetry*. 2002: Royal Society of Chemistry.
248. Wunderlich, B., *Thermal Analysis of Polymeric Materials*. 2005: Springer.
249. Ferreira, E.B., M.L. Lima, and E.D. Zanotto, *DSC Method for Determining the Liquidus Temperature of Glass-Forming Systems*. *Journal of the American Ceramic Society*, 2010. **93**(11): p. 3757-3763.
250. Chandler, H., *Hardness Testing*. 1999: ASM International.
251. Zhou, Y., L. Yang, and Y. Huang, *Micro- and Macromechanical Properties of Materials*. 2013: Taylor & Francis.
252. Cocchi, M., C. Durante, G. Lusvardi, G. Malavasi, and L. Menabue, *Evaluation of the behaviour of fluorine-containing bioactive glasses: reactivity in a simulated body fluid solution assisted by multivariate data analysis*. *Journal of Materials Science: Materials in Medicine*, 2012. **23**(3): p. 639-648.
253. Abou Neel, E.A., W. Chrzanowski, and J.C. Knowles, *Effect of increasing titanium dioxide content on bulk and surface properties of phosphate-based glasses*. *Acta Biomaterialia*, 2008. **4**(3): p. 523-534.
254. Ahmed, I., A. Parsons, A. Jones, G. Walker, C. Scotchford, and C. Rudd, *Cytocompatibility and Effect of Increasing MgO Content in a Range of Quaternary Invert Phosphate-based Glasses*. *Journal of Biomaterials Applications*, 2010. **24**(6): p. 555-575.
255. ElBatal, H.A., E.M.A. Khalil, and Y.M. Hamdy, *In vitro behavior of bioactive phosphate glass-ceramics from the system P_2O_5 - Na_2O - CaO containing titania*. *Ceramics International*, 2009. **35**(3): p. 1195-1204.
256. ElBatal, F. and G. El-Bassyouni, *Bioactivity of Hench Bioglass and Corresponding Glass-Ceramic and the Effect of Transition Metal Oxides*. *Silicon*, 2011. **3**(4): p. 185-197.
257. Walter, G., J. Vogel, U. Hoppe, and P. Hartmann, *Structural study of magnesium polyphosphate glasses*. *Journal of Non-Crystalline Solids*, 2003. **320**(1-3): p. 210-222.
258. Karakassides, M.A., A. Saranti, and I. Koutselas, *Preparation and structural study of binary phosphate glasses with high calcium and/or magnesium content*. *Journal of Non-Crystalline Solids*, 2004. **347**(1-3): p. 69-79.
259. Dias, A.G., M.A. Lopes, A.T. Trigo Cabral, J.D. Santos, and M.H. Fernandes, *In vitro studies of calcium phosphate glass ceramics with different solubility with the use of human bone marrow cells*. *Journal of Biomedical Materials Research Part A*, 2005. **74A**(3): p. 347-355.
260. Valerio, P., M.H.R. Guimarães, M.M. Pereira, M.F. Leite, and A.M. Goes, *Primary osteoblast cell response to sol-gel derived bioactive glass foams*. *Journal of Materials Science: Materials in Medicine*, 2005. **16**(9): p. 851-856.
261. Valerio, P., M.M. Pereira, A.M. Goes, and M.F. Leite, *The effect of ionic products from bioactive glass dissolution on osteoblast proliferation and collagen production*. *Biomaterials*, 2004. **25**(15): p. 2941-2948.

262. O'Donnell, M.D., S.J. Watts, R.V. Law, and R.G. Hill, *Effect of P2O5 content in two series of soda lime phosphosilicate glasses on structure and properties – Part II: Physical properties*. Journal of Non-Crystalline Solids, 2008. **354**(30): p. 3561-3566.
263. Juhasz, J., Kapadia, A., *21432/6/3/11: Feasibility Study to Investigate the Failure Strength of Bulk Glasses for the Medical Industry*. 2011, The Welding Institute (TWI): Cambridge. p. 1-9.
264. ASTM, *C158-02 Standard Test Methods for Strength of Glass by Flexure (Determination of Modulus of Rupture)*. 2012, ASTM: ASTM International.
265. Clement, J., P. Torres, F.J. Gil, J.A. Planell, R. Terradas, and S. Martinez, *Evaluation by Vickers indentation of fracture toughness of a phosphate biodegradable glass*. Journal of Materials Science-Materials in Medicine, 1999. **10**(7): p. 437-441.
266. Nychka, J.A., D. Li, and B. Alexander, *In vitro bioactivity of 45S5 bioactive glass as a function of indentation load*. Journal of the Mechanical Behavior of Biomedical Materials, 2008. **1**(3): p. 243-251.
267. Hosmani, S.S., *Introduction to Surface Alloying of Metals*. 2014: Springer (India) Private Limited.
268. Bhushan, B., *Handbook of Micro/Nano Tribology, Second Edition*. 1998: Taylor & Francis.
269. Bourhis, E.L., *Glass: Mechanics and Technology*. 2008: Wiley.
270. Rinehart, J.D., T.D. Taylor, Y. Tian, and R.A. Latour, *Real-time dissolution measurement of sized and unsized calcium phosphate glass fibers*. Journal of Biomedical Materials Research, 1999. **48**(6): p. 833-840.
271. Kokubo, T. and H. Takadama, *How useful is SBF in predicting in vivo bone bioactivity?* Biomaterials, 2006. **27**(15): p. 2907-2915.
272. Chavan, P.N., M.M. Bahir, R.U. Mene, M.P. Mahabole, and R.S. Khairnar, *Study of nanobiomaterial hydroxyapatite in simulated body fluid: Formation and growth of apatite*. Materials Science and Engineering: B, 2010. **168**(1-3): p. 224-230.
273. Clement, J., J.M. Manero, J.A. Planell, G. Avila, and S. Martinez, *Analysis of the structural changes of a phosphate glass during its dissolution in simulated body fluid*. Journal of Materials Science-Materials in Medicine, 1999. **10**(12): p. 729-732.
274. Adams, R.L.P., *Cell Culture for Biochemists*. 1990: Elsevier Science.
275. Harrison, M.A. and I.F. Rae, *General Techniques of Cell Culture*. 1997: Cambridge University Press.
276. Hughes, D. and H. Mehmet, *Cell Proliferation and Apoptosis*. 2003: Taylor & Francis.
277. Blumenthal, R.D., *Chemosensitivity: Volume I: In Vitro Assays*. 2005: Humana Press.
278. Hayes, A.W., *Principles and Methods of Toxicology, Fifth Edition*. 2007: Taylor & Francis.
279. Hannun, Y.A. and R.M. Boustany, *Apoptosis in Neurobiology*. 1998: Taylor & Francis.
280. BSI *BS EN ISO 10993-5:2009 Biological evaluation of medical devices, Part 5: Tests for in vitro cytotoxicity* 2009.
281. Sen, K. and N.J. Ashbolt, *Environmental Microbiology: Current Technology and Water Applications*. 2011: Caister Academic Press.
282. Kimura, D., *Cell Growth Processes: New Research*. 2008: Nova Biomedical Books.

283. Oswal, V., S. Jovanvic, S.M. Zeitels, J.P. Krespi, and C. Hopper, *Principles and Practice of Lasers in Otorhinolaryngology and Head and Neck Surgery*. 2014: Kugler Publications.
284. Sahu, S.C. and D.A. Casciano, *Nanotoxicity: From In Vivo and In Vitro Models to Health Risks*. 2009: Wiley.
285. Das, S.S., P.K. Srivastava, and N.B. Singh, *Fast ion conducting phosphate glasses and glass ceramic composites: Promising materials for solid state batteries*. Journal of Non-Crystalline Solids, 2012. **358**(21): p. 2841-2846.
286. Schwarz, J., H. Ticha, L. Tichy, and R. Mertens, *Physical properties of PbO-ZnO-P₂O₅ glasses - I. Infrared and Raman spectra*. Journal of Optoelectronics and Advanced Materials, 2004. **6**(3): p. 737-746.
287. Elisa, M., B.A. Sava, R. Iordanescu, I. Feraru, C. Vasiliu, M. Calin, A. Diaconu, L.D. Ursu, L. Boroica, Z. Plaiasu, F. Nastase, C. Nastase, and A. Dumitru, *Obtaining and characterization of calcium/magnesium/iron lithium phosphate glasses*. Optoelectronics and Advanced Materials-Rapid Communications, 2010. **4**(9): p. 1301-1303.
288. Moustafa, Y.M. and K. El-Egili, *Infrared spectra of sodium phosphate glasses*. Journal of Non-Crystalline Solids, 1998. **240**(1-3): p. 144-153.
289. Kiani, A., J.V. Hanna, S.P. King, G.J. Rees, M.E. Smith, N. Roohpour, V. Salih, and J.C. Knowles, *Structural characterization and physical properties of P₂O₅-CaO-Na₂O-TiO₂ glasses by Fourier transform infrared, Raman and solid-state magic angle spinning nuclear magnetic resonance spectroscopies*. Acta Biomaterialia, 2012. **8**(1): p. 333-340.
290. Tricot, G., B. Revel, and S. Wegner, *Thermal stability of a low T_g phosphate glass investigated by DSC, XRD and solid state NMR*. Journal of Non-Crystalline Solids, 2011. **357**(14): p. 2708-2712.
291. Karabulut, M., B. Yuce, O. Bozdogan, H. Ertap, and G.M. Mammadov, *Effect of boron addition on the structure and properties of iron phosphate glasses*. Journal of Non-Crystalline Solids, 2011. **357**(5): p. 1455-1462.
292. Srivastava, A.K., Pyare, R., *Characterization of CuO substituted 45S5 Bioactive Glasses and Glass-ceramics*. International Journal of Scientific & Technology Research, 2012. **1**(2): p. 28-41.
293. Abou Neel, E.A., W. Chrzanowski, G. Georgiou, M.J. Dalby, and J.C. Knowles, *In vitro biocompatibility and mechanical performance of titanium doped high calcium oxide metaphosphate-based glasses*. Journal of tissue engineering, 2010. **2010**: p. 390127-390127.
294. Thompson, I.D. and L.L. Hench, *Mechanical properties of bioactive glasses, glass-ceramics and composites*. Proceedings of the Institution of Mechanical Engineers, Part H: Journal of Engineering in Medicine, 1998. **212**(2): p. 127-136.
295. Baikova, L.G., V.P. Pukh, Y.K. Fedorov, A.B. Sinani, L.V. Tikhonova, and M.F. Kireenko, *Mechanical properties of phosphate glasses as a function of the total bonding energy per unit volume of glass*. Glass Physics and Chemistry, 2008. **34**(2): p. 126-131.
296. Rouxel, T., *Elastic Properties and Short-to Medium-Range Order in Glasses*. Journal of the American Ceramic Society, 2007. **90**(10): p. 3019-3039.
297. Inaba, S., S. Fujino, and K. Morinaga, *Young's Modulus and Compositional Parameters of Oxide Glasses*. Journal of the American Ceramic Society, 1999. **82**(12): p. 3501-3507.
298. Crobu, M., A. Rossi, and N. Spencer, *Effect of Chain-Length and Countersurface on the Tribochemistry of Bulk Zinc Polyphosphate Glasses*. Tribology Letters, 2012. **48**(3): p. 393-406.

299. Kurkjian, C.R., *Mechanical properties of phosphate glasses*. Journal of Non-Crystalline Solids, 2000. **263–264**: p. 207-212.
300. Bourhis, E.L., *Glass: Mechanics and Technology*. 2014: Wiley.
301. Pukh, V.P., L.G. Baikova, M.F. Kireenko, L.V. Tikhonova, T.P. Kazannikova, and A.B. Sinani, *Atomic structure and strength of inorganic glasses*. Physics of the Solid State, 2005. **47(5)**: p. 876-881.
302. Clément, J., P. Torres, F.J. Gil, J.A. Planell, R. Terradas, and S. Martinez, *Evaluation by Vickers indentation of fracture toughness of a phosphate biodegradable glass*. Journal of Materials Science: Materials in Medicine, 1999. **10(7)**: p. 437-441.
303. Ashizuka, M. and R.C. Bradt, *Fracture Toughness of Metaphosphate Glasses*. Journal of the American Ceramic Society, 1982. **65(5)**: p. c70-c70.
304. Park, J. and R.S. Lakes, *Biomaterials: An Introduction*. 2007: Springer.
305. Chu, P.K. and X. Liu, *Biomaterials Fabrication and Processing Handbook*. 2008: Taylor & Francis.
306. Lee, K.Y.S., K.M.C. Chin, S. Ramesh, J. Purbolaksono, M.A. Hassan, M. Hamdi, and W.D. Teng, *Characterization of forsterite ceramics*. Journal of Ceramic Processing Research, 2013. **14(1)**: p. 131-133.
307. Salama, S.N. and H.A. El-Batal, *Microhardness of phosphate glasses*. Journal of Non-Crystalline Solids, 1994. **168(1–2)**: p. 179-185.
308. Limbach, R., B.P. Rodrigues, and L. Wondraczek, *Strain-rate sensitivity of glasses*. Journal of Non-Crystalline Solids, 2014. **404(0)**: p. 124-134.
309. Smedskjaer, M.M., M. Jensen, and Y. Yue, *Effect of thermal history and chemical composition on hardness of silicate glasses*. Journal of Non-Crystalline Solids, 2010. **356(18–19)**: p. 893-897.
310. Richerson, D., D.W. Richerson, and W.E. Lee, *Modern Ceramic Engineering: Properties, Processing, and Use in Design, Third Edition*. 2005: Taylor & Francis.
311. Pattanayak, D., B.T. Rao, and T.R.R. Mohan, *Calcium phosphate bioceramics and bioceramic composites*. Journal of Sol-Gel Science and Technology, 2011. **59(3)**: p. 432-447.
312. Venkateswara Rao, G. and H.D. Shashikala, *Structural, optical and mechanical properties of ternary CaO-CaF₂-P₂O₅ glasses*. Journal of Advanced Ceramics, 2014. **3(2)**: p. 109-116.
313. Hayden, J.S., A.J. Marker Iii, T.I. Suratwala, and J.H. Campbell, *Surface tensile layer generation during thermal annealing of phosphate glass*. Journal of Non-Crystalline Solids, 2000. **263–264**: p. 228-239.
314. Jacobson, M.Z., *Air Pollution and Global Warming: History, Science, and Solutions*. 2012: Cambridge University Press.
315. Gao, H., T. Tan, and D. Wang, *Effect of composition on the release kinetics of phosphate controlled release glasses in aqueous medium*. Journal of Controlled Release, 2004. **96(1)**: p. 21-28.
316. Navarro, M., M.-P. Ginebra, J. Clément, M. Salvador, A. Gloria, and J.A. Planell, *Physicochemical Degradation of Titania-Stabilized Soluble Phosphate Glasses for Medical Applications*. Journal of the American Ceramic Society, 2003. **86(8)**: p. 1345-1352.
317. Feih, S., A. Thraner, and H. Lilholt, *Tensile strength and fracture surface characterisation of sized and unsized glass fibers*. Journal of Materials Science, 2005. **40(7)**: p. 1615-1623.
318. BSI, *BS ISO 11567:1995 Carbon fibre - Determination of filament diameter and cross-sectional area*. 1995, BSI.
319. BSI, *BS ISO 11566:1996 Carbon fibre - Determination of the tensile properties of single-filament specimens*. 1996, BSI.

320. Derby, B., D.A. Hills, and C. Ruiz, *Materials for engineering: a fundamental design approach*. 1992: Longman Scientific & Technical.
321. Reynoso, V.C.S., K. Yukimitu, T. Nagami, C.L. Carvalho, J.C.S. Moraes, and E.B. Araujo, *Crystallization kinetics in phosphate sodium-based glass studied by DSC technique*. Journal of Physics and Chemistry of Solids, 2003. **64**(1): p. 27-30.
322. De, S. and J.R. White, *Short Fibre-Polymer Composites*. 1996: Taylor & Francis.
323. Gibson, R.F., *Principles of Composite Material Mechanics, Third Edition*. 2011: Taylor & Francis.
324. Rosato, D.V. and D.V. Rosato, *Reinforced Plastics Handbook*. 2004: Elsevier Advanced Technology.
325. Onal, L., S. Cozien-Cazuc, I.A. Jones, and C.D. Rudd, *Water absorption properties of phosphate glass fiber-reinforced poly- ϵ -caprolactone composites for craniofacial bone repair*. Journal of Applied Polymer Science, 2008. **107**(6): p. 3750-3755.
326. De Diego, M.A., N.J. Coleman, and L.L. Hench, *Tensile properties of bioactive fibers for tissue engineering applications*. Journal of Biomedical Materials Research, 2000. **53**(3): p. 199-203.
327. Lehtonen, T.J., J.U. Tuominen, and E. Hiekkänen, *Dissolution behavior of high strength bioresorbable glass fibers manufactured by continuous fiber drawing*. Journal of the Mechanical Behavior of Biomedical Materials, 2013. **20**: p. 376-386.
328. Lutisanova, G., M.T. Palou, and J. Kozankova, *Comparison of Bioactivity In Vitro of Glass and Glass Ceramic Materials During Soaking in SBF and DMEM Medium*. Ceramics-Silikaty, 2011. **55**(3): p. 199-207.
329. Rehman, I. and W. Bonfield, *Characterization of hydroxyapatite and carbonated apatite by photo acoustic FTIR spectroscopy*. Journal of Materials Science-Materials in Medicine, 1997. **8**(1): p. 1-4.
330. Combes, C. and C. Rey, *Amorphous calcium phosphates: Synthesis, properties and uses in biomaterials*. Acta Biomaterialia, 2010. **6**(9): p. 3362-3378.
331. Clupper, D.C., J.E. Gough, P.M. Embanga, I. Notingher, L.L. Hench, and M.M. Hall, *Bioactive evaluation of 45S5 bioactive glass fibres and preliminary study of human osteoblast attachment*. Journal of Materials Science-Materials in Medicine, 2004. **15**(7): p. 803-808.
332. Franks, K., I. Abrahams, G. Georgiou, and J.C. Knowles, *Investigation of thermal parameters and crystallisation in a ternary CaO-Na₂O-P₂O₅-based glass system*. Biomaterials, 2001. **22**(5): p. 497-501.
333. Grover, L.M., A.J. Wright, U. Gbureck, A. Bolarinwa, J. Song, Y. Liu, D.F. Farrar, G. Howling, J. Rose, and J.E. Barralet, *The effect of amorphous pyrophosphate on calcium phosphate cement resorption and bone generation*. Biomaterials, 2013. **34**(28): p. 6631-6637.
334. Uskoković, V. and T.A. Desai, *Phase composition control of calcium phosphate nanoparticles for tunable drug delivery kinetics and treatment of osteomyelitis. I. Preparation and drug release*. Journal of Biomedical Materials Research Part A, 2013. **101A**(5): p. 1416-1426.
335. Leeuwen, Y.M.v., K.P. Velikov, and W.K. Kegel, *Morphology of colloidal metal pyrophosphate salts*. RSC Advances, 2012. **2**(6): p. 2534-2540.
336. BSI, *BS EN ISO 14125:1998+A1:2011 Fibre-reinforced plastic composites - Determination of flexural properties*. 1998, BSI.
337. Harris, B., *Fatigue in Composites: Science and Technology of the Fatigue Response of Fibre-reinforced Plastics*. 2003: CRC Press.
338. Karbhari, V.M. and H. Strassler, *Effect of fiber architecture on flexural characteristics and fracture of fiber-reinforced dental composites*. Dental Materials, 2007. **23**(8): p. 960-968.

339. Motherway, J., P. Verschueren, G. Van der Perre, J. Vander Sloten, and M. Gilchrist, *The Mechanical Properties of Cranial Bone*, in *6th World Congress of Biomechanics (WCB 2010). August 1-6, 2010 Singapore*, C.T. Lim and J.C.H. Goh, Editors. 2010, Springer Berlin Heidelberg. p. 776-779.
340. Tjong, S.C., *Polymer Composites with Carbonaceous Nanofillers: Properties and Applications*. 2012: Wiley.
341. Khan, R.A., A.J. Parsons, I.A. Jones, G.S. Walker, and C.D. Rudd, *Preparation and Characterization of Phosphate Glass Fibers and Fabrication of Poly(ϵ -caprolactone) Matrix Resorbable Composites*. *Journal of Reinforced Plastics and Composites*, 2010. **29**(12): p. 1838-1850.
342. Pan, J., *Modelling Degradation of Bioresorbable Polymeric Medical Devices*. 2014: Elsevier Science.
343. Hannink, G. and J.J.C. Arts, *Bioresorbability, porosity and mechanical strength of bone substitutes: What is optimal for bone regeneration?* *Injury*, 2011. **42**, **Supplement 2**: p. S22-S25.
344. Peña, J., T. Corrales, I. Izquierdo-Barba, A.L. Doadrio, and M. Vallet-Regí, *Long term degradation of poly(ϵ -caprolactone) films in biologically related fluids*. *Polymer Degradation and Stability*, 2006. **91**(7): p. 1424-1432.
345. Kelter, P.B., M.D. Mosher, and A. Scott, *Chemistry: The Practical Science*. 2008: Houghton Mifflin.
346. Han, F.X. and A. Singer, *Biogeochemistry of Trace Elements in Arid Environments*. 2007: Springer.
347. Shen, L., H. Yang, J. Ying, F. Qiao, and M. Peng, *Preparation and mechanical properties of carbon fiber reinforced hydroxyapatite/polylactide biocomposites*. *Journal of Materials Science-Materials in Medicine*, 2009. **20**(11): p. 2259-2265.
348. Kolarik, L. and A. Priestley, *Modern Techniques in Water and Wastewater Treatment*. 1996: CSIRO PUBLISHING.
349. Agrawal, C.M. and K.A. Athanasiou, *Technique to control pH in vicinity of biodegrading PLA-PGA implants*. *Journal of Biomedical Materials Research*, 1997. **38**(2): p. 105-114.
350. Schiller, C. and M. Epple, *Carbonated calcium phosphates are suitable pH-stabilising fillers for biodegradable polyesters*. *Biomaterials*, 2003. **24**(12): p. 2037-2043.
351. Lc, C., *Next generation calcium phosphate-based biomaterials*. *Dental materials journal*, 2009. **28**(1): p. 1-10.
352. McKetta, J.J., *Encyclopedia of Chemical Processing and Design: Volume 6 - Calcination Equipment to Catalysis*. 1978: Taylor & Francis.
353. Andreasen, J.O., F.M. Andreasen, and L. Andersson, *Textbook and Color Atlas of Traumatic Injuries to the Teeth*. 2013: Wiley.
354. Santos, M.H., M.d. Oliveira, L.P.d.F. Souza, H.S. Mansur, and W.L. Vasconcelos, *Synthesis control and characterization of hydroxyapatite prepared by wet precipitation process*. *Materials Research*, 2004. **7**: p. 625-630.
355. Mei, H.Y. and A.W. Czarnik, *Integrated Drug Discovery Technologies*. 2002: Taylor & Francis.
356. Glencross, H., N. Ahmed, C. Smith, and Q. Wang, *Biomedical Science Practice: Experimental and Professional Skills*. 2010: OUP Oxford.
357. Danoux, C.B., D. Barbieri, H. Yuan, J.D. de Bruijn, C.A. van Blitterswijk, and P. Habibovic, *In vitro and in vivo bioactivity assessment of a polylactic acid/hydroxyapatite composite for bone regeneration*. *Biomatter*, 2014. **4**(1): p. e27664.

358. Zinck, P., E. Mäder, and J.F. Gerard, *Role of silane coupling agent and polymeric film former for tailoring glass fiber sizings from tensile strength measurements*. Journal of Materials Science, 2001. **36**(21): p. 5245-5252.
359. Friedrich, K., S. Fakirov, and Z. Zhang, *Polymer Composites: From Nano- to Macro-Scale*. 2005: Springer.
360. Bregg, R.K., *Frontal Polymer Research*. 2006: Nova Science Publishers.
361. Liang, J.-Z., *Toughening and reinforcing in rigid inorganic particulate filled poly(propylene): A review*. Journal of Applied Polymer Science, 2002. **83**(7): p. 1547-1555.
362. Kane, R.J., G.L. Converse, and R.K. Roeder, *Effects of the Reinforcement Morphology on the Fatigue Properties of Hydroxyapatite Reinforced Polymers*. Journal of the mechanical behavior of biomedical materials, 2008. **1**(3): p. 261-268.
363. Cech, V., E. Palesch, and J. Lukes, *The glass fiber-polymer matrix interface/interphase characterized by nanoscale imaging techniques*. Composites Science and Technology, 2013. **83**: p. 22-26.
364. Wang, T., L.C. Chow, S.A. Frukhtbeyn, A.H. Ting, Q. Dong, M. Yang, and J.W. Mitchell, *Improve the Strength of PLA/HA Composite Through the Use of Surface Initiated Polymerization and Phosphonic Acid Coupling Agent*. Journal of research of the National Institute of Standards and Technology, 2011. **116**(5): p. 785-796.
365. Joseph, R., W.J. McGregor, M.T. Martyn, K.E. Tanner, and P.D. Coates, *Effect of hydroxyapatite morphology/surface area on the rheology and processability of hydroxyapatite filled polyethylene composites*. Biomaterials, 2002. **23**(21): p. 4295-4302.
366. Zhang, Y. and K.E. Tanner, *Effect of filler surface morphology on the impact behaviour of hydroxyapatite reinforced high density polyethylene composites*. Journal of Materials Science: Materials in Medicine, 2008. **19**(2): p. 761-766.
367. Fu, S.-Y., X.-Q. Feng, B. Lauke, and Y.-W. Mai, *Effects of particle size, particle/matrix interface adhesion and particle loading on mechanical properties of particulate-polymer composites*. Composites Part B: Engineering, 2008. **39**(6): p. 933-961.
368. Tham, W.L., W.S. Chow, and Z.A.M. Ishak, *Simulated body fluid and water absorption effects on poly(methyl methacrylate)/hydroxyapatite denture base composites*. Express Polymer Letters, 2010. **4**(9): p. 517-528.
369. Speidel, M.O. and P.J. Uggowitzer, *Materials in Medicine*. 1998: vdf, Hochschulverlag AG an der ETH Zürich.
370. Vallittu, P., *Non-Metallic Biomaterials for Tooth Repair and Replacement*. 2012: Elsevier Science.
371. Persson, M., G.S. Lorite, H.E. Kokkonen, S.-W. Cho, P.P. Lehenkari, M. Skrifvars, and J. Tuukkanen, *Effect of bioactive extruded PLA/HA composite films on focal adhesion formation of preosteoblastic cells*. Colloids and Surfaces B: Biointerfaces, 2014. **121**: p. 409-416.
372. Partini, M. and R. Pantani, *FTIR analysis of hydrolysis in aliphatic polyesters*. Polymer Degradation and Stability, 2007. **92**(8): p. 1491-1497.

Publications

Abstracts

- R.C. Colquhoun, K.E. Tanner, Development of a bioresorbable phosphate glass fibre composite and its potential as an alternative to metallic medical devices for the repair of cranial defects, accepted for presentation, Niigata Research Forum, Niigata, Japan, January, 2013.

- R.C. Colquhoun, K.E. Tanner, Evaluation of Polyhydroxybutyrate-co-valerate as a Degradable Matrix Material, 25th European Conference on Biomaterials, Madrid, Spain, September, 2013.

- R.C. Colquhoun, K.E. Tanner, The Degradation Relationship Between Mechanical and In Vitro Testing of a Phosphate Glass Fibre Composite, 26th Annual Conference of the European Society for Biomaterials, Liverpool, UK, September, 2014.

Evaluation of polyhydroxybutyrate-co-valerate as a degradable matrix material

Ross Colquhoun¹ and K.E. Tanner¹

Biomedical Engineering Division, School of Engineering, University of Glasgow, Scotland
r.colquhoun.1@research.gla.ac.uk

INTRODUCTION

Phosphate based glass fibre (PGF) composites have advantages as potential degradable implant materials for treatment of bone defects. However the retention of mechanical properties when immersed in aqueous media remains an issue due to the breakdown of the fibre/matrix interface¹.

Polyhydroxybutyrate-co-valerate-12% (Goodfellow® PHBV-12%) presents a promising composite matrix material with beneficial properties that include its natural origin, hydrophobic/piezoelectric nature and applicability with conventional manufacturing methods². Thus PHBV-12% could allow for advantageous PGF composites with improved retention mechanisms by retarding the breakdown of the fibre/matrix interface given its increased hydrophobicity compared to polylactic acid (NatureWorks® 3001D PLA)³.

MATERIALS/METHODS

Glass composition Giltech® CorGlaes® Pure 107. PGF diameter $\varnothing \approx 20\mu\text{m}$ manufactured by gravity melt spin method were manipulated to form random continuous fibre mats.

Matrix sheets made by compressing 8g of PLA or PHBV-12% granules under 1 MPa at 190°C for 30 seconds.

Composites of 0.2 fibre volume fraction (V_f) produced by film stacking method by alternatively stacking fibre mats with matrix sheets inside a cavity mould. The mould was heated to 195°C (PLA) or 175°C (PHBV-12%) for 15 minutes at 4MPa and cooled under pressure.

Degradation properties evaluated by immersing 60 x 15 x 2mm samples stored individually within 100ml of de-ionised water. Samples subsequently weighed (wet/dry) and mechanically tested periodically across 6 weeks in accordance with BS EN ISO 14125:1998+A1:2011. Samples of non-filled polymer were used as controls.

REFERENCES

- Ahmed, I. et al., JBMR PB:AB. (2008) 89B:18-27
- Köse, G.T. et al., Biomat. (2003) 24 4999-5007
- Ramalingam, M., et al., IBTE, John Wiley & Sons. (2012)

RESULTS AND DISCUSSION

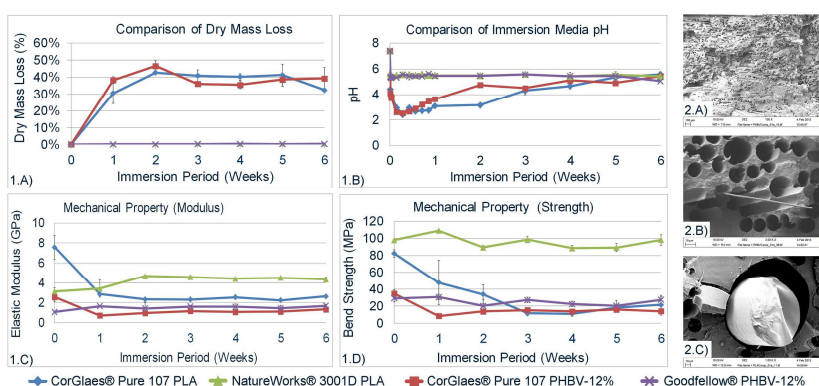


Figure 1 (Left): A) Dry mass loss comparison over immersion period B) Sample media pH comparison over immersion period
C) Retention of Elastic Modulus over immersion period D) Retention of Bend Strength over immersion period

Figure 2 (Right): A) SEM image of bulk porosity generated throughout matrix of composite
B) SEM image demonstrating successful impregnation of fibres with polymer matrix indicated by pore-to-pore separation
C) SEM image highlighting reduction in fibre cross-section through dissolution in relation to breakdown of fibre/matrix interface

- CorGlaes® Pure 107 PHBV-12% composites displayed reduced initial $[T_0]$ mechanical properties compared to a PLA matrix - attributed to the reduced elastic modulus of PHBV-12% ($E \approx 0.5$ GPa) in relation to alternative NatureWorks® 3001D PLA matrix ($E \approx 3.5$ GPa).
- Large deviations observed in initial mechanical properties $[T_0]$ due to continuous random fibre architecture used in the composites design.
- All composite samples showed a rapid mass loss over first week of immersion $[T_0 \rightarrow T_1]$ (Figure 1.A) that correlated with pH drop in immersion media (Figure 1.B) and reduction in mechanical properties (Figure 1. C/D) below those of the control samples. SEM analysis confirmed fibre dissolution over immersion period and generation of porous matrix throughout composite (Figure 2).
- Rate of reduction in bend strength appeared reduced in PLA composites reaching plateau after three weeks of immersion $[T_0 \rightarrow T_3]$ compared to first week of immersion $[T_0 \rightarrow T_1]$ with PHBV-12% matrix composites.
- Minimal discrepancy observed in rates of reduction of elastic modulus between PHBV-12% and PLA composites - 64% and 73% reduction in modulus (E) over $T_0 \rightarrow T_1$ for PLA and PHBV-12% respectively.
- Influence of CorGlaes® Pure 107 fibre dissolution, formation of phosphoric acid (H_3PO_4) and resulting auto-catalysis effect attributed to observed rapid mass loss and sharp drop in pH (related to glass composition).

CONCLUSIONS

- PHBV-12% offers a potential alternative candidate matrix material for PGF composites however mechanical testing indicates that current PGF-PHBV-12% composites would not be suitable for load bearing applications.
- Increased hydrophobicity of PHBV-12% matrix failed to improve retention of composite mechanical proper-

ACKNOWLEDGEMENTS

The authors would like to thank Giltech® for their collaboration and EPSRC in providing DTA financial support.



INTRODUCTION

Phosphate glass fibres (PGF) have potential as bio-active reinforcement agent in degradable composites for bone tissue regenerative applications such as fracture fixation pins and plates. A key factor in the success of these materials is the gradual transfer of mechanical loading from the implant to the native bone tissue during fracture healing (8-12 weeks) and is dependant on the PGF dissolution rate (D_r)^[1].

Ultraphosphate glasses (>50 mol% P_2O_5) are a compositional group highly suitable for fibre formation but are susceptible to autocatalysis effects that accelerate PGF D_r due to their acidic dissolution by-products (H_3PO_4). This can alter the mechanical property retention of a PGF-composites, its bioactivity and cytotoxicity due to the associated reductions in pH and accelerated release of ions from PGF^[2].

However it has been observed that the D_r of PGF can be influenced by the ionic strength of the soaking media due an ionic buffering effect. Thus given the interdisciplinary nature of characterising these materials it is important to consider how their degradation profile's translate across the different media employed during testing. The degradation properties of a PGF composition and PGF-PLA composite were assessed during a mechanical degradation procedure as well as conditions replicating those experienced *in vitro*.

MATERIALS AND METHODS

PGF: Giltech® CorGlaes® Pure 107 PGF ($\varnothing \approx 20\mu m$) manufactured by melt spin method. Fibres were manipulated to form random continuous fibre mats

PGF-PLA Composites: 0.2 fibre volume fraction (V_f) produced by compression molding (200°C, 4MPa, 15 minutes) using a film stacking method with Nature-Works® 3001D PLA matrix.

PGF Dissolution: 20mm fibres degraded over 24 hours in static distilled water (D.water), simulated body fluid (SBF), phosphate buffered saline (PBS) and protein free, acellular Dulbecco's Modified Eagles Medium (DMEM) at 15 cm²/ml. Initial media ionic strength and mass loss were recorded and D_r calculated.

Composite Degradation: 60 x 15 x 2mm samples were statically immersed in distilled water and DMEM at 37°C (0.21 cm²/ml). Sample weight (wet/dry) as well as media pH measured across 6 week (T₀-T₆) incubation period. Media was change every 3-4 days. Samples were tested by a three point bend technique following BS EN ISO 14125:1998+A1:2011.

REFERENCES

- Jones, J. and Clare, A. () Bio-Glasses: An Introduction (2012) Wiley&Sons
- Cozien-Cazuc, S. et al. J. Non-Crystalline Solids (2009) 355 2514-2521
- Satyavratra, S. et al. Acta Biomaterialia (2013) 9 8037-8045

RESULTS AND DISCUSSION

PGF DISSOLUTION

- All PGF D_r were greater than those measured for annealed bulk disks ($4 \times 10^{-3} \text{ mg cm}^{-2}/\text{hour}$) due to high surface area:volume ratios (SA:V) with fibres and autocatalysis effects (Figure 1. - 2.).
- Decreased D_r was observed with increasing ionic conductivity of different immersion media (Figure 2.).
- DMEM contradicted the trend - showing significantly higher pH buffering and reduced D_r , compared to the ionic conductivity of distilled water, PBS and SBF.
- Observed results were attributed to solution saturation with the least soluble ion relevant to the PGF composition. DMEM showed the greatest saturation rates.
- However no significant difference in initial ionic concentrations between DMEM and SBF (except for (HCO_3^-) ion) to account for solution saturation theory of DMEM (Table 1.)

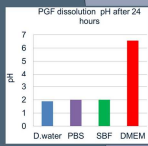


FIGURE 1. Media pH after 24 hours of H₃P₄ dissolution

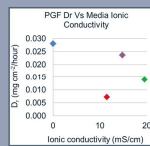


FIGURE 2. PGF Dr with different medias of ionic strength.

TABLE 1. Ionic concentrations (mM/l) of DMEM and SBF media

| ION | DMEM | SBF |
|--------------------------------|--------|-------|
| Na ⁺ | 154.56 | 141.8 |
| K ⁺ | 5.37 | 5.0 |
| Ca ²⁺ | 1.82 | 2.5 |
| Mg ²⁺ | 0.8 | 1.5 |
| HCO ₃ ⁻ | 44.0 | 4.2 |
| Cl ⁻ | 120.5 | 148.0 |
| HPO ₄ ²⁻ | 1.0 | 1.0 |
| SO ₄ ²⁻ | 0.8 | 0.5 |

PGF-PLA COMPOSITE DEGRADATION

- Rapid decreases in composite dry weight and flexural modulus were observed — attributed to PGF dissolution over first week of immersion (T₀-T₁) despite significant differences between media pH (Figure 3. A/B/C)
- PGF dissolution confirmed by SEM analysis (Figure.5 A) with the formation of a porous PLA matrix.
- Rapid dissolution attributed to high SA:V ratio at the fibre-matrix interface that superseded potential buffering effect of DMEM media as observed in fibres.
- Surface precipitate formed over the surface of DMEM degraded composite and within vacated fibre pores of degraded composite (Figure. 5 B-6)
- FTIR (Figure. 3.D) and XRD data (not shown) indicates the formation of possible amorphous calcium phosphate (ACP) [Ca₃(PO₄)₂·3H₂O] due to saturation of DMEM with Ca²⁺ and PO₄³⁻ ions from glass dissolution^[3].
- Consumption of ions from solution to form ACP precipitate may have aided the rapid dissolution by preventing complete solution saturation and thus retardation of PGF dissolution rate.

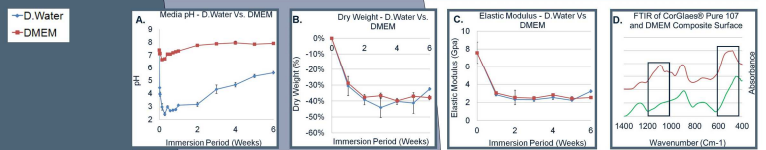


FIGURE 3: Composite degradation D.Water Vs. DMEM A) Degradation media pH over 6 week period B) Dry weight over 6 week degradation period C) Elastic modulus over 6 week immersion period D) FTIR of PGF and DMEM degraded composite precipitate

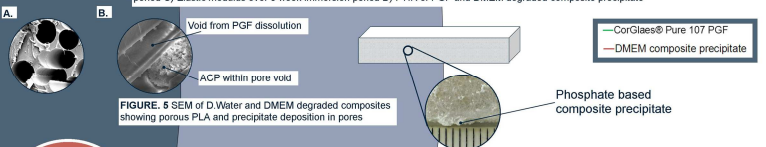


FIGURE 5 SEM of D.Water and DMEM degraded composites showing porous PLA and precipitate deposition in pores

FIGURE 6 Surface deposition on DMEM degraded composite

CONCLUSIONS

- PGF D_r data will vary across testing media and thus different dissolution behaviour can be expected between mechanical degradation and during *in vitro* cell culture (i.e. ion release and weight loss).
- Evidence that better representation of *in vivo* degradation is attained when degrading PGF in DMEM media.
- Equal rate of mechanical property depreciation and mass loss for PGF-PLA composites in D.water and DMEM signal that mechanical data of PGF composites is reflective of *in vitro* dissolution behaviour.
- Presence of osteoinductive ACP advantageous for bone regenerative applications^[3]

ACKNOWLEDGEMENTS

The authors would like to thank Giltech® for their collaboration and EPSRC in providing DTA financial support .

